UNIVERSITY OF NEWCASTLE UPON TYNE

DEPARTMENT OF MINING ENGINEERING

THE LONG TERM STABILITY OF ROOM AND PILLAR WORKINGS IN A GYPSUM MINE

A thesis submitted for the degree of
Doctor of Philosophy in the Faculty of Engineering.

by

MEHMET DOKTAN, Dip. Eng. (HACETTEPE UNIV.)

SEPTEMBER 1983

PAGE
NUMBERS
CUT OFF
IN
ORIGINAL

ACKNOWLEDGEMENTS

I would like to express my deepest gratitude to my supervisor, Andrew Szeki, for providing the opportunity to conduct this research, for his constant aid, encouragement and interest in the welfare of myself and my family during the research and production of this thesis.

Sincere thanks are due also to Tom Shepherdson, John Moore, Bill Clasper, Colin Dixon, Lyndsey Moore, Alex Blyth and Mel Paisley, for their technical expertise offered to me and for photographic evidence.

I am grateful also for the assistance provided by the management and men of Sherburn-in-Elmet Mine and to Parvis Mottahed, previous rock mechanics engineer.

Special thanks to Chris Woodford for his prompt attention to problems encountered during the computer modelling studies.

I am most appreciative of all the helping hands, and the entertainment of my colleagues, particularly Nick Taggart, Ömer Aydan, Necdet Turk, Happy Sinyangwe, Enver Erkiliç and Alparslan Ersen.

I am grateful to TKI (The Turkish Coal Mining Engerprises) and management for financial backing.

Particular thanks to Mrs. Edna Gannie for her considerable patience and expertise in typing the thesis.

Last, but not least, loving thanks to my wife, Seher Doktan, for her endurance, participation and encouragement throughout the project.

* * *

CONTENTS

* * *

ABSTRACT

The factors influencing the long term stability of mine workings at Sherburn-in-Elmet have been isolated and studied through laboratory experimentation and theoretical studies.

A series of physical models were constructed and tested in order to appreciate the behaviour of the strata overlying the gypsum deposit in the event ofa single or multiple gypsum roof beam failure.

The effect of water on the long term stability of gypsum pillars was investigated through long term creep testing of gypsum specimens submerged in mine water.

The time-dependent deformation of submerged gypsum was appraised mathematically and an empirical equation was developed for the description of creep behaviour.

A procedure for the prediction of failure time of submerged gypsum specimens under a constant load was developed and graphical and computerised versions of solutions are presented.

The influence of the satinspar bands on pillar degradation was investigated through servo-controlled testing of simulated pillars.

A possible roof structure, a linear arch, was modelled photoelastically and the presence of tensile stresses in the structural elements was proved.

Finite element modelling studies were carried out to demonstrate separately the change in the state of stress around the workings due to a roof beam failure and in the pillars due to the presence of satinspar bands.

* * *

LIST OF FIGURES

SECTION FOUR

SECTION FIVE

SECTION EIGHT

* * *

LIST OF TABLES

* * *

1. INTRODUCTION TO RESEARCH

1.1 Introduction

In mining, routine or standard practice to solve problems, especially in rock mechanics, does not exist, except on a very limited scale. The extremely variable nature of rocks and particular circumstances in mining application usually necessitates special attention and also long term research for the solution of problems.

Only during the last two decades has it been recognised that the science of rock mechanics is a valuable tool to be used rationally and as an alternative to years of underground experience during which, undoubtedly, a considerable amount of practical knowledge was accumulated and utilised to solve underground problems successfully.

Because of a general increase in mining depths of working low grade deposits and the need to work problematic horizons for which often little or no previous mining experience is available, more and more resources have been channelled towards the rock mechanics branch of mining engineering in the hope of finding solutions to the problems encountered.

A substantial amount of time and effort have already been allocated to the understanding of the mechanical behaviour of laboratory size samples of rocks and, no doubt, extremely valuable information has been acquired in this field.

The use of physical and idealised models has certainly increased the usefulness of the science of rock mechanics which for some time remained locked in itself by using analytical techniques which had little significance to people directly involved in the operation of rock excavations.

In-situ experimentations have been implemented on the full-scale underground structures in order to correlate the laboratory findings and to monitor the actual behaviour of rock structures. This has become increasingly popular and valuable in the understanding of the true behaviour of rock structures.

A stage has now been reached where information concerned with the behaviour of rock structures in the distant future - say hundreds of years after the completion of mining - is required by the mining industry. An increase in urban development, together with the probability of expansion of property and population above the exhausted mining areas, has provided further momentum to the research in this aspect.

It is this requirement which forms the basis of the present investigations discussed in this thesis. This research is part of a long term investigation by the Department of Mining Engineering of the University of Newcastle upon Tyne into the rock mechanics aspects of a number of gypsum mines owned by British Gypsum Limited. This particular study is confined specifically to one mine at Sherburn-in-Elmet in Yorkshire.

1.2 Geological features of the area

The Sherburn Mine in Elmet is situated in the extensive post-glacial plains which cover a considerable area of the East Riding of Yorkshire. These plains extend inland to a distance of 24 Km from the coast and form an extremely prosperous farming area on the surface.

The gypsum deposits mined at Sherburn date from Permian times and are considered to have been associated with the western edges of the ancient Zechstein Sea, which is also associated with the formation of the extensive evaporite deposits in North-East Yorkshire.

Gypsum is an evaporite which is deposited in saline water isolated from through flow. Two possible mechanisms are proposed for the formation of the thick evaporite beds:

(1) Formation in a Sabkha environment.

(2) Evaporation of brine pools.

The formation in a Sabkha environment is a capillary effect in which sea water lost due to high surface evaporation is replaced by saline water by a 'sponge-like' action. The salts deposited by this process form Algal Mats at tidal horizons (Blyth 1960).

Evaporites formed by the second method are precipitated when the concentration of salts dissolved in seawater is 50% of their saturation level. Since there is no outlet to the isolated water, as the water evaporates, salts commence to form in the reverse order of their solubilities. The gypsum is the first salt to be deposited when

37% of the water has evaporated, followed by anhydrite ($CaSO_4$). Climatic conditions (ambient temperature, humidity, etc.) are important factors in the formation of evaporites such as gypsum.

1.3 Petrology of Gypsum

Gypsum is hydrated calcium sulphate ($CaSO_4 2H_2O$) and has a monocline structure. It is usually found in laminated, granular or compact masses. A fibrous form is known as satinspar. The colour is white or sometimes grey, yellowish or red, and the lustre of the massive varieties is described as generally glistening, but sometimes dull and earthy, whilst the fibrous kinds appear silky. Gypsum is clearly transparent to translucent and even opaque from the admixture with impurities.

1.4 Gypsum Deposits at Sherburn

The gypsum at Sherburn is quite pure and varies in thickness from 5 to 7 metres. The bed sub-outcrops to the West of the workings. There are two separate working sections of the mine. The North district is the more recent development. The gypsum in the South is extremely pure and uniform but the North tends to have an impure rock. Certain small monoclines are associated with the workings in these blocks which can be either diagenetic or post-depositional in nature. The gypsum tends to peter out into anhydrite towards the South and East of the lease area.

The seam is cut by a number of discontinuities which can be filled with marl or recrystallised gypsum. Anhydrite is present in

varying quantities at the base of the seam. Bands of gypsum variants, crystalline, selenite and fibrous satinspar are frequently found in the strata. The gypsum bed is sandwiched between two marl seams, each approximately 13 metres thick. These beds are termed 'Upper Permian Marl'.

Boreholes have indicated the presence of a pressurised aquifer beneath the seam.

The seam lies 10.5 metres above the Upper Magnesian Limestone with the intervening strata consisting of red mudstone with grey shales and gypsum.

A soft mudstone exists above the gypsum seam (34.5-25.5 metres below the surface). This material has a very low permeability and is rather soft and well-jointed. As the depth increases from 35.5 metres to 36 metres, the mudstone increases in sand content until, at 36 metres depth, it becomes a sandstone which is rather porous. This is underlain by a relatively thick bed of satinspar, erosion of which could lead to water ingress.

Above the soft mudstone, the 13.5 metres of strata has been named the Upper Permian Marl, which is a very mixed strata of muddy fine-grained sandstones, pure mudstone and silty mudstone with gradations between. In general, these mudstone beds would not permit the passage of water vertically.

Two water bearing sand deposits are present above the Upper Permian Marl, the upper one 1 metre in thickness and at a depth of

approximately 8 metres and the lower one, 3 metres in thickness, is approximately at a depth of 19.5 metres. Any disturbance of these beds of sand could present a considerable problem to the mine, as they become fluid when disturbed.

The upper 23 metres of post-glacial strata at Sherburn have been termed 'lake deposits' which consist mainly of varve clays and fine silts and sands. The varves, however, become more silty with depth until an area of almost pure laminated silt is found at a depth of 21 metres. Due to the presence of large amounts of clay in the deposits, they are almost impervious to the vertical movement of water.

A detailed borehole log is given in Figure 2.1

1.5 Mining Method

Because of the problems associated with the petrological nature of the material overlying the gypsum seam and the presence of two water bearing sand beds in the overlying strata, the initial mining method chosen was bord and pillar mining, wholly within the seam leaving a protective roof beam of gypsum to preclude disturbance of the weak and water bearing sands.

On this basis, the mining layout was designed to provide support for an indefinite period for the area, leaving 1.8 metres of gypsum as the immediate roof with pillar sizes of 7.6 metres, roadway width of 4.67 metres and a mining height of 3.05 metres. Approximately 0.6 metres of gypsum was also left in the floor to minimise water flow from the underlying aquifer and provide a good transport roadway surface.

Based on the initially available data and the extremely variable nature of the rock material, the preliminary design was implemented with a large safety factor of 3 or 4. As the mining progressed the behaviour of mine design became better known and with the application of various rock mechanics techniques, the optimum mining dimensions and hence maximum exploitation of the deposits within the rulings of the governing institutions were achieved.

Extensive laboratory and in-situ experimentation programmes undertaken by the Department of Mining Engineering warranted a modification to the mining dimensions at Sherburn. These alterations included a reduction in the pillar base area to 5 metres square with increase in extraction height to 4 metres, where continued maintenance of the roof beam thickness was permitted. This configuration of pillars retained the width to height ratio of the pillar such that the important confined central core still existed. With a roadway width of 4 metres, areal extraction has increased from 61% to 69%, while the volumetric extraction ratio has increased from 61% to 84.3%.

The gypsum deposit has been exploited by blocking out large panels by a five advancing roadway system along the periphery of the block to prove the ground. It was envisaged that the panels would be mined later on a broad-panel configuration.

The gypsum has been excavated by a conventional drill and blast cyclic technique, using short distance dumping vehicles and a conveyor system. Egress is by inclined drift and ventilation shaft.

1.6 Research Objectives

As previously mentioned, the main objective of the present research is to provide information as to the long term stability of the mine workings at Sherburn. For this reason, research has developed from in-situ observations to various forms of laboratory testing and theoretical studies.

The convergence measurements at Sherburn Mine have been recorded by an employee of the mine. Assessment of the data received revealed a rather inconsistent roof behaviour; sometimes unbelievable upward movement of the roof beam! Therefore, most of the data were considered to be erroneous and discounted. Some selected convergence data taken over the years have been presented in Section Seven.

Convergence measurements in roadways at some sections of the mine have been reported by earlier investigators. In the light of high convergence rates it was suggested that part of the roof may fail in the distant future after mining has been completed. Failure of the immediate layer of gypsum in the roof of roadways may result in two different conditions.

(1) If roof failure occurs while the mine is still in production, water ingress could create adverse conditions or, in the worst case, the flooding of the mine.

(2) Should failure occur after the mine has been abandoned and the workings are flooded, then the broken rock

would settle by gravitation, fill in the open spaces, and the void might migrate towards the surface.

The presence of two water bearing sands with a high potential of flow rate and local variations in the competence of overlying strata above the mining horizon make it extremely difficult to estimate the likely consequences of such an event on the surface. The peculiar characteristics of the Upper Permian Marl in contact with water complicates the problem further. To provide a realistic answer to the problem, physical scale modelling was considered appropriate and this is discussed fully in Sections Two and Three.

After completion of mining the continuous pumping of water will cease and the workings will be allowed to flood. Flooding of the mine workings will certainly affect the stability of pillars which have been considered extremely stable in dry conditions. On this basis the effect of water on the short- and long-term strength of various gypsum beds has been investigated and will be discussed in Sections Four and Five.

In order to use experimental results for prediction within or beyond the limits covered by the experimental programme, it is essential to describe the testing results in mathematical form correctly. Two new equations have been developed and their uses have been illustrated. By use of one of the equations it is possible to predict the time of a pending failure of a rock structure under a constant load. Only three readings of convergence or deformation are necessary in order to obtain a rapid, fairly accurate prediction. Graphical

arithmetical, computerised methods of prediction process are described and demonstrated in Section Five of this thesis.

One of the factors affecting pillar stability at Sherburn is the presence of soft fibrous satinspar bands at different horizons of the pillar. The mechanical properties of satinspar and its effect on the deformational and strength characteristics of laboratory size gypsum samples have been studied at some length in Section Six.

Investigations into the roof stability at Sherburn Mine have been reviewed and one possible form of roof structure; that is, the linear arch; has been photoelastically modelled in order to obtain an idea of the stress distribution and to establish a relationship between the governing parameters. Section Eight has been allocated to this topic.

Finite element analysis has been employed in numerical modelling studies in Section Nine. The studies have been conducted in order to provide theoretical support to the experimental programmes discussed in Sections Two, Three and Six.

* * *

2. INVESTIGATION OF ROOF FAILURE BY MODELLING

2.1 Introduction

In mining, structural theories are often based upon simplified hypothesis because of the complex nature of rocks and the difficulties experienced in dealing with them. The best way of solving the problems associated with rock materials is to conduct investigations on the actual structures. However this is not always possible because of the high costs involved. The most commonly employed alternative is that of modelling the actual structure as accurately as possible.

Modelling techniques can be examined broadly under three headings:

(1) Mathematical Modelling;

(2) Photoelastic Modelling; and

(3) Physical Scale Modelling.

The scope of mathematical methods of the theory of elasticity is limited to relatively simple boundary conditions. The photoelastic modelling technique has some advantages in relation to the mathematical modelling technique. Interpretation of photoelastic analysis is based also on the perfect elasticity of the materials used. In these circumstances, physical scale modelling gives usually more realistic results about the behaviour of the rock structures.

The applicability of physical scale modelling depends entirely upon the similitude achieved in material parameters for the model with respect to the prototype. This technique has been widely used in technology with success (Hobbs 1966, 1968, 1970; Moss 1973; Singh 1978;

Mair 1980; Yenge 1981; Güloglu 1982; Smith 1963; Lawrence 1973; and Lajtai et al. 1975).

2.2 Condition of the mine workings at Sherburn

Despite the shallowness of the mine workings at Sherburn, peculiar geological and geographical circumstances in the area combine to give a rather special situation at the Sherburn Mine.

The surface land in Sherburn is a prosperous farming area and is drained by a complex canal system. The rivers in the area, the Ouse and the Wharf, are tidal and the level of the rivers can be higher at high tides than the land, which is only a few metres above sea level. Any substantial subsidence on the surface can cause the reversal of the flow of the distribution system which, in turn, can be extremely detrimental to the area from an environmental point of view. Bearing these environmental considerations in mind, and in order to prevent land subsidence, the Mines Inspectorate, the Local Planning Authority and the Mining Company imposed tight restrictions on the mining dimensions and methods.

The stability of mine workings has been complicated by many factors mostly related to local geology. These factors can be broadly examined in four categories:

(1) The complex nature of the overlying strata;

(2) The blocky character of the gypsum seam;

(3) An increase in the span of openings; and

(4) The presence of water.

2.2.1 The complex nature of the overlying strata

The gypsum seam at Sherburn is overlain by a number of incompetent sedimentary layers. Most of these layers vary in their thickness in different zones. A detailed log of an early borehole (Figure 2.1) demonstrates the critical geological succession.

2.2.1.1 Upper Permian Marl

The gypsum deposit is sandwiched between two marl layers which are termed Upper Permian Marl. Each marl layer is approximately 0.3m thick, and consists of muddy fine sandstone, sandy and silty mudstone and marl, with gradations between.

The geologists' report of this marl seam overlying the gypsum indicate that the vertical permeability of this layer is low, although well developed jointing in the marl is recorded in places.

However, at certain places in the mine, seepage of reddish marly water through the cracks in the roof beam was observed by previous investigators and by the author. It is obvious that the erosion of a satinspar bed overlying the fine mudstone beds has led to a channel for the passage of water from overlying sand beds.

Marl behaves very peculiarly when it comes into contact with water. Due to the presence of clay minerals

(e.g. montmorillanite-type minerals), it would swell and disintegrate almost immediately on immersion in water. This will be discussed later in this Section.

The importance of the Upper Permian Marl, which essentially acts as a barrier between the upper sand beds and the gypsum beam is dictated by the fact that if water finds access to this layer, it loses its load-carrying capacity and, in addition, it exerts extra pressure on the gypsum beam. Thus this adds another component of deflection to the total roof deflection.

2.2.1.2 Quick Sands

The Upper Permian Marl is overlain up to the surface by the strata, called 'glacial deposits'. Due to its natural characteristics, this succession is rather loose and combines to make the surface soil.

The importance of this strata from the stability point of view is enhanced by the fact that two water-bearing sands are deposited in this section. The upper sand bed is about 1 metre in thickness and approximately 8 metres below the surface. The lower one is 3 metres thick and is about 23 metres below the surface. These beds consolidate towards the eastern side of the mine to form the Bunter Sandstone, but remain water bearing. The flow rate of these beds are considered to be high and reports of flow of the Upper Sand bed into exploratory boreholes have been recorded.

Should a breakthrough occur from the workings reaching these beds, the sand beds may flow down into the workings affecting large areas on the surface.

2.2.2 The Blocky nature of the gypsum seam

The gypsum seam at Sherburn is intersected by a series of well orientated fractures. There are also planes of weakness which are filled with marl or recrystallised satinspar in association with marl. These 'filled-in' planes of discontinuity are observed in the mine generally in all districts, but their presence is more evident near the zones which are tectonically disturbed.

Due to the nature of the overlying strata, as previously discussed, these planes of weakness can act as channels for the passage of water into the workings. Inspection of the cores has indicated that the Upper Permian Marl consists of finely laminated beds and the intersection of these laminations by vertical discontinuities facilitates the ingress of water into the horizons below (Mottahed 1974). Obviously, the swelling properties of these strata, which depends largely upon the amount of clayey material present, may inhibit the passage of water to a certain degree.

A sample joint survey carried out by Mottahed (1974) revealed that a certain orientation of joint-planes exists in the mine. Three distinct joint sets are orientated in the following directions:

1st Set : Strike NW-SE trend NE-SW

2nd Set : Strike NE-SW trend NW-SE

3rd Set : Strike $N10^{o}$-$10^{o}W$ trend NE-SW

It was reported that the third set of joints particularly were infilled mainly by red marl washed down from above, satinspar, selenite and a grey clay. The inclination of the joints was generally sub-vertical (75° or greater) and the direction of the perpendicular joint sets was 45° to the mine layout. The frequency of joint was variable from 7.76 joints per 30 metres to 3 joints per 30 metres (Haque 1974). The total number of open joints were found to vary from 0 to 21 on the sections considered. The roof could, therefore, be considered as a series of gypsum blocks.

In fact, in-situ convergence and stress measurements proved conclusively that the roof was not acting as a continuous-clamped beam on elastic supports, but was acting as a linear-arch or voussoir beams. This subject will be discussed more fully in Section Seven of this thesis. For this reason, it will suffice to quote here that if the roof is acting as a linear arch, substantial roof deflections which may be as much as 30 to 40 times the maximum for a solid beam (Seymour 1968) can be observed.

2.2.3 Increase in the span of openings

With the development of the mine it became clear that the gypsum seam was not homogeneous and continuous rock, but there was a marked vertical variation in the rock material. This variation gives rise to a laminated effect to the gypsum. A large number of joint planes in the seam quite often result in the formation of blocks of gypsum of varying sizes which are completely free from the rest of the seam material.

The existence of satinspar bands, varying in thickness at different sections of the pillars, also contribute to the gradual deterioration of pillar corners. Due to the soft and fibrous nature of the material, the pillars containing substantial amounts of satinspar can be expected to exhibit larger deformations than those which contain less satinspar. Perhaps a more important consideration is that, as the satinspar bands are squeezed out, radial and tangential tensile stresses are set up in the surrounding gypsum material. Hence these stresses may enhance the speed of deterioration of pillar corners.

As a consequence of loosening of gypsum blocks at the periphery of the pillars, the span of unsupported roof beam effectively increases. In the long run, this process adds another component to the total roof deflection in the mine.

2.2.4 The presence of water

It was reported by Mottahed (1974) that the inclined roof boreholes drilled at regular intervals in the headings, in order to ensure that a minimum 1.83m thick gypsum was left between the roof of the workings and the overlying marl, often produced water of varying quantities. These holes were subsequently plugged and the plugs were inserted within the seam boundary. Whilst these plugs prevent the water from entering the workings through the boreholes, this will not restrict the passage of water to the seam itself, through horizontal planes and vertical cracks present in the seam.

More precise appreciation of the hydrogeological situation at Sherburn may be gained through an experience: The drivage of the roadway 38 South in a geologically disturbed zone resulted in the ingress of large quantities of water in excess of 275-450 lt/min. into the mine workings. The drivage of the roadway was abandoned and the flow of water was restricted by the erection of a 6-metre thick dam across the roadway. The inflow of a large quantity of water suggests that the water from the two sand beds finds access to the working zone through the channel created by a multiplicity of vertical fractures above the dam.

In addition, the boreholes drilled to the underlying material have indicated the presence of an aquifer approximately 50 metres below the seam and with an artesian head of water of nearly 60 metres. Although the gypsum left on the floor and the Lower Permian Marl underneath the gypsum floor would prevent water ingress from the aquifer, highly fractured zones of gypsum floor would pose similar problems.

Hydrogeological problems of a parallel nature have been encountered during the investigations carried out by the National Coal Board for the development of the Selby Coal Field, very close to the Sherburn location (Forrest 1978; Aydan 1982). A total inflow of water to an unlined shaft of the order of 13500 lt/min was recorded. Two-thirds of this was encountered in the Bunter Sandstone and the remaining third in the Lower Magnesian Limestone between 240 and 262 metres below the surface.

2.3 The need for modelling

The exceptional circumstances prevailing at Sherburn Mine have already been discussed at some length in the foregoing sections.

When the mineable gypsum deposits in the area are exhausted, the mine workings will have to be abandoned, which will mean that pumping of water out of the workings and continuous monitoring of mine structures (roof, pillar, etc.) will be terminated.

On this basis, it is not difficult to forecast a complete or partial water flood into the workings.

It is known that, at shallow depths, even in the presence of water, pillars may continue to support the overlying strata for a considerable period of time. Although the gradual deterioration is accentuated by the water, depending on many factors (see Section Four), it is found that in the case of Sherburn, the effect is relatively small on the pillar deterioration and the pillars with stipulated dimensions are able to carry the load imposed by the overburden in the foreseeable future.

Alternatively, roof structure spanning the distance between the pillars may fail with time. The reasons for the roof failure at Sherburn may, in the long run, be numerous. The time-dependent deformation of cracked roof beam, aided by the gradual water penetration into the marl above the gypsum roof at critical sections would exceed the limiting deformation. Gradual failure of pillar corners, which gives rise to the unsupported roof span may also contribute to the roof

instability. One of the factors which governs the loosening of pillar corners is the existence of satinspar bands in the pillars at different sections of the mine at Sherburn (see Section Six).

While any pillar failure would seem to be highly unlikely at Sherburn in the future, the same guarantee cannot be given for the roof with any degree of certainty. The fact that this may be followed by, or subsequent to, a water flood is difficult to assess.

Then the question may be formulated in respect of the consequences of a roof beam failure at Sherburn. What will be the consequences on the surface if a roof failure occurs in the future after the abandonment of the mine workings? The peculiar characteristics of the strata above the gypsum seam which were discussed previously renders the approaches of 'rule of thumb' in order to assess the likelihood of surface subsidence rather limited in value. The numerical modelling elaborated in Section Eight of this thesis and the photoelastic modelling discussed in Section Seven of this thesis also offer very little in this aspect. The case histories and solutions presented by Orchard 1956, 1958; Wardell et al. 1969; Bell 1975, 1978; Littlejohn 1978; and Singh 1979 throw much valuable light onto likely behaviour of strata overlying room and pillar workings in the case of roof failure. Due to variation in the lithological properties, it is still difficult to speculate on the likely outcome of a roof failure at Sherburn merely by examining case histories.

On these grounds the physical scale modelling of mine workings and overlying critical successions of strata would appear to be a more realistic approach to resolving the problem under consideration.

2.4 Physical Scale Modelling

The rocks characterised by numerous complex joint systems together with water do not exhibit normal elastic behaviour patterns and hence their behaviour cannot yet be modelled by the use of analytical or numerical methods currently available (Fumagalli 1974; and Goodman and John 1977). The use of physical models, on the other hand, provides the means of ascertaining the influence of various critical parameters on the stability of underground openings outside the elastic limits as well as within the elastic limits. They can be used not only for producing qualitative, but also for quantitative information required by the researcher provided that they are properly constructed and tested.

With the use of modelling, certain engineering problems can be isolated and investigated separately (Barton 1976, 1980; Watson 1979; Hoffman 1964; Didev and Berichuili 1974; Moss 1973; Güloglu 1982; Brook 1982; Yenge 1981; and Bonsall *et al.* 1982).

2.4.1 Dimensional Analysis

Prior to modelling a dimensional analysis should be carried out and a functional relationship between model and prototype variables established and the direction to be followed in the experimental design determined.

The fundamental dimensions of physical quantities are usually taken as mass, length and time and are denoted by M, L and T respectively. The dimensions of other quantities can be derived from their definitions.

Some of the relevant quantities and their dimensions are shown in Table 2.1. In addition, there are other, non-dimensional, quantities which are given by pure numbers; for example Poisson's ratio (γ), angle of internal friction (ϕ) or a strain (ε).

The concept of similitude and hence the theory of models is based upon the principles of homogenity of physical relationships, one of which is the Buckingham's Pi theorem.

Buckingham's theorem states that if an equation is dimensionally homogeneous, it can be reduced to a relationship among a complete set of dimensionless products (Langhaar 1951; Obert and Duvall 1967; and Fumagalli 1974).

It has been shown that if there are n variables and the rank of the dimensionless matrix is r, there will be p dimensionless products or dimensionless Π terms.

$$\Pi_p \quad : \quad p = n - r$$

Furthermore, a functional relationship exists among the Π terms and is given by:

$$\Pi_1 = f(\Pi_2, \Pi_3 \ldots \Pi_p)$$

There are an infinite number of complete sets of Π terms. However, it is sufficient to find one complete set which includes at least one reference to every variable and rank. A function of this kind can be written for both the model and the prototype and a relationship between Π_{1m} and Π_{1p} can be obtained from the ratio:

$$\frac{\Pi_{1p}}{\Pi_{1m}} = \frac{f(\Pi_{2p}, \Pi_{3p}, \ldots \Pi_{9p})}{f(\Pi_{2m}, \Pi_{3m}, \ldots \Pi_{9p})}$$

if, $\Pi_{2p} = \Pi_{2m}$

$\Pi_{3p} = \Pi_{3m}$

$\vdots$

$\Pi_{9p} = \Pi_{9m}$

then, $f(\Pi_{2p}, \Pi_{3p}, \ldots \Pi_{9p}) = f(\Pi_{2m}, \Pi_{3m}, \ldots \Pi_{9m})$ and hence:

$\Pi_{1p} = \Pi_{1m}$.

The relevant variables can be formed into the dimensional matrix shown in Table 2.2. Since all third order determinants vanish, the rank of matrix is two, hence the number of dimensionless product in a set is four, which may be as follows:

$$\frac{U_p L_p}{E_p} = \frac{U_m L_m}{E_m} \quad - 2.1$$

$$\frac{C_p}{E_p} = \frac{C_m}{E_m} \quad - 2.2$$

$$\frac{T_p}{E_p} = \frac{T_m}{E_m} \quad - 2.3$$

$$\frac{\tau_p}{E_p} = \frac{\tau_p}{E_m} \quad - 2.4$$

and $\gamma_p = \gamma_m$, $\varepsilon_p = \varepsilon_m$

From the above equations if the ratio of the model dimensions to the prototype dimensions is chosen as:

$$\lambda = \frac{L_p}{L_m}$$

and the ratio of the unit weight of model material to that of the prototype as:

$$\alpha = \frac{U_p}{U_m}$$

and if $\tau = \frac{E_p}{E_m}$, the equation 2.1 becomes:

$$\lambda \times \alpha = \tau \qquad \ldots\ldots (2.5)$$

and (2.2), (2.3) and (2.4) become:

$$\frac{C_p}{C_m} = \frac{T_p}{T_m} = \frac{\tau_p}{\tau_m} = \frac{E_p}{E_m} = \tau \qquad \ldots\ldots (2.6)$$

where τ is the degree of efficiency.

It is sometimes difficult to increase body forces by increasing the unit weight of the modelling material because of the limitations in the range that weight can be conveniently varied. In these cases, a centrifuge system can be used to scale the gravitational forces. Another method is to conduct the experiment by pushing the model along a roughened surface or, alternatively, the base on which the model rests can be moved at a calculated speed thus creating gravity effect in the model (Goodman 1976).

Equation (2.5) suggests that if the ratio of both unit weights is equal to unity (that is, $U_p = U_m$), then the degree of efficiency must be the same as the scale of geometrical dimensions. And the mechanical properties of rock and modelling material are related to each other by a single scale factor (i.e. geometrical scale factor).

2.4.2 Modelling Materials

The use of natural rock as a modelling material is highly desirable since this eliminates the need to form numerous similarity conditions which must otherwise be satisfied. If the actual material is used for modelling the only condition that remains to be satisfied is the geometric similarity.

The use of a prototype material instead of the modelling material brings about certain limitations. Firstly, if the rock possesses a high compressive strength, it will require substantial boundary loads in order to achieve measurable deformations which, in turn, necessitates a costly loading system. Secondly, although the geometrical scale is reduced, the weakness zones, fractures and crystal size cannot be reduced. Moss (1973) used prototype material, potash, for modelling purposes. It was observed that the individual salt crystals caused absurd convergence due to the large crystal size and the slippage of crystals during the course of testing.

Modelling can be carried out using equivalent modelling materials. In choosing an equivalent material, requirements of similarity and reproducibility must be taken into consideration.

Lee and Coates (1957) investigated the usability of Plaster of Paris, subjected to vacuum pressure, mainly for civil engineering orientated modellings.

Rankilor (1970) used soft polyurethane rubber called Solithane which could be manufactured in the laboratory with a wide range of Young's modulus and could be loaded by its own weight. He simulated the strata over mine workings and observed the subsidence reaching the surface as the excavation of seams proceeded.

Hoffmann (1964) made use of Moltopren, an artificial foam material, in order to reproduce movements between mine workings and the surface.

Rosenblad (1968), sought a rock-like material for the investigation of the failure mechanism of a discontinuum. He indicated that, in searching for such a material, the scaled modulus of elasticity would not be adequate, since the behaviour of material would be very different under increased confining pressure. He eliminated many modelling materials used in the past on the basis of cost, availability, reproducibility, and the brittle behaviour of the materials.

Fumagalli (1973) divides various modelling materials into two categories. The first category comprises materials for use in the elastic region, e.g. celluloid, rubber and thermo-plastic materials, and the second comprises material for use up to failure, e.g. cement, plaster, lime. Baumgartner et al. (1979) used ordinary cooking flour mixed with methanol. Barton (1970; 1974); Nelson et al. (1968);

Saučier (1967); and Güloglu (1982) have conducted experiments using sand with other additives such as red lead, galena, and ballotins-plaster, water, etc.

2.5 Development of a modelling material

Already available and commonly used equivalent materials are considered unsuitable for modelling a roof failure above mine workings where water, in association with marl, is expected to play a major part. Characteristics of marl-water association will be discussed further in the forthcoming sections.

The use of actual marl as a modelling material was eliminated mainly for two reasons: The workability and availability of prototype material were not sufficient to build up a number of models. Secondly, it would require sophisticated and expensive loading arrangements.

Therefore, an apt method of producing a substitute material was adopted. The method will be described fully in the following sections but involves mainly crushing, grinding the prototype material and the recompacting of ground marl with water into steel moulds. It is possible to produce modelling materials with various strength characteristics including those required by the similitude of the intended model by altering some of the parameters involved in the production process.

2.5.1 Compaction

One of the most commonly used methods of mechanical stabilisation in soil mechanics is that of compaction. Compaction is described by

Bowles (1979) as the densification of soils by the application of mechanical energy. The most significant effect of compaction is the improvement of the engineering properties of soil mass through an increase in the unit weight or, alternatively, a decrease in the void ratio of the soil mass. An increase in the unit weight is accompanied by an increase in the angle of friction; e.g. for a uniform fine sand an increase in unit weight from 1.4 tons/m^3 to 1.6 tons/m^3 increases the angle of internal friction from about 34^o to 39^o. This results in more than doubling the physical properties of the soil mass such as compressibility, modulus of deformation, and coefficient of permeability (Wilson 1952).

Koido and Hoshino (1979) investigated the characteristics of deformation of sedimentary rocks under confining pressure in terms of geological compaction. They observed that the modulus of deformation clearly increased with the reduction of porosity in compacted soils.

2.5.2 Compaction Methods

Fine-grained cohesive soils may be compacted in the laboratory by falling weights and hammers, by special kneading compactors, by hand tamping or by using static pressure, as would be applied in a common compression testing machine.

In soil mechanics practice, the impact compaction is often used for soil tests. During impact compaction a hammer is allowed to drop several times on a soil sample, placed in a mould. The size of the hammer, height of drop, number of drops, number of layers of soil and volume of mould are specified. Then the impact compactive effort, which is a measure of mechanical energy applied, is computed from the formula below:

$$CE = \frac{\text{Weight of ham. x Layers x Blows/Layer x Thickness of layer}}{\text{Volume of mould}}$$

For kneading and static compaction methods the calculation of compaction energy is extremely complex (Bowles 1979). In static compaction, the soil sample is simply pressed into a mould by a static pressure of some known magnitude and side friction developed on the mould becomes a significant factor, since a lateral pressure is created in relation to the equation below:

$$\sigma_h = k x \sigma_v \qquad k = \left(\frac{\nu}{1-\nu}\right) \quad \nu \text{ - Poisson's ratio.}$$

The physical properties of compacted specimens are greatly affected by the method of compaction employed.

For modelling purposes, large quantities of ground marl had to be compacted. Therefore, for convenience, it was decided to employ static compaction during the experimental programme.

2.5.3 Characteristics of Compacted Soils

When a compacted soil or material is subjected to an external load, the load is initially only partially carried by grain-to-grain contact with a balancing effect of the pore water or the air filling of the voids between the particles. The stress in the voids is called the neutral stress, and that in the soil structure is termed effective stress. Naturally, the ability of a compacted material to resist deformation or to carry load is proportional to the effective stresses acting between the grains. The distribution between effective and neutral

stresses upon loading depends not only on the original degree of compaction, but also on changes in void ratio and the degree of saturation of the material.

2.5.4 Principles of Compaction

The principles of standard compaction were first laid down by Proctor in 1933 (B.S.1377:1948, No.9). The standard laboratory compaction test is, therefore, usually called the Proctor Test. In soil compaction, four variables may be considered important:

(a) Dry unit weight;

(b) Water content;

(c) Compaction effort; and

(d) Soil type (presence of clay, gradation, etc.).

In the standard compaction test, samples (five are usually sufficient) of the same material as that to be compacted, but with different water contents, are compacted with the constant compactive effort into the standard mould of known volume. The wet unit weight and water content of samples are determined. After the water content for each test is obtained, the dry unit weight is computed and the curve of dry unit weight versus water content is plotted.

The compaction curve is unique for a given soil type, method of compaction and compactive effort. The peak point of the compaction curve corresponds to the maximum dry unit weight and optimum moisture content (OMC). The compaction curve can be divided into two sections; namely: the dry of optimum and the wet of optimum. The importance of

compaction curve is that the amount of water to be compacted with marl is determined from the compaction curve of a specific compactive effort (Figure 2.2).

2.5.4.1 Soil Type

In general, the finer the particles, the better the compaction obtained. Moreover, uniform and well graded mixtures provide higher dry unit weight when compacted than that of unbalanced gradations and thus they produce better compaction.

In order to define the degree of gradation of a sample of ground marl, the particle size analysis is carried out. Mechanical sieving was adopted for this purpose. Approximately 1703 gr. of marl sampled from a total amount of marl chunks received for modelling purposes was crushed in a jaw crusher then ground in a laboratory mill. The whole of the ground material was poured onto the sieve of the largest size and sifted through the whole set of sieves. On completion of the sieving (about 10 minutes), the material retained on each sieve was weighed. The calculations for percentage passing were made using the following equation:

$$P_p = \frac{W_o - \max_{n=1}^{i} \sum W_i}{W_o} \times 100$$

where W_o = Total weight

W_i = Weight retained

P_p = Percentage passing.

By plotting the percentages (P_p) against the corresponding sieve sizes, the grain size distribution curve is obtained (Figure 2.3).

Mainly three chracteristics of the curve are of major practical importance in compaction; namely, the maximum grain size in the assemblage, the general slope of the curve (uniformity coefficient) and the degree of grading. The maximum grain size (d_{max}), which is read from the plot as the largest sieve size, is important in the choice of a method of soil compaction and also in the permeability of compacted material. If the uniformity coefficient ($U = d_{60}/d_{10}$) is close to unity, the distribution of particles is said to be very uniform. This indicates that there are coarse grains, as well as fine grains in the material, which is beneficial in accomplishing a good compaction. Inspection of Figure 2.3 suggests that fairly uniform material is obtained for the purpose of compaction of marl.

The presence of clay in the material is a major factor in the strength of compacted material. A particular phenomenon of clay is that a clay mass which has dried from some initial water content forms a mass which has a considerable strength. If the dried marl lumps are broken down to elementary particles, the material behaves as a cohesionless particulate medium. When water is again added it becomes plastic with some strength intermediate to the dry lump strength. If the wet clay is again dried it forms hard, strong lumps. In this process, the role

of water is not fully understood. However, in drying, surface tension certainly pulls the particles into a maximum contact with minimum interparticle spacing so that the interparticle forces are maximum. It appears that these interparticle forces are responsible for this high strength. It is interesting to note that the use of water which is a dipolar agent will produce this effect, whereas a non-polar agent, such as Carbon Tetrachloride (CCL_4), does not (Michaels 1952).

2.5.4.2 Water Content

Water content or moisture content (the ratio of the weight of the water present in the material to the weight of dried material) is the main factor determining the strength and also the deformation characteristics of cohesive soils and compacted soils.

A clay when mixed with a sufficient amount of water becomes a thick paste that has practically no cohesion and would flow under its own weight, even on gentle slopes. If the paste is gradually dried, it passes from the liquid state to plastic state, so that it can be readily moulded. On further drying, the clay becomes stiff, its colour turns into a lighter shade, its strength gradually increases until, finally, it becomes quite hard and rigid. The boundaries of these phases are, in terms of water content, called 'Consistency Limits'. The implications of these limits with respect to modelling will be discussed later in this Section.

The compaction test curves (Figure 2.2) illustrate that, at low water contents, the soil is dry and there does not exist sufficient water to affect a breakdown or softening of clay lumps. Success in compaction in this moisture content range depends primarily on whether the energy input is sufficient to crush the lumps. As the water content increases, the particles have sufficient water to slake the lumps and develop water films. The water films on the clay particles reduce the inter-particle bonding by increasing the spacing so that the compaction energy tends to produce a more dispersed structure. A small contribution of water lubrication at the particle contact points may be developed. A water content is reached where this condition is optimised and is termed Optimum Moisture content for this particular compactive effort. Beyond this point, the degree of saturation becomes such that further compaction effort produces soil displacement and local shearing instead of particle packing.

2.5.4.3 Dry Unit Weight

In compaction tests, the main objective is to obtain the maximum possible dry unit weight of a compacted material at a constant compactive effort. In the Proctor tests, for each specimen with different water content, the dry unit weight is computed as follows:

$$V_{wet} = \frac{\text{Weight of wet soil in compaction mould}}{\text{Volume of compaction mould}} \quad \text{and}$$

$$V_{dry} = \frac{V_{wet}}{1 + \text{The water content at each step}}$$

The highest value obtained is the maximum dry unit weight and corresponds to the optimum moisture content.

2.5.4.4 Compactive Effort

Compactive effort is a measure of the mechanical energy applied to the soil mass to be compacted. As the compactive effort is increased, the void ratio of compacted soil and the optimum moisture content decrease (Bowles 1979 and Glanville 1974). A line drawn through the peak points of a family of compaction curves obtained from different compactive efforts on the same soil will be approximately parallel to the zero-air-voids curve. This line is called the line of optimums (Figure 2.4).

It is obvious that at higher compactive efforts, the optimum moisture content and hence the maximum dry unit weight is achieved at lower moisture content levels. However, in practice the choice of compactive effort is limited due to practical considerations.

2.6 Production Procedure of Modelling Material by Static Compaction

The production principles of a modelling material from the prototype material (marl) can be laid down. The main steps to be followed can be given as follows:

(1) Crush and grind the marl chunks available. Well graded material gives better compaction.

(2) Determine the geometrical scale factor of modelling.

(3) Using similitude law, determine physical properties that modelling material should possess.

(4) Assuming an arbitrary moisture content, produce a number of specimens compacted at various compactive efforts.

(5) By testing ready made specimens, compare the results with those required and determine the most suitable compactive effort.

(6) At this compactive effort using various amounts of water, produce at least 7 specimens and determine therefrom the compaction test curve for ground marl.

(7) From the compaction test curve, determine the maximum dry weight and optimum moisture content to be used in the production of model material.

(8) Using optimum moisture content and compactive effort, produce a number of specimens to be tested and compare the testing results with those required for a final check.

The above developed steps will be followed in the present modelling study and results commented upon in the final part of this Section.

2.6.1 Crushing and Grinding the Prototype Material

Approximately 100 kg of marl supplied by British Gypsum Ltd. was crushed in a jaw crusher in order to reduce the size of chunks to enable them to be fed into the grinding machine. For grinding, a small-scale laboratory mill available within the Department of Mining Engineering was used.

Particle size analysis of a sample from ground material was carried out to ensure a well graded grain size distribution (Figure 2.3).

2.6.2 Geometrical Scale Factor and Required Model Material Properties

Geometrical scale factor has been chosen from practical considerations such as: The size of the model should allow observation of a progressive failure of simulated roof strata to be made. It should be large enough to simulate three adjacent roof beam failures so that any likely interaction could be viewed. It should be managable in size. On these grounds, a scale factor of 1:50 was considered appropriate.

In Section 2.4.1, the law of similarity was discussed at some length. It was deduced that if the unit weights of model material and prototype material are equal, the model material properties (compressive, tensile, strength, Young's modulus, etc.) are related to the prototype material properties by the geometrical scale factor. On this basis, required modelling material properties are determined and these are set out in Table 2.3.

2.6.3 Determination of Compactive Effort

An appropriate amount of ground, dried marl was mixed with water. The water content was chosen arbitrarily as 9%. Using a cylindrical metal mould (80mmϕ, 250mm height) and two steel plungers of the same diameter as the mould (Figure 2.5), a total of 8 compacted marl specimens were prepared at various compactive effort levels.

Prepared specimens were tested for uniaxial strength and tensile strength (Brazilian). The results of these tests are set out in Figures 2.6 and 2.7. Since the required values were already known, a suitable compactive effort was chosen; that is, 11 kN (2.188 MPa).

2.6.4 Compaction Test for Marl

At the determined compactive effort (11 kN), a further 8 specimens, each having different moisture content, were prepared in the same way as previously. For every specimen, moisture content and corresponding dry unit weights were calculated as described previously. A graph showing dry unit weights versus moisture contents was drawn, and a curve passing through the points in the graph was plotted (Figure 2.2). The highest point (the peak point) for dry unit weight and corresponding moisture content was found as optimum moisture content of the compacted specimens.

Optimum moisture content and dry density were found to be 12.5% and 20.75 kN/m^3 respectively. It is known that the strength of cohesive materials compacted dry of optimum is usually larger than that of those compacted wet of optimum (Bowles 1979). Furthermore, the

samples compacted dry of optimum show more swelling properties than those compacted wet of optimum. For these reasons, the working moisture content of marl specimens was chosen as 11% and corresponding dry unit weight as 20.25 kN/m^3.

2.7 Physical Properties of developed Modelling Material

It is essential to ensure that the modelling material produced as described in the preceding sections possesses the required physical properties, because the degree of reliance with which model results will be evaluated is largely related to the similarity achieved in the modelling material with regard to prototype material. If the similarity is not satisfactory, the model results may be misleading, even if they are considered only qualitatively.

For this reason, numerous specimens have been prepared. The moisture content and compaction effort has been maintained constant in all preparations as determined (11% and 2.188 MPa respectively). Compaction was carried out using circular steel mould as mentioned earlier (Figure 2.5) on a 25-ton loading machine. The loading rate was approximately 2 kN/min. in all compactions.

2.7.1 Uniaxial Compressive Strength

A total of 17 specimens have been tested uniaxially on the 25-ton machine with matching steel end platens. The heighth-width ratio was 1:1 for practical reasons, although slight variations have occurred.

6 specimens were tested immediately after production and yielded an average strength value of 375.5 kPa.

4 specimens were tested 2 days after their production in order to observe the effect of change in the moisture content on the strength values. The remaining specimens were tested 4 days after their production for the same reason.

The results clearly indicate that as the age increases the strength of the specimens also increases (Figure 2.6). The failure modes of specimens were usually diagonal shear fractures in a brittle manner. Some specimens (those tested immediately) exhibited barrelling and multiple shear planes intrinsic to plastic failure or semi-plastic failure.

2.7.2 Tensile Strength (Brazilian Disc)

14 specimens having a height to width ratio of 1:2 were tested for tensile strength. An average tensile strength value of 40 kPa was obtained (Figure 2.7).

The observed failure mode was generally crushing at the contact points and associated vertical splitting.

2.7.3 Young's Modulus

Two specimens were tested with a servo-controlled testing machine (see Section Six). The full load-deformation curves are shown in Figure 2.8. The compacted specimens behaved in a brittle manner. At 50% of ultimate peak load, tangent moduli of specimens were calculated. The average value was 3.3 MPa.

2.7.4 Shear Strength

In order to determine the values of cohesion and angle of internal friction of modelling material, 8 specimens were tested in shear using a direct shear testing equipment often used in soil testing. The apparatus will be referred to in Section Six of this thesis in relation to shear testing of satinspar. It is, therefore, considered appropriate to describe the equipment used briefly (ASTM D3080-72).

The sample, cast in a rectangular shear box, was forced to fail along a predetermined plane and direction. The normal stress was applied on the specimen by the dead weights suspended by a yoke. Shearing load is produced at a known rate by a motor coupled to the shear box. The details of shear box used are given in Figure 2.9. Applied shearing load and displacements were recorded at certain time intervals by means of a dial gauge mounted on the shear box. Dial gauge readings and time readings were converted to load with a conversion factor provided on the charts for the machine.

For the model material tested, applied normal and shear stresses at peak for each specimen are shown in Figure 2.10. By fitting a straight line to the points, the cohesion (c) and the internal angle of friction (ϕ) are found to be 69.62 kPa, and 45^{o} respectively.

$$\tau = c + \sigma_n \times \tan\phi = 69.62 \text{ kPa} + \sigma_n \tan 45^{o}.$$

2.7.5 Slake Durability of Prototype and Modelling Material

Some rocks disintegrate to a considerable extent when they come into contact with water. Particularly, due to their complex nature, most clayey materials show significant slaking, swelling properties under wetting and subsequent drying conditions. This can result in severe instability problems leading suddenly to localised roof falls in cases where these materials are exposed to water above the mine roofs.

The early analysis at Sherburn Mine by I.W. Jones (1968) indicated that the marl would be self supporting and that the roof beam would be loaded only by its own weight plus a hydrostatic head. Subsequent investigations showed that the marl was closely following the deflection of the gypsum beam. Hence Mottahed (1974) undertook an extensive investigation into the mechanical and swelling properties of the Upper Permian Marl.

The Upper Permian Marl is red in colour and massive in its make-up, with varying degrees of siltstone content. Inspection of the borehole cores suggested that this layer was not uniform in its content and that its petrology changes from one location to the next. The x-ray diffractograms of marl specimens examined by Mottahed (1974) indicated the presence of certain clay minerals (illite, kaolinite and small amounts of chlorite) in the Upper Permian Marl. Although the abundance of montmorillonite clay minerals was not confirmed, the result of analysis by x-ray was conclusive in showing certain amounts of montmorillonite clay minerals. Moreover, the abundance of calcium ions in the form of carbonate or chloride salts (NaCl, $CaCO_3$) in the marl,

and the ease of access of water to the workings through joints and fracture planes from the two sand beds form suitable conditions of the leaching of the carbonate and chloride salts. Hence the leaching of soluble salts from the marl will provide volume for the further swelling of clay minerals.

The slake durability tests were intended for the determination of the degree of disintegration of rocks when subjected to subsequent two cycles of wetting and drying processes. Since it is an index test, the results are not directly applicable to the in-situ cases, but can be compared with the indices obtained from other rocks.

Mielenz and King (1955) postulate the mechanism of slaking in shales as follows:

(1) During drying, shrinkage cracks are formed which are filled with air.

(2) Swelling of shale during re-adsorption cycle causes air to be trapped causing tensile stresses in shale.

(3) Differential swelling pressures are set up during re-adsorption cycle and

(4) Combination of tensile stresses and differential swelling causes slaking of shales.

In order to compare the prototype material and the developed modelling material in terms of disintegration in subsequent wetting and drying conditions, the slake durability index tests were carried out (Franklin and Candra 1972). The procedure has been described in detail elsewhere (Suggested methods for rock mechanics). Ten lumps of prototype

and modelling material, each weighing approximate 20 grammes and fairly rounded, were tested simultaneously using four test drums (Figure 2.11). In the tap water, two cycles of wetting (10 minutes each) in rotating drums and drying in an oven (103°C)was adopted.

The slake durability index for the prototype material and the modelling material have been found to be 78.7% and 58.2% respectively. Watson (1979) reports the index of slake durability of Upper Permian Marl as 80%. The results clearly indicate that the modelling material is less resistant to the subsequent two standard cycles of wetting and drying than the prototype material.

2.7.6 Swelling Strain and Stress Index Test for Modelling Material

Swelling can be defined as a time-dependent volume increase of the natural material caused by stress changes, increase in water content, or by a combination of both.

The reasons for potential swelling of a material are given by Olsen and Engen (1974) and are shown in two main categories. Firstly, the internal factors such as the type and amount of clay minerals (montmorillonite, illite, kaolinite), grain size and contents of exchangeable ions. The external factors, which depend on the local conditions such as the consolidating pressure, the access of water, and the temperature. A heavily consolidated clay with low potential swellability will mobilise a higher swelling pressure than a clay with low consolidation.

The swelling of natural and artifically compacted shale and marl has been extensively discussed by many authors (Gromko 1974; Sowers and Kennedy 1967; Alpan 1957; Madsen 1979; Mottahed 1974; and Brekke 1965).

Swelling properties of Upper Permian Marl are of paramount importance in the loading mechanism of roof beam at Sherburn (Mottahed 1974). In an attempt to see whether developed modelling material has similar swelling properties to those of the Upper Permian Marl, two swelling tests were conducted (Suggested methods for rock mechanics). Apparatus used for this purpose is similar to that employed by Mottahed (1974) (Figure 1.12).

The results of testing are shown in Figures 2.13 and 2.14. The maximum swelling pressure index and swelling strain index for modelling material were found to be 6.5 ± 0.22 kPa and $2.25 \pm 0.19\%$ respectively. The values are in good agreement with those having high clay content tested by Mottahed (1974).

2.7.7 Coefficient of Permeability of Modelling Material

In order to examine the propensity for water to flow and penetrate, two permeability tests were carried out. The apparatus was a modified triaxial cell connected to a water head. A constant head of pressure was adopted for this purpose (ASTM 02434-68).

The coefficient of permeability of the modelling marl was calculated to be 12.3×10^{-8} mm/sec. Watson (1979) gives a value of 2.2×10^{-8} mm/sec for the prototype marl. It infers that modelling marl is more permeable than actual marl, which is beneficial for modelling purposes.

2.7.8 Absolute gravity and voids ratio

Absolute gravity and voids ratio of modelling material was determined by the pycnometer method (suggested Methods for Rock Mechanics). The specific gravity and voids ratio of the modelling material were found to be 2.0723 gr/cm^3 and 6% respectively.

2.7.9 Plastic and Liquid limits (Atterberg Limits) of Marl

Atterberg Limits tests are well known in soil mechanics for the evaluation of the behaviour of a cohesive soil at different moisture content levels. The water content above which soil-like materials behave as a viscous liquid (a soil-water mixture with no measurable shear strength) is called the liquid limit of specific soil types. The water content below which the soil no longer behaves as a plastic material is termed the 'plastic limit' of that particular soil.

The significance of these limits with respect to modelling is apparent. The liquid limit sets up the moisture content that is sufficient to render the modelling material a viscous fluid. On the other hand, at moisture contents below the plastic limit, marl-water mixture becomes rigid, i.e. it sets up the upper limit of moisture content for compaction.

The procedures for determination of the liquid limit and the plastic limit of modelling material will not be described here since they are given elsewhere (B.S.1377:1975). The cone penetration method was adopted for the liquid limit determination.

The liquid limit and plastic limit of compacted marl were found to be 26% and 16% respectively.

2.8 Comparisons between the prototype marl and modelling marl properties

In order to model a roof beam failure with accompanying water inrush at Sherburn Mine, an equivalent material has been developed. Since the water is expected to play a major role in the failure of the immediate roof, particular attention was paid to produce a material which would exhibit similar behaviour, when it comes into contact with water, to that of the actual material.

In Table 2.3, the relevant properties of the prototype material (Upper Permian Marl), the developed model material are given, together with the scaled-down (1:50) values of actual material. Inspection of the table suggests that although there are variations between the target values and those achieved, in general results can be considered to be appropriate for modelling purposes. Thus the similitude requirements set out at the beginning of this Section appear to be satisfied.

Moreover, simplicity of the production process developed, re-useability of the same material over and over, workability of the material, makes the compacted marl an attractive equivalent material, and it is advisable to use it in future modelling studies for similar circumstances.

2.9 Modelling Material for Upper Glacial Deposits

It has been discussed in earlier sections that the Upper Glacial Deposits have negligible load-bearing strength. The existence of flowing sand beds in this section of the overlying strata accentuates

its critical situation. On these grounds, fine river sand with appropriate amounts of water added was considered to be suitable for simulating the Upper Glacial Deposits in the model studies.

River sand was placed on top of the compacted marl blocks by hand tamping at appropriate intervals. An abundant amount of water was then added from the top, allowing the sand to achieve flowing properties.

In order to compensate the difference in the gravitational forces between the Upper Glacial deposits and the river sand, a number of steel bars weighing approximately 10 kg were placed on top of the sand layers. This arrangement was considered sufficient for the purpose.

2.10 Construction of Model Box

A box made of timber and perspex components was constructed in order to accommodate the model during testing. The size of the box was chosen in such a way that at least three scaled-down rooms and four scaled-down pillars could be simulated up to the surface. The relevant dimensions of the box are given in Table 2.4.

In order to enable visual inspection of the model during testing, all the sides of the box were made of perspex sheets. The front perspex plate could be removed during the construction of the model and after the testing terminated.

Since large amounts of water were anticipated being involved, all the edges were sealed off and the timber components were varnished

to prevent decay and undue swelling. Considerable difficulties associated with the model box were experienced during the course of the testing programme. These will be mentioned in the following Section (Section Three) where appropriate.

The gypsum beam was simulated by timber planks. The roof beam failure was modelled by pulling the dowells which supported the collapsible timber-roof-planks. In order to make the collapsible parts heavier to sink in the water, metal weights were glued to the bottom of the timber planks.

Tap water was poured into the model via a plastic hose.

* * *

FIG 2.1 A

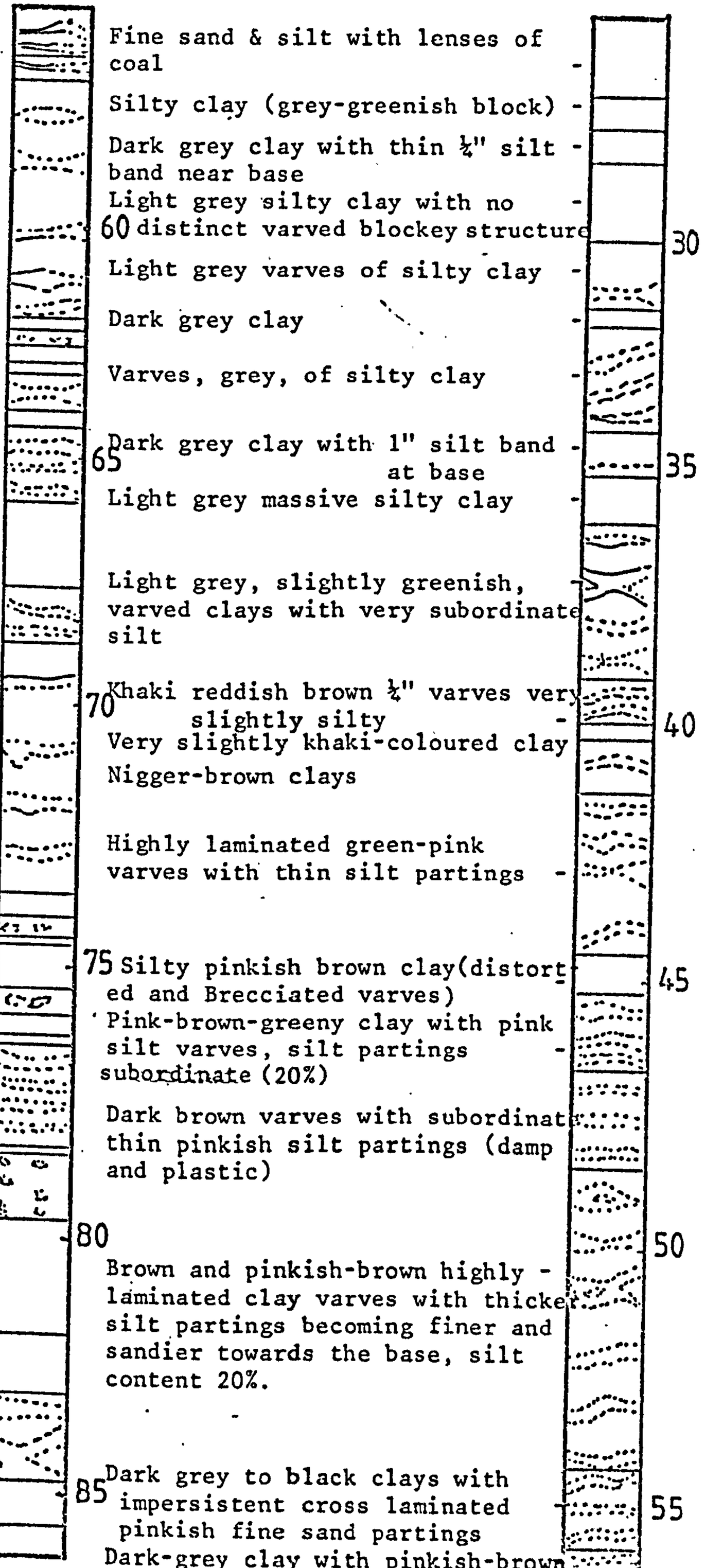

Highly laminated silty clays with subordinate silt.

Light brown varves of silty clay with silt partings up to 30% of total.

Khaki-brown compact silty clay
Dk.brown clay varves with cross-laminated silts
Dark reddish-brown plastic clay.
Highly laminated dark clay with light brown clay and silt.
Silts cross-laminated of equal proportion of dark and light brown clay partings.
Dark brown clay.
Dark & light brown clays,cross-bedded lenses of silt & fine sand(20-25%total)
Light grey-brown clayey silt.
Laminated silts & dark brown clays.

Laminated silt with a very small proportion of clay

Laminated silt with a very small clay content.
Fine sand with a clay binder
Poorly bedded silt & clay laminate
Brecciated red marl.
Partly laminated red marl.
Green siltstone with subordinate red stained layers.
Red Laminated marls.
Green silt or fine sand
Brown fine sandy marl with small layers of clay-like marl.
Light green and brown fine sandstone masses irregularly distributed in brown marl

Mixed brown sandy marl and brown marl-

Light brown fine sandy marl

Mixed green and red fine muddy sandstone, impersistent layering

Green sandstone

Red-brown muddy fine sandstone

Fine sand & silt with lenses of coal
Silty clay (grey-greenish block)
Dark grey clay with thin ¼" silt band near base
Light grey silty clay with no distinct varved blockey structure
Light grey varves of silty clay

Dark grey clay

Varves, grey, of silty clay

Dark grey clay with 1" silt band at base
Light grey massive silty clay

Light grey, slightly greenish, varved clays with very subordinate silt

Khaki reddish brown ¼" varves very slightly silty
Very slightly khaki-coloured clay
Nigger-brown clays

Highly laminated green-pink varves with thin silt partings

Silty pinkish brown clay(distorted and Brecciated varves)
Pink-brown-greeny clay with pink silt varves, silt partings subordinate (20%)

Dark brown varves with subordinate thin pinkish silt partings (damp and plastic)

Brown and pinkish-brown highly laminated clay varves with thicker silt partings becoming finer and sandier towards the base, silt content 20%.

Dark grey to black clays with impersistent cross laminated pinkish fine sand partings
Dark-grey clay with pinkish-brown silts & fine sands of almost equal proportions.

60 65 70 75 80 85

30 35 40 45 50 55

FIG 2.1 B

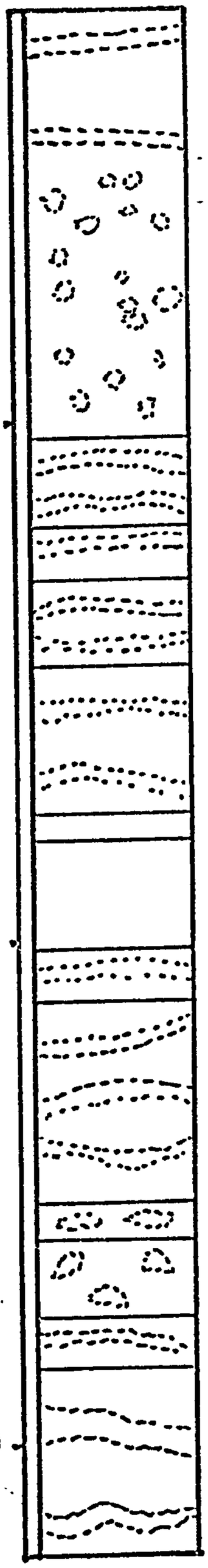

- Red-brown muddy fine sandstone with occasional bands of thin marl, some green sandstone masses up to ½ diameter especially in the bottom two feet.

- Layers of brown marl with siltstone partings.

- Fine green sandstone with some thin layers of red sandstone; some marl partings near top and bottom.

- Red-brown mudstone with thin siltstone partings.

- Fine-grained reddish sandstone with mudstone partings.

- Red-brown and green fine sandstone with a few brown mudstone partings near top.

- Fine sandy mudstone, blocky and soft.

- Green sandstone.

- Red-brown mudstone, angular fragments, with subordinate red fine sand and siltstone layers.

- Irregular green fine sandstone with red patches and some thin bands of reddish-brown mudstone.

- Light brown silty fine sandstone with irregular plates of mudstone.

- Green and light brown fine sandstone with bands of disturbed fine laminae of reddish-brown mudstone.

- Large plates of laminated reddish brown marl and brown siltstone, essentially a muddy siltstone area.

FIG 2.1 C

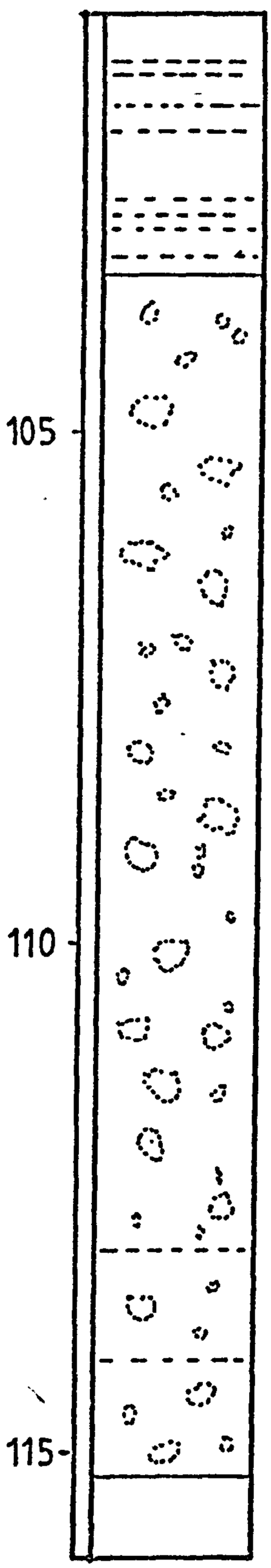

- Green fine sandstone with subordinate bands of brown siltstone with reddish-brown mudstone, sometimes highly laminated.

- Muddy fine sandstone with no distinct bedding and with irregularly distributed muddier areas, small green eyes scattered throughout, satinspars at 114 feet. Material is hard and sandy.

- Purplish-brown fine sandy mudstone with no obvious bedding plane. Blocky and soft compared to material above.

FIG 2.1 D

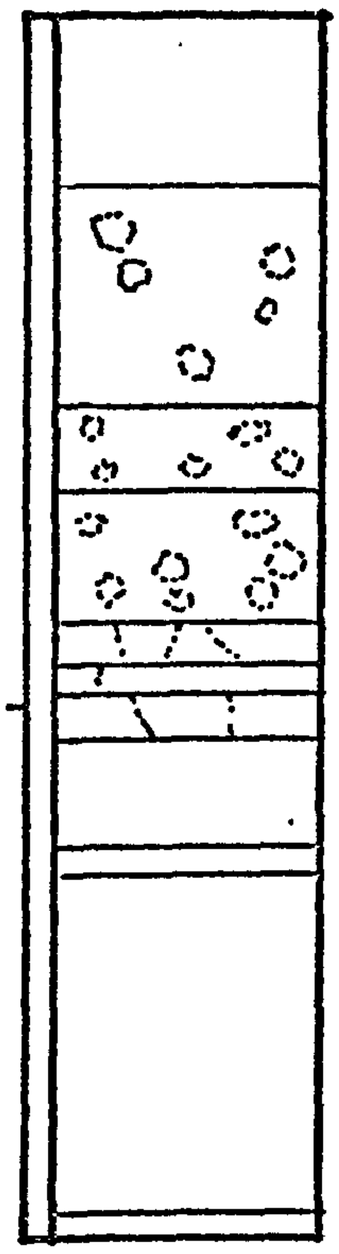

- Purplish-brown fine, sandy mudstone with no obvious bedding plane. Blocky and soft compared with material above.

- Purplish-brown mudstone, less silty, blocky with green eyes.

- Muddy fine sandstone with poor bedding, fairly hard, green eyes.
- Reddish-brown fine sandstone, poor beeding, many green eyes.
-Satinspar with green silty marl (talc-like).
- Pink dolomite with green areas.
- Satinspar, red marl parting.

- Pink and white gypsum, impersistent bands.
- White saccharoidal gypsum.

- Pink gypsum.

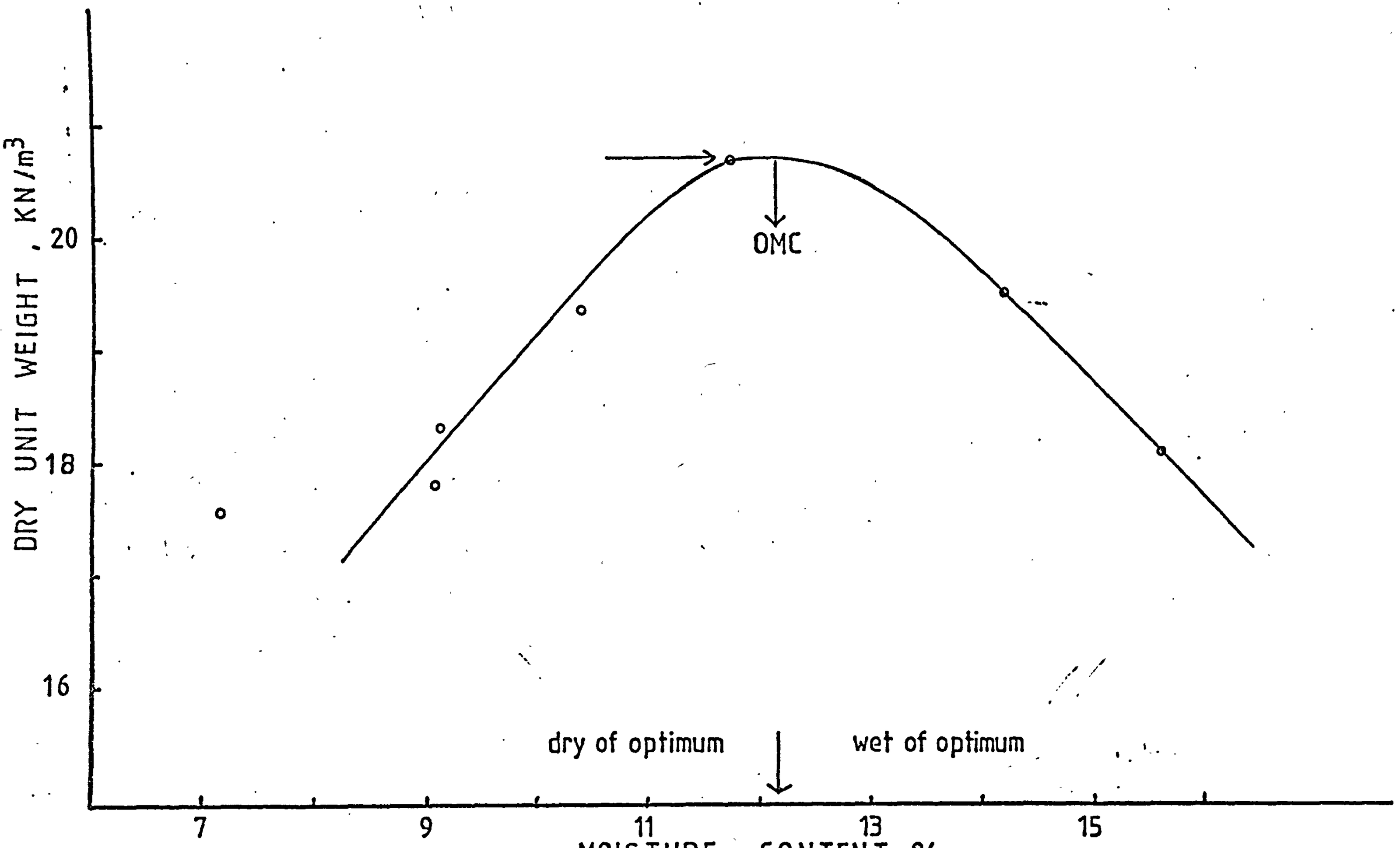

FIG 2.2 COMPACTION CURVE OF MARL

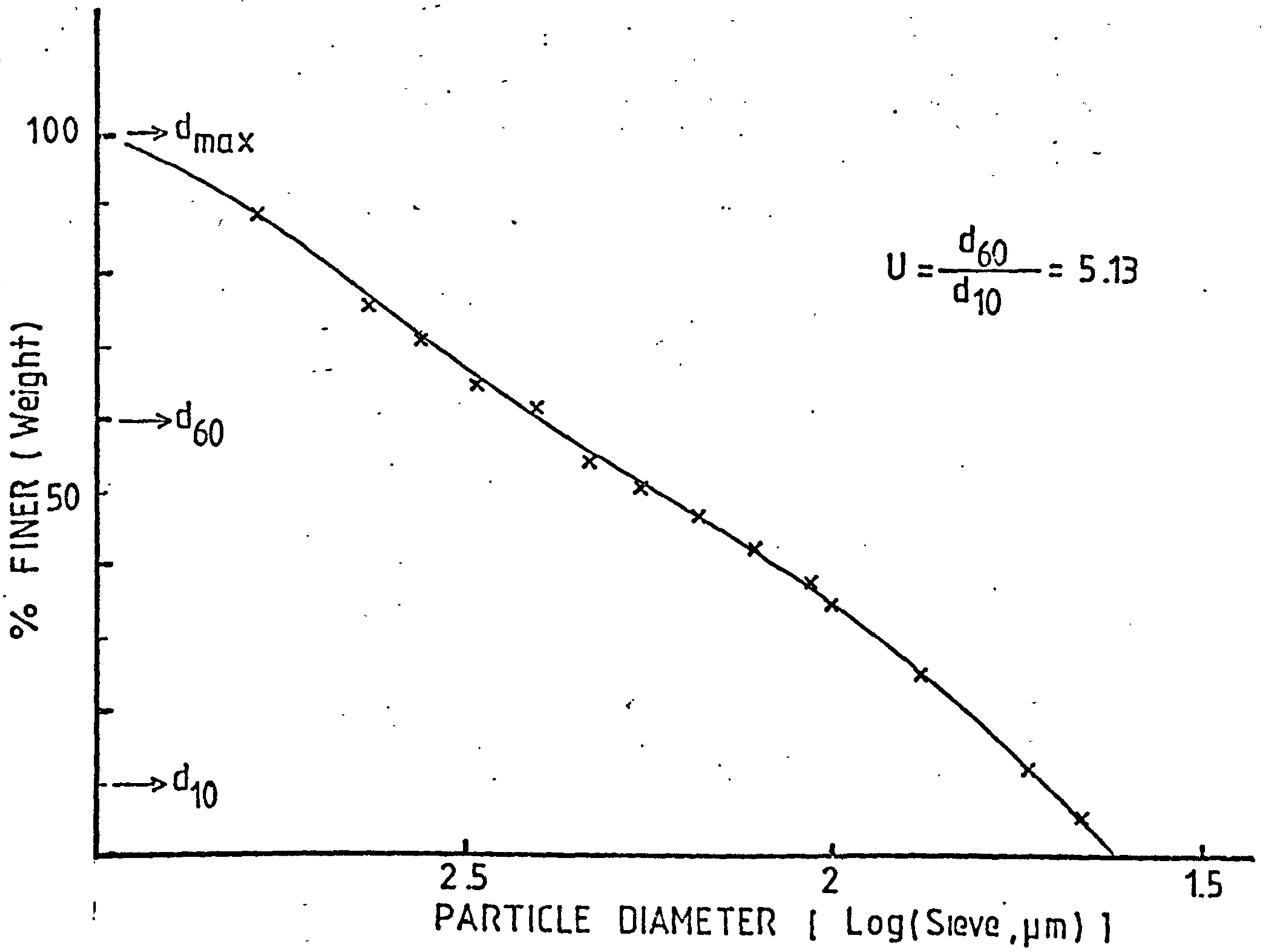

FIG 2.3 GRAIN SIZE DISTRIBUTION CURVE

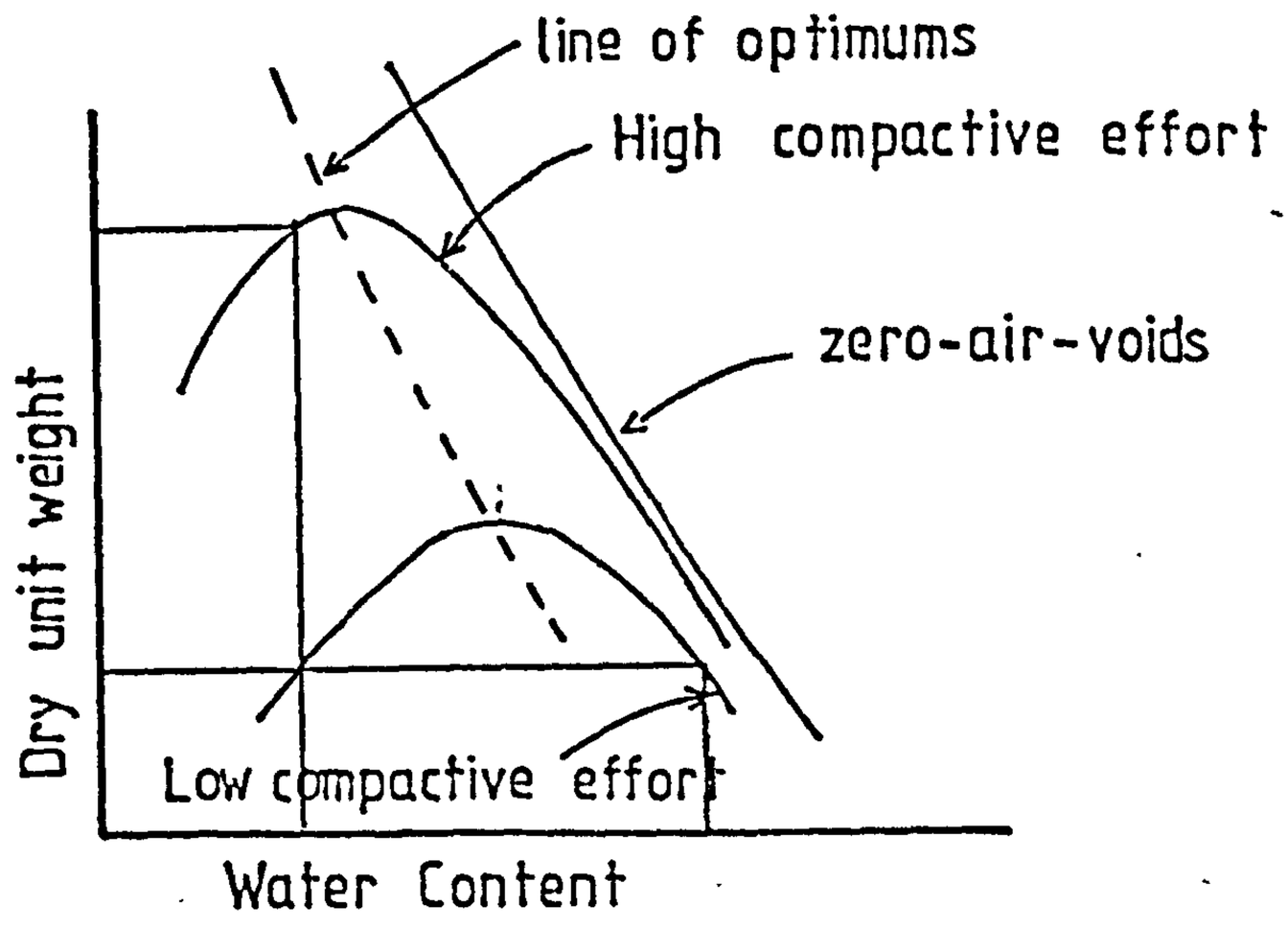

FIG 2.4 EFFECT OF COMPACTIVE EFFORT
(AFTER BOWLES ,1979)

FIG 2.5 Steel moulds

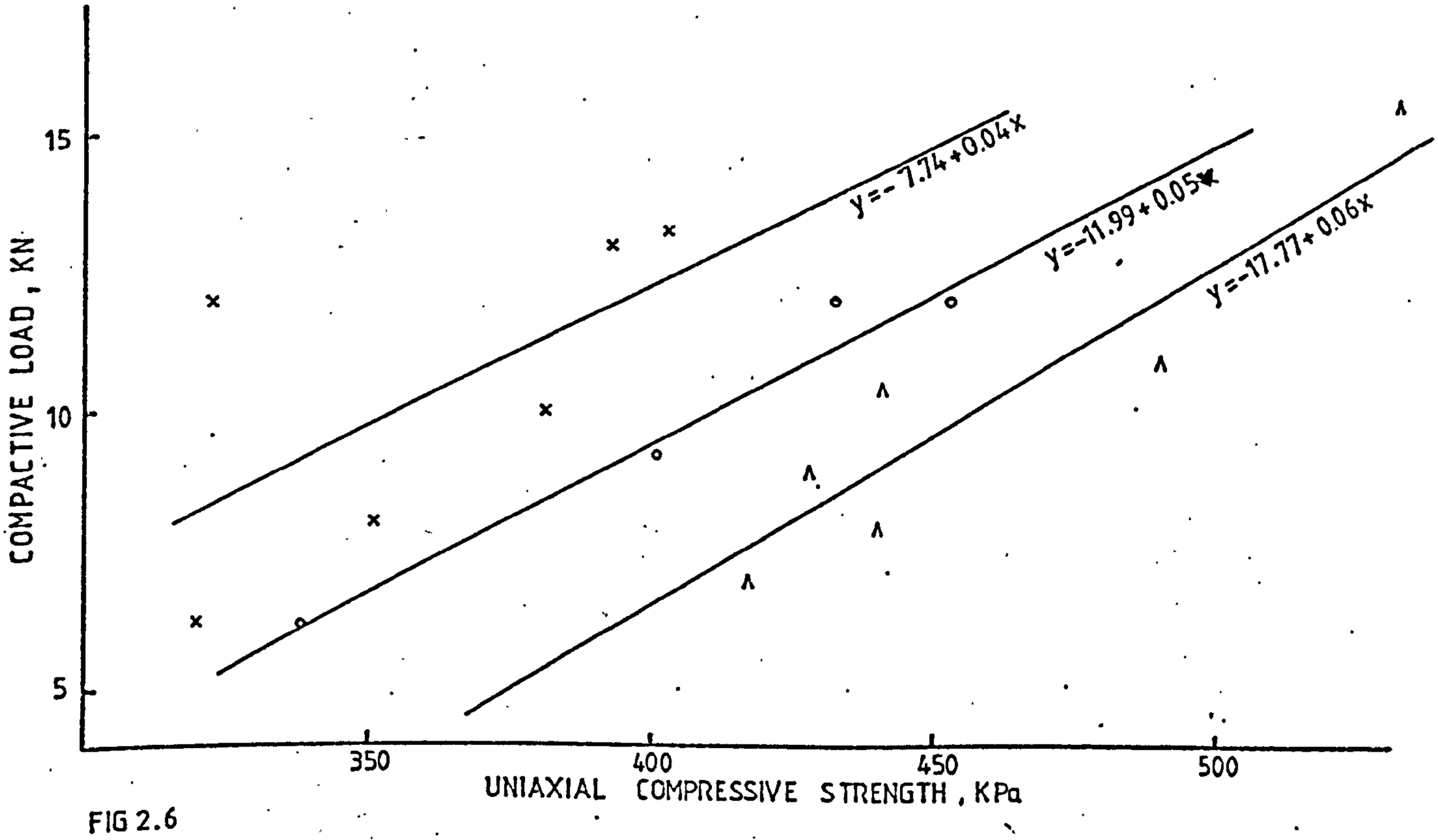
Curing time
2 Days
4 Days
y=-7.74+0.04x
y=-11.99+0.05x
y=-17.77+0.06x
COMPACTIVE LOAD, KN
15
10
5
350
400
450
500
UNIAXIAL COMPRESSIVE STRENGTH, KPa

FIG 2.6

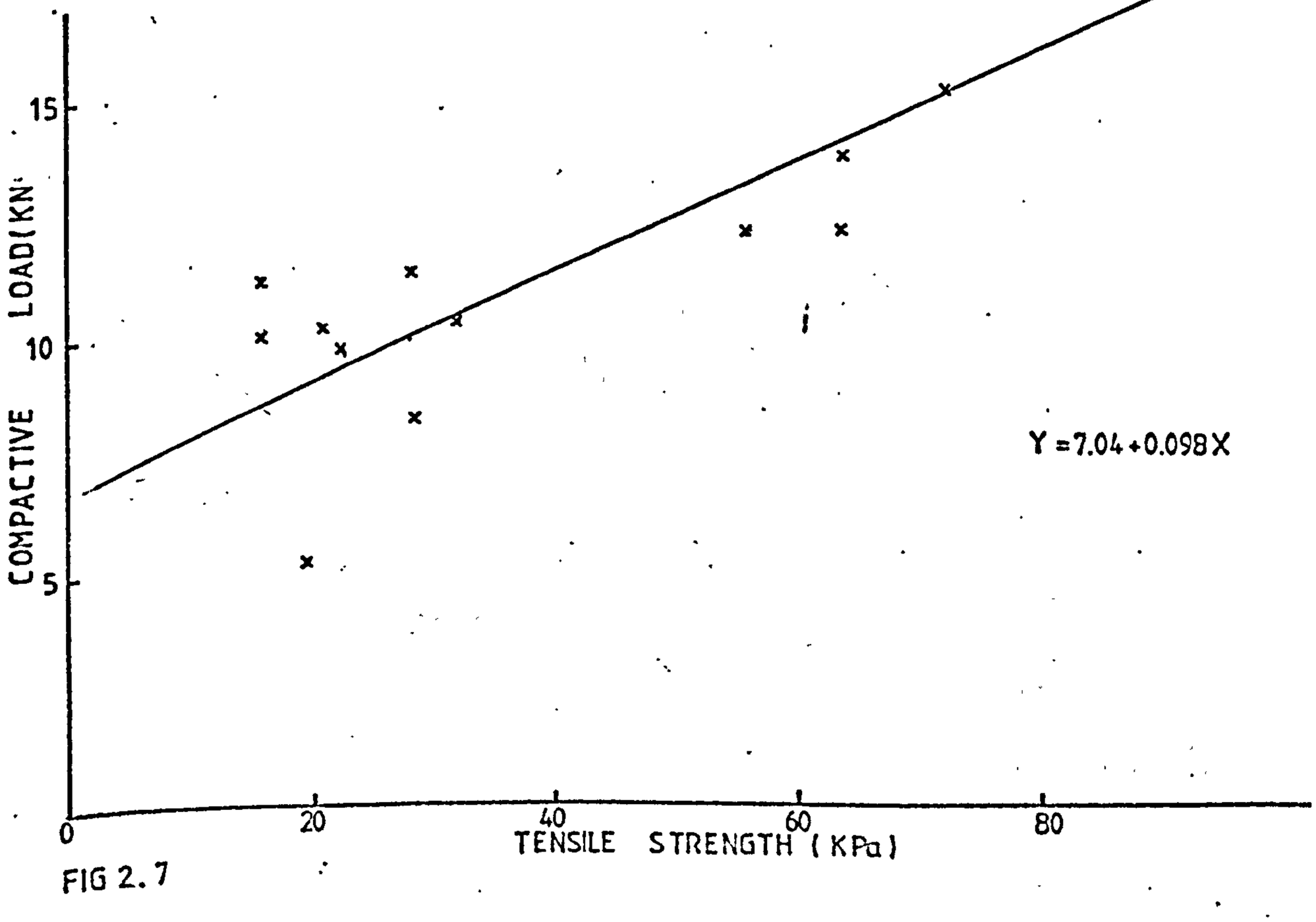
LOAD(KN
COMPACTIVE
15
10
5
0
20
40
60
80
TENSILE STRENGTH (KPa)
Y =7.04+0.098X

FIG 2.7

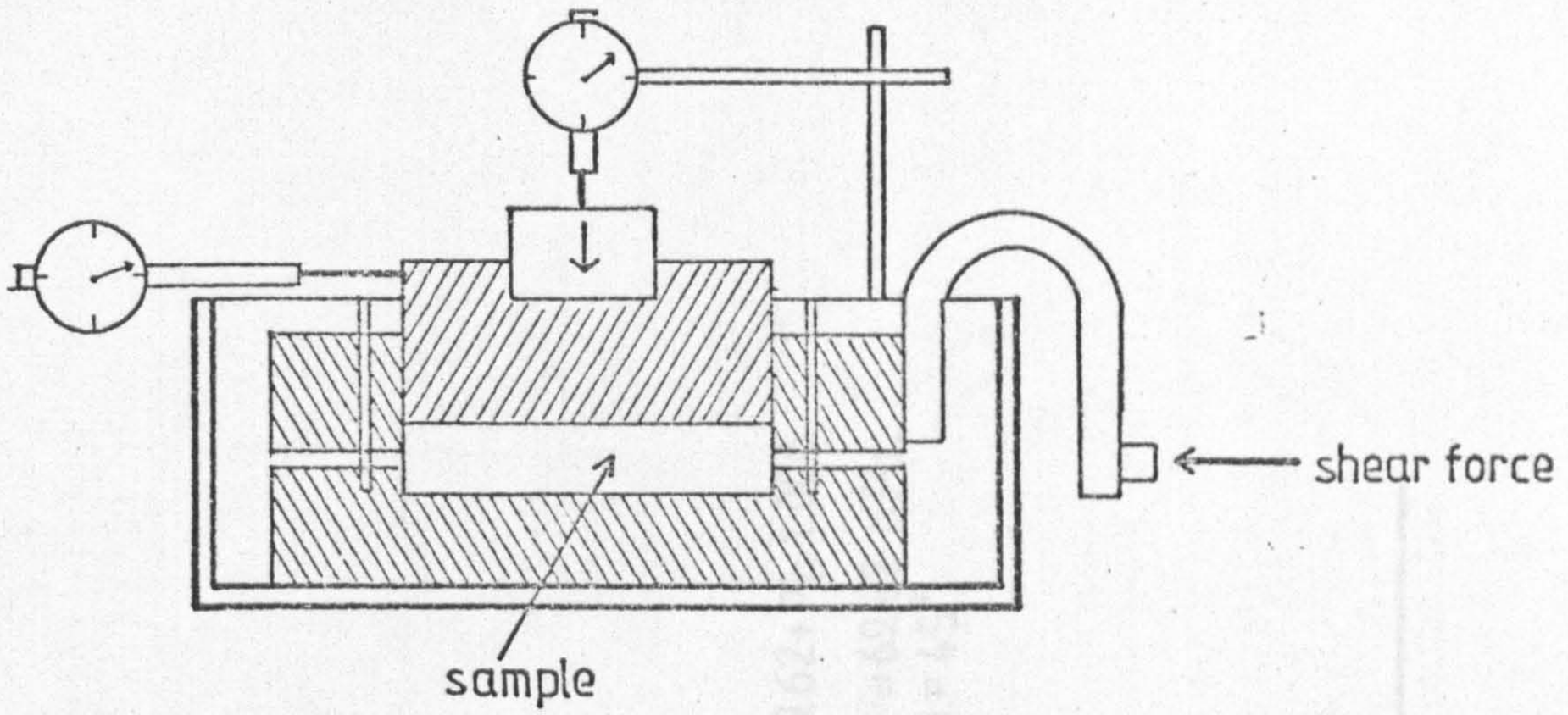

FIG 2.9 DETAILS OF SHEAR BOX

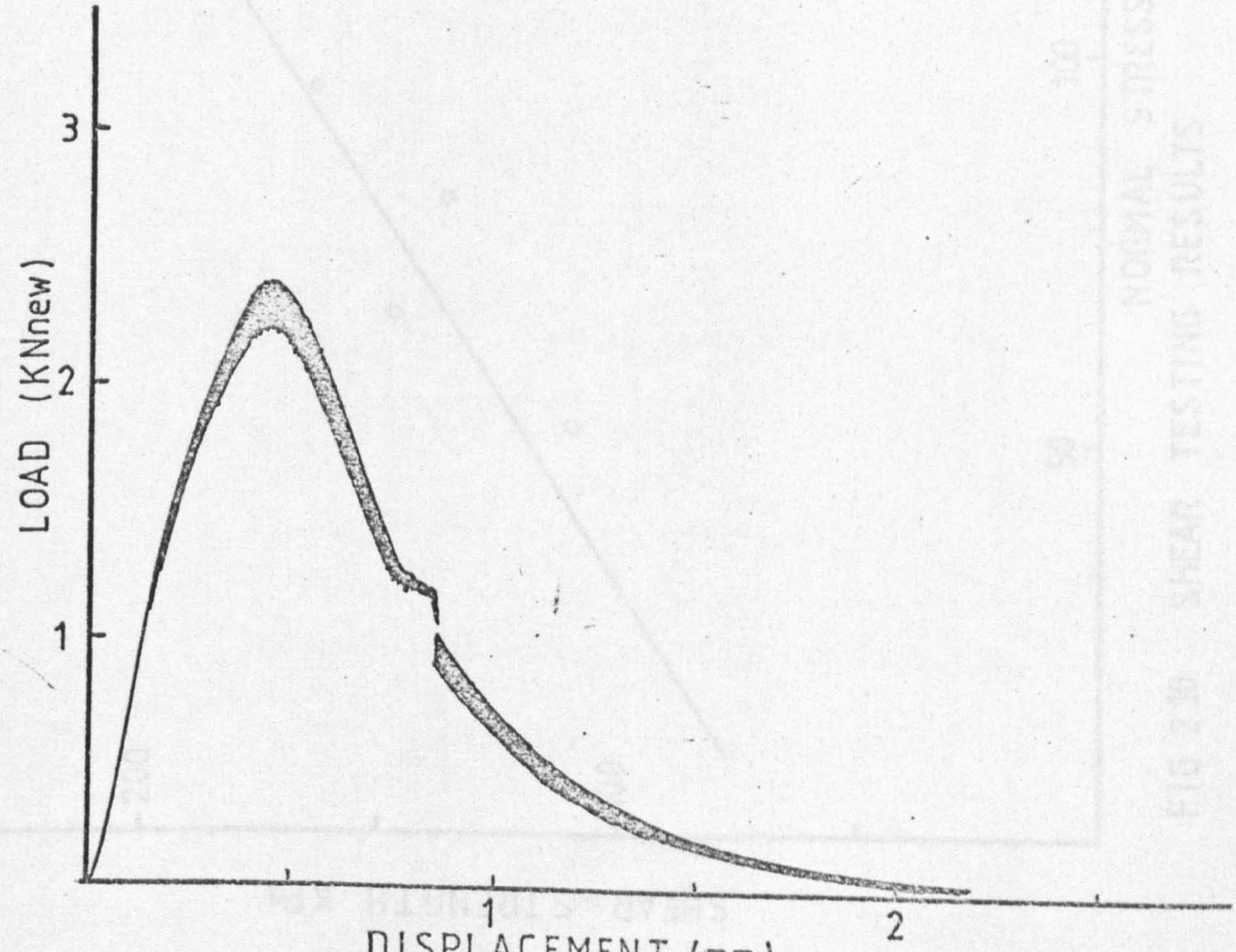

FIG 2.8 SERVO CONTROLLED TESTING OF MARL

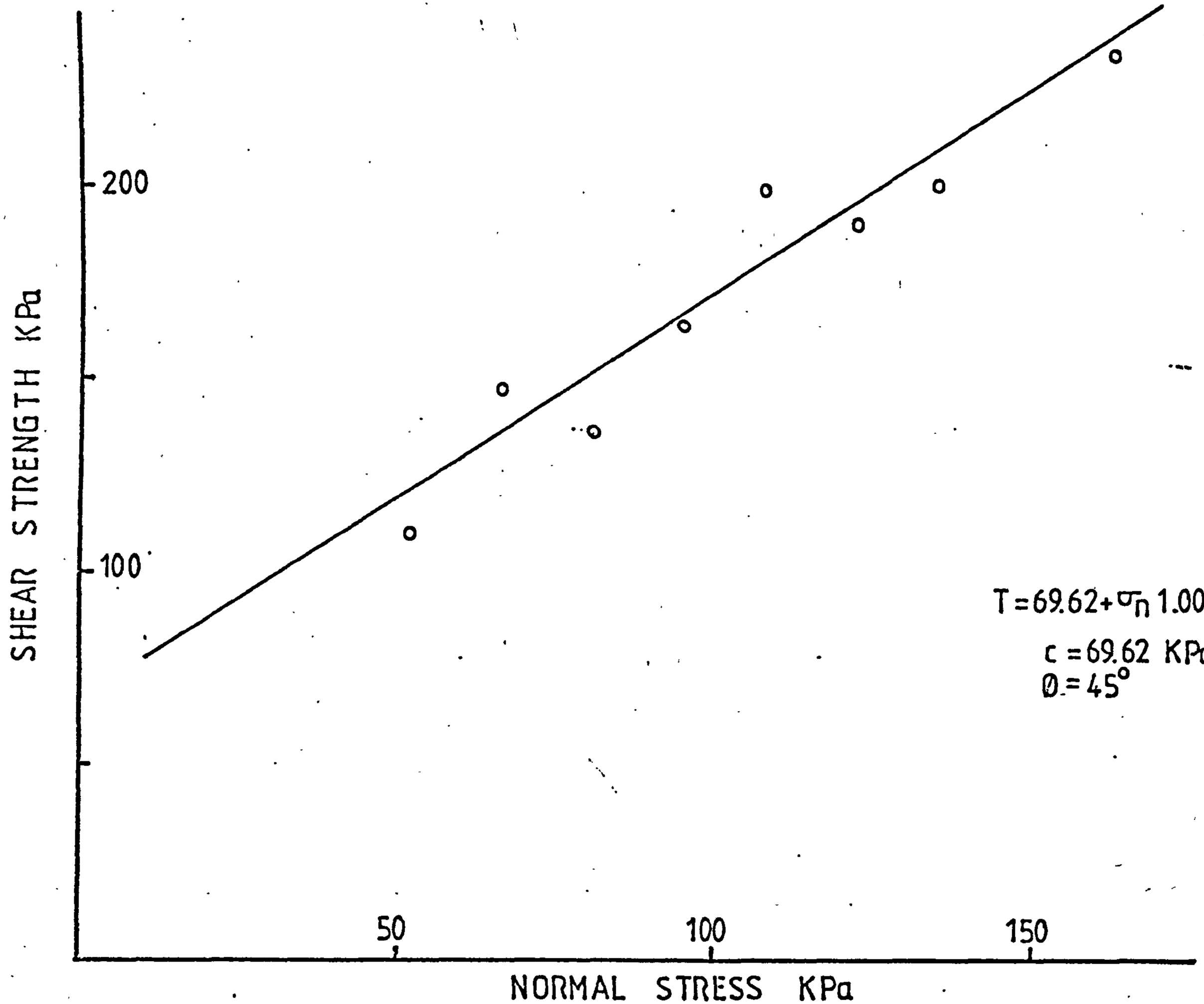

FIG 2.10 SHEAR TESTING RESULTS

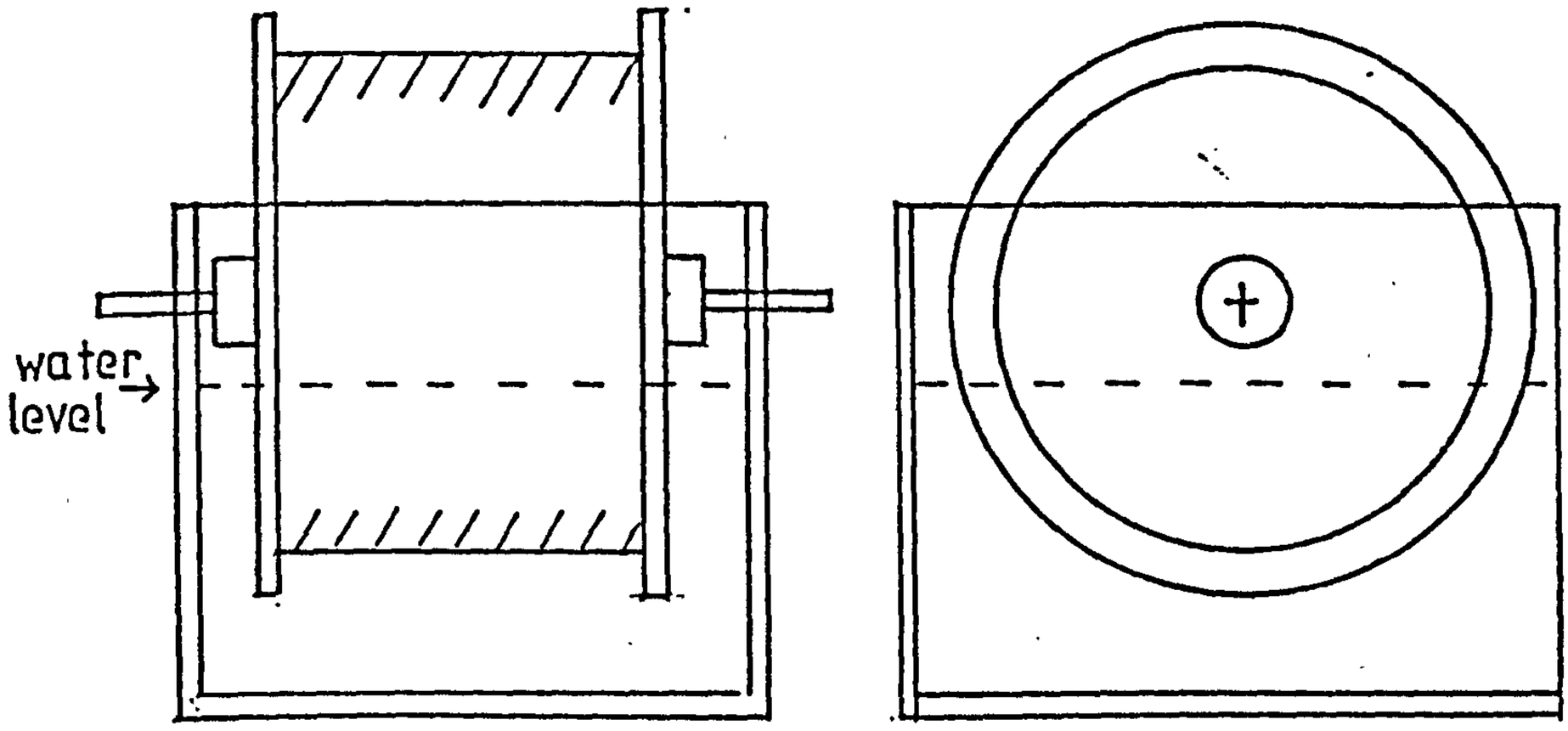

FIG 2.11 SLAKE DURABILITY TEST EQUIPMENT

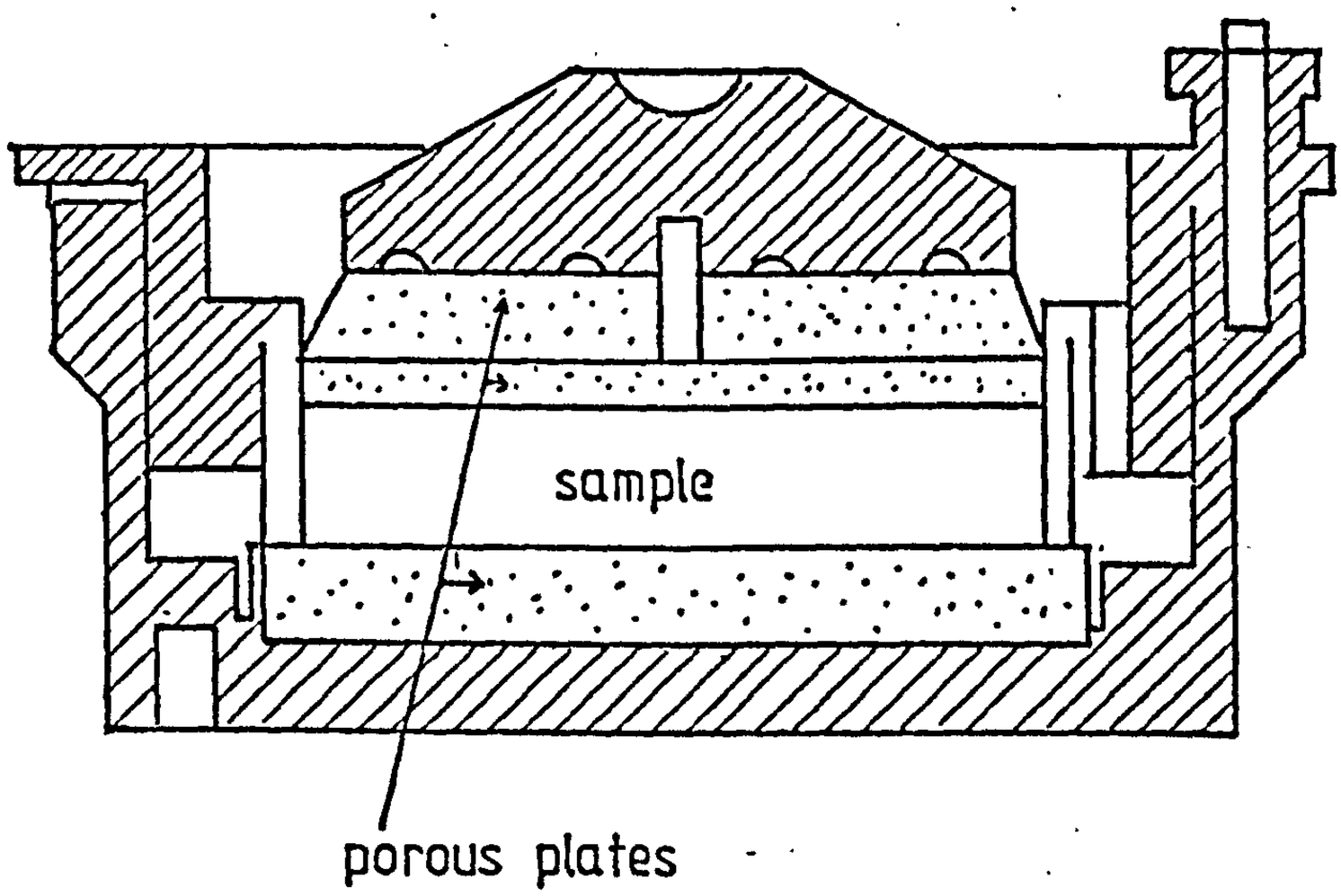

FIG 2.12 SWELLING TEST EQUIPMENT

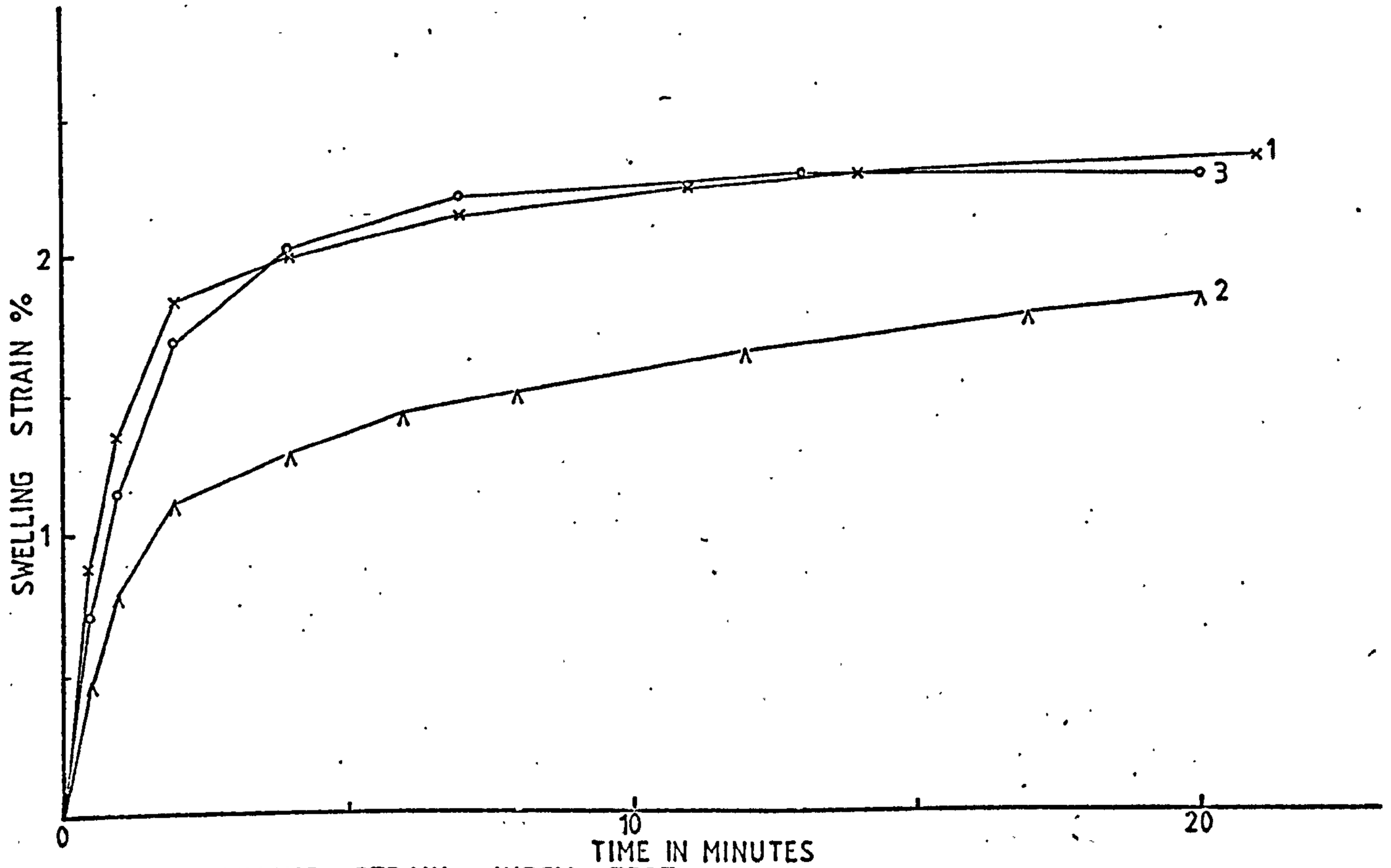

FIG 2.13 SWELLING STRAIN INDEX TEST

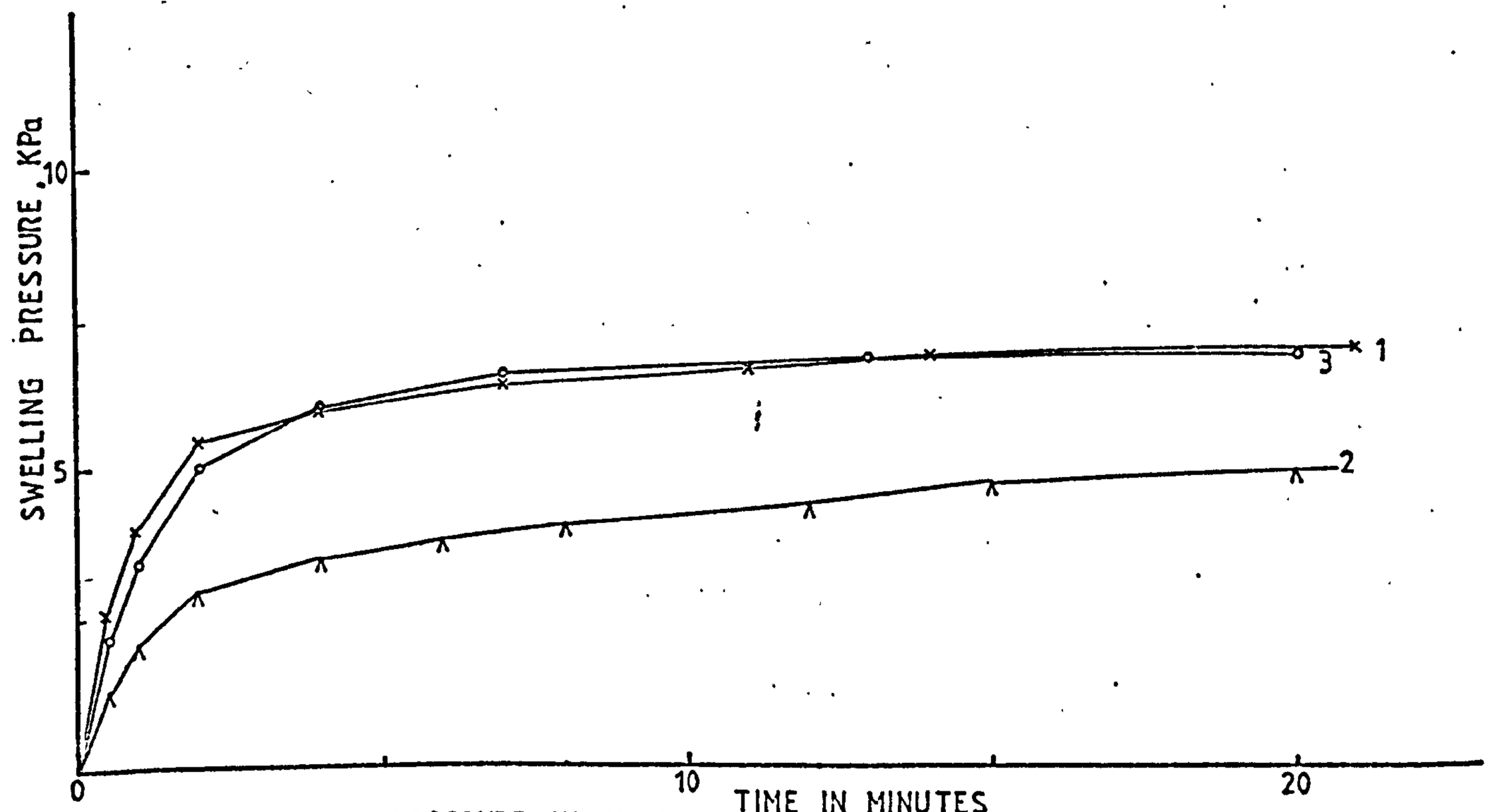

FIG 2.14 SWELLING PRESSURE INDEX TEST

TABLE 2.1 VARIABLES IN DIMENSIONAL ANALYSIS

	SYMBOL	DIMENSION
POISSON'S RATIO	V	1
STRAIN	E	1
YOUNG'S MODULUS	E	$ML^{-1}T^{-2}$
SHEAR STRENGTH	τ	$ML^{-1}T^{-2}$
COMPRESSIVE STRENGTH	C	$ML^{-1}T^{-2}$
TENSILE STRENGTH	T	$ML^{-1}T^{-2}$
HEIGHT OF MODEL	H	L
JOINT SPACING	J	L
SUBSIDENCE	S	L
WATER PRESSURE	P	$ML^{-1}T^{-2}$
UNIT WEIGHT	U	$ML^{-1}T^{-2}$

TABLE 2.2 DIMENSIONAL MATRIX

	V	B	E	τ	C	H	T	J	S	P	U
M	0	0	1	1	1	0	1	0	0	1	1
L	0	0	-1	-1	-1	1	-1	1	1	-1	-2
T	0	0	-2	-2	-2	0	-2	0	0	-2	-2

TABLE 2.3 PROPERTIES OF UPPER PERMIAN MARL AND MODEL MARL

PROPERTY	PROTOTYPE	SCALED VALUE	MODEL
COMPRESSIVE STR.	21.6 MPa	432 KPa	375.5 KPa
TENSILE STRENGTH	1.65 MPa	33 KPa	40.0 KPa
YOUNG'S MODULUS	308.7 MPa	6.17 MPa	3.3 MPa
ANGLE OF INTER.FRIC.	43°	43°	43°
COHESION	5.5 MPa	110.3 KPa	69.6 KPa
SLAKE DUR.INDEX	78.7 %	78.7 %	58.2 %
SWELLING STRAIN INDEX	2.1 %	2.1 %	2.3 %
SWELLING STRESS INDEX	7.8 KPa	7.8 KPa	6.5 KPa

TABLE 2.4 RELAVANT DIMENSIONS OF PROTOTYPE AND MODEL

	PROTOTYPE	MODEL
TOTAL HEIGHT	40.75 m	81.5 cm
TOTAL WIDTH	7.5 m	15.0 cm
TOTAL DEPTH	46.0 m	92.0 cm
THICK.OF UPPER SANDS	24.0 m	48.0 cm
THICK.OF MARL	13.0 m	26.0 cm
THICK.OF GYPSUM BEAM	0.75 m	1.5 cm
HEIGTH OF ROADWAYS	3.0 m	6.0 cm
WIDTH OF ROADWAYS	4.6 m	9.2 cm
PILLAR WIDTH	7.6 m	15.2 cm
PILLAR BREADTH	7.6 m	15.2 cm

3. MODEL TESTS

3.1 Situations Modelled

It is extremely difficult, if not impossible, to simulate an engineering structure in every aspect in detail. This is because many engineering prototypes are often too complex and thus their accurate scaling is not always possible within the limitations of resources available (time and money). Sometimes accurate information on the prototype parameters may not be available.

In such cases, the main interest should be to concentrate upon scaling the most essential and technically feasible parameters. If the model is over-simplified, the testing results may be invalidated. Therefore, a compromise between these two extremes without undue simplicity or impractical complexity is necessary.

In view of this, the immediate roof, i.e. the Upper Permian Marl, was simulated in the model with various degrees of crack intensity ranging from a solid layer to a layer having 12 cracks per 60cm. This was achieved by cutting the compacted marl block to square pieces of small size. It is believed that the range covered in the model tests is sufficient to represent two extreme cases (i.e. a fairly strong immediate roof and relatively incompetent immediate roof) as well as representing intermediate cases.

For simplicity, all cracks modelled were assumed to be vertical and equal in spacing.

In the first four models, a single roof beam failure was simulated. In the last model, three simultaneous roof beam failures were modelled in order to observe a likely interaction between the three failed zones.

3.2 Production of Marl Blocks for Modelling

In all tests with the exception of the second modelling, marl blocks were prepared following the procedure discussed in the foregoing sections. A square, steel, dismountable mould (Figure 2.5) was used in compaction on the 25-ton machine. The compacted marl blocks had dimensions of 15 x 15 x 10cm, although slight variations occurred in the thickness of the blocks. An average of 15 blocks were produced for each model.

In order to obtain small size square pieces, blocks of compacted marl were cut using a Clipper saw.

Immediately after each block was produced, the blocks were covered with cling-film in order to prevent excessive evaporation of water from the faces of the compacted marl blocks and hence preventing them from becoming relatively stiffer. This was considered particularly important as, during the preparation stage, long delays were unavoidable for numerous practical reasons.

Upon completion of the testing of each model, the marl, which often became a mass of mud, was allowed to dry in the air completely; it was then used for the next modelling.

Dry ground marl was mixed thoroughly with the required amount of water; thereafter, each block was compacted separately.

3.3 Model Testing I

The blocks of compacted marl (15 x 15 x 10cm) were placed on the timber components of the box which simulated the gypsum roof in such a way that the vertical crack frequency was approximately 1 crack per 10cm in the horizontal direction. The river sand was laid on top of the marl blocks, tapping by hand at required intervals.

Upon the introduction of water the front perspex started to bulge. After a while, due to excessive lateral load imposed by the sand, which became almost fluid, the front perspex burst. Hence the testing was discontinued.

Although this testing was not successful, a number of drawbacks, mostly associated with the box, were brought to light. These drawbacks can be summarised as follows:

(1) The model box should be stiffened in the lateral direction.

(2) The running down of the saturated sand in the gaps between the perspex plates and the marl blocks should be prevented.

(3) The deterioration of marl blocks from their side faces due to freedom of water at these faces must be reduced.

(4) The turbidity of water in the simulated rooms should be reduced to allow clearer observations.

(5) The water seepage through the edges of the box should be reduced.

3.4 Model Testing II

3.4.1 Preparations

Prior to building the second model, the drawbacks mentioned earlier had to be carefully considered and the necessary remedial measures taken.

In order to preclude the perspex plates from bulging, two timber runners were bolted onto the main frame approximately mid-height.

The rear faces of the marl blocks were covered with a thin layer of wax in order to minimise the premature disintegration of the blocks. Care was exercised in applying minimal amounts of wax because undesirable thickness of wax would strengthen the blocks adversely. A relatively thicker wax layer was applied along the slit to close the gap between the marl blocks and perspex plate in order to prevent the upper sand from flowing down through this slit.

The edges of the box were sealed off carefully to reduce water seepage from the box.

To minimise the murky appearance of the water during testing, a small quantity of flocculent, known commercially as 'Sedimax H.P.' (I.C.I.) was added to the water.

Due to failure of the first testing, the second modelling was carried out by arranging the blocks of marl in the same manner as in the previous test.

3.4.2 Testing and Observations

Approximately 4 hours after the water was introduced into the model, two dowels supporting the simulated roof beam were pulled and the roof was allowed to fail.

It is interesting to note that the form of the immediate roof failure was not a sudden inrush, but a slow and progressive slaking, although the marl blocks had been soaked for sufficiently long periods prior to initiation of roof beam failure.

The detachment of small flakes of marl from the roof could be clearly observed as the failed zone progressed upward. These flaked off particles formed a small heap at the base (Figure 3.1).

The speed of immediate roof deterioration was seen to decrease with time. This indicated that the structure was attaining a stable condition.

The type of failure zone in the marl was apparently an arch (Figure 3.2). The deterioration of the marl faces along the perspex plate may give a misleading impression about the failure pattern of the immediate roof as being 'V'-shaped (Figure 3.2), but it is clear that this is caused by the gap between the marl blocks and the perspex plates in which water can freely act. In fact, at the rear face, where the marl blocks had been covered with a thin layer of wax, this type of failure was evident to a much lesser extent.

About two hours later, the upward migration of the failure zone and slaking of marl layer appeared to have almost stopped. In order to

ensure that the progressive failure ended, observations were continued for two hours, then after the testing was discontinued.

The final type of failure zone was an arch with a height of 7.5cm from the simulated roof beam. When this was connected to the prototype, the height of the failure zone was found to be 3.75m. It is evidenced in Figure 3.2 that the failed material on the floor of the box has reached a level where it can provide additional side restraint to the marl despite the fact that the bulking factor of the marl is considerably lower, mainly because of the grain sizes of the particles.

It can be deduced that under simulated conditions, a roof beam failure is likely to induce an arch-shaped void migration in the immediate marl layer. The migration of void is terminated well before it reaches the marl-sand interface and bulking of the spalled material may choke the cavity.

3.5 Model Testing III

3.5.1 Preparations

In this testing, the fracture frequency in the simulated Upper Permian Marl was increased considerably in order to achieve least stable conditions in the immediate roof.

The compaction process was carried out as before and each ready-made marl block (15 x 15 x 10cm) was cut into 18 discrete cubes, each measuring approximately 5 x 5 x 5cm. A total of 120 cubes were obtained in this way.

In modelling fracture planes in a rock mass, tight packing of blocks is essential (Barton 1970, 1982). Therefore, care was exercised in packing the cubes of compacted marl tightly in the model box (Figure 3.3).

The joint frequency was 1 joint per 5cm in three directions, corresponding to 1 joint per 2.5m in the prototype.

It was believed that the blocky nature of marl layer in the model would enable the water to penetrate and deteriorate the simulated immediate roof freely, thus creating the potentially least stable condition.

3.5.2 Testing and Observations

The tap water was introduced to the model until the water level in the box reached the marl-sand intersurface. Meanwhile, sufficient quantities of water were also given to the upper sands.

In order to obtain highly saturated state of marl blocks, the model was immersed in water for at least two hours. Thereafter, two dowells were removed, leaving the roof unsupported. Two plastic bungs were tucked into the holes to prevent water from escaping.

It was observed that upon the removal of the support, none of the marl blocks had fallen out from the unsupported roof, but marl cubes had remained stable for a while, forming some sort of linear arch in the unsupported roof. It is likely that swelling of the marl provided a lateral thrust which, in turn, aided a temporarily stable position in the unsupported roof.

The slaking and deterioration of marl had started in the lower-central section of the formed linear arch. It was noticed that, with time, the cube in the left hand side was affected substantially more than the other one and, subsequently, the one in the right hand side dropped out from the roof.

The failure form was, again, an arch, but the development of a failed zone was largely controlled by the simulated fracture planes in the marl. The void migration was upward in a chimney-like manner, with little sideward expansion.

By the time the crown of the failure arch reached the second level of marl cubes, the collided particles on the floor had almost closed the initial gap up to the simulated gypsum roof. The pose angle was approximately 30^{o} from the floor. As the height of the pile increased, the consolidation of collided particles became apparent.

After approximately 4 hours it was noted that visible upward void migration had ended. The height of disintegrated zone in the front was about 13cm, whereas at the back, it was about 18cm. This discrepancy was related to the gap between the blocks and the perspex plate at the back where water could more freely disintegrate the marl blocks.

It is of importance to note that the spalled material was able to choke the cavity created by the void migration. This cannot be clearly seen in Figures 3.4 and 3.5, because the photographs were taken after the water had been removed from the model, which caused consolidation and lowering of the pile.

In Figures 3.6 and 3.7 the final shape of the immediate roof is shown. It is clear that the type of failure is an arch-progressed upward and is largely controlled by the crack orientation in the marl. The void migration ceased well before it reached the marl-sand interface. When the height of void migration in the model was converted to the prototype, the height of the failed zone was found to be 8.75m from the level of the gypsum beam.

Upon the dismantling of the model, inspection of marl cubes revealed that the water was able to penetrate into the marl blocks in the stressed zones (above the pillars) to a much lesser extent than those in relatively stress relieved zones (the crown). This, in fact, suggests that redistribution of stresses after the roof beam failure is also a controlling factor in the deterioration of marl above the simulated gypsum beam. The redistribution of stresses due to roof beam failure will be examined in the elastic range in Section Eight of this thesis.

3.6 Model Testing IV

3.6.1 Preparations

The objective in this testing is to observe the behaviour of relatively loose and saturated marl above the simulated roof beam in the event of a roof breakage.

Therefore, the usual compaction procedure was not followed in the preparation of Model IV. Instead, highly broken and saturated mass of marl was laid on the timber planks in the box and, by hand tapping, the mass of marl was loosely compacted inside the model box

The upper sand layers and metal weights were laid on the marl layer as before.

3.6.2 Testing and Observations

After the testing was commenced by pulling the dowells out, it was realised that the speed of disintegration of the marl was very much slower than in previous tests. When the degree of compaction performed in this test is considered, the speed of void migration is found to be surprisingly small.

By examining the model it was detected that a film of trapped air was acting as a protective cushion between the marl and the water underneath the arched roof. This phenomenon was not observed in the previous models.

It was obvious that since the saturated mass of marl was moulded into the box, most of the channels through which air would escape had been clogged up and upon the introduction of water some air was trapped in the roof.

The trapped air was released by drilling a tiny hole across the model and the experiment was continued.

However, the improvement in the speed of deterioration of the simulated immediate roof was not as significant as would be expected. It was decided, therefore, to keep the experiment running overnight.

The result was not much different next day. The ultimate height of the failed zone was measured and found to be 4.6cm, corresponding to

2.3m in the prototype (Figure 3.8). The shape of the failed zone was clearly an arch.

Relatively small void migration was obtained and this may be accounted for mainly by two reasons:

Firstly, it is known from the swelling stress and strain tests of marl (Section Two) that the rate of swelling strain and stress decreases with increasing moisture absorption of the marl. Having reached saturation level, the swelling properties are diminished with time. Hence, since marl mass was in a saturated state prior to testing, little or no swelling would be expected during testing. This, in turn, resulted in slowing down the failure process.

Secondly, due to direct moulding of the marl mass into the model box, elastic deformation of the perspex plates occurred, inevitably, to a certain extent. Therefore the mass of marl was provided with some lateral constraint which reduced the rate of deterioration effectively.

It is difficult to determine which factor has played a major role in the testing, although they both may be expected to prevail in the case of the prototype to some degree.

3.7 Model Testing V

3.7.1 Preparations

In the preceding models, a single roof beam failure was simulated and the resultant void migration was observed in the simulated Upper

Permian Marl, the competency of which was altered by modifying crack frequency and orientation. It is clearly demonstrated that, under the conditions modelled, upward migration of voids is stabilised well below marl-sand interface and the cavity underneath is largely filled by spalled material.

In this test, it was envisaged that three simultaneous roof beam failures would be modelled and the behaviour of simulated Upper Permian Marl would be observed.

For this purpose, 15 compacted marl blocks (15 x 15 x 10cm) were prepared as described in the previous section. Each block was then cut into 18 cubes (5 x 5 x 5) using a Clipper saw. A total of 270 discrete cubes were obtained in this way for the construction of the model.

The crack frequency was in all three directions 1 crack per 5cm, corresponding to 1 crack per 2.5m in the prototype. This arrangement was considered to be a pessimistic representation of an incompetent section of the Upper Permian Marl.

A new set of timber planks to simulate gypsum pillars and collapsible simulated roof beams were made, together with a sufficient number of dowells.

In the models tested previously it was not possible to observe any subsidence on the surface. On this basis it was decided to force a cavity to fail if no failure took place naturally. This would provide an opportunity of evaluating the extent of subsidence on the surface.

A fork-like metal rod was constructed in order to exert force on the central cavity at the end of testing. The lower end of the rod was placed across the central crack inside the sand layers.

To enable observation of subsidence at the surface a number of white-coloured sand layers were laid in the box. The model prior to testing can be seen in Figure 3.9.

3.7.2 Testing and Observations

Having initiated three simulataneous roof beam failures by removing the supporting dowells, the slaking and flaking of marl cubes began to progress. The failure of the roof by slipping of individual members was not observed.

During the initial stages, arching action was predominant at the mid-lower section of the unsupported openings where the least stressed region would be expected (see Section Seven).

The heights of failed zones were slightly different from each other possibly because of variation in the degree of tightness of packing.

When the height of voids were approximately 10cm the common abutments appeared to have been slightly affected, particularly at the rear.

The development of upward deterioration of marl took the form of an arch above each individual opening with slight interactions between each zone (Figures 3.10, 3.11 and 3.12). It is noticeable that interactions between the adjacent failure zones are confined to the

outer surfaces of common abutments. This surface deterioration is purely related to the gap between the marl blocks and the perspex plate, where water can more freely disintegrate the surface of marl blocks. In fact, at the front face (Figure 3.10), where the marl blocks were tightly packed against the perspex sheet, surface deterioration was not evident.

The model testing was continued overnight. Due to excessive water seepage, frequent replenishment of water, and constant care, were required.

Visible slaking of marl pieces and upward progress of voids ceased almost completely after two days.

The final appearance was rather murky and there was an indication that undercutting of common abutments had not developed to the extent that an overall collapse would be imminent, despite contradictory appearance. In fact, no disturbance of overlying sands took place apart from some settlement due to consolidation of sands.

At the rear side, the first four rows of marl cubes appeared to have been badly affected, while the common abutments were still able to carry the overlying weights. On the other hand, at the front face, only the first two rows of marl cubes above the unsupported roof had failed. The common abutments were undisturbed with the exception of slight undercuts which were possibly created by the circulation of water.

The model was kept in the water for another day to see whether any visible deterioration took place with time. This did not seem to have altered the situation significantly. On this basis it was decided to induce an artificial roof breakage.

The fork-like rod which had already been placed over the central opening was knocked from the top in order to induce an upbreak in the simulated marl. The successive stages of this failure can be seen in Figures 3.13, 3.14, 3.15 and 3.16. The lowering of sand beds above the central void can also be clearly seen in these Figures.

The resulting subsidence on the surface was very shallow and flat-bottomed. A subsidence profile, constructed from the photographs taken, is set out in Figure 3.17. The angle of draw is approximately 59^{o} from the horizontal. Probably the most important observation is that even if the void is migrated to the level of marl-sand interface, due to the loose nature of the overlying sands, the disturbance on the surface is not likely to be in the form of a crown hole or a 'plump' hole, but rather in a shallow-bottomed settlement. Since the cavity created in the marl is largely filled with spalled marl pieces (despite low bulking) it is highly unlikely that the upper quick sands can find access to the working zone. This is further substantiated by the inspection of the model after the testing was completed (Figures 3.18 and 3.19).

In Figures 3.18 and 3.19, the induced deformation of marl cubes over the central zone can be seen clearly. Tension cracks around the subsurface subsidence trough in the marl are typical examples of an induced upbreak.

Figures 3.20 and 3.21 show the condition of simulated Upper Permian marl layer upon the removal of the first row and the second row of marl cubes. It is interesting to note that the common abutments remained virtually unaffected. This is attributed to the fact that the spalled material has choked the cavity substantially thus providing lateral thrust and to the fact that the common abutments have been highly stressed thus preventing penetration of water. The stress redistribution due to roof beam failure in the central opening will be discussed in Section Eight of this thesis.

3.8 Results of the Modelling Studies

The physical modelling is a valuable means of scientific research from which the mining engineer can benefit a great deal when predictions concerning the structural behaviour of rocks are to be made. The degree of realism is dependent upon the similitude achieved between the prototype and the model with respect to material properties.

Modelling studies undertaken by the author are intended to produce evidence on the likely behaviour of a rather incompetent section of the strata overlying gypsum deposits at Sherburn in the event of a roof beam failure after abandonment of the mine.

3.8.1 Modelling Material

In order to achieve a reliable simulation of anticipated prototype behaviour, a model material which would exhibit slaking and swelling properties in water similar to those of the prototype material, and at the same time whose mechanical properties could be varied over a range required by the similitude law was a prerequisite.

A technique for the production of model material from the prototype material utilising the method of static compaction of soils has been developed. Various tests conducted on the produced model material indicated that the material produced could be used satisfactorily as a substitute material for the Upper Permian Marl.

3.8.2 Model Box

The performance of the test-box was not completely trouble free during the testing programme. Because of the involvement of large quantities of water in the testing, constant attention was necessary to the reduction of water seepage through the edges and joints.

In future modelling studies of this nature, it is advisable that precautions be taken in sealing off the possible leakage zones in the box or, alternatively, to construct a steel-framed box.

3.8.3 Model Tests

The model tests carried out provided useful information on the progress of a failure zone in a strata with varying degrees of weakness planes. The main points of practical importance are listed below:

(1) The failure of the immediate roof was not a sudden occurrence, but a gradual slaking and spalling in all of the situations considered.

(2) A draw channel which would be observed in a cohesionless medium was not observed in the models tested.

(3) Arching with progressive upward migration was evident in the tests conducted.

(4) Void migration ceased naturally well below the sand-marl interface in all cases, but the ultimate height of upbreak was dependent upon the degree of incompetency of the immediate roof (Table 3.1).

(5) The development of void migration was effectively controlled by the weakness zones present in the immediate roof strata.

(6) The pose angle of the spalled material was approximately 30^{o} in all cases (Table 3.1).

(7) The spalled material was able to choke the cavity to a large extent, despite its low bulking factor.

(8) Deterioration of water was effective, particularly at stress relieved zones.

(9) Trapped air in the crown served as a protective cushion, thus reducing the speed of slaking.

(10) In the case of three simultaneous roof beam failures, the common abutments above the simulated pillars were able to stand up and carry the overburden load until a stable position was obtained.

(11) When the migrating void reached the sand-marl interface, the overlying sands subsided, creating a shallow, flat-bottomed subsidence on the surface.

(12) Since the cavity was filled largely with the spalled material flowing sands could not gain access to the simulated working zone.

3.9 Appraisal of Results

It appears that in places where the Upper Permian Marl overlying the gypsum seam is not heavily disturbed by the fracture planes and weakness zones this strata may be sufficiently strong to withstand to the full overburden load imposed and also the deteriorating effect of water. The void migration may be arrested before it reaches the marl-sand interface and a stable condition established.

In places where the Upper Permian Marl is in a badly fractured state, the void migration may breach the marl-sand interface in a manner controlled by the orientation and spacing of the joints. This type of roof collapse is associated with void migration and has been exemplified by many researchers (Wardell and Wood 1965; Bell 1975, 1980; Lutton 1971; Littlejohn 1979; and Attewell and Farmer 1976).

The occurrence of such a process is likely to take place at a slow rate because of the cohesive nature of the Upper Permian Marl.

Since the fallen material loosely fills the cavity created substantially, the flow of quick sands into the remaining gap will be minimal and hence resultant settlement on the surface will be correspondingly minimal.

However, model testing and experience (Price et al. 1969; and Littlejohn 1979), indicate that a minimal disturbance occurring in the subsurface (at the marl-sand interface) is likely to be accentuated on the surface by the loose water-bearing, essentially non-cohesive deposits such as quick sands, silts, etc. Thus the ultimate disturbance on the surface due to a breakdown in the roof beam is reflected as a shallow, flat-bottomed, well spread subsidence trough.

If a multiple roof beam failure takes place simultaneously at a similar section of Upper Permian Marl it is likely that the individual subsidence troughs will overlap and the combined effect will be a wider, flat-bottomed subsidence trough on the surface.

It must be pointed out that any disturbance on the surface in the form of crown holes, plump holes or humps, as observed by various authors, mainly over the old coal workings (Orchard 1969; Bell 1975; and Littlejohn 1979), is highly unlikely to occur over the gypsum deposits at Sherburn under the conditions considered in the modelling studies.

* * *

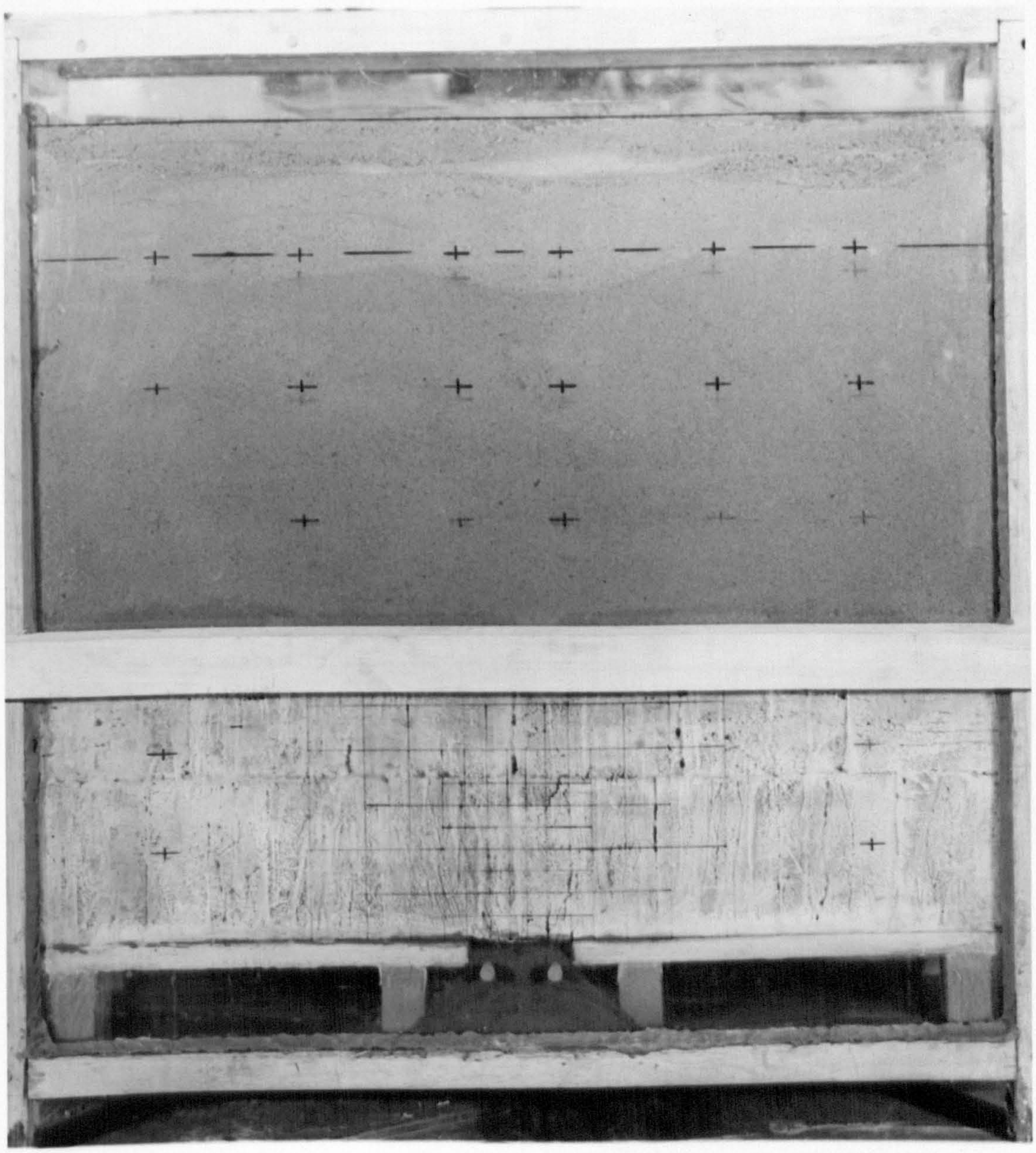

FIG 3.1 Model 1

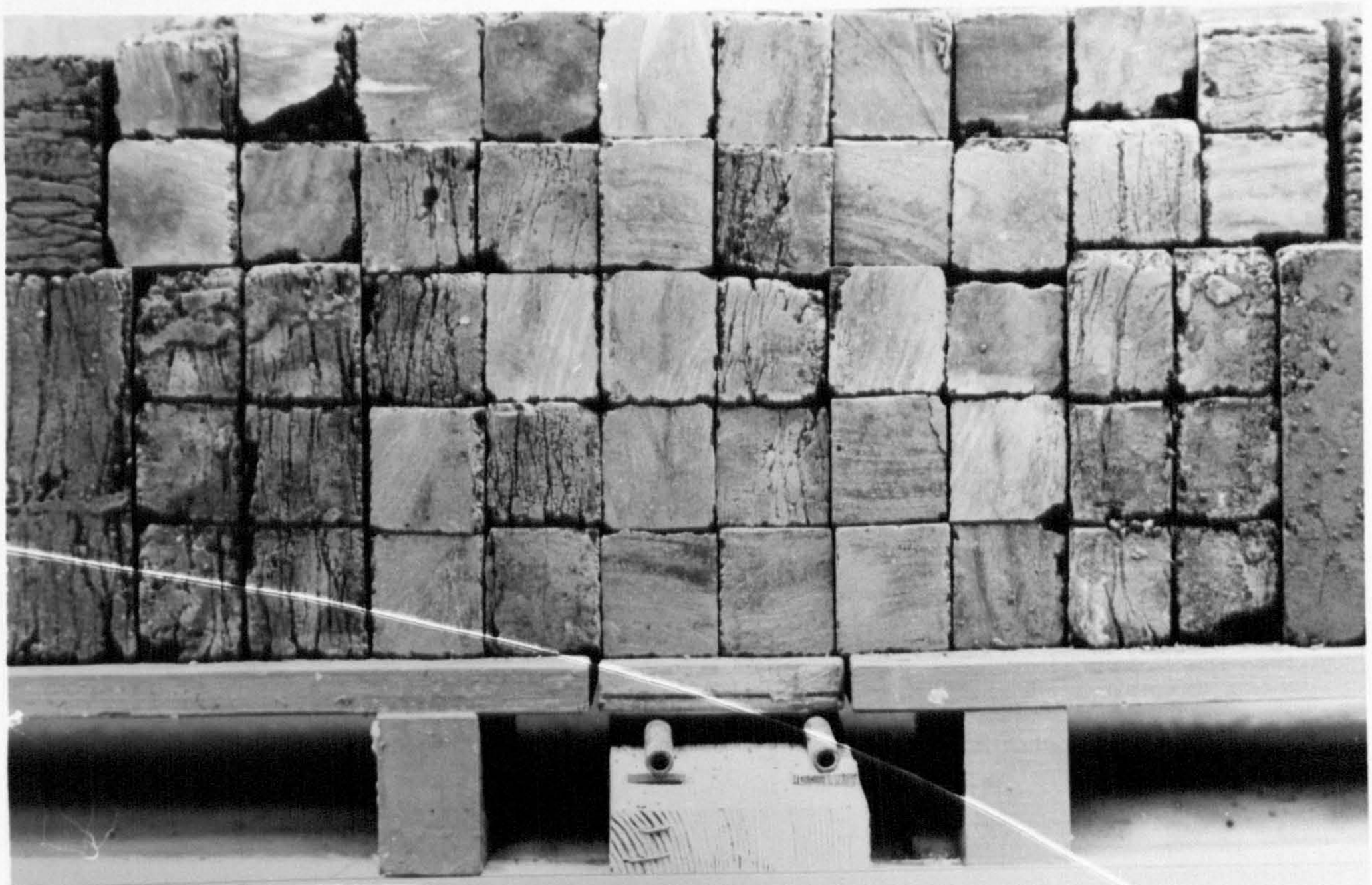

FIG. 3.2 Model 3

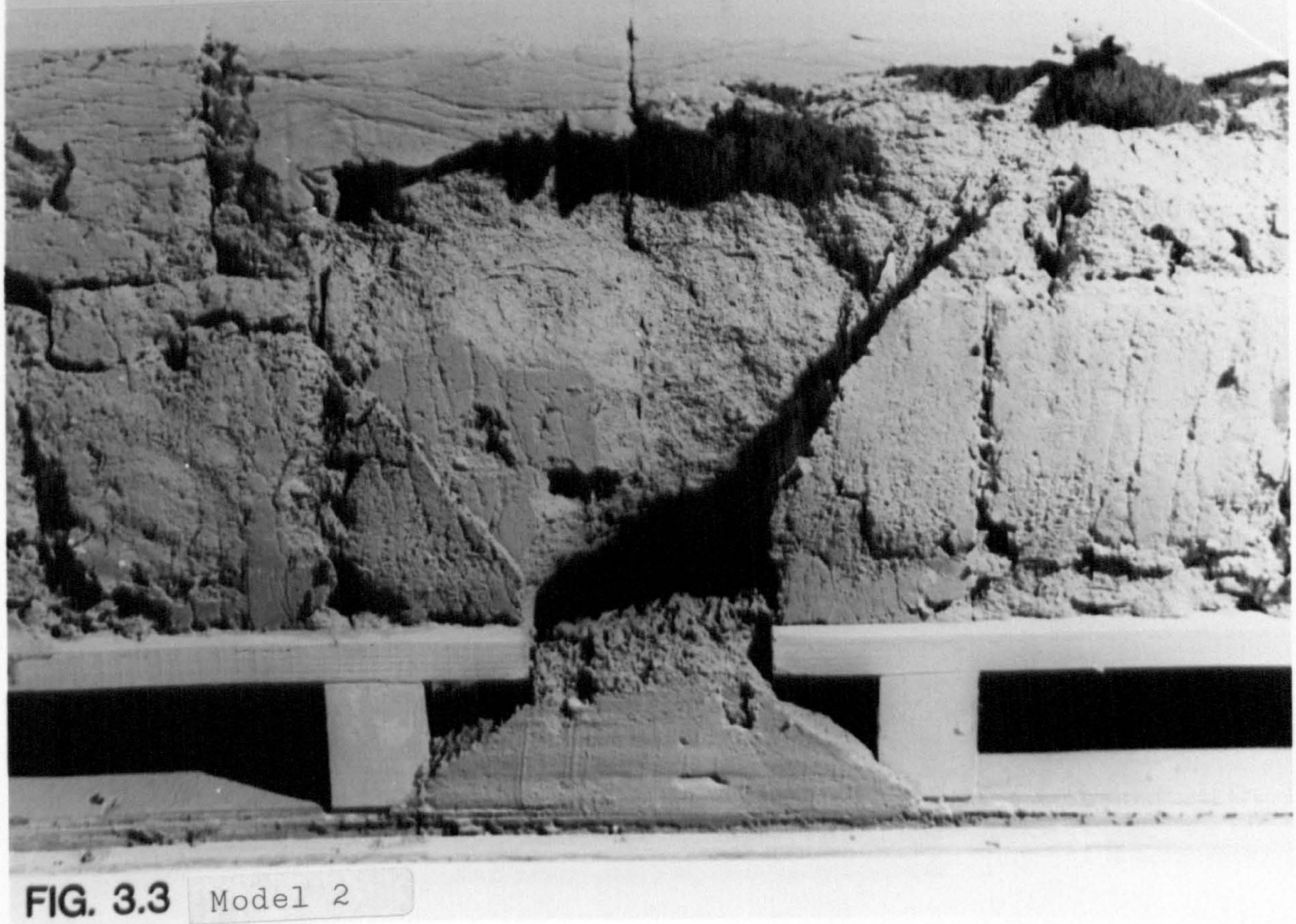

FIG. 3.3 Model 2

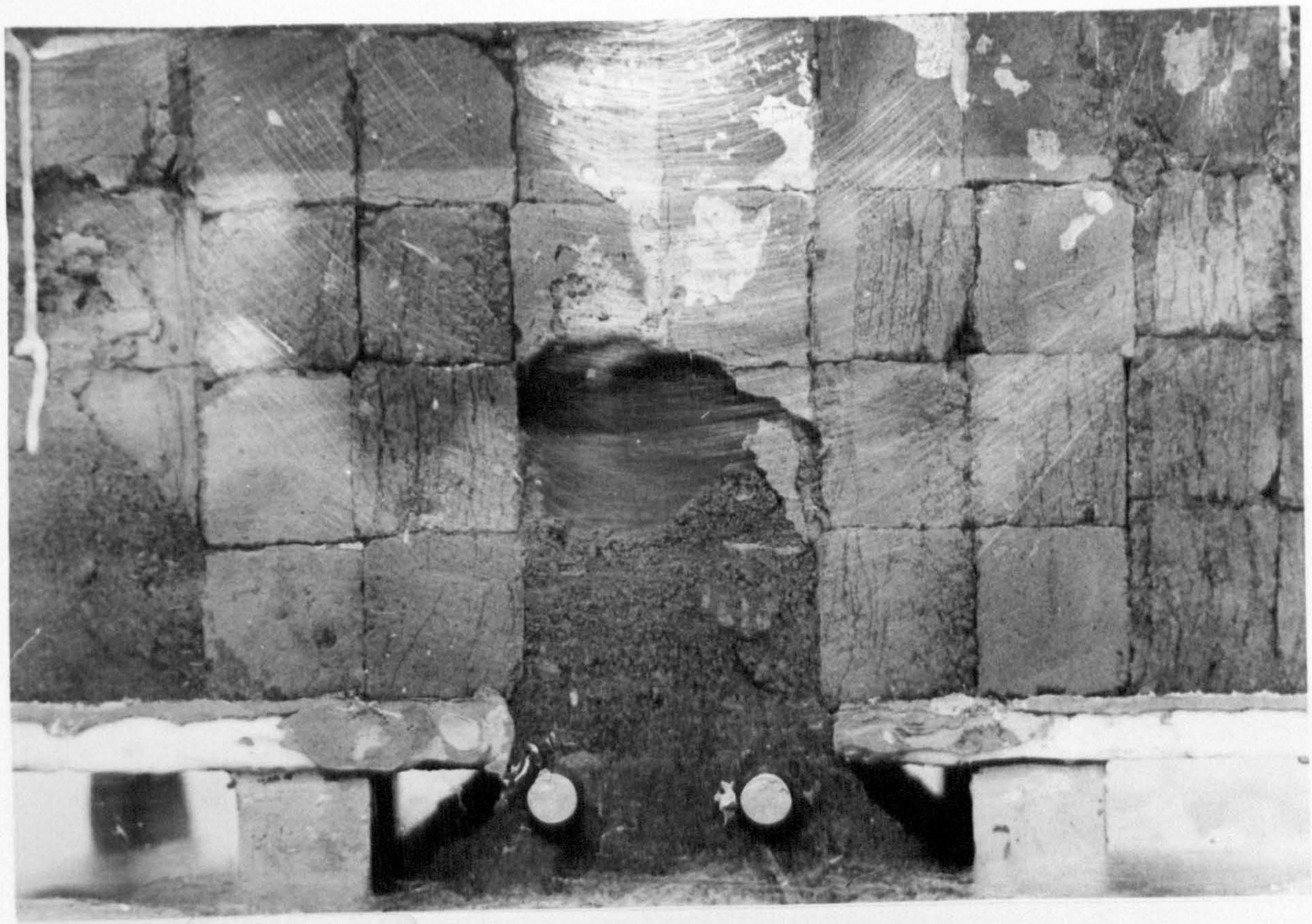

FIG. 3.4 Model 3

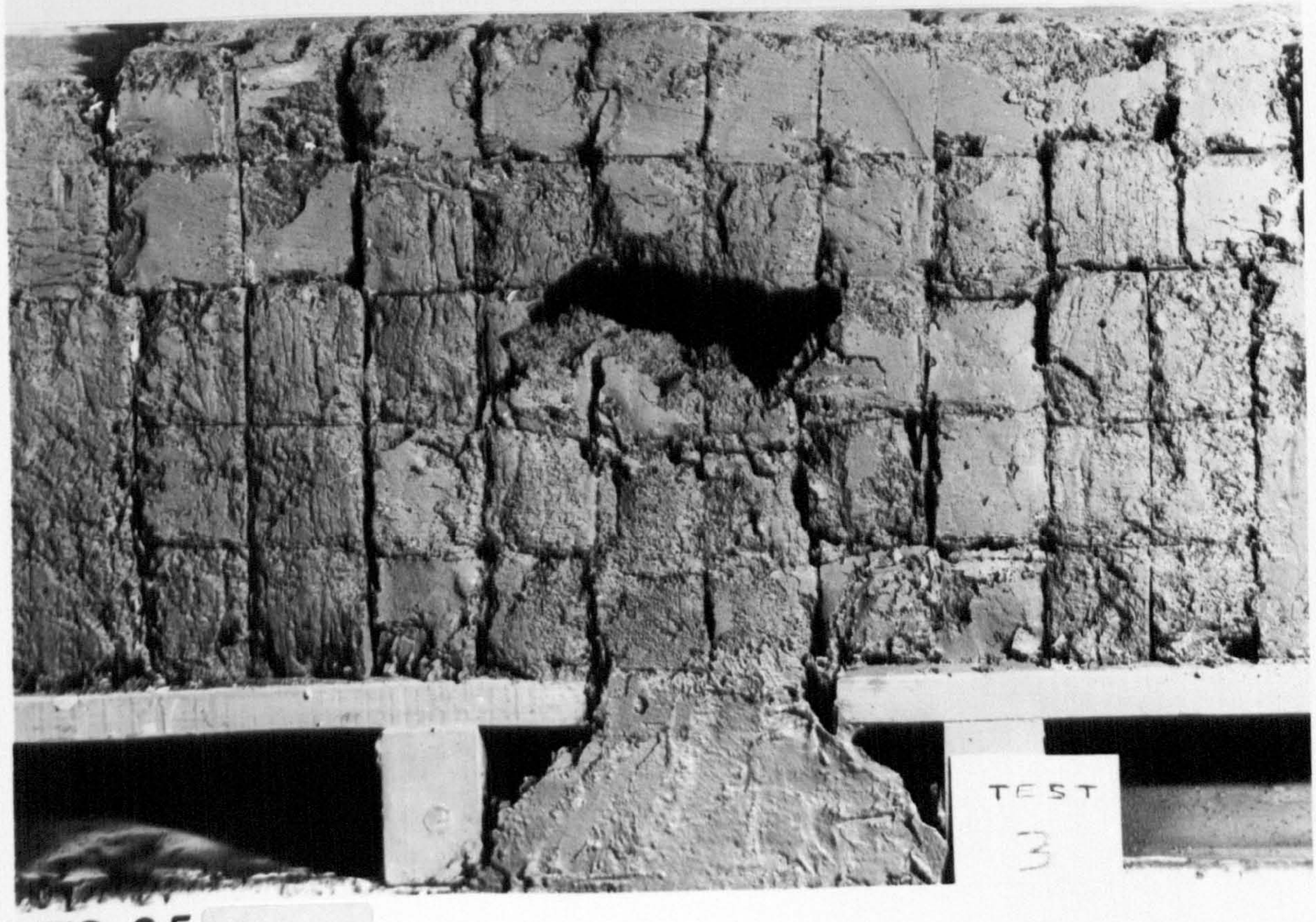

FIG. 3.5 Model 3

FIG. 3.6 Model 3

FIG. 3.7 Model 3

FIG. 3.8 Model 4

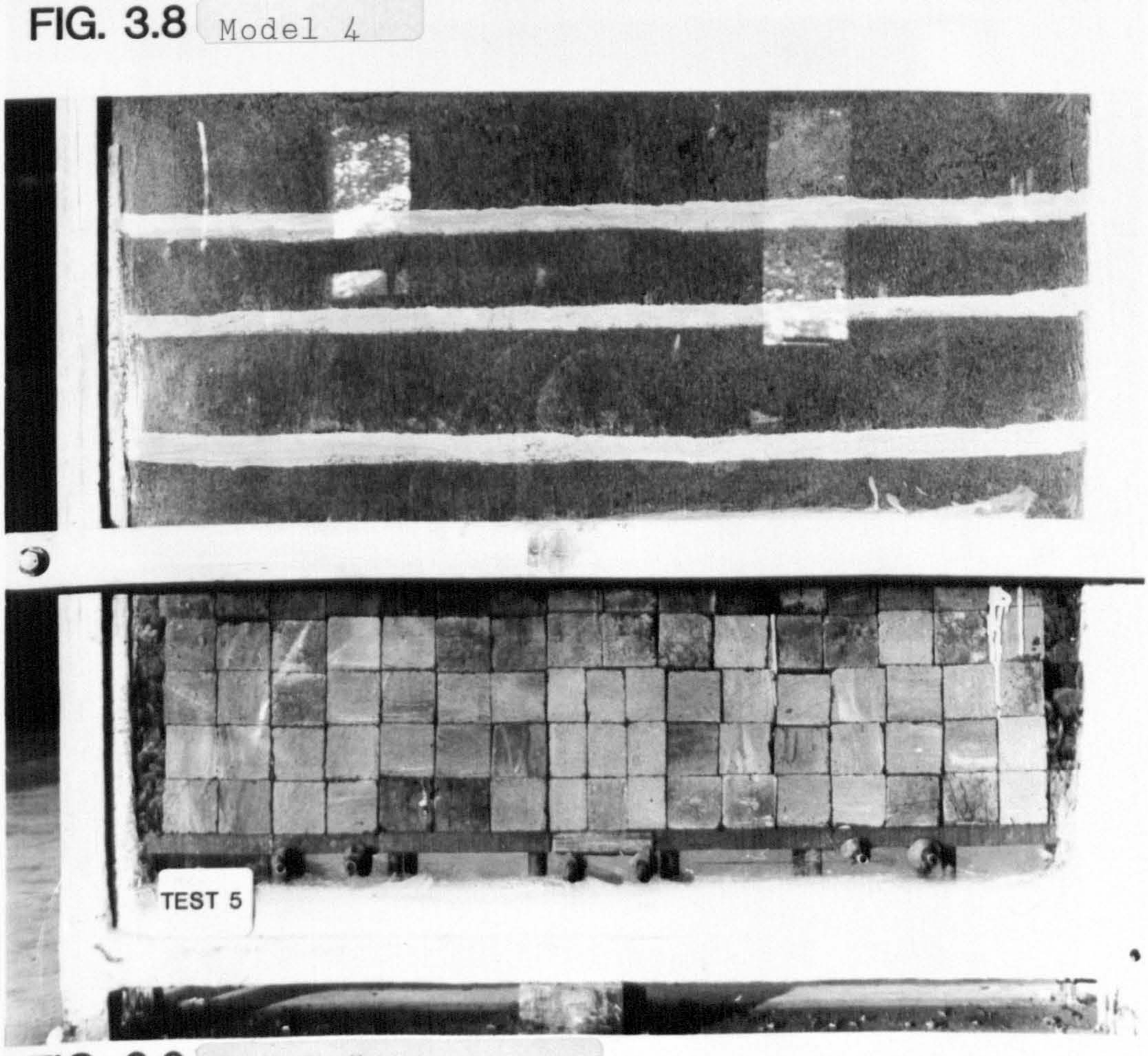

FIG. 3.9 Model 5

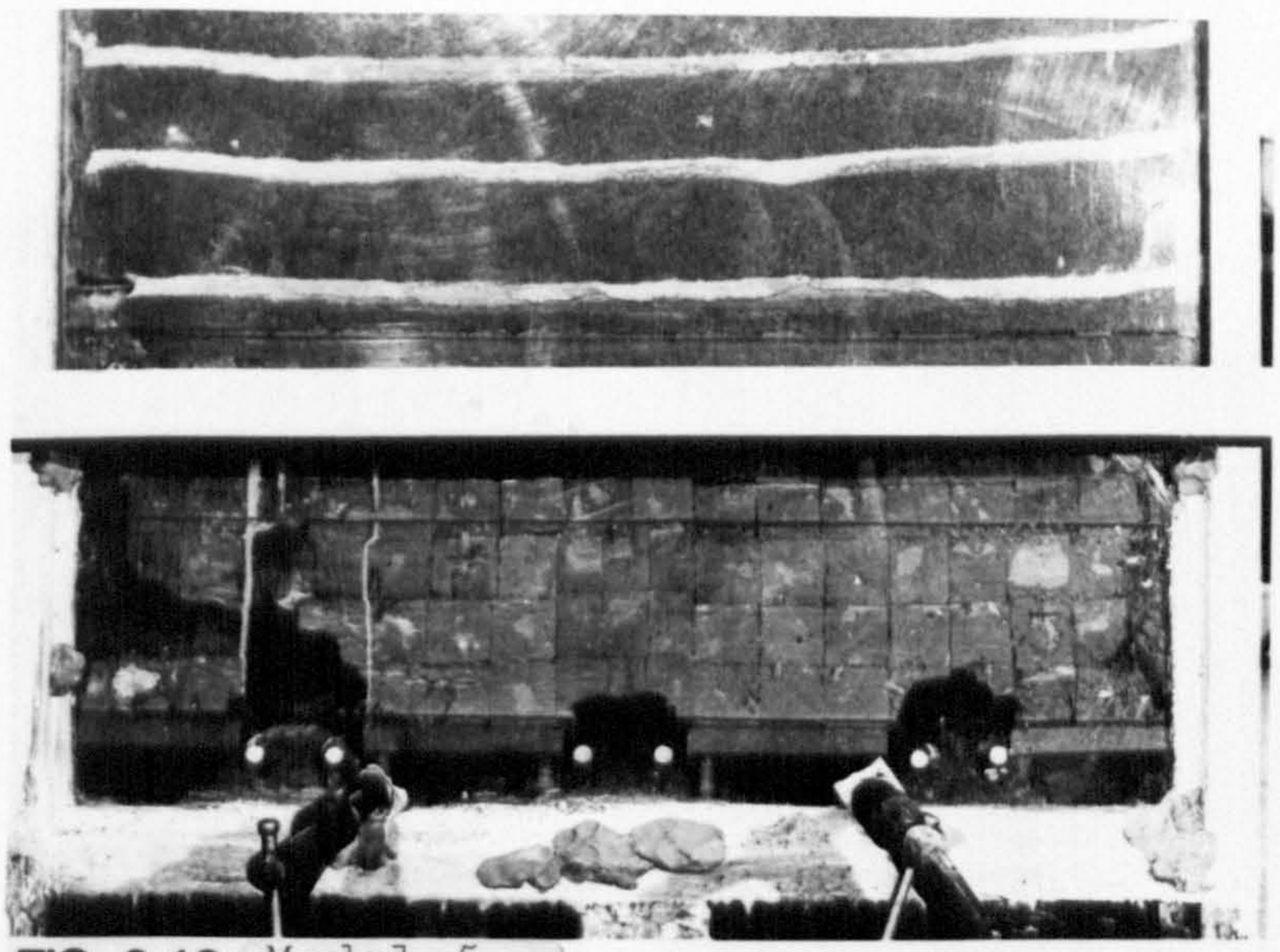

FIG. 3.10 Model 5

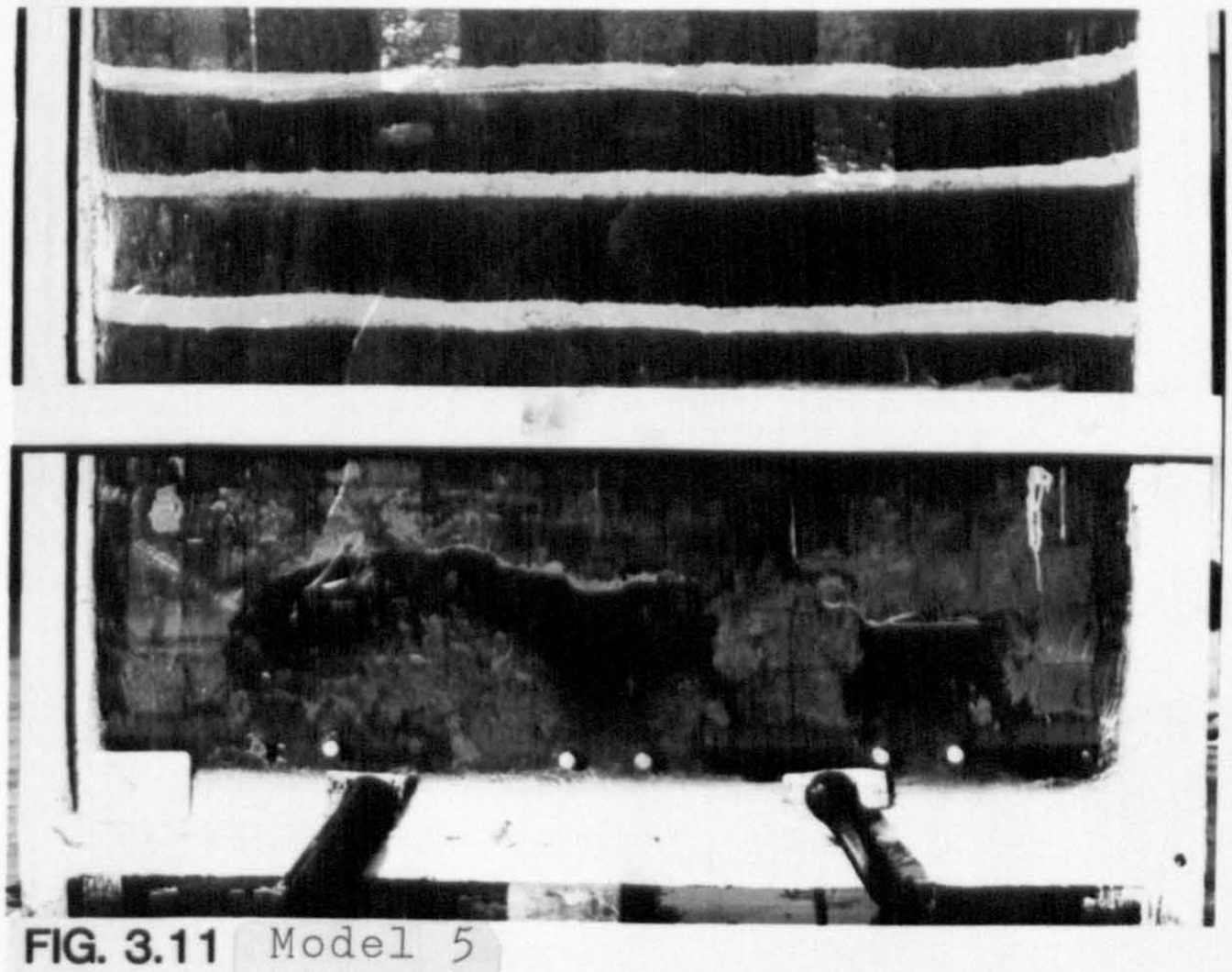

FIG. 3.11 Model 5

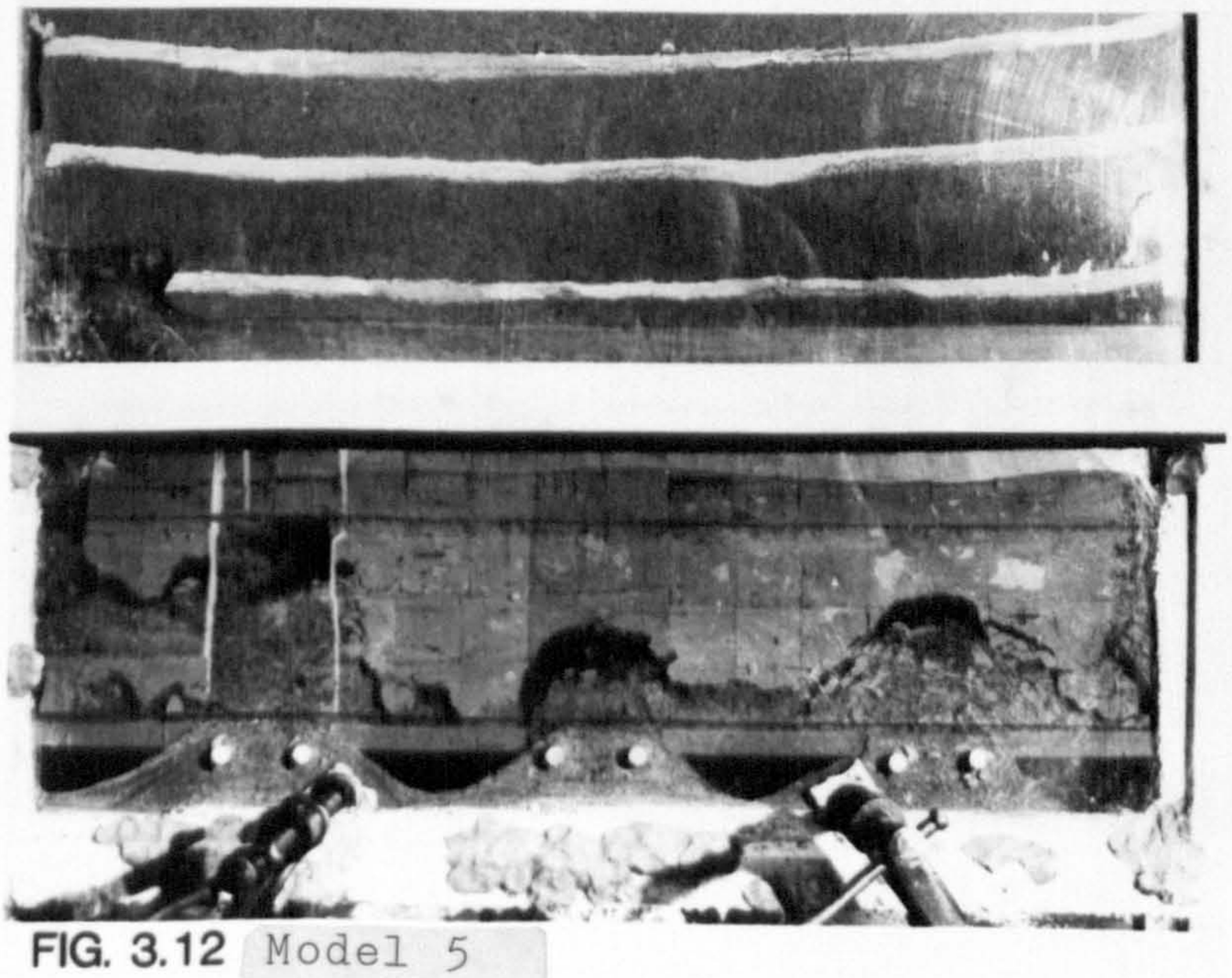

FIG. 3.12 Model 5

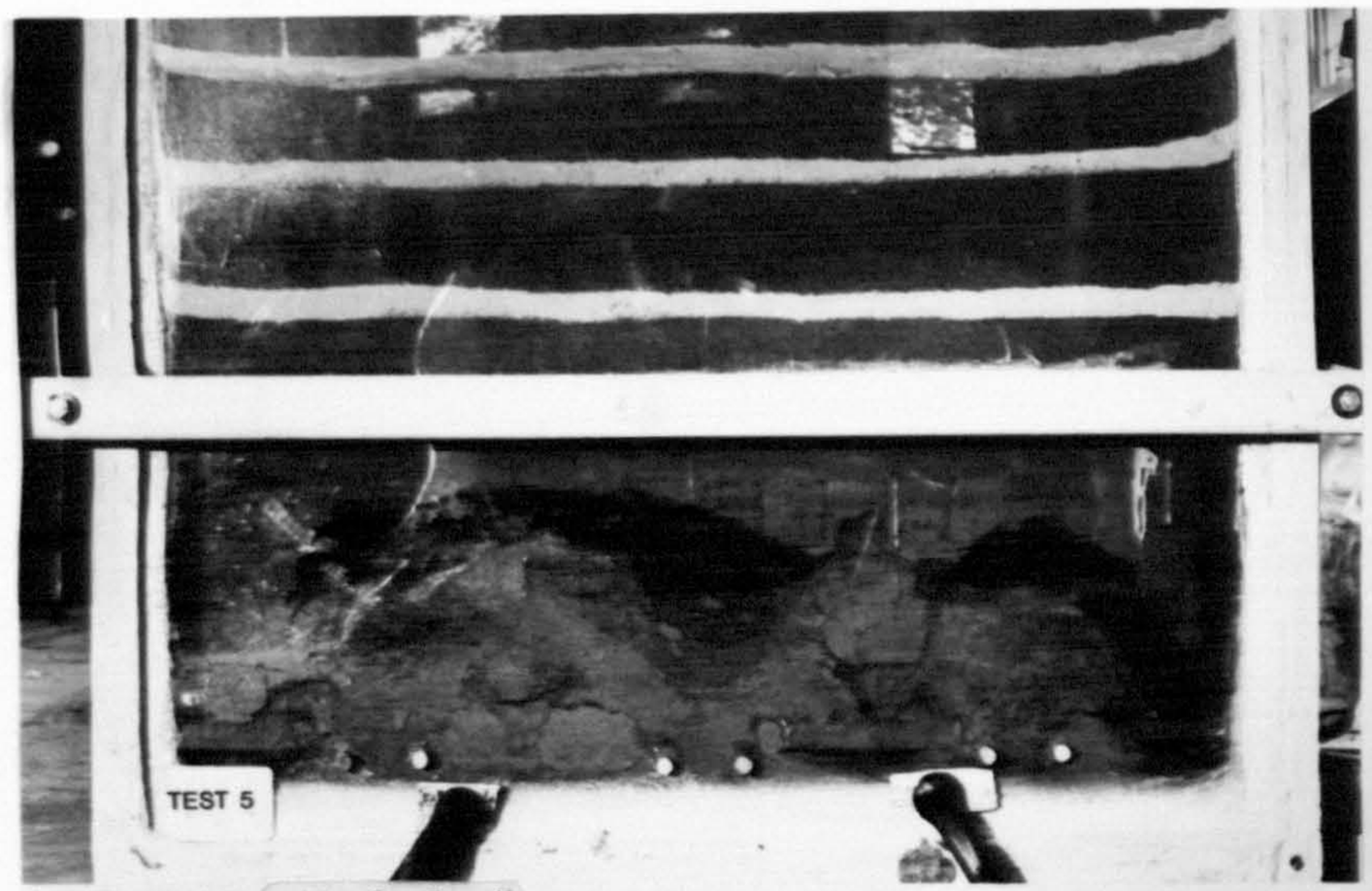

FIG. 3.13 Model 5

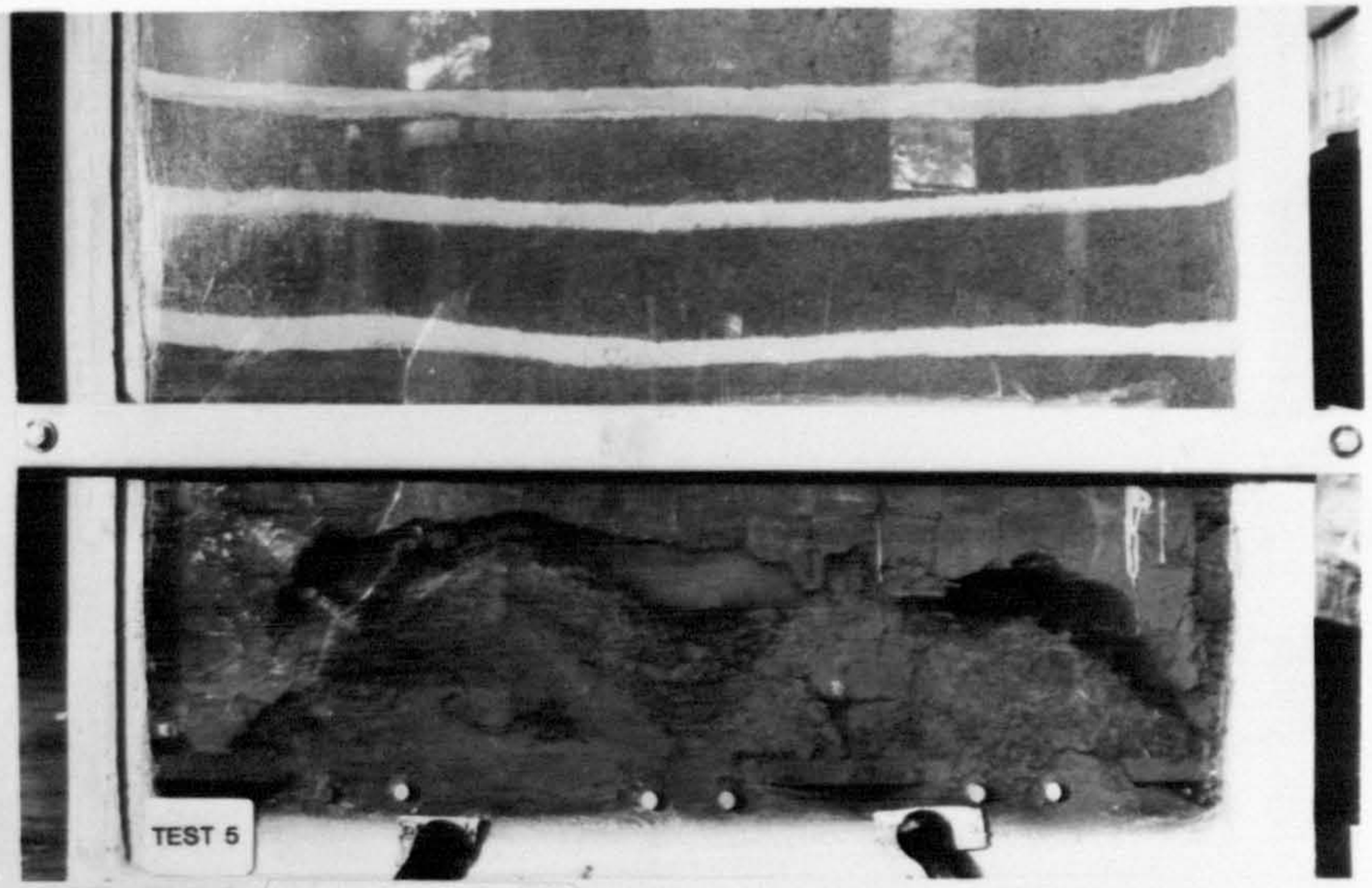

FIG. 3.14 Model 5

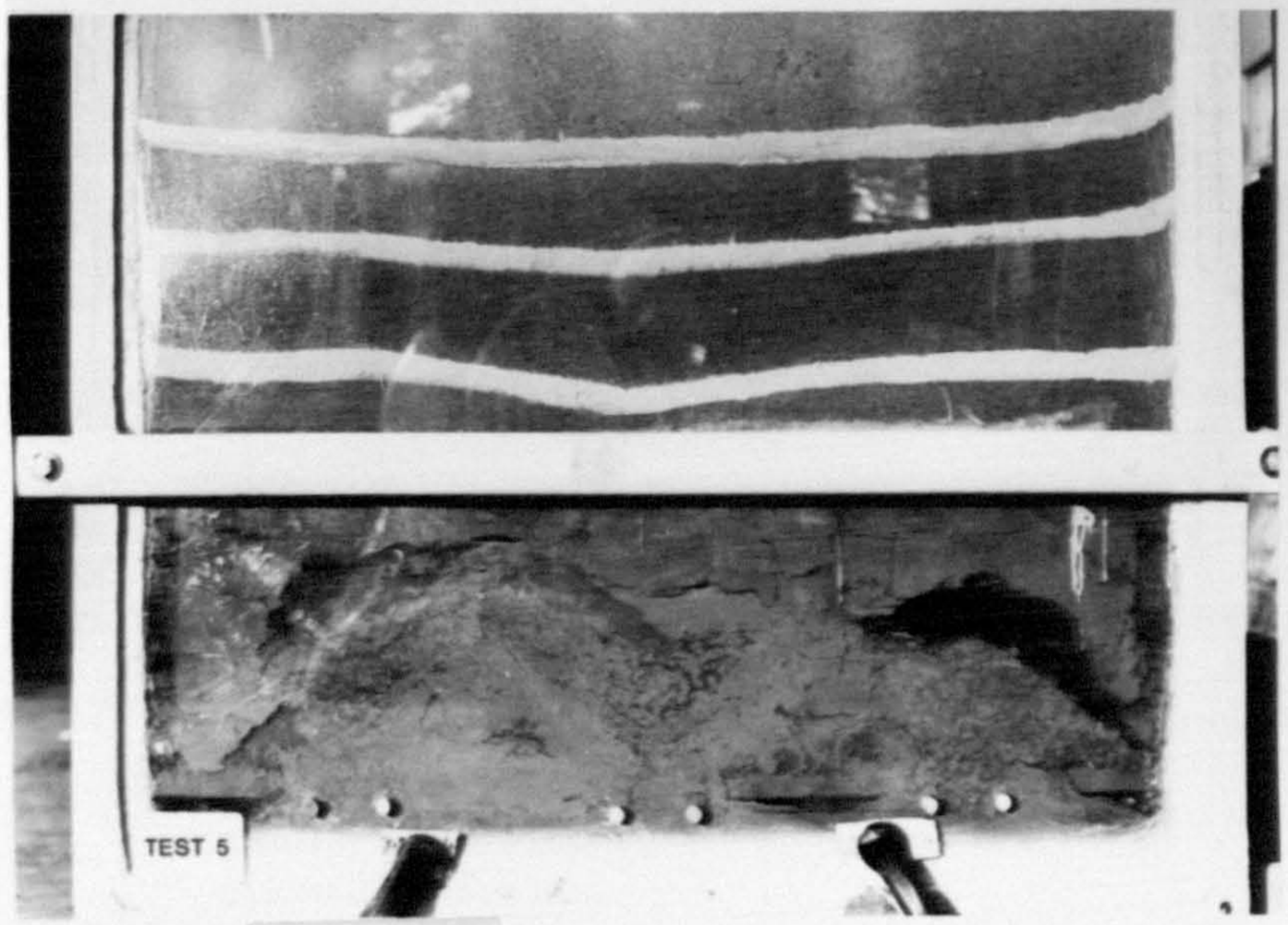

FIG. 3.15 Model 5

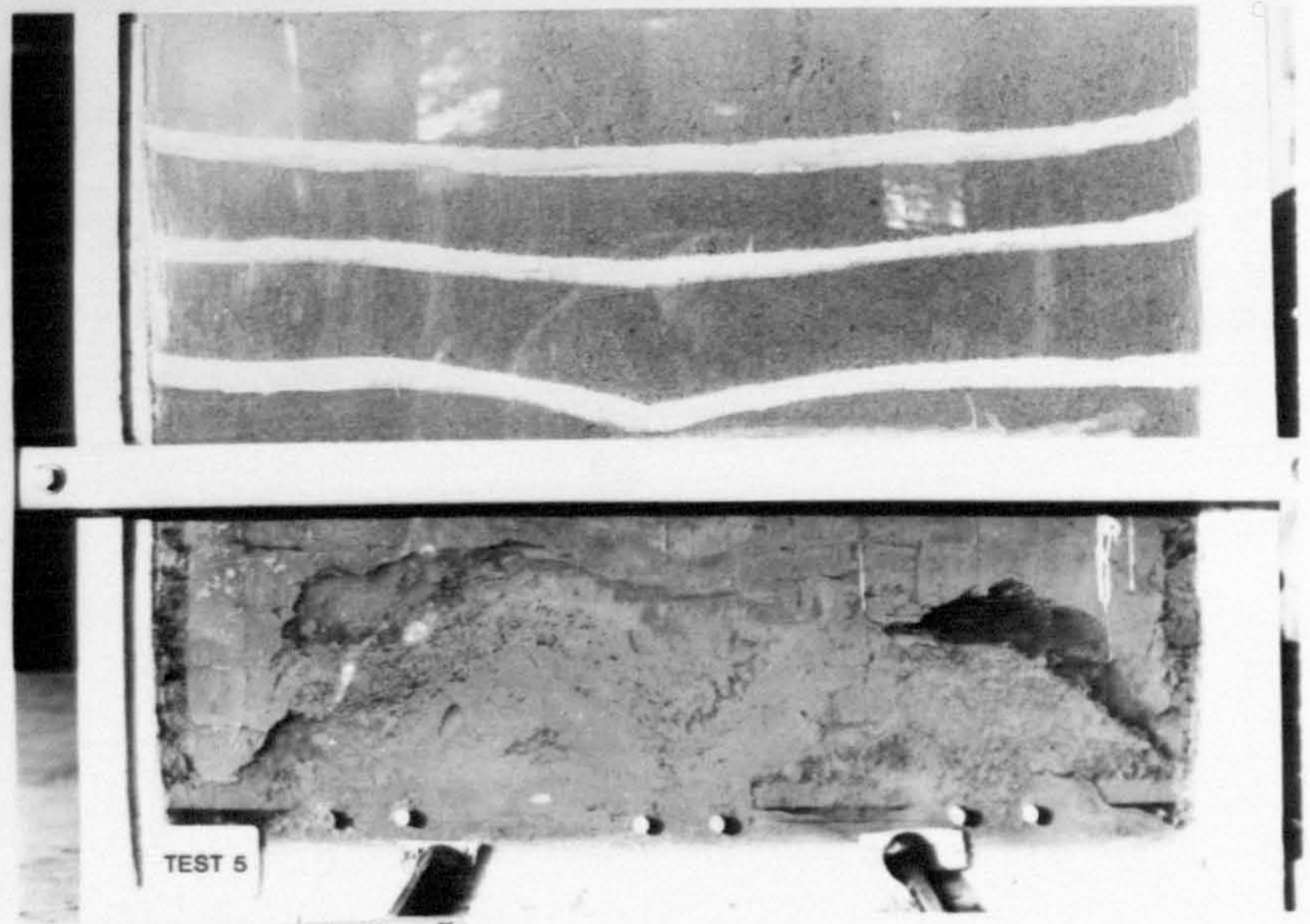

FIG. 3.16 Model 5

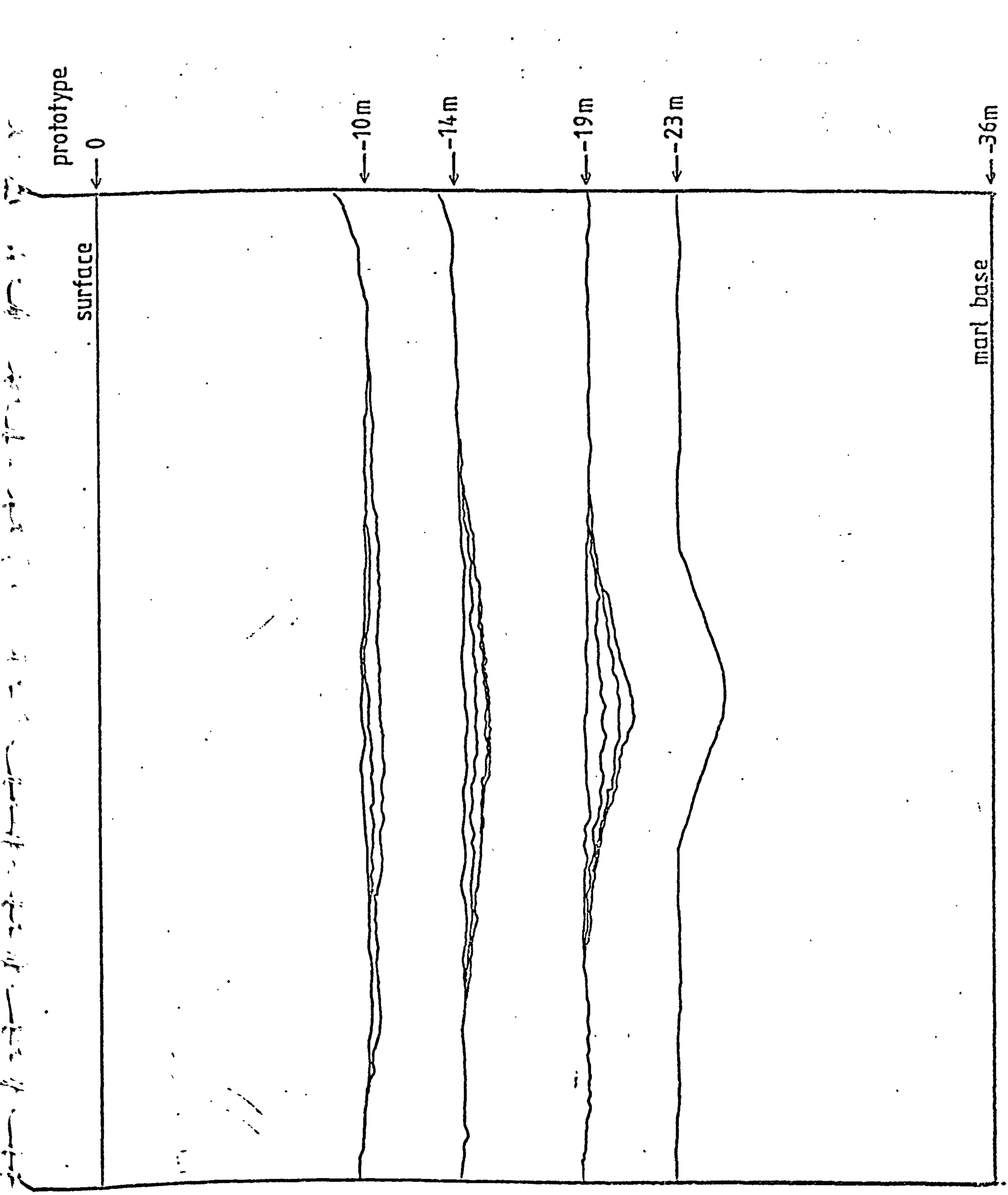

FIG 317 SUBSIDENCE PROFILE (scale : 1 / 208)

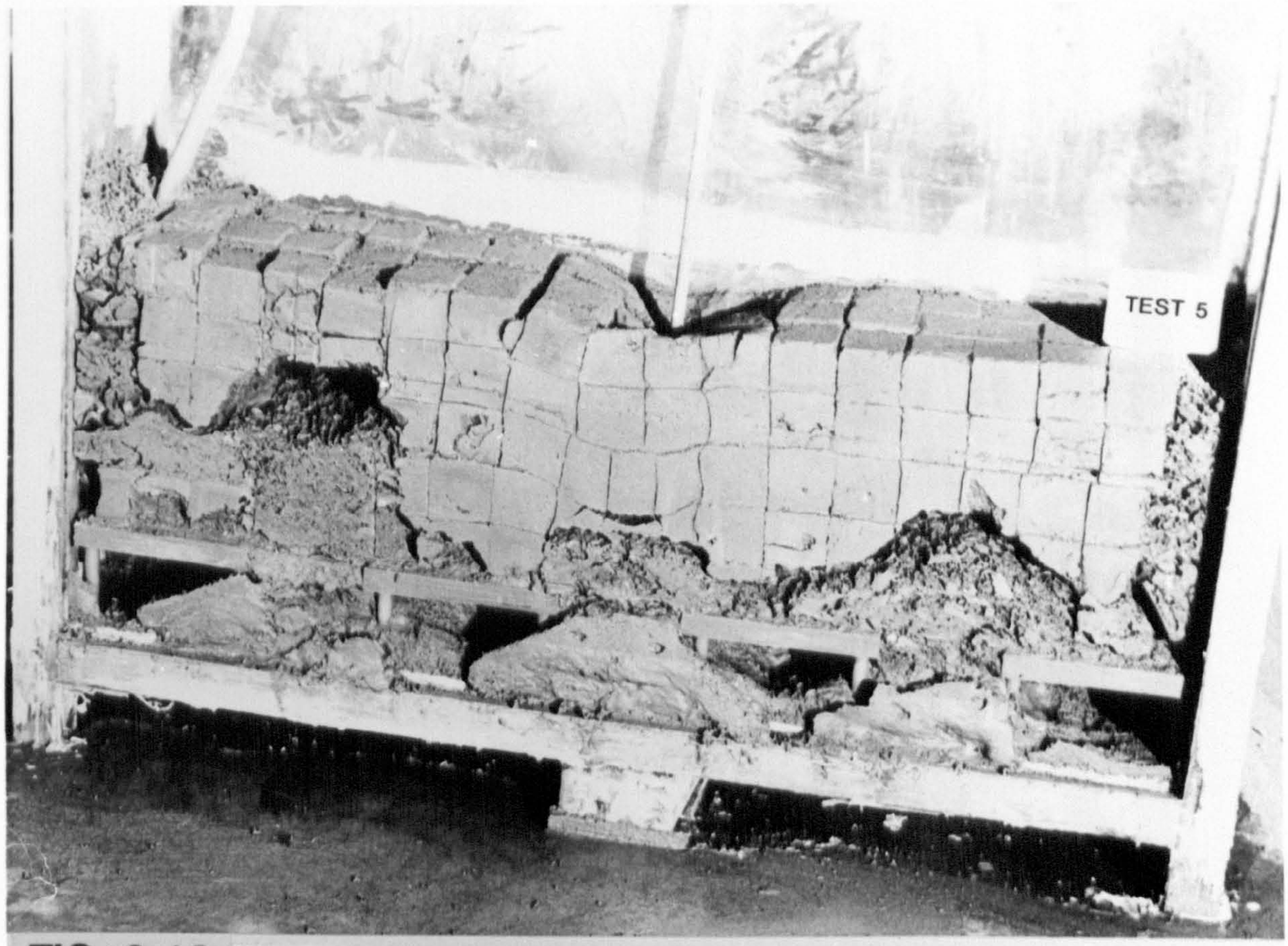

FIG. 3.18 Model 5

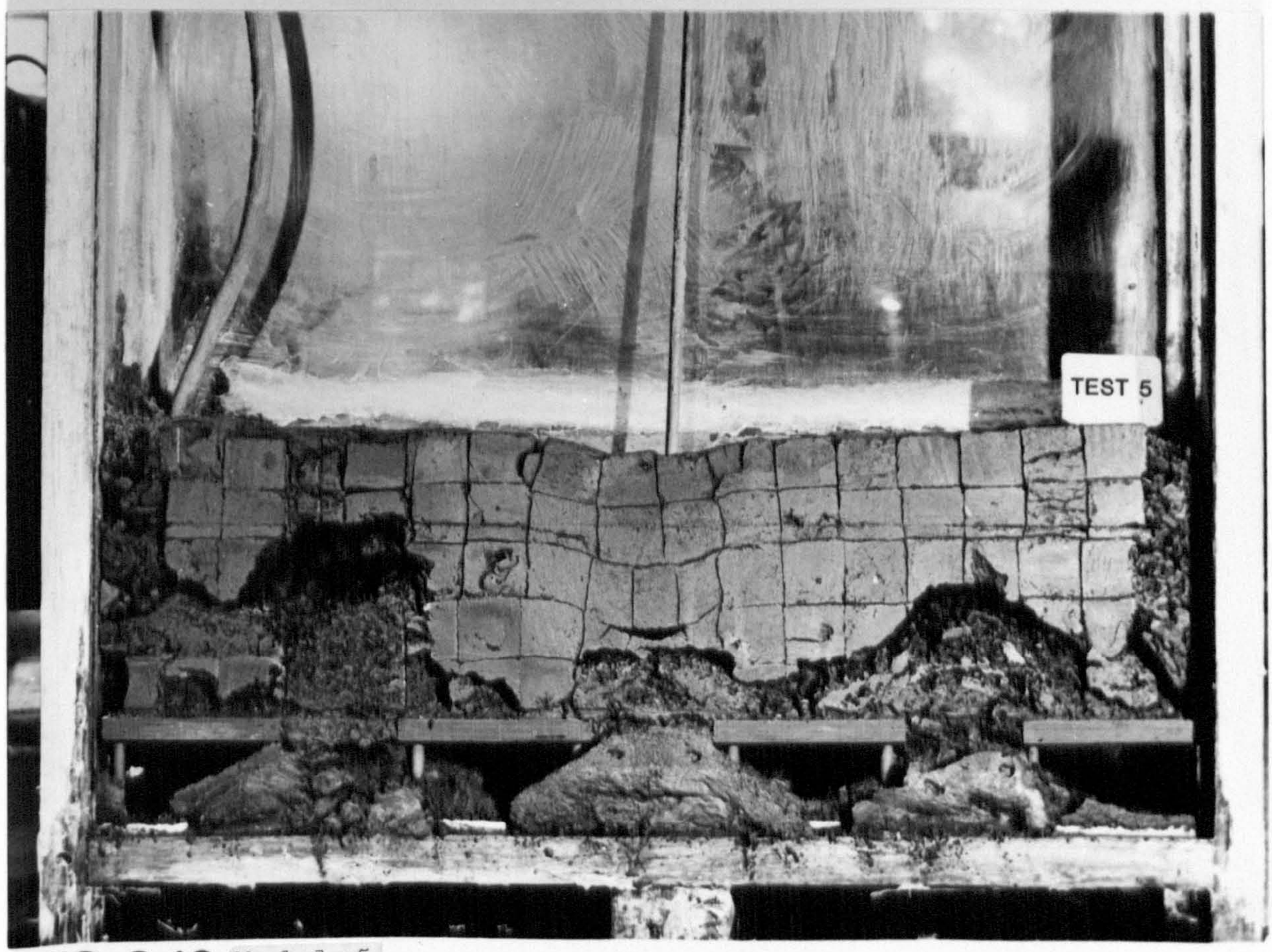

FIG. 3.19 Model 5

FIG. 3.20 Model 5

FIG. 3.21 Model 5

TABLE 3.1 MODEL RESULTS

MODEL NO:	CRACK FREQUENCY MODEL	CRACK FREQUENCY PROTOTYPE	HEIGTH OF UPBREAK MODEL	HEIGTH OF UPBREAK PROTOTYPE	WIDTH OF UPBREAK MODEL	WIDTH OF UPBREAK PROTOTYPE	ANGLE OF POSE
1	2per10cm	7per30m	----	----	----	----	------
2	2per10cm	7per30m	5.5 cm	2.75 m	9.2	4.6	30-33
3	3per10cm	13per30m	16.2 cm	8.10 m	19.0 cm	9.5 m	27-32
4	solid	body	6.5 cm	3.15 m	9.2 cm	4.6 m	30
5	3per10cm	13per30m	18.3 cm	9.15 m	15.7 cm	7.8 m	29-34

4. THE EFFECT OF WATER ON PILLAR STABILITY

4.1 Introduction

The many factors affecting the stability of underground workings have an influence to a variable extent on the rock structure. Two of these factors, however, have a significant influence on stability; namely, the deformation characteristics of the pillars and the presence or absence of water. Water is ingressing into the workings at different locations and in variable quantities. It is reasonable to assume that, after abandonment of the mine in the distant future, pumping will cease and the workings will be inundated.

The likely consequences of this flooding of the workings, with special reference to roof failure, has been investigated by means of physical modelling techniques, which have been reported in Sections Two and Three. In this Section the effect of water on the strength characteristics of gypsiferous rock in general, and the long-term time-dependent behaviour of submerged gypsum in particular, will be dealt with. It is believed that testing has provided valuable data on which forecasts of the stability of mine pillars in the event of flooding can be made.

4.1.1 Deterioration of Rock Properties due to Water

The experimental evidence suggests that the strength of most rocks is substantially altered by the presence of water (Griggs 1939; Serdengecti *et al.* 1962; Colback and Wiid 1965; Broch 1974, etc.).

The magnitude of the deterioration is particularly pronounced in rocks which contain clay material, being susceptible to water. (The term 'water' may also imply humidity.) The association of gypsiferous deposits with irregular pockets and bands of clay, marl or mudstone, is also often observed. The reduction in strength of such rocks may be rapid when the rock mass in dry condition comes into contact with the water. In the following sections the mechanisms of deterioration due to water will be discussed.

4.1.1.1 Effect on short-term strength

Rock can be regarded as an aggregate of mineral grains which are either crystalline or amorphous, or both. The fragments are held together by a bonding material, friction and interlocking between the grains. Generally, the boundaries between particles are the weakness zones in the structure. The nature of the bonding material and its frictional properties have an influence on the mechanical characteristics to a greater extent than does the composition of individual grains. The pores between the grains may be filled completely or partially with water. This pore water is believed to affect the strength of rocks in several ways.

If the pore water is pressurised, the hydrostatic force adds algebraically to the stress acting on the rock. The effect is a reduction in contact load between the grains which, in turn, results in a decrease of frictional resistance, and thus of load-bearing capacity of the rock. This phenomenon

has been studied mathematically and experimentally by Terzahgi 1945; Robinson 1959; Handin et al. 1963; and Murrel et al. 1963.

If the absorbed moisture is not under pressure, the strength properties of the rock are affected largely by chemical and physical alteration of the materials at the boundary of the mineral grains or in the binding material. It has been shown for a variety of materials that, at a crack tip subjected to tensile forces, chemical reactions can weaken the molecular bonds and crack propagation will occur (Pomeroy 1978). This is true for silicates when water can penetrate to the highly stressed crack tips, where silicon-oxygen bonds are hydrated and the cracks propagate. Crack development reduces the effective modulus of the rock so that additional deformation takes place.

If the rock contains active minerals such as clay, a strength reduction due to change in the moisture is a result of a change in the absorptive pore pressure (Serdengeçti et al. 1962).

Rutter (1972a) explains that water causes weakening at grain boundaries due to polar interaction between water and grain surfaces and this leads to a reduction in the surface energy of calcite which has relatively high porosity.

Colback and Wiid (1965), referring to test results on quartzitic sandstone immersed in different fluids, showed that the uniaxial compressive strength of specimens is inversely proportional to the surface tension of the liquids. Since the

surface free energy of a solid submerged in a liquid is a function of the surface tension of the liquid, by reducing the surface free energy of the rock, the strength is reduced, or by reducing the surface energy, the energy required for holding stable cracks is decreased and thus stable microcracking is initiated.

An interesting physico-chemical process of rock deterioration due to water is presented by Winker and Wilhelm (1970). They calculated that hydration pressures in excess of 30,000 psi (207 MPa) may be generated in conversion of bassinite ($CaSO_4.^1/2.H_2O$) to gypsum ($CaSO_4.2H_2O$). Therefore, if the rock contains this kind of material in the pores accessible to water, the hydration pressures acting on the pore walls can cause the disintegration of the rock. It is noted that anhydrite is not included in the calculations because it hydrates too slowly.

4.1.1.2 The effect of water on the long-term strength

The mechanism of the effect of water on the short-term strength of rock is valid also for the long-term strength, but there are additional mechanisms which must be taken into consideration.

Griggs (1939) carried out the first known systematic work on alabaster specimens immersed in various solutions. He explained the high strain rate of the immersed specimens by the 'Riecke's Principle', which states that the solution will

take place at the surfaces of maximum stress and recrystallisation at the surfaces of no stress. One test, involving a solution in which the solubility of gypsum is higher than that in water, has resulted in an increase in strain rate, hence it conformed to the recrystallisation process. However, further tests conducted with a specimen immersed in calcium chloride in which the solubility of gypsum is about 45% less than that in water because of the common-ion effect of calcium in solution and in gypsum has produced greater creep rate than that obtained with distilled water. If the recrystallisation process were controlled by solubility, the creep rate of the specimens immersed in calcium chloride would be lower than that in distilled water. Thus, he suggests that the creep rate should be a function of the ionic mobility of the gypsum in the solvent but not the solubility.

Griggs also examined the contribution of pore pressure to the increased creep rates of submerged rocks. The creep rate of specimens immersed in distilled water for 68 days was similar to that of the specimens initially dry but later surrounded by water. The use of penetrating oil instead of solvent has provided the same creep rate as the dry specimens. It was concluded, therefore, that pore pressure was active in cracks formed during the deformation of the specimen upon the application of load.

Varo and Passaris (1977) studied the role of water on the creep properties of another evaporite, halite. Although

halite is a fundamentally different rock to gypsum, it is thought that it would be worth mentioning the process involved, since it constitutes an extreme case and demonstrates to what extent the controlling mechanism can change with different rocks. They reported that the humidity, particularly above 75% of the relative humidity of the environment, has a marked effect on the creep properties of halite because, due to the high humidity salt goes into solution. The effect of humidity is explained on the basis of the 'Joffe Effect', which is observed upon immersing halite in water. The theory states that halite is an 'inherently ductile' material and if this is stored in the air for a long time, it becomes brittle (used as a relative term). This is attributed to the reaction between certain gases in the air (e.g. ozone) and the halite. The ozone is adsorbed onto the surfaces of halite and this prevents dislocations from 'escaping' by forming a barrier and so prevents slip occurring. On the other hand, creep of saturated halite specimens in brine was proved to have been controlled by recrystallisation. Using a coloured dye diluted in the surrounding water, they demonstrated freshly coloured crystals on the surface of the specimens and along the fracture planes. Due to the high solubility of halite in distilled water, the creep rate of specimens was largely controlled by the solution of halite.

It is believed that in the case of gypsum submerged in the mine water, possibly a combination of many processes is involved. Some factors which are considered relevant to the deterioration process will be discussed briefly later.

4.1.2 Solubility and Solution Rate

The solubility of a material is defined as the amount of material that can dissolve in a given quantity of solvent to reach the equilibrium concentration. The speed of dissolution is termed the rate of solution. These two concepts are of great importance when comparing the degree of alteration of different rocks produced by water or by a solvent. In Tables 4.1 and 4.2, the solubility and the constant of solubility rate of different materials are set out. The difference in solubility rates of different materials is attributed to the type of bonding between the molecules making up the material, such as covalently bonded quartz and ionicly bonded gypsum or halite. Although the solubility of gypsum is similar to that of anhydrite, the rate is much higher with the latter. Therefore, anhydrite is potentially more prone to be affected by water than gypsum where appreciable water flow is expected.

It is proposed by James and Kirkpatrick (1980) that the chemical composition of the mineral is a sufficient definition of the solubility and specific solution rate characteristics. For example, gypsum has the same solution rate and solubility whether it is in the form of selenite, alabastine or satinspar.

It is, however, noted by James and Lupton(1978) that the dissolution rate of satinspar is lower than that of gypsum. But this may be attributed to the size of sample used, which was comparatively smaller than the size of gypsum and, hence, to the short flow path.

The dissolution of minerals by the diffusion of ions into the solution has been given by the following equations (Crank 1975):

$$\frac{d_m}{d_t} = kA\ (C_s - C) \qquad \ldots\ldots (4.1)$$

$$\frac{d_m}{d_t} = kA\ (C_s - C)^2 \qquad \ldots\ldots (4.2)$$

where k = solution rate constant

m = mass dissolved

t = time

A = area of exposure

C_s = solubility of material

C = concentration of material in the solution.

The dissolution rate of gypsum obeys the first order equation (4.1), whereas the dissolution rate of anhydrite obeys the second order equation (4.2) (James and Lupton 1978).

The factors which influence the solution rate of gypsum are:

(1) solubility;

(2) exposed surface area;

(3) flow velocity of water;

(4) temperature and pressure;

(5) presence of other dissolved salts; and

(5) subsaturation concentration of ground water.

4.1.2.1 Solubility

The solubility of gypsum is a function of temperature, presence of other dissolved salts and the saturation level of the water. Considering a flooded mine situation, with no appreciable flow velocity of water after the initial states, the solubility of gypsum is likely to be a controlling factor in the pillar deterioration process. Since the mine water and the evaporite deposits contain finely disseminated sodium chloride, a higher solution rate of gypsum and anhydrite can be expected in-situ.

4.1.2.2 Exposed Surface Area

An increase in the surface area of gypsum pillars linearly increases the rate of solution of gypsum, according to the equation (4.1). In the areas where pillars are fragmented by the presence of satinspar bands, natural joints and bedding planes, rate of solution will increase. However, this increase may be regarded as an advantage from the point of view of the mine because, for a given volume of solvent, an increased surface area of solute will require the removal of less material per unit surface area than in the case of a small surface area in order to reach equilibrium conditions. On the other hand, the presence of marl bands, due to their rapid decomposition upon immersion in water, can create weak spots in the pillar.

4.1.2.3 Flow Velocity

The flow velocity of water effectively controls the rate of solution, allowing rapid removal of diffusing ions from the surface of gypsum. It was calculated by James and Lupton (1978) that the flow velocities larger than about 10^{-3} m/s can cause extensive dissolution of gypsum, leading to a 'run-away' situation within a few years in a massive gypsum adjacent to a confined permeable strata. Fortunately, this factor is of limited importance in the case of mine flooding, except during the first stages of the occurrence, after which water movement literally stops.

4.1.2.4 Temperature and Pressure

In solutions the stable phase can change appreciably over quite short ranges of temperature, especially in hydrated systems (Mullin 1972). Liu and Nancollas (1971) reported the influence of temperature on the dissolution of small gypsum crystals as being an exponential function of temperature. It is, however, also indicated that solubility of gypsum decreases after a certain temperature is exceeded, which is termed as 'negative solubility' or 'inverted solubility' (Mullin 1972). It must be pointed out that the effect of temperature can be safely considered to be negligible in the case of a flooded mine, since no appreciable variation in temperature can be expected.

If an area likely to be affected by ingress of water is sealed off prior to flooding, the incoming water will build up pressure in the trapped mine air which will be inversely proportional to the volume displaced by the water. This

pressure increase is based on the fact that ideal gas law (PV=MRT) isothermally holds in this situation (Lee 1969; and Sushkov 1965). Then it follows from 'Le Chatelier's Principle' which, for the present purpose can be stated as: when a system in equilibrium is subjected to a change in temperature or pressure the system will adjust itself to a new equilibrium state in order to relieve the effect of change and the process of dissolution will be reversed and recrystallisation will take place. Contrary to this logic, Griggs (1940) found that the steady state creep rate of immersed alabaster increased even further when the solution in which it was immersed was put under pressure. The reason for this seems obvious because the solution under pressure was not saturated, and hence was not in a state of equilibrium. Applied pressure forced the liquid to penetrate deeper into the rock structure, thus rendering it weaker. Which case is the most appropriate to the in-situ condition depends largely on the subsaturation concentration of ground water, the presence of other salts and many other local conditions. A more detailed research towards the thermodynamic aspects of the subject is recommended.

4.1.2.5 <u>The presence of other dissolved salts</u>

James and Lupton (1978) showed that even a concentration of 1% NaCl solution could increase the solution rate of gypsum considerably (more than twice that of pure water at the flow velocities up to 0.25 m/s and at 23^{o}C). The same phenomenon was reported for carbonate and carbon dioxide by Weyl (1958)

and Wigley (1973). Since gypsum deposits contain finely disseminated sodium chlorite, the rate of solution will be increased.

4.1.2.6 Subsaturation concentration of ground water

James and Lupton (1978) report the linear relationship found between the solution rate of gypsum and the subsaturation concentration of ground water with respect to concentration of calcium sulphate.

Since water percolating through a medium containing fragmented gypsum material will tend to form a saturated condition very rapidly because of the increase in the exposed surface area, even if the subsaturation level of the original ground water is not high, it will become saturated quickly. Therefore, the presence of small pieces of material and dust will be helpful in bringing the groundwater to saturation rapidly before it can penetrate deep into the rock. However, it is important to note that if the particles of a solute suspended in a solvent are small enough, concentrations greater than the concentration represented by the normal solubility of the substance can temporarily be obtained. Hulett (Mullin 1972) investigated the effect of fine grinding on the solubilities in water of various substances and reported a 19% increase in the solubility of gypsum for 0.4 μm particles.

4.1.3 Mine Water Analysis

Chemical analysis of the mine water samples from Fauld and Marbleagis is given in Table 4.3 (reproduced from Preston 1980). With pH values of 7.3 and 7.2 for Fauld and Marbleagis respectively, samples are slightly alkaline and both samples are highly saturated with calcium sulphate at levels of 76% for Fauld and of 71.5% for Marbleagis. The relatively higher level for Fauld samples is attributed to the presence of anhydrite as it is revealed in thin section analysis. The similarity of the host rocks through which ground water percolates is also reflected in the analysis.

4.1.4 Porosity of Gypsum

The apparent porosity of gypsum specimens from different sources has been determined by Preston (1980). He used water absorption methods in order to estimate the apparent porosity. Since, in this case, it was not possible for water to penetrate into the pores which are not interconnected, the values obtained would probably underestimate the actual porosity. He reports fairly consistent results for different gypsum specimens ranging from 0.5% to 1.0%. Comparatively high porosity for Mountfield Seam 4 is explained by the coarser grain size and the presence of a thin satinspar band. Jones (1968) also produced a value (0.88%) very close to the estimates of Preston.

4.2 Short Term Testing of Dry and Wet Gypsum

The effect of water on the microscopic scale and the parameters associated with the deterioration process due to water have been discussed in the foregoing sections. Experimental evidence in the literature

suggests that the strength of widely different rocks is substantially reduced by the water (Price 1960; Colback and Wiid 1965; Wiid 1970; Rutter 1972; and Broch 1974).

The simplest and most convenient way of determining the strength properties of rocks is the uniaxial compressive test. Uniaxial compressive strength of rocks is dependent upon the size and shape of the specimen, platens used for testing, loading rate, temperature and humidity of the environment, pore water, petrology, fabric and weathering level of the rocks. Therefore, laboratory testing should be considered rather as an index test for comparative purposes and not as absolute values.

In Table 4.4 the variation of uniaxial compressive strengths of various rocks having variable moisture contents is shown. Large discrepancies between the results of tests conducted by Lisk (1976) and Ali (1979) indicated the importance of the fabric, composition, grain size and weathering state of the rock. This is reflected also in the results of Preston (1980) in Table 4.5 using gypsums from Fauld, Mountfield and Marbleagis.

The tests involved the use of 63mm diameter cores with a height to width ratio of 1:1 in order to make results comparable with the pillars and also with the creep tests. Saturated specimens were kept in mine water under the vacuum for a time (usually 3 weeks), while the dry specimens were allowed to dry in the laboratory. Because of the chemical composition of gypsum ($CaSO_4.2H_2O$) it was not possible to test the samples to high temperatures in an oven to achieve a perfectly dry condition as this would have caused recrystallisation and physical alteration of the mineral structure.

Testing was conducted on the 25-ton Avery testing machine, employing steel platens having the same diameter as the specimen. The loading rate was maintained constant according to suggestions by the ISFRM. Failure mode of the specimens was in the form of two opposite shear cones with small pieces around. No appreciable difference in the mode of fracture of dry and wet specimens was detected.

Due to the limitations of material available it was not possible to test a large number of specimens. However, inspection of Table 4.5 suggests that consistent results were obtained. The percentage reduction of the uniaxial strength due to water was highest (42%) for the material from Mountfield No.4 Seam, which also produced the lowest dry strength of 32.4 MPa. This may be explained on the basis of the material being coarser-grained than the others. The lowest reduction in strength was observed in Sherburn gypsum (25%) and Fauld gypsum (26%) respectively.

Brazilian disc tests were carried out on the gypsum discs (42mm in diameter and 21mm in thickenss). Four specimens were submerged in mine water and another four specimens in a humidity and temperature controlled room at 60% relative humidity and at 13.3^{o}C were kept for at least 60 days. Therefore, specimens were not truly dry, but possessed a moisture content approximately similar to the in-situ moisture conditions. The results are set out in Table 4.6. An average 44.9% strength reduction was obtained. Mottahed (1974) using larger discs (76.2mm in diameter and 19mm in thickness) reported 63% reduction due to wetting the specimens for 10 days. The difference could be accounted for by the size effect and also he compared his wet results with the air-dried specimen results.

4.3 Long Term Testing of Submerged Gypsum

4.3.1 Introduction

The short term strength of rocks must be considered as being a useful index of rock properties and should be used for comparison purposes only. Under certain conditions, most rocks undergo time-dependent deformation well below their ultimate short term strength levels. Therefore, rock structures designed on the basis of short term strength may stand for a long time but, eventually, may collapse if their long term strength is not taken into consideration. In metals, where creep behaviour is extensively studied, high temperatures are usually required for creep to take place, whereas in most rocks, high confining pressure or the presence of solutions are necessary. Some rocks, such as halite, potash, would creep at relatively low stress levels. Other types of rocks may creep under certain conditions.

Creep is generally seen as a form of flow which becomes apparent soon after the initial elastic deformation has taken place. The subsequent non-elastic deformation is related to displacement on the microscopic scale within the crystal lattice structure. On the macroscopic scale the creep behaviour is characterised in the simplest form by the plot of strain versus time. A typical creep curve (Figure 4.1) may be divided into three parts: primary stage (transient), secondary stage (the steady state) and tertiary stage.

Creep behaviour of rocks is influenced by specimen size and shape, applied-stress level and rate, temperature, humidity, the presence of solutions and rock properties (strength, composition, grain size, porosity, weathering, fabric, etc.).

4.3.2 Time-Dependent Deformation of Dry Gypsum

Jones (1968) observed negligible creep of gypsum specimens from Sherburn with a height-width ratio of 1.4 when the sustained stress was below 17 MPa.

Later, Williams and Elizzi (1977) conducted uniaxial and triaxial creep tests on the Sherburn Gypsum with a height-width ratio of 3:1. The stress levels for creep testing adopted were 30, 40, 50, 65 and 80% of the short term compressive strength of the specimens. The creep strains obtained were very small, mostly less than 0.1%. They found that at low stresses (30 and 40%) creep of gypsum followed a logarithmic law while, at high stresses, it followed a power law. Triaxial creep testing also indicated that increasing confining pressure decreased creep rate at constant stress difference.

Ali (1979),studied the dry and wet creep of gypsum from Sherburn, found similar results. He employed air-dried specimens with height to to width ratio of 3:1 at stress levels varying from 15 MPa to 34 MPa.

Watson (1979) used specimens with h/w ratios of 2:1 at a stress level of approximately 75% of the ultimate dry strength. He used fine grained and the coarser, 'sugary' gypsum. The latter showed no time dependent movement, whereas the fine grained gypsum underwent 0.3% strain during a period of 500 days.

Preston (1980), using Marbleagis specimens with a width to height ratio of 1:1 and a stress level of 75% of the ultimate short term strength, obtained 318 microstrain over 27 days and creep was confined to the primary stage only.

4.3.3 The Mechanism of Time-Dependent Deformation

Numerous theories exist on the creep mechanism of rocks, ranging from crack formation on macroscopic scale to the dislocations of the crystal lattice on the microscopic scale. It is more likely that more than one mechanism contributes to the time-dependent deformation.

Nadai (1950), emphasising the complexity of the mechanism of plastic deformation in the crystal lattice of solid materials, postulates four elementary creep phenomena:

(1) Slip : Parallel displacements (translations) of the elements of the crystal lattice. Sliding in the grains often occurs in numerous parallel planes. Evaporites may deform by translation of gliding on prominent cleavage planes.

(2) Formation of twins : Shifting, as a whole, of a part of a crystal to a second position, symmetrical with respect to certain planes in the lattice of the remaining part of the crystal.

(3) Deviations from regular positions of atoms and their thermal agitation in the lattice cause motion of dislocations under stress. Evaporites are especially susceptible to this type of deformation as they are characterised by ionic bonding which may be broken to form a dislocation.

(4) Breakdown of structure, occurring often quite gradually under an increasing load. Displacements of crystal grains are accompanied by a partial distruction of the cohesion. This results in a gradual loosening or tearing apart of the structure even under constant stress.

Pomeroy (1978) argues about the validity of the mechanisms suggested above on the basis that the elementary creep phenomenon is proposed for metals and the rock structure is much more complicated than that of metals. He explains the creep mechanism with the uneven stress concentrations that occur in a non-homogeneous material like most rocks. Since rocks contain voids and inherent cracks, when they are stressed, these cracks will be opened up and grow until stress concentration is reduced by coalescing, branching, or by running into a pore. For this reason, the initial rate of strain decreases as a consequence of limited crack propagation. The subsequent deformation is controlled by the diffusion of 'corrosive' substances into the crack tips. This 'corrosive' substance may be water, or any other solvent which can weaken the molecular bonds of the material at the crack tips chemically where high tensional forces act, hence crack propagation is re-started. New crack development would reduce the effective modulus of the rock; consequently, additional deformation would occur.

Schols (1972A) suggested a slightly different approach from the one discussed above. He assumes rock contains very small homogenous regions each of which undergoes static fatigue by the stress-aided corrosion at crack tips. When one of these small regions fails it contributes to the total volumetric strain and with time, the number of unfailed regions decreases together with the strain rate. Each failed region may fail again and this sort of re-activation of regions may lead to a secondary stage and, eventually, tertiary stage is entered.

Attewell and Farmer (1976) explain the creep mechanism on the basis of Griffith's crack deformation concept: the cracks develop under progressive load with each crack movement being accompanied by a stress relaxation at its tip, so tending to re-concentrate the stress at the tip of an adjacent crack. These local stress redistributions lead to an increasing density of crack propagation under increasing load while, if the load is constant, local stress redistributions lead to a reduction in the rate of increase of crack density with time, which is reflected in a logarithmic strain-time relationship.

The mechanism proposed by Cruden (1971) is also based on the 'stress activated corrosion at crack tips'. Cracks will grow gradually extending in their own plane until a critical length is reached, after which they propagate towards the direction of maximum compressive stress until a stable configuration is attained. Due to increasing probability of crack coalescence or crack interaction, the onset of the tertiary stage is reached.

Kranz (1979),using samples of Barre granite subjected to a uniaxial stress equal to 87% of their fracture strength, examined the crack growth and development with a scanning electron microscope. He postulates that crack growth and development as a function of time under constant load is similar, but not exactly the same as, crack growth and development as a function of stress at constant strain rate. After the appearance of the first new stress-induced cracks upon the application of load, the region around the crack relaxes and the local stress drops to a value insufficient to let further growth continue. They will not propagate further unless the crack tip stress is increased or the crack tip strength is decreased. Since the macroscopic stress is being held

constant, local stress can increase only through the interaction between two cavities. Crack tip strength can be decreased by temperature or by moisture. Thus crack growth and development are limited by the rate at which corrosive agents can decrease crack tip strength.

It emerges from the approaches suggested by Pomeroy (1978), Attewell and Farmer (1976), Cruden (1971), and Kranz (1979) that creep of rocks is essentially related to the corrosion of highly stressed crack tips by the environmental agents such as temperature and moisture. In the case of submerged gypsum, the ionic mobility of gypsum at the crack tips will be controlled by a number of factors such as subsaturation concentration of the fluid, temperature, permeability, porosity and the surface area of the exposed material. If, for example, under-saturated fluid is added, ionic mobility of gypsum will increase at crack tips where high tensional stresses act and solution of the material will take place rendering crack tip weaker, hence crack development continues. When the water becomes saturated recrystallisation takes place at the unstressed surfaces. It is possible that even slight change in the environmental temperature can affect the solubility either directly or indirectly by creating agitations in the surrounding water.

4.3.4 Creep of Submerged gypsum

The first systematic work on the submerged creep properties of rocks including alabaster was carried out by Griggs (1939). He tested dry and submerged alabaster under a stress of 52 MPa, equivalent to 40% of ultimate short term strength. Creep of dry specimens is confined to only the primary stage, whereas specimens surrounded by distilled water showed an accelerated creep rate with the tertiary stage commencing

at about 0.5% of strain level (Figure 4.2). Tests with various stress levels revealed that the full creep curve would be produced at stress levels greater than 20% of the ultimate compressive strength below which only the primary stage would be obtained (Figure 4.3). Griggs reports that, by immersing specimens in water, the creep law is changed from logarithmic to power law.

Ali (1979), with specimens having height/width ratio of 3:1, reported a 45% increase in the elastic strain rate and a fivefold increase in the strain rate when specimens were saturated with water. He also indicated the change of creep law from logarithmic to power, as did Griggs and Williams and Elizzi (1977).

Lisk (1975), employing specimens from Kirkby Thore area, Cumbria, with a h/w ratio of 1:1, carried out creep tests at different stress levels varying from 23 to 50% of ultimate strength. At stress levels between 36 and 43% of ultimate strength, creep law obeyed a power law.

Preston (1979), using 1:1 specimens and water from four different mines, observed the creep behaviour for at least 50 days at stress levels of 40 to 75% of ultimate wet strength. His work confirmed the change of creep law at low stresses in the presence of water. With material from Marbleagis, a change in the height to width ratio from 1:1 to 0.5:1.0 resulted in fourfold reduction in creep rate, indicating the importance of specimen size on the overall creep deformation. The use of distilled water showed that the creep rate was markedly influenced by the level of saturation of the surrounding water with calcium sulphate.

A twofold increase in creep rate was obtained on the first day. The difference in creep rates of various gypsum specimens is related to the fabric and petrology of gypsum.

4.3.5 Test Procedure

Specimens from Fauld, Marbleagis and Mountfield had been already installed by Preston (1979) when the author began this study. The measurements were taken for a further 1250 days approximately. Due to very small rates of deformation at later stages of creep, experimental errors affected the calculated creep rates. For this reason, the frequency of taking readings on instruments were reduced from daily to fortnightly, according to the state of a particular specimen during the testing programme.

It is essential, in creep testing, to have a complete control of stress level. Otherwise one or two stages may be missed, or very little effect produced. Based on the previous experience, the stress level adopted was chosen as 75% of the nominal ultimate wet strength of the gypsum specimens. For the Sherburn specimens, the stress level imposed was 65% of the ultimate nominal dry strength. The procedure was to allow the specimens to creep unsubmerged until the stability was reached and then the cell was filled with water and the effect of submerging the specimen in water was observed.

4.3.6 Specimens and Specimen Preparation

Gypsum specimens from four different sources were used in the programme:

(1) Mountfield gypsum consisted of coarse crystalline gypsum enclosed in a matrix of alabastrine gypsum and calcite. A thin section analysis of failed pieces of this material revealed cracks along the boundaries of the coarse grains and also cleavage splitting (Preston).

(2) Fauld gypsum contained many bands and pockets of anhydrite with apparent cleavages and enclosed in alabastrine gypsum.

(3) Marbleagis gypsum contains coarse grained crystals of gypsum enclosed in a fine grained matrix with an absence of corroded relics of anhydrite within the individual crystals.

(4) Sherburn gypsum is pink, crystalline material and thin fragments are translucent.

Cylindrical specimens having a height to width ratio of 1:1 and 63.2mm in diameter, were used. The coring was carried out from blocks of gypsum in the laboratory using paraffin as drilling fluid. .They were sized approximately with a clipper saw, then ground in order to obtain perfectly flat surfaces.

In an attempt to reduce frictional end effects, and to prevent rusting of platens in the long run, dolerite platens were used during testing. The top platen was 50.8mm thick, while the bottom one was 25.4mm thick and both had the same cross-sectional area as the specimen.

4.3.7 Particulars of Testing

In order to obtain comparable results from the long term creep testings, a close simulation of the actual situation, as far as possible, was necessary. Moreover, since change in the strain over the weeks was very small, a slight variation in the atmospheric condition could influence the specimen, despite the fact that the specimen was surrounded with the water, and resulted in incorrect observations. Therefore, a full control over the environmental temperature and humidity was an essential requirement. This was achieved by maintaining the creep rigs and specimens in a creep room climatically controlled.

The temperature and relative humidity of the creep room were maintained at 13^{o}C and 60% respectively throughout the testing programme. Minor changes in temperature and humidity which were detected on a chart recorder occurred accidentally, but these were found to have had negligible effect on the creep of specimens. Replenishment of the water to the cells had to be carried out from time to time to counteract evaporation in the rooms.

Creep rigs were designed within the Department of Mining Engineering and consisted of a rectangular steel framework. Details of applied stresses and specimens can be seen in Table 4.7. The pressure applied to the system was controlled by accumulators consisting of steel gas bottles

containing pressurised nitrogen which forces hydraulic fluid into the jacks. An allowance of 3% of the ram load was made in order to overcome piston friction (Mirza 1978).

The pumping of the oil in the hydraulic rams to the required level was a continuous process, not stepwise.

During the course of creep testing, changes in the cross-sectional area of the samples occur and this inevitably causes a decrease in the stress acting on the specimen. This is especially pronounced if the axial strains are greater than 1 percent. Rutter (1977), demonstrated that the creep curves obtained with wet Solenhofen Limestone were sensitive to the change in the cross-sectional area. No account of this effect was taken into consideration in the testing because of the equipment. used. It can be proposed that, if the area compensation is required, it is necessary to introduce some form of computerised control system.

Hawkes and Mellor (1970) discuss the factors affecting strength testing of rocks. The end constraint effects are especially important causing abnormal stress distributions, and the platen effect is particularly pronounced in samples with low height to width ratios due to Saint Venant's principle. Problems arising during the use of platens or inserts having different elastic modulus than the specimens were investigated theoretically by Balla (1966), Al-Chalabi and Huang (1974), and many others. Balla (1960) treated the case as an elastic boundary problem with differing degrees of end constraint. Al-Chalabi and Huang criticise this approach for its performance in the region of contacts.

The specimens and the dolerite platens were positioned in specially made creep cells. The cell was made of a circular mild steel base onto which a perspex cylinder was secured in order to allow observations of specimen behaviour.

To measure the vertical deformation, two dial gauges were mounted on the opposite sides of the specimen. These dial gauges were able to record any displacement up to 1/1000th part of an inch. A typical rig, cell and specimen are shown in Figure 4.4.

4.3.8 Presentation of Creep Data

Creep data obtained in the form of time-displacement measurements have been processed in the computer using package program 'PADAS', details of which can be found elsewhere (Watson 1979). The computer output in graphical form shows time elapsed in days versus percentage strain. This is the simplest and most convenient way of presenting creep data and clearly describes the behaviour of the specimens. For the sake of comparison and curve fitting purposes, data were also plotted in logarithmic scale.

4.4 Creep Results

4.4.1 Marbleagis Gypsum

Three specimens from Marbleagis Mine (numbers 11, 8 and A) were tested. Specimens 11 and 8 showed similar behaviour within the testing period with strain levels of 0.3246% on the 854th day (Figure 4.5) and 0.358% on the 254th day (Figure 4.6) respectively. Testing of specimen No. 8 had to be terminated on the 254th day because of equipment failure

while readings from rig 11 were taken up to 854 days without any interruption. Only the primary stage was present for these two specimens. Creep rates of all the specimens tested with corresponding time intervals are shown in Table 4.8. Due to deterioration of the glue at the perspex base interface, water leakage occurred on the 854th day of specimen 11. For this reason, testing was temporarily interrupted and the cell was repaired without removing the load on the specimen. However, no discernible creep was recorded afterwards.

Specimen A underwent comparatively larger time-dependent deformation than the other two specimens (Figure 4.7). As can be seen in Table 4.8, the specimen attained very high strain rates (7.88×10^{-3}/day) within the first five days, which was approximately four to five times that of specimens 11 and 8 and, in fact, was the highest of all specimens tested. Gradually decreasing strain rate had reached (0.47×10^{-3}/day) on the 150th day. This specimen was characterised by fine grained pure alabaster, which is particularly affected by water. On the 179th day, the stress on the specimen was increased by 3% from 75% to 78% of the ultimate short term wet strength. This immediately raised the strain level from 0.6048% to 0.6424%, and the specimen entered the tertiary creep stage. With progressively increasing strain rate (Table 4.8), specimen eventually ruptured on the 394th day with a total strain of 2.12%.

The top dolerite platen also failed, apparently in tension, forming longitudinal columns (Figure 4.8). A likely explanation of this failure although it possesses a higher strength than the gypsum, is that the radial expansion of gypsum induces radial tensile stresses in the

platens which promote longitudinal splitting of the platen. In creep testing, although the axial and radial strains go through the same three creep phases, at later stages before the rock fails the radial strain always shows a higher strain rate than the axial strain (Singh 1975; and Sangha and Dhir 1972). This is related to the difference in rate of growth between the crack width and crack length (Kranz 1979). Since there were no irregularities in the observations it is probable that the platen had failed simultaneously with the specimen. The bottom dolerite platen was not broken because of the low h/w ratio and the frictional restraint of the metal base would contribute also to restrain the base dolerite platen from radial expansion.

The failure mode of gypsum specimens was in the form of shear cone at the base and was surrounded with rather small prismatic fragments (Figure 4.9).

It is difficult to compare the results with those of Preston (1980) because of the different stress levels used. Preston tested two specimens from Marbleagis, one being stressed at 81% of ultimate wet strength and failing within 11 days with an ultimate strain of 0.7%, the other being stressed at 73% of wet strength and showing only primary creep in 75 days, with a strain level of 0.257%. The latter specimen, taking the difference in the stresses into account, may be said to have exhibited similar behaviour to the specimens 11 and 8 in the present study. The ultimate total strain for the failed specimen was less than that of specimen A, which is attributed to the short duration of testing.

4.4.2 Fauld Gypsum

The creep behaviour of three submerged specimens (numbers 10, 12, and 13) from Fauld Mine have been monitored over approximately 1250 days. The specimens experienced substantial deformations in the primary stage compared to Marbleagis specimens (Figures 4.10, 4.11 and 4.12). In all of the specimens, the rate of decrease in strain rate was not as great as it was in the Marbleagis specimens. This distinct variation in behaviour is an excellent example of specimen composition on creep behaviour.

The specimens from Fauld Mine contained significant amounts of anhydrite. Therefore, the dissolution rate of the anhydrite was much higher because the process of hydration was the controlling factor. The precipitation of calcium sulphate around the creep cell and platens was a distinctive feature of these specimens.

The highest instantaneous strain was shown by Specimen No. 10 (0.4880%) and after 400 days the decreasing trend of strain rate was overshadowed by sporadic increases and decreases in the strain rate (Table 4.8). If this region is regarded as the secondary creep stage on the macroscopic scale, the constant strain rate can be approximated to a value of 0.19×10^{-3}/day.

Specimen No. 12 (Figure 4.11) exhibited lower instantaneous strain (0.3882%) than Specimen No. 10 when load was applied, whilst the rate of straining was similar (2.7×10^{-3}/day for No.10 and 2.2×10^{-3}/day for No.12) at early stages. Apparently the inflexion point was reached on day 710, with a strain level of 0.5876% and a strain rate of 0.1×10^{-3}/day. After this day strain rate steadily increased and reached

a value of 0.27 x 10^{-3}/day on day 964 when, unfortunately, due to the failure of a nitrogen bottle, the specimen had to be removed from the rig. Recommissioning of another rig caused a slightly higher load to be applied on the specimen; therefore, a small primary-stage-like behaviour was produced.

Specimen 13 deformed with decreasing strain rate from 1.86 x 10^{-3}/ day on the 10th day, to 0.52 x 10^{-3}/day on the 200th day. The instantaneous strain was the lowest of all three (0.2450%) which may be attributed to the high anhydrite content. On the 229th day, the stress was increased by 3% - from 75% to 78% of wet strength - which caused an immediate increase in the strain of 0.322% magnitude which compared very well with that of specimen 14 from Marbleagis. The rate of strain continued to decrease until the 537th day when a strain level was 0.8220%. The inflexion point was reached between the 547th and 624th days. It was not possible to determine the exact inflexion point because of the irregular behaviour of the specimen during this period. On the 716th day it was noted that the upper platen had already been broken at one side. Consequently, the stress on the specimen dropped and, from then on, the strain rate remained almost constant (1.1 x 10^{-3}/day) for a period of 150 days. Finally, the specimen failed on the 1098th day with a total strain of 1.866% (Figure 4.12).

4.4.3 Mountfield Gypsum

Due to the limitation of material available, it was possible to test one specimen only (No.6) from Mountfield Mine. The specimen produced 0.4797% instantaneous strain upon application of the load and exhibited

primary stage creep until the 282th day, with decreasing strain rate from 3.1 x 10^{-3}/day to 0.6 x 10^{-3}/day. After inflexion point on the 282th day, with a strain level of 0.7288%, the creep rate increased dramatically from 0.6 x 10^{-3}/day to 93.4 x 10^{-3}/day, just one day prior to failure occuring (on the 699th day) with an ultimate strain of 1.802% (Figure 4.13).

In fact, the specimen No.6 was the only one out of seven submerged specimens which failed under a stress corresponding to 75% of uniaxial wet strength. Table 4.5 also indicates that the Mountfield specimen had the largest amount of strength reduction (42%) as well as the lowest dry strength (32.4 MPa). This can be explained by the coarse grained and porous nature of this material.

The mode of fracture of specimen and upper dolerite platen was similar to that of specimen A (Figure 4.14).

4.4.4 Sherburn Gypsum

Three specimens numbers 1N, 14N and 6N were tested under a load equivalent to 65% of dry strength and corresponding to 88% of wet strength. The specimens were allowed to creep in a dry condition in the creep room (R.H.=63%) for approximately 50 days, then water was poured into the cells. The specimens 14N and 6N failed within three days, while specimen 1N sustained the load for a further 40 days (Figure 4.15).

Specimen 1N showed very little creep prior to wetting, with the strain level increased from 0.5590% to 0.5658% over 46 days. Upon introduction of water into the cell, the specimen started to creep

markedly, displaying first the primary stage with creep rate decreasing from 56.6 x 10^{-3}/day to 13.1 x 10^{-3}/day, which was almost constant in the following secondary stage and then a tertiary stage leading to rupture with a recorded strain level of 1.46%.

* * *

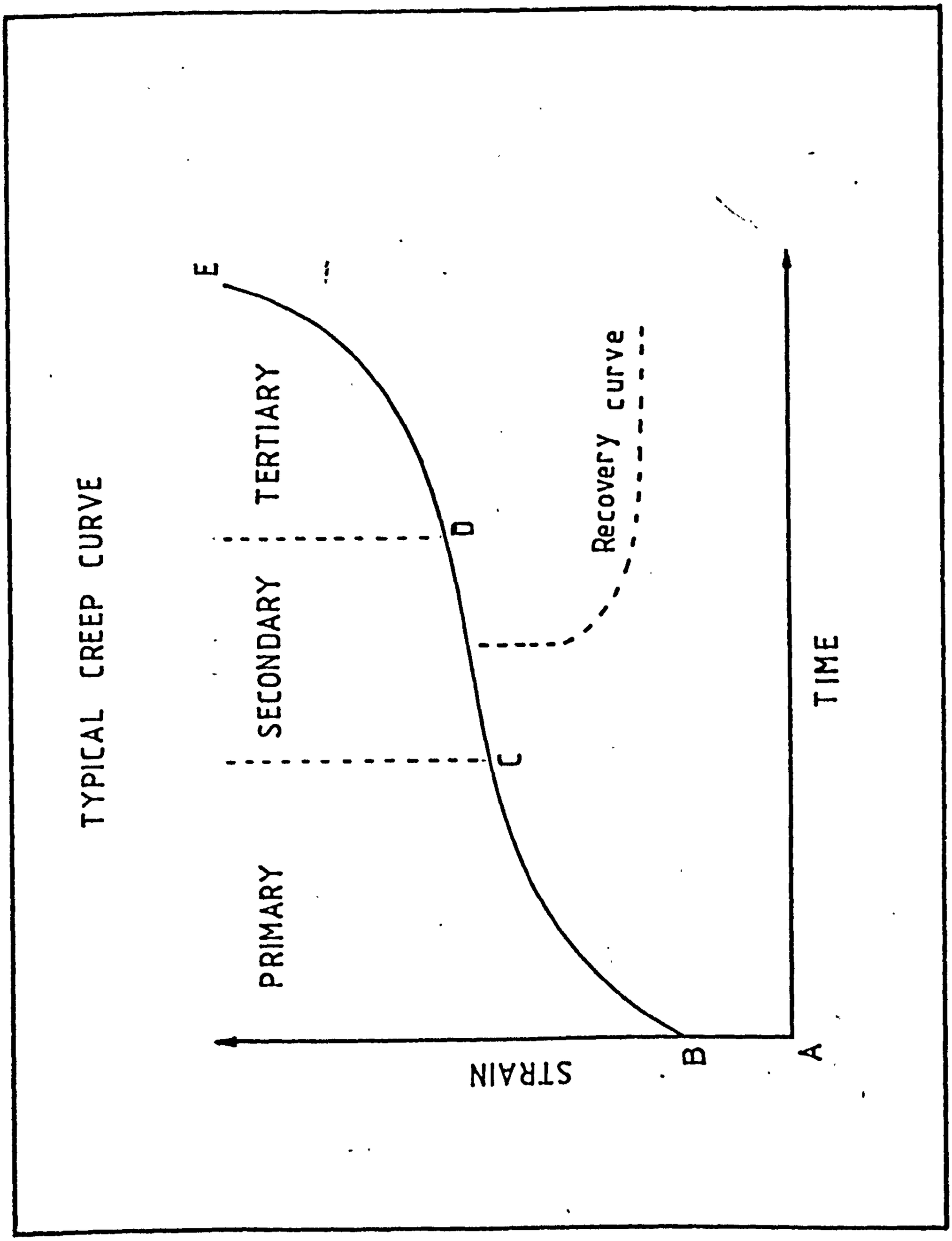
TYPICAL CREEP CURVE
PRIMARY
SECONDARY
TERTIARY
STRAIN
TIME
A
B
C
D
E
Recovery curve

FIG 4.1

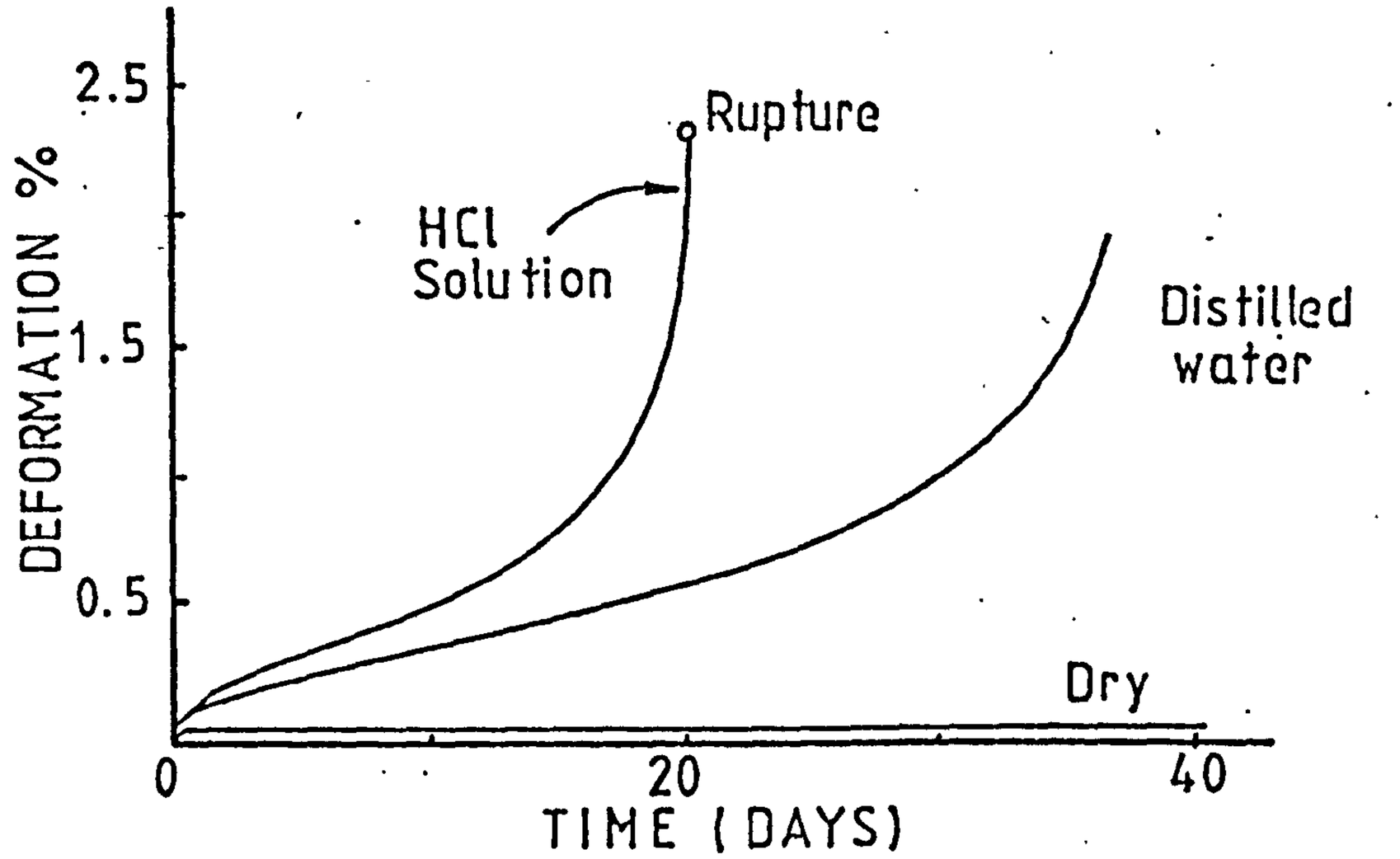

FIG 4.2 CREEP OF ALABASTER IN VARIOUS ENVIRONMENTS
(Stress = 20.5 MPa) (GRIGGS, 1940)

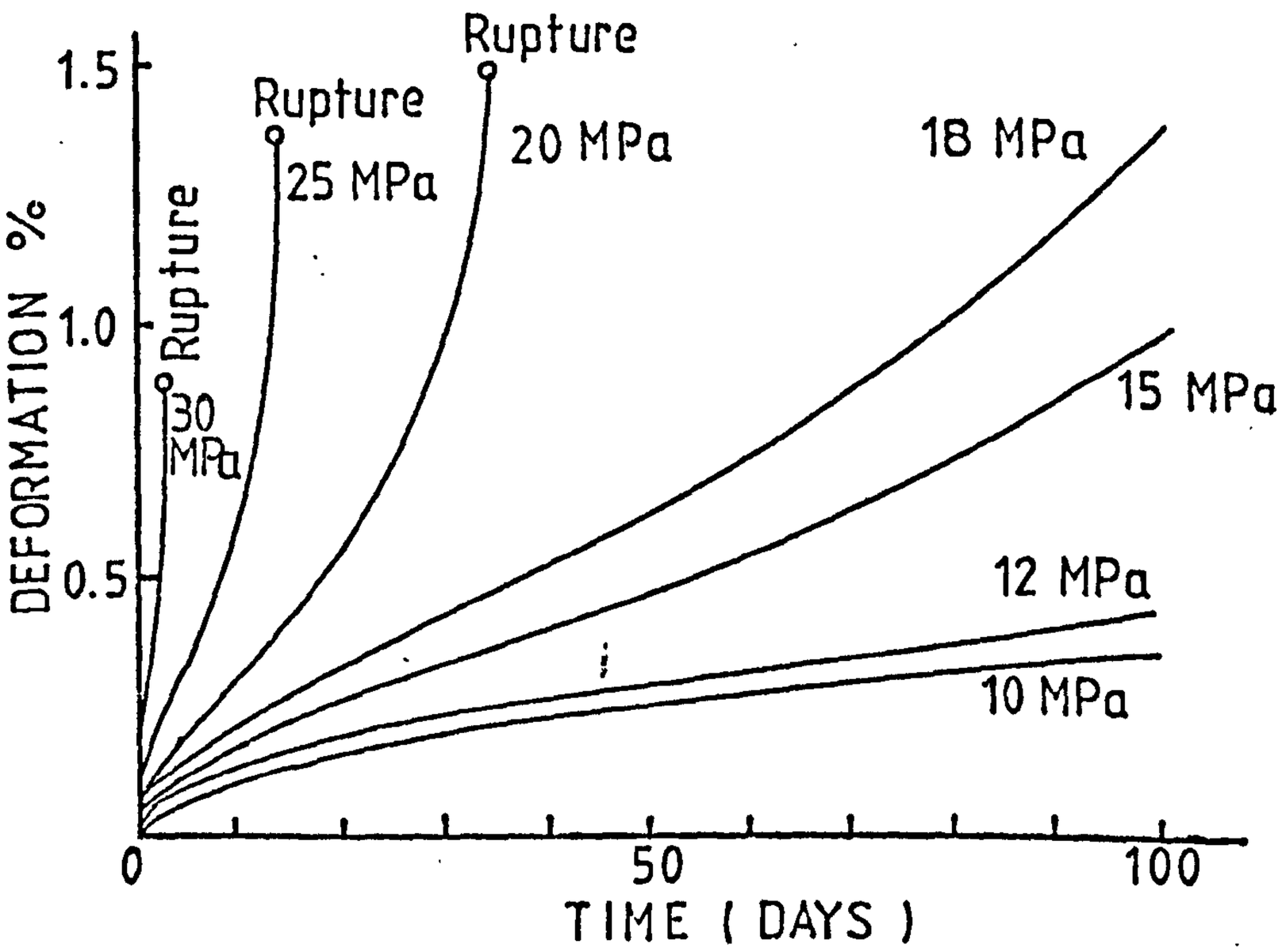

FIG 4.3 CREEP OF ALABASTER IN WATER (24°C)
(GRIGGS, 1940)

FIG 4.4 A creep rig.

FIG 4.5

LONG TERM CREEP OF SUBMERGED MARBLEAGIS GYPSUM

RIG NO:11 (75 % WET STRENGTH)

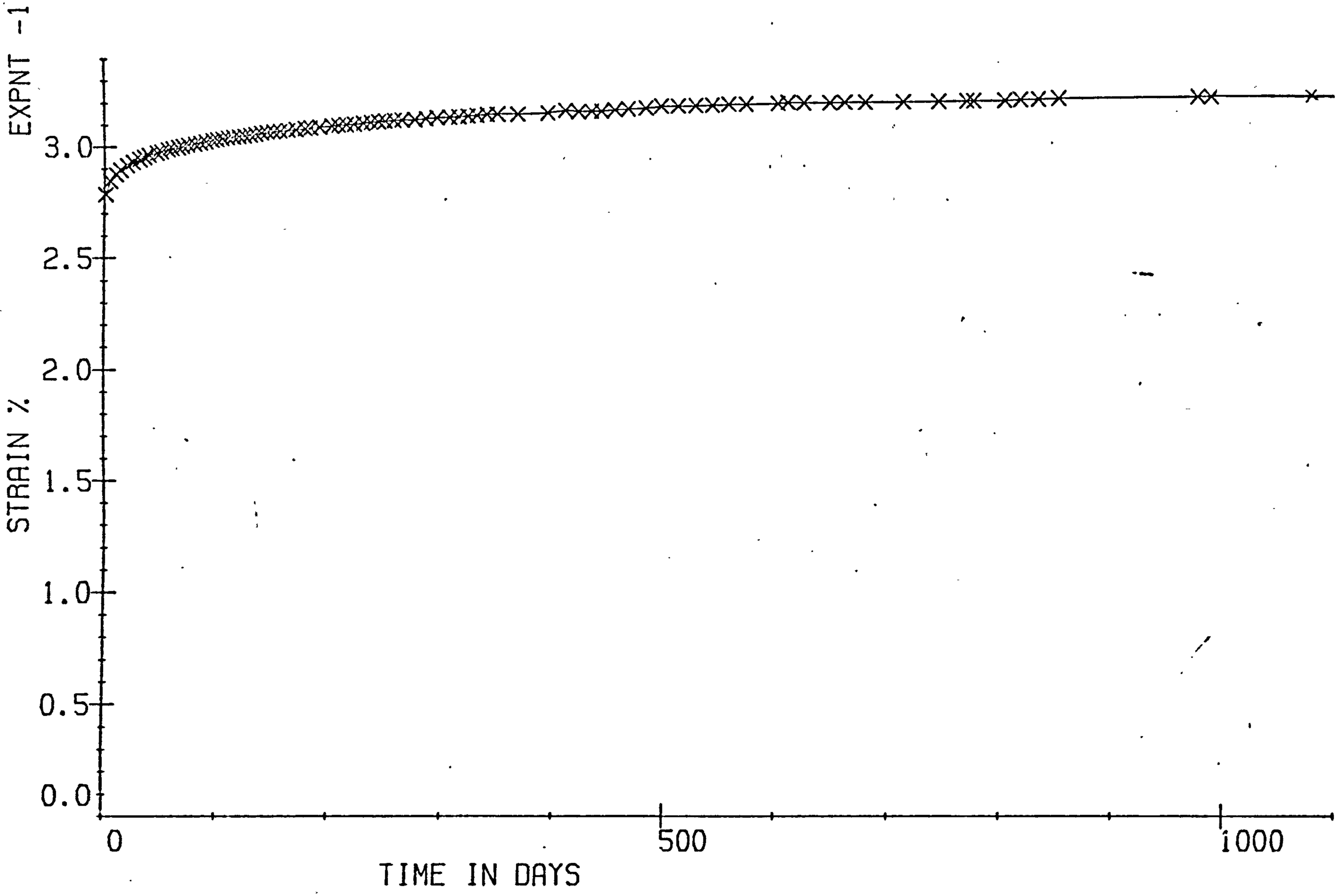

FIG 4.6

LONG TERM CREEP CURVE OF SUBMERGED MARBLEAGIS GY

RIG NO:8 (75 % WET STRENGTH)

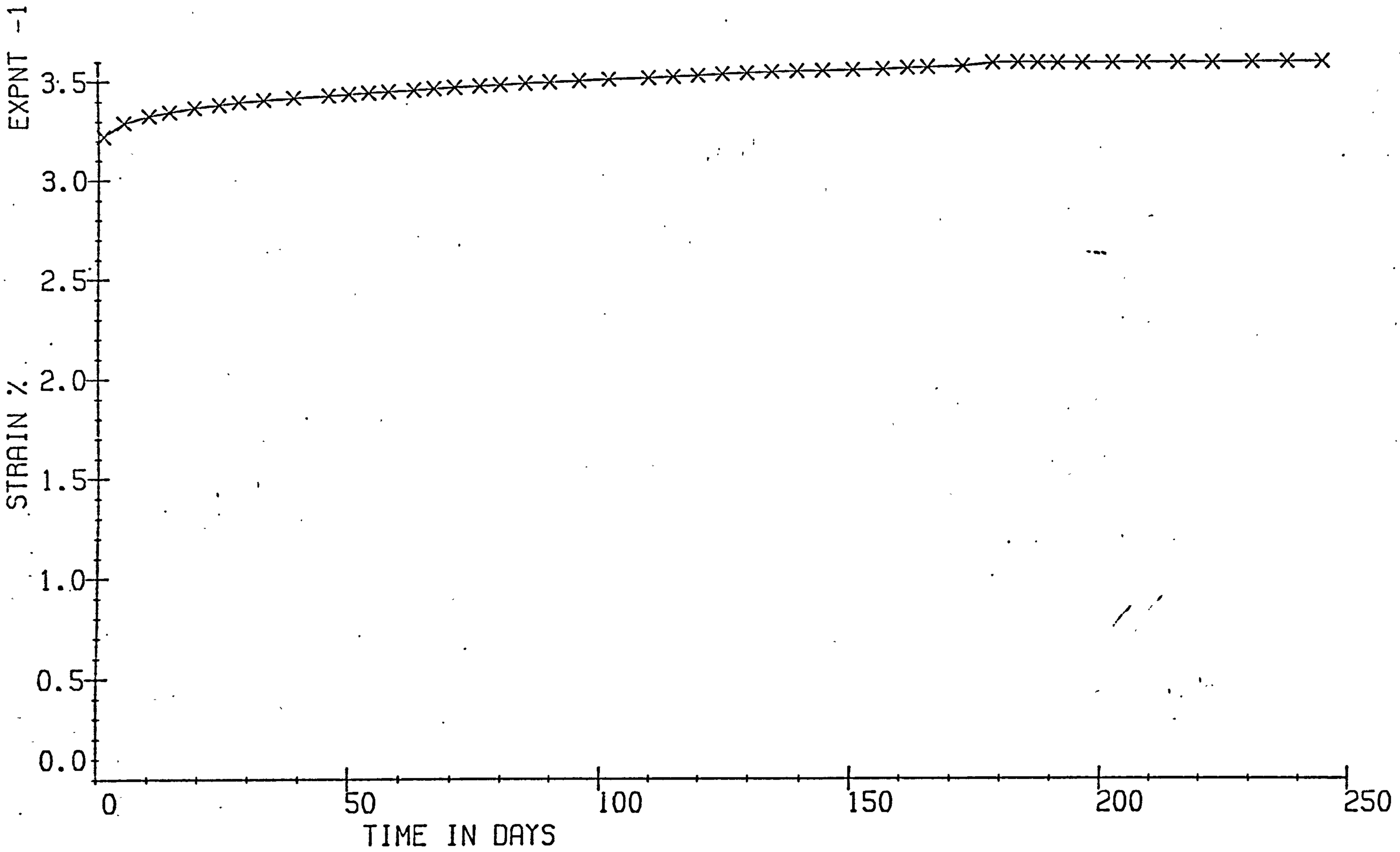

FIG 4.7

LONG TERM CREEP CURVE OF SUBMERGED MARBLEAGIS GY

RIG NO:A (75 % WET STRENGTH)

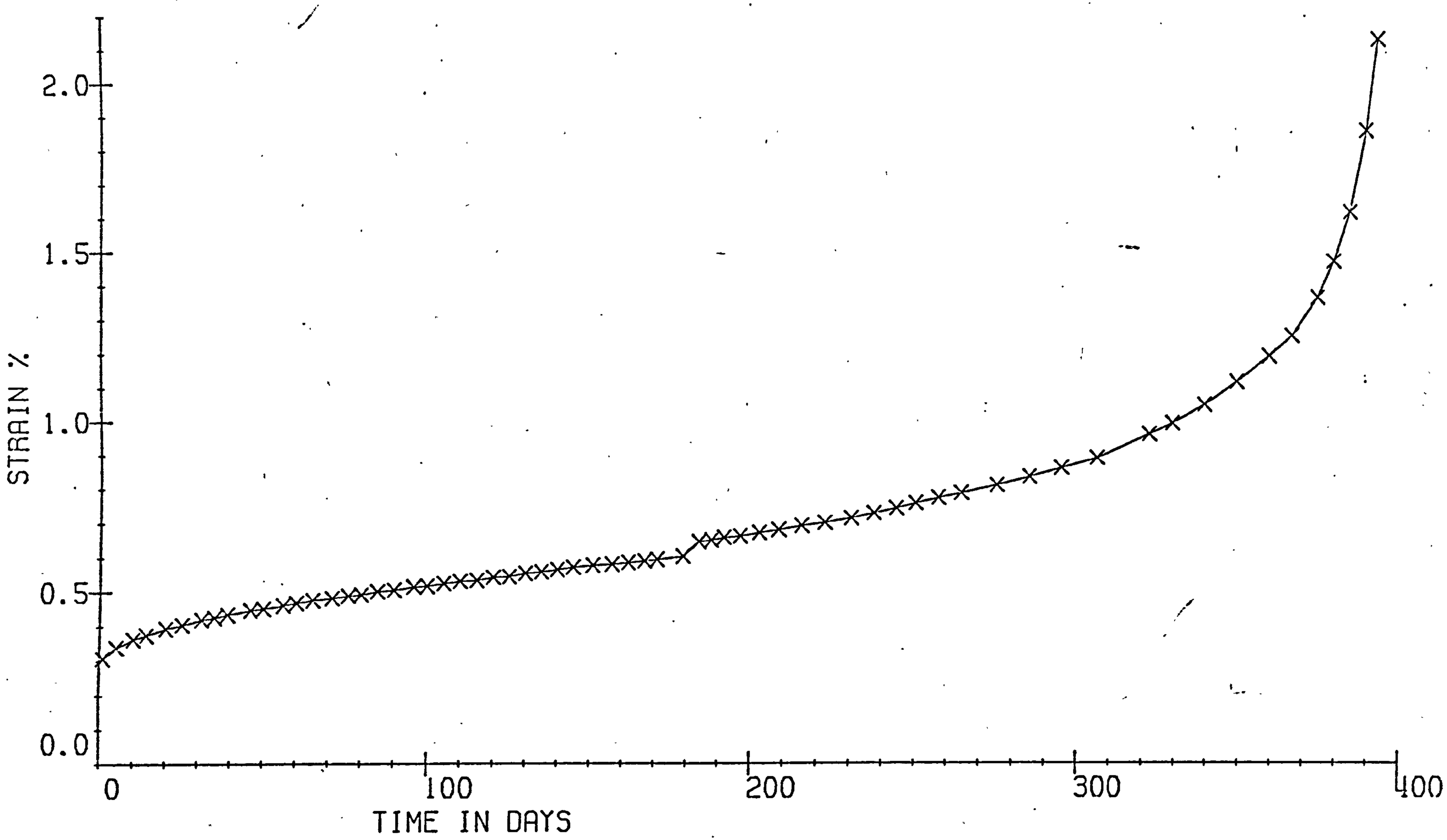

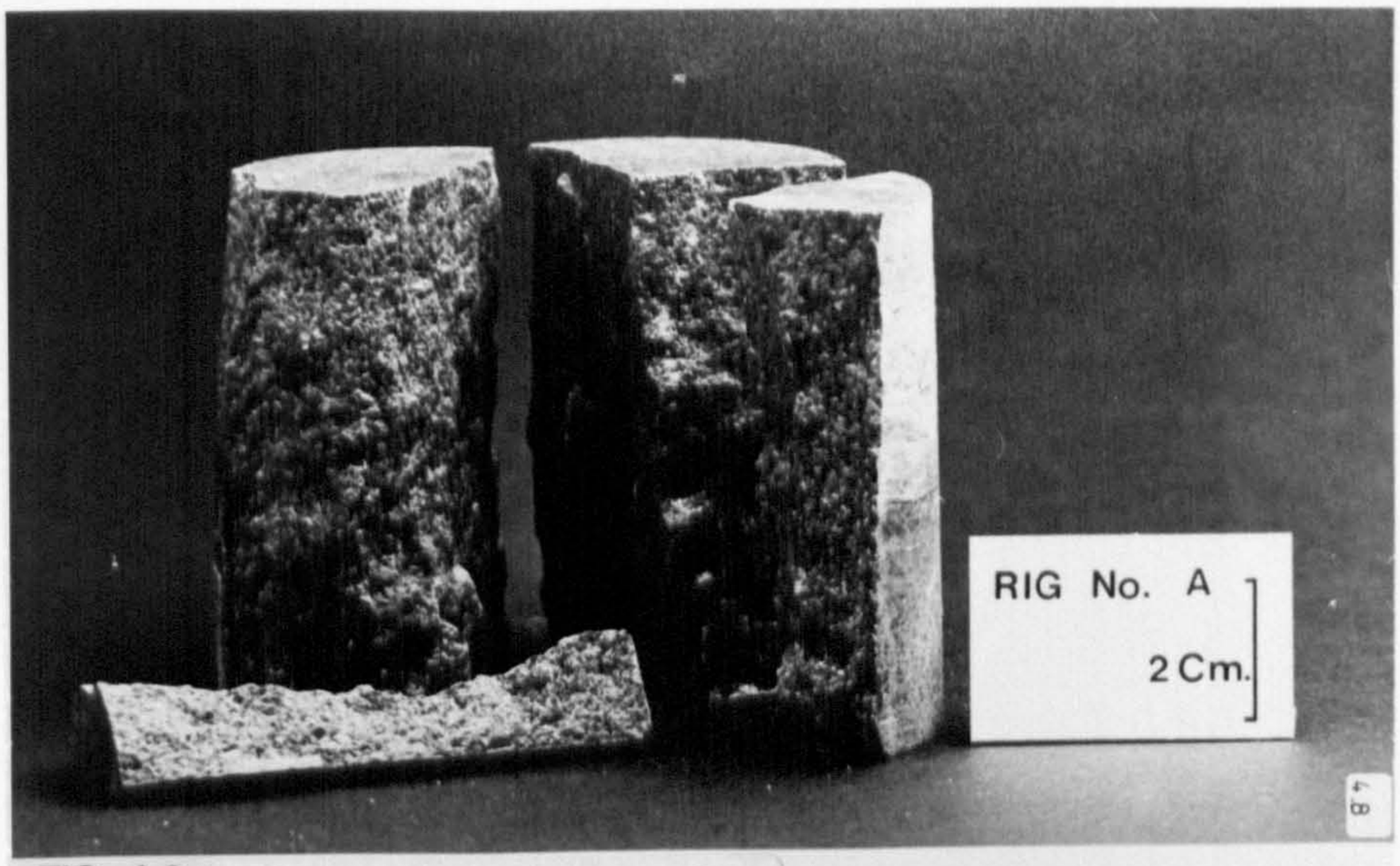

FIG. 4.8 Broken Dolerite

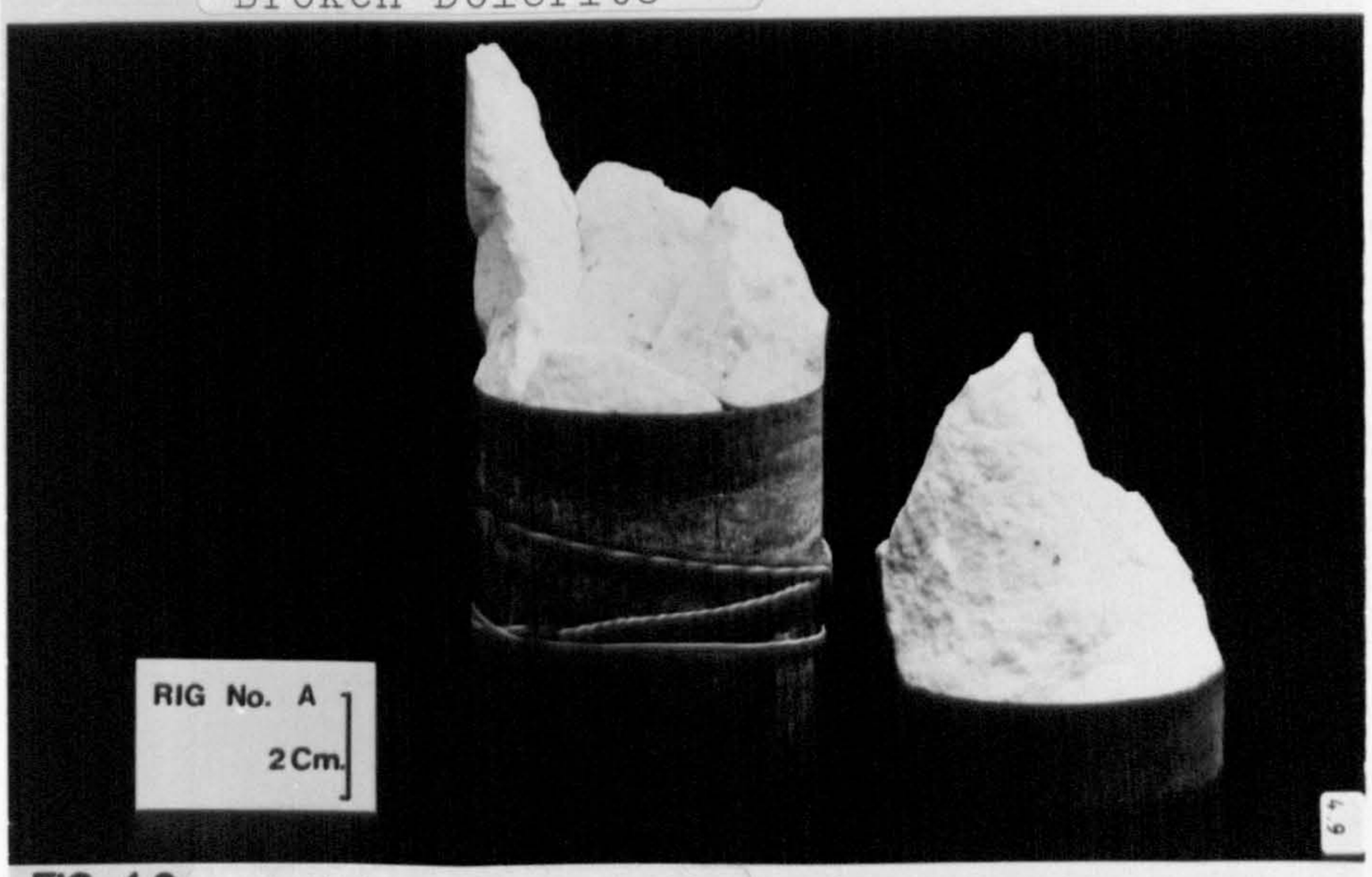

FIG. 4.9 Broken Specimen A

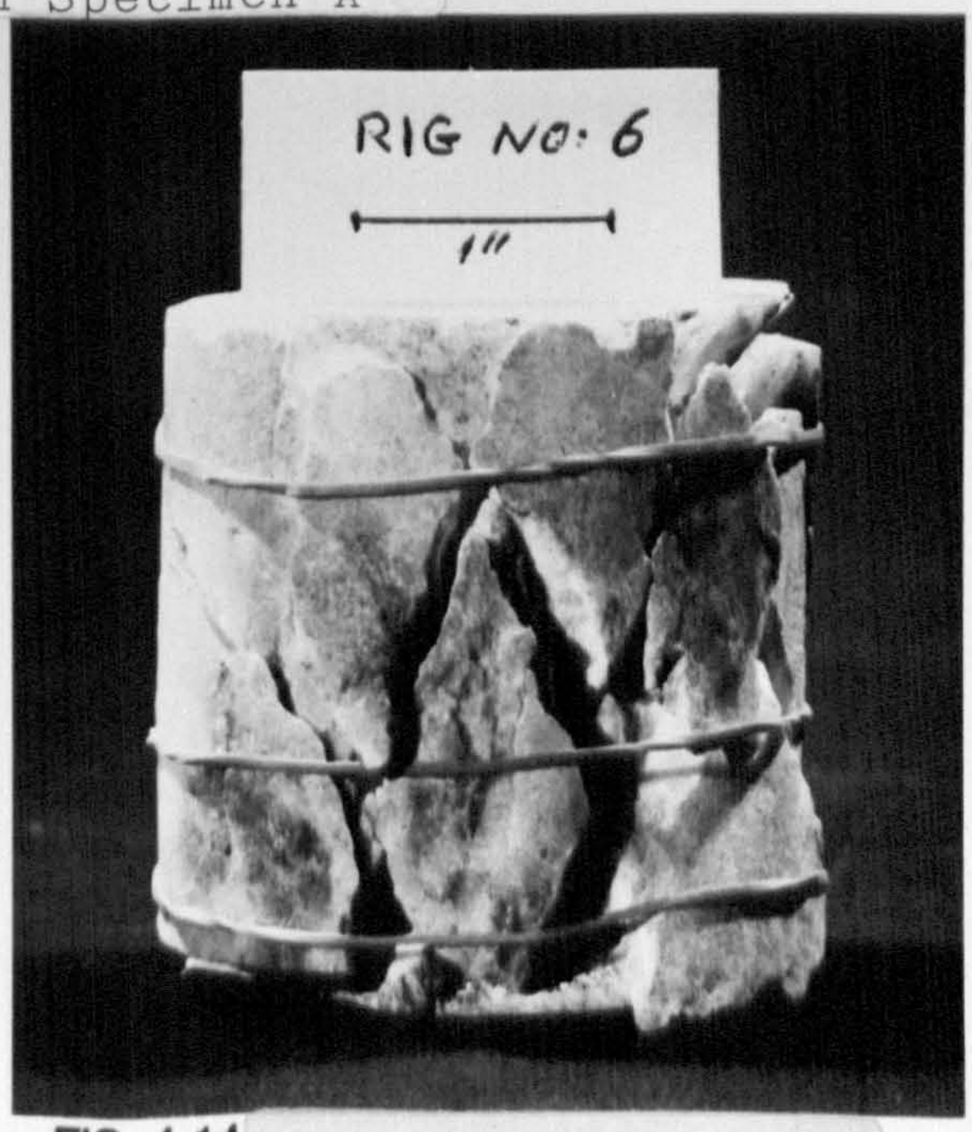

FIG. 4.14 Broken Specimen 6

FIG 4.10

LONG TERM CREEP OF SUBMERGED FAULD GYPSUM

RIG NO:10 (75 % WET STRENGTH)

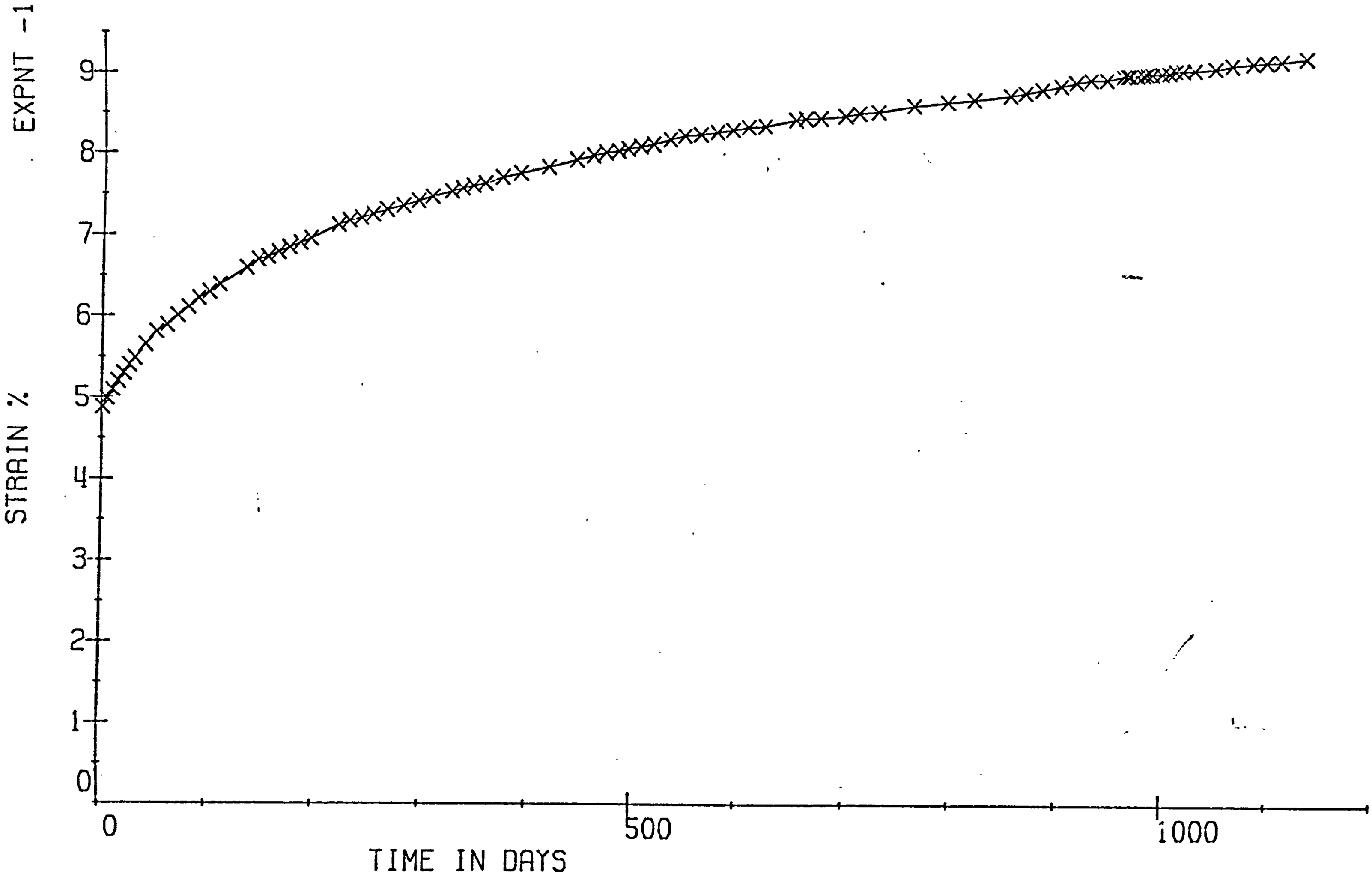

FIG 4.11

LONG TERM CREEP OF SUBMERGED FAULD GYPSUM

RIG NO:12 (75 % WET STRENGTH)

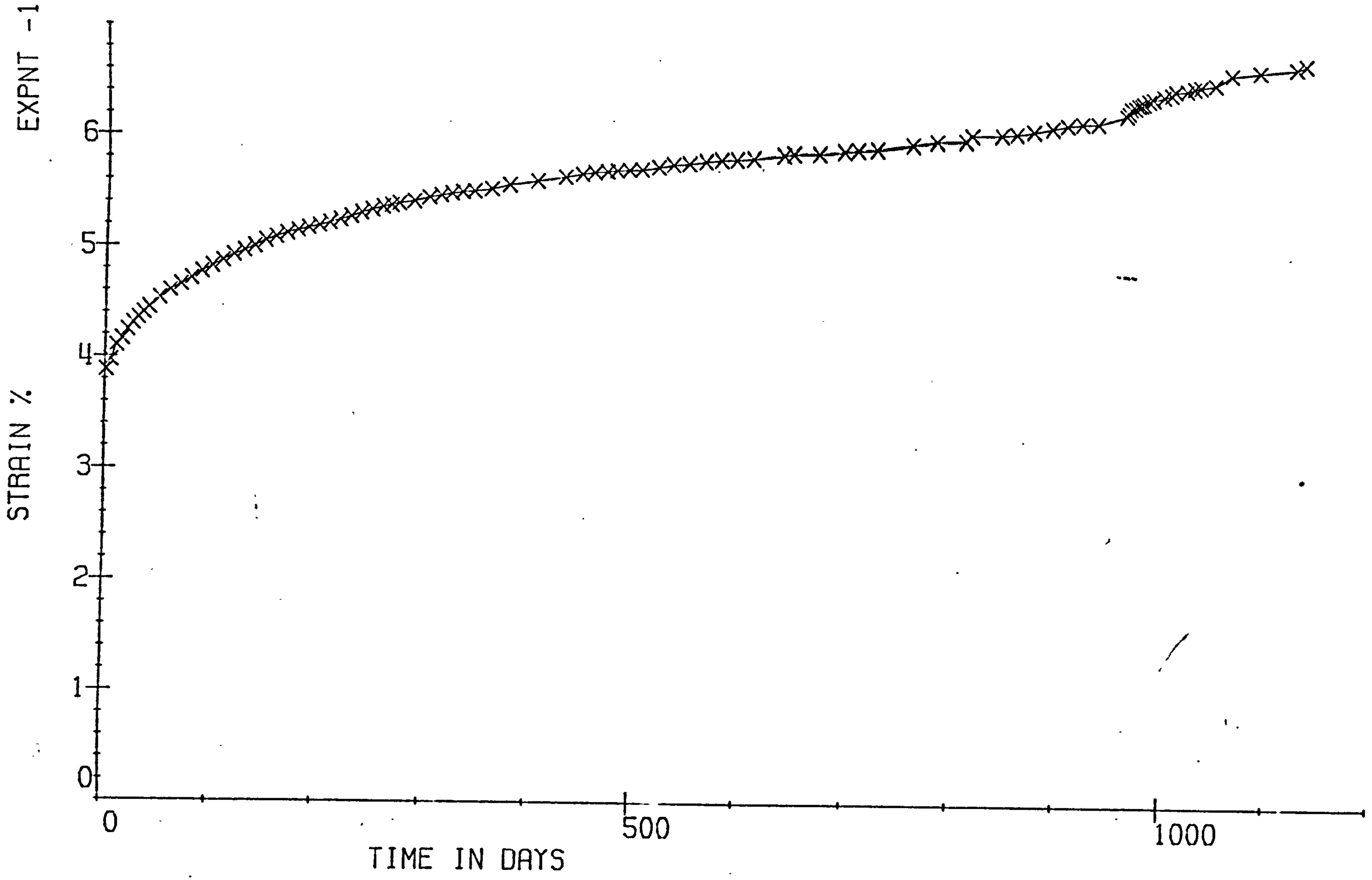

FIG 4.12

LONG TERM CREEP OF FAULD GYPSUM

RIG NO:13

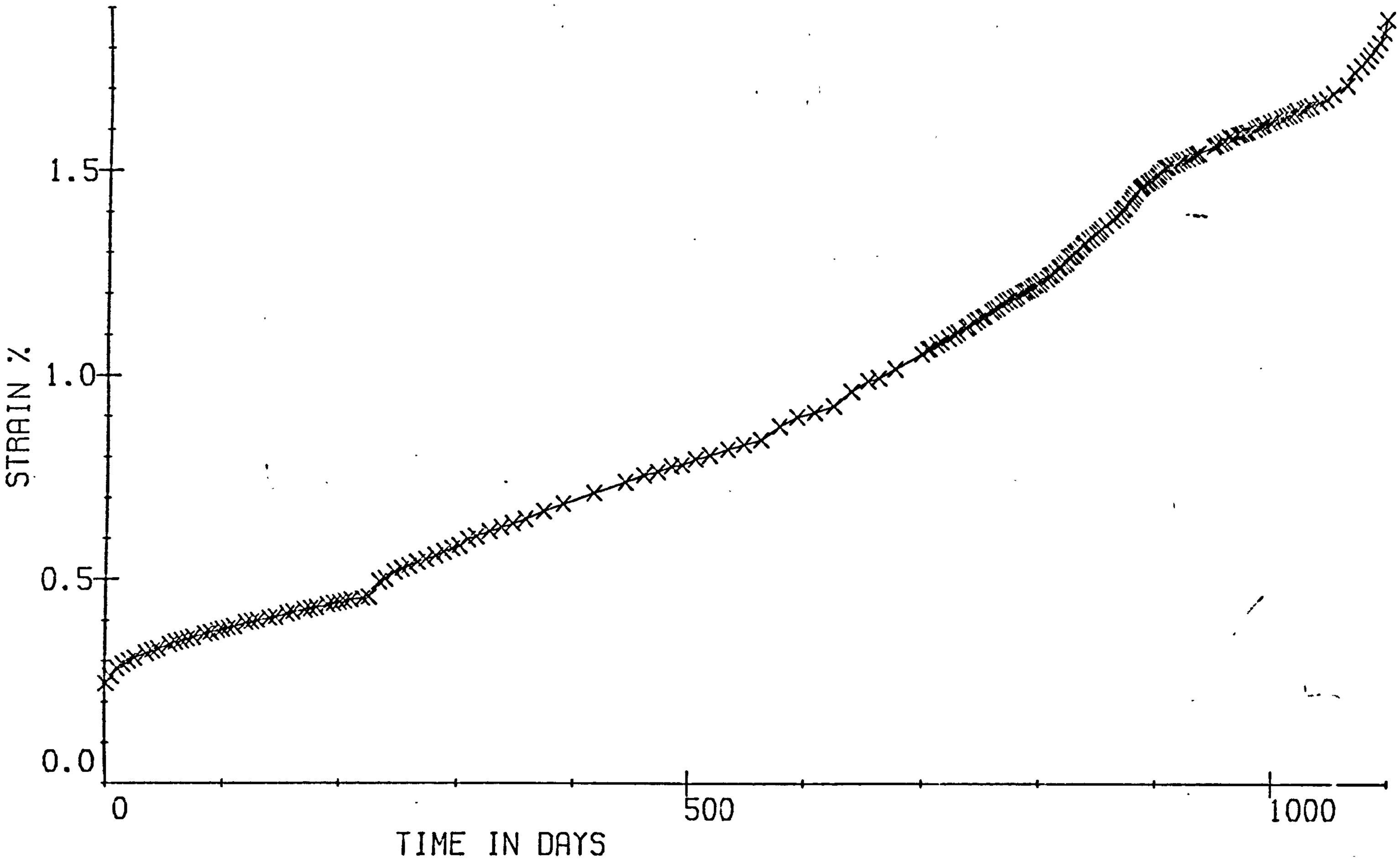

FIG 4.13

FIG 4-13 LONG TERM CREEP CURVE OF SUBMERGED MOUNTFIELD GY.

RIG NO: 6 (75 % WET STRENGTH)

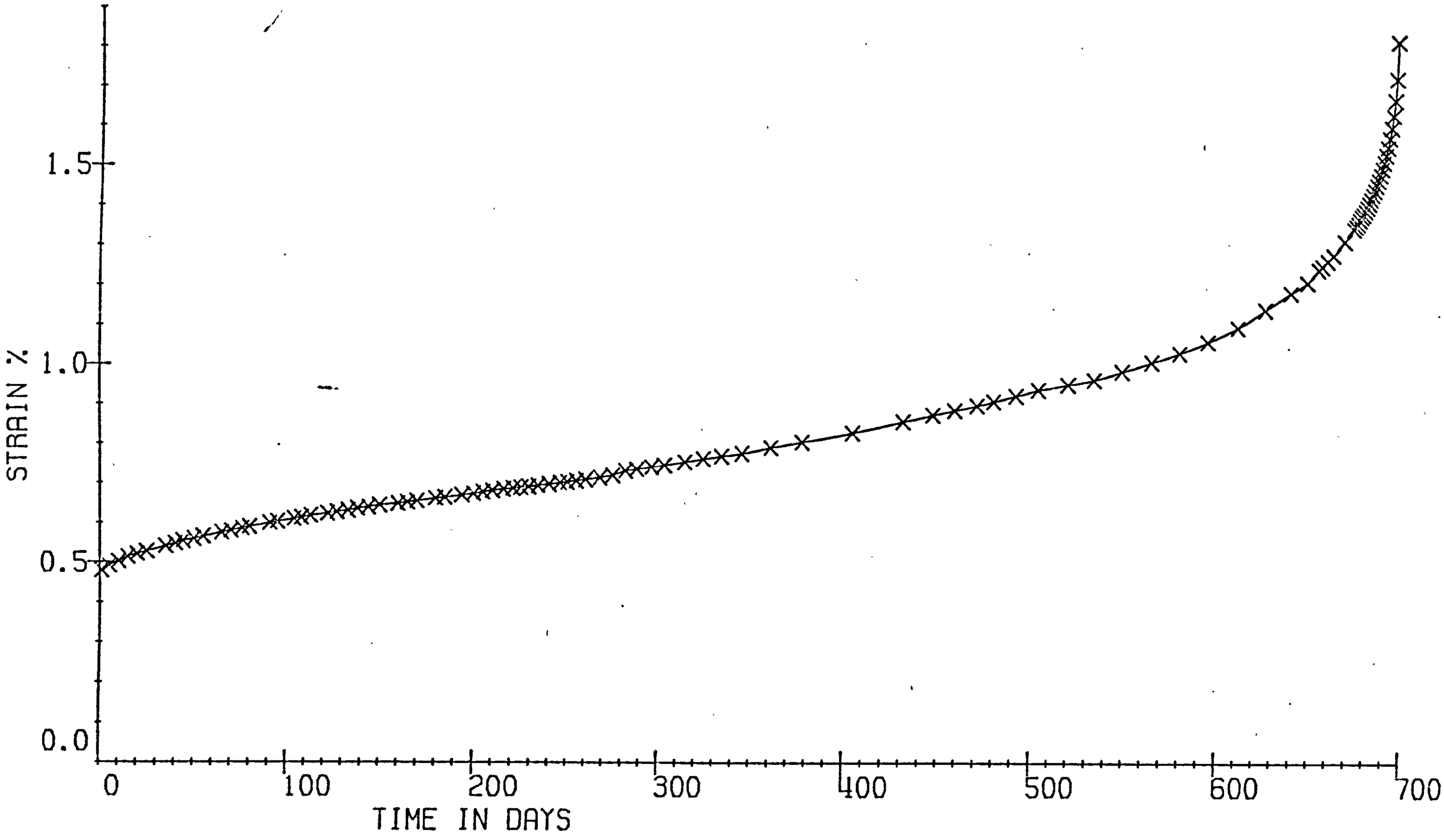

FIG 4.15

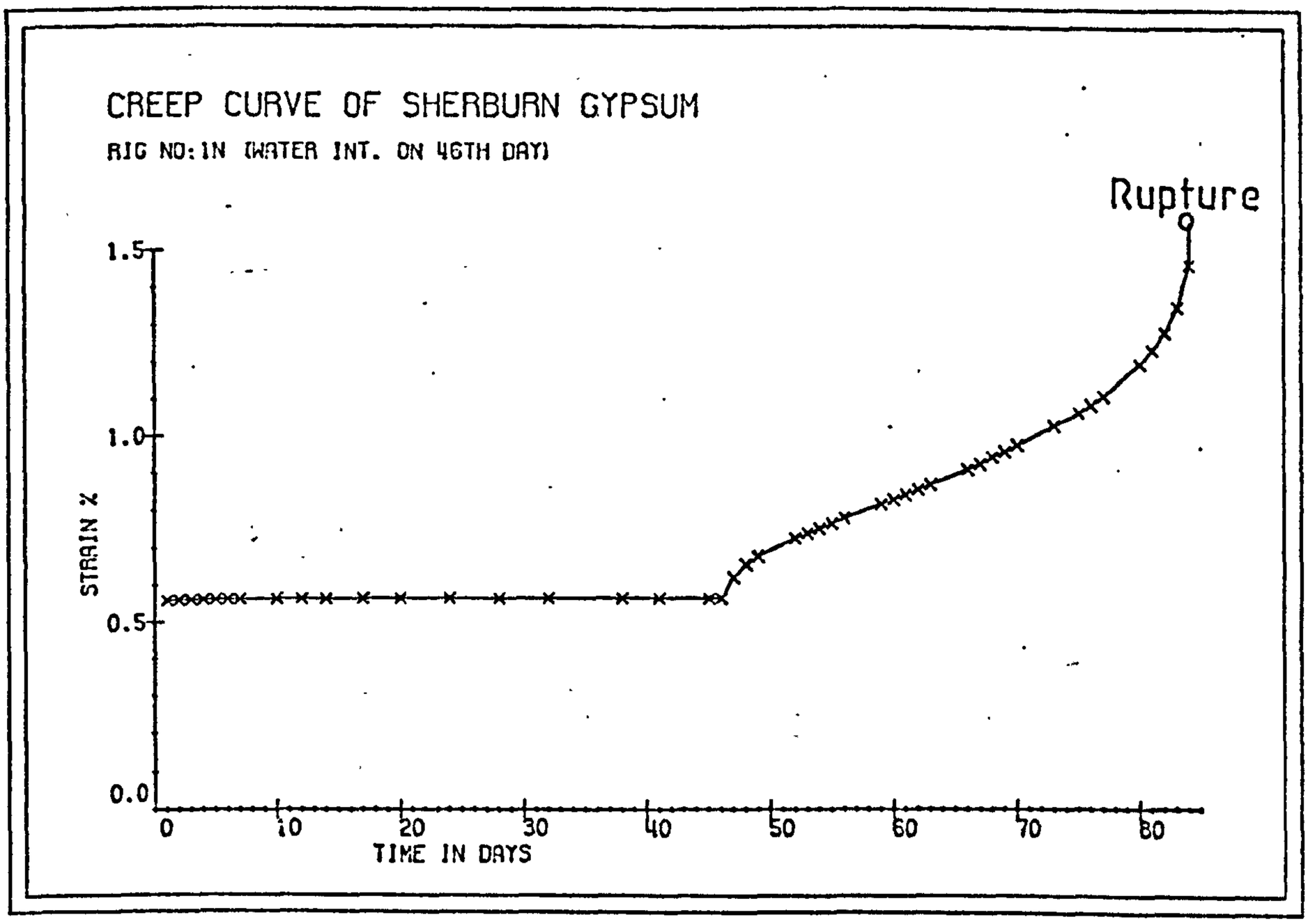
CREEP CURVE OF SHERBURN GYPSUM
RIG NO:1N (WATER INT. ON 46TH DAY)
Rupture
1.5
1.0
0.5
0.0
STRAIN %
0
10
20
30
40
50
60
70
80
TIME IN DAYS

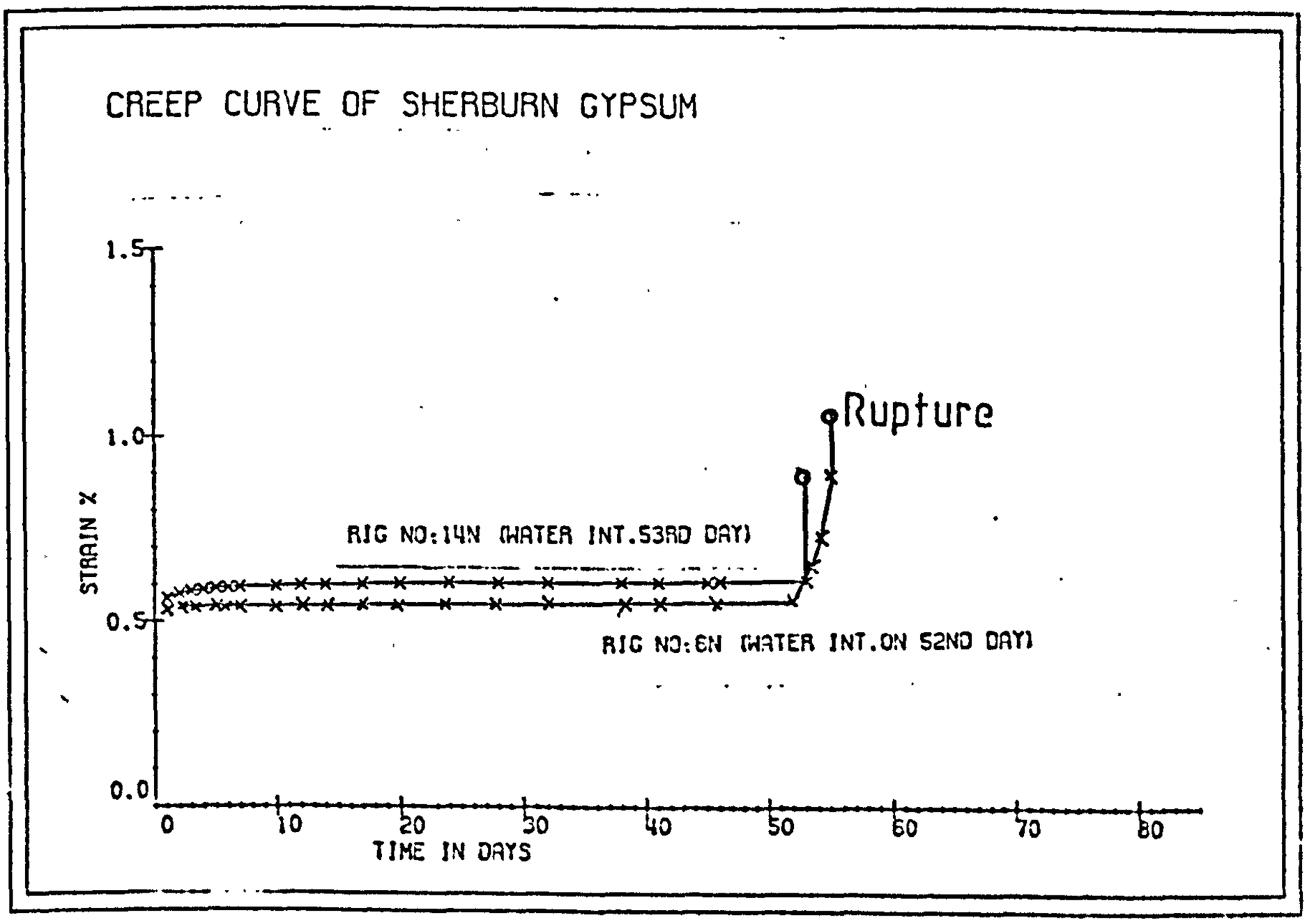
CREEP CURVE OF SHERBURN GYPSUM
1.5
1.0
0.5
0.0
STRAIN %
Rupture
RIG NO:14N (WATER INT.53RD DAY)
RIG NO:6N (WATER INT.ON 52ND DAY)
0
10
20
30
40
50
60
70
80
TIME IN DAYS

TABLE 4.1

SOLUBILITY OF MATERIALS (JAMES & KIRKPATRIC 1980)

MATERIAL	SOLUBILITY IN PURE WATER (10°C)) (Kg/m^3)
GYPSUM	2.5
ANHYDRITE	2.0
HALITE	360.0
LIMESTONE	0.015
QUARTZ	0.01

TABLE 4.2

SOLUTION RATE CONSTANTS AT 10°C (JAMES & KIRKPATRICK 1980)
(FLOW VELOCITY 0.05 m/s -PURE WATER)

MATERIAL	$K(ms^{-1})*10^5$ ($\theta=1$)	$K(m^4kg^{-1}s^{-1})*10^6$ ($\theta=2$)
GYPSUM	0.2	-
ANHYDRITE	-	0.8
HALITE	0.3	-
LIMESTONE	0.4	-
QUARTZ	$dc/dt=10^{-17}*(s/v)Kgm^{-2}s^{-1}$	-

TABLE 4.3

MINE WATER ANALYSIS EXPRESSED AS EQUIVALENT SULPHATE CONTENT (ppm) (PRESTON,1930)

SAMPLE	FAULD	MARBLEAGIS
Calcium as CaO	1836.0	1707.0
Magnesium as MgO	416.0	426.0
Iron as Fe_2O_3	-	-
Sodium as Na_2O	86.0	117.0
Potassium as K_2O	7.0	25.0
Aluminium as Al_2O_3	-	-
TOTALS	2345.0	2275.0
TOTAL SOLUBLE SOLIDS (Dried at 175°C)	2410.0	2390.0
ERROR (%)	2.7	4.8
AMOUNT OF SATURATION WITH $CaSO_4$	76.0	71.5
ACIDITY (pH)	7.3	7.2

TABLE 4.4

VARIATION OF STRENGTH WITH MOISTURE IN UNIAXIAL COMPRESSION

RESEARCHER	CONDITION	ROCK TYPE	APPARENT POROSITY (%)	STRENGTH REDUCTION (%)
PRICE (1960)	SATURATED	SANDSTONE	-	55
COLBACK AND WIID (1965)	SUBMERGED	SHALE	0.28	50
		SANDSTONE	15.0	
WIID (1970)	SATURATED	DOLERITE	1.0	35
		SANDSTONE	21.0	32
		SANDSTONE	15.0	49
RUTTER (1972)	SATURATED	LIMESTONE	-	30
BROCH (1974)	SATURATED	VARIOUS	0.3-1.2	33-55
LISK (1976)	SATURATED	GYPSUM	2-4	22
ALI (1979)	SATURATED	GYPSUM	-	47-49

TABLE 4.5

COMPRESSIVE STRENGTH DATA (PRESTON-1980)

MATERIAL SOURCE	DRY STRENGTH MPa(psi) VALUES	MEAN	STND.DEV.	WET STRENGTH MPa(psi) VALUES	MEAN	STND.DEV.	STRENGTH REDUCTION %
MOUNTFIELD NO:1 SEAM	48.8 44.2	46.5 (6743)	2.3 (334)	32.2 28.1	30.2 (4379)	2.05 (297)	35.0
MOUNTFIELD NO:4 SEAM	33.2 31.6	32.4 (4698)	0.8 (116)	25.7 22.3	24.0 (3480)	2.0 (290)	42.2
FAULD	41.1 36.7	38.9 (5641)	2.2 (319)	24.5 20.5	22.5 (3263)	1.7 (247)	25.9
MARBLEAGIS	48.4 38.2	43.3 (6279)	5.1 (740)	20.5 31.5	26.0 (3770)	5.0 (725)	40.0
SHERBURN	44.9 46.1	45.6 (6605)	0.8 (120)	32.9 35.0	33.9 (4920)	1.5 (220)	25.5

TABLE 4.6

TENSILE STRENGTH (BRAZILIAN DISC) OF GYPSUM

NO:	1	2	3	4	MEAN	REDUCTION %
DRY MPa	3.753	3.306	4.698	3.840	3.899∓0.582	---
DRY (psi)	544.2	479.4	681.2	556.8	565.4∓84.4	---
WET MPa	2.793	2.533	1.610	1.660	2.149∓0.132	44.9
WET (psi)	405.0	367.3	233.5	240.7	311.6∓19.1	44.9

TABLE 4.7

CREEP TEST RAM AND SPECIMEN SPECIFICATION

CREEP TESTS AT 75 % OF THE WET STRENGTH						
NO	SPECIMEN TYPE	σ wet (MPa)	σ applied (MPa)	RAM TYPE	RAM PRESSURE Psi	RAM PRESSURE MPa
8	MARBLEAGIS	24.0	16.0	P131	889	6.13
A	MARBLEAGIS	24.0	18.0	P230	450	3.13
11	MARBLEAGIS	24.0	18.0	P230	450	3.13
6	MAUNTFIELD	30.2	22.6	P131	1117	7.71
10	FAULD	22.5	16.8	P131	830	5.72
12	FAULD	22.5	16.8	P131	830	5.72
13	FAULD	22.5	16.8	P131	830	5.72
14N	SHERBURN	34.0	30.0	P230	755	5.21
1N	SHERBURN	34.0	30.0	P230	755	5.21
6N	SHERBURN	34.0	30.0	P131	1506	10.39

**SPECIMENS 2.5"x2.5" (6.35cmX6.35cm Cylindirical)
SUBMERGED IN MINE WATER

DETAILS OF HYDRAULIC RAMS IN CREEP RIGS

EPCO P230-100 TON

RAM AREA:28.27 sq in. (0.01824 sq m.)

EPCO P131-50 TON

RAM AREA:14.16 sq. in (0.00915 sq m.)

TABLE 4.8

STRAIN RATES ($X10^{-3}$/DAY)

SPEC.TYPE	MARBLEAGIS			MOUNTFIELD	FAULD		
SPEC.NO: TIME	8	A	11	6	10	12	13
1-5	1.75	7.88	1.50	3.08	2.75	2.20	4.50
5-10	0.70	4.60	0.60	2.10	2.10	2.60	3.84
10-14	0.48	3.00	0.50	2.34	2.10	1.20	1.86
20-25	0.30	2.20	0.30	1.26	2.00	1.20	1.40
30-35	0.18	1.50	0.25	1.12	1.65	0.90	0.90
45-50	0.18	1.13	0.13	0.92	1.60	0.85	1.00
75-80	0.13	0.95	0.07	0.88	1.05	0.55	0.77
100-105	0.08	1.50	0.08	1.10	0.92	0.50	0.66
150-155	0.05	0.47	0.05	0.40	0.33	0.32	0.76
200-205	0.01	1.53	0.05	0.74	0.64	0.25	0.52
250-255	--	2.23	0.03	0.60	0.42	0.25	1.33
300-305	--	2.62	0.02	0.63	0.42	0.18	2.34
350-355	--	7.50	0.01	0.94	0.29	0.13	0.95
400-405	-	-	--	0.87	0.28	0.13	0.99
450-455	-	-	0.03	0.96	0.34	0.13	1.03
500-505	-	-	--	1.25	0.23	0.05	1.15
550-555	-	-	0.03	1.44	0.11	0.13	0.76
600-605	-	-	0.04	2.20	0.23	0.06	0.75
650-655	-	-	0.02	5.33	0.16	0.13	1.84
698-699	-	-	0.01	93.40	0.13	0.09	1.56
750-755	-	-	0.01	-	0.24	0.12	1.30
800-805	-	-	0.03	-	0.13	0.03	1.04
900-905	-	-	--	-	0.26	0.19	2.68
1000-1005	-	-	--	-	0.09	0.23	1.07

5. ANALYSIS OF CREEP RESULTS

5.1 Introduction

Mathematical description of the mechanical behaviour of an inelastic material is a broad field for investigation with many facets. The ultimate aim is to establish a relationship between the relevant parameters such as time, strain, stress and temperature, so that predictions for the actual behaviour can be made. What is most required, but too often ignored, is the simplicity and the ease in the use. In this Section, some of the different approaches will be discussed briefly with regard to the creep data of the submerged gypsum and two new equations will be derived and the application to the data will be presented.

Methods of analysis of creep data can be divided into three broad categories, namely theoretical, phenomenological and empirical.

5.2 Theoretical Approach

The theoretical approach is mostly used in the field of metals and attempts to explain the creep behaviour on atomic or molecular scale. The theory is based on the lattice imperfections known as dislocations and their movement under a certain stress.

Gordon (1976) defines a dislocation as an irregularity consisting of a line of defects which allow a large number of molecules to move on a broad front. Two basic types of dislocations are known to exist: the edge dislocation and the screw dislocation. The edge dislocation is an extra partial layer of ions in a crystal lattice. The screw dislocation

is equivalent to a partial plane of shear and is more difficult to visualise. Besides the dislocations, crystals contain other defects such as lattice faults, impurity, ions, voids within the lattice and mosaic boundaries and fluid inclusions (Friedel 1964).

Mott (1953), based on the creep theory of the intersection of dislocations moving through a forest of dislocations and on the dynamic recovery by cross-slip of screw dislocations, derived a creep equation which is the same as the β-creep law (Andrade 1910). Lecomte (1965), using a similar theory, found a power law for creep data.

Höfer and Knoll (1969), applying the dislocation theory on the creep of Carnallite specimens which were minerologically pure, arrived on a power relationship for high stresses and on a logarithmic relationship for low stresses.

Apart from the fact that most rocks are inhomogeneous and anisotropic, the theoretical approach requires detailed experimental information on the parameters involved on the microscopic scale and thus violates the rule of simplicity.

5.3 Rheological Approach

Rheology which is the study of flow in general is used for the description of creep behaviour of materials by building up the models as combinations of simple mechanical models which represent the basic concepts of linear elasticity by the use of springs (Hookean substance), viscosity by the use of dash pots (Newtonian substance) and plasticity

by the use of a frictional element (St. Venant's substance). More complicated systems can be generated by arranging these basic elements in series or in parallels.

The most often used rheological models are the Maxwell, Kelvin-Voigth, Generalised Kelvin and Burger models as depicted in Figure 5.1, together with the corresponding empirical equivalents.

The Burger's model includes instantaneous elastic and transient creep deformations both of which are recoverable upon the removal of the applied stress and a steady state creep deformation which is non-recoverable upon the removal of the stress. On this basis, according to some investigators, Burger's model offers the most realistic representation of the four models mentioned in Figure 5.1, with regard to the actual behaviour of rocks (Hardy 1959; Ross 1958; and Watson 1979).

Scheidegger (1970), discussing the inadequacy of the conventional exponential forms of rheological models to describe the creep behaviour of materials which show low strain rates, has deduced a logarithmic form of rheological equation by the correspondence principle.

Shoua and Mase (1966), investigating the influence of confining pressure on polycrystalline rock behaviour, derived a rheological model composed of two independent systems, one representing the crystal properties and the second the properties of grain boundaries. Each system contained a Maxwell unit, the dash pot of which was replaced by a Bingham body in order to provide a yield strength and used in series with the spring and Voigth units. The two systems are fixed at the bottom to a rigid base and are coupled together by a rigid bar hinged to each

system at the top. The position of the applied differential stress along the hinged bar varies relative to the degree of confining pressure. This model shows how refined models may be produced that suit the need of a particular system.

When the rheological approach is adopted, the parameters of the creep law, not the creep law itself, are determined by means of best fit analysis of the experimental data. Numerical difficulties, therefore, increase noticeably as the equation becomes complex. Obviously, it is a matter of opinion whether this feature is compensated by the improvement gained in the results.

Since the structure of the law is derived from a rheological model and is not related to a particular test, it can be applied to a general creep problem without requiring additional assumptions. On the other hand, they do not allow basic changes in the properties of the system to take place such as the incorporation of a fluid which radically changes the creep behaviour of the rocks.

5.4 Empirical Approach

For many years, empirical relationships between the creep strain and time have been used for the description of creep behaviour of metals, concrete and rocks. They can describe the full creep behaviour with sufficient accuracy and are essentially simple and flexible. The main drawback is, however, that each relationship is specific for a particular case and they do not give any information on the actual mechanism of the deformation process. Therefore, extrapolations and predictions may not produce accurate results.

The complete creep strain in relation to creep time can be represented by the general equation in the form:

$$\varepsilon = \varepsilon_e + \varepsilon_p(t) + V.t + \varepsilon_T(t)$$

ε = total strain

ε_e = instantaneous strain

ε_p = primary strain as a function of t

ε_T = tertiary strain as a function of t

V = slope of secondary creep curve.

t = creep time.

Greater attention is paid in this field to the primary and secondary stage creep because of their importance in the design of the structures. Kennedy (1963), Conway (1967), Mirza (1978), and Gilbert (1981), provide a good review of the innumerable empirical equations which can be employed in the creep analysis of metals, concrete and rocks. The equations for convenience are listed in Table 5.1.

Andrade (1910), who published the first modern work on the creep properties of lead, copper and soft alloy metals under tension, fitted this well known one-third power equation to his data:

$$\varepsilon = A.t^{1/3}$$

Griggs (1939, 1940) suggested a power law at high stresses and a logarithmic law at low stresses for alabaster:

$$\varepsilon = At^B \text{ and } \varepsilon = C + \alpha \text{Log } t$$

Lomnitz (1956) and Robertson (1960) used a modified form of logarithmic law:

$$\varepsilon = A\,(1 + B\mathrm{Ln}\,(1 + Ct))$$

Michelson (1917, 1920), proposed an exponential law for the creep of a number of materials, including marble, subjected to torsion:

$$\varepsilon = A\,(1 - \exp\,(-B.t^{\frac{1}{2}})) \qquad \ldots\ldots(5.4.1)$$

He compares the equation above (5.4.1) with the one having (t) instead of ($t^{\frac{1}{2}}$) and concludes that the equation above provides much better fit for the long term data.

Glanville (1930) and Evans (1940) used a slightly different equation:

$$\varepsilon = A\,(1 - \exp\,(B - CT^{n}))$$

For the gypsum, Griggs (1960), Ali (1979), Williams and Ellizzi (1979) and Preston (1980) fitted a power law at high stresses, a logarithmic law for low stresses and dry condition, whereas only a power law for saturated condition.

With power, one-third power and logarithmic laws, strain continually increases with time, instead of tending to a constant value and as time approaches zero ($t \rightarrow 0$), the rate of strain becomes infinite.

Exponential forms offer a more realistic tendency in this respect. This issue is of considerable importance when a prediction is attempted over long periods of time. Further, improvements in the exponential forms can be made by summing a series of exponential terms but this inevitably violates the rule of simplicity.

Logarithmic law fits the early part of the data reasonably well but in the later stages generally underestimates the creep strain as a function of time. With the power law, the early fit is often good but the overestimate of the later creep is worse than that of the logarithmic law.

Coefficients appearing in the empirical law referring to the particular conditions of experiments such as temperature, confining pressure, presence of solutions, etc. and are determined by means of curve-fitting techniques. The goodness of fit, i.e. the ability of the proposed law to describe the data, can be expressed by the correlation coefficient, sum of squares of residuals, randomness and distribution of residuals. Cruden (1971a) discusses the problems arising when using curve-fitting techniques to identify the best curve from the many curves available. He has suggested a statistical method to examine the various functions. After some consideration he rejected the exponential law of creep.

5.5 Preliminary Analysis of Creep Data

An assessment of strain rates suggests that the creep behaviour of all specimens consisted of either a mainly primary stage, with very small decrease in the strain rate with time, or a primary stage immediately followed by a tertiary stage. The absence of a well defined secondary stage conflicts with the findings of Hedley (1965) on rock salt, though it is difficult to reach a definite conclusion due to the limited number of tests. On these grounds, the division of the full creep curve into two parts, for the purpose of regression analysis, was thought to be justified.

Bias due to the frequency of observations can occur when a considerable amount of data points are recorded at the start of the test and gradually becomes less frequent. This effectively produces a weighting effect on the transformed data; as a result, the 'fit' becomes biased towards the more important later stages. This is overcome by a careful selection of a roughly even range of data before analysis begins.

The creep data of submerged gypsum specimens, stored in separate files, have been analysed on the computer, using a curve fitting program which is available in the N.MTS system as a part of PADAS package, details of which can be found elsewhere (Watson 1979). The program employs the least squares method to regress the data against seven standard curves, as follows:

LINEAR	$Y = A + B * X$
POWER	$Y = A \times (X^B)$
EXPONENTIAL	$Y = A \times EXP\ (B \times X)$
LOGARITHMIC	$Y = A + B \times LOG(X)$
HYPERBOLIC	$Y = A \times (B/X)$
HYPERBOLIC	$Y = 1/(A+B \times X)$
HYPERBOLIC	$Y = X/(A+B \times X)$

where A and B are constants, Y and X are the variables supplied by the user in any form desired.

Thus by making suitable arrangements of input it is possible to obtain most of the equations listed in Table 5.1 or further refined forms.

Creep data have been inputted in two forms. The percentage creep strain versus the creep time in days, and the logarithm of percentage creep strain and the logarithm of creep time in days, so as to double the number of equations against which the data is regressed.

This also allows us to check the goodness of the power fit which yields a straight line on the log-log scale as suggested by Griggs (1939); Ali (1979); and Preston (1980).

The nature of some of the functions prevented data with an origin at (0,0) from being fitted. In such cases, zero was replaced by the smallest value that could be placed in a formatted reading, that is 0.0001. This was considered particularly important, as previous experience indicated that a power law for normal data and an hyperbolic or linear law for the log-log data was likely to be a good fit.

The results of analysis are outputted in two different ways; firstly, for the different equation used in the analysis the calculated constants A and B are given in Table 5.2, along with the Index of Determination. Secondly, after the best fit was selected, based on the Index of Determination, a plot of the selected equation with the observation points was drawn.

5.6 Appraisal of the Analysis

The numerical output of the analysis using the least squares method which attempts to minimise the distance of the line from the data points (Alder and Roessler 1968), together with the analysis of the processed data, which will be dealt with in the following subsections, can be seen in Appendices 5.1a and b. The best fit out of seven equations for each set of data was chosen from the full analysis based on the Index of Determination and is shown in Table 5.2 along with the plots from Figures 5.2 to 5.8.

In Table 5.2 it appears that the power and linear laws are superior to others in describing the primary stage data in the form of creep time and creep strain. However, substantial deviations of the corresponding correlation coefficients from unity clearly indicate the disagreement of the power and linear laws with the experimental data. Inspection of the Figures 5.2 to 5.8 will clearly indicate the severity of the deviations. The data from specimens 8 and 11 (Figures 5.2 and 5.6) would seem to obey a power law slightly better than others. Nevertheless, in all cases the best fit power law over-estimates the data during the early stages and underestimates it in the later stages.

The results of analysis of the primary stage creep data inputted in the form of log strain-log time can be seen in Table 5.3. The best fit in this case would seem to be a linear law which, when transferred to normal scale yields a power law. The correlation coefficients and the visual check of the fits (Figures 5.9 to 5.15) clearly demonstrate the poorness of the relationship. It must, however, be pointed out in this context that there are two extremely important points which may lead to misunderstanding in the interpretation of the results when the curve fitting attempts are made on the log-log scale. Because of the nature of the logarithmic function, the differences in the successive strain values and time values are largely suppressed during later stages, whereas this is not so pronounced during the early stages. This, firstly, reduces the effect of the magnitudes of the differences in the least squares fitting process, which attempts to find an optimum line for the observation points by reducing the distance between the points and the

line and, secondly, creates a bias due to the weighting effect. The evidence for this phenomenon is provided in Tables 5.2 and 5.3. The specimens 8, 11, 10 and 12 are found to obey a power law, both in normal scale and in log-log scale. Despite the close similarity between the correlation coefficients, the constant B, which is supposed to be the same in both cases is assigned to various values.

The deviations of the data points from a straight line in the log-log scale implies either an overestimate or an underestimate of a power law, but not necessarily an inflexion point. As can be seen from Figures 5.9 to 5.15, substantial deviations are evidenced, although specimens are still in the primary stage.

The tertiary stage data is also regressed in order to establish a relationship between the creep strain and creep time, by which a prediction of the failure time may be made. The results of the numerical analysis are presented in Table 5.5 and also in Figures 5.16 and 5.17. It is evident from the correlation coefficients and the figures that the predictions based on the best fit (that is, a hyperbolic function) can produce unrealistic failure times (540.5 days for speciman A, and 1079.4 days for specimen 6).

Consequently, it can be concluded that creep laws in the form of power, logarithmic, exponential and hyperbolic equations in the form used above are not suitable to describe the creep behaviour of submerged gypsum in undisputable form and hence these may be rejected.

5.7 Development of a formula for primary stage creep data

Failure to describe the creep behaviour of submerged gypsum by means of conventional forms of power, logarithmic, exponential and log-log hyperbolic equations with reasonable accuracy necessitated the development and application of a new equation.

With a power equation, whose derivative with respect to time is, strictly speaking, again a power relationship, the rate of decrease in the strain rate with time appears to be relatively slow compared to that of the actual data. This is illustrated in Figure 5.18, where curve number 2 shows the decrease of strain rate with time, according to a best fit power law and the curve number 1 is (for the time being) assumed to show the decrease of the strain rate of the experimental data with time. The difference between the rate of strain increases as the time elapses and this is reflected on the creep curve as an overestimate. In Figure 5.19, the strain rates of the power law curve and the data in relation to the time are plotted on the logarithmic scale. Examination of the results shown in Figure 5.19 may be carried further as follows:

When a power law in the form of $\dot{\varepsilon} = AxT^{B}$ is differentiated with respect to time, it becomes:

$\frac{d\varepsilon}{dt} = A.B.T^{B-1}$ and taking the logarithm of it, a linear function in the form of

$Ln.\ (\frac{d\varepsilon}{dt}) = LnA + lnB + (B-1)Lnt$ is generated which is, in fact, curve number 2 in Figure 5.19. However, the curve of the observations

at a certain point deviates from the straight line and attains a curved nature. It is logical, therefore, to express the first linear portion of the curve of the data in the form of:

$$\text{Ln}\ (\frac{d\varepsilon}{dT}) = A + B\ \text{Ln}(T)$$

To this equation, for the remaining part of the curve, an equation in the general form of f(T) can be added. Thus it becomes:

$$\text{Ln}\ (\frac{d\varepsilon}{dT}) = A + B\ \text{Ln}(T) + f(T)$$

We can now examine the possible types of the function f(T). A logarithmic form can be easily ruled out since, when the antilogarithm is taken, another power equation is obtained:

$$\text{Ln}(\frac{d\varepsilon}{dT}) = A + B\ \text{Ln}(T) + C\ \text{Ln}(T) \Rightarrow \text{Ln}(\frac{d\varepsilon}{dt}) = A + \text{Ln}\ (T^{B+C})$$

and $\quad \frac{d\varepsilon}{dT} = D.T^{B+C}$

Also an exponential function can be ruled out because when

$$\text{Ln}\ (\frac{d\varepsilon}{dT}) = A + B\text{Ln}(T) + e^{T} \Rightarrow \text{Ln}\ (\frac{d\varepsilon}{dT}) = \text{Ln}\ (T^{B}.e^{e^{T}}) + A$$

and $\quad \frac{d\varepsilon}{dT} = D.\ T^{B}.\ e^{(e^{T})}$. Integration of this is extremely difficult.

A linear function can also be discounted since, when:

$$\text{Ln}\ (\frac{d\varepsilon}{dT}) = A + B\ \text{Ln}(T) + C.T \Rightarrow \text{Ln}\ (\frac{d\varepsilon}{dT}) = A + \text{Ln}\ (T^{B}.e^{c.t})\ \text{and yields:}$$

$$\frac{d\varepsilon}{dT} = D.T,^{B}e^{C.T}.$$

However, a power function produces the easiest possible answer to the problem:

$$\text{Ln}\left(\frac{d\varepsilon}{dT}\right)=A + B\ \text{Ln}(T)+CT^{n} \Rightarrow \text{Ln}\left(\frac{d\varepsilon}{dT}\right)=A + \text{Ln}\left(T^{B} \times K^{T^{n}}\right) \text{ where } C = \text{Ln}K$$

and $$\frac{d\varepsilon}{dT} = D \cdot T^{B} \cdot K^{(T^{n})}.$$

If $B = n - 1$ and $A = n.\varepsilon_{o}.\text{Ln}\,K$, are taken, the integration of this equation with respect to time yields an equation of the form:

$$\varepsilon = \varepsilon_{o} \times K^{(T^{n})} \qquad \ldots\ldots 5.1$$

Further support to the development of this formula comes from the log-log graphs of the experimental data. Inspection of Figures 5.9 to 5.15 clearly suggest that if the double logarithm of the strain is taken, it is possible to transform the curve to a straight line. Thus, if:

$$\text{Ln}\,(\text{Ln}\,(\varepsilon/\varepsilon_{o}))=\text{Ln}A + n\cdot\text{Ln}\,T$$

taking antilogarithm, it becomes:

$$\text{Ln}\,(\varepsilon/\varepsilon_{o}) = A \times T^{n} \text{ and taking}$$

$$A = \text{Ln}\,K \quad \Rightarrow \text{Ln}\,(\varepsilon/\varepsilon_{o}) = \text{Ln}\,K \times T^{n}$$

and second antilogarithm equation is reduced to:

$$\varepsilon/\varepsilon_{o} = K^{(T^{n})} \text{ and } (\varepsilon = \varepsilon_{o} \times K^{T^{n}})$$

In fact, this rather unusual equation provided exceptionally good fit to the data as will be shown later. Furthermore, when the second

derivative of the equation with respect to time is taken, the presence of an inflexion point is found.

$$\frac{d^2\varepsilon}{dt^2} = n.\varepsilon_o.\text{Ln } K.K^{(T^n)}.T^{(n-2)}((n-2) + T^n \; n.\; \varepsilon_o.\text{Ln } K)$$

in order $\frac{d^2\varepsilon}{dt^2} = 0 \Rightarrow ((n-2) + T^n\; n.\; \text{Ln } K) = 0$ thus

$$T = \left(\frac{1-n}{n.\varepsilon_o.\; \text{Ln } K}\right)^{1/n}$$

is obtained. It must be pointed out, however, that time obtained for the inflexion point using relevant constants was too far to be acceptable. Therefore, the full extent of the formula is not used, and it is suggested that the inflexion point should be determined experimentally.

In equation 5.1, if the time is zero (T = 0), the initial strain is obtained ($\varepsilon = \varepsilon_o$) and if the time is one day, strain becomes equal to $\varepsilon = \varepsilon_o$. K, thus a reasonably accurate estimate of K and ε_o can be obtained. However, it is preferable to calculate the constants from the complete data so as to avoid errors due to individual incorrect observations.

For this purpose, a non-linear curve fitting technique can be adopted. The program, using an iterative algorithm by Fletcher (1979), needed initial estimates of the constants and the final results were dependent upon these estimates. Another program described by Afrouz and Harvey (1974) considered fifteen possible equations reduced to general forms subjected to a least squares fit by stepwise by Gauss-Newton iterations. However, none of the programs were available for

use; therefore, an algorithm was developed for data processing, making use of least squares linear curve fitting program already available.

5.7.1 Mathematical Solution

The logic followed in this section forms the basis of graphical and computerised solutions of the proposed equation.

The three points from the experimental strain-time data can be chosen in such a way that between the relevant time values, the conditions as follows hold:

$$\frac{T_1}{T_2} = \frac{T_2}{T_3} \quad \text{or} \quad \text{Ln } T_1 - \text{Ln}T_2 = \text{Ln}T_2 - \text{Ln}T_3$$

Substituting these points into the formula 5.1, three equations are derived:

$$\text{Ln } \frac{\varepsilon_1}{\varepsilon_o} = T_1^n \cdot \text{Ln } K \qquad \ldots\ldots (5.2)$$

$$\text{Ln } \frac{\varepsilon_2}{\varepsilon_o} = T_2^n \cdot \text{Ln } K \qquad \ldots\ldots (5.3)$$

$$\text{Ln } \frac{\varepsilon_3}{\varepsilon_o} = T_3^n \cdot \text{Ln } K \qquad \ldots\ldots (5.4)$$

dividing 5.2 by 5.3

$$\frac{\text{Ln } (\frac{\varepsilon_1}{\varepsilon_o})}{\text{Ln } (\frac{\varepsilon_2}{\varepsilon_o})} = (\frac{T_1}{T_2})^n \quad \Rightarrow \quad \text{Ln } (\frac{\text{Ln}(\varepsilon 1/\varepsilon o)}{\text{Ln}(\varepsilon 2/\varepsilon o)}) = n \cdot \text{Ln } \frac{T_1}{T_2} \qquad \ldots\ldots (5.5)$$

and also dividing 5.3 by 5.4:

$$\frac{\text{Ln}(\frac{\varepsilon_2}{\varepsilon_o})}{\text{Ln}(\frac{\varepsilon_3}{\varepsilon_o})} = (\frac{T_2}{T_3})^n \quad \Rightarrow \quad \text{Ln } (\frac{\text{Ln}(\varepsilon 2/\varepsilon o)}{\text{Ln}(\varepsilon 3/\varepsilon o)} = n \cdot \text{Ln } \frac{T_1}{T_2} \qquad \ldots\ldots (5.6)$$

and dividing 5.5 by 5.6, n is eliminated and since $\text{Ln}\ \frac{T_1}{T_2} = \text{Ln}\ \frac{T_2}{T_3}$:

$$\frac{\text{Ln}\ (\frac{\varepsilon_1}{\varepsilon_o})}{\text{Ln}\ (\frac{\varepsilon_2}{\varepsilon_o})} = \frac{\text{Ln}(\frac{\varepsilon_2}{\varepsilon_o})}{\text{Ln}(\frac{\varepsilon_3}{\varepsilon_o})} \Rightarrow$$

$(\text{Ln}\ \varepsilon_2 - \text{Ln}\ \varepsilon_o)^2 = (\text{Ln}\ \varepsilon_1 - \text{Ln}\ \varepsilon_o)\cdot(\text{Ln}\ \varepsilon_3 - \text{Ln}\ \varepsilon_o)$ resolving

this equation for $(\text{Ln}\ \varepsilon_o)$:

$$(\text{Ln}\ \varepsilon_2)^2 - 2(\text{Ln}\ \varepsilon_2)(\text{Ln}\ \varepsilon_o) + (\text{Ln}\ \varepsilon_o)^2 = (\text{Ln}\ \varepsilon_1)\cdot(\text{Ln}\ \varepsilon_3) - (\text{Ln}\varepsilon_1)(\text{Ln}\ \varepsilon_o) - (\text{Ln}\ \varepsilon_o)\cdot(\text{Ln}\ \varepsilon_3) + (\text{Ln}\varepsilon_o)^2$$

and:

$$\text{Ln}\ \varepsilon_o = \frac{(\text{Ln}\ \varepsilon_1)\cdot(\text{Ln}\ \varepsilon_3) - (\text{Ln}\varepsilon_2)^2}{(\text{Ln}\ \varepsilon_1) + (\text{Ln}\ \varepsilon_3) - 2(\text{Ln}\varepsilon_2)} \qquad \ldots\ldots (5.7)$$

is obtained. Thus initial strain (ε_o) can be calculated using only three strain values. The other constants can be easily determined:

$$n = \frac{\text{Ln}(\frac{\text{Ln}\ \varepsilon_1 - \text{Ln}\ \varepsilon_o}{\text{Ln}\ \varepsilon_2 - \text{Ln}\ \varepsilon_o})}{\text{Ln}\ T_1 - \text{Ln}\ T_2} \quad \text{and}$$

$$\text{Ln}\ K = \frac{\text{Ln}\ \varepsilon_1 - \text{Ln}\ \varepsilon_o}{T_1^{\,n}}$$

5.7.2 Graphical Solution

The equation 5.7 can be re-written by subtracting Ln ε_3 from each side:

$$(Ln\varepsilon_3 - Ln\varepsilon_o) = \frac{(Ln\ \varepsilon_3 - Ln\ \varepsilon_2)^2}{(Ln\ \varepsilon_3 - Ln\ \varepsilon_1) - 2\ (Ln\ \varepsilon_2 - Ln\ \varepsilon_1)} \quad \text{and}$$

and re-arranging,

$$(Ln\ \varepsilon_3 - Ln\ \varepsilon_2) = \frac{(Ln\ \varepsilon_3 - Ln\ \varepsilon_1) - 2\ (Ln\ \varepsilon_2 - Ln\ \varepsilon_1)}{(Ln\ \varepsilon_3 - Ln\ \varepsilon_2)} (Ln\ \varepsilon_3 - Ln\ \varepsilon_o)$$

dividing each side by 2 and adding (Ln T_2-LnT_1) to each side.

$$\frac{(Ln\ \varepsilon_3 - Ln\ \varepsilon_2)}{2} + (LnT_2 - LnT_1) =$$

$$\frac{\left(\frac{(Ln\ \varepsilon_3 - Ln\ \varepsilon_1)}{2} - (Ln\ \varepsilon_2 - Ln\ \varepsilon_1)\right) \cdot (Ln\ \varepsilon_3 - Ln\ \varepsilon_o)}{Ln\ \varepsilon_3 - Ln\ \varepsilon_2} + (LnT_2 - LnT_1)$$

On the logarithmic strain-time graph, the left hand side of the above equation represents a straight line parallel to Lnε axis, while the right hand side represents a straight line with a slope of value:

$$m = \frac{\left(\frac{(Ln\ \varepsilon_3 - Ln\ \varepsilon_1)}{2}\right) - (Ln\varepsilon_2 - Ln\varepsilon_1)}{Ln\ \varepsilon_3 - Ln\ \varepsilon_2}$$

The intersection of these two lines yields the logarithm of instantaneous strain on the Ln (ε) axis. In Figure 5.20 the procedure of the graphical solution is set out. The three points which satisfy Ln T_1 - Ln T_2 = Ln T_2-LnT_3 are found on the Ln T axis and vertical lines are drawn to the experimental curve. From the points where the lines intersect the curve horizontal lines are drawn and Ln (ε_1), Ln (ε_2) and Ln (ε_3) are found. On the line passing Ln (T_2), P, R and O are marked as indicated. M as the mid-point of the distance between P and R and N as the mid-point of the distance between O and P, are determined on the same line. M and N are reflected as M' and N' on the horizontal line passing through O and Ln (ε_2). The line passing N' and parallel to Ln ε axis and the line passing P and M', are drawn. From where they intersect each other, a horizontal line drawn to Ln (ε) axis yields Ln (ε_o). Calculations carried out using a number of three points should converge to the same value. Small deviations can be attributed to the incorrect individual measurement, whereas serious divergence can be either because the primary stage is completed or the data is not following the proposed formulae.

Having determined initial strain, the constants K and n could be calculated easily by plotting double logarithmic strain versus logarithmic time. In this graph the observation point should be viewed as a straight line. The slope of the line gives n and K is easily calculated (Figure 5.21).

A graphical method of solution, as described, is extremely easy and can be carried out rapidly in the field with a pocket calculator. Serious deviations of the calculated ε_o with newly recorded data from

the previous values, may be an indication of the onset of the tertiary stage.

5.7.3 Computer Application

An algorithm for the linearisation of the proposed formula was essential in order to determine the constants, making use of the least squares curve fitting program available on N.MTS as a part of package program PADAS (Watson 1979).

A program written in FORTRAN was prepared for the estimation of initial strain (ϵ_o) from the data. The program (Appendix 5.2) selects all possible sets of three points from the data, which satisfies the condition of $T_1/T_2 = T_2/T_3$ and utilising equation 5.7 calculates ϵ_o for each set and yields the average as a result.

Using the average ϵ_o, the data is processed. Each strain value is divided by ϵ_o and by taking logarithm of the resultant values with corresponding time values; are stored in a separate file. The processed data is then subjected to the least squares curve fitting analysis.

By taking logarithm and by re-arranging, equation 5.7 may be written as follows:

$$\text{Ln}\ (\epsilon / \epsilon_o) = T^n \times \text{Ln}\ K$$

Thus the processed data should yield an ordinary power equation from which the constants n and K are found, and the Index of Determination is calculated, providing evidence of the goodness of the fit. of the fitted equation with the observation points are also provided in order to allow the visual inspection of the fits (Figures 5.22 to 5.28).

The results of the analysis which are extracted from the full analysis of the processed data (Appendix 5.1b) are tabulated in Table 5.4. Comparison of the Index of Determination in Table 5.4 with those in Table 5.2 demonstrates the magnitude of the improvement made by employing the proposed formula instead of standard forms of creep laws. The proposed formula overestimated slightly the creep behaviour of specimens 10 and 12 (Figures 5.26 and 5.27). The reason for this rather tolerable overestimate is that both specimens have entered the secondary stage after approximately 450 days (Table 4.8), but the data have not been exempted from the analysis. However, even though this is so, the formula is found to be superior to the power law.

5.8 Construction of a chart for the prediction of creep behaviour in the primary stage

Hitherto, the various methods of determining the constants (ε_o, K,n) appearing in the proposed formula have been discussed. Yet because the equation is essentially non-linear, it may still seem to be confusing relative to how the creep behaviour described by the formula is governed by each individual constant and to what extent improvement is achieved by expressing creep behaviour by the formula over the conventional power and logarithmic laws.

It was decided that a chart incorporating the most common forms of logarithmic law, power law and the proposed law would serve this purpose. The logic of sequence of the chart is as follows:

Let us begin with the proposed equation (5.1), which may be rewritten as two parametric equations of the parameter Z:

$$\varepsilon = \varepsilon_o \cdot K^{(T^n)} \quad , \quad \text{taking } Z = T^n \quad ,$$

it becomes:

$$\varepsilon = \varepsilon_o \cdot K^Z \quad \text{and} \quad \varepsilon/\varepsilon_o = K^Z.$$

If T and n are given appropriate values from 0 to 250 and 0.2 to 0.4 respectively, and making use of parametric equation $Z = T^n$, the curves on the right hand side of the plot in Figure 5.29 are produced.

Similarly, using the parametric equation, $\varepsilon/\varepsilon_o = K^Z$, and assigning values from 1.15 to 1.0 to the constant K, together with the calculated Z values, the left hand side of the plot in Figure 5.29 is obtained.

Before going any further, it must be pointed out that the plot in Figure 5.29 is sufficient to explain how the variables(ε,T) in the proposed formula are related to the constants (ε_o, K, n). At a given time if the constant n is changed, say, from 0.2 to 0.4, the magnitude of the increase in the strain is dependent upon the value of the constant K. If K is very close to unity, the increase in the strain proportional to ε_o, is small. If, however, it is close to, say, 1.20, the increase in the strain is much more pronounced. The constants K and n are interrelated to each other such that when the given time (T) is small, or at early stages of creep, different values of n and K produce very close strain values yet, as the time increases, the calculated values become sensitive to the selected constants.

The constant K is easily estimated when the strain value of the first day is available in the following way: putting T = 1 in the equation (5.1) it becomes:

$$\varepsilon_1 = \varepsilon_o \cdot K \quad \text{and} \quad K = \varepsilon_1/\varepsilon_o.$$

If another point is taken from the data it is possible to calculate the constant n from the chart. A vertical line is drawn from the $\varepsilon/\varepsilon_o$ axis, passing the point of known ε to the curve of determined K and from the intersection point a horizontal line is passed towards the curves on the right hand side. Another vertical line, drawn from the T axis, passing the point of known T will cut the horizontal line at some point which yields the value of constant n. This process may well be reversed to calculate or extrapolate the strain value for longer periods.

The power law may be re-examined in the same fashion: a general form may be written as:

$$\varepsilon = \varepsilon_o + AT^n$$

When T = 0, $\varepsilon = \varepsilon_o$, and when T = 1, $\varepsilon_1 = \varepsilon_o + A$, thus $\varepsilon_1 - \varepsilon_o = A$, and:

$$\frac{\varepsilon_1}{\varepsilon_o} - 1 = \frac{A}{\varepsilon_o} \quad \text{if } B = \frac{A}{\varepsilon_o} \text{ it becomes}$$

$$\frac{\varepsilon_1}{\varepsilon_o} - 1 = B, \text{ since in the chart for the proposed formula,}$$

$\varepsilon_1/\varepsilon_o = K$, it becomes $B = K - 1$.

Now the power equation above may be expressed in the form of two parametric equations thus:

$$Z = T^n \quad \text{and} \quad \epsilon/\epsilon_o = 1 + B \times Z.$$

Using the same T and n values as used in the previous chart, Z values are obtained. Using the resultant Z values and B values as calculated from $B = K - 1$, ϵ/ϵ_o values are determined. When T versus Z and ϵ/ϵ_o versus Z are plotted, the plot in Figure 5.30 is obtained.

As can be seen, the right hand side of the plot is the same as the one in Figure 5.29, while on the left hand side, lines are straight instead of curved. This change, in fact, characterises the only difference between the proposed equation and the power law. However, before attempting to discuss the difference, it is worth evaluating the Figure 5.30 in more detail.

As in the case for the proposed formula, estimating B from the initial strain and the strain on the first day alone and taking any arbitrary point from the data, it is possible to determine the constants of the power law rapidly. Alternatively, if the data is known to obey the one-third power law, better known as 'Andrade's Law', the strain at a given time or vice-versa can be estimated rapidly.

When the plot in Figure 5.29 is superimposed on the plot in Figure 5.30, the plot in Figure 5.31 is obtained, which is of particular importance in comparingthe two equations.

As can be seen in Figure 5.31, the straight lines (broken lines) tangentially converge to the curves towards the point where ϵ/ϵ_o is unit. Away from the unity, straight lines diverge from the curves, but

the amount of divergence decreases as the value of K and also B approach unity and nil respectively. Since the horizontal distance between the points, where an horizontal straight line is drawn for a given time and n value intersects the curve and the broken line of given K and B values shows the difference between the strain values of the proposed equation and the power law, it can be deduced that if B is close to zero, both forms of equations yield almost identical results or fits, but if B deviates from zero, although they both still yield similar results at very early stages of creep, the power law underestimates the values calculated by the proposed equation (5.1) which has been proven in the previous section to be well representative of the actual creep data. Thus the reason why the power law underestimates creep data at later stages has been explained with the help of the chart. It is, in fact, often the case where a power law overestimates the data at early stages but, underestimates at later stages (as shown in Figures 5.6 and 5.7), as shown for specimens 10 and 12. In such situations, the least squares curve fitting programme selects a value of B such that the line cuts the curve in two points overestimating at early and underestimating during later stages in order to obtain a high Index of Determination for the fit.

It is now possible to proceed one step further and include the logarithmic law to the chart in order to complete derivations. A general form of the logarithmic equation may be written in the following manner:

$$\varepsilon = \varepsilon_1 + A \ln (T)$$

Since $T \neq 0$, taking $T = 1$, it becomes $\varepsilon = \varepsilon_1$, and taking $\varepsilon_1/\varepsilon_o = K$, the equation is rewritten:

$$\varepsilon = K.\varepsilon_o + A \text{ Ln } (T), \text{ which becomes:}$$

$$\varepsilon/\varepsilon_o - K = \frac{A}{\varepsilon_o} \text{ Ln}(T)$$

Taking anti-logarithm, it is reduced to:

$$e^{\varepsilon/\varepsilon_o - K} = T^{A/\varepsilon_o} \quad \text{putting } A/\varepsilon_o = n$$

and separating it into two parametric equations such that

$$Z = T^n \text{ and } \varepsilon/\varepsilon_o = K + \text{In } (Z),$$

by assigning the usual values to n, T and K, the chart is constructed(Fig 5.32). As can be seen, the nature of the curves on the left hand side is completely changed from downward concave in the proposed formula, the straight line in the power law to upward concave in the logarithmic function. This is an obvious indication of continually decreasing strain rate-with time. Moreover, the curves of various K values have become squeezed, which implies the fact that creep behaviour characterised by the logarithmic law is less responsive to the value of $\varepsilon_1/\varepsilon_o$ than the developed equation and the power law equation. Clearly, the creep behaviour is confined to relatively smaller changes in creep strain as time elapses. It must, however be stated that in practical cases where a logarithmic law was found to be adequate, the constant n should attain much lower values (close to zero) than those appearing in Figure 5.32. But for purposes of comparison, the same n values as

used in the previous charts are chosen in the logarithmic chart. The inadequacy of the logarithmic law for the creep results of the submerged gypsum is revealed very well in this chart (Figure 5.32). If an attempt is made to describe the behaviour of submerged gypsum with a logarithmic law, an excessively high overestimate in the early stages and underestimate in the later stages is bound to occur.

A chart incorporating all three laws can now be prepared (Figure 5.33) with the aid of which the form of creep equation can rapidly be determined using at least two data points and a good estimate of the constants can also be made. In order to enhance the accuracy charts much more refined than those demonstrated can be constructed in similar fashion to suit any particular need.

5.9 Development of a formula for tertiary stage creep data

During the long-term creep testing of submerged gypsum, two specimens, A and 6, entered into the tertiary stage of creep and ended in complete failure. Due to the slow rate of increase in strain, the time taken for the specimens to reach failure stage was characteristically long (Figures 4.7 and 4.13) and thus a greater proportion of the creep process was dominated by the tertiary stage of creep. The likelihood of observing a similar and possibly further prolonged deformational behaviour of actual pillars underground cannot be ruled out. The question could be raised, when would be the time of the failure! A reliable estimate of the time of a pending failure could be of extreme value to the rock mechanics engineer, enabling him to consider the necessary preventive measures, if failure is not permitted, or to take steps to evacuate the area in time, preventing injury to persons or damage to equipment if failure or collapse cannot be prevented in time.

Theoretical and experimental efforts have been understandably concentrated on the determination of the onset of the tertiary stage (Sangha and Dhir 1972; Singh 1975; Munday et al. 1979; Genevois and Prestininzi 1979; and Dedame 1979) but, to a lesser extent, on the prediction of the actual failure time during the tertiary stage.

Griggs and Coles (Glen, 1958) expressed the results of their measurement of accelerating tertiary stage of creep with a parabolic equation which may be written in the following form:

$$\varepsilon = A - B \times T^2$$

The preliminary analysis of the tertiary stage data of specimens 6 and A by regressing against seven standard curves have indicated that the best fit out of seven is in the form of a hyperbolic function (Table 5.5).

However, extremely poor correlation between the fitted curves and the data as indicated by the Index of Determination and as seen in Figures 5.16 and 5.17, necessitated a new form of equation which would produce a better mathematical description of the tertiary stage data.

In the development of a new formula for the tertiary stage, similar approaches to those of Saito (1965a,b, 1969) have been followed and will be elaborated in the following subsections.

The rate of strain of specimens 6 and A increases hyperbolically in the tertiary stage (Table 4.8) with respect to time and asymptotic to failure time, towards which the rate goes to infinity. This requires an equation of the form:

$$\frac{d\varepsilon}{dT} = \frac{M}{T_F - T} \quad \text{where} \quad M = \text{constant}$$

T_F = time of failure

T = time

Taking $\frac{d\varepsilon}{dT} = 0$ when T = To and integrating with respect to T, one obtains

$$\varepsilon = M \times \text{Ln} \frac{TF - To}{TF - T} \qquad \ldots\ldots (5.8)$$

It must, however, be pointed out that the formula (5.8) which is essentially a logarithmic-hyperbolic function is to be used only partially for the tertiary stage creep data. (For this reason, the data will be assumed to be tertiary creep data.)

When $\frac{TF - To}{TF - T} = e = 2.7183$

i.e. $T = \frac{TF\ (2.7183 - 1) + To}{2.7183}$

the equation (5.8) becomes $\varepsilon = M$.

On the other hand, when T = To, the equation (5.8) becomes $\varepsilon = 0$. The results have indicated that the values of To are negative, thus no meaning can be attached to them in terms of creep behaviour. The determination of the constants appearing in the equation will be carried out in a fashion similar to that of the formula for the primary stage.

5.9.1 Mathematical Solution

Three pairs of strain-time points may be selected from the data such that the relationship $\varepsilon_1 - \varepsilon_2 = \varepsilon_2 - \varepsilon_3$ is satisfied. Putting these three points into the equation (5.8), three sets of euqations can be obtained.

$$\varepsilon_1 = M \text{ Ln } \left(\frac{TF - To}{TF - T1}\right) \quad \ldots\ldots (5.9)$$

$$\varepsilon_2 = M \text{ Ln } \left(\frac{TF - To}{TF - T2}\right) \quad \ldots\ldots (5.10)$$

$$\varepsilon_3 = M \text{ Ln } \left(\frac{TF - To}{TF - T3}\right) \quad \ldots\ldots (5.11)$$

Subtracting (5.9) from (5.10) and rearranging gives:

$$\varepsilon_2 - \varepsilon_1 = M \text{ Ln } \left(\frac{TF - T1}{TF - T2}\right) \quad \ldots\ldots (5.12)$$

and similarly subtracting (5.10) from (5.11) and rearranging obtains:

$$\varepsilon_3 - \varepsilon_2 = M \text{ Ln } \left(\frac{TF - T2}{TF - T3}\right) \quad \ldots\ldots (5.13)$$

and dividing (5.12) by (5.13) and also, since $\varepsilon_2 - \varepsilon_1 = \varepsilon_3 - \varepsilon_2$, one obtains:

$$\text{Ln } \left(\frac{TF - T1}{TF - T2}\right) = \text{Ln } \left(\frac{TF - T2}{TF - T3}\right) \quad \text{which becomes:}$$

$$\frac{TF - T1}{TF - T2} = \frac{TF - T2}{TF - T3} \quad \ldots\ldots (5.14)$$

and $T_2^2 = 2T_FT_2 - T_FT_1 - T_FT_3 + T_1T_3$

by adding $- 2 T_1T_2 + T_1^2$ to each side and rearranging, it results in:

$$(T_2 - T_1)^2 = (TF - T_1)(2T_2 - T_1 - T_3) \text{ and finally,}$$

$$T_F - T_1 = \frac{(T_2 - T_1)^2}{2\,T_2 - T_1 - T_3} \qquad \ldots\ldots (5.15)$$

is obtained. The equation above (5.15) is of particular value since for the prediction of the failure time, no further information except the three time values is required, provided the relationship of $\varepsilon_1 - \varepsilon_2 = \varepsilon_2 - \varepsilon_3$ is observed when selecting the three pairs of creep data. Creep data obtained at later stages of tertiary creep can be incorporated into the calculation easily. No further comments will be made here because the issue is discussed in detail in the following subsections.

Having determined T_F in equation (5.8), it is possible to calculate arithmetically the constants T_o and M (Appendix 5.3).

$$T_o = T_F - \sqrt{\frac{(T_F - T_2)^{\varepsilon_1}}{(T_F - T_1)^{\varepsilon_2}}}^{\varepsilon_1 - \varepsilon_2} \qquad \text{and}$$

$$m = \frac{\varepsilon_1}{\mathrm{Ln}(T_F - T_o) - \mathrm{Ln}(T_F - T_1)} \qquad \text{can be found.}$$

5.9.2 Graphical Solution

Equation (5.15) can be rewritten as follows:

$$T_F - T_1 = \frac{(T_2 - T_1)^2}{2(T_2 - T_1) - (T_3 - T_1)} \qquad \ldots\ldots (5.16)$$

and

$$T_2 - T_1 = (T_F - T_1) \times \frac{2(T_2 - T_1) - (T_3 - T_1)}{(T_2 - T_1)} \qquad \text{by}$$

dividing each side by 2 and adding $\varepsilon_2 - \varepsilon_1$ to each side it becomes:

$$\frac{(T_2 - T_1)}{2} + (\varepsilon_2 - \varepsilon_1) = \frac{(T_2 - T_1) - \frac{(T_3 - T_1)}{2}}{T_2 - T_1}(T_F - T_1) + (\varepsilon_2 - \varepsilon_1)$$

Each side of this equation represents a straight line on the normal strain-time scale. The left hand side is a line of zero slope and the right hand side is inclined with a constant slope which is given as:

$$m = \frac{(T_2 - T_1) - \frac{(T_3 - T_1)}{2}}{T_2 - T_1}$$

The common solution of these two lines yields the failure time (T_F) on the strain-time scale. This is illustrated in Figure 5.34. Three points which satisfy the condition ($\varepsilon_1 - \varepsilon_2 = \varepsilon_2 - \varepsilon_3$) are selected on the strain axis, and corresponding T_1, T_2 and T_3 values are marked on the time axis, as shown. A line passing through the point ε_2 on the strain axis and parallel to a time axis can be drawn and points O, P and R are marked on this line. The mid-point of O, P, as N and the mid-point of R, P as M are found, then N and M are reflected on the vertical line passing O, as N' and M'. The failure time can be obtained as abscissa of an intersection of a line passing through N' and parallel to the time axis, with another line passing through P and M'.

Repetition of this procedure for different sets of three points should ideally yield the same result. However, due to errors in observations, a band of failure times is likely to be produced. In this case, it is advisable to carry out graphical solutions on a graph as large as possible, hence errors due to drawing are reduced or, alternatively, a statistical method may be adopted in order to determine the exact failure time. Since the solution is originally based on the

rate of strain, even though it does not enter in the solution, the larger the time span covered, the more precise becomes the prediction. Therefore, the incorporation of the forthcoming observations as time is progressing will result in improved estimates. It must be remembered that the failure time (T_F) is theoretically an asymptote of the equation (5.8), along which the strain rate is assumed to be infinite and thus the limiting strain sustainable by the specimen is reached slightly before the predicted time. However, this is found to have been confined to a fraction of a day when the failure time prediction is made within a 30-day period prior to failure (Specimen 6).

Having calculated the failure time (T_F) the remaining constants of equation (5.8) can be determined graphically also. Equation (5.8) can be arranged as follows:

$$\varepsilon = M \text{ Ln } (T_F - T_o) - M \text{ Ln } (T_F - T)$$

If the time left to failure on the logarithmic scale is abscissa and the strain values on the normal scale are ordinate and are placed a straight line is produced. The slope of this line gives the value of M, and the intersection of the line on the ε-axis gives the value of strain one day before failure. This is illustrated in Figure 5.35 for the tertiary stage data of specimen 6. In fact, this property of the proposed equation allows us to estimate the strain of the specimen just one day prior to failure with fairly high accuracy and, if this is incorporated into the graphical solution (Figure 5.34), the behaviour of the specimen with successive readings can be compared with the predicted behaviour.

5.9.3 Computer Application

An algorithm similar to that used for the primary stage formula has been adopted in this case.

First the tertiary stage data is separated from the rest of the data with the rate of strain being the decisive factor. By means of another program written in FORTRAN (Appendix 5.4), all the possible sets of three points which satisfy the condition $\varepsilon_1 - \varepsilon_2 = \varepsilon_2 - \varepsilon_3$ have been found and using corresponding time values and utilising equation (5.15) the failure times are calculated. Since the calculation is carried out with three points, if the three points are chosen very close to each other, small errors in observations are magnified in the result. If the time span covered by the three points is sufficiently large, the fractional error in any observation is less pronounced. On this basis it was decided not to average the calculated T_F values. In two cases (specimens 6 and A) the failure time had been predicted by graphical methods; therefore, by the time computer application was attempted, the two failure times were already available.

Another program was used to convert the time values to $T_F - T$ and together with the corresponding strain values this was stored in a file. By applying the least squares method to the processed data, constants of the equation and the Index of Determination of the fit were established (Table 5.6).

The fitted curves and the observation points are plotted for both specimens in Figures 5.36 and 5.37. Inspection of the fitted curves and the Index of Determination in Table 5.6 evidence the excellent correlation between the data and the equation.

5.10 Construction of a chart for the failure-time prediction

It is now possible to reduce the steps of failure prediction process to a more simplified form.In equation:

$$(T_F - T_1) = \frac{(T_2 - T_1)^2}{2(T_2 - T_1) - (T_3 - T_1)} \quad \ldots\ldots (5.16)$$

arbitrary values are assigned to the terms $(T_2 - T_1)$ and $(T_3 - T_1)$, the corresponding values of $(T_F - T_1)$ can be calculated. By plotting $(T_3 - T_1)$ versus $(T_F - T_1)$ for each $(T_2 - T_1)$ value, a set of curves are obtained as Figure 5.38. The density of the $(T_2 - T_1)$ curves can be varied at will as well as the range of $(T_3 - T_1)$ values.

Taking three points from the data such that $\varepsilon_1 - \varepsilon_2 = \varepsilon_2 - \varepsilon_3$, the values of $(T_3 - T_1)$ and $(T_2 - T_1)$ become available. A vertical line from the $(T_3 - T_1)$ axes passing through the point of known $(T_3 - T_1)$ is drawn. This line intersects the curve of known $(T_2 - T_1)$ value at a point from which horizontal line is passed. The point at which the horizontal line cuts the $(T_F - T_1)$ axes gives the time of failure relative to the time of the first point (T_1).

Time values can be of any unit (minutes, days, months, etc.) and the points may be chosen as displacements instead of strains.

Since the chart shown in Figure 5.38 serves the purpose of demonstration, very few $(T_2 - T_1)$ values were chosen. When it is required to use the chart in practice a much refined chart may be prepared in the same fashion, as previously stated.

5.11 Prediction of failure time of rock structures

In engineering applications probably the most important information is the correct life span of the structure designed. The significance of this information is further enhanced if the structure happens to be a rock structure in the form of a tunnel, mine pillar or an open pit slope where unforeseen factors may initiate failure which may endanger lives, damage equipment and disrupt production.

Several collapses, both major and minor, of room and pillar workings have occurred in the not too distant past (Bryan et al. 1964; Wilson 1965; Salomon 1969; Mottahed 1974; Mottahed and Szeki 1982). Although in many cases, rock mechanics observations indicated the probability of pending collapse, few attempts have been made to determine the exact time of failure.

An interesting study was reported by Saito and Uzzawa (1965) who suggested a relationship for the failure prediction of soil samples subjected to creep testing in the laboratory. The equation can be written in its simplest form as follows:

$$T_R \times \dot{\varepsilon} = 214,$$

where $\dot{\varepsilon}$ is the steady state creep rate in x 10^{-4}/min. and

T_R is the rupture time of the sample.

They applied this empirical relationship to the full-scale experiments of slope failure and obtained good correlation.

Saito (1965) verified the above formula on actual soil structures. The collapse of a large retaining wall in the Ooigawa Railroad was successfully predicted and the area was evacuated one day before the collapse occurred.

Later, Saito (1969) reported the equations (5.8) and (5.16) which are shown in Section 5.9. By the use of these equations and a graphical method, he was able to forecast the failure time of a landslide at Asamushi on the Tohoku Line in Japan. Forecasting, carried out with data obtained three days before the failure, was within a day's accuracy.

Kennedy and Niermeyer (1967) have predicted a major slope failure at Chuquicamota Mine in Chile, thus preventing an extended shut-down of the mine. Their prediction was made by curve fitting techniques and by extrapolation for the rupture. Although they do not report the type of curve, or equation of the curve, fitted, they predicted the actual failure time about one month prior to the failure.

With the equations developed in Section 5.9 it was possible to forecast the failure times of the submerged gypsum specimens subjected to long-term creep testing with reasonable accuracy. It would, however, be advisable to carry out further long-term experiments in order to confirm the applicability of the equations.

5.12 Discussion of the application of the proposed equations to creep data

Equations (5.1) and (5.8) have been applied to the relevant data by means of computer, and results have been presented in graphical and numerical form. The agreement between experimental data and theoretical prediction was very good.

Originally it was thought that the full creep behaviour may be described by one equation similar to the formulae derived for the primary stage. In fact, the equation, as shown, does have an inflexion point and is capable of representing, decelerating and accelerating creep stages. It was, however, found that for the stress levels and testing conditions adopted, it was not feasible to extend it to the full range. It may, however, be possible under high stress loading conditions, both stages (primary and tertiary) may be approximated by one single formula of creep. If the applied stresses are not high the experimental data may be divided into two separate stages according to the strain rates, and each stage is then analysed individually.

The interrelationship between the constants, n, K, ε_o, and variables $\dot{\varepsilon}$, T in the proposed formula (5.1) is expressed with the aid of two parametric functions which are utilised for the construction of the chart (Figure 5.33). Although it is difficult to speculate at this stage how the constants K and n are related to the parameters of deformation processes, the fact that the Mountfield specimen (no. 6), which is the only specimen which failed without being affected by any change during the creep experiment, possessed a coarse-grained structure and a high porosity, attained the highest value of n (Table 5.4). This suggests that the constant n is dependent upon specimen fabric and structure.

The student-t test has been carried out on the paired data of Marbleagis and Fauld specimens to see whether any significant differences exist between the constants of K and n. The test indicated that even at 10% significance level, the difference was not significant. When the results are averaged, 0.334 and 1.075 for n and K are found respectively.

It was observed that when ε_o is calculated from the data, either graphically or arithmetically, the instantaneous value of the strain upon the application of load is obtained with a deviation of less than 1% in all cases.

The constant K can be approximated by dividing the strain attained on the first day by the instantaneous strain with a fair accuracy. The curve fitting analysis has substantiated this.

Although it was not possible to verify the applicability of the suggested tertiary stage creep formula on numerous specimens because only two specimens entered the tertiary creep stage, the application to the tertiary stage data of specimens A and 6 provided excellent results. Prediction of failure time by using only three points, independent of other constants, offers unique versatility of the new predicting method. It is hoped that further research on other rocks and at various stress levels will provide more factual data and will support the proposed equations and lead to wider applications.

5.13 Conclusions

The effect of water on pillar stability has been investigated through short- and long-term laboratory testing of saturated gypsum specimens.

The tests on the short-term uniaxial strength of saturated Sherburn gypsum has indicated a reduction of the order of 25% which is in good agreement with the results of Preston (1980), and slightly lower than those of Ali (1979). The highest reduction obtained from Mountfield gypsum(42%) is related to the material having a coarser grain size. Brazilian disc tests yielded a 45% reduction in the dry strength under saturated conditions.

The long-term creep testing of various specimens submerged in mine water at a stress level equivalent to 75% of short-term wet strength provided more realistic data as to the long-term effect of water on the deformational characteristics of gypsum. At this stress level the only specimen which failed in 706 days was from Mountfield Mine. The comparatively low long-term strength is attributed to the high porosity which results in rapid deterioration due to water. All specimens have undergone comparatively large deformations with decreasing creep rate in the primary stage. The rate of decrease of strain rate (i.e. $\dot{\varepsilon} = \frac{d^2\varepsilon}{dt^2}$) has shown a time-dependent decrease towards the end of the primary stage (Figures 5.18 and 5.19) which led to the rejection of a power law widely used by other investigators (Griggs, Ali and Preston).

Specimens have exhibited either a continuously decreasing rate of strain or reached an inflexion point along the creep curve at a certain strain level. Thus the Time-Safe-Strain concept evolved by Hedley (1965) appears to be superior to the Time-Safe-Stress concept which assumes that the creep rate eventually reaches zero with time.

It is likely that the 'recrystallisation process' is the controlling factor in the time-dependent deformation of submerged gypsum. The contribution of other mechanisms varies depending on the rock fabric and petrological properties and cannot be excluded. The subsaturation level of underground water and the level of fracturing of the mine pillars are of leading importance.

The long-term creep data have been analysed on the computer and found to have obeyed the proposed formula extremely well. Various simple techniques developed for solution offer flexibility and wider horizons. The tertiary creep data is fitted to a logarithmic-hyperbolic function which has an asymtothe at the failure time, thus enabling the rupture time to be estimated with reasonable accuracy.

The issue of to what extent the laboratory testing is applicable to the actual cases has been a subject of much research (Salomon and Munro 1967; Denkhaus 1965; Lama 1970; and Bienawski 1968). It is believed that, by simulating in-situ conditions faithfully, the actual in-situ behaviour can be approximated in the laboratory.

On this basis, the climatic conditions are simulated in the tests. The duration of testing can also be considered to be sufficiently long to allow transformation of the results to the actual case to be made. The pillars underground are usually fractured or a layer of

soft satinspar band may be present in the pillar, plus there are many other visible defects. On the other hand, this discrepancy can be assumed to have been cancelled out by the stress level imposed on the specimens which is approximately 6 to 8-fold of the in-situ calculated stress and by the height to width ratios of the specimens (1:1). End restraint effect is eliminated to a certain degree by employing matching dolerite platens instead of the normal steel platens.

With a conservative approach it can be concluded that the pillars with stipulated dimensions are able to sustain the load imposed by overburden, even if they are surrounded by mine water.

* * *

NAME	BEHAVIOR	MECHANICAL MODEL	EQUATION	EMPIRICAL EQUIVALENT
MAXWELL	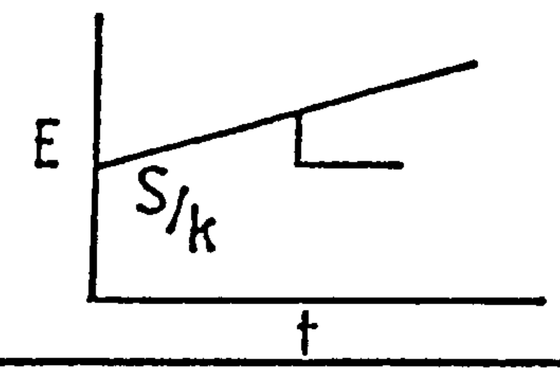	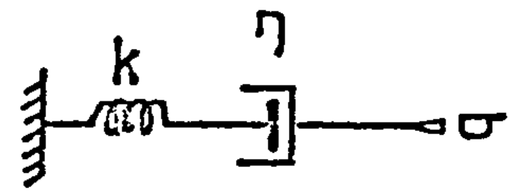	$E=(S/k)+S(t/\eta)$	$E=A+Bt$
KELVIN – VOIGT	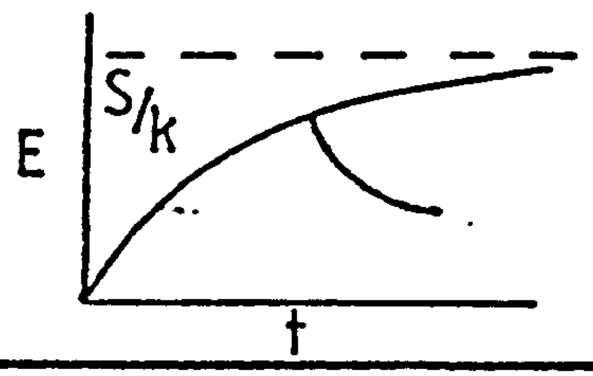	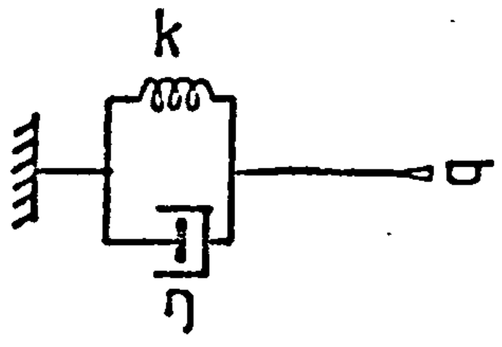	$E=(S/k)[1-e^{-\frac{k}{\eta}t}]$	$E=A[1-e^{Bt}]$
GENERALIZED KELVIN	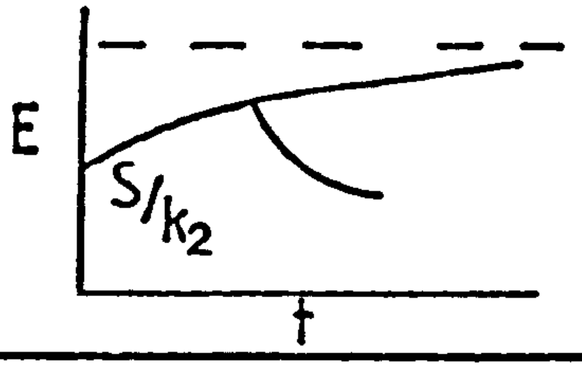	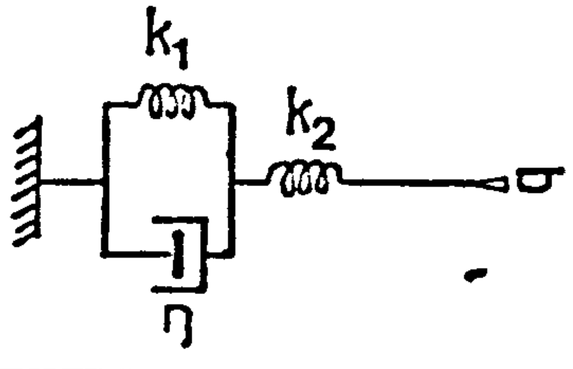	$E=S/k_2+(S/k_1)[1-e^{-\frac{k_1}{\eta}t}]$	$E=A+B[1-e^{Ct}]$
BURGERS	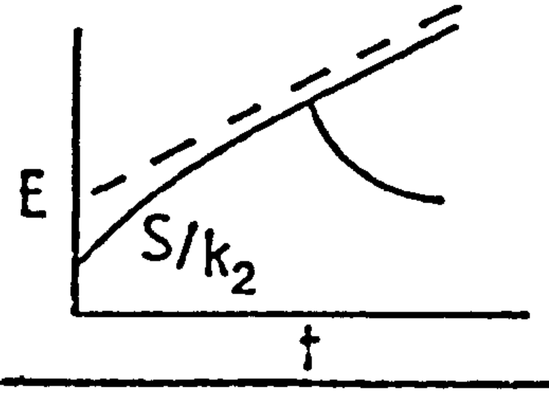	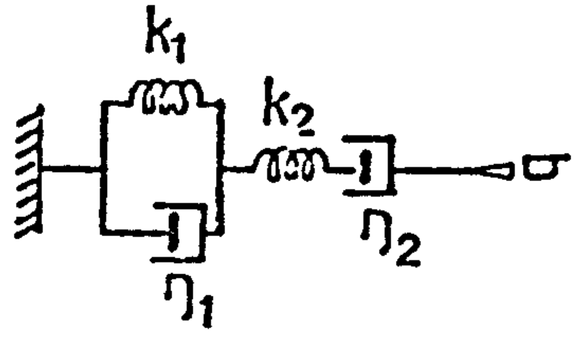	$E=S/k_2+(S/\eta_2)t+(S/k_1)[1-e^{-\frac{k_1}{\eta_1}t}]$	$E=A+Bt+C[1-e^{Dt}]$

FIG 5.1 RHEOLOGICAL MODELS

FIG 5.4

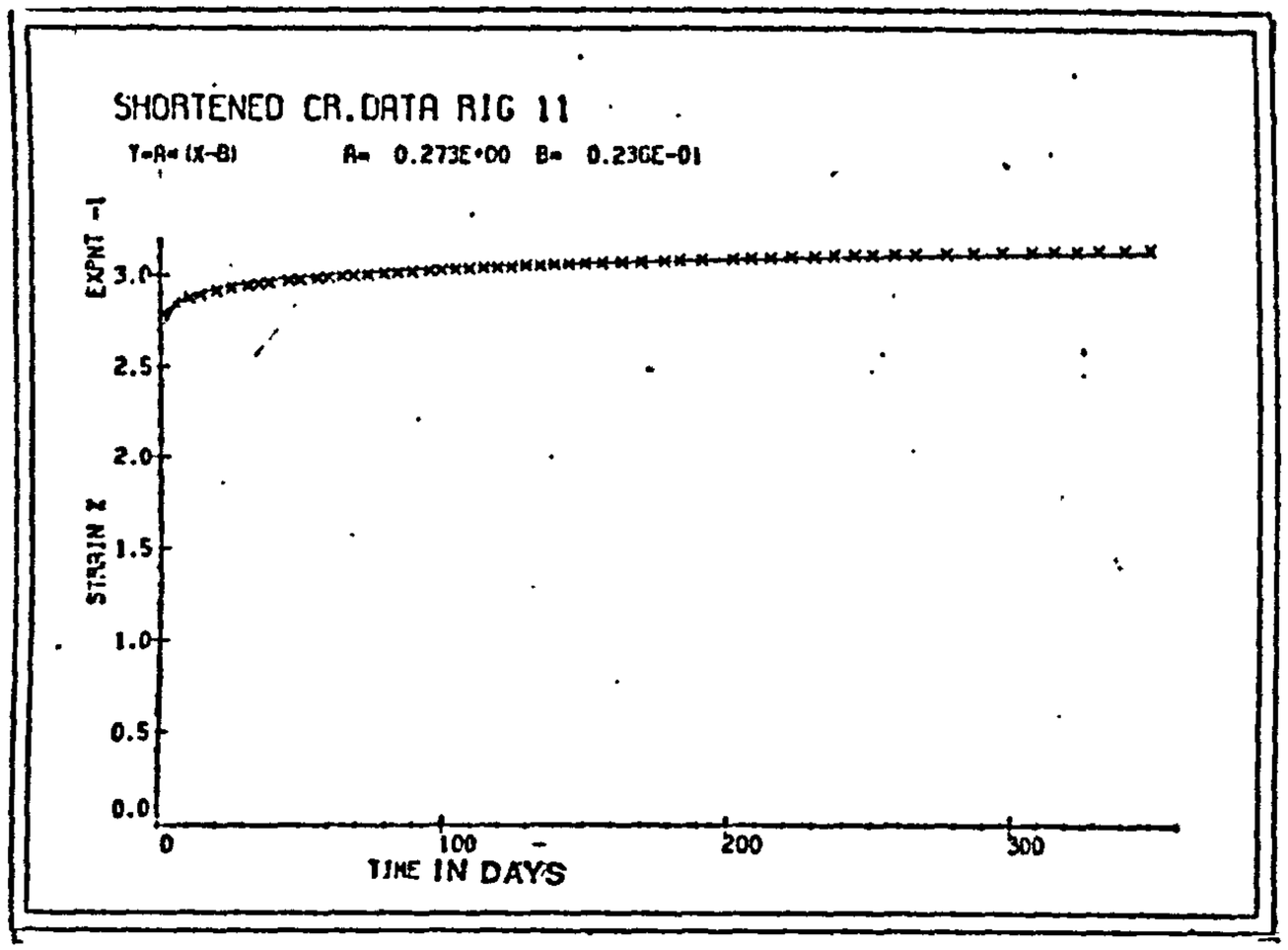

FIG 5.2

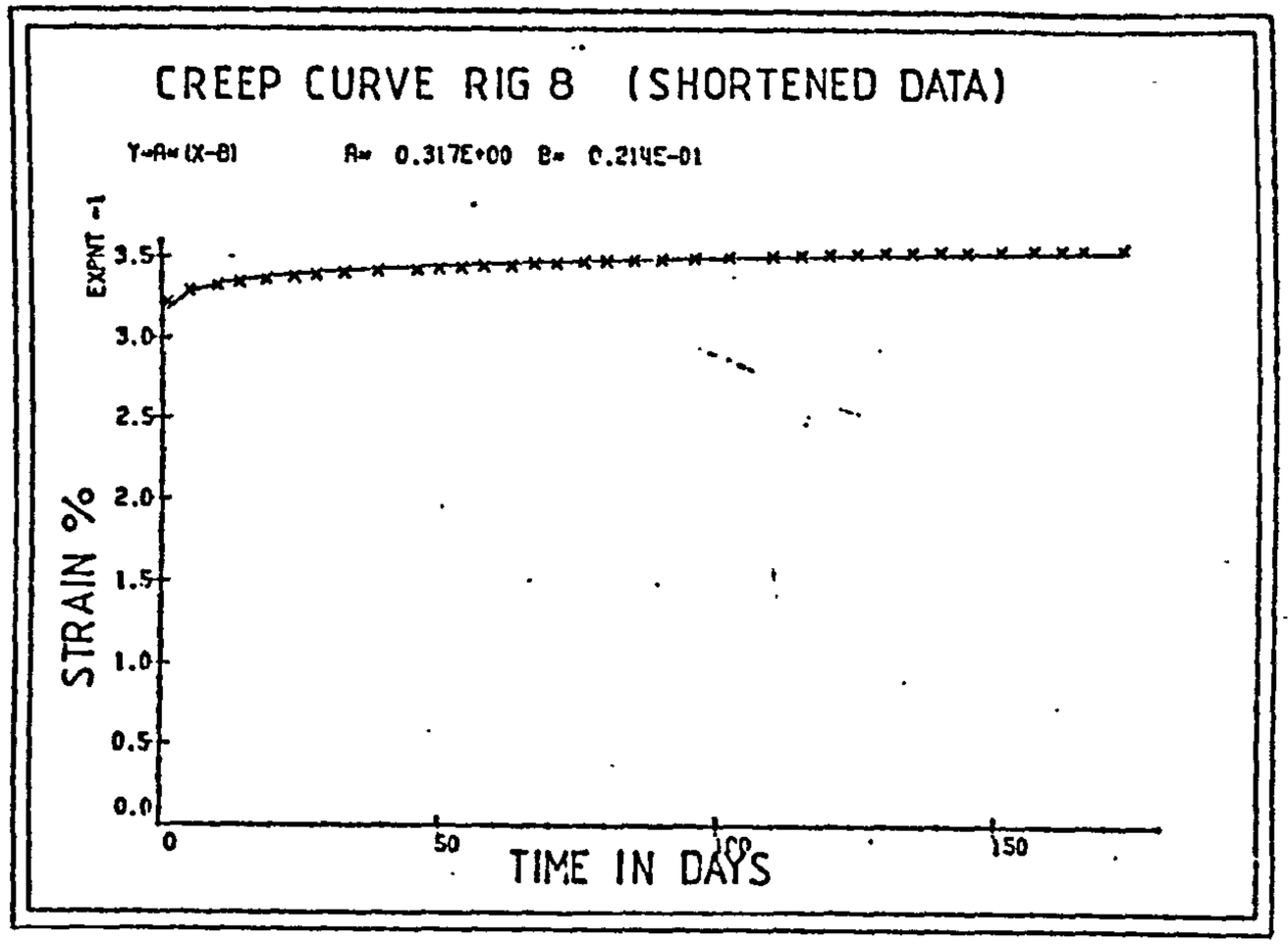

FIG 5.5

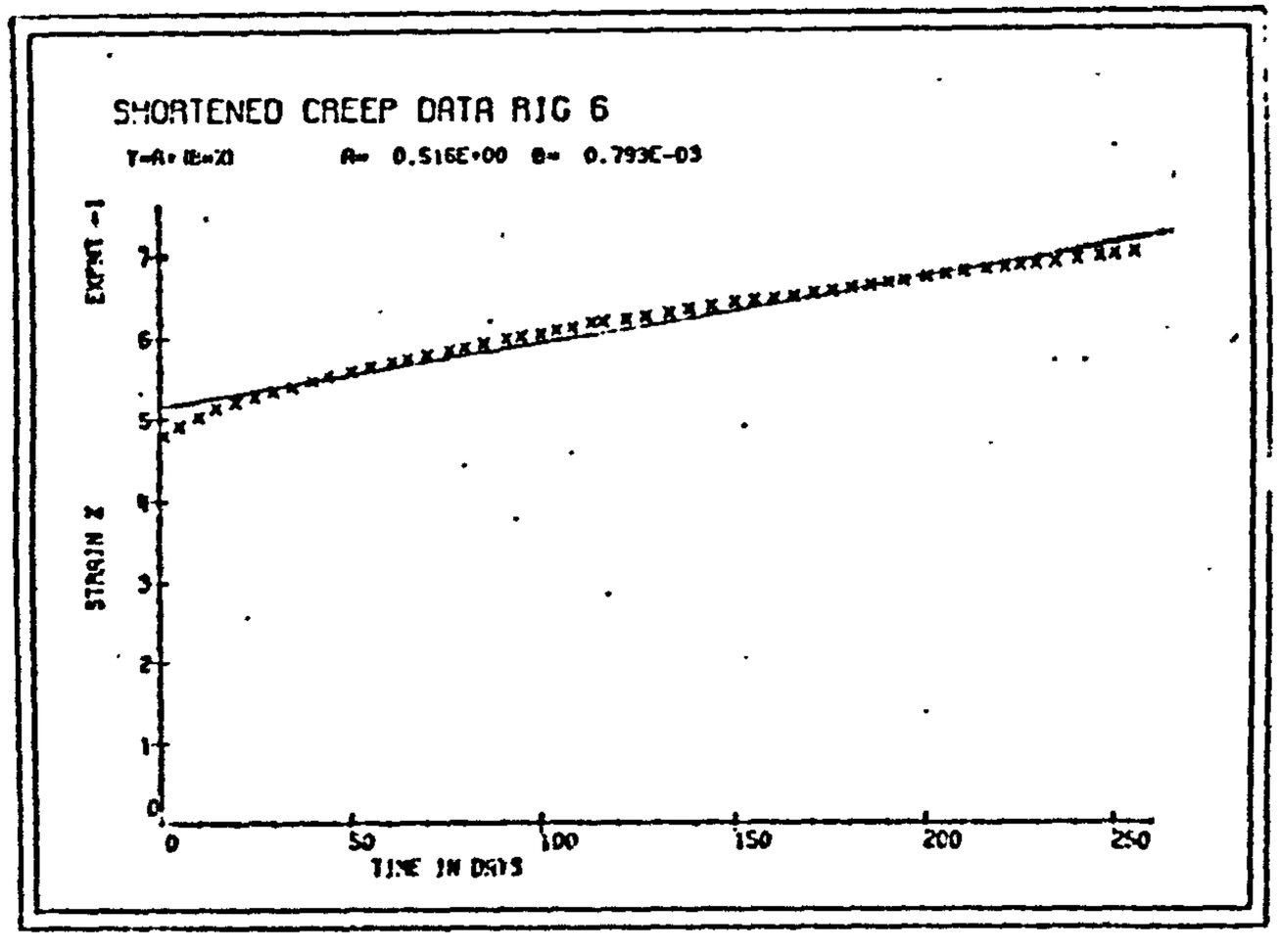

FIG 5.3

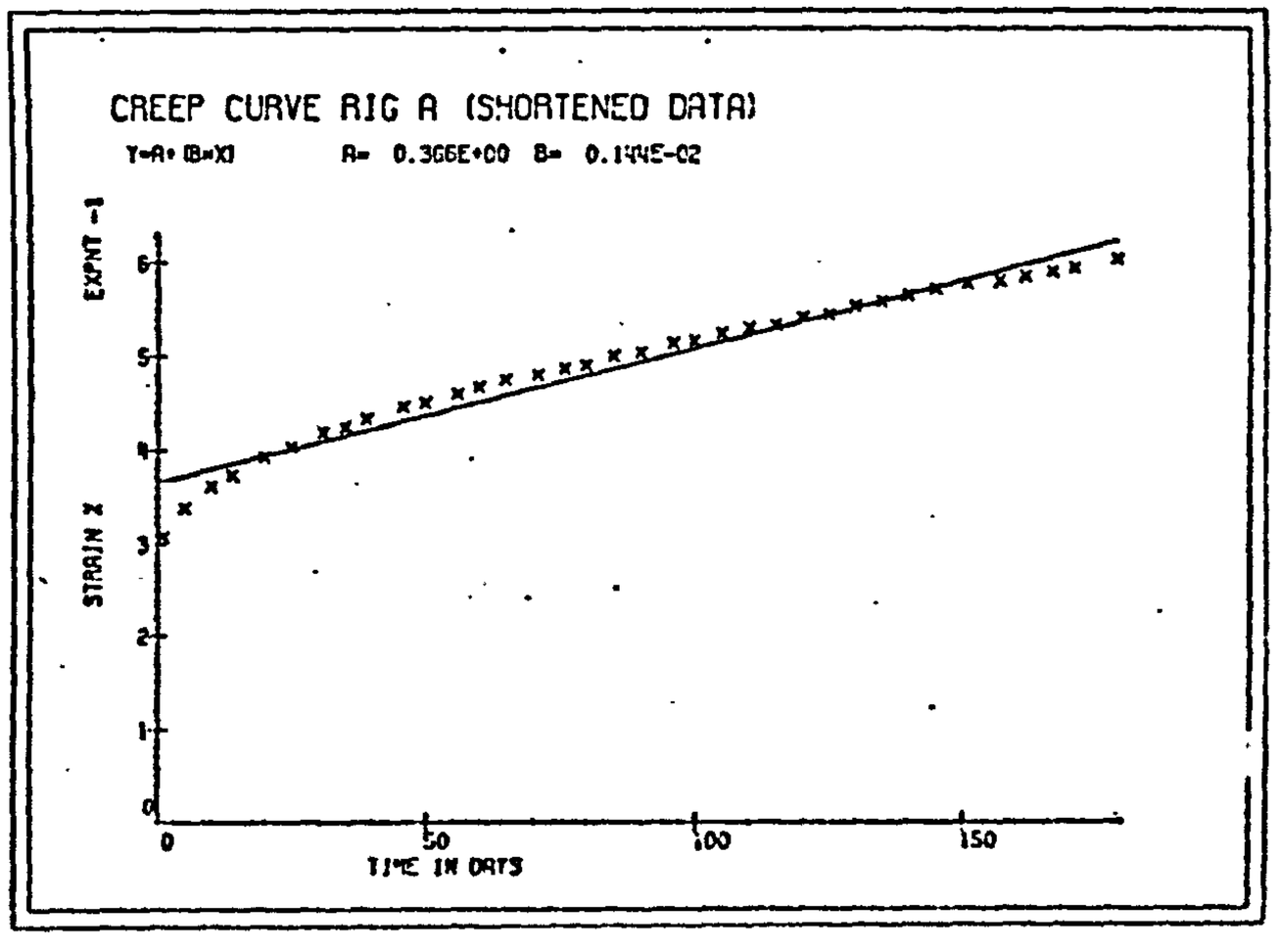

FIG 5.8

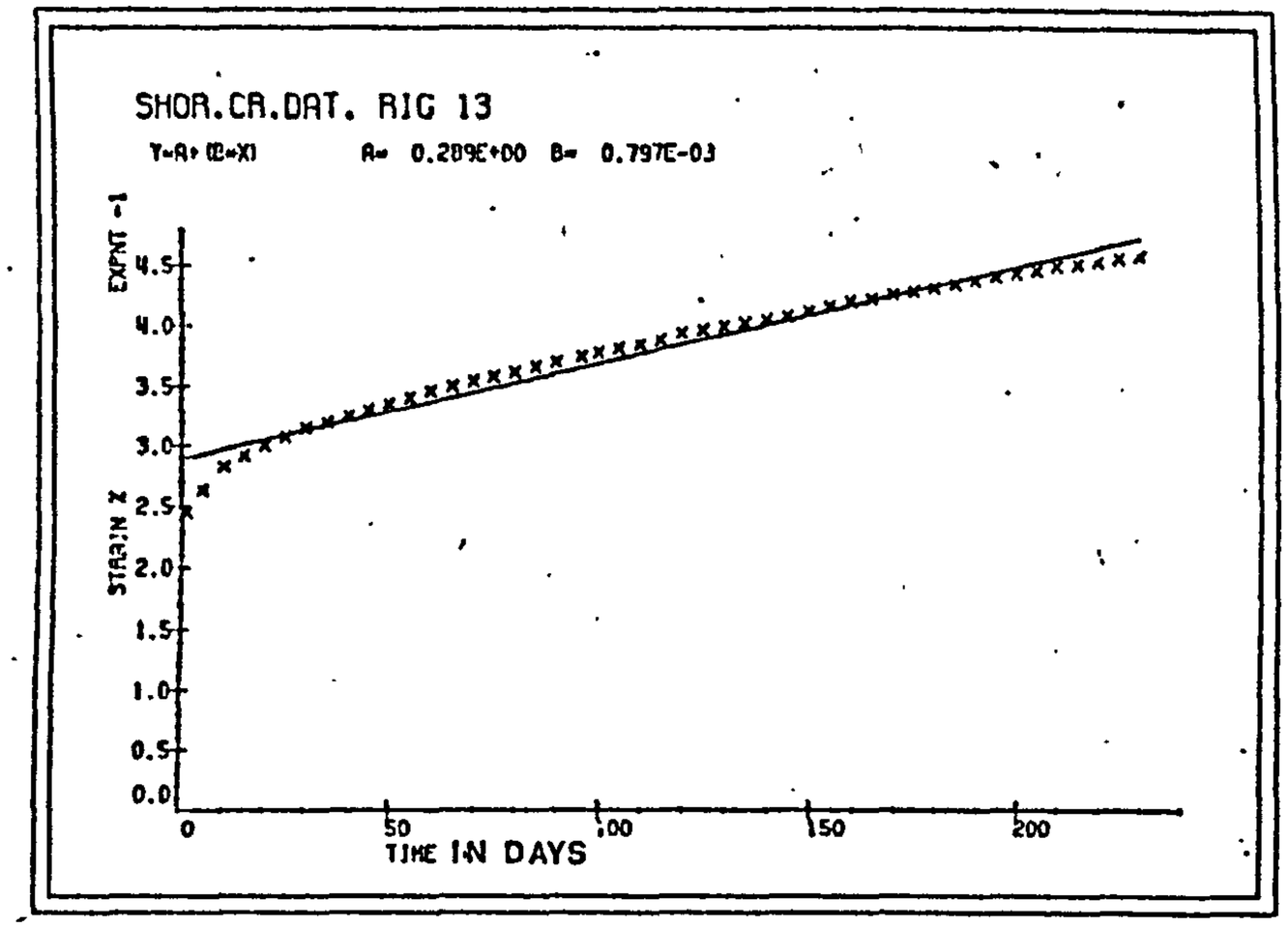

FIG 5.6

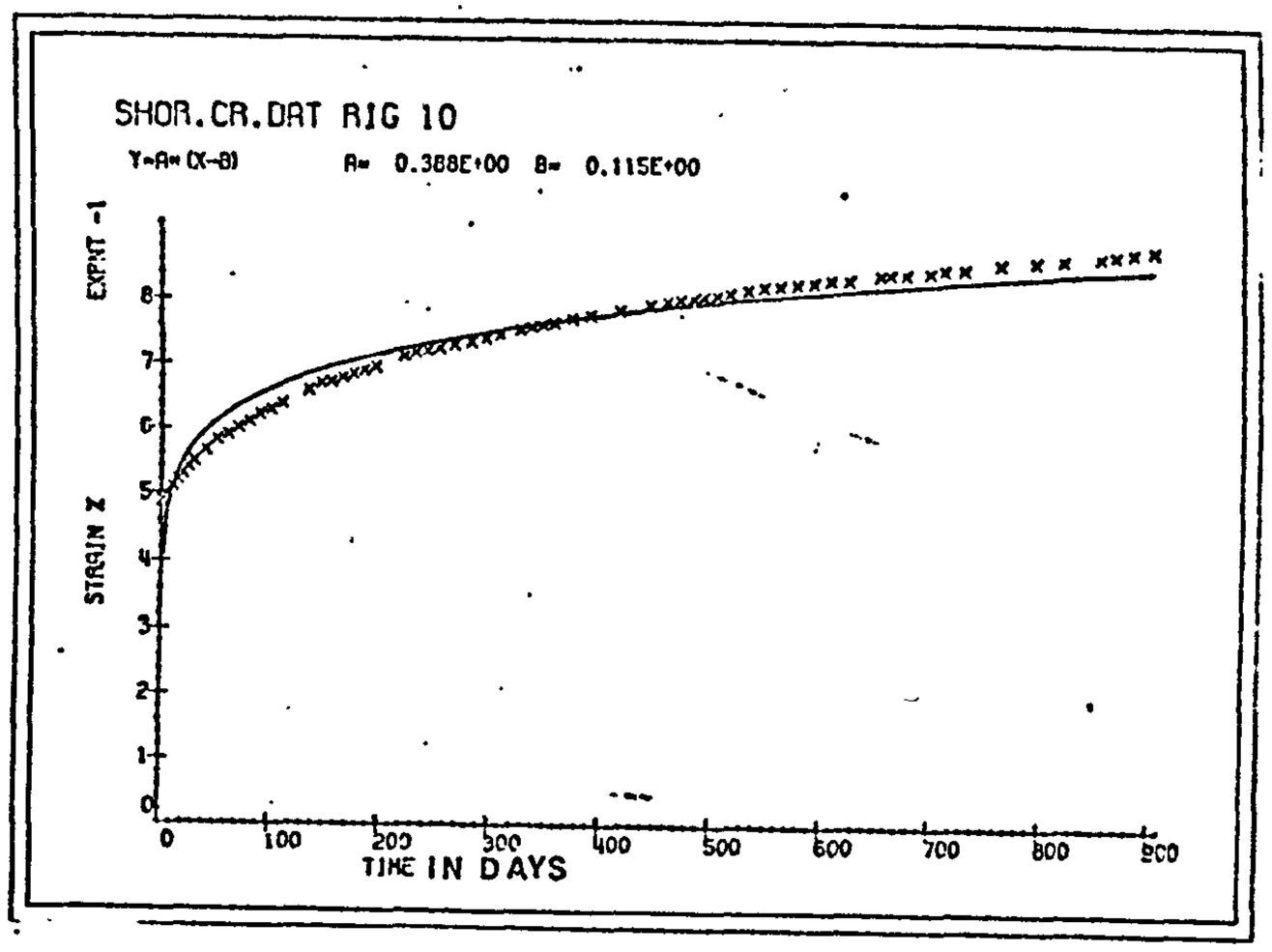

FIG 5.9

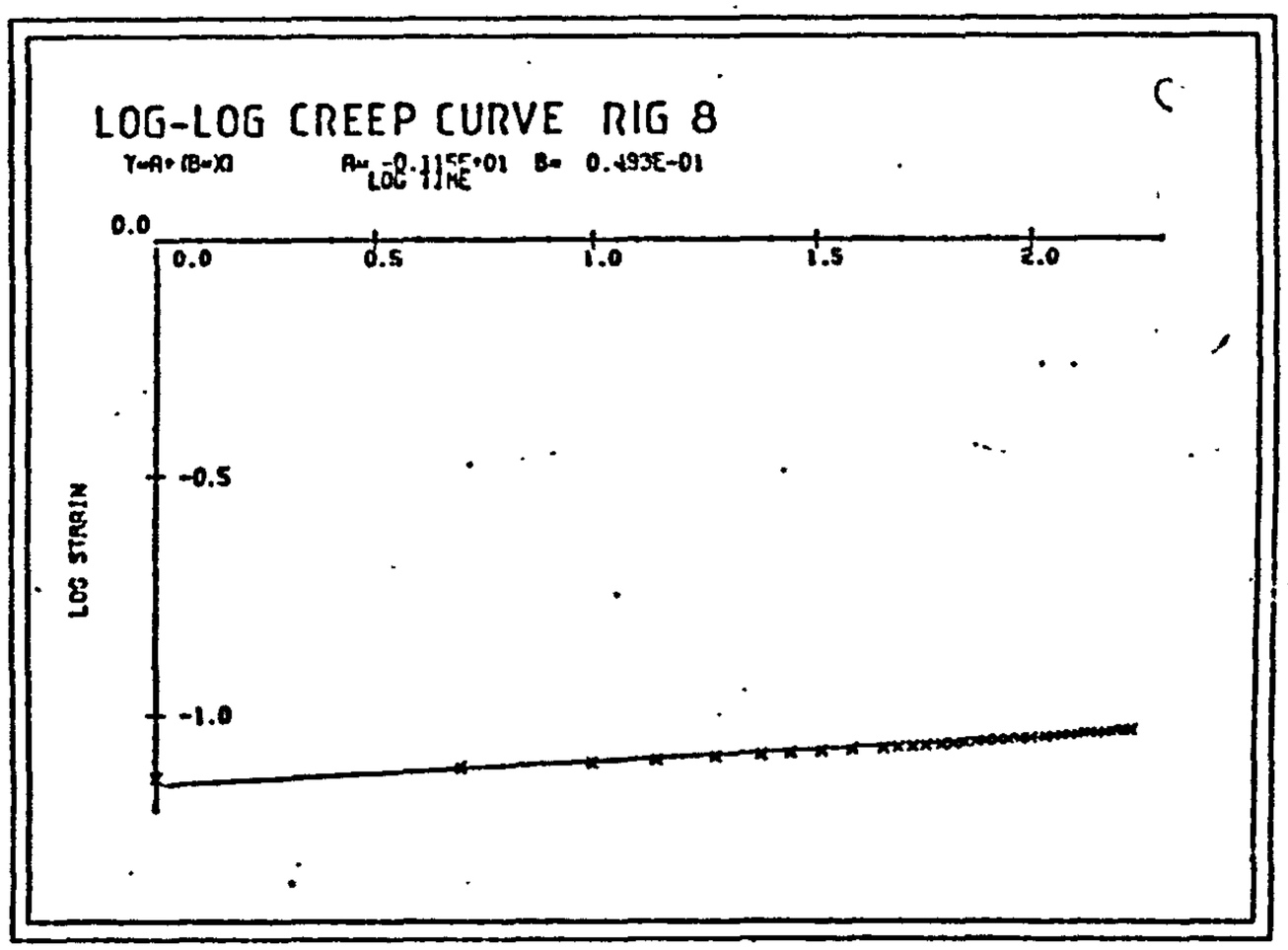

FIG 5.7

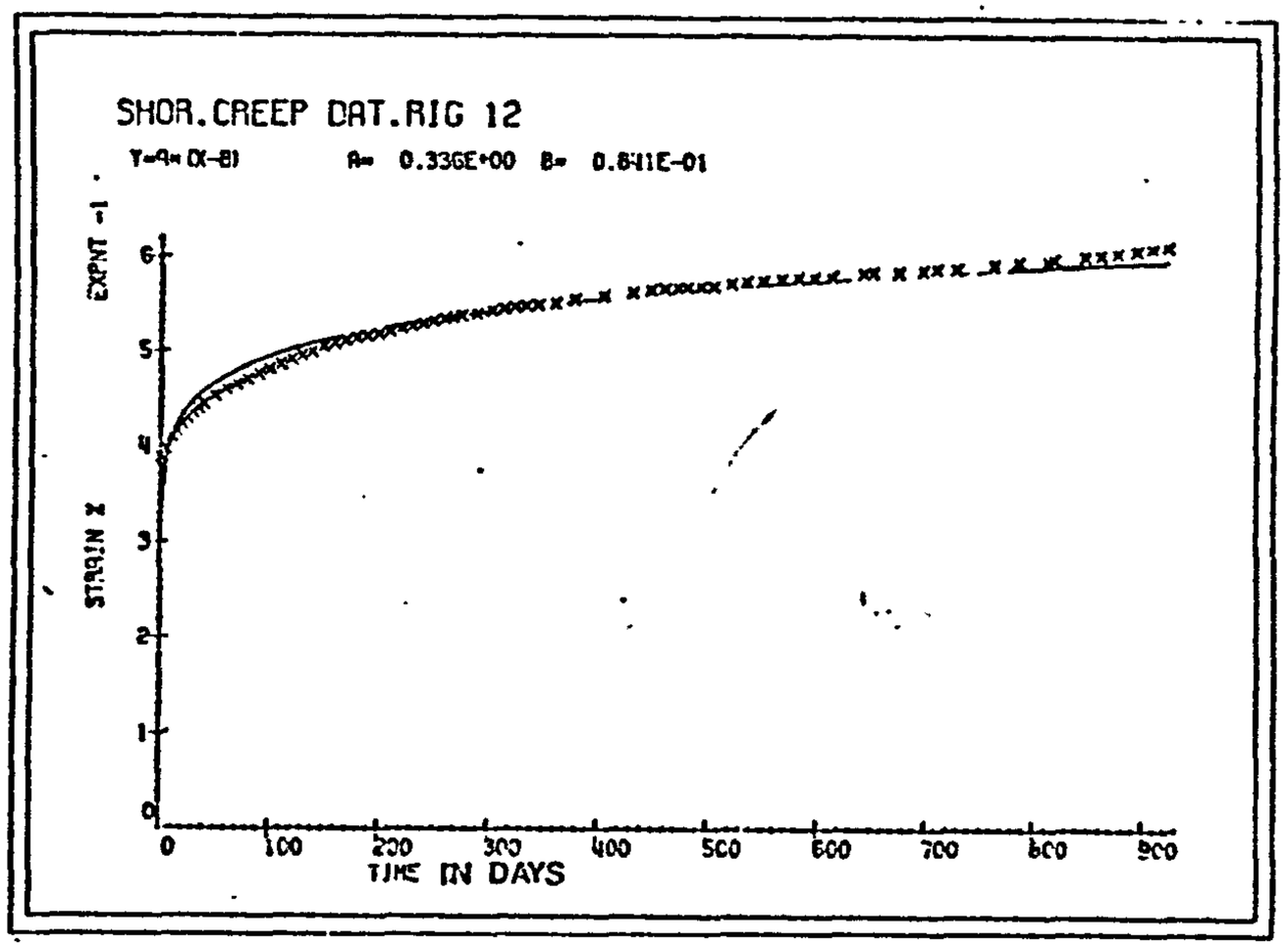

FIG 5.12

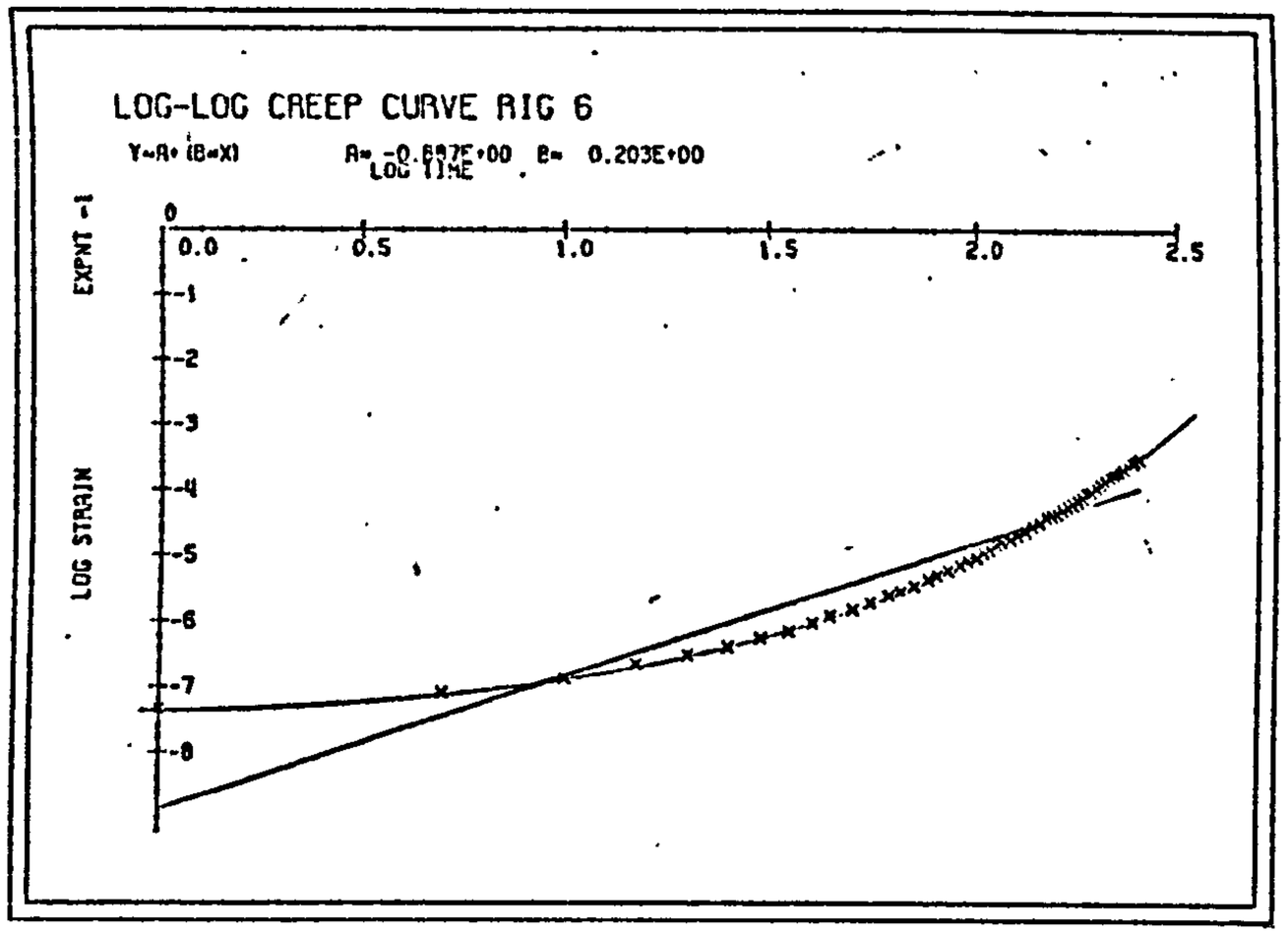

FIG 5.10

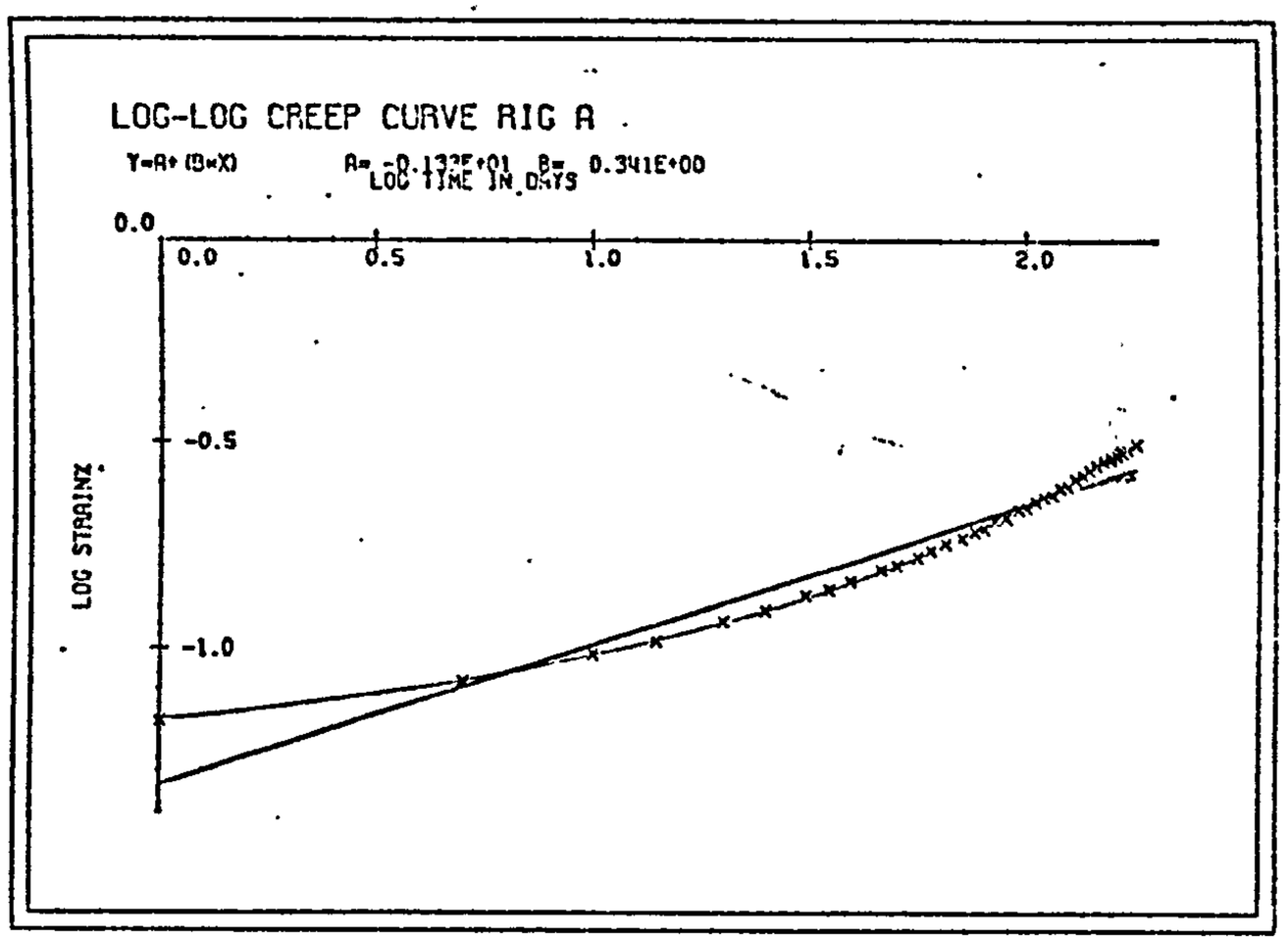

FIG 5.13

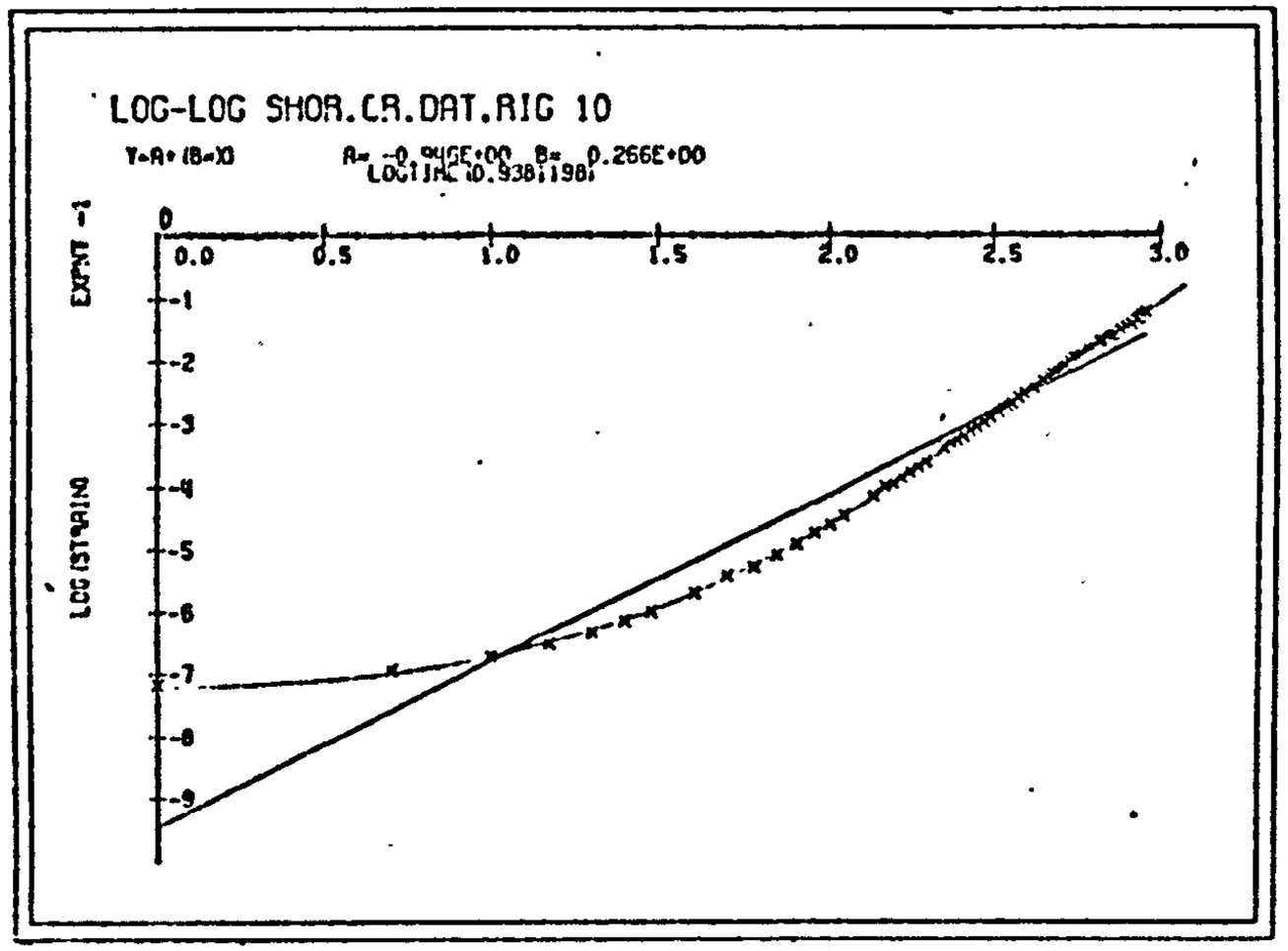

FIG 5.11

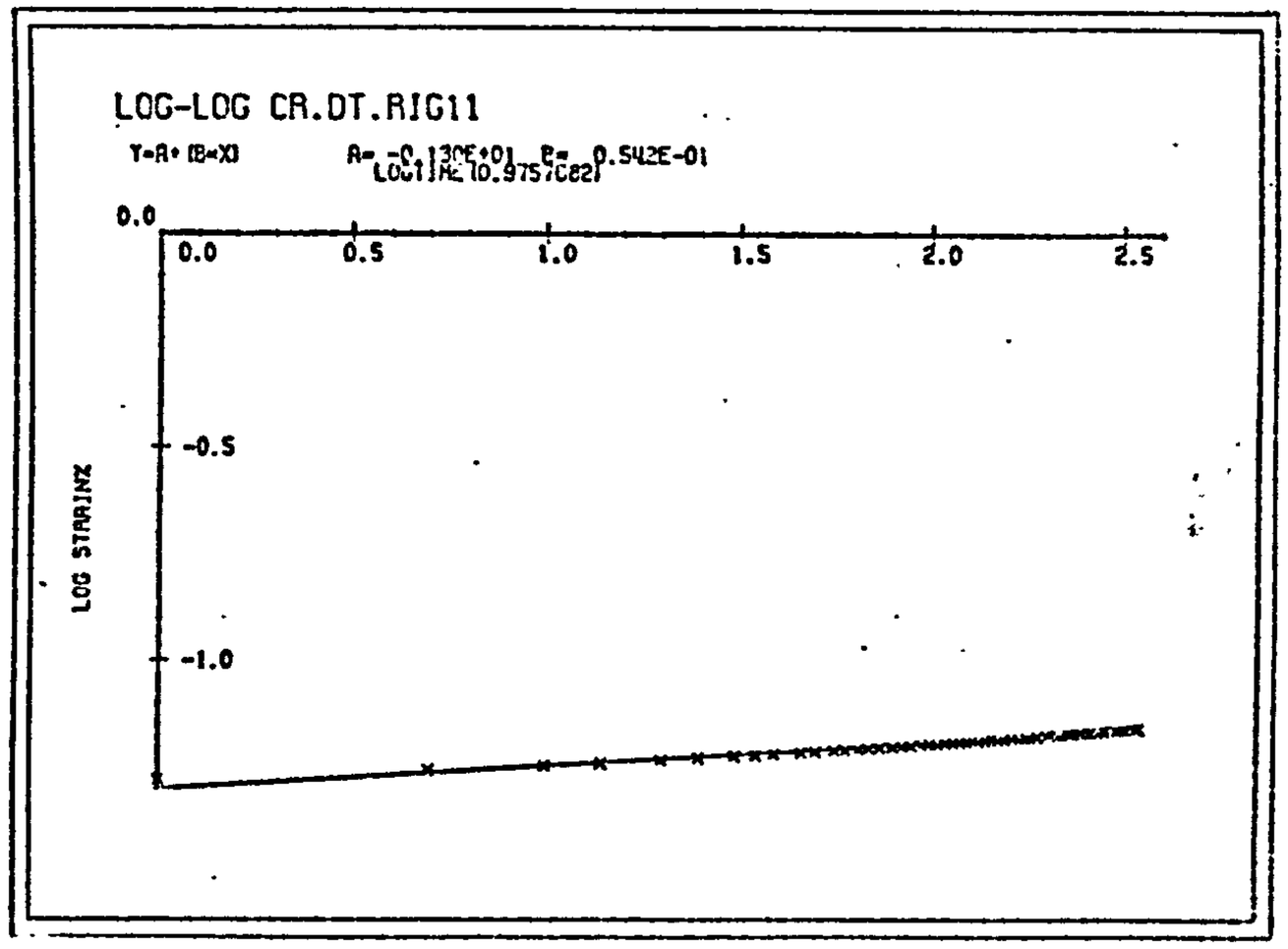

FIG 5.16

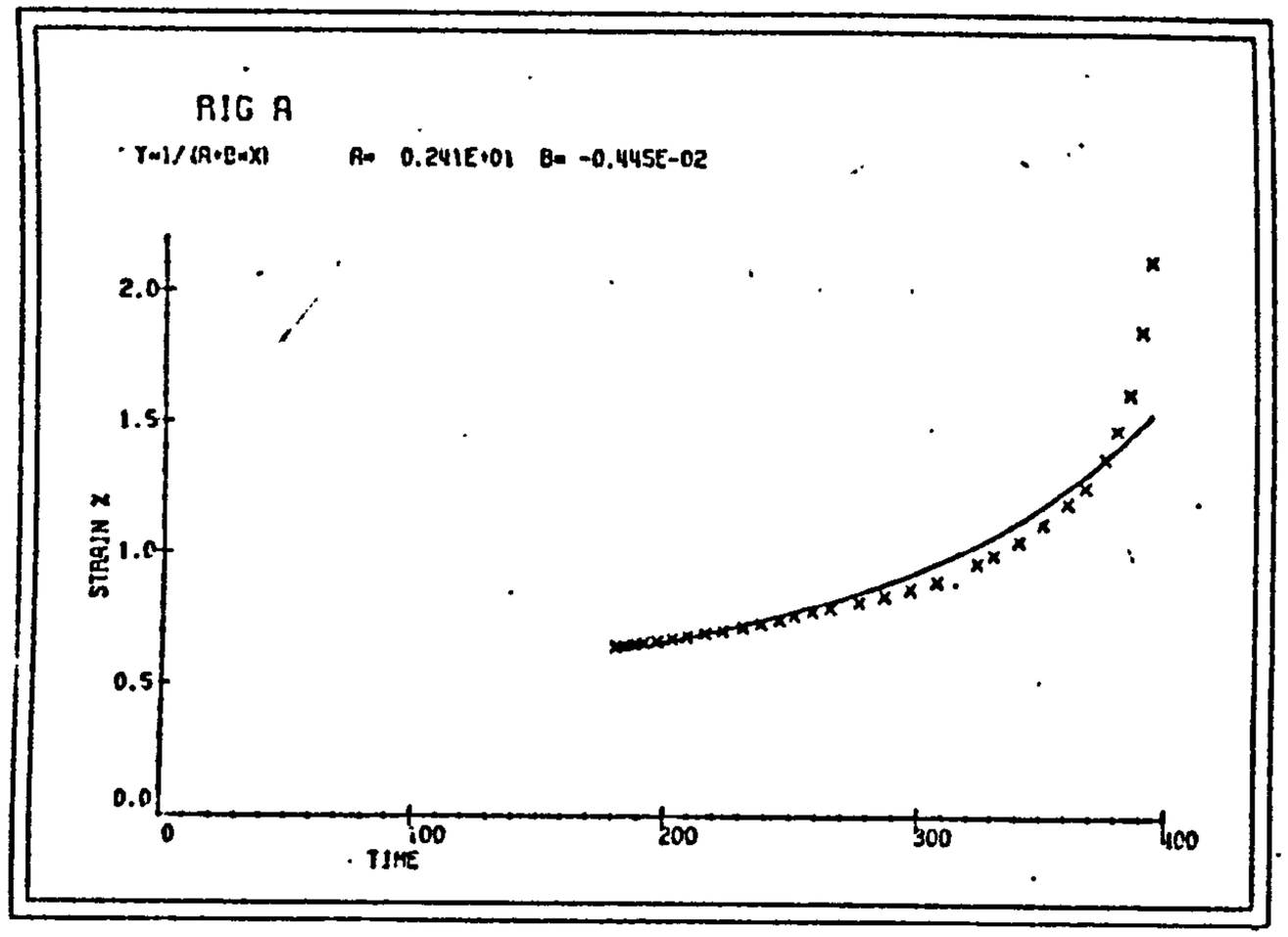

FIG 5.14

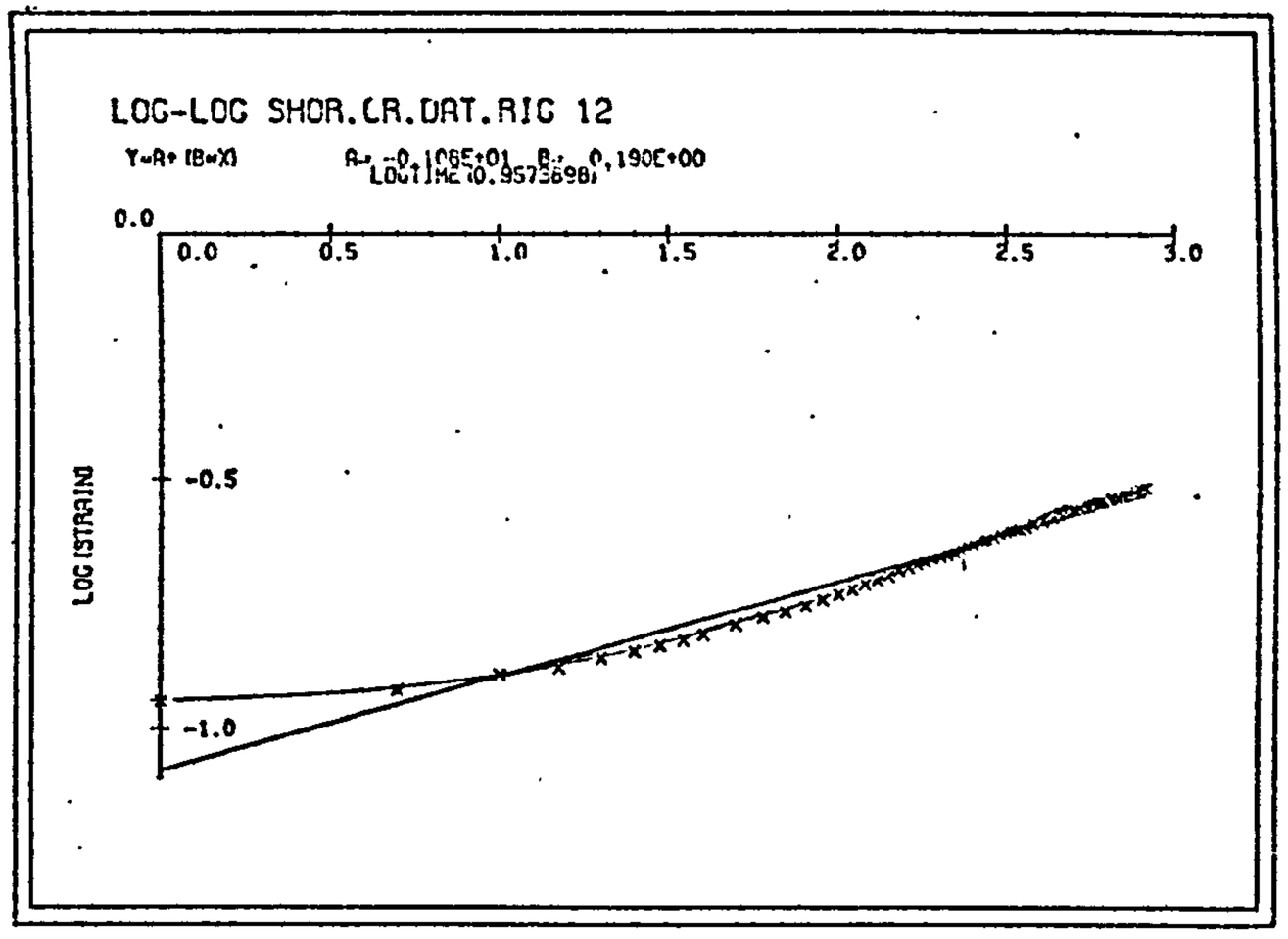

FIG 5.17

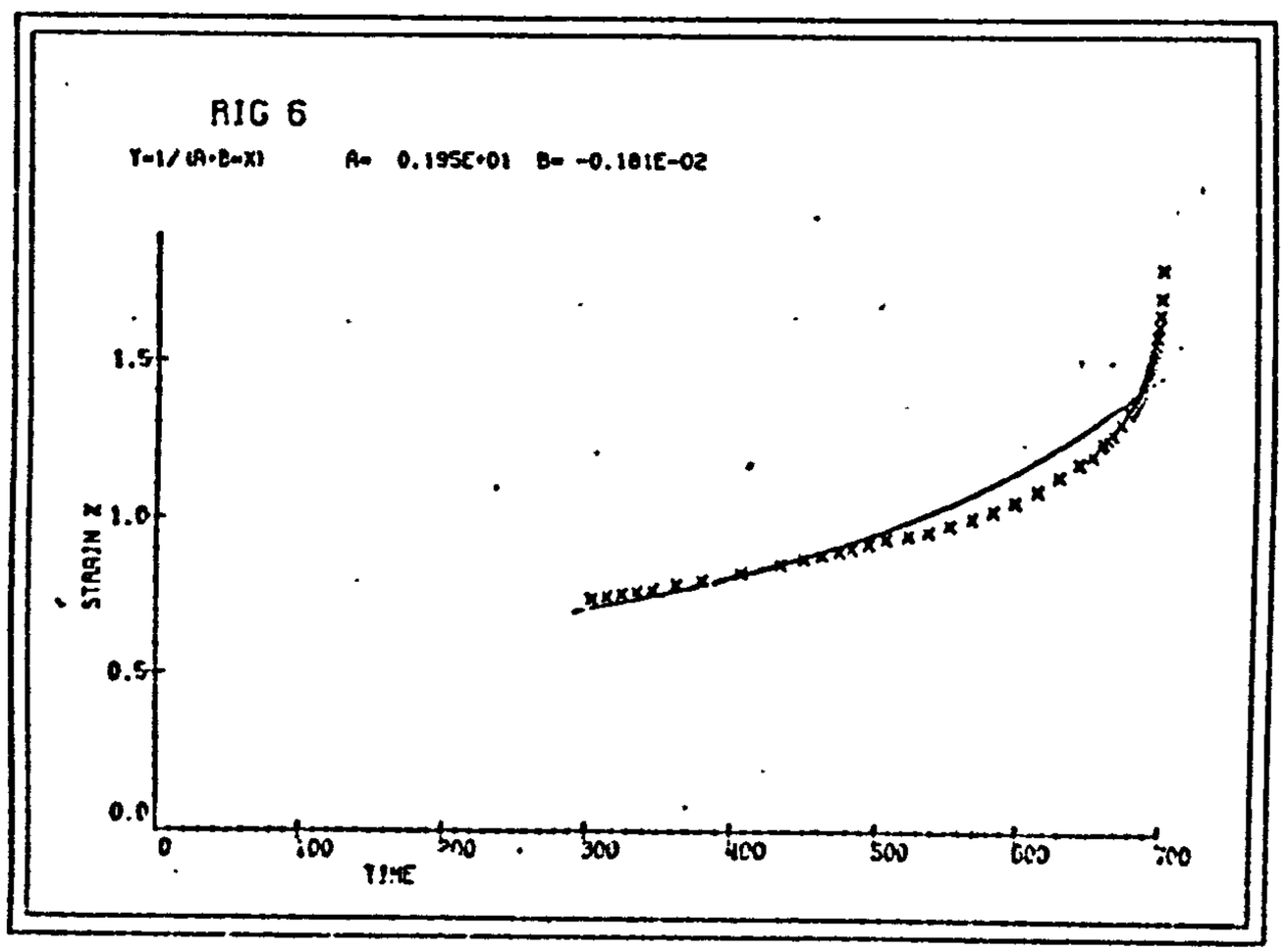

FIG 5.15

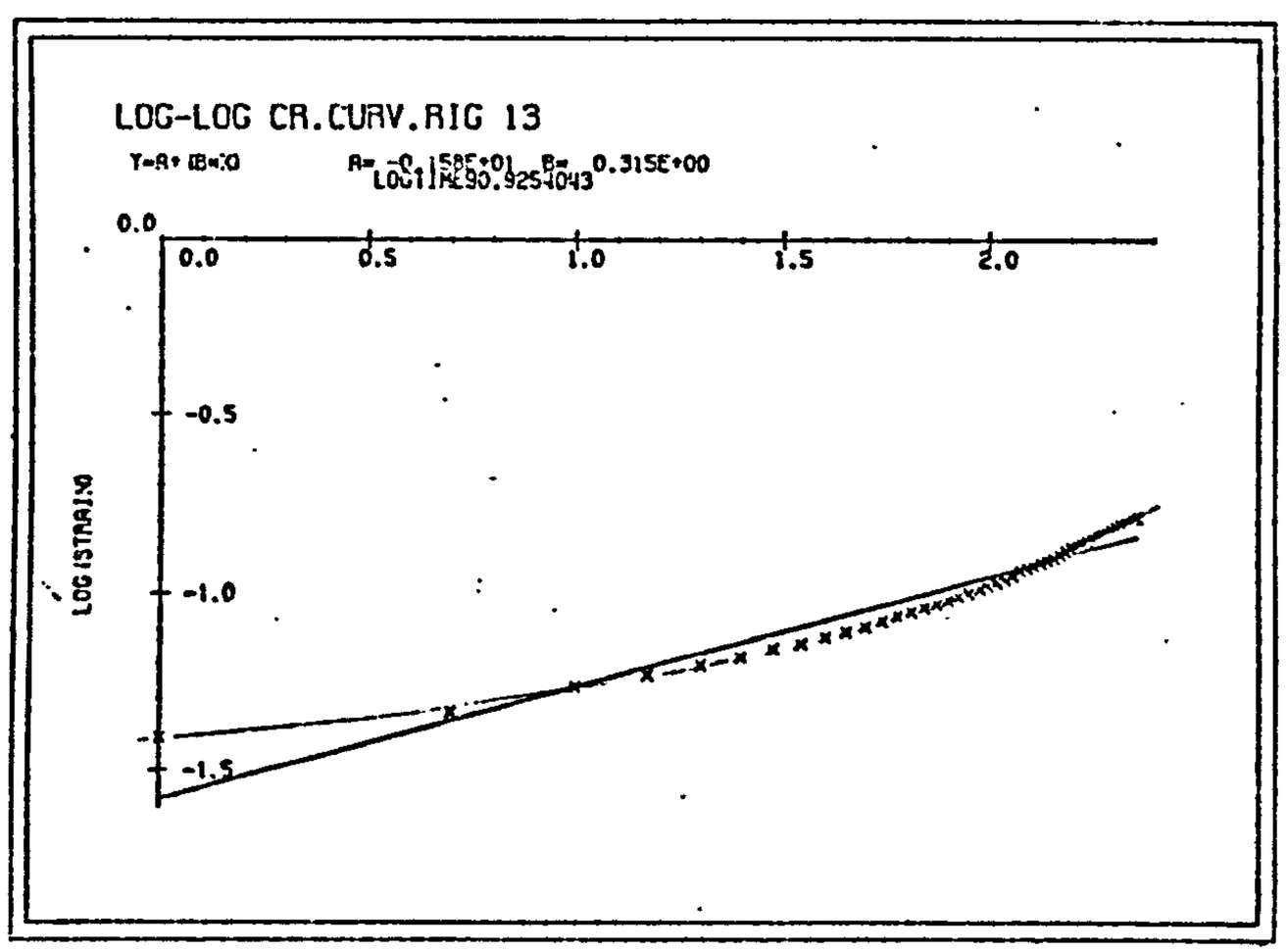

FIG 5.18

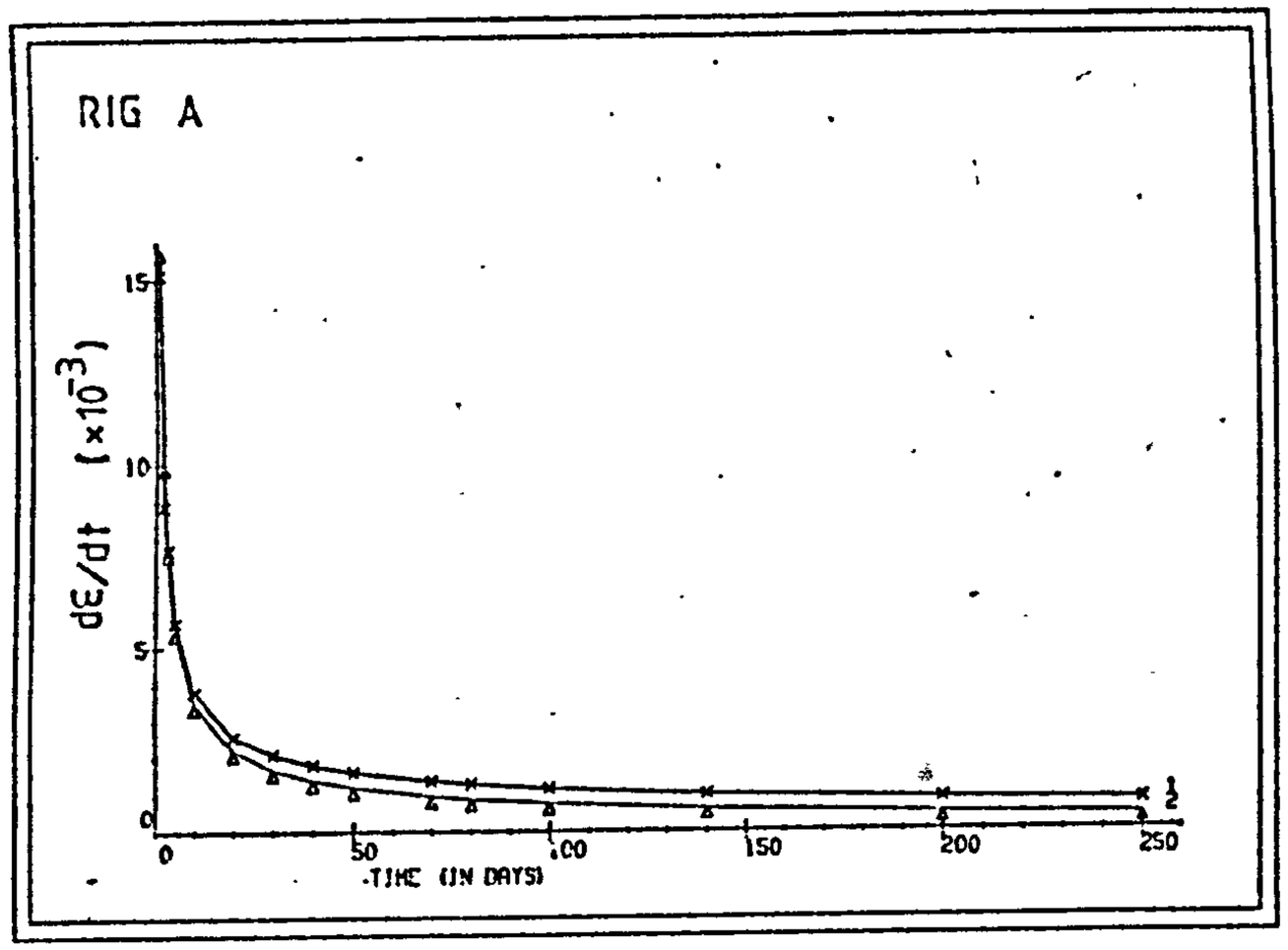

CURVE 1 . Decrease of strain-rate with time according to the proposed formula

$$\varepsilon = \varepsilon_o \times K^{(t^n)}$$

Where ε=Strain (%), t=Time (days), ε_o=0.2630, K=1.1636, n=0.3262

and

$$\frac{d\varepsilon}{dt} = n \times \varepsilon_o \times \ln K \times t^{n-1} \times K^{(t^n)}$$

CURVE 2 Decrease of strain-rate with time according to the best-fit power law

$$\varepsilon = A \times t^B$$

Where ε=Strain (%), t=Time (days), A=0.04636, B=0.341362

and

$$\frac{d\varepsilon}{dt} = A \times B \times t^{B-1}$$

FIG 5.19

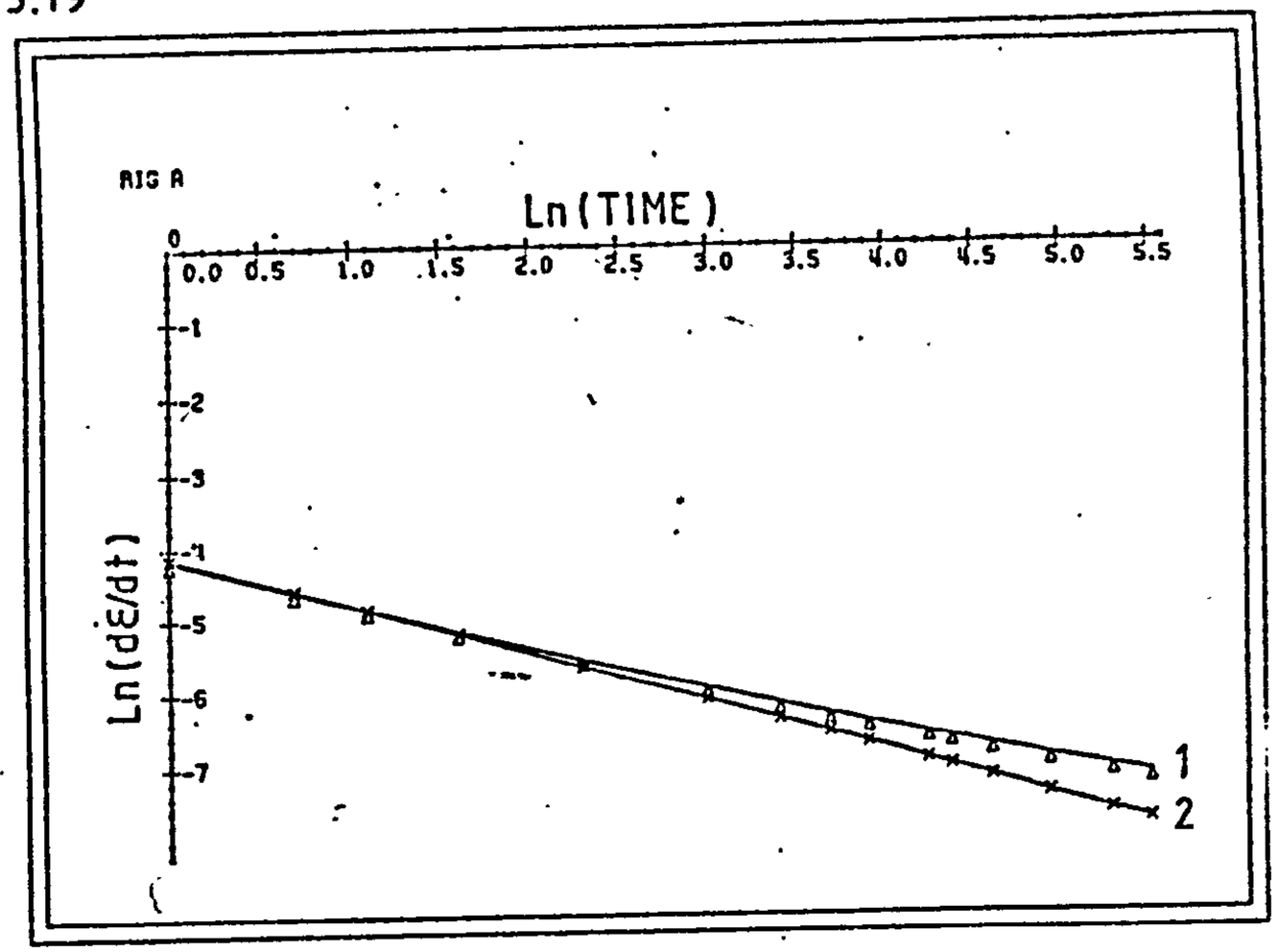

CURVE 1

$$\ln(d\varepsilon/dt) = \ln n + \ln\varepsilon_o + \ln(\ln K) + (n-1)\ln t + (t^n)\ln K$$

CURVE 2

$$\ln(d\varepsilon/dt) = \ln A + \ln B + (B-1)\ln t$$

FIG 5.20 GRAPHICAL SOLUTION OF FORMULA 1.

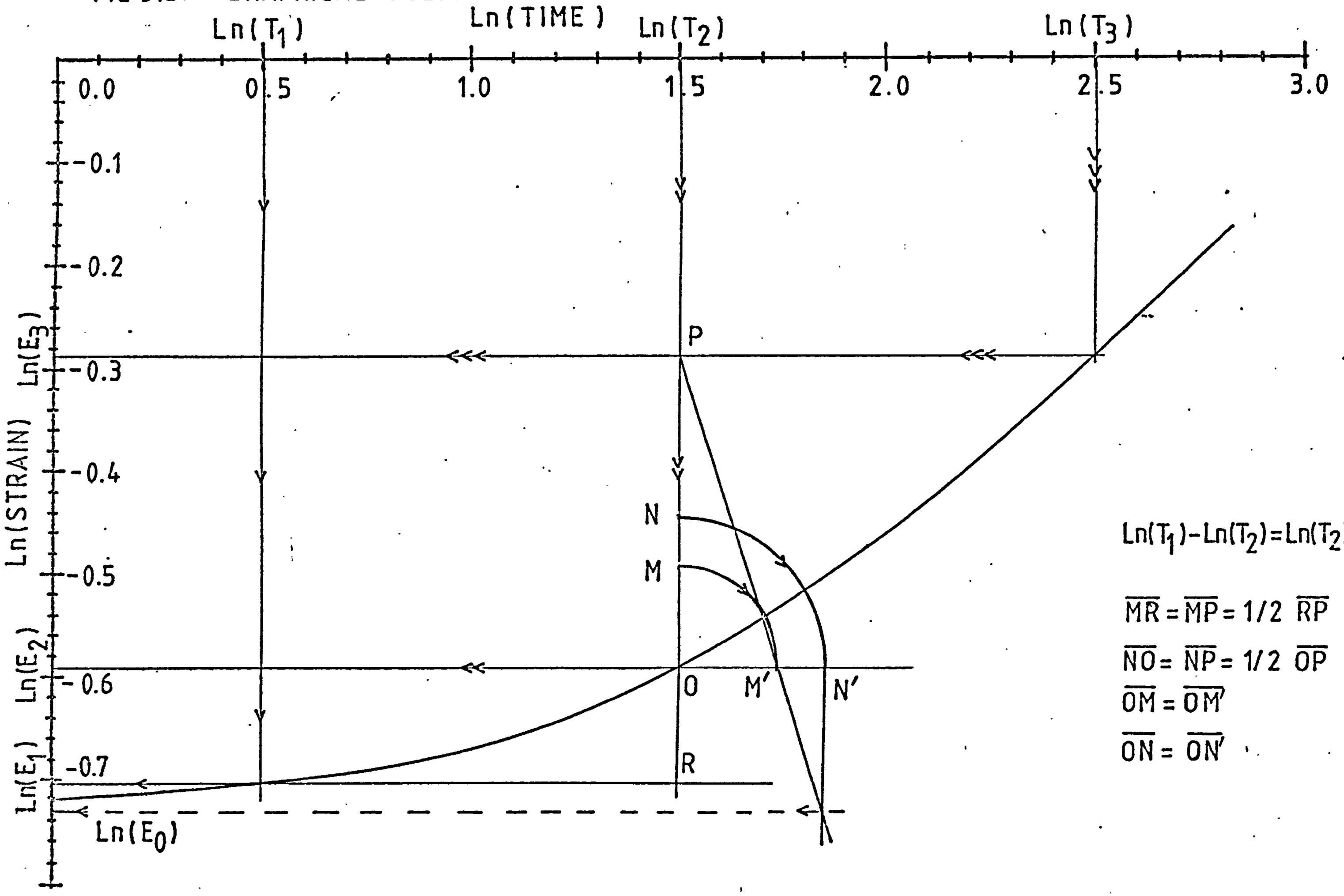

$Ln(T_1)-Ln(T_2)=Ln(T_2)-Ln(T_3)$

$\overline{MR}=\overline{MP}=1/2\ \overline{RP}$

$\overline{NO}=\overline{NP}=1/2\ \overline{OP}$

$\overline{OM}=\overline{OM'}$

$\overline{ON}=\overline{ON'}$

FIG 5.21

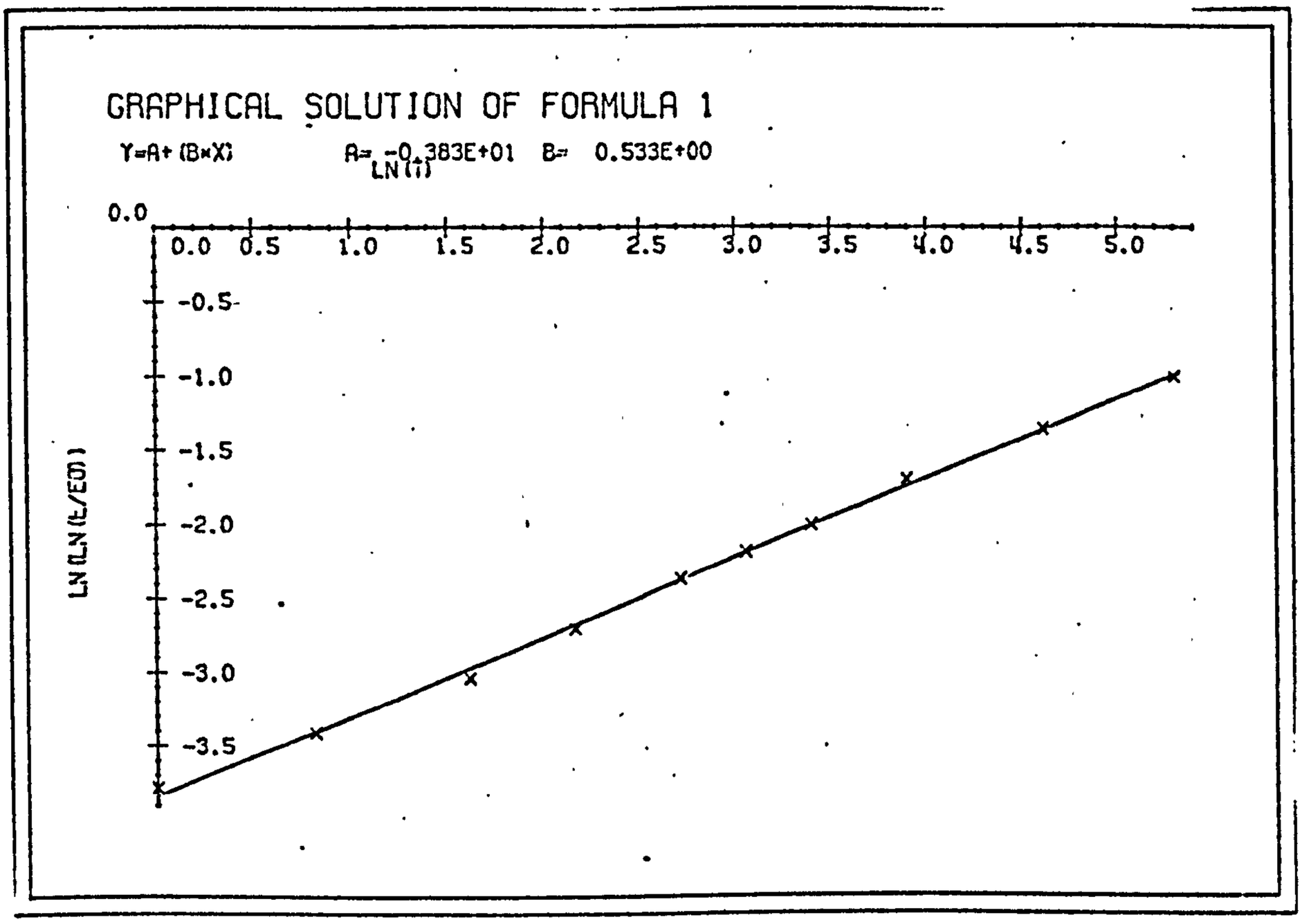
GRAPHICAL SOLUTION OF FORMULA 1
Y=A+(B*X)
A= -0.383E+01
B= 0.533E+00
LN(t)
0.0
0.0 0.5 1.0 1.5 2.0 2.5 3.0 3.5 4.0 4.5 5.0
-0.5
-1.0
-1.5
-2.0
-2.5
-3.0
-3.5
LN(LN(1/E(t)))

FIG 5.24

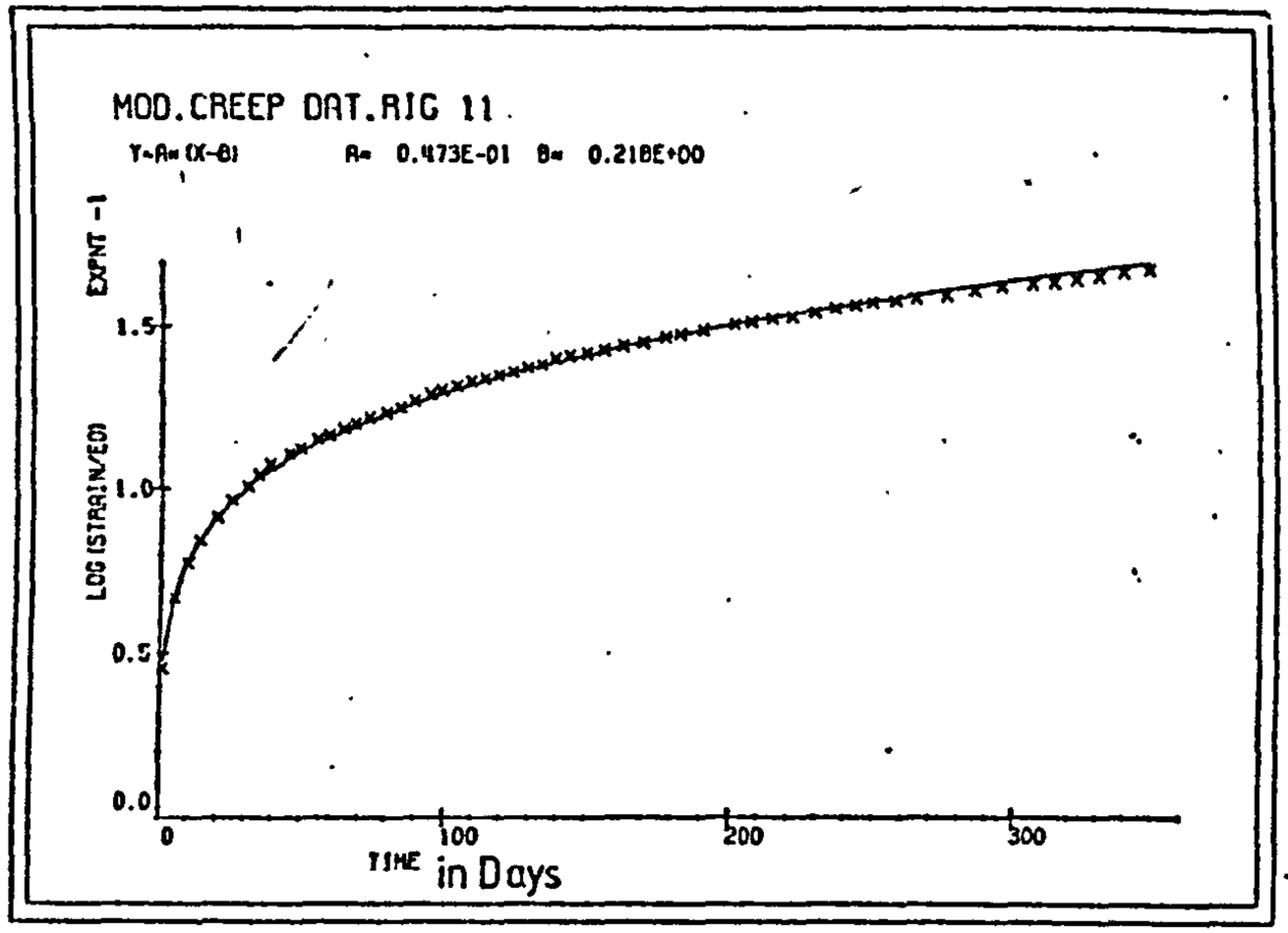

FIG 5.22

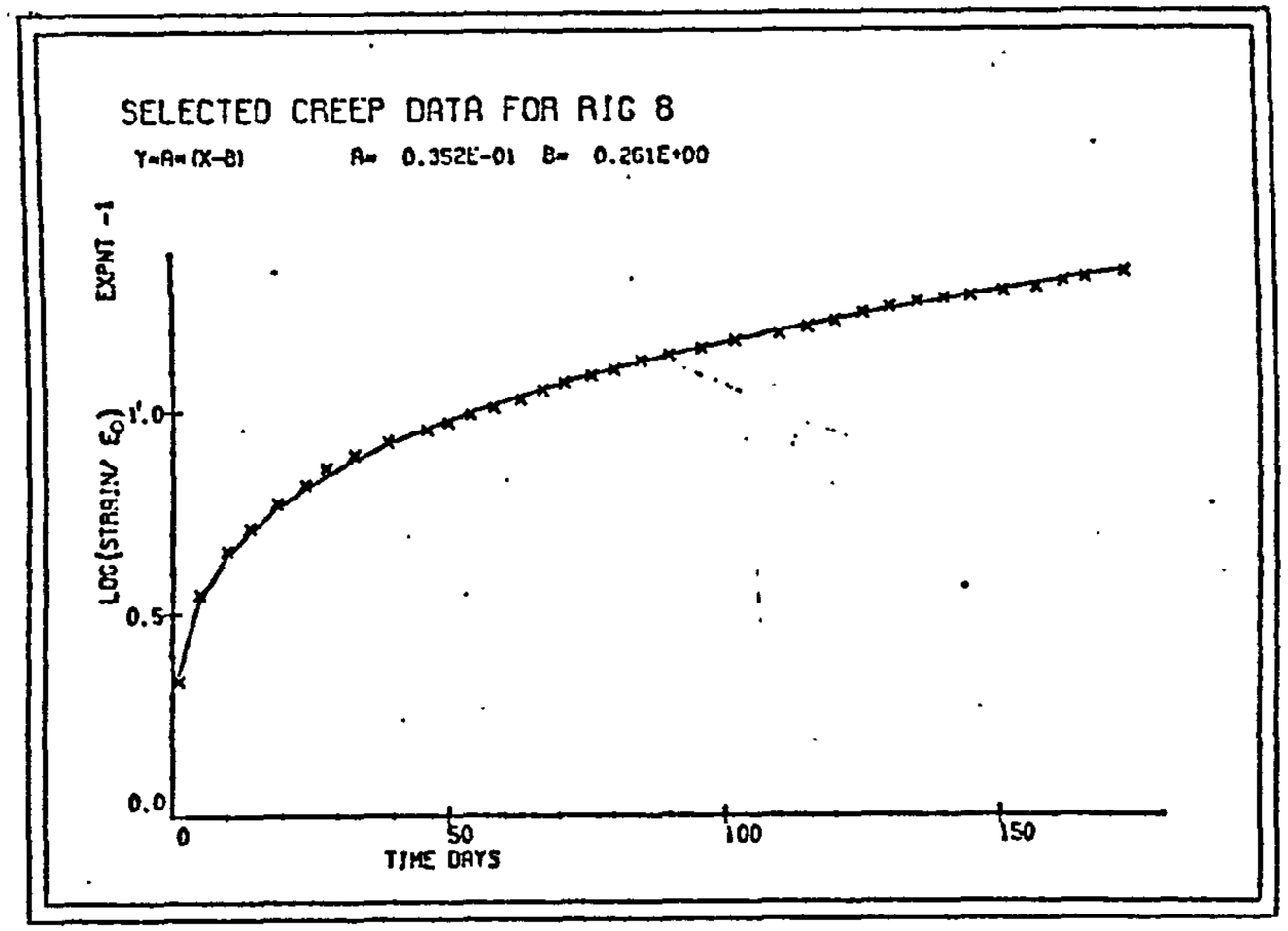

FIG 5.25

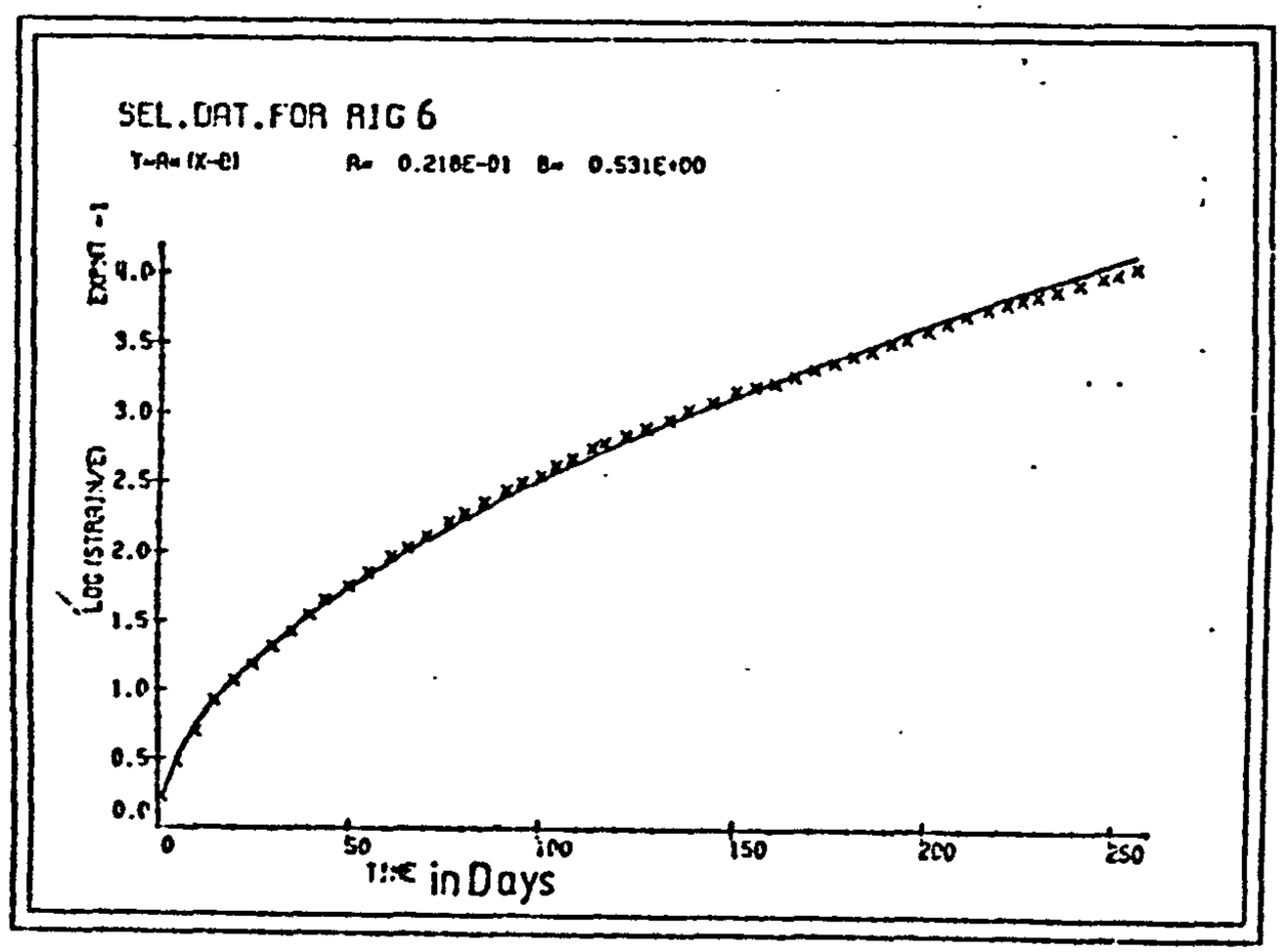

FIG 5.23

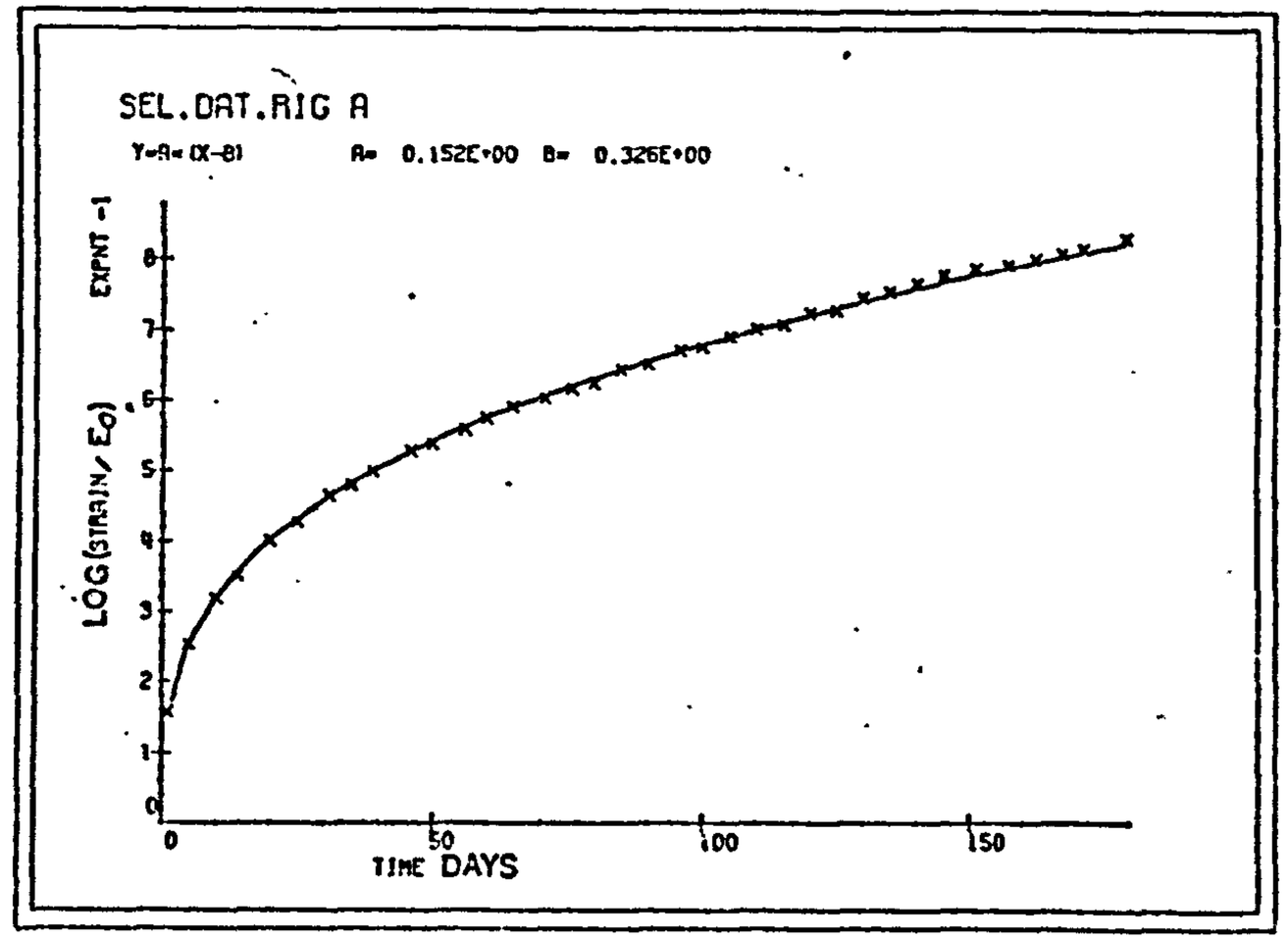

FIG 5.26

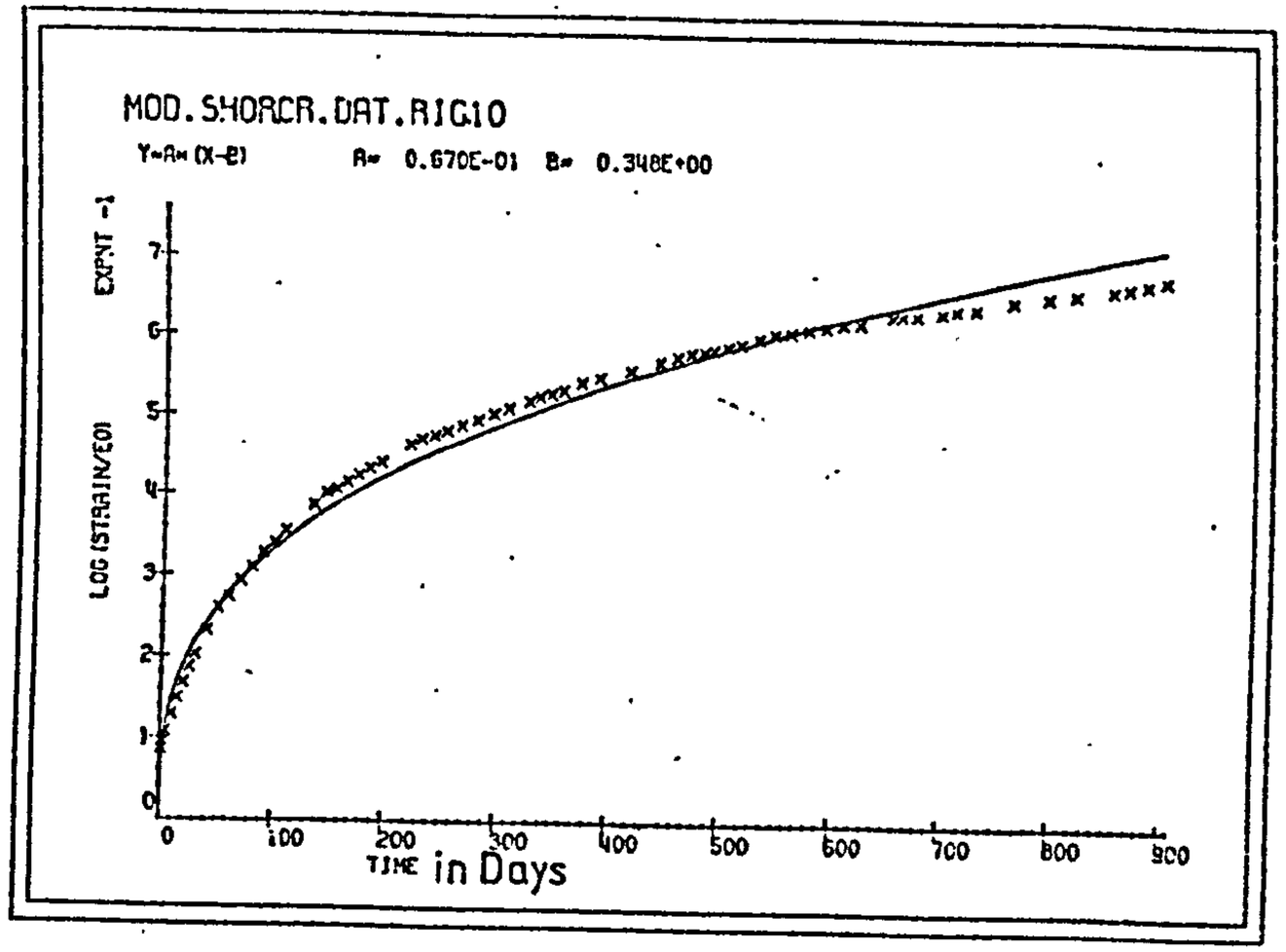

FIG 5.28

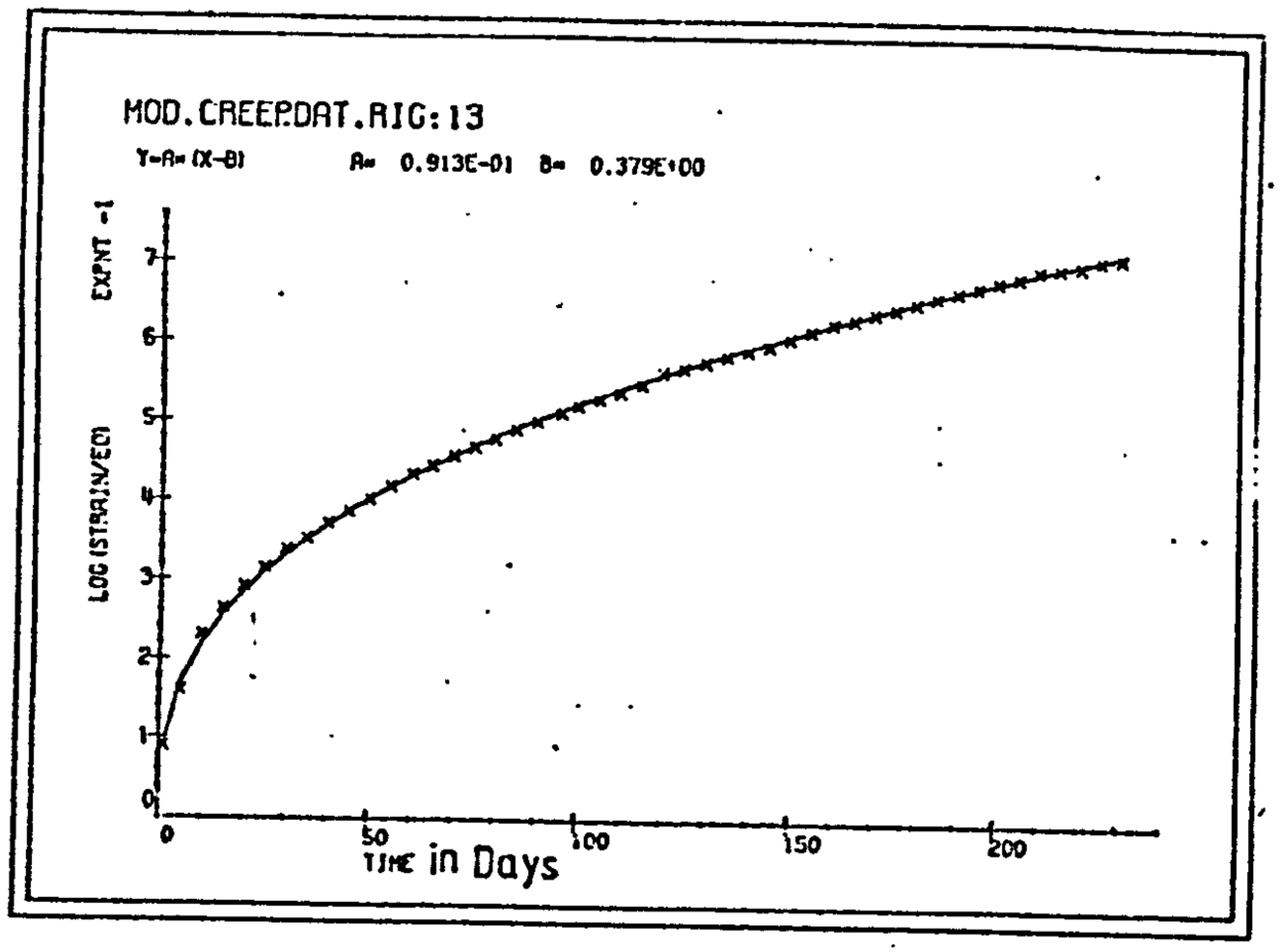

FIG 5.27.

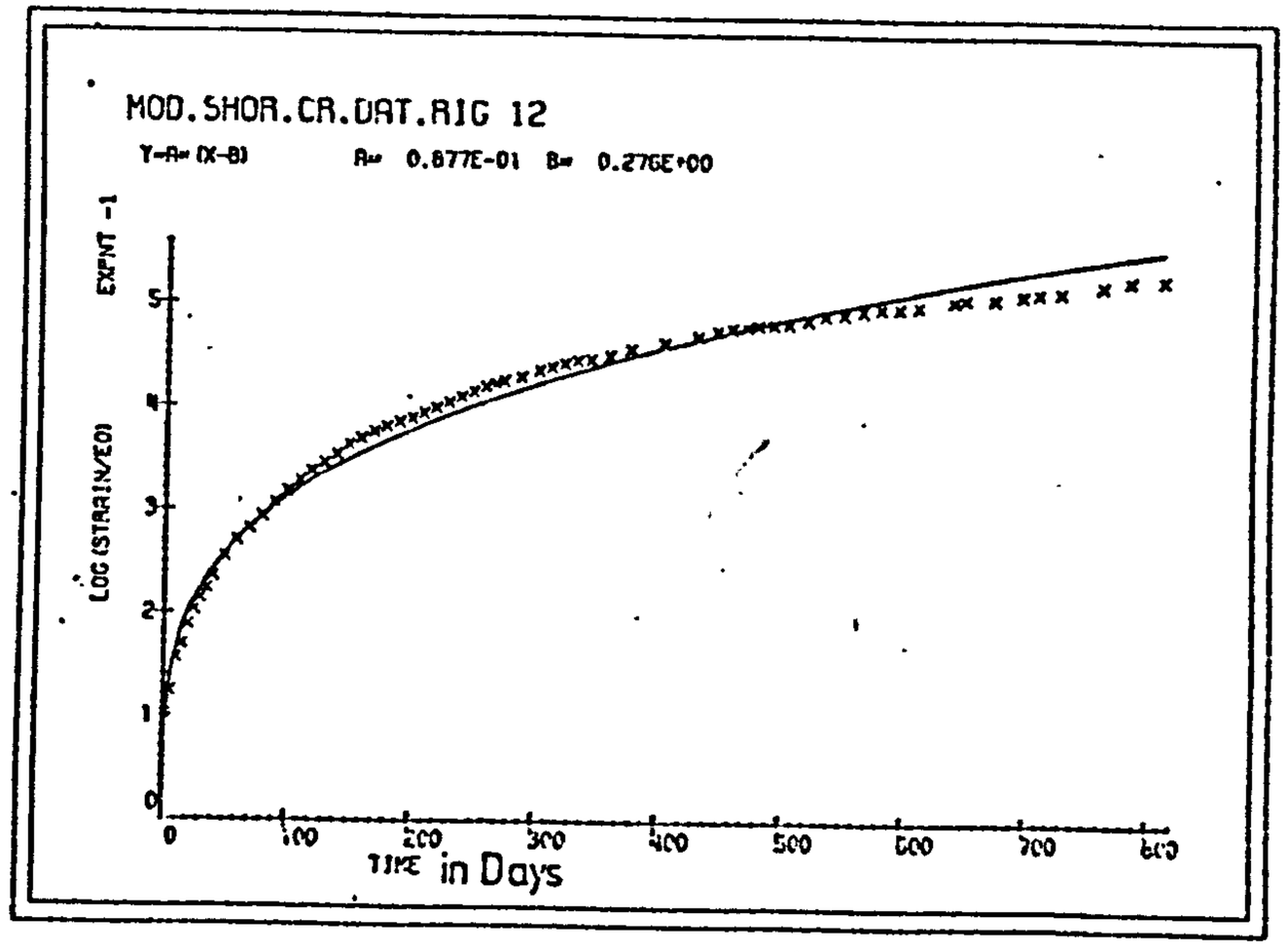

FIG 5.29

CHART FOR PROPOSED FORMULA

Where $Z = t^n$

$\varepsilon/\varepsilon_o = K^Z$

($K = \varepsilon_i/\varepsilon_o$)

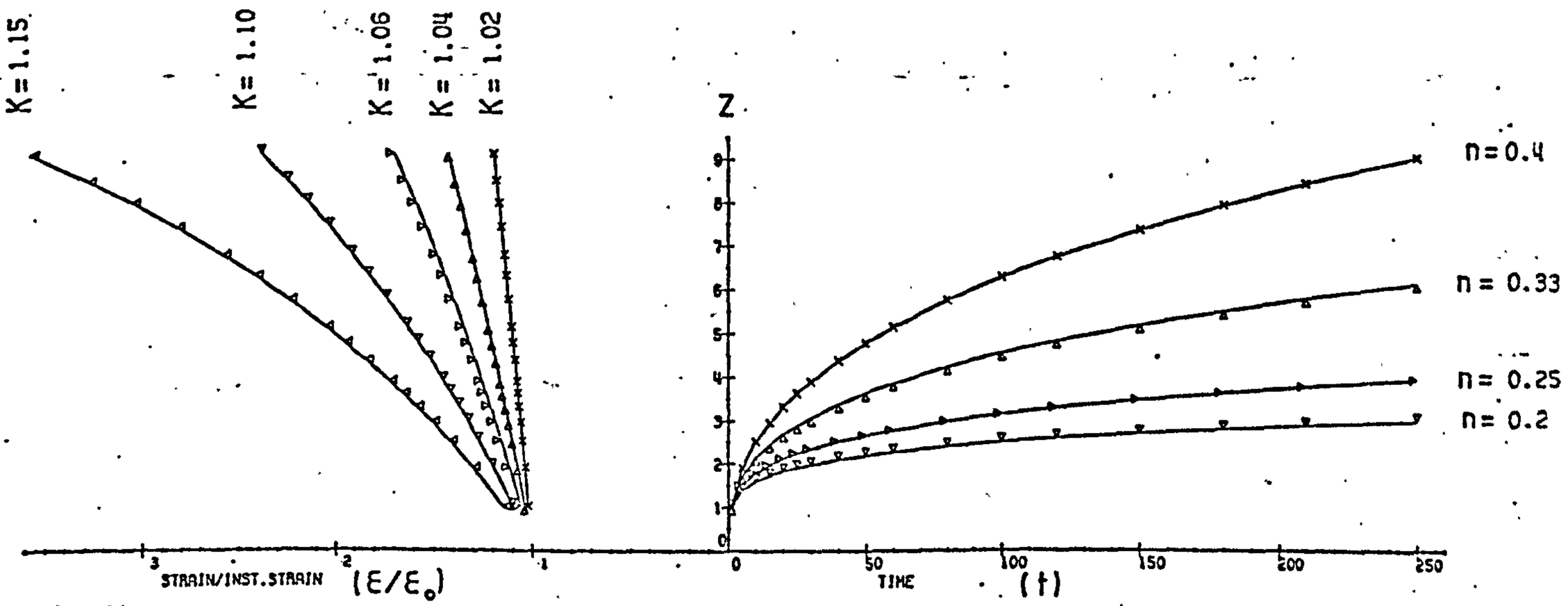

FIG 5.30

CHART FOR POWER LAW

Where $Z = t^n$

$\varepsilon/\varepsilon_o = 1 + B \times Z$

($B = K - 1 = \varepsilon_i/\varepsilon_o - 1$)

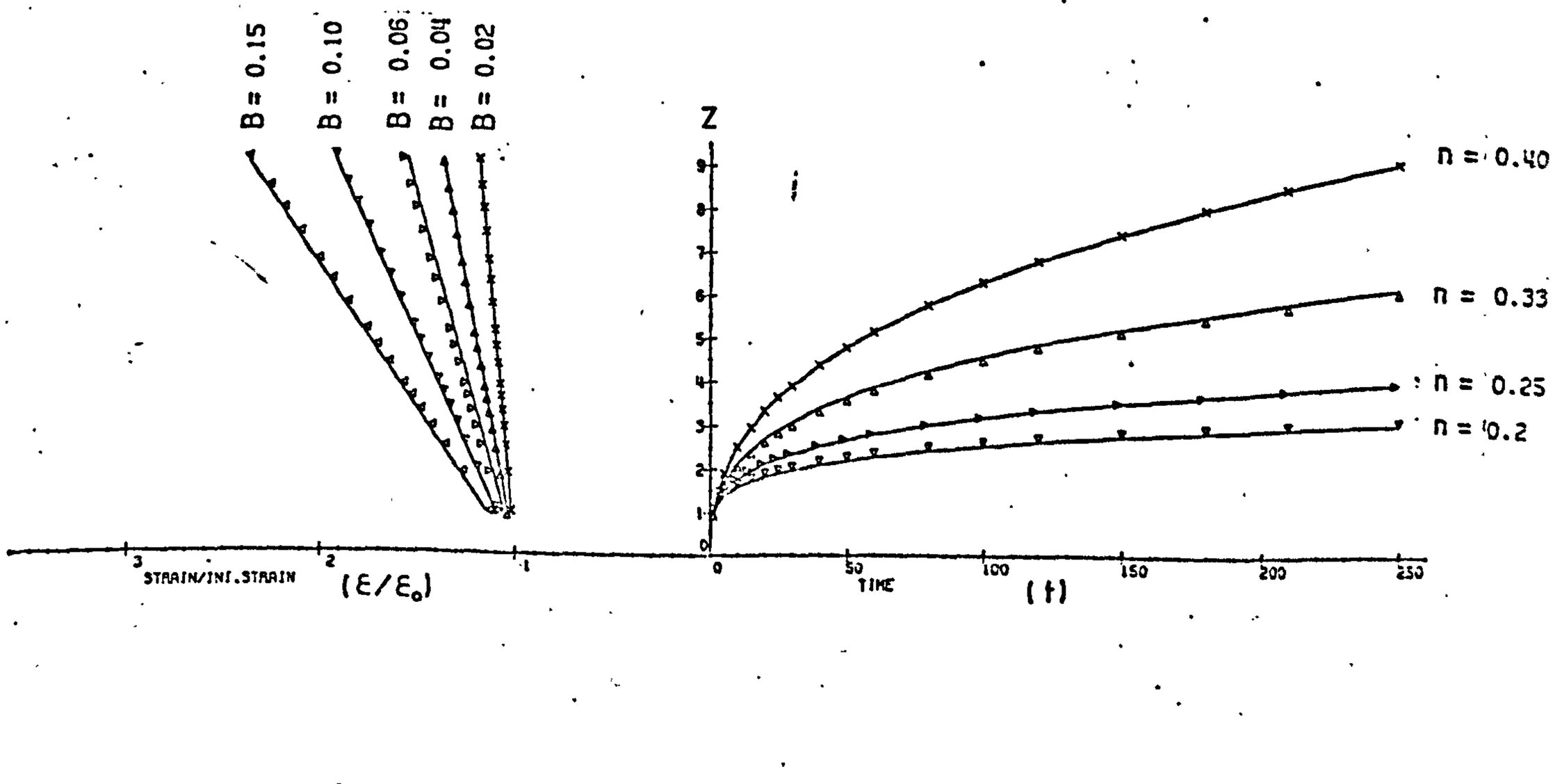

FIG 5.31 CHART FOR THE ESTIMATION OF CREEP BEHAVIOR

$K=\varepsilon_1/\varepsilon_o$, $B=K-1$

Proposed equation : $\varepsilon/\varepsilon_o = K^Z$

Power law : $\varepsilon/\varepsilon_o = 1+(K-1)\times Z$

$Z = t^n$

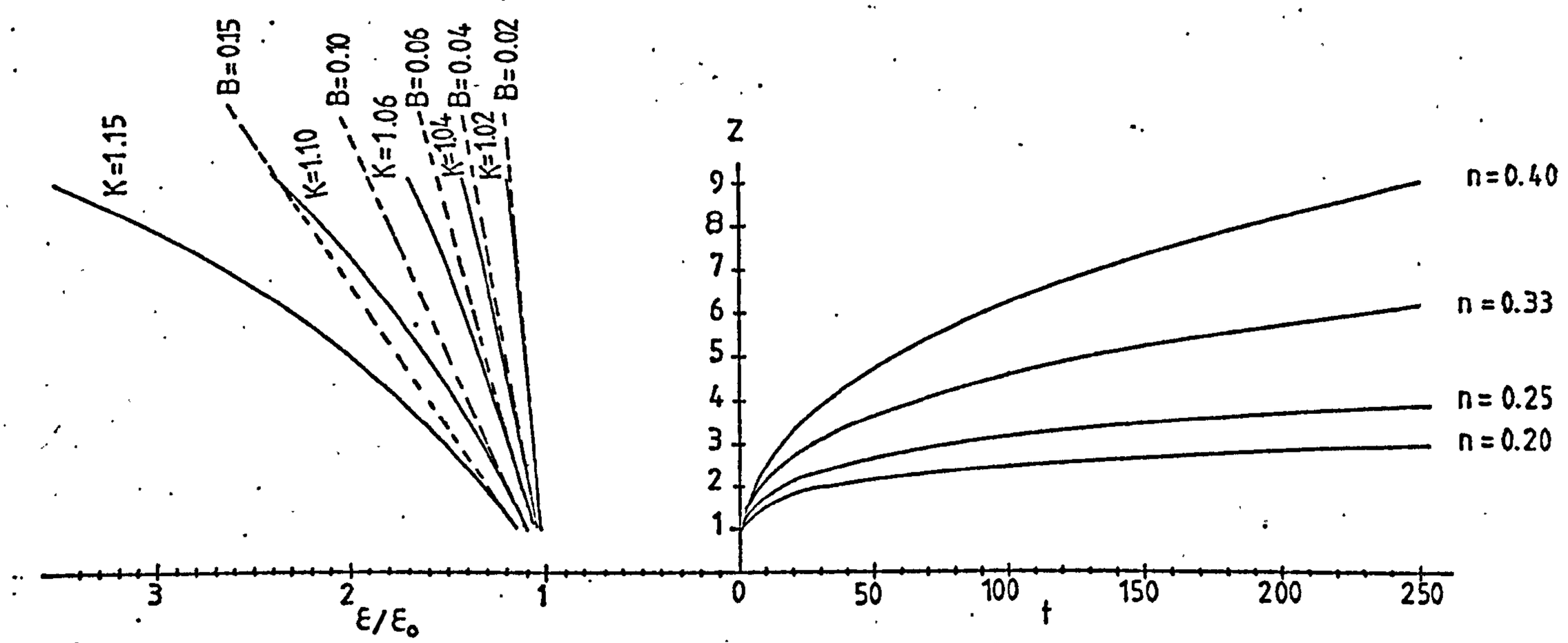

FIG 5.32 CHART FOR LOGARITHMIC LAW

Where $Z = t^n$

$\varepsilon/\varepsilon_o = K + \mathrm{Ln}\, Z$

$(K = \varepsilon_1/\varepsilon_o)$

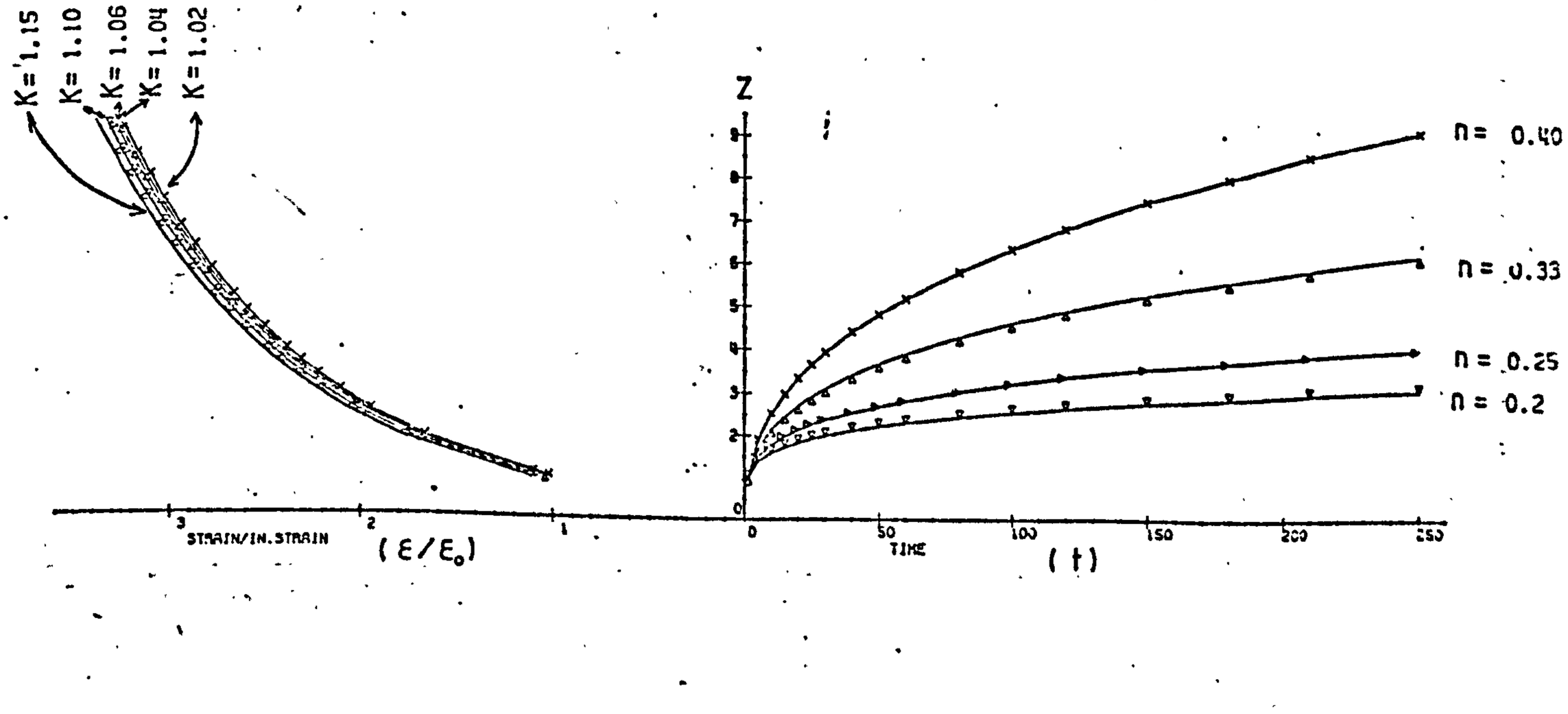

FIG 5.33 MULTI PURPOSE CHART

Curve	K
1	1.02
2	1.04
3	1.06
4	1.10
5	1.15

$Z = t^n$, $K = \varepsilon_1/\varepsilon_o$

——— Proposed equation: $\varepsilon/\varepsilon_o = K^Z$

- - - - - - Power law : $\varepsilon/\varepsilon_o = 1+(K-1)\times Z$

—·—·— Logarithmic law : $\varepsilon/\varepsilon_o = K + \ln Z$

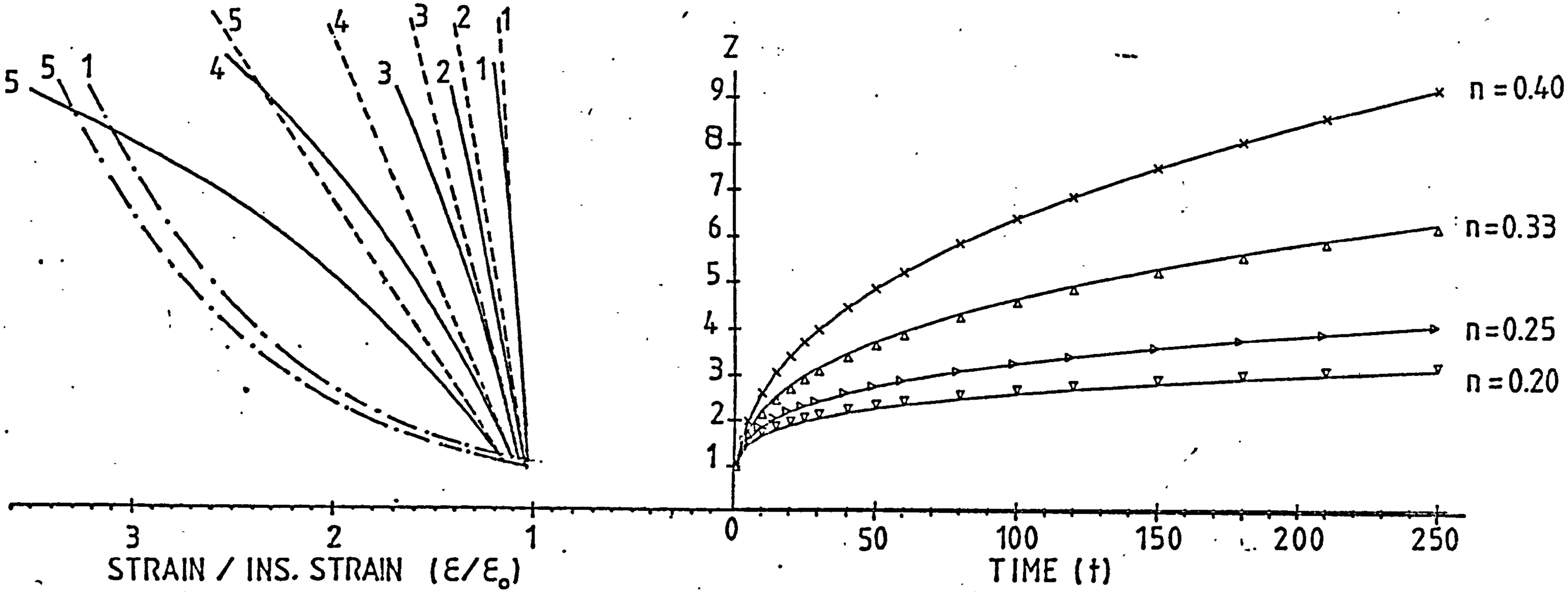

FIG 5.34 GRAPHICAL SOLUTION OF FORMULA 2.

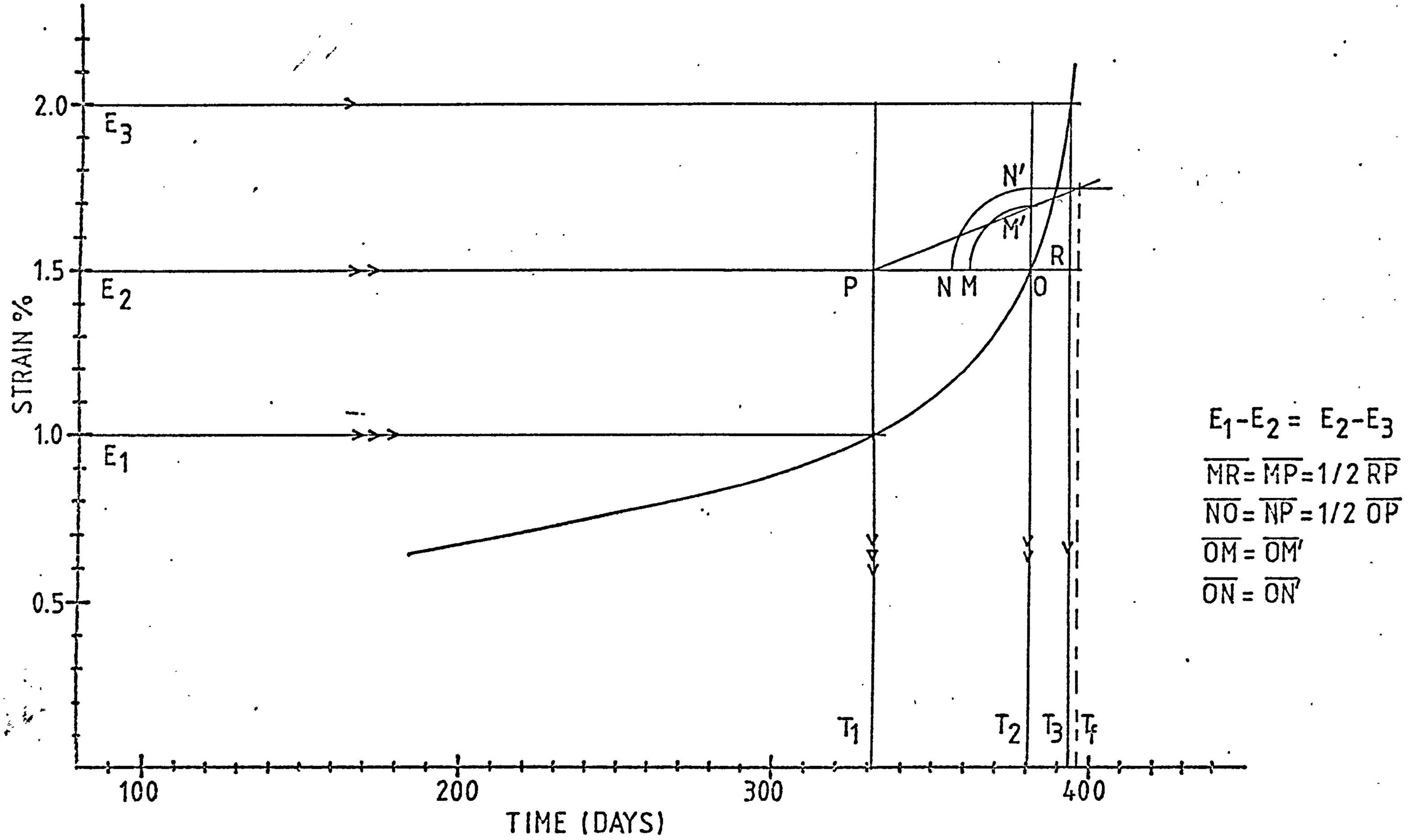

FIG 5.35

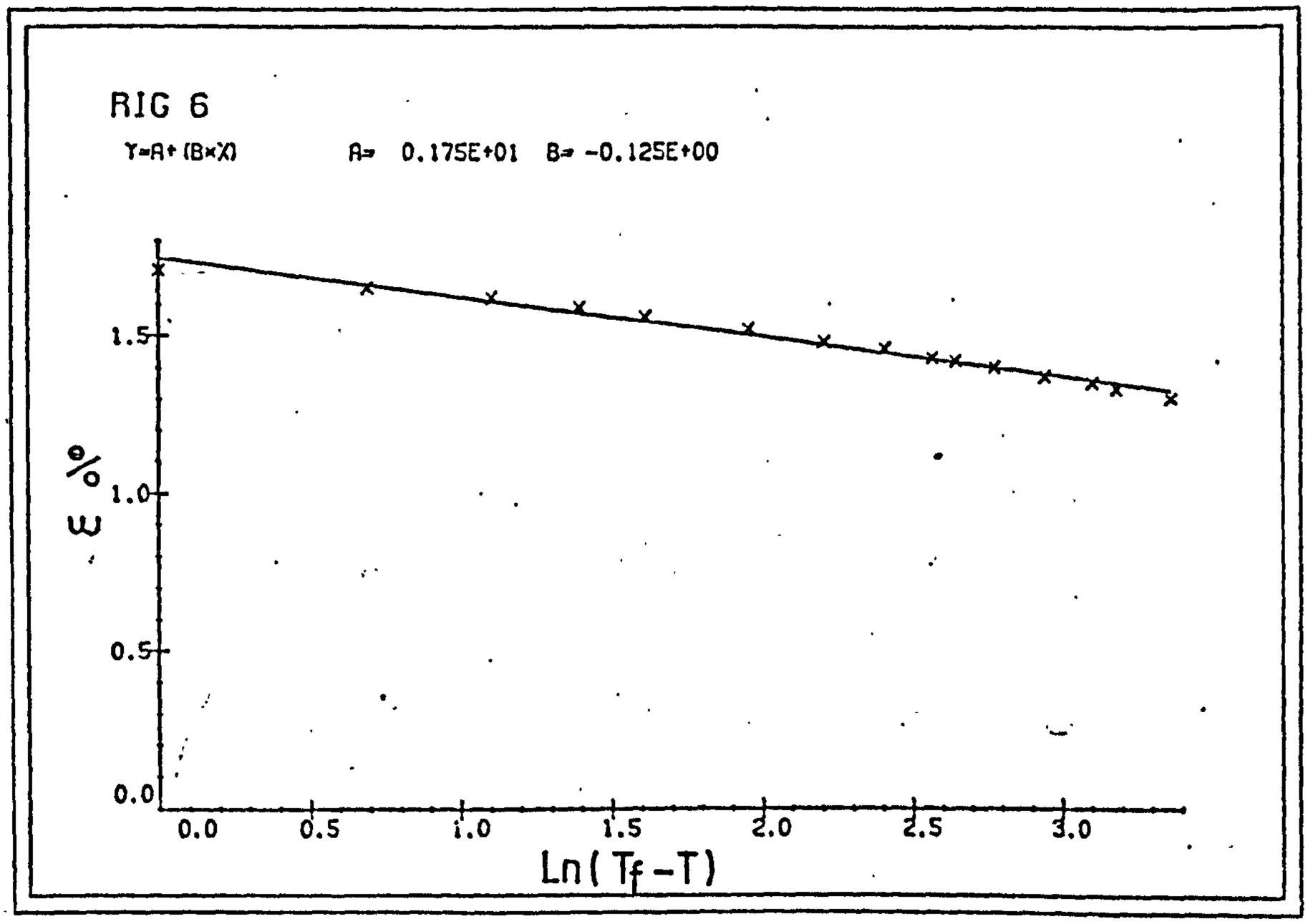

FIG 5.36

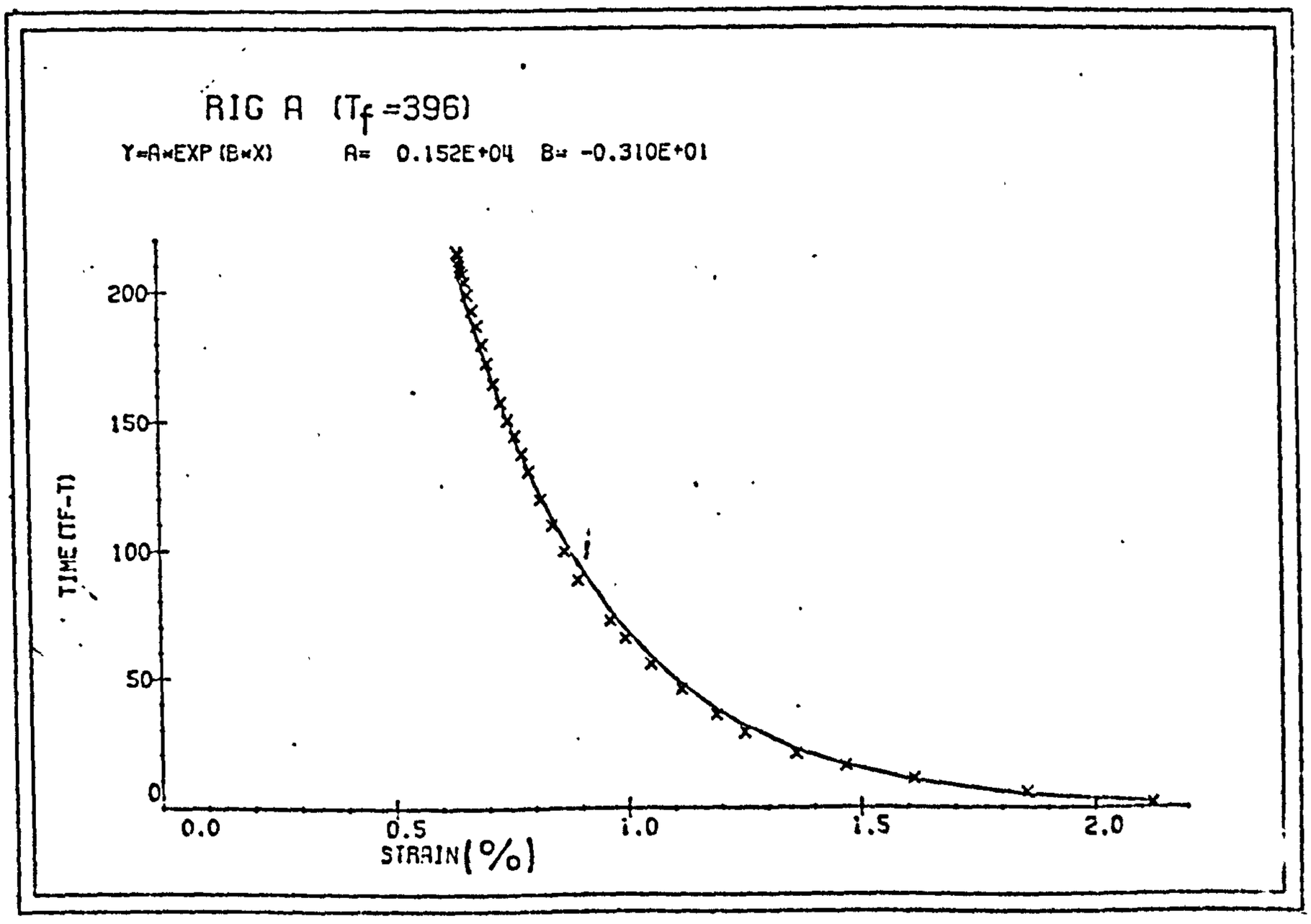

FIG 5.37

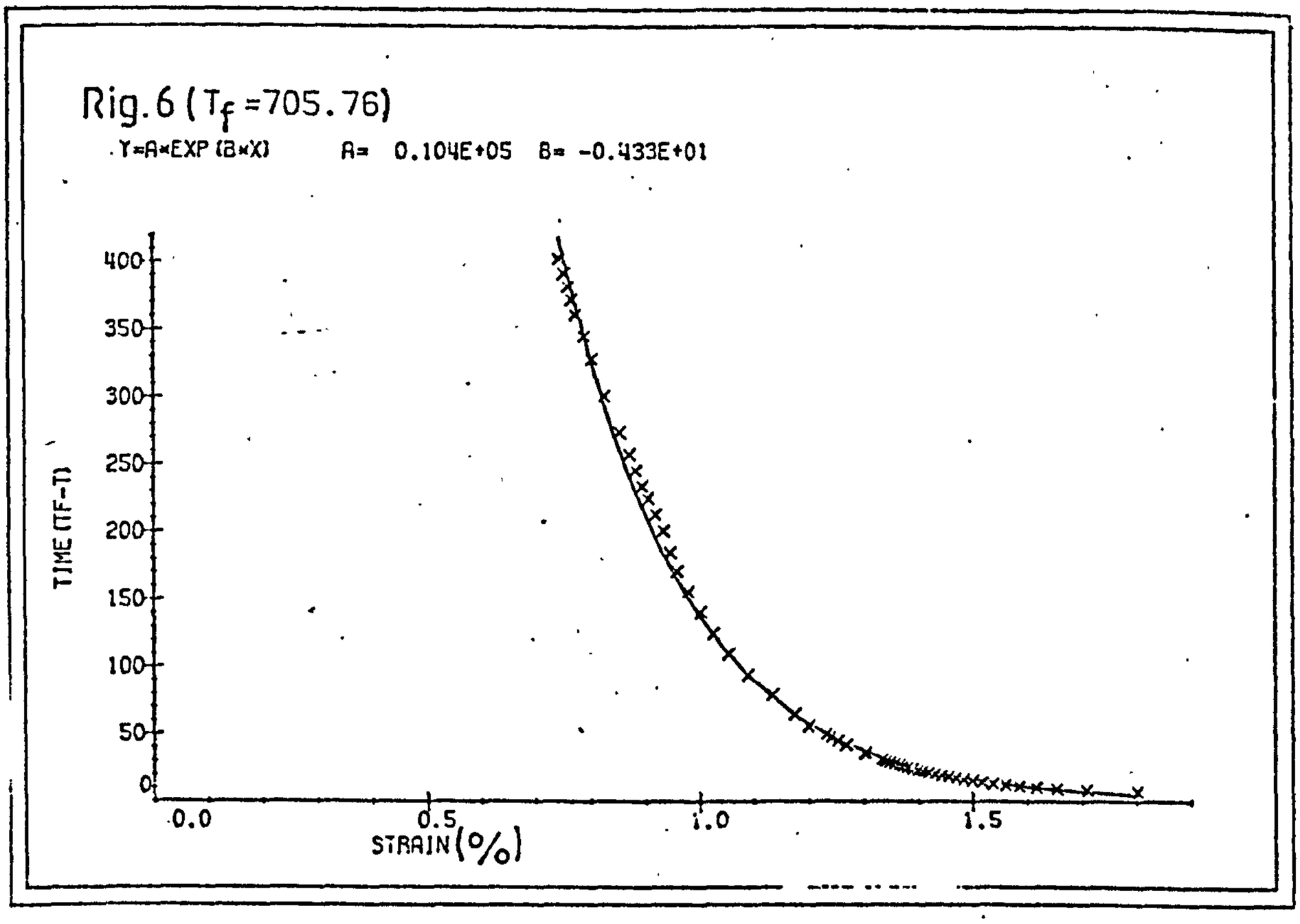
Rig.6 (T_f =705.76)
Y=A*EXP (B*X)
A= 0.104E+05 B= -0.433E+01
TIME (TF-T)
400
350
300
250
200
150
100
50
0
0.0
0.5
1.0
1.5
STRAIN (%)

FIG 5.38

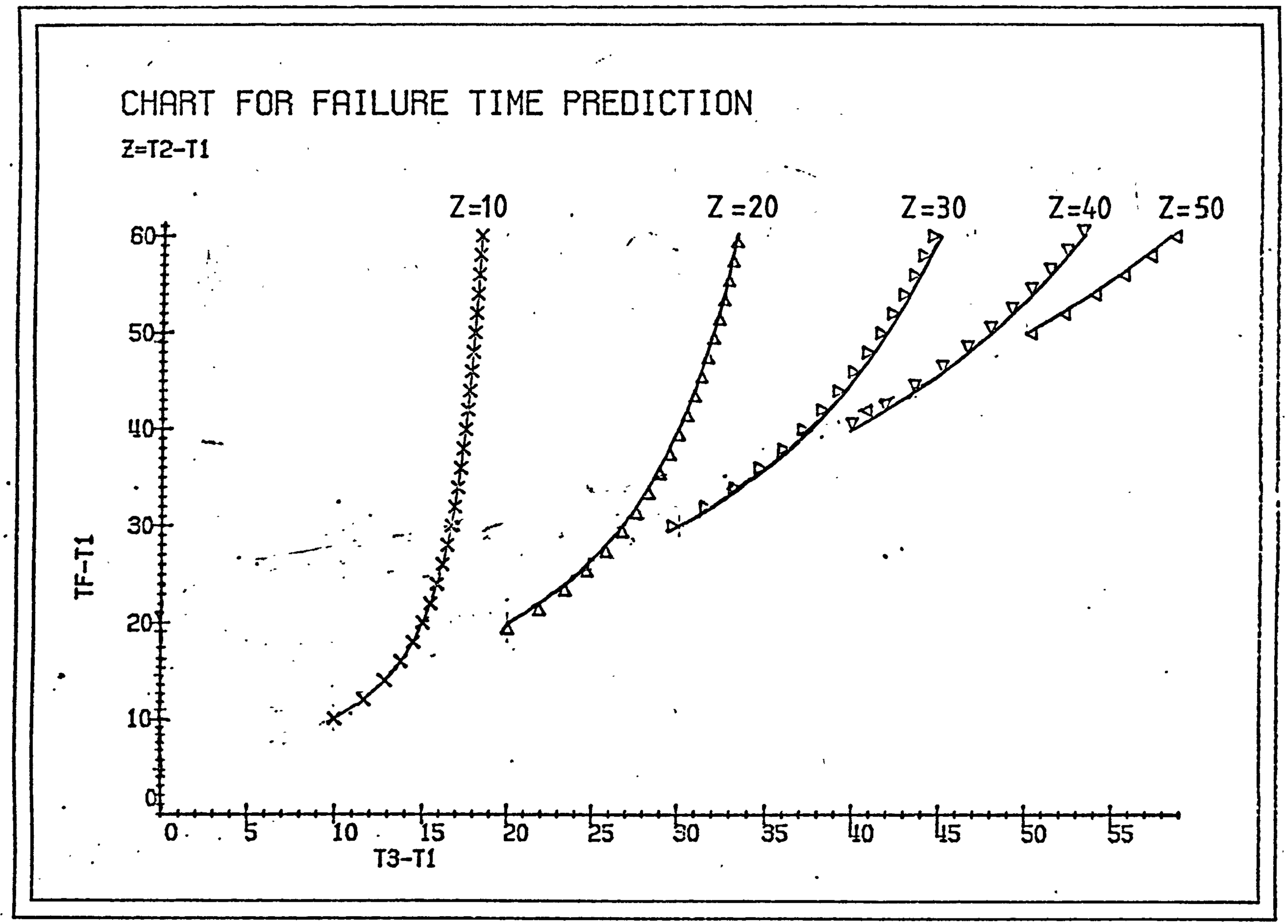
CHART FOR FAILURE TIME PREDICTION
Z=T2-T1
Z=10
Z=20
Z=30
Z=40
Z=50
TF-T1
T3-T1
0
10
20
30
40
50
60
0
5
10
15
20
25
30
35
40
45
50
55

Table 5.1 Some common creep laws

1.	$\varepsilon = At^m$
2.	$\varepsilon = A + Bt^m$
3.	$\varepsilon = A + Bt + Ct^n$
4.	$\varepsilon = A + Bt^m + Ct^n + Dt^p$
5.	$\varepsilon = At^m + Bt^n + Ct^p + Dt^q + \ldots\ldots$
6.	$\varepsilon = A \log t$
7.	$\varepsilon = A + B \log t$
8.	$\varepsilon = A \log (B + t)$
9.	$\varepsilon = A \log (B + Ct)$
10.	$\varepsilon = A + B \log (C + t)$
11.	$\varepsilon = A + B \log (t + Dt)$
12.	$\varepsilon = At/(1 + Bt)$
13.	$\varepsilon = A + B \text{ Sinh } (Ct^n)$
14.	$\varepsilon = A + Bt - C \text{ Exp } (-Dt)$
15.	$\varepsilon = At + B (1 - \text{Exp } (-Ct))$
16.	$\varepsilon = A(1 - \text{Exp } (-Bt)) + C (1-\text{Exp}(-Dt))$
17.	$\varepsilon = A + B \log t + Ct^n$
18.	$\varepsilon = A + Bt^n + Ct$
19.	$\varepsilon = A + B \log t + Ct$
20.	$\varepsilon = \log t + Bt^n + Ct$
21.	$\varepsilon = A \log (1 + (t/B))$
22.	$\varepsilon = A (1 - \text{Exp } (B - Ct^n))$
23.	$\varepsilon = A (1 - \text{Exp } (-Bt))$
24.	$\varepsilon = A \text{ Exp } (Bt)$.

TABLE 5.2

STRAIN-TIME CREEP RESULTS						
RIG NO	SPECIMEN TYPE	BEST FIT	CORR.COEFF.	A	B	PLOT NO
8	MARBLEAGIS	Y=A*(X^B)	0.9663770	0.3171776	0.0214196	5.2
A	MARBLEAGIS	Y=A+B*X	0.9585706	0.3656479	0.0014395	5.3
11	MARBLEAGIS	Y=A*(X^B)	0.9757652	0.2727000	0.0235548	5.4
6	MOUNTFIELD	Y=A+B*X	0.9692676	0.5157006	0.0007930	5.5
10	FAULD	Y=A*(X^B)	0.9381191	0.3883573	0.1154874	5.6
12	FAULD	Y=A*(X^B)	0.9573906	0.3383145	0.0823036	5.7
13	FAULD	Y=A+B*X	0.9626964	0.2888888	0.0007970	5.8

TABLE 5.3

LOG-LOG STRAIN-TIME CREEP RESULTS						
RIG NO	SPECIMEN TYPE	BEST FIT	CORR.COEFF.	A	B	PLOT NO
8	MARBLEAGIS	Y=A+B*X	0.9663766	-1.1482926	0.0493206	5.9
A	MARBLEAGIS	Y=A+B*X	0.9357070	-1.3338838	0.3413680	5.10
11	MARBLEAGIS	Y=A+B*X	0.9757682	-1.2993832	0.0542372	5.11
6	MOUNTFIELD	Y=A+B*X	0.8840610	-0.8867451	0.2034141	5.12
10	FAULD	Y=A+B*X	0.9381198	-0.9458326	0.2659211	5.13
12	FAULD	Y=A+B*X	0.9573898	-1.0837788	0.1895105	5.14
13	FAULD	Y=A+B*X	0.9254043	-1.5800373	0.3150648	5.15

TABLE 5.4

PRIMARY STAGE
PROCESSED DATA CREEP RESULTS

RIGNO	SPEC.TYPE	CORR.COEFF.	Eo	K	n	PLOT NO
8	MARBLEAGIS	0.9981147	0.3114	1.035837	0.2612324	5.22
A	MARBLEAGIS	0.9994201	0.2630	1.163584	0.3262470	5.23
11	MARBLEAGIS	0.9985784	0.2661	1.048488	0.2182198	5.24
6	MOUNTFIELD	0.9988191	0.4689	1.022073	0.5309576	5.25
10	FAULD	0.9861063	0.4480	1.069274	0.3483567	5.26
12	FAULD	0.9893609	0.3510	1.091632	0.2760348	5.27
13	FAULD	0.9988909	0.2242	1.095569	0.3792179	5.28

FORMULA 1: Ln(E)=Ln(Eo)+(T^n)*Ln(K)

TABLE 5.5
TERTIARY STAGE CREEP DATA ANALYSIS

SHORTENED DATA BEST FIT RESULT

RIG NO	SPEC.TYPE	BEST FIT	CORR.COEFF.	A	B	Tf	PLOT NO
A	MARBLEAGIS	Y=1/(A+B*X)	0.9703506	2.4057616	-0.0044514	540.5	5.16
6	MOUNTFIELD	Y=1/(A+B*X)	0.9583391	1.9523499	-0.0018087	1079.4	5.17

TABLE 5.6
SHORTENED AND PROCESSED DATA RESULTS

RIG NO	SPEC.TYPE	CORR.COEFF.	Tf	M	To	PLOT NO
A	MARBLEAGIS	0.9978516	396	0.3229730	-1121.326378	5.36
6	MOUNTFIELD	0.9955179	705.8	0.2307875	-9741.408408	5.37

FORMULA 2:

E=_(M)XLn[(Tf-To)/(Tf-T)]

6. EFFECT OF SATINSPAR BANDS ON THE PILLAR STABILITY

6.1 Introduction

The stability of pillars in Sherbern in Elmet has been the subject of research over the years ever since mining activities commenced in the area. It was conclusively demonstrated that the load bearing capacity of the pillars with originally stipulated dimensions was far in excess of the load imposed by overburden (Jones 1970; Mottahed 1974; Szeki 1978; and Watson 1979).

However, in certain districts, the deterioration of some pillars (conspicuous to the naked eye) required further study. Apparently, blocks of gypsum from the periphery of the pillars have been dislodged into the roadways, leaving freshly formed, almost vertical cracks exposed at the side of the pillars. It is possible to detect cracks having a width of that of a pencil in some places. It is noticeable also that these cracks are heavily concentrated around the pillar corners.

The most probable explanation for this gradual degradation of some pillars is the presence of soft, fibreous satinspar bands throughout the gypsum seam. Upon formation of the pillars, the soft satinspar bands are squeezed and extruded from the pillars. This radial expansion, in turn, creates radial and tangential tensile stresses which may be sufficient to overcome the tensile strength of the pillar forming material. Alternatively, or in addition, due to local variations

in the satinspar thickness, compaction of this soft material may result in differential axial deformation of the pillar and thus this may cause a shear failure along a vertical plane.

Although this phenomenon has been widely recognised by previous researchers, the views as to what extent the pillar stability is affected by the presence of satinspar bands in the pillar have remained controversial and very little has been done to quantify it.

In view of these, a laboratory experimental scheme has been undertaken in order to demonstrate the effect of satinspar bands on the deformational characteristics of gypsum specimens so that the actual pillar behaviour can be appreciated more precisely.

Satinspar bands or gypsum associated soft materials are most commonly seen in the northern part of the mine at Sherburn. The thickness of the material can vary, even in the same pillar, but in general, the cumulative thickness may vary from a couple of mms to one metre. A single, or as many as 6 bands may be present at different horizons in the pillar.

6.2 A short review of the research related to the pillar stability in Sherburn

Extensive laboratory tests on the mechanical properties of gypsum were first carried out by Jones (1968) and the gypsum was found to be isotropic and homogeneous with an average uniaxial compressive strength of 41 MPa and with a tensile strength (Brazilian disc) of 3.1 MPa. These findings have been confirmed largely by successive investigators.

It was reported by Jones that the gypsum strength was not particularly sensitive to specimen size but was dependent on the geometry of the specimens pronounced as an increase in the strength with decreasing height: width ratio. Using the theoretical approach of Tincelin and Sinou (1960), a pillar stress of 3.3 MPa at 38 metres below the surface with a 75% extraction ratio was calculated. Jones, referring to Stamphill and Birk's Head Mine stated that if the pillars contained only a small amount of weak material, the presence of this material would not reduce the absolute limiting compressive strength of the overall pillar, because of the lateral restraint and consequential triaxial loading caused by the presence of the stronger rock type. However, he was not able to produce any in-situ or laboratory evidence to substantiate this statement.

As mining proceeded, the homogeneity of the gypsum seam became suspect as the pillars appeared to be laminated, although with no definite partings. There were steeply inclined planes of discontinuity sometimes creating large blocks separated from the main body of pillars. Therefore, subsequent investigator, B. Jones (1970), initiated in-situ instrumentation schemes in order to confirm the previous work.

Pillar deformation has been measured using wire extensometer techniques developed by Potts (1963). The results of measurements over a period of years showed that most of the deformation took place in the outer one-metre zone of the pillar and the central section was in a confined state. The majority of the strain was due, apparently, to the opening and closing of cracks or discontinuities as mining advanced further. The stress measurements utilising a door-stopper plug device indicated a pillar stress of 2.56 MPa and 1.68 MPa in vertical and in horizontal directions respectively.

Mottahed (1974) using a levelling technique has confirmed the extremely low rate of pillar deformation and attributed most of the pillar skin deformation to the presence of thin bands of crystalline gypsum material, which showed considerably high strains when squeezed. This was shown qualitatively by using a piece of satinspar (3" x 3") which was loaded to 6 MPa in a testing machine. The rock underwent a reduction of about a third of its original thickness, but was still capable of accepting more load.

Watson (1979) found a major principal stress of 2.5 MPa and an intermediate stress of 1.3 MPa in the pillar, making use of the Talbot stressmeter.

Thus the pillar stability in Sherburn Mine was verified with great confidence and subsequent researches were directed towards the roof stability.

6.3 Mechanical properties of satinspar bands

To date, any information on the mechanical properties of satinspar from Sherburn Mine is most difficult to find in the literature. This is partly because of the difficulty in obtaining sufficient amounts of pure satinspar large enough to be cored and partly because of the difficulty in specimen preparation.

It was, therefore, thought worth determining some of the mechanical properties of the satinspar prior to investigating its effect on the deformational behaviour of gypsum. Limited amounts of material have been used for this purpose. Shear strength, uniaxial

compressive strength, tensile strength, Young's modulus and ultrasonic pulse velocity of satinspar have been determined. By using measured Young's modulus, its ultrasonic pulse velocity, and the unit weight of satinspar an estimate of Poisson's ratio was made.

6.3.1 Specimen preparation and equipment

The slabs of satinspar were removed from different parts of Sherburn Mine, mostly from the roof, where satinspar layers had already been exposed; hence it can be assumed that these satinspar slabs had not been squeezed excessively prior to testing. The average thickness of the slabs varied from 5mm to 25mm with undulated surfaces.

A Clipper rock cutting saw proved to be too robust for cutting the satinspar which tended to flake away. For this reason, a diamond impregnated cutting blade was used in the preparation of the specimens, which were cut to the required size, faced in a lathe turning at the slowest rate. To finish the faces of satinspar specimens, a fine emery paper was applied to the faces while the specimen was between the jaws of the rotating lathe.

For direct shear testing, it was not necessary to grind the faces of the specimens, as they were to be cast in a steel shearing box with plaster of paris. The testing equipment was originally designed for soil testing but, since a low strength was anticipated, it was considered to be appropriate for use in the present work. The equipment was described, briefly, in Section Two of this thesis.

Beam testing was adopted for tensile strength determination because of the relative ease in preparation of rectangular specimens. The equipment used can accommodate specimens having dimensions of 160mm x 160mm x 60mm and was tested in a 5-ton loading machine.

In the absence of a specimen of the required size in one piece (50mm x 50mm) or larger, it seemed justifiable to test three thick, square satinspar pieces placed on top of each other to make up the correct height. Einstein et al. (1969), studying the effect of joint configuration and spacing on fabricated gypsum models, noted that the strength of the jointed model at a given normal stress is highest for vertical joints and lower for horizontal joints and for each joint configuration, there is a systematic strength increase with increasing joint spacing. For convenience, horizontal jointing was adopted in satinspar testing. Testing was conducted on the 500-ton servo controlled stiff testing machine.

6.3.2 Test Results

Fourteen specimens were tested at a constant displacement rate of 0.845 mm/min, and at various normal stress levels, in an attempt to determine the angle of friction and the cohesion of satinspar. In the samples tested, crystals were almost parallel to the shearing plane and the directions of crystals on the shearing plane were approximately measured after the testing had been completed. The results of the shear tests and the relevant information are given in Table 6.1. As would be expected, the directions of crystals relative to loading direction influenced substantially the peak shear strength.

For an orientation of 90^{o}, the cohesion is 0.7 MPa and the coefficient of friction is 0.37. Even though the results are considered to be qualitative, the low values clearly suggest that the satinspar bands are the weakest zones in the pillar forming material and it should be taken into consideration, particularly if an inclined seam is envisaged to be extracted by mining.

The results of four-point beam bending tests of satinspar are presented in Table 6.2, together with relevant information. Three specimens were tested but the results for the third sample were ignored in the calculations because a malfunction of the equipment was detected after testing. The average tensile strength was calculated to be 0.96 $\pm$ 0.03 MPa which is almost one-third of the tensile strength of gypsum

Two satinspar specimens (nos. 1 and 2), tested with a servo controlled stiff testing machine, gave an average compressive strength of 10.9 $\pm$ 1.2 MPa and a tangent modulus at 50% of the peak strength of 0.68 $\pm$ 0.09 GPa. The full load-deformation curves of these specimens are shown in Figure 6.1. The uniaxial compressive strength and Young's modulus values appear to be slightly higher than those found by Lisk (1975) for specimens from Stamphill Mine. The difference can, however, be attributed to the variations in the loading rates and in the texture of specimens employed. The uniaxial peak strength of satinspar is approximately one-quarter of the value of gypsum, while the tangent modulus is approximately 24 times less than that of gypsum. (16.3 GPa).

Four specimens were tested for ultrasonic pulse velocity, using the Pundit equipment. Averaged value was 0.928 x 10^{3} m/sec.

The same specimens were used for determination of the average density, which was found to be 2182 Kg/m^3. An estimate of the Poisson's ratio was obtained; that is, 0.26, using appropriate values in the following equation:

$$V^2 = \frac{E(1-\nu)}{P(1+\nu)(1-2\nu)}$$

where: E = Young's modulus

P = Density

ν = Poisson's Ratio and

V = Ult. Pulse Velocity.

6.4 Servo-controlled testing of gypsum with and without satinspar inclusions

6.4.1 Objectives

The main objectives of the experimental programme elaborated in this section may be given as follows:

(a) To demonstrate the magnitude of reduction in the strength of gypsum due to satinspar.

(b) To observe the change in the mode of fracturing due to satinspar bands.

(c) To investigate the effect of satinspar thickness on the strength reduction.

(d) To examine the prefailure and postfailure characteristics of gypsum with and without satinspar bands.

(e) To relate the laboratory behaviour to in-situ observed pillar behaviour.

It is believed that information gathered from the experimental programme will be supplementary to the appreciation of the apparent pillar degradation in some areas of the mine at Sherburn.

6.4.2 Preliminary study

Various methods have been considered for the purpose of demonstrating the effect of satinspar bands on the pillar deterioration. Originally, casting the satinspar slabs into a concrete block and by coring from the block to obtain specimens seemed to be the least complicated and the most realistic way of simulating the natural occurrence of satinspar in gypsum. In this case, it would be possible to test the satinspar bands with undulations and ripples on the surface. A trial cast has proved the method practical and feasible. On this basis, a suitable concrete mixture which, at a certain age, would reach approximately the uniaxial compressive and tensile strength of the gypsum was sought. Using fine river sand and 100% high alumina cement, a mixture having a sand-cement ratio of 3 and water-cement ratio of 0.5 was found to give the target values at the age of 12 days under laboratory conditions. A large block of concrete with satinspar slab at mid-height was cast. However, during the coring process, despite many attempts, it was realised that it was not possible to obtain a sufficient number of proper cores from the block, mainly due to excessive chipping and flaking of the satinspar inclusions. Apparently, the bond between the satinspar and the concrete was also

insufficiently strong to withstand the torsional forces induced during coring. In fact, examination of the trial specimens after testing revealed that the satinspar had already fractured inside the concrete, thus providing a much stronger bond between the concrete and the satinspar. On this basis, it was decided to abandon this alternative.

The most common practice used in investigating the effect of soft layers such as shales, satinspar, clay seams on the pillar deformation is to model such a soft layer using an artificial material such as rubber, graphite, molybdenum disulphide, greased polyethene sheets or teflon sheets.(Lomenick and Bradshaw 1969; Meikle and Holland 1968; Starfield and McClain 1973; and King 1973). However, the use of another material instead of the actual material poses the question of to what extent it is modelling the actual behaviour, and whether its application to the factual case under investigation is applicable. Lomenick and Bradshaw (1969) report that the effect is exaggerated with the use of teflon sheets lubricated with grease and the actual behaviour of salt pillars with thin shale partings, at Lyons, Kansas, falls between the models with lubricated teflon and the models without simulated shale partings.

As early as 1958, Ahmed found 50% reduction in the cube strength of concrete when a thin rubber sheet was used as an insert between the platens of the loading machine and the end of the specimens.

Brady (1971a, b), investigating the effects of inserts on the elastic behaviour of cylindrical materials loaded between rough end-plates, emphasises the importance of the Poisson's ratio to Young's and Length to Diameter ratios of the insert material on the resulting induced stresses in the material.

Peng (1970) has shown that the uniaxial compressive strength of Chelmsford granite ranges from at least as high as 207 MPa to at least as low as 97 MPa, depending on the types of inserts used between the specimen ends and the loading machine platens.

On this basis, it was decided to cut and grind the surface of the satinspar and use it as insert material, interposed between the loading machine platens and the gypsum cores. By so doing, although local variations in thickness and the ripples, undulations of the surface would be overlooked, more realistic insights would be obtained than in the case of a simulated material.

6.4.3 Testing Programme

As indicated previously, satinspar partings may appear at the top and the bottom of the pillars, a single layer at mid-height, or a number of bands in the different heights of the pillar.

On the other hand, the range in which the size of the specimens can be conveniently varied was very narrow because of the difficulty in cutting and grinding the faces of satinspar of large dimensions. Thus the option of multiple layers was eliminated in the first stage.

From the remaining two, concepts, the first was considered more crucial than the second; when the satinspar bands are situated at the bottom and the top of the pillar, they serve as effective friction reducers which, consequently, allows deformation of the pillar more independently of the roof and the floor, i.e. the confining effect of roof and floor is not transmitted into the pillar, thus rendering the pillar potentially less stable than in the case of satinspar at mid-height.

The effect of end-restraintor confinement on the strength of rocks has been investigated by many researchers over the years, with an ultimate objective of transforming the laboratory testing results into in-situ cases (Meikle and Holland 1965; Holland and Olsen 1968; Babcock 1969; Lama 1969; and 1972; and Panek 1980).

Babcock (1969) reports that the resulting strength obtained from the end-constrained specimen with H/W ratio greater than 0.5 is significantly different from specimens tested without any end restraint. As the H/W ratio becomes smaller than 0.5, end constraint becomes more effective in uniaxial strength which is also in agreement with the St. Venant principle. He reports an increase of 58% for sandstone and 55% for marble with H/W ratios of 0.25 and 0.5 respectively when a constraining load of 30% of axial load is applied.

The above evidence infers that by testing gypsum specimens having scaled down dimensions of a typical pillar with and without thin satinspar bands separating the pillar from the roof and floor, it was thought the net effect of satinspar could be demonstrated. A number of cylindrical specimens having H/W ratio of 1 and a cross-sectional area of $4.4 \times 10^{-3} m^2$ and a number of specimens with square cross-sections having H/W ratios and 0.6 with a cross-sectional area of $2.5 \times 10^{-3} m^2$ together with essential number of satinspar end pieces varying in thickness from 3 to 17mm was considered to be sufficient for the purpose of demonstrating the effects of satinspar insertions.

6.4.4 Specimen Preparation

The soft and crumbly nature of satinspar made the cutting and grinding processes extremely difficult and resulted in wastage of substantial amounts of material. A small, diamond impregnated cutting blade was used to cut the satinspar to cylindrical and square shapes as required. The diameter of the pieces was left slightly larger than that of gypsum in order to avoid crumbling of the edges. The faces of the pieces were finished in a lathe to produce smooth and perfectly parallel faces. More than 60 in total were prepared in this way.

In the preparation of the gypsum specimens no problem was experienced using conventional rock cutting equipment. All the relevant dimensions are set out in Tables 6.3 and 6.4.

All specimens were kept in a temperature and humidity controlled room (13^{o}C and 63% R.H.) prior to testing to enable direct comparisons with the mine pillars from the temperature of the environment point of view.

6.4.5 Servo-controlled stiff testing and equipment

In the tests carried out with conventional hydraulic testing machines (soft machines) stored elastic energy during loading produces spontaneous energy discharges which crush the specimen as soon as the peak strength is reached. In such systems, it is difficult to study the post-failure characteristics of rocks. The advent of stiff machines or servo-controlled machines made it possible to obtain pre-

failure and post failure load deformation curves of rocks (Cook and Hojem 1966; Bieniawski 1967; Wawersik 1972; Rummel and Fairhurst 1970; Hudson et al. 1972a,b; Price 1979; and Wright and Ahmed 1968).

In order to fully appreciate the effect of satinspar bands, the use of a servo-controlled loading machine was indispensable. The equipment, a 500-ton capacity machine, is described in detail elsewhere (Price 1979) and consists of a servo-loop system based on a program signal supplied by a digital ramp generator responding to a feedback signal from an LVDT (Figure 6.2).

Testing the effect of strain rate on the elastic constants of tuff in the pre-failure region, Peng and Podnieks (1972) found that the stress-strain curves in cyclic testing for cycles from two to seven are essentially the same, except for slight differences due to the compaction of microcracks within the specimens. At lower strain rates there is more time for relaxation to take place and thus a lower ultimate strength is obtained. Moreover, the curves above the elastic limit, where relaxation behaviour starts, the slope of the stress-strain curves increases with increased applied strain rate. In the post-failure region, higher strain rates produce stress-strain curves with lower negative slope whereas slower strain rates result in higher negative slope and produce a stepwise drop in load as a result of stress relaxation. In this region, frictional behaviour of fractured specimen and shearing of asperities play an important role. (Peng 1973; Wawersik 1972; Rummel and Fairhurst 1970; and Bieniawski 1970). Therefore, the strain rate was maintained fairly constant during

the testing programme (1.5×10^{-5}/sec), although slight variations occurred during the testing due to operator error and due to changes in the satinspar thickness.

The finite response time of the servo-controlled machine may be too slow for some extremely brittle rocks and thus the control over the specimen deformation is temporarily lost. However, because of the low H/W ratios of the prepared specimens, this was not anticipated.

The axial deformation of, and the load on the, specimen during testing have been recorded graphically on an X-Y recorder, connected to a servo-controller. The set-up can be seen in Figure 6.2.

6.5 Discussion of the servo-controlled test results

A total of 30 gypsum specimens of varying size and shape, with and without using satinspar end pieces, were tested. The relevant data and calculated peak strength and strain are shown in Table 6.3.

Test results with respect to the test objectives will be briefly discussed in the following sections.

6.5.1 Comments on the load/deformation curves

The load-deformation curves of specimens tested with steel end platens and with satinspar end pieces were traced in appropriate pairs on the same paper so that they could be evaluated more easily. The load was converted to engineering stress, whereas deformation was not scaled to engineering strain because of the changes in the satinspar thickness (Figures 6.3 to 6.17).

The outstanding features of interest are:

(1) There is a clear reduction in the peak strength of gypsum when tested with satinspar but the magnitude of reduction is variable depending on the size of the specimen and the relative thickness of the satinspar bands.

(2) In general, specimens tested with satinspar exhibited a reduced slope in the pre-failure curve, thus larger deformations were exhibited at a given load.

(3) The specimens without satinspar behaved in a linear-elastic manner in the pre-failure region. In all instances, the peak of the curve is acute, which indicates a brittle behaviour. On the other hand, in the majority of cases with satinspar, the curve before the failure point showed three or four intermediate peak points where the load-bearing capacity of the specimen was temporarily lost, but very rapidly recovered with increasing load. This behavioural change is one of the most marked effects of the presence of satinspar bands and is attributed to pre-failure fracturing of the specimen. Further elaborations on this issue will be made in the following section. Considering the shape of curves around the peak-region, it is not so acute as that obtained without satinspar inclusions, and has a rather rounded nature, indicating that the specimen is behaving in a semi-brittle/ductile manner.

(4) Examination of post-failure sections of all curves reveals an apparent slip-stick behaviour which is not as

pronounced in the post-failure behaviour of pure satinspar (Figure 6.1). The load on the broken specimen increases until a sudden slip occurs between the surfaces, which subsequently lock together again.

Stick-slip behaviour is related to mineralogy, porosity, water pressure, and temperature. In general, low effective pressurc, high porosity, weak minerals, high temperature and high partial pressure of water favour stability and stable sliding instead of stick and slip (Brace 1972). It is reported also that the strain rate has little or no effect on stick-slip (Byerlee and Brace 1968; and Coulson 1970).

It is, then, reasonable, to assume that by inserting satinspar bands (which is softer than gypsum) between the specimen ends and the platens, the amplitude of slip-stick should reduce. In fact, as can be seen in Figures 6.15, 6.16, and 6.17, this is found to be so.

It is of great importance to note that specimens no. 3 and 4 (Figure 6.3), have exceeded the peak load, hence the residual strength has started to increase with axial deformation. This is ascribed to the specimens having low H/W ratios (0.6 and 0.74). The implication of this in terms of actual pillars is straight forward; if the pillars are designed with the lowest possible H/W ratio, even if the pillar strength is exceeded, after a certain amount of deformation, they can bear indefinitely high loads. Comparison of Figures 6.3 and 6.4 will substantiate the effect of H/W ratios of specimens on the peak strengths and residual strengths.

Inspection of the post-failure section of the curves of the specimens tested with steel end platens and of the specimens tested

with satinspar end pieces shows that the drop in load-bearing capacity of specimens with satinspar is not so pronounced as in the specimens tested with steel platens. Hence specimen behaviour is slightly changed from strain softening to semi-strain hardening (Specimens 16, 17 and 18; Figures 6.8, 6.9 and 6.10), i.e. from brittle to semi-ductile behaviour. This suggests that with the presence of satinspar bands in the pillars, the pillars are less prone to a sudden and violent rupture than those pillars with the absence of satinspar bands.

It is known that for brittle-ductile transition, a high confining pressure, high temperature, presence of solutions, is usually required for rocks (Heard 1960; Bieniawski 1967; Rutter 1972; and Farmer 1980). From the results of tests conducted, it would appear also that, as the proportion of soft, ductile materials increase in the rock mass, the rock system gradually loses its brittleness.

6.5.2 Mechanism and mode of Specimen fracture

It is neither possible nor necessary to examine the failure theories and mechanisms of rock fracture in detail in this context. Therefore, the change in mode of fracture will be reasoned comparatively briefly and reference will be made to Section Eight of this thesis, where relevant finite element analysis is elaborated.

The gypsum specimens tested between the matching steel platens failed generally leaving two possible shear cones with either a number of accompanying fragments or two wedge-shaped fragments (Figure 6.18). Specimen 7 failed, sliding along two inclined pre-weakness zones, as illustrated in Figure 6.18. It is logical to assume that the post-failure characteristics of these specimens are, to a large extent,

governed by the frictional properties of rock and the size and shape of the two opposite cones, as they slide on each other. As the H/W ratio is lowered, the contact area on which the two cones slide is proportionally increased (because of the cones becoming flatter) thus, with the help of confinement supplied by the surrounding material, the load-bearing capacity increases after the initial compaction period.

Specimens tested with satinspar end pieces exhibited distinct features of tensile splitting. Longitudinal columns surrounded a broken, but highly compacted, inner core (Figures 6.19 and 6.20). With the square-shaped specimens, the columns in the corners are comparatively larger than other sides. In fact, as can be seen in Figure 6.21 (which depicts the fracturing process of specimen no. 23 at different stages) the first crack appeared around the corner of specimen 1, and then the cracking spread to other regions. The stages of fracturing are also marked on Figure 6.22 which depicts general behaviour of rock loaded with a constant strain rate.

Examination of the satinspar end pieces after testing revealed that they were crushed only from the corners and the regions near to the centre of the pieces remained intact and without distortion. This is shown in Figure 6.23 which shows slip-lines or shear-lines in a flat material loaded between rough end plates. In the shaded area, the yield stress is not exceeded so that they remain intact, whereas, in the remaining regions, material is extruded (Nadai 1950; Bishop 1957; Jeager and Cook 1979; and Johnson and Miller 1975).

The mechanism involved in this type of failure is not something new, but has been experimentally and theoretically investigated by a number of persons over the years (Lomenic and Bradshaw 1969; Meikle and Holland 1968; Ahmed 1958; Brady 1969; Peng 1970; Babcock 1969; Al-Chalabi and Huang 1974; and King 1973). It will be sufficient, therefore, to say here that when a soft, flat material is present between the specimen ends and the loading machine platens, radial and tangential tensile stresses, the magnitude of which is dependent upon Poisson's ratio and Young's modulus and Thickness / Diameter values of the specimen and inserted material are induced on the specimen. When the induced stresses exceed the material strength, failure takes place. The nature and the distribution of the stresses induced will be further discussed in Section Eight with respect to mine pillars.

One of the more significant observations made during testing was that literally all of the specimens fractured substantially into long columns well before peak strength was attained. This visible, pre-failure fracturing was reflected by the load-displacement curves as intermediate peak points before the ultimate peak load point was reached. Despite this, the specimens continued to take up more load which was shared by the individual columns and blocks of gypsum. It is most likely that this is the very reason why the post-failure strength of the specimens tested with satinspar end pieces was greater than that of the specimens without satinspar end pieces. The implications of this are that the pillars may be adversely fractured in the periphery by the satinspar bands, but this does not necessarily indicate that the pillars are excessively loaded or they are on the verge of an imminent rupture.

6.5.3 The effect of satinspar thickness

It is experimentally and theoretically shown that, when a friction reducer (i.e. rubber, cardboard sheet, etc.) is interposed between the test specimen and loading end plates to eliminate end effects, the magnitude of radial and tangential tensional stresses set up in the specimen increases as the thickness of the insert is increased and the rate of increase depends initially on the relative Poisson's ratio/Young's modulus of the specimen and the insert.

Similarly, if the thickness/width values of the lubricant are sufficiently low, the effect may disappear. Brady (1969) quoted a thickness/width value of 0.01 for a low modulus insert ($E = 4 \times 10^{-3}$ psi, 27.59 MPa and $\nu = 0.45$), for which he observed that the end effect had vanished. However, this conclusion was reached for specimens having a height/width ratio of 2; thus for those having lower height/width ratios than 2 the end effect can be expected to be much higher.

The evidence on the effect of satinspar thickness on the peak strength of gypsum of various height/width ratios and sizes is already given in Table 6.4. With few exceptions (Specimens 11, 16 and 27), it can be said that, as the satinspar thickness increased, the peak strength value of the gypsum specimens decreased. This is further substantiated in Figure 6.24, where the peak strength values are plotted against the ratio of gypsum thickness to satinspar thickness. The wide scatter of data points may be related to the fact that no attempt was made to eliminate the gypsum specimens which had apparent weakness zones from the testing programme, as well as to the fact that slight variations in strain rate was inevitable, due to different thicknesses of the satinspar pieces. The least square regression analysis of data

using PADAS, which has been described in Section Five at some length, yielded an hyperbolic function of the following form:

$$\text{Peak Strength (MPa)} = 22 - 7.49 \times \left(\frac{\text{Satinspar : Thickness}}{\text{Gypsum Thickness}}\right)$$

Thus this equation sets the upper limit of strength as being 22 MPa when the thickness of satinspar attains small values compared to that of gypsum thickness. Probably a better appreciation can be made, when the results of testing with satinspar end pieces (Table 6.4) are compared with the results of tests with steel end platens (Table 6.3). Two important points emerge; firstly, for the gypsum specimens with square cross-section as the height to width ratio of gypsum decreases the strength reduction due to satinspar end pieces becomes more pronounced and, secondly, it appears that, for the same height to width ratio (1:1), the cylindrical specimens having a cross-sectional area of $4.4 \times 10^{-3} m^2$ are more susceptible to change in loading platen than the cubic ones with a cross-section of $2.5 \times 10^{-3} m^2$. For the latter, the most likely explanation can be the probability of containing weak zones being higher in a large size than in a small size which, in turn, renders the specimen less resistant to tensional forces induced by satinspar.

Another interesting observation comes from the inspection of post-failure sections of the curves in Figures 6.8, 6.12, 6.16 and 6.17. It is apparent that, in the majority of cases, the residual strength of specimens with high T/W ratios is greater than that of specimens with comparatively lower T/W values, in contrast to the peak strength values. This can be accounted for largely by a decrease in the brittleness of the specimen upon an increase in the satinspar thickness. The

presence of a virtually undisturbed inner core of satinspar end pieces of reasonable thickness after testing (as depicted diagrammatically in Figure 6.23 as a shaded area) is likely to bear the responsibility to a great extent. Since this section is in a highly confined state during post-failure loading, further deformation is allowed without losing much load resisting ability, thus this is reflected accordingly in the load deformation curve of the specimen.

6.6 Applicability of testing results to in-situ pillar behaviour

It would seem that, in spite of numerous theoretical and applied approaches made over the years by many individuals, a sound method for prediction of actual failure strength from tests of small size samples of the pillar material in the laboratory is beyond reach (Denkhaus 1965; Bieniawski 1968; Lama 1969, 1970, 1972; Salomon 1969; Panek 1980; and Mottahed and Szeki 1982). Apart from many other factors, it emerges that the size effect and the end conditions are of particular importance. Especially in the presence of horizontal tensile stresses, vertical jointing and weakness planes, tensile strength, which in most cases, is negligible in horizontal direction, play a predominant role in the overall strength of rock mass.

It must also be recognised that in the underground environment rock will be subjected neither to constant displacement nor to a constant load because of continuing ore extraction, but to a condition dictated by the unloading characteristics of the surrounding rock.

In summary, it would be entirely incorrect to consider the results of laboratory testing of gypsum with satinspar bands as quantitatively correct in respect of in-situ pillar strength. However,

by fulfilling the objectives set out at the beginning of the experimental programme, it is believed that much valuable information regarding pillar deformation can be obtained. With little circumspection the in-situ behaviour of pillars can be qualitatively correlated to the observed behaviour of small size gypsum specimens tested with satinspar end pieces in the laboratory. The following section, therefore, deals with the examination of the validity of laboratory tests.

6.7 Implications of test results on the pillar deformation

The resemblance between mode of fracture of the specimens tested with satinspar and the mode of actual pillar fracturing observed in the mine suggests that the mechanism of pillar deterioration is largely controlled by the presence of ubiquitous satinspar bands.

The mechanism of pillar disintegration is essentially similar to that of a laboratory specimen being loaded between two soft inserts but further complicated by local variations in the satinspar thickness within the pillar, by the presence of undulations and by the relative position and spacing along the pillar section.

Local variations in the thickness of satinspar partings is likely to have an adverse influence on the fragmentation process. Due to differential deformation under a constant load, vertical shearing associated with horizontal tensile splitting can lead to separation of large blocks of gypsum from underground pillars.

As the spacing of satinspar bands, relative to their thickness, increases the effect is accordingly reduced because of a decrease in the tensional stresses acting horizontally.

The presence of satinspar bands at the top and at the bottom of a pillar may seem to be critical on first consideration based on the idea that the confining effect of the roof and floor is not transmitted to the pillar. However, it is more likely that upon the creation of a pillar, either a slight punching of the pillar into the roof and floor and a deflection of the roof beam and the floor beam towards the opening, or a combination of the two, may take place. Hence the pillar becomes rather barrel-shaped. Because of this action, satinspar bands are effectively prevented from expanding. Whereas, if the satinspar bands are located at a distance, say 10 to 50cm from the roof and floor, the expansion of satinspar bands can occur more freely and the situation becomes more crucial.

Probably one of the most significant findings of the testing was that almost all of the specimens tested with satinspar bands had fractured well before the peak strength value was reached. This was evident on the load deformation curves appearing as intermediate peaks along the pre-failure section of the curves. Visual inspection of the specimens during testing also confirmed this phenomenon. Hence observations strongly suggest that the separation of large blocks of gypsum from the main body of the pillar does not necessarily indicate that the pillar is loaded to its limiting load bearing capacity or in excess of it. In fact, as long as blocks remain in contact with the surrounding rock mass they will continue to contribute in sharing the overall load bearing capacity of the pillar effectively.

It would also appear that the pillars with square cross-sections are affected more by the presence of satinspar bands than pillars having

circular cross-sections and having the same cross-sectional area. This can be related to the fact that high stress concentrations occur around the corners. The fracturing of specimens of square cross-section begins at the corners of the specimens which may be considered similar to the fracturing of pillar corners in-situ.

The presence of satinspar bands causes a change in the deformational behaviour of pillars from a brittle manner to a semi-ductile manner. The change becomes more marked as the proportion of satinspar bands relative to the amount of gypsum increases. The implication of this is that even if the pillar strength is exceeded a sudden and violent failure is most unlikely to occur.

Large variations in the abundance of satinspar bands in the pillars can cause differential lowering of the roof and this can adversely affect the roof structure.

In conclusion, the average ratio of gypsum thickness to the total thickness of satinspar bands in a typical pillar taken as being 25 and using the equation given in Section 6.5.3, a peak strength of 21.7 MPa is obtained. This value is still much greater than the value of stress imposed on the pillars.

* * *

FIG 6.1

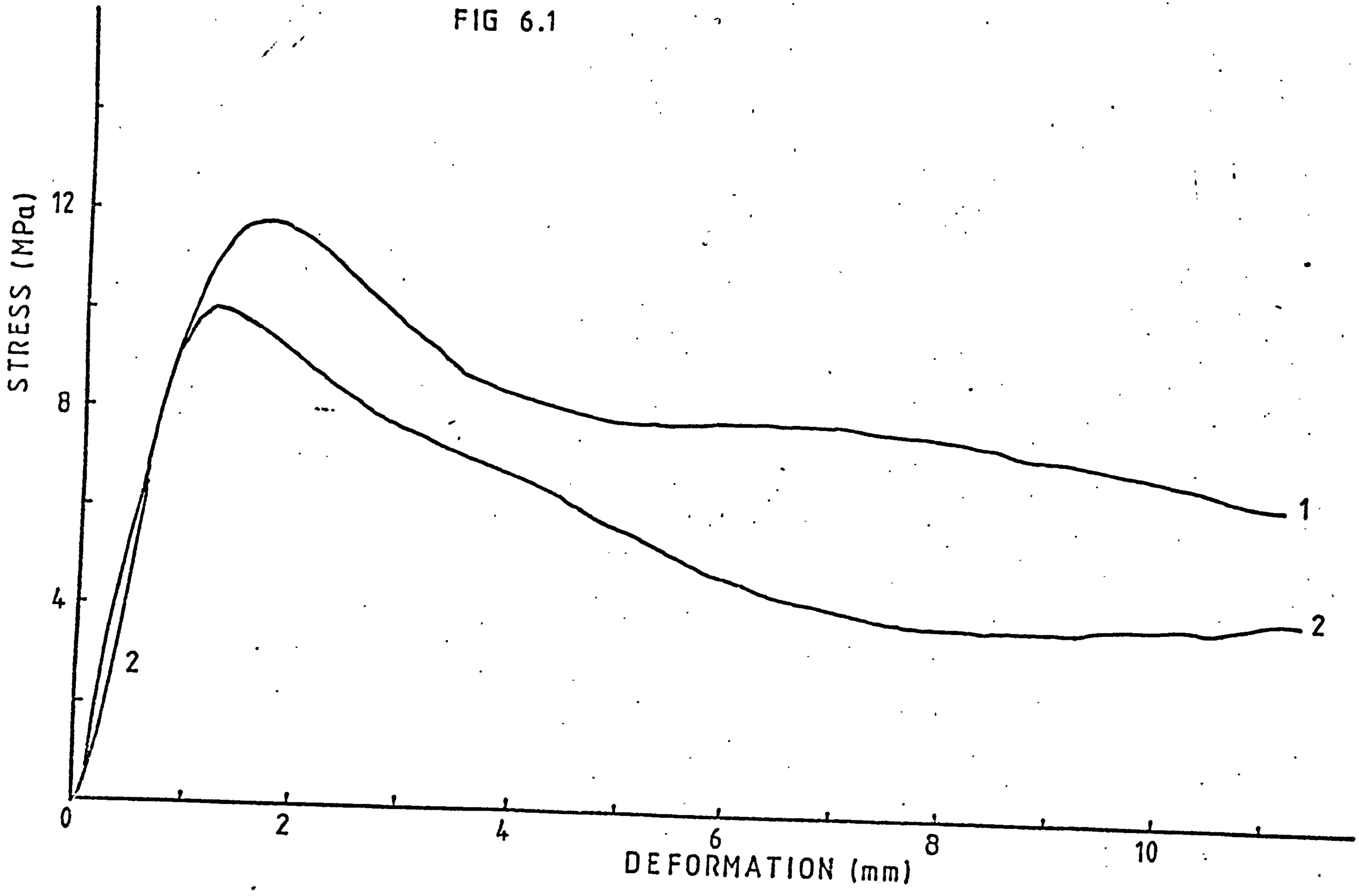

FIG 6.2 Servo-controlled testing machine

FIG 6.3

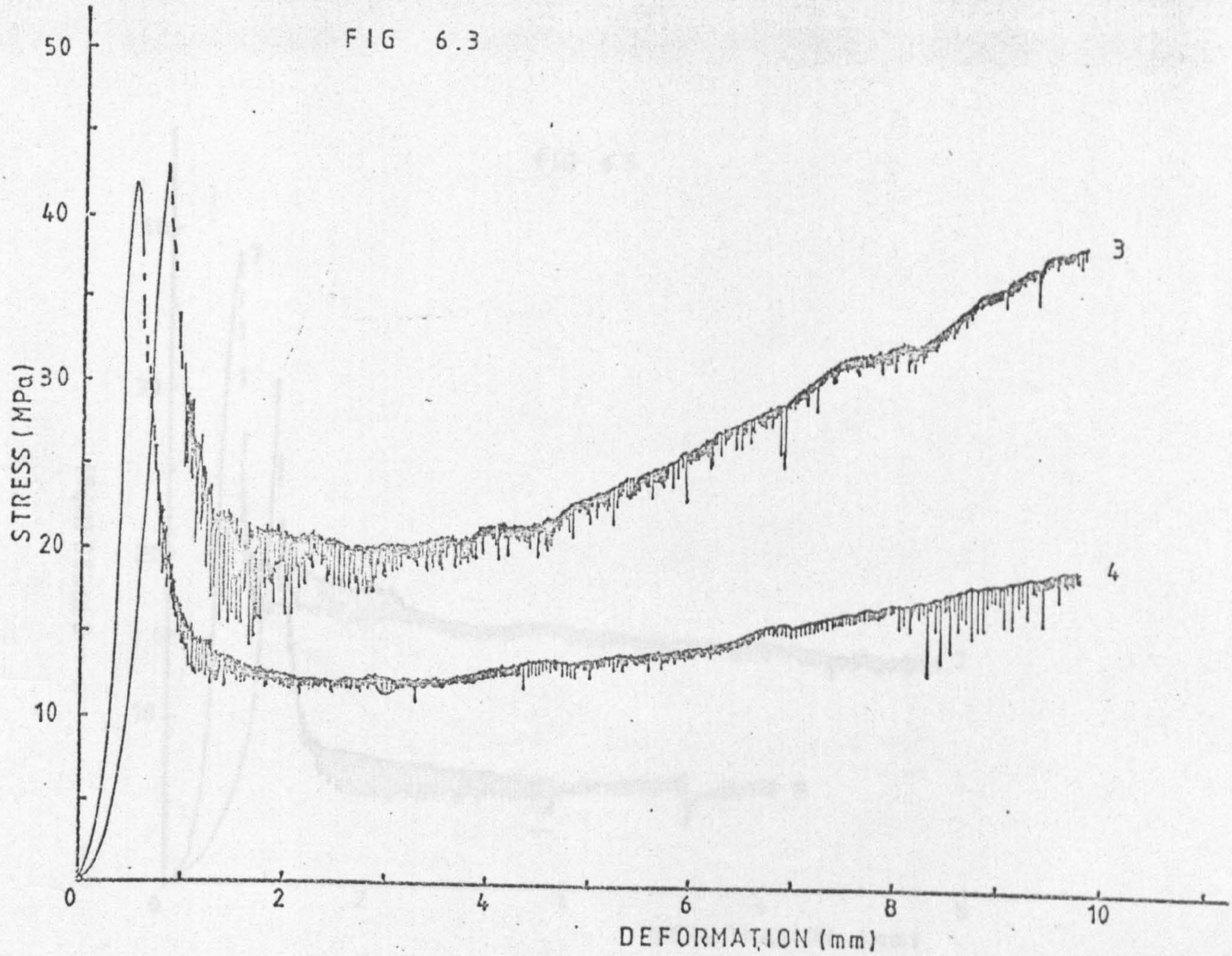
50
40
30
20
10
STRESS (MPa)
0
2
4
6
8
10
DEFORMATION (mm)
3
4

FIG 6.4

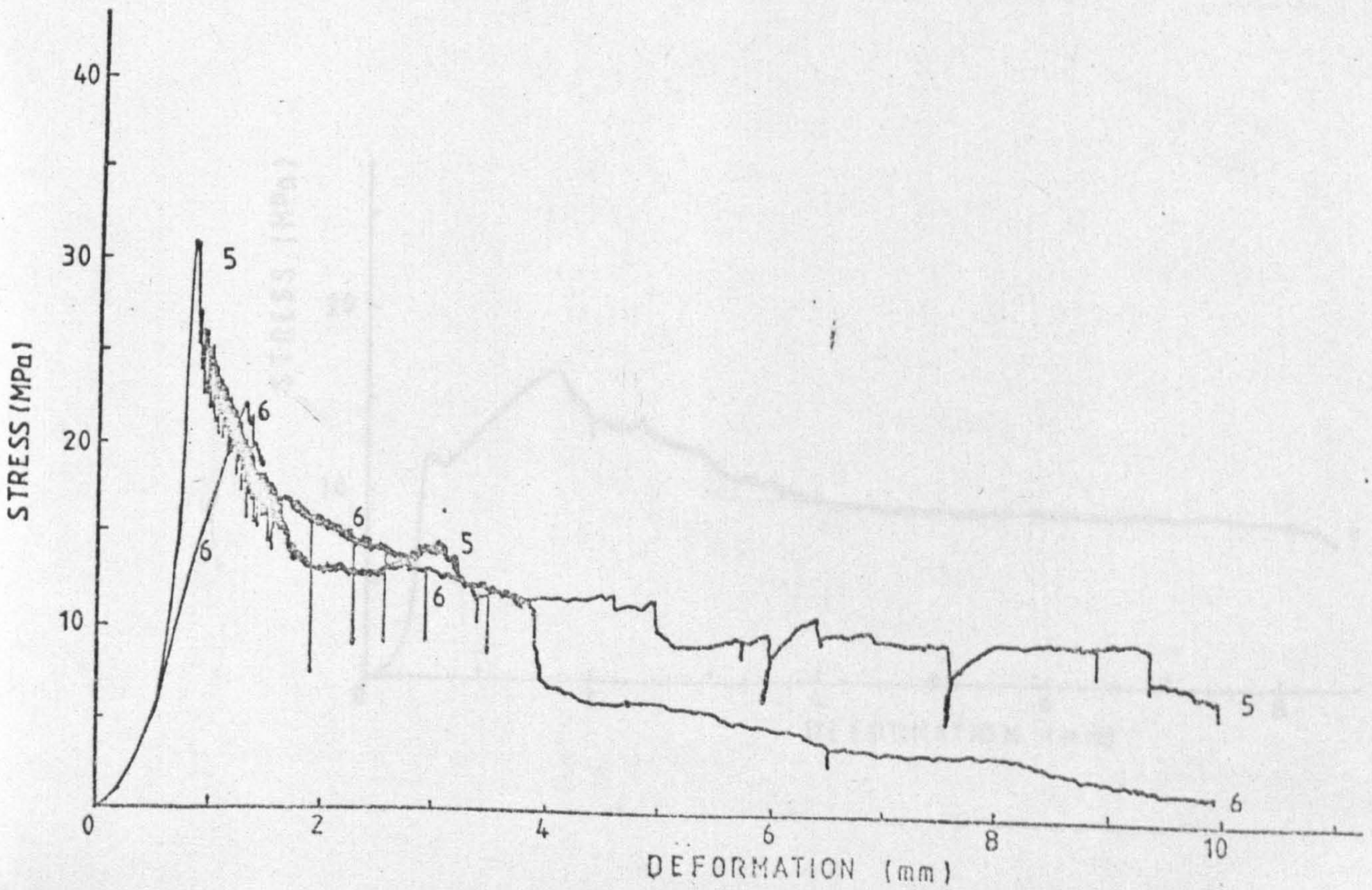
40
30
20
10
STRESS (MPa)
0
2
4
6
8
10
DEFORMATION (mm)
5
6

FIG 6.5

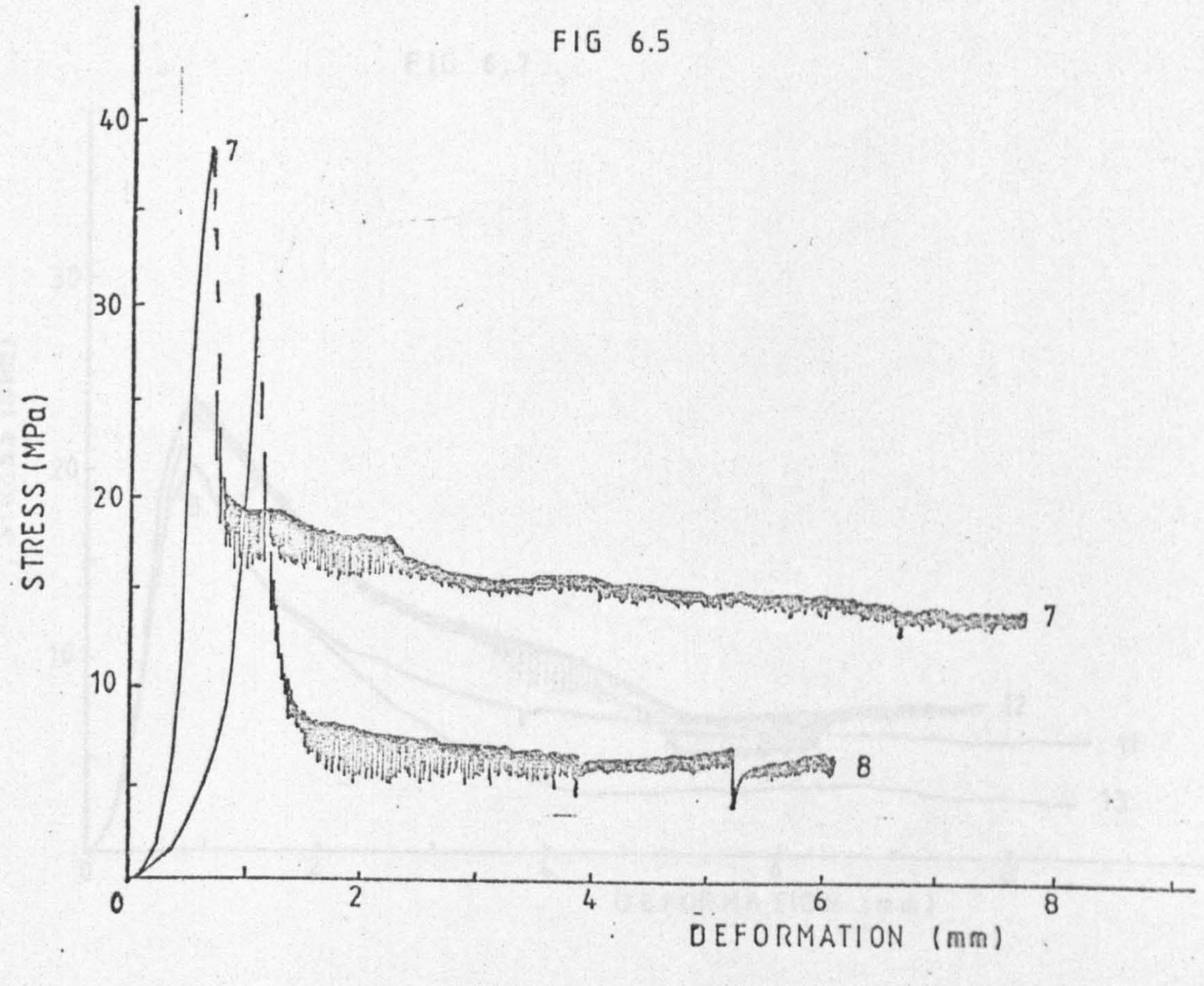
STRESS (MPa)
40
30
20
10
0
2
4
6
8
DEFORMATION (mm)
7
8

FIG 6.6

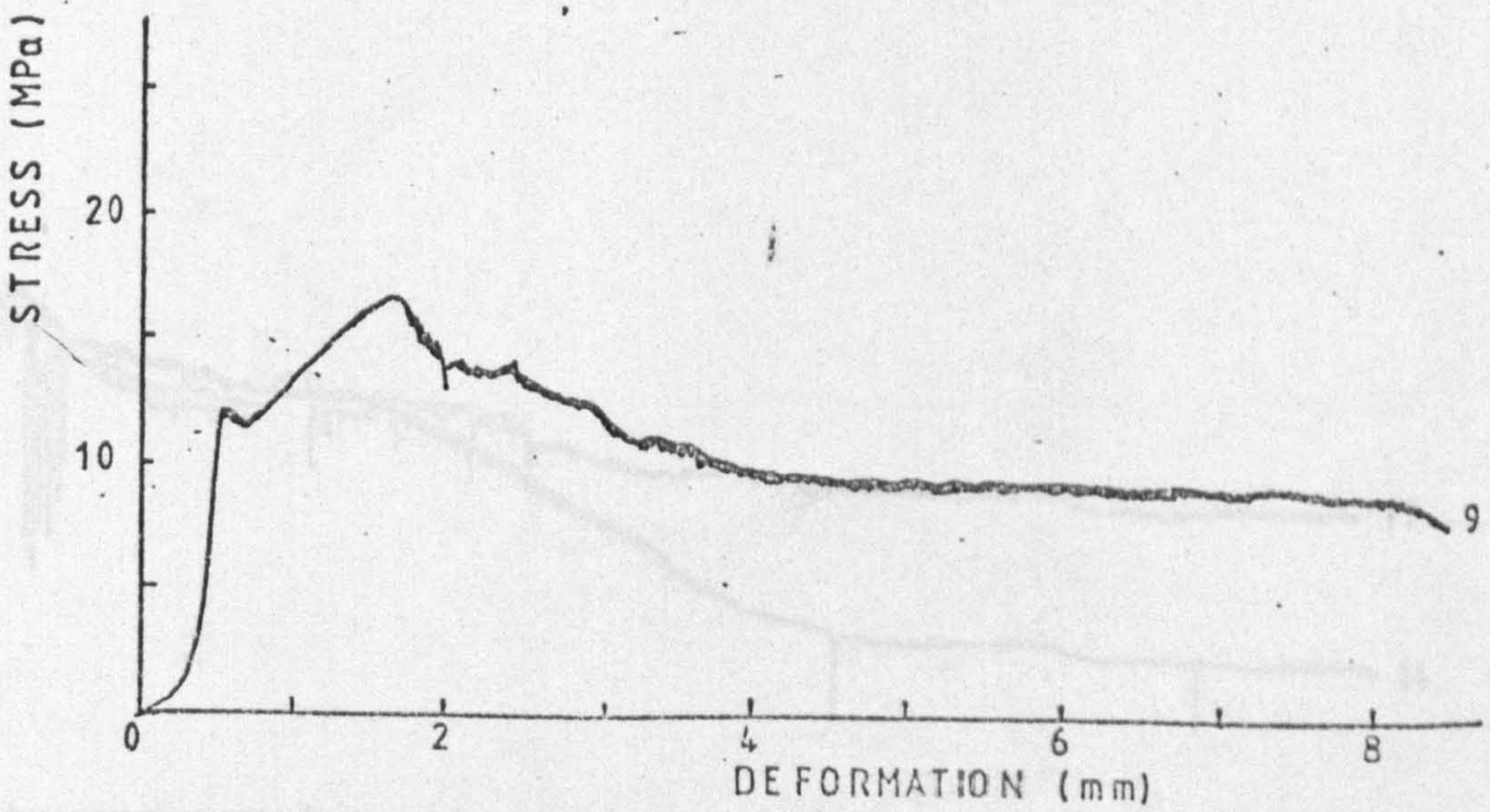
STRESS (MPa)
20
10
0
2
4
6
8
DEFORMATION (mm)
9

FIG 6.7

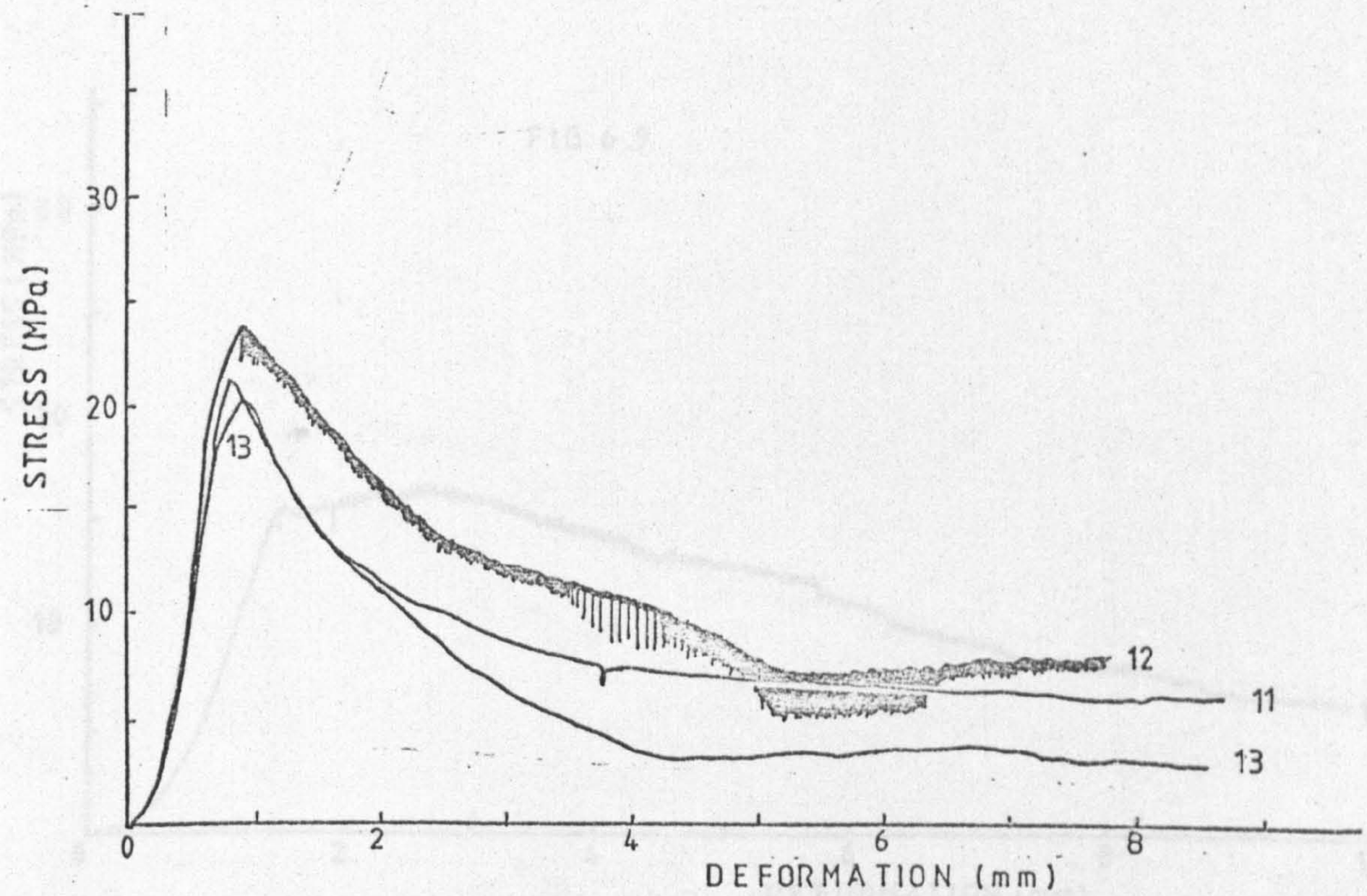
STRESS (MPa)
30
20
10
0
2
4
6
8
DEFORMATION (mm)
13
12
11
13

FIG 6.8

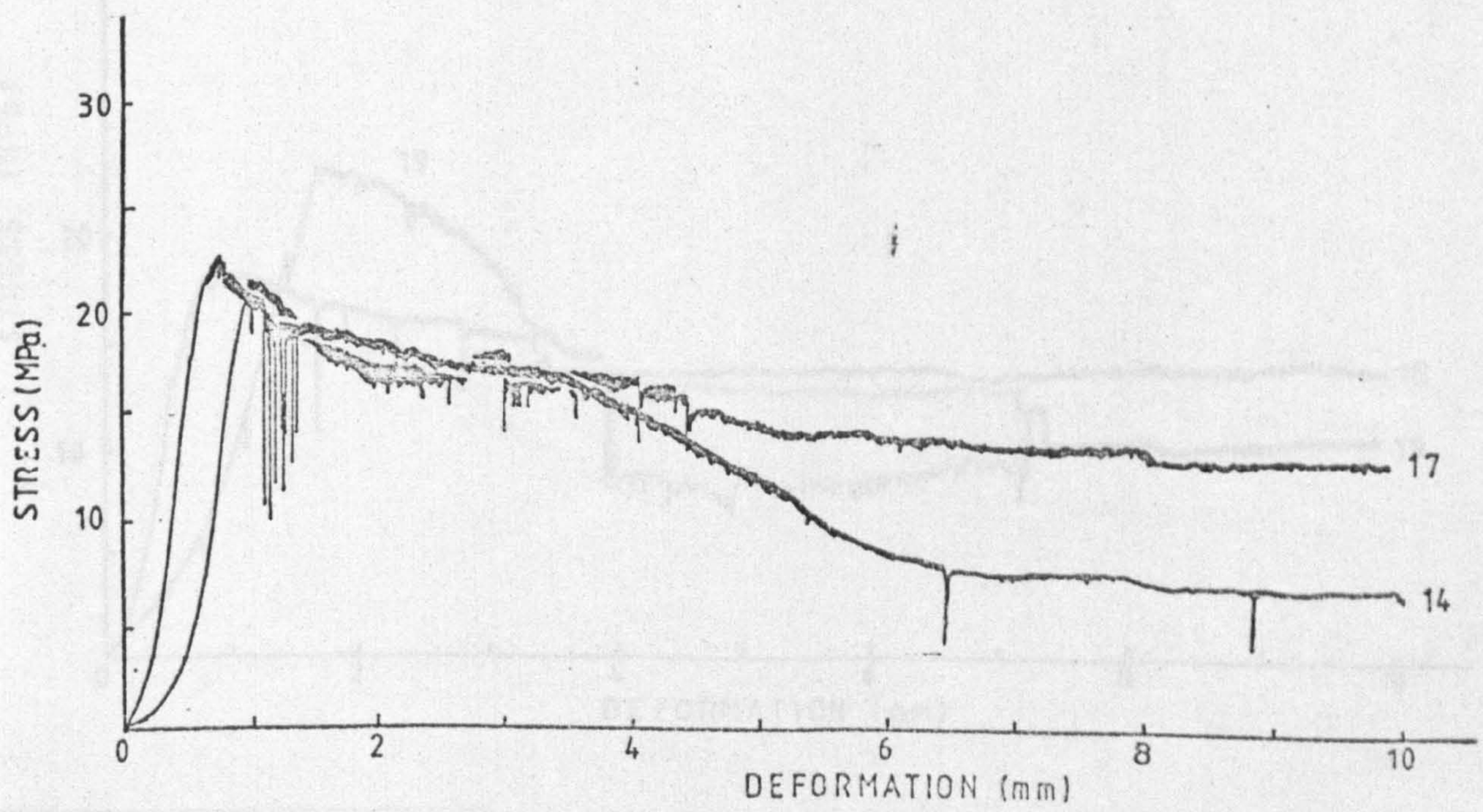
STRESS (MPa)
30
20
10
0
2
4
6
8
10
DEFORMATION (mm)
17
14

FIG 6.9

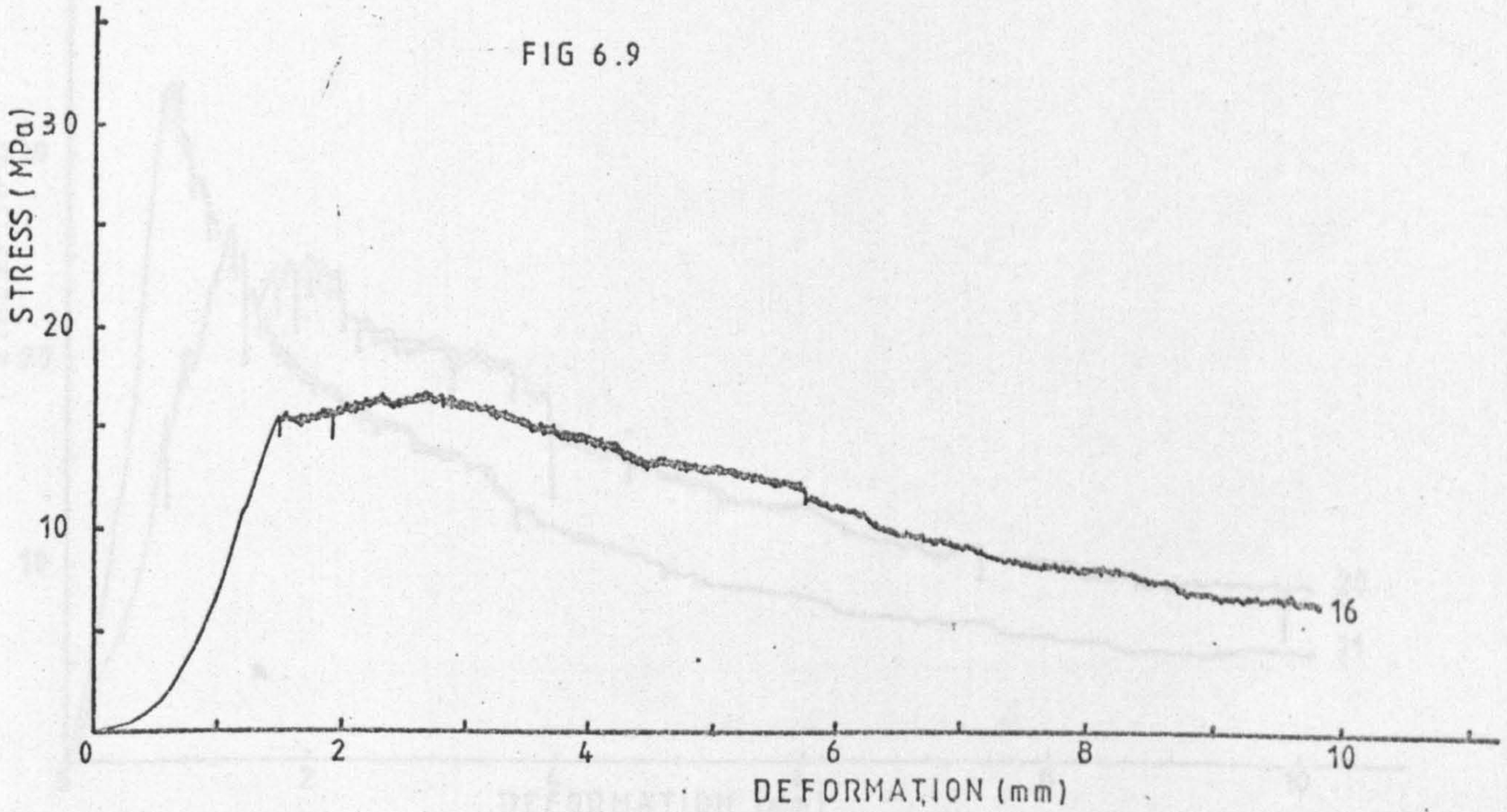

FIG 6.10

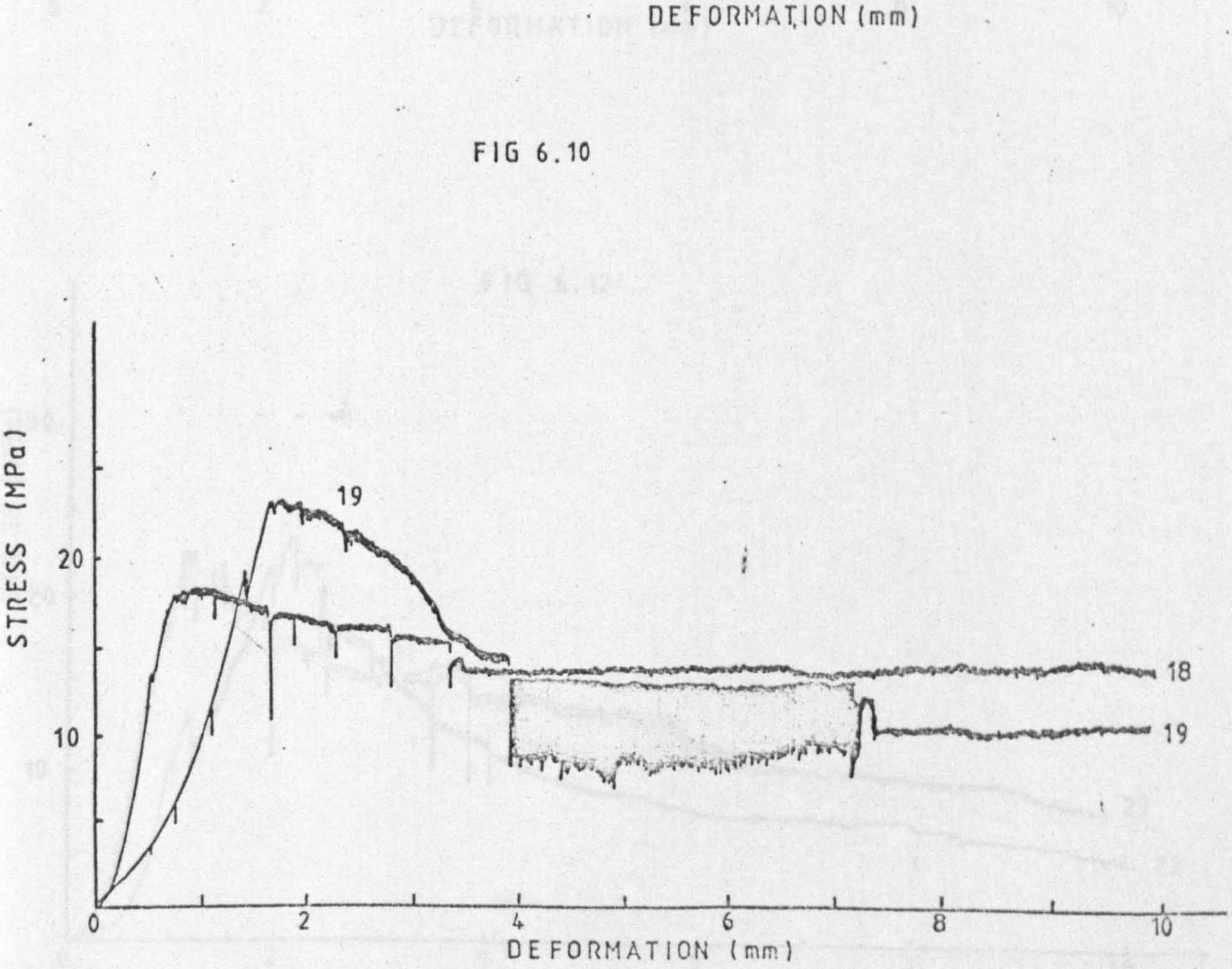

FIG 6.11

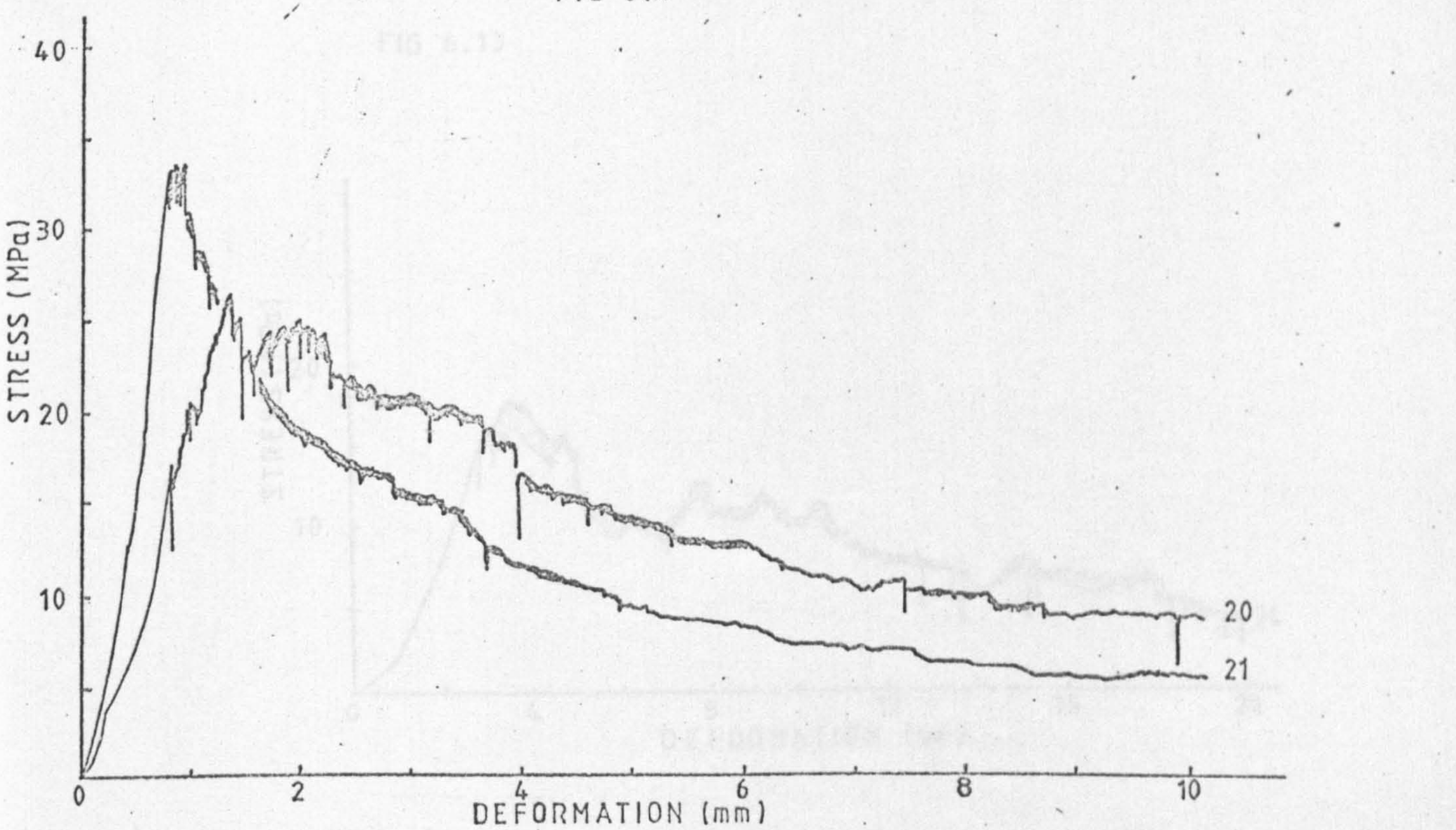

FIG 6.12

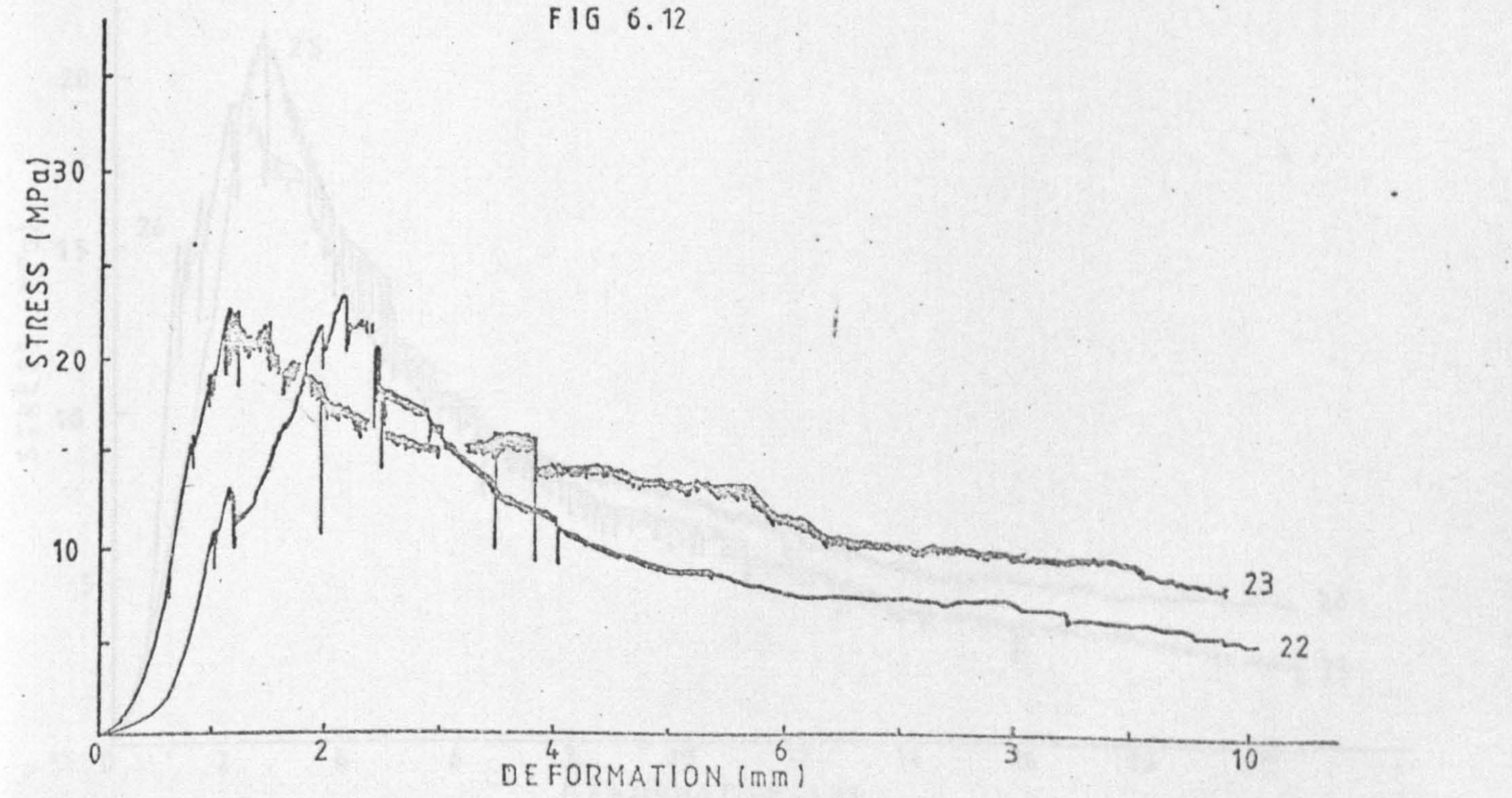

FIG 6.13

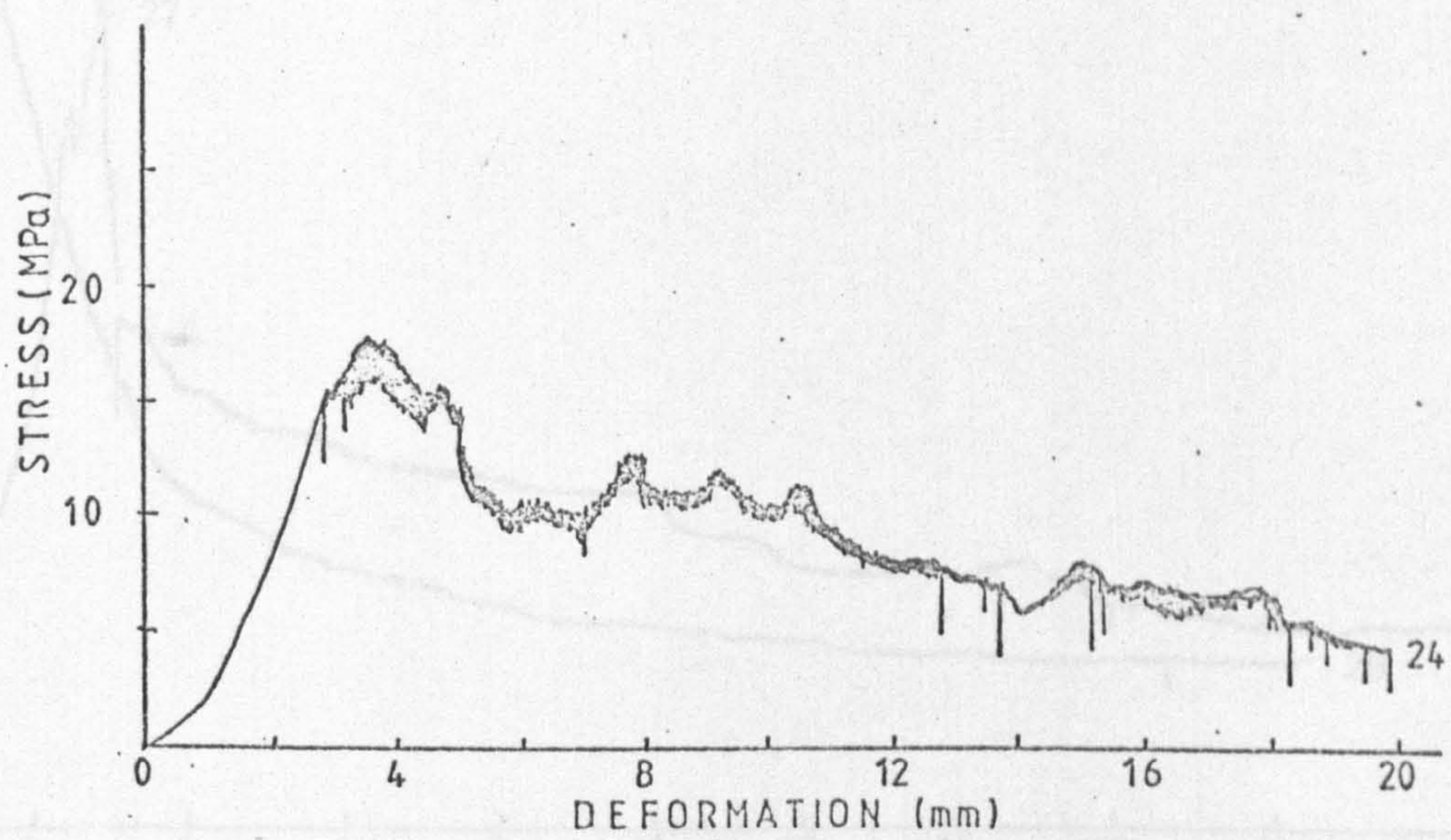

FIG 6.14

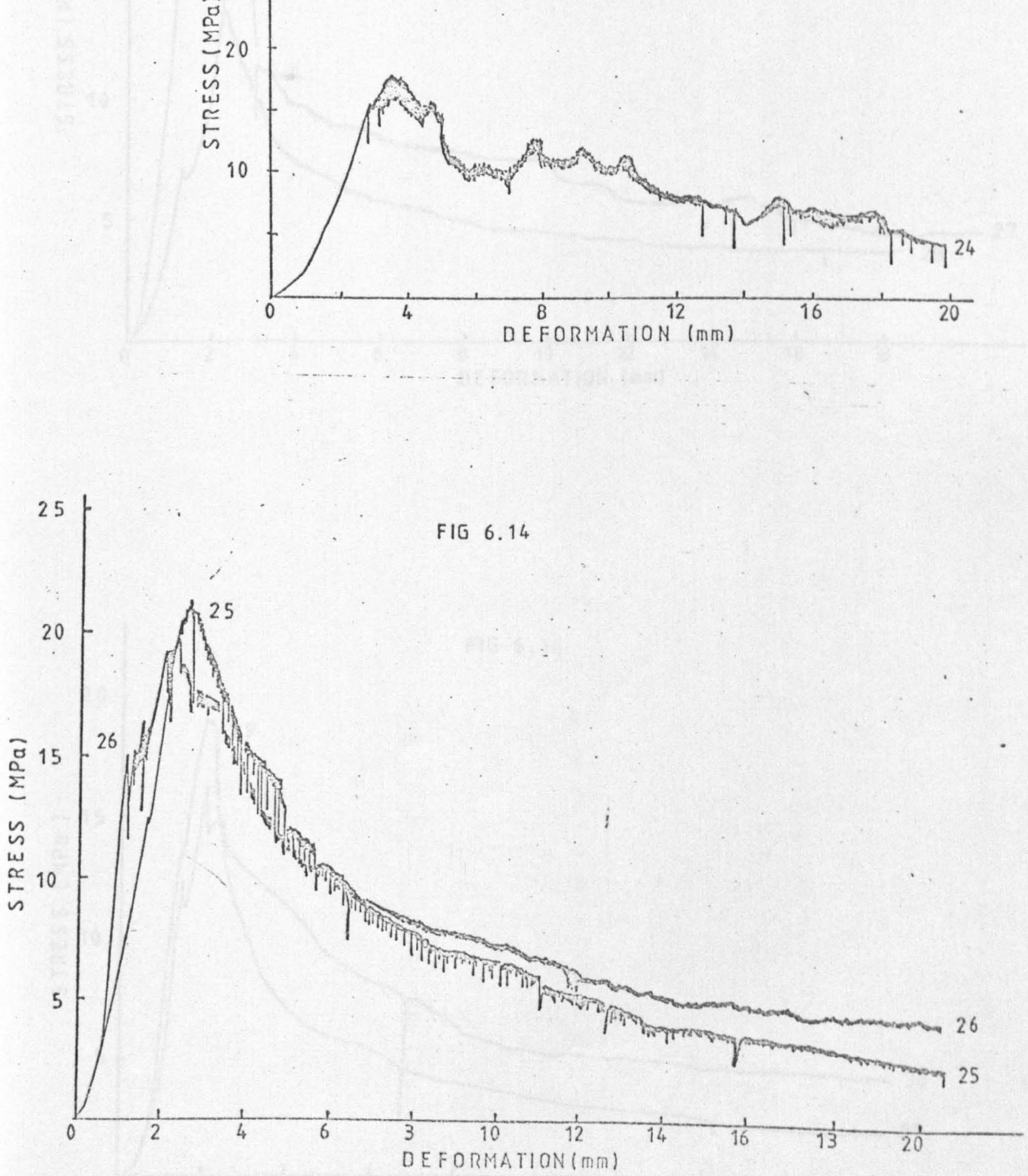

FIG 6.15

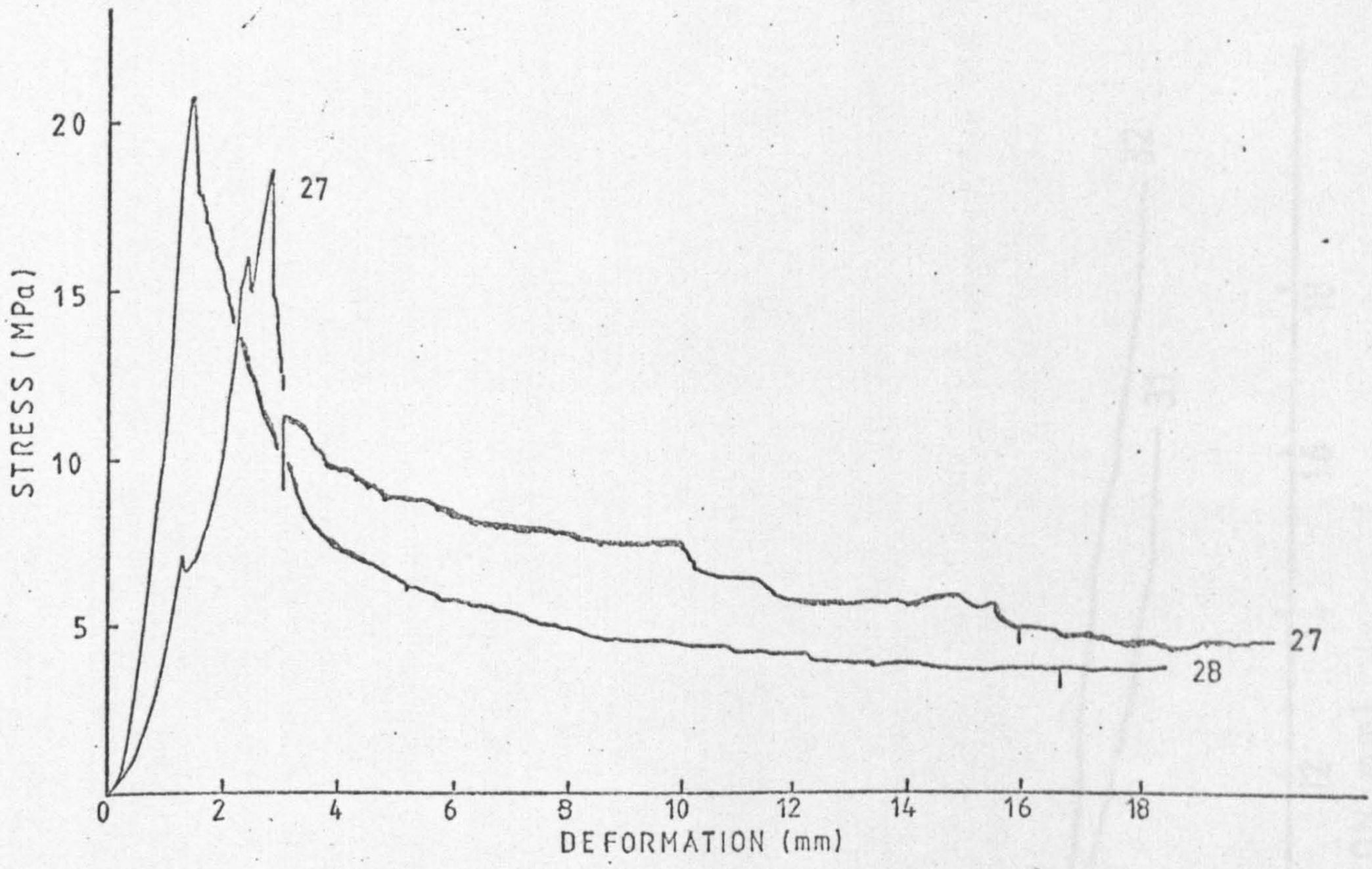

FIG 6.16

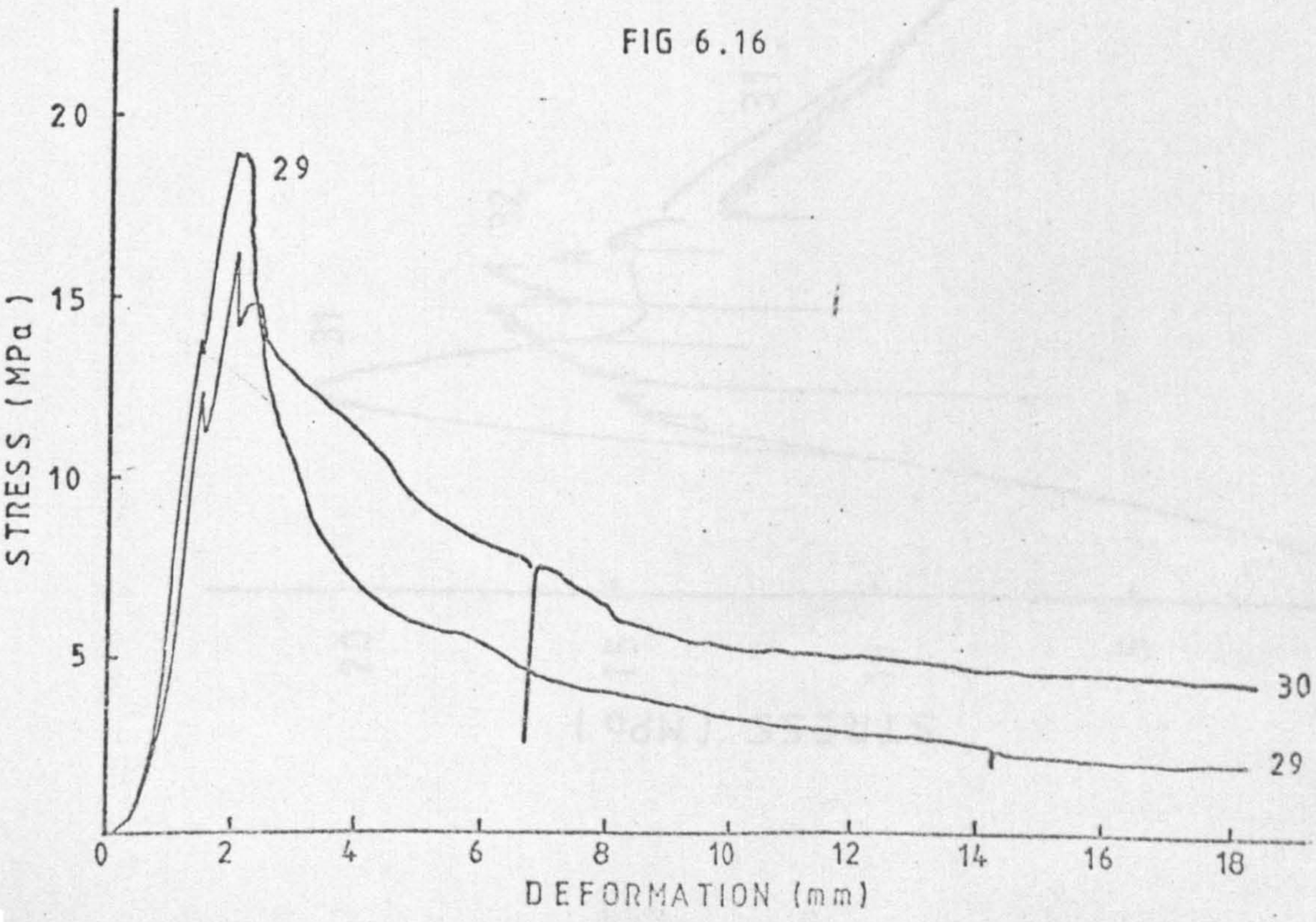

FIG 6.17

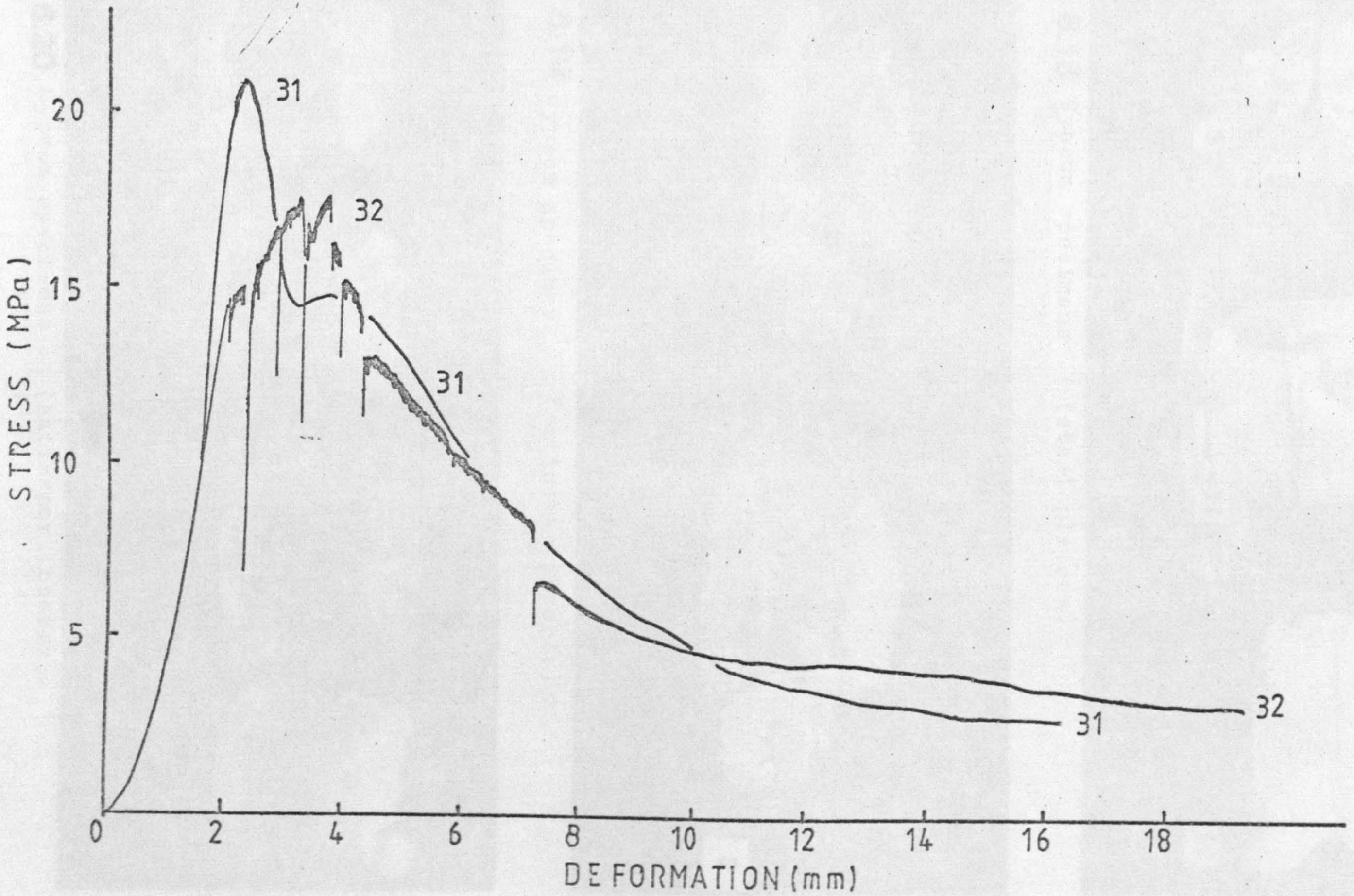
STRESS (MPa)
20
15
10
5
0
2
4
6
8
10
12
14
16
18
DEFORMATION (mm)
31
32
31
32
31

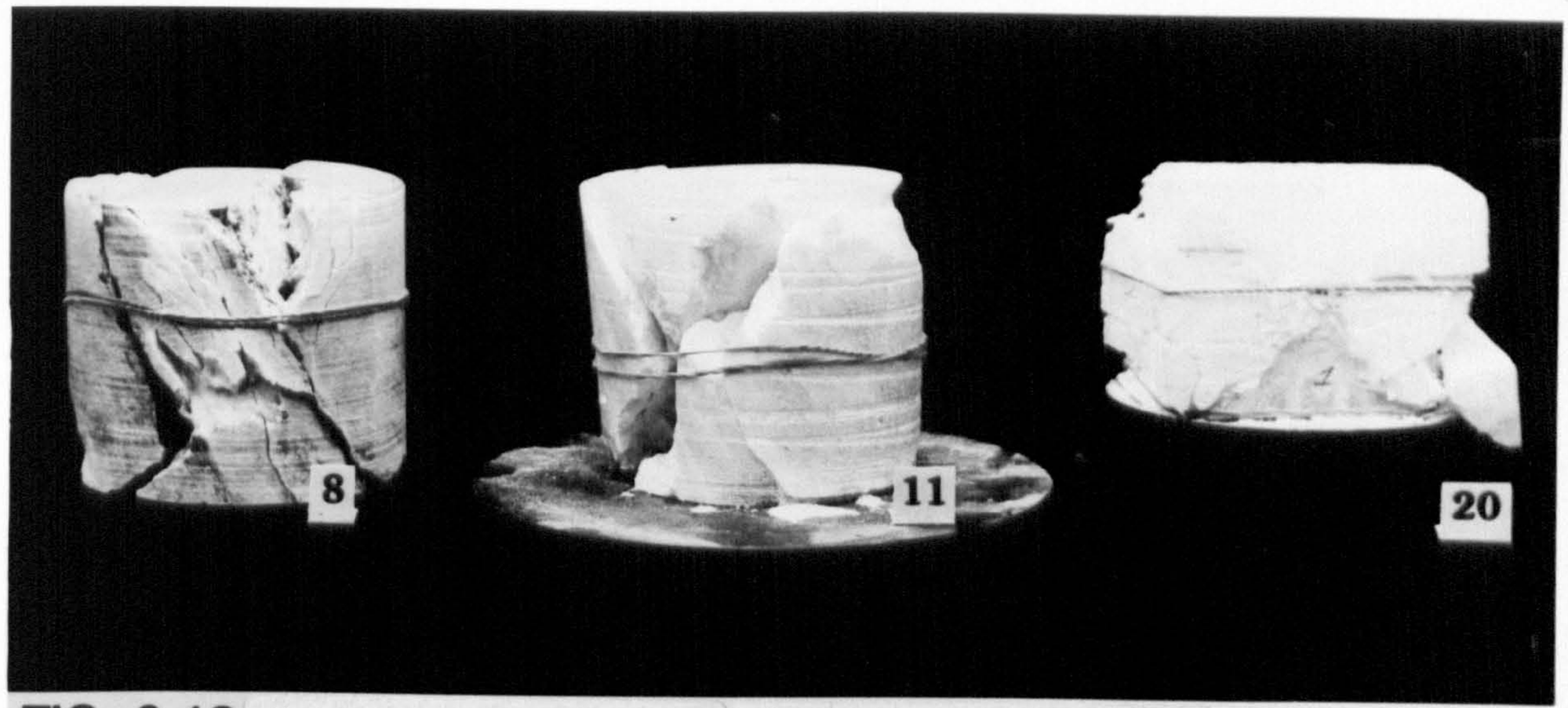

FIG. 6.18 Gypsum specimens (steel platens)

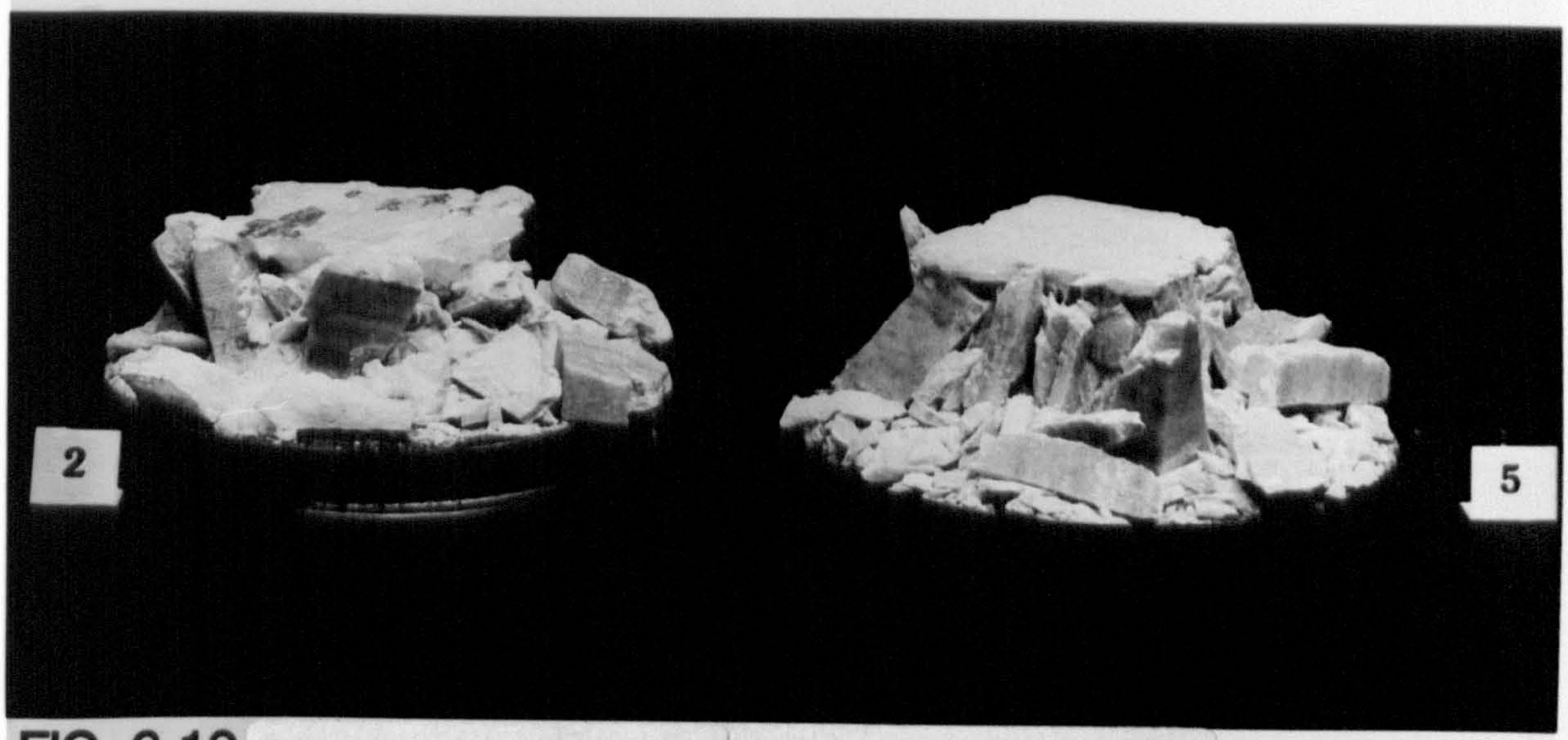

FIG. 6.19 Gypsum specimens (satinspar inserts)

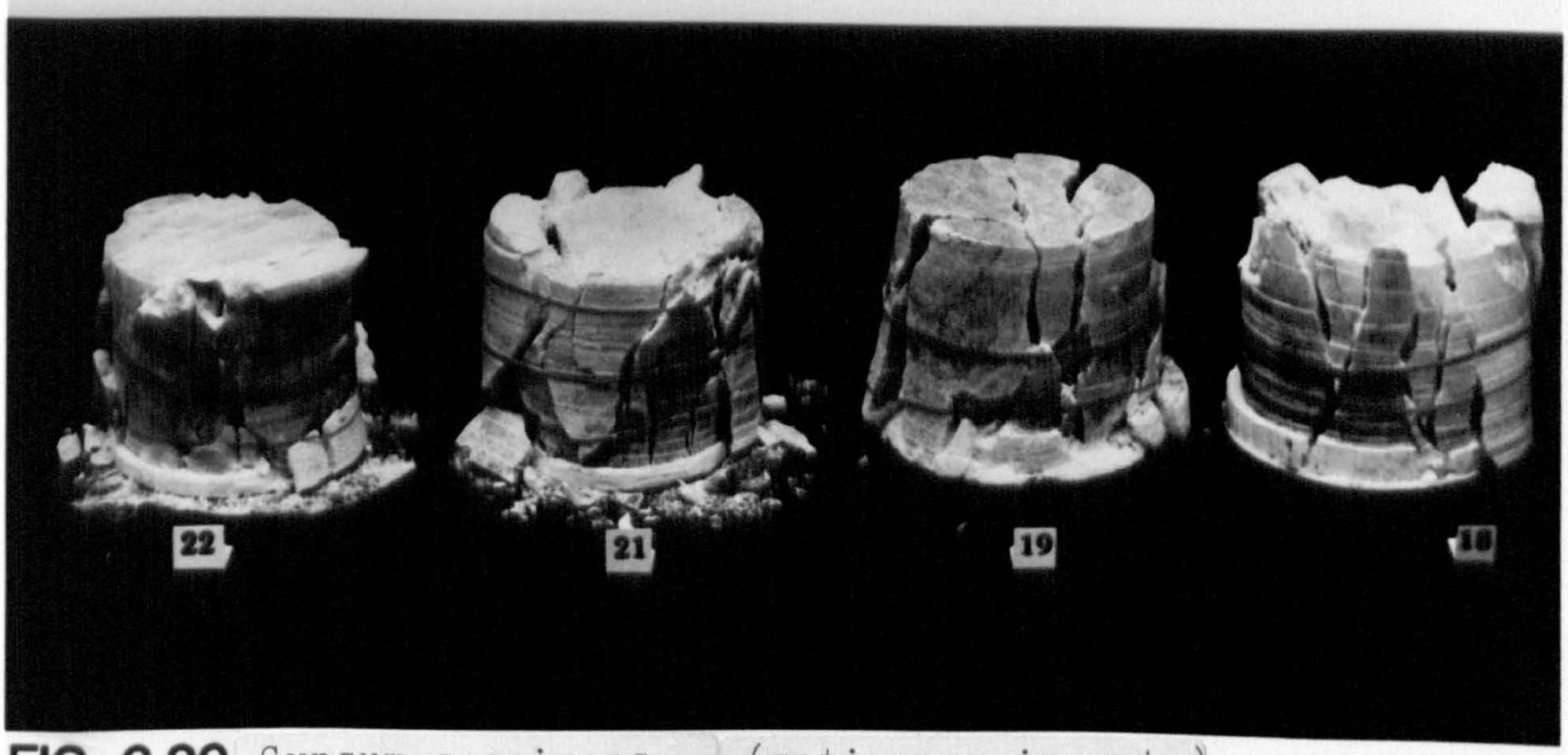

FIG. 6.20 Gypsum specimens (satinspar inserts)

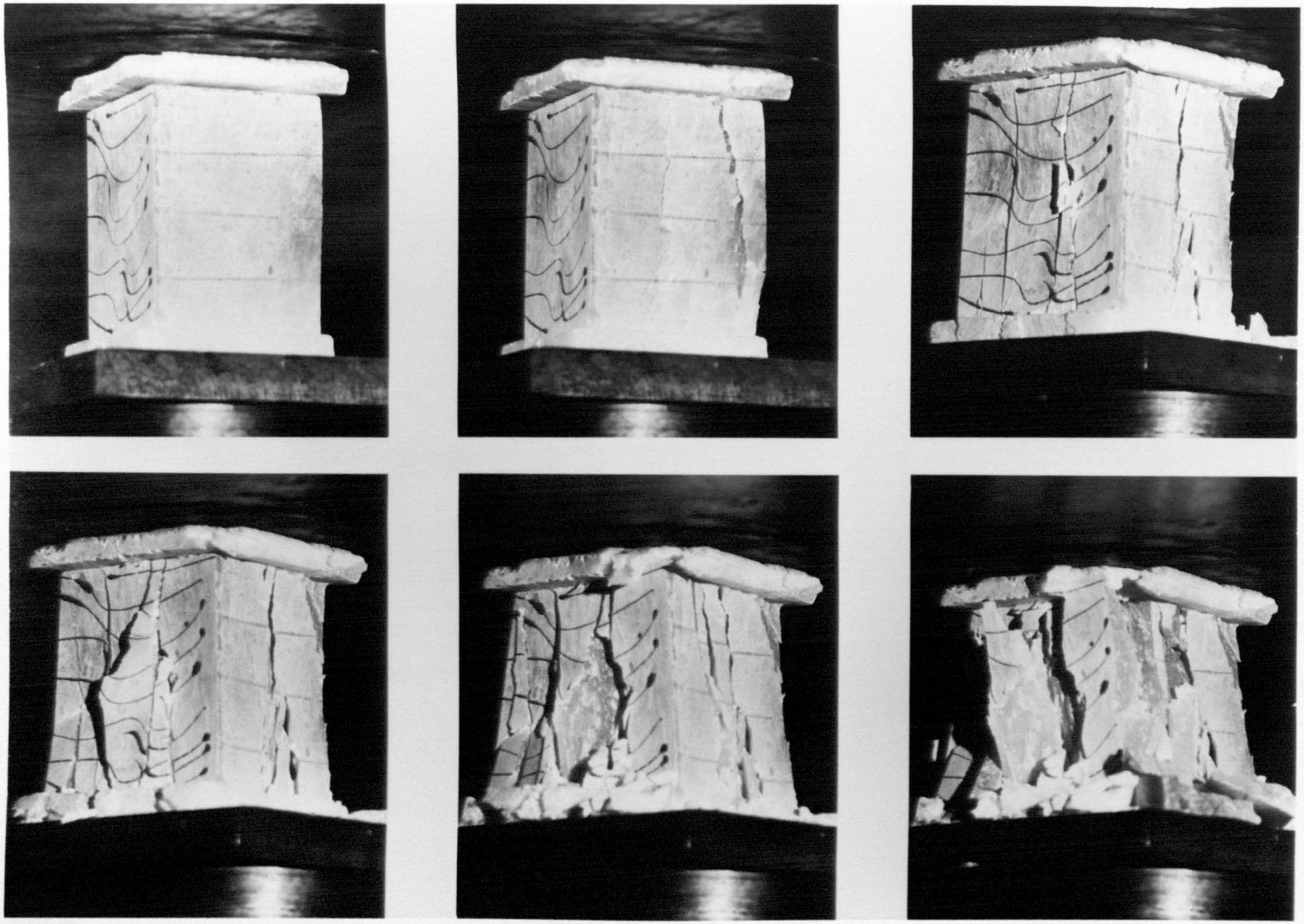

FIG 6.21 Failure of specimen no.23

FIG 6.22 Full load-deformation curve
(adapted from literature)

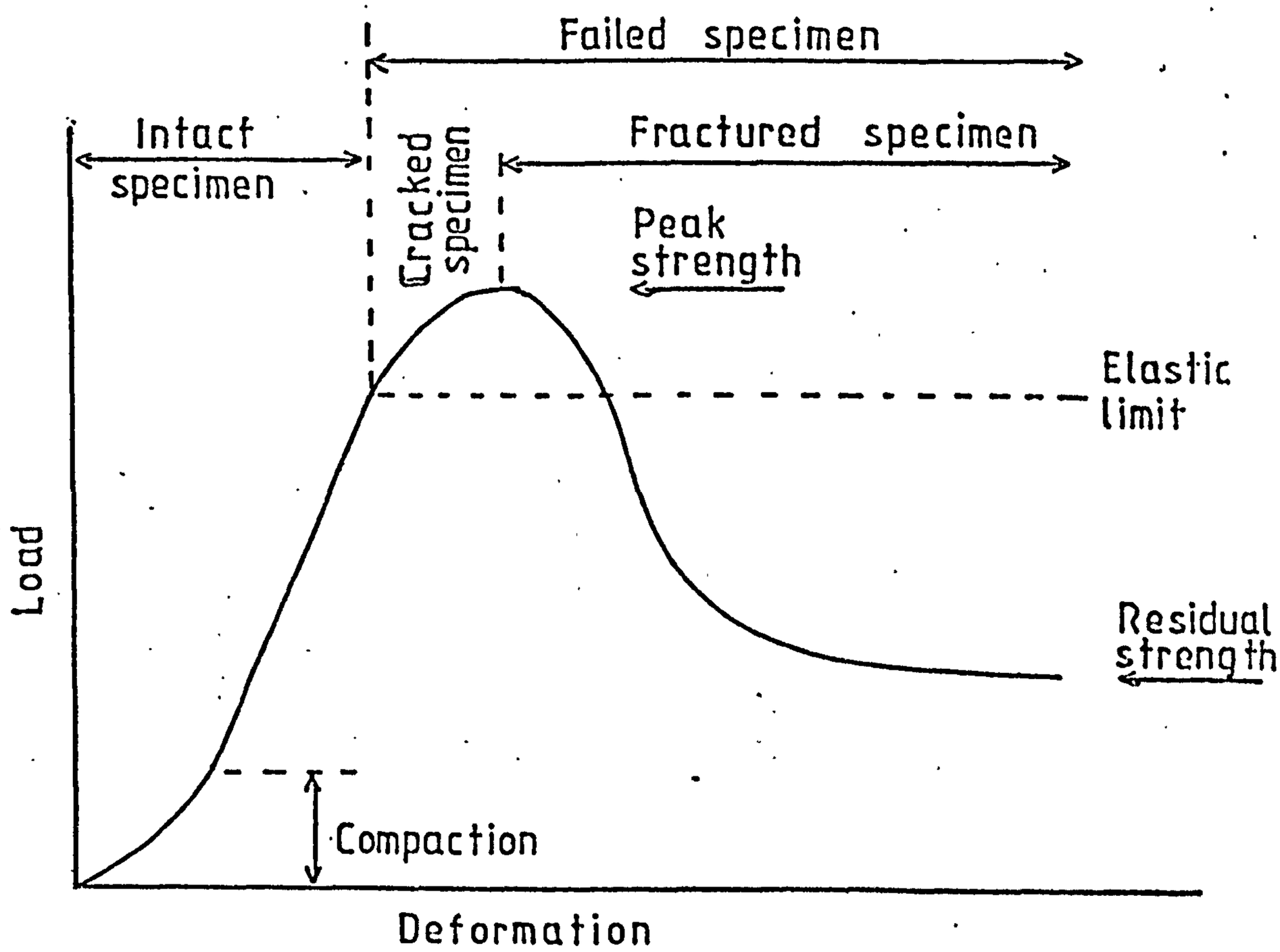

FIG 6.23 Slip-line field for compression between rough parallel platens when $2w/2h = 6.6$
(JOHNSON AND MELLOR, 1975)

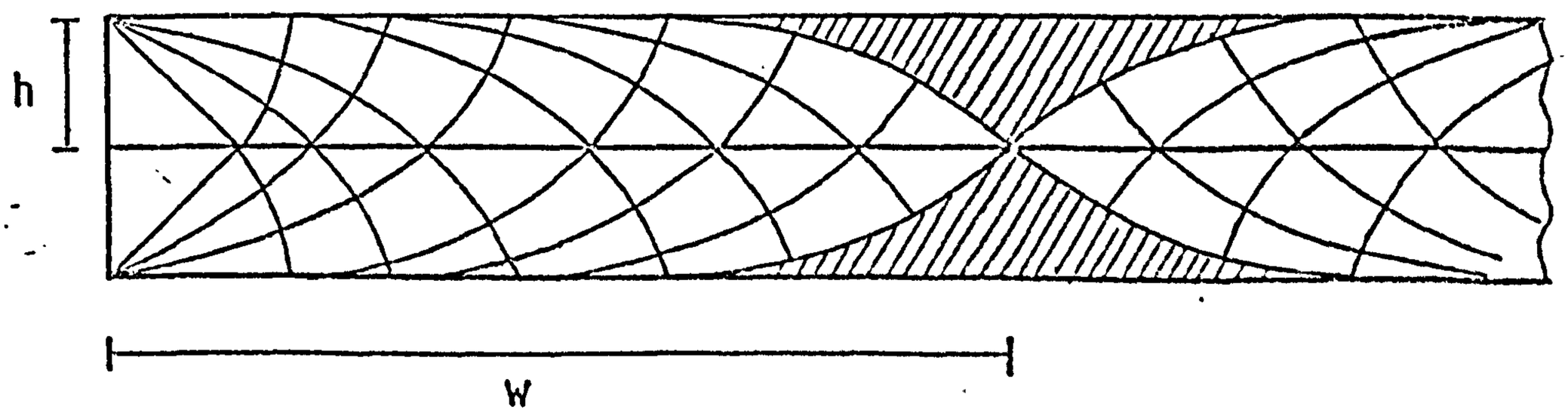

FIG 6.24

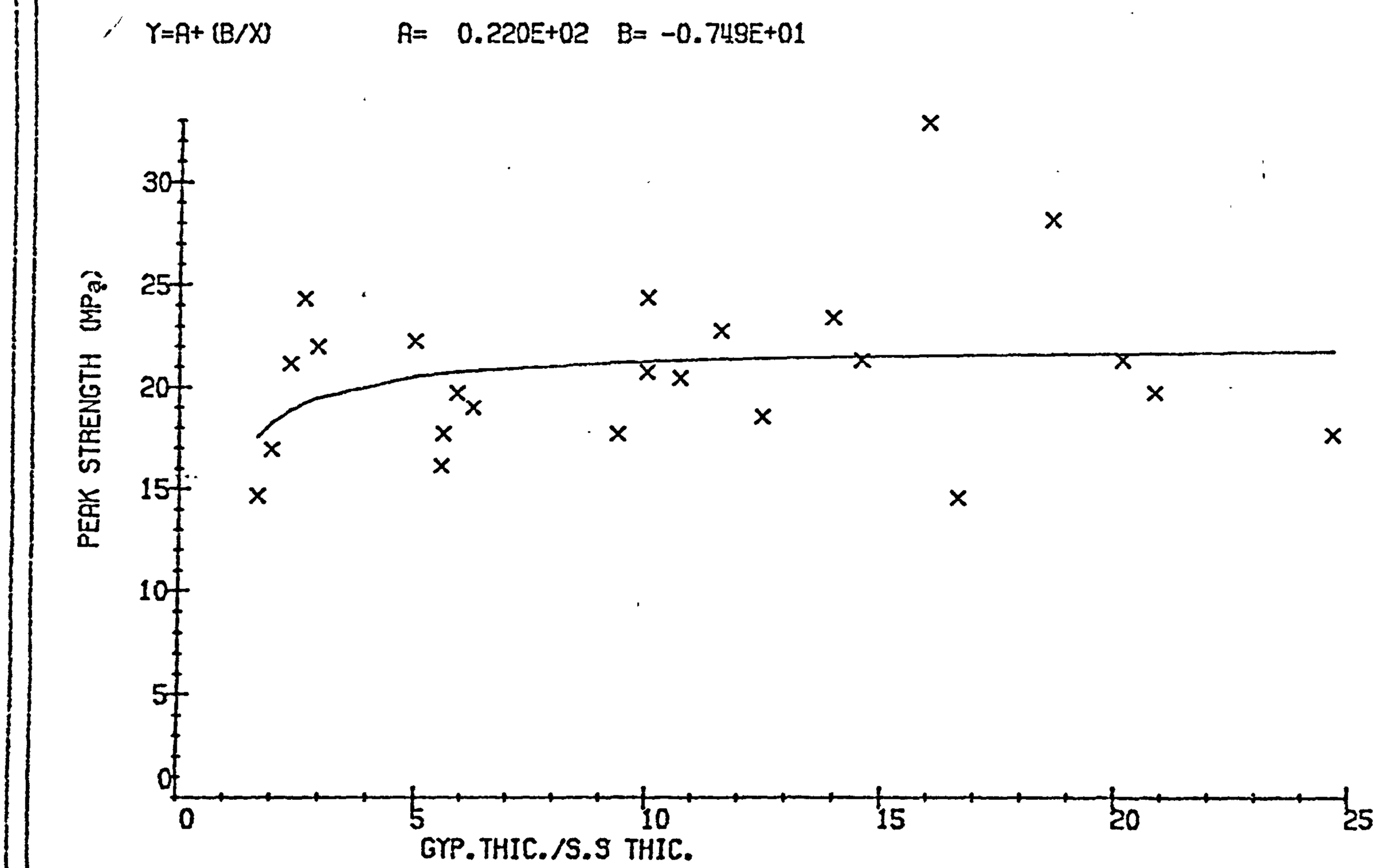
Y=A+(B/X)
A= 0.220E+02 B= -0.749E+01
PEAK STRENGTH (MPa)
30
25
20
15
10
5
0
0
5
10
15
20
25
GYP.THIC./S.S THIC.

TABLE 6.1 DIRECT SHEAR TESTING RESULTS

NO:	AREA(m^2)	σ_N (MPa)	T (MPa)	ANGLE OF ANISOTROPY
1	2.025	1.75	1.245	90^o
2	1.404	4.20	2.030	90^o
3	3.600	0.59	1.316	75^o
4	3.540	1.33	1.707	75^o
5	3.074	1.77	1.830	75^o
6	1.444	4.40	2.390	65^o
7	1.775	0.94	2.000	45^o
8	2.026	1.06	1.640	30^o
9	1.971	2.28	2.960	30^o
10	2.082	0.80	2.090	25^o
11	2.284	2.17	2.28	25^o
12	3.480	0.88	2.02	20^o
13	2.100	1.69	2.015	20^o
14	1.873	3.90	2.615	10^o

TABLE 6.2 FOUR POINT BEAM BENDING TEST RESULTS

NO:	LOAD (N)	THICKNESS ($X10^{-2}m$)	WIDTH ($X10^{-2}m$)	I ($X10^{-3}$)	M (N/m)	σ (MPa)
1	371.28	1.52	5.26	1.536	1.912	0.944
2	388.96	1.56	5.03	1.591	2.003	0.982
*3	912.29	1.56	5.38	1.702	4.698	2.153

* Discounted because of unintentional error in the equipment

$$I=\frac{a\times b^3}{12}\quad,\quad M=\frac{10.3\times10^{-3}}{2}\times LOAD\quad,\quad \sigma=\frac{M\times Y}{I}$$

MEAN TENSILE STRENGTH = 0.963 ± 0.026 MPa

TABLE 6.3 SERVO-CONTROLLED TEST RESULTS OF SATIN-SPAR AND GYPSUM SPECIMENS WITH MATCHING STEEL PLATENS

SPEC. NO:	SPECIMEN AND SHAPE	AREA ($X10^{-3}m^2$)	H/W	PEAK STRENGTH (MPa)	PEAK STRAIN (%)	FIGURE NO:
1	S.SPAR/CUBE	3.4	1.02	12.0	2.65	6.1
2	S.SPAR/CUBE	3.4	1.08	9.8	1.95	6.1
3	GYPSUM/CUBE	2.5	0.60	43.2	3.04	6.3
4	GYPSUM/CUBE	2.5	0.74	20.75	1.20	6.3
5	GYPSUM/CUBE	2.5	1.00	31.08	1.94	6.4
6	GYPSUM/CUBE	2.5	1.22	22.75	2.15	6.4
7	GYPSUM/CYL.	4.4	1.00	21.76	0.83	6.5
8	GYPSUM/CYL.	4.4	1.00	30.16	1.38	6.5

TABLE 6.4 SERVO CONTROLLED TEST RESULTS OF GYPSUM WITH SATIN SPAR END PIECES

SPEC. NO:	SPEC. SHAPE	AREA ($X10^{-3}M^2$)	GYPSUM H/W	S.SPAR THICK.(mm)	S.SPAR T/W	TOTAL H/W	GY.TH. / SS.TH.	PEAK STRENGTH	PEAK STRAIN	FIGURE NO:
9	CUBE	2.5	0.6	15.0	0.3	1.2	2.0	16.94	2.76	6.6
10	CUBE	2.5	0.6	17.0	0.34	1.28	1.7	14.64	---	----
11	CUBE	2.5	0.74	12.5	0.25	1.24	2.96	21.96	1.27	6.7
12	CUBE	2.5	0.74	14.0	0.28	1.3	2.67	24.28	1.33	6.7
13	CUBE	2.5	0.74	15.5	0.31	1.36	2.39	21.15	1.31	6.7
14	CUBE	2.75	0.95	5.0	0.095	1.14	10.0	20.75	1.19	6.8
15	CUBE	2.75	0.95	5.0	0.095	1.14	10.0	24.33	---	----
16	CUBE	2.75	0.95	3.0	0.057	1.06	16.66	14.55	2.7	6.9
17	CUBE	2.75	0.95	8.5	0.16	1.27	5.9	19.72	1.55	6.8
18	CUBE	2.61	0.97	9.0	0.18	1.32	5.6	17.72	1.62	6.10
19	CUBE	2.61	0.97	10.0	0.19	1.36	5.0	22.24	2.37	6.10
20	CUBE	2.35	1.15	3.0	0.06	1.27	18.66	28.15	2.15	6.11
21	CUBE	2.5	1.12	3.5	0.07	1.26	16.00	32.90	1.26	6.11
22	CUBE	2.5	1.12	4.0	0.08	1.28	14.00	23.39	3.29	6.12
23	CUBE	2.5	1.16	5.0	0.1	1.36	11.6	22.75	1.52	6.12
24	CUBE	2.3	1.04	6.5	0.14	1.26	9.38	17.73	4.19	6.13
25	CYLIND.	4.4	0.97	5.0	0.066	1.10	14.60	21.33	1.54	6.14
26	CYLIND.	4.4	0.97	3.5	0.047	1.06	20.86	19.74	1.44	6.14
27	CYLIND.	4.4	1.0	6.0	0.08	1.16	12.5	18.58	1.65	6.15
28	CYLIND.	4.4	1.0	7.0	0.093	1.19	10.71	20.46	0.84	6.15
29	CYLIND.	4.4	1.0	12.0	0.16	1.32	6.25	18.98	1.05	6.16
30	CYLIND.	4.4	1.0	13.5	0.18	1.36	5.56	16.11	1.01	6.16
31	CYLIND.	4.4	1.6	6.0	0.08	1.76	20.16	21.33	1.54	6.17
32	CYLIND.	4.4	2.0	6.0	0.08	2.16	24.66	17.66	1.86	6.17

7. LINEAR ARCH STRUCTURE AND PHOTOELASTIC MODELLING OF A LINEAR ARCH

7.1 A short review of research related to the roof stability at Sherburn

The Department of Mining Engineering of the University of Newcastle upon Tyne have been engaged in research relative to all aspects of stability of the mine at Sherburn ever since the beginning of mining activities in the area. A detailed chronological synopsis of the extensive research which has been carried out over the years can be found elsewhere (Watson 1979, Chap. 1). It was, however, considered appropriate to review the previous research concerned with roof stability at Sherburn briefly to establish a connection between the subject which is discussed in this Section and the roof stability at Sherburn Mine.

Investigations into roof stability at Sherburn Mine were carried out simultaneously with the pillar research, but proved to be complex and substantially more decisive in respect of mine stability. Considering the limited availability of structural considerations, the 'clamped beam theory' was thought appropriate for an initial theoretical approximation regarding roof stability. Three possible situations were postulated in respect of the probable load carried by the roof beam:

(a) self weight of the gypsum beam only;

(b) self weight plus a hydrostatic head; and

(c) self weight plus the full weight of the superincumbent strata.

Considering the roof as a beam on elastic supports (i.e.pillars), I.Jones (1968) calculated stresses in the roof for all three cases. The maximum tensile stresses are found to occur at the pillar corners and for the three cases the theoretical values are (a) 0.28 MPa, (b) 3.03 MPa and (c) 5.51 MPa.

A similar theoretical study was made by B. Jones (1970) using a technique derived by Stephanson (1971). The results under identical loading were of the same order of magnitude as those obtained by I. Jones.

The convergence measurement at stations installed in the roadways by B. Jones indicated unexpected deflections of the roof greatly in excess of those predicted by the theoretical studies. Deflections were occurring at a slow, but consistently linear, rate. In the light of this continuous downward movement of the roof beam a concern was expressed that an unabated convergence may result in roof collapse at an indeterminate time.

Simultaneously with convergence observations, it was established that the pillars were deforming by a comparatively small amount and could not account for total roof deflection. Precise levelling of some areas indicated that the floor movement was also negligible. Hence the assumption that the roof can be approximated as a clamped beam is an over-simplification.

A comprehensive in-situ instrumentation programme was initiated by Mottahed (1979) to identify intrinsic characteristics of the roof structure and the effect of mining techniques on roof deflection.

Continuous monitoring of the roadway closure using LVDTs showed that vibration from blasting and the use of different continuous miners (Greenside, McAlpine tunnelling machines, Dosco roadheader, Mavour and Coulson roadheader) had virtually no effect on roof deformation.

By monitoring anchor movements fixed in the marl above the seam and at the lower surface of the beam, it was found that the marl was following the lowering of the gypsum beam and the immediate roof was carrying the whole weight of the superincumbent strata.

Approximately 1000 days after installation of the convergence stations measurements indicated a decreasing rate, hence Mottahed fitted a decreasing exponential curve to the data. However, some stations still exhibited a linear rate of increase as quoted in an internal report to British Gypsum Ltd. by Szeki (1978) (Figures 7.1, 7.2 and 7.3).

In sections of the mine where the roadway intersections had large spans, the opening of tensile cracks was monitored using a Demec strain measuring device. A linear relationship was found between time and convergence. Subsequently, artificial pillars were erected at these intersections in order to reduce the effective roof span and prevent any likely roof failure.

Extensive joint distribution surveys carried out by Mottahed (1974), Haque (1974) and, later, by undergraduates from the University, provided a better picture of the blocky nature of the roof beams. The joints were mostly subvertical (75^{o} to 90^{o}) and the frequency varied from 7.76 joints per 30 metres to 3 joints per 30 metres.

Stress measurements undertaken in the roof, using the 'Potts' high modulus inclusion stress meters indicated a lateral compressive force along the beam axis. In view of this, Mottahed concluded that the roof was behaving as a linear arch, Voussoir beam, or cracked roof beam.

On this basis, in order to reduce the convergence rate, the roadway width was reduced from 5m to 4m, which was the smallest roadway distance that the operators could consider mining. With an accompanying reduction in pillar size, the reduction in the roadway size caused only a small decrease in extraction ratio (to 64%), but resulted in a decreased convergence rate.

Instrumentation carried out by Watson (1979), utilising the Talbott MKII strain cell, produced further evidence on the presence of linear arch structure. In subhorizontal direction in the roof beam measurements of compressive stresses supported the assumed existence of the linear arch structure. It was noted that, since the magnitude of the normal stresses were low, the initial pre-thrust on the beam was also minimal which, in turn, would reduce the effective resisting force preventing vertical sliding of blocks in the roof. Due to the low stress field and the accuracy of the recording apparatus, a high percentage of error accompanied the results (0.6 MPa). However, the probability of a linear arch structure was verified with confidence.

7.2 Linear Arch Structure

The fact that a cracked roof beam can stand up safely as long as a sufficient lateral force exists has long been recognised.

After Bucky (1934), who had published results of tests on model beams restrained at the ends with vertical or steeply inclined cracks, Evans (1941) introduced the term 'Voussoir Beam'. He proposed an analytical solution in order to define the maximum stress in the beams by considering a contact length equal to one-half of the beam thickness and horizontal compressive stress normal to vertical planes at mid-span and which had a triangular distribution at the abutment. These considerations were, however, to be found subsequently in error.

It was reported by Mohr (1954, 1956) that the horizontal force necessary to prevent bending was much less with a thick beam than with a thin beam in the linear arch.

Under the blast loading, the behaviour of masonry walls and unreinforced brick beams is similar to that of a linear arch (Anderson et al.1955; McDowell et al.1956). An approximate solution, considering an elasto-plastic material and the development of plastic zones at the top of the beam or flat arch at centre and at the bottom at abutments was suggested by McDowell et al. The pre-failure and post-failure resistance-deflection curve of a linar arch with three cracks based on the equation suggested by McDowell was similar to that obtained experimentally by Sterling and Nelson (1978) using a servo-controlled loading machine.

Haycocks (1962) modified Evan's solution by considering the effect of shear stress component of the resultant force at the abutment. However, he also assumed a triangular stress distribution and a contact length of half the crack length.

The modification to the approach suggested by McDowell (1956) by taking the axial force into account, was made by Trollope (1965). He calculated the maximum resisting moments of the immediate roof under varying axial loads for elastic, plastic and non-tension plastic types of roof beam.

Elaborate stress analysis of a cracked room beam was first carried out by Wright and Mirza (1963). They modelled the linear arch photoelestically and found that the maximum stresses were much higher than those predicted by Evan's solution and the contact area along the cracks much less than half the depth of the beams (18% of beam depth).

In 1972, Wright postulated three possible mechanisms of failure of the linear arch structure.

(a) Sliding, if the resistance provided by the thrust, the frictional charcteristics and the angle of dip of the dip of the joint surfaces are not great enough..

(b) Rock crushing at points of high compressive stress thereby permitting rotation of blocks.

(c) A plastic or elastic buckling of the rock beams without exceeding rock crushing strength at the points of rotation.

The cracked roof beam was examined by a finite element method as well as by physical models. All finite element models were self loaded and cracks were modelled by thin columns of elements which were assigned the same Modulus of Elasticity as the rest of the beam where the cracks were closed and much lower Modulus of Elasticity where the cracks were open. It was deduced that the crack length of half the beam depth was in error, but a triangular stress distribution was sufficiently accurate for engineering purposes. He also suggested that the worst case which produced the highest compressive stress would occur when a beam was cracked only at the abutments and at the centre of the span. The calculated stresses at abutments were surprisingly found to be higher than at the centre. It is most likely that this is caused by the rigid abutments employed. The formulae proposed by Wright for the linear arch is complex and the parameters are mutually dependent.

At Newcastle, following the work by Seymour (1968), who tested blocks of sandstone and concluded that the deflections as much as 30 to 40 times the solid beam could be obtained with linear arch, Smethurst (1975) modelled the linear arch using gypsum blocks from Sherburn. The vertical failure load was found to be linear for beams having span to depth ratios from 2.5 to 7, and for beams with span to depth ratios above 7, the failure load decreased at a slower rate. He did not observe the failure type by elastic-plastic buckling of the beams as described by Wright, but rather, he observed diagonal failure accompanied by a vertical tensile crack over the abutment. Crushing of corners and rotation of beams were noted for beams having three joins and a span to depth ratio of 3.5 and 7.

Chugh (1977) presented a numerical step-by-step procedure for the analysis of a single-layer jointed rock beam subjected to gravity loads and in-plane, in-situ formation pressure. The joints are permitted to open where the flexural stress exceeds the flexural strength and the material properties of joint and block can be varied freely. The procedure assumes a number of conditions, including the following:

For a single-layer jointed beam, the deflections and rotations are independent of the y-coordinate and remain relatively small compared with the depth of the blocks. However, experience has shown that the deflections of the linear arch are significant. Wright (1972) gives a deflection up to 14 percent of the depth of the beam.

The material blocks cannot interpenetrate beyond a point contact. However, in reality, due to crushing of the beam corners, the line contact of the adjacent blocks is considerably more than a point contact as implied by Chugh.

Sterling and Nelson (1978) reported the results of rock beams restrained at the ends acting as a continuous beam first, then after tensile failure as a cracked beam. They utilised a servo-controlled loading machine and recorded the pre-failure and post-failure load deflection curves of linear arch. The ultimate bearing load of the cracked beams was approximately 6.5 times that of tensile cracking load. They also observed diagonal failure mode of the beam blocks, as previously noted by Smethurst (1975). They criticise the elastic computerised solutions of Wright (1972) on the basis of the fact that rock crushing takes place at the highly stressed corners (at the top of the central crack and the bottom of the abutment cracks).

Watson (1979) embarked upon model testing investigations to provide data on the short-term and long-term behaviour of broken gypsum beams. The ultimate bearing load of the broken beams was reported to be up to five times the first tensile failure load. For the beams tested, a linear relationship between the induced axial thrust and the applied transverse load was found for the low applied pre-axial thrust. Beams with high initial axial thrust showed a curve becoming asymptotic to a straight line at higher loads, as indicated also by Wright (1972). The position of the centroid of the thrust acting at the abutments gradually moved towards the centre of the beam as the transverse load increased in the pre-peak load region. With the exception of an elastic-plastic buckling and subsequent rotation of the beams, Watson observed all the modes of failure of a linear arch noted by previous investigators. The crushing of high stress regions can be identified as a series of shear planes occupying an approximately triangular area. He noted the mode of axial shearing for beams having span to depth ratio of less than 6:6 and the crushing of corners and subsequent rotation for beams having span to depth ratio higher than 6:6 (Figures 7.26 and 7.27).

7.3 Objectives of the photoelastic modelling of the linear arch

The linear arch structure was photoelastically modelled for the following objectives:

(a) To obtain an idea of the stress distribution in the cracked beam.

(b) To examine the effect of span to depth ratio of the cracked beams on the stress distribution.

(c) To enlarge upon the aspects of linear arch.

The stress distribution in a linear arch was studied by Watson (1979) using a non-linear finite element program (ANNOLIN 4). The idea was to employ a thin no-tension strength joint element between the two beam blocks. The joint elements duly cracked but, instead of transferring the load to the compression areas and hence acting as a linear arch, the tensile stresses were simply passed to the adjacent, non-limited tension elements. Further attempts also yielded unrealistically high deflections of the linear arch and he concluded that the present capabilities of ANNOLIN 4 were not sufficient to model the linear arch.

Another finite element package prgram, PAFEC 75, which is available at Newcastle, is also incapable of modelling joints in a cracked beam. This program will be referred to in the following Section for other modelling purposes.

On these grounds it was thought expedient to model the linear arch structure photoelastically.

7.4 The contribution of photoelasticity to the solution of the problem being considered

Photoelastic analysis is a method commonly applied in engineering to determine the stress distribution in a structural element for which the mathematical solution is often difficult. The principles of photoelasticity will not be described here since they are dealt with in detail in several standard textbooks (Frocht 1948; Heywood 1952; Cookeret al.1957; and Hendry 1966 and 1977).

It is sufficient to quote that, in the polariscope, polarised light passes through a stressed material which becomes optically anisotropic under applied stress and suffers optical interference. If the light is circularly polarised the fringe order at any point is directly proportional to the difference between the principal stresses at this point, which is also equal to twice the maximum shear stress at that point. These fringes are usually called 'isochromatics'. If the light is plane polarised, black interference appears wherever the direction of one of the principal stresses lies in the plane of polarisation of the light. These lines are called 'isoclinics'. By rotating the polarising and analysing plates at known intervals, the direction of the principal stresses at every point in the model can be found. When the stresses at all the boundaries of the model are available, the sum of the principal stresses can be calculated. Thus each principal stress and its direction can be determined at every point in the model subjected to loading. This information specifies completely the state of stress in the model.

Photoelastic methods of stress determination have been widely used in rock mechanics for various specific cases by many researchers (Dixon 1955; Banerji 1968; Stevic and Jasarevic 1977; Wright and Mirza 1963; Carey 1965; and Chappel 1974, 1979).

In order to model the linear arch structure photoelastically, the following assumptions had to be made:

(a) Prototype material (that is, gypsum) is assumed to exhibit linear strain-stress relationship.

(b) Prototype beams are assumed to be perfectly rectangular and there is no crack filling material.

(c) Loading the photoelastic beams from the bottom edge uniformly is assumed to be representing the body forces in the beams.

(d) No pre-axial load is taken into consideration for simplicity.

In the photoelastic tests, two-dimensional beams were subjected to a plane stress loading condition. Therefore, the deformation of the front and rear surfaces of the beams took place in relation to the equation below:

$$\varepsilon_2 = -\frac{\nu}{E}(\sigma_1 + \sigma_3)$$

ν = Poisson's ratio

E = Young's modulus

σ_1 & σ_3 = principal stresses

ε = Strain.

7.5 Construction of model beams

7.5.1 Selection of photoelastic material

There are many materials commercially available which may be used in photoelastic stress analysis work. The selection of a suitable material is based on transparency, machinability, high optical sensitivity, absence of creep effects, freedom of initial stresses, linear stress-strain and stress-fringe relations, isotropy, rigidity, availability and

low cost. The relative merits of photoelastic materials are sometimes compared by their figures of merit which is the ratio of the elastic modulus to the material fringevalue (i.e. Q = E/f). For low stress fields, a material with a high figure of merit is required so that a sufficient number of fringes can be generated. On this basis, Grieves (1961) used models made of Gelatine, Wright and Mirza (1963) employed model beams made of Kriston and Chappel (1979) preferred Araldite for modelling discontinuous rock media. Alternatively, gravitational field may be replaced by a centrifugal field in order to obtain sufficient fringes from a model made of a material with a low figure of merit, as did Panek (1952).

Considering the linear arch structure and the loading device which is described in the following sections, Araldite CT-200, which has a high degree of merit, was found to be appropriate for modelling purposes. The relevant properties of Araldite CT-200 are given in Table 5.1.

7.5.2 Preparation of model beams

The rectangular model beams were first sawn out from the sheets of Araldite avoiding the portions that indicated initial anisotropy when viewed through polarised light. A small thickness of material along the edges was left for machining. The beams were then machined to the final size using side milling techniques and a template of the same size with the beams. Induced anisotropy and chipping of material was avoided by allowing a very small feed to the machine tool in the final phases of machining and by using a sharp cutter. In order to minimise time-edge effect, one model was prepared at a time.

Two steel end pieces (Figure 7.4) were bonded to the araldite beams using an adhesive (Araldite 2003A) which had somewhat similar properties to those of the beams. Care was exercised to apply the minimum possible quantity of adhesive for bonding because the quality of adhesion would affect the stress distribution around and at the interface.

7.5.3 Initial Stresses

Initial stresses up to the order of half a fringe, possibly resulting from the manufacturing process, existed in the material. There are certain annealing techniques to eliminate these stresses, but it was thought it would be satisfactory to make allowances for them in the calculations rather than resorting to an annealing method which may affect adhesion between the steel end pieces and the araldite beams.

At freshly exposed surfaces of the photoelastic materials due to the evaporation or absorbtion of water at these edges, time-edge effect takes place. This can distort the fringes in a narrow zone bordering the edges of the beams together with the equilibriating stresses distributed through the interior. For this reason, model beams were tested immediately after the beams had been made.

7.6 Calibration of the photoelastic material

In carrying out a photoelastic analysis, it is necessary to establish the relationship between the relative retardation and the principal stress difference in appropriate units. Therefore, an

araldite specimen, as shown in Figure 7.5, was subjected to tensile loading in the field of view of the polariscope. The fringes appearing at the shank of the specimen were recorded against each applied load and by converting the load to stress, the fringe order was plotted against the applied stress (Figure 7.6). The slope of the line was calculated as being the unit fringe value which was 0.651 MPa/per fringe. As can be seen in the graph (Figure 7.6), the straight line did not pass through the origin of the axis. This is an indication of the presence of initial stresses in the material.

7.7 Loading mechanism and construction of loading apparatus

Faulty loading conditions would lead inevitably to the introduction of irrelevant or unintentional stress concentrations which may not be easily identified in the model. A simple loading system was designed for this purpose.

Two identical rectangular model beams in juxtaposition were simplified to represent a horizontal mine roof that had cracked over the supports and in the centre of the span. The span and the thickness of the beams were to be fixed at 20.28cm and 1.27cm respectively throughout the experimental program. Yet the depth of the beams could be varied to obtain different span to depth ratios.

To approximate a uniform loading, two steel end plates, having an identical span and thickness to that of the beams but of a triangular shape with a hole in the lower middle corner, were fabricated. These steel elements were bonded to the bottom of the photoelastic members. The loading was carried out by hanging weights on a hanger connected to the steel beams through the holes (Figure 7.4).

Two metal brackets were constructed, one being fixed to the straining frame, the other being movable horizontally (maximum 3cm) by means of two screws attached at the end of the bracket. In order to prevent the beams from sliding downward, two L-shaped abutment pieces made of the same photoelastic material as the beams were fixed onto the sides of the end brackets. The lips of the L-shaped abutments made a 60^{o} angle with the horizontal axis hence leaving 15^{o} clearance with the steel end pieces for the deflection of beams. The set-up can be seen in Figure 7.4.

Wright and Mirza (1963) employed similar loading mechanisms for photoelastic modelling of a cracked roof beam. They loaded the beams by means of eight holes drilled to the bottom of each kriston model beam and adopted rigid abutments rather than using photoelastic material.

7.8 Optical System

A large field polariscope was used for the experiments. The apparatus was composed of a light source with a diffuser to produce a uniform field of parallel light, a Wratten filter (number 77A) to be fitted onto the camera at the other end of the apparatus, two $\lambda/4$ wave plates, a polarising plate, an analysing plate, a white screen and a camera (Figure 7.4).

Isochromatics and isoclinics were in a few cases photographed for better inspection but were, in general, traced from the white screen. All tests with the exception of the last one were carried out on a dark background.

7.9 Testing Programme

Numerous beams having different span to depth ratio were tested in order to establish a relationship between the maximum induced stress and the span to depth ratios of the beams within the elastic limit.

The effect of increasing the applied transverse load on the stress concentration was also examined within the experimental programme.

Upon discovery of a tensile zone in the simulated beams, suspicions arose over the correctness of the loading mechanism. For this reason a number of auxilary tests were carried out by loading the photoelastic members from the top by hand.

In a separate test, the beams having a span to depth ratio of 4 were tapered from the top middle corners of the beams in order to achieve larger contact area.

Finally, a beam having 4 cracks and a span to depth ratio of 6.66 was modelled. Relevant information regarding the beams tested is presented in Tables 7.2.

7.10 Photoelastic Observations

The isoclinic lines were determined by rotating the polariser and analyser at 5^{o} intervals under plane polarised light. However, for the sake of clarity, they were presented in the order of 10^{o} in Figures 7.7 to 7.10. They were generally drawn on tracing paper

covering a white screen in place of the camera. It was found that very often the isoclinic fringes were poorly defined and a great deal of judgement was needed to trace them correctly.

Isochromatic fringe patterns of the beams under various loads were obtained in a circularly polarised light. Every isochromatic fringe is a line along which $(\sigma_1 - \sigma_3)$ has a certain value thus the relationship between the fringe order and the relative retardation is given by:

$$d\ (\sigma_1 - \sigma_3) = n \times f,$$

where d is the thickness of the model,

n is the fringe order and

f is the unit fringe value.

The first order fringe always appears at the highly stressed locations and as the load is increased it gradually spreads to the lower stressed regions. The fringe orders were identified by observing the model as the load was applied.

In order to determine the fractional fringe order at a point, the Tardy method may be adopted. Tardy (Frocht 1948) revealed that if the direction of one principal stress coincided with the plane of polarisation, then by rotating the analyser the change in the fringe order would be directly proportional to the amount by which the analyser was rotated. Hence, for a rotation of θ degress, the resulting change in the fringe order would be $\theta/180$ fringes for angles up to 90^{o}. Because the stresses were concentrated over a small area, the fringe

orders were determined to $\pm$ ½ of a fringe and this was found to be satisfactory. At high applied loads, sometimes it was not possible to count the exact fringe order at the top of the central crack. In such cases, the fringes were approximated from the edge stresses. The photographs of the fringes of some of the model beams are shown in Figures 7.11 to 7.20.

7.11 Utilisation of photoelastic data

7.11.1 Construction of stress trajectories

The stress trajectories were drawn directly from the isoclinic lines. The isoclinics of different parameters were cut by the short lines drawn at appropriate angles from the horizontal axis and thereafter the lines of principal stress were sketched in so as to be tangential to these short lines. The stress trajectories of some beams are shown in Figures 7.21 and 7.22. Diagonal thrust zone has shifted slightly up as the span to depth ratio of the beams increased.

7.11.2 Calculation of individual stresses

There are several methods for the calculation of separate principal stresses in a stressed body from the data obtained by photoelasticity. All the methods are based on the equations of equilibrium. In general, the accuracy of these methods depends upon the accuracy of the measured optical data and the values derived from them. The reader is referred to textbooks by Kuske and Robertson (1977) and Frocth (1948). In order to minimise experimental errors it was decided to separate principal stresses by the numerical solution of Laplace's equation.

7.11.2.1 Calculation of the sum of the principal stresses

The sum of the principal stresses at all points in an elastic plate in equilibrium under two-dimensional stress system obeys Laplace's differential equation:

$$\frac{d^2 (\sigma_1 + \sigma_3)}{dx^2} + \frac{d^2 (\sigma_1 + \sigma_3)}{dy^2} = 0$$

Thus from the fringe pattern alone, if the sum of the principal stresses at all points on the edge of the stressed beams becomes available, the sum of the principal stresses at all points within the beams can be found with the aid of this rule without taking recourse to any other expcriment.

In a stressed body, where there is a free boundary one of the principal stresses is zero, so that the edge stresses are equal to the boundary values of $(\sigma_1 + \sigma_3)$. On a boundary subjected to normal distribution of load of known value, the sum of the principal stresses can also be calculated by using the formula:

$$(\sigma_1 + \sigma_3) = (\sigma_1 - \sigma_3) + 2p,$$

where p is the intensity of the load (load per unit thickness).

In a numerical solution of Laplace's equation, the first step is to prepare a coarse network of square lines covering the surface of the model. Then the sum of the principal stresses are calculated at every point along the

free edges of the model. Thereafter, initial values of $(\sigma_1 + \sigma_3)$ are assigned to each intersection of the network. Then every value is iterated until sufficient accuracy is obtained using the well-known Liebman's equation:

$$\varepsilon_o = \frac{\sigma_1 + \sigma_2 + \sigma_3 + \sigma_4}{4}$$

This formula is inferred from the fact that in a stressed body the value of $(\sigma_1 + \sigma_3)$ at any point must be the mean of the quantities at four equidistant nearby points. The interaction process is sometimes called 'Harmonisation'. In this way, although the arithmetical work may be considerable, it is simple and by no means prohibitive. Nair et al.(1964) used a 4-point influence equation and utilised a computer in his interpretation of the photoelastic data.

The application of a computer was not attempted in this study mainly for two reasons: firstly, all the methods of separations give correct results when the stresses in a body do not change abruptly. However, as will be elaborated in the following sections (and as illustrated in the isochromatic fringe photographs in Figures 7.11 to 7.19), the principal stresses change magnitude and sign in a relatively small region around the central crack. Secondly, probably a fault in the loading mechanism caused unintentional stresses around the bottom corner of the abutment crack. For these reasons, only the mid-quarter of the beams were subject to the analysis of each principal stress and iteration was carried out with a pocket calculator until reasonable approximation was achieved.

7.11.2.2 Calculation of individual principal stresses

Using the difference and the sum of the principal stresses each principal stress was calculated at every point on the network. The separate principal stresses can be seen in Figures 7.23 and 7.24. Figure 7.38 shows the effect of increasing transverse load on the major principal stresses along the upper edge of the beams.

7.11.2.3 Calculation of shear stresses

Having obtained each principal stress and the directions of the principal stresses, the shearing stresses at every point throughout the model beam were calculated using the equation:

$$\tau_{xy} = \frac{\sigma_1 - \sigma_3}{2} \text{ Sin } 2\theta$$

7.11.3 Effective shear stresses in the beam

Maximum shear stress occurs on planes which make angles of 45^{o} with the major principal stress. Since one principal stress is zero at the boundary of the beams, the shear stress will be maximum at the upper edge of the beams around the central crack and will decrease away from the edge.

However, fracturing is not likely to take place along the planes in which shear stresses are maximum, but along the planes of maximum effective shear stress. These planes make angles of $45^{o} - \phi/_{2}$ with the major principal stresses (ϕ is the angle of internal friction). Thus effective shear stresses, τ_{ef}, can be calculated from the equation below (Woodruff 1966).

$$\tau_{ef} = \frac{\sigma_1 - \sigma_3}{2} \text{ Sin } (45^o - \phi/_2)$$

Taking the angle of internal friction as 50^o (Smethurst 1975), effective shear contours can be constructed, as shown in Figure 7.25. It can be seen that the likely failure planes are similar to those of actual failure planes (Figures 7.26 and 7.27) (Watson 1979).

7.12 Discussion of Results

7.12.1 Transformation of photoelastic results to the prototype

From the equations of equilibrium and compatibility it can be inferred that the distribution of stress in the elastic state is independent of the magnitude of the loads and the scale of the model. In two-dimensional problems it is also independent of the elastic constants if the body forces are zero or uniform. On this basis, the photoelastic material, the scale of the model and the magnitude of the load may be chosen as convenient, provided that the model and the prototype are geometrically similar and the type of loading is the same for both. The model results can then be transferred to the prototype following the laws of similarity. If $\gamma_m = \gamma_p$:

$$\sigma_p = \sigma_m \left(\frac{d_m}{d_p}\right) \left(\frac{t_m}{t_p}\right) \left(\frac{p_p}{p_m}\right)$$

where γ is unit weight,

d is linear dimension,

t is thickness,

p is load and

σ is stress, and

m and p stand for model and prototype respectively.

7.12.2 Fringe patterns obtained

The fringe patterns of all models undoubtedly indicate that the difference in principal stresses and hence the shear stresses are maximum at the top of the cnetral crack and at the bottom of the abutment cracks (Figures 7.11 to 7.19). An interesting observation, which may be better seen in Figures 7.13 and 7.18, is that in all cases there was a zero order fringe in each photoelastic member. In Figures 7.13 and 7.18 these zero order fringes can be distinguished from their distinct locations and shapes (rather like two bent lines) from the well known pressure bubbles in the upper corner of the central crack. In fact, these lines are made literally of a number of singular points (i.e. the points where σ_1 and σ_3 are zero), and they separate a pure radial tension zone from a pure radial compression zone. Hence they can be called 'the neutral axis' of the beams. Since this finding is fundamentally new in linear arch concept, it will be discussed fully, with its justifications, in the following subsections.

As the transverse load is increased on the beams, the fringes move towards the interior of each member and at a certain load, the outer fringes (that is, the first order fringes) approach each other. It is obvious from the fringe patterns that there is a compression zone acting like a diagonal compression member in each beam.

At the lower part of the abutment crack an unexpected, but irrelevant fringe was generated (Figure 7.11). This was caused, most probably by the resistance against straining of the lower section of the beams which had been bonded to the steel loading pieces by the induced axial thrust at the abutment. If this was disregarded, the fringes appeared more rounded in nature, compared to those at the centre. It was

also clear that the resultant thrust was acting approximately at an angle of 45^{o} to the horizontal axis of the beam at the abutment crack. However, it was almost horizontal at the central crack (Figure 7.11).

As the span to depth ratio of the beams was increased, the stress concentration at the abutment and central cracks increased also. When the stress concentration factor K ($K = \sigma_{induced}/\sigma_{applied}$) is regressed against span to depth ratio of the beams ($S_{/D}$), the equation below is obtained with an Index of Determination of 0.999 (Figure 7.28).

$$K = \frac{(S_{/D})}{0.1426212 - 0.0063993\ (S_{/D})}$$

Hence it may be inferred that for beams having a span to depth ratio of approximately 22, the induced stress attains infinitely high values. It must be remembered that the above equation is derived from the test results of the beams with span to depth ratios ranging from 2.66 to 8 and with a transverse stress of 0.37 MPa in the absence of pre-axial thrust.

Wright and Mirza (1963) give a linear relationship between stress concentration factor and depth to span ratios from $^{1}/3$ to $^{1}/6$ as:

$$\frac{\sigma_{max}}{W} = 159.3 - 427.7\ (D_{/S})$$

The difference between results obtained from both equations above for the span to depth ratios tested can be attributed to the variations in the applied transverse loads and the materials used.

The fringe patterns did not change substantially their forms as the span to depth ratio is altered from 2.66 to 8.00 at the loading ranges employed, though there was a slight shifting of the fringes at mid-span upwards and a slight widening of the tension region, i.e. the neutral axis moved upwards (Figures 7.7 to 7.10).

Since cracked beams deform elastically further when the transverse load is enhanced, the effective contact area between the two members of the linear arch also increased. This in turn caused a reduction in rate of increase in the induced stress at the mid-span crack with increasing applied transverse stress (Figure 7.29). For the photoelastic beams having a span to depth ratio of 5.33 and for applied stresses from 0.17 MPa to 0.37 MPa, the relationship was in the form of a power law:

$$\sigma_{induced} = 11.5841987\ (\sigma_{applied})^{0.8348832}$$

I.D. = 0.990.

This type of behaviour is also recorded between induced axial thrust and transverse stress by Watson (1979) on actual gypsum beams.

In an attempt to achieve uniform compressive stresses at the upper corners of the central cracks, beams having a span to depth ratio of 4 were tapered from their corners and tested with some pre-axial load. At a certain applied transverse load (45lb), a reasonably uniform pure compressive stress was obtained over the full contact area (Figure 7.19). As soon as the load was increased, fringes swiftly drifted to the upper corner, as previously observed.

Distribution of stresses at different sections of a beam including the contact area is shown in Figure 7.30. It is clear that distribution of stresses across the contact length was not in the form of a triangle, but may be approximated with a triangular shape for engineering purposes, as suggested also by Wright and Mirza (1963).

7.12.3 Isoclinics obtained

Isoclinics of the photoelastic models are shown in Figures 7.7 to 7.10. It can be noticed that the isoclinic of zero parameter and some sections of the isoclinics of other parameters pass through the same line (i.e. the same line as the isochromatic fringe of zero order and, as previously named, 'the neutral axis'), around the upper section of the mid-crack. Since, through singular points, isoclinics of many parameters may pass and since singular points located on free boundaries usually represent a transition from compression to tension (Frocth 1948), it is obvious that there is a tension zone in the beams examined. In fact, stress trajectories constructed using isoclinic lines, also provide support for this conjecture. Stress trajectories in Figures 7.21 and 7.22 show the direction of the principal stresses acting in the photoelastic members, as well as their signs.

Increasing the span to depth ratio also shifts up the position of isoclinics slightly but the general pattern remains the same.

7.12.4 Principal Stresses

The maximum and minimum principal stresses, in terms of fringe order, for photoelastic model beams having a span to depth ratio of 4 are given in Figures 7.23 and 7.24. Since along a free boundary one of the principal stresses vanishes, the other principal stress parallel to the upper edge of the beams attains maximum value at the top fibres of the beams around the central crack, and these are compressive in nature.

As can be seen both principal stresses become zero along the neutral axis and these attain tensile values below the neutral axis. The maximum tensile principal stress is found just below the point where the neutral axis intersects the central crack in the photelastic models. The magnitudes of the principal stresses in this region are comparatively smaller than those above the neutral axis. In general, the maximum compressive principal stress at the top fibres of the beams is four to five times the maximum tensile principal stress vertical to the horizontal axis of the linear arch underneath the neutral axis.

7.12.5 Contact area at mid-span crack

The contact area between the beams at the central crack was limited to a small portion of the total crack length. There is a tendency to increase as the transverse load is increased, but this is quite small in real terms, mainly because of the load range adopted. As measured from the fringe photographs, an average contact area of 15% of the total crack length is found at a stress level of 0.37 MPa.

This is slightly smaller than 18% which is given by Wright and Mirza (1963). This is attributable to the stress levels applied.

7.13 Justification of the presence of tensile zone in the cracked beam

The discovery of a tensile zone in the linear arch as a result of photoelastic analysis carried out by the author is contradictory in concept to the previously accepted forms of stress distributions in the cracked roof beams. This, therefore, casts some doubt over the way in which the loading was implemented in the tests and over the interpretation of results obtained. For this reason, this concept requires elaboration.

Wright and Mirza (1963) simulated the linear arch photoelastically using kriston beams. The loading was achieved through eight holes drilled in the lower edge of the photoelastic beams and hanging weights from the bottom. They noted that stress free areas occurred in the outer top corners and in the lower section of the beams; they also noted tensile stresses in the lower sections of the beams. However, they attributed these tensile stresses purely to the body weight of the beams and they thought that, because the loading was carried out by hanging weights from the bottom, these stresses were largely magnified in the model tests.

Since the loading mechanism employed is basically similar to that used by Wright and Mirza, it is natural to expect that similar magnification in the magnitudes of the tensile stresses underneath the neutral axis noticed by the author. However, although some contribution due to the loading system cannot be ruled out completely, the loading mechanism alone cannot be held responsible for the larger proportion of

tensile stresses generated in this region. To prove this, photoelastic members having a span to depth ratio of 8 and 5.33 and without steel end pieces, were loaded by hand from the top (Figures 7.15, 7.16 and 7.17). As can be clearly seen in these figures, there are still fringes underneath the highly stressed region at the top section of the mid-span crack. It is noticable on comparison of Figures 7.16 and 7.17 with Figure 7.12 that the fringes in the tensile zone became more rounded in the case of hand loading from the top. This may be a consequence of eliminating tensile forces introduced by the pulling action from the lower edges of the beams. It is thus clear that, even if the beams are transversely loaded from the top, there are stresses in the lower section of the central crack and it may be misleading to name this area as a stress-free zone. It must be borne in mind that during the tests, no pre-axial thrust was present. It is an integral part of the linear arch mechanism and is likely to affect the stress distribution in the beams to a certain degree. This subject remains to be investigated in future experiments.

The lines referred, up to now, as 'neutral axis' can now be proved to be made of a number of singular points (i.e. where $\sigma_1=\sigma_3=0$). It is known that there are three cases in which black dots appeared in the photoelastic models:

(a) black points where $\sigma_1 - \sigma_3$ reaches a maximum value. These points may be present in the model for certain values of applied load and they are not permanent.

(b) black points where $\sigma_1 = \sigma_3 \neq 0$; these are called 'isotropic points'.

(c) black points where $\sigma_1 = \sigma_3 = 0$ and they are called 'singular points'.

The first case (a) can be easily eliminated as the black dots do not disappear when the load is altered (Figures 7.15 and 7.17). From the remaining two, case (b) can also be discarded, because, as can be seen in Figures 7.15 and 7.17, the black lines below the highly stressed region intersect a free boundary of the model where one of the principal stresses is bound to be zero and thus rendering $\sigma_1 = \sigma_3 = 0$. It is obvious also that along this line shear stress is equal to zero.

As a rule, if the directions of σ_1 and σ_3 stresses are known at one point in the body, then a simple inspection of the stress trajectories makes it possible to determine the signs of all free boundary stresses. It is seen in Figure 7.21 that trajectory abruptly changes its course along a zero degree isoclinic,hence this indicates that stresses change sign. Thus since it is certain that the stresses in the upper fibres of the beams are compressive, the stresses below the singular points must be tensile. The lines made of numerous singular points can, therefore, be called the 'neutral axis' of the beams along which $\sigma_1 = \sigma_3 = 0$ and also σ_1 and σ_3 change sign.

Further support comes from the fact that, when a singular point is found on a free boundary, the stresses are changed from compression to tension, or vice-versa. It is seen that the black line intersects the boundaries of the beam at two points (i.e. at the lower edge and at the mid-crack).

7.14 Appreciation of tensile stresses in the linear arch structure

The presence of tensile stresses in individual blocks of the linear arch have been pointed out implicitly by some of the previous researches investigating arching mechanisms of block-jointed rock masses.

Trollope (1966), examining the linear arch mechanism analytically and experimentally, noted that at the ends of the beams in the lower fibres (i.e. in the roof corners), a region of high compression field would develop which, in turn, would create high tensions in this zone. He attributes the spalling and flaking of rock surfaces as an indication of effective tensile stresses that are generated under applied high compressive stresses.

Goodman et al.(1968) also observed the occurrence of tensile stresses induced by the lateral thrust in beam block elements above the roof. They concluded that the opening of joints caused eccentric loading of joint blocks and led to the development of tension stresses.

Chappel (1974, 1975a, 1975b, 1975c, 1979a, 1979b) investigated extensively the stress distributions between the individual members making up the discontinuous media around the openings by means of photoelastic models comprised of a system of blocks where both the stresses and deformations were measured. He notes that, although the tensional stresses within the joints are impossible, this does not necessarily preclude the development of tensional stresses within individual blocks. The blocks which have loads imposed on them (Figure 7.31) will develop either tensile stresses or effective tensile strains. Effective tensile strain is a Poisson-type strain which is the tensile strain induced transversely in a body loaded uniaxially in compression (Brown and Trollope 1967).

In the case of Figures 7.31a and c, the effective tensile strain concept is evident and slabbing is possible. In the case of Figures7.31b and d tensile stresses were induced by a punching or 'digging in' action of continuous blocks as their tendency to rotate or slip is inhibited. Chappel (1979a) was able to postulate that the rupture of failure of the individual blocks is initiated by the induced tensile stresses or strains. The magnitude of these induced tensile stresses were found to be approximately one-tenth the maximum induced compressive stress which was also in agreement with Heymans' (1966) recommendation that the working stresses in the Voussoir beams be limited to one-tenth of that associated with the compressive strength of the rock.

The evidence presented above provides positive support to the view that the induced tensile stresses are present in the members of linear arch, as observed by the present author in the photoelastic models. It is important, however, to distinguish them from those obtained in the lower fibres of a continuous beam when transversely loaded.

In particular, induced tensile stresses may be of great importance when the linear arch is composed of three beam blocks. In this case, as was observed in the photoelastic models (Figure 7.32b) slabbing is likely to take place in the lower section of the central block. The presence of bedding planes and weakness zones in the roof augments the importance of induced tensile stresses.

7.15 Sources of tensile stresses in the linear arch

It is now possible to examine the occurrence of tensile stresses underneath the compressed region at the top of the central crack of the linear arch in an explicit manner.

When a semi-infinite rectangular photoelastic material is loaded with a concentrated load acting vertically at a point along the centroid of the section, as in Figure 7.33a, the stresses induced in the material are pure radial compression and the isochromatic fringes form a system of concentric circles which are tangent to the upper edge at the point of application of the load, as depicted in Figure 7.33a.

If the position of the vertical concentrated load is changed along the upper edge relative to the axis of symmetry, say to a distance of d from the axis, as in Figure 7.33b, the fringe patterns are substantially altered. In fact, two distinct semi-circular fringe sets, which are similar to those obtained in the photoelastic models of the linear arch around the top of the central crack, are generated. The circles in front of the load represent loci of radial compression and those at the side of them are loci of equal radial tension. The line dividing the two zones is the 'neutral axis' along which radial stresses are zero. As marked in Figure 7.33b, the photoelastic layers in front of the load are compressed, while those at the side of the load are stretched. Therefore, as the eccentricity of load (e) is increased, tensional stresses are created. It is obvious that the highest tensile stress occurs when the load acts at the tip of the material.

Frocth (1948), Lancaster et al.(1980) give excellent examples of photoelastic analysis of various loading conditions and equations

derived with elastic theory so that radial and tangential stresses can be theoretically calculated (Figure 7.33b).

Till now, only the eccentricity of a concentrated load acting vertically on the edge of a semi-infinite plate has been examined with respect to the generated tensile stresses. However, the direction of the load is also important in the generation of tensile stresses. In Figure 7.34b it can be seen that the concentrated load is acting at the tip of the plate with an angle of 45^{o} from the vertical direction. In this case, all the stresses induced in the corner of the plate are in pure radial compression and tensile stresses have completely disappeared.

It can be concluded, therefore, that there are two factors which effectively control the generation of tensile stresses as well as the magnitude of tensile stresses in a semi-infinite square plate loaded with a concentrated load; these are:

(a) eccentricity of the load; and

(b) direction of the load.

On the other hand, based on the similarity between the fringe patterns obtained in the central section of the model beams tested and those of a semi-infinite rectangular plate loaded at its corner vertically with a concentrated load, it can be deduced that the two factors above are also valid for the case of a photoelastic model of linear arch. It was found in the previous sections that the effective contact area through which horizontal thrust was acting was limited to a very small proportion of the total crack area (Author: 15% of total; Wright and Mirza: 18% of total), and the stress distribution could be approximated

with a triangular form. Hence the resultant thrust can be safely assumed to be acting almost at the tip of the individual beams (at a distance of approximately 5% of the total crack depth from the top fibres of the beam). It is thus this eccentricity that is largely responsible for the development of high tensile stresses just below the neutral axis.

It was found that the direction of the resultant thrust acting at the central crack was not horizontal but slightly inclined. This was deduced from the fact that, if the resultant thrust were acting strictly normal to the plane of vertical crack, the angle between the neutral axis and the horizontal edge of the beam should be $57^{o}30'$ (Frocht 1948) (see Appendix 7.1). However, the measured angle from the fringe photographs is approximately $61^{o}50'$.

It is clear, therefore, that the development and the magnitude of tensile stresses around the central crack below a compression zone are markedly related to a combination of high eccentricity, direction of the resultant thrust relative to the axis of beams, and the magnitude of resultant thrust.

Since eccentricity is naturally expected to be higher in the beams having small span to depth ratios than in beams having relatively high span to depth ratios, assuming that the percentage of effective contact area is the same for both cases, the beams with low span to depth ratios are more likely to fail in tension than those with high span to depth ratios. In fact, experimental evidence (Wright 1972; Smethurst 1975; Watson 1979) appears to comply with this hypothesis.

7.16 Eccentrically loaded beams

It seems prudent to assume that the change in the form of individual block failure from corner crushing to axial failure approximately at a span to depth ratio of 7, as noted by Smethurst (1975) and Watson (1979), is associated with relatively high eccentricity and hence with the induced tensile stresses below a compression zone.

From photoelastic observations, it is obvious that the ratio between maximum compressive stress and maximum tensile stress at a given transverse load increases with an increase in the span to depth ratio, indicating that with slender beams compressive stresses, and hence shear stresses, at the outer fibres are predominant, whereas for beams with smaller span to depth ratios, the tensile effect is more pronounced. Yet very little is known about the combined effect of eccentricity and the span to depth ratios on the load-bearing capacity of rocks which are often very weak in tension.

On this basis, a limited experimental programme was carried out to see whether eccentric loading could cause a change in failure mode of gypsum beams with different span to depth ratios.

Three gypsum beams with span to depth ratios of 6.04, 7.95, and 10.10 (Table 7.3) were loaded between the steel platens of a hydraulic machine in such a manner that the angle between the specimen end and the steel platen was approximately 5^{o} in all three cases (i.e. the direction of applied eccentric load was constant relative to the edges of the specimen in all cases) (Figure 7.35a). The broken specimens are shown in Figure 7.36.

The specimen with a span to depth ratio of 6.04 failed along an axial plane, whereas the specimens with span to depth ratios of 7.95 and 10.10 failed by crushing at their corners. It is obvious, therefore, that the change in failure mode as observed on numerous samples by Watson (1979) is largely related to eccentric loading hence to induced tensile stresses. It is also interesting to note that the failure types are very similar to those obtained by Watson (1979) (Figures 7.26 and 7.27) who used large-scale gypsum beams.

In a further set of experiments with three beams having span to depth ratios of 4.03, 7.95 and 10.10 (Table 7.3), the combined effect of eccentricity and the direction was examined utilising a shear testing apparatus (Figure 7.35b). Gypsum beams were placed in the apparatus (as illustrated in Figure 7.35b) and then the top platen of the hydraulic machine was brought into contact with the upper edge of the specimen. Loading was carried out by using a hand pump which forced the bottom steel platen to slide over the rollers, as indicated in Figure 7.35b. Since specimen ends were inhibited from sliding, induced axial thrust was recorded from the load indicator of the hydraulic machine. The beam with span to depth ratio of 4.03 failed axially but the other by crushing at their corners, as expected (Figure 7.37).

It would appear that the change in failure mode of eccentrically loaded beams is governed by the degree of eccentricity which is a function of the span to depth ratio of the beam and hence most likely by the magnitude of the induced tensile stresses.

7.17 Sources of errors

As with all experiments, a number of errors were encountered during experiments. Some sources of error were known and all possible remedial measures were employed, but other errors were inherent in the experimental technique and hence were unavoidable. In this subsection, all possible types of errors are discussed and the extent to which the accuracy of the results may have been affected by the errors is evaluated.

7.17.1 Errors due to experimental technique

The experimental procedure involve analysis of stress distribution from the isochromatic fringe pattern and the isoclinic lines. The accuracy of the results were limited, therefore, by the accuracy of the precise positions of the fringe lines and the isoclinic lines. Neither the fringes nor the isoclines appear as sharp, fine lines, but as wide, dark and sometimes hazy lines across the photoelastic models.

In order to determine the separate principal stresses, the method of mathematically solving the Laplace differential equation was adopted. The reason for this was to avoid the introduction of further possible experimental errors. This method, along with others, is reasonably accurate where the stresses do not change rapidly. Due to an erroneous fringe around the lower section of the abutment crack, and to rapid change in the stresses around the top section of the central crack, a full analysis of the model face was not attempted.

At highly stressed zones, it was sometimes difficult to determine the maximum fringe order exactly, due to excessive concentration of fringes. Whenever this situation arose either a magnifier was used or extrapolation from the edge stresses was made.

7.17.2 Errors due to loading arrangement

The loading arrangement designed had inherent drawbacks. Firstly, the photoelastic members were loaded with a tensile load to simulate the body forces of an actual arch. This inevitably introduced tensile stresses to the material sometimes in unknown quantities because of the deflection of the beams. Secondly, by loading the lower edges of the beams to the perfectly flat ends of steel pieces, a restraint at the lower edges of the beams in the horizontal direction was applied. This, in turn, created an unintentional fringe around the lower corner of the abutment crack.

It is possible also that an unknown amount of shear stresses were induced along the lower edges of the beams by the steel pieces as a result of elastic deflection of the beams during loading.

7.17.3 Errors due to photoelastic material

Despite the fact that careful attention was given to the selection of parts of plates without initial anisotropy and that very low feed was allowed to the machine tool in order to avoid machining stresses, some initial stresses were still present in the models. This was evident by the fact that the fringe lines in some models tended to deviate from regular shapes. Machining stresses are always compressive at the edges and may cause slight distortions along the boundary.

Unfortunately, the model beams had to be kept 24 hours to allow the adhesive to set. Therefore, time-edge effect took place to a certain extent. This manifested itself in the folded fringes on the compression side and by flattened fringes on the tension side.

7.18 Conclusions

Photoelastic modelling of linear arches has highlighted many points which may be of practical importance in appreciation of the linear arch mechanism. It should be borne in mind that test results should be considered to be valid for the elastic range of deformational behaviour of a linear arch structure. The results are summarised below:

(1) The highest compressive stress occurred at the top fibres of the beam block around the central crack, and radial and tangential stresses were compressive around the contact area. In each beam block an approximately diagonal compression zone is present.

(2) The effective contact length between the two beam blocks was about 15% of the total crack length and there was a tendency to increase as the transverse load was increased.

(3) The stress distribution at the contact length was not triangular but may be approximated with a triangular distribution for practical purposes.

(4) Maximum compressive stress at the upper fibres of the beams around the mid-span crack increased hyperbolically with increased span to depth ratio of the beams.

(5) An increase in the span to depth ratio did not alter the fringe pattern substantially but a slight upward shifting was noticable.

(6) The relationship found between the stress concentration at the top fibres around the mid-span crack and the applied transverse load is a power relation which yielded slightly better fit than a linear one. This is related to increasing contact area as load increased.

(7) At the lower section of the mid-span crack a tension zone is present. The highest vertical tensile stress occured along the vertical edge of the mid-span crack, just below the neutral axis and may be as much as one-fourth of the maximum compressive stress at the top fibres for beams with low span to depth ratios. It is likely that change of failure mode of beam blocks from corner crushing to axial failure, as observed by previous investigators, was largely governed by eccentricity and thus by induced tensile stresses.

In future experiments for the photoelastic study of a cracked roof beam, it is recommended that centrifugal testing apparatus, possibly similar to those used by Panek (1952) and Wang et al.(1967), should be employed. The equipment should have facilities for pre-axial thrust and should enable the beams to be loaded to failure, so that failure modes can be correlated with the distribution of stresses in the beams. Because stresses change sign and magnitude over a relatively small area, it is essential to employ an experimental technique for the resolution of principal stresses.

* * *

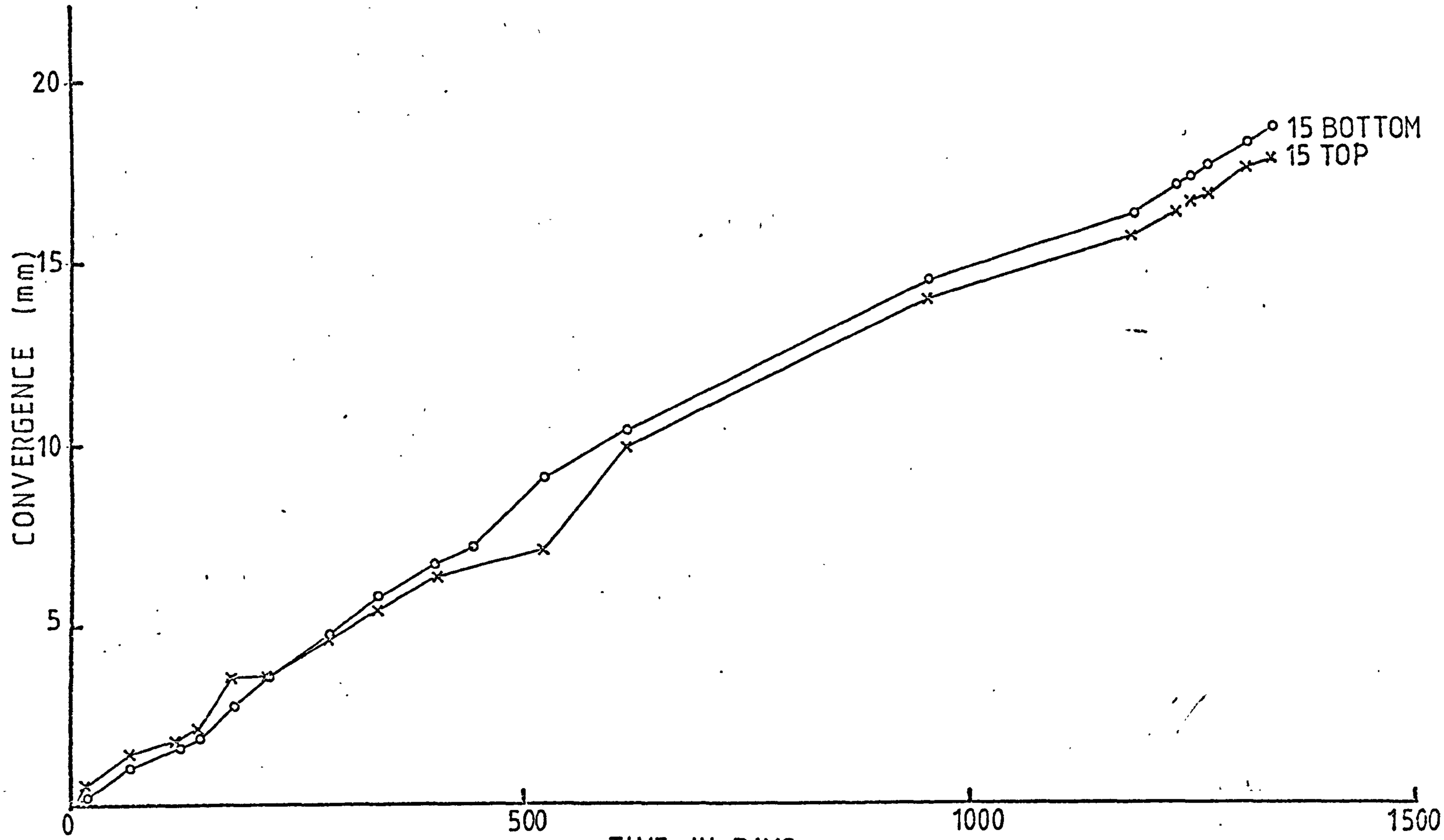

[26.11.1971]

FIG 7.1 CONVERGENCE RESULTS FOR LOCATION 8 NORTH - 6 EAST INTERACTION

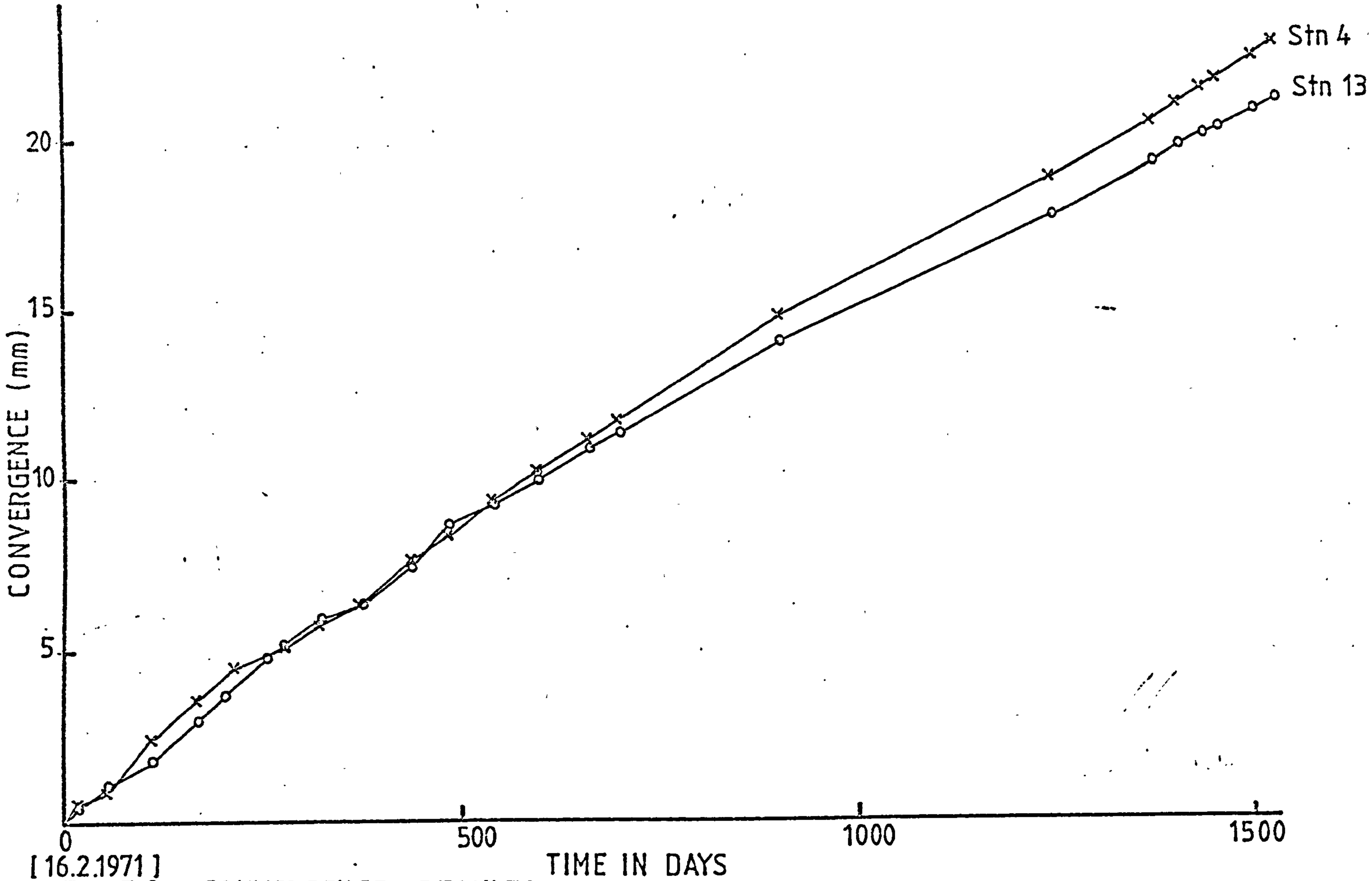

[16.2.1971]

FIG 7.2 CONVERGENCE RESULTS

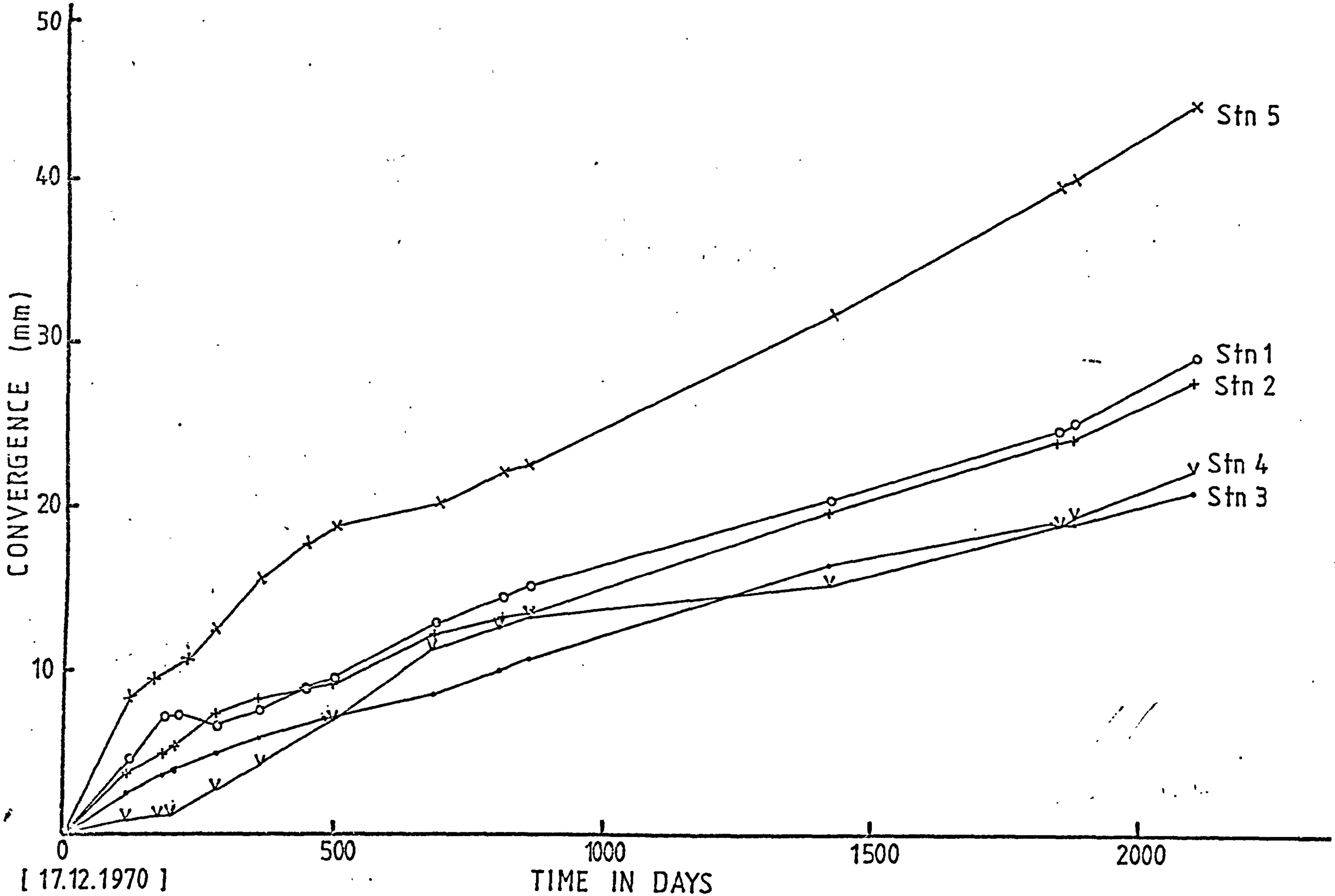

[17.12.1970]

FIG 7.3 CONVERGENCE RESULTS FOR MACHINE DRIVEN HEADING 7E / 9 - 11 S

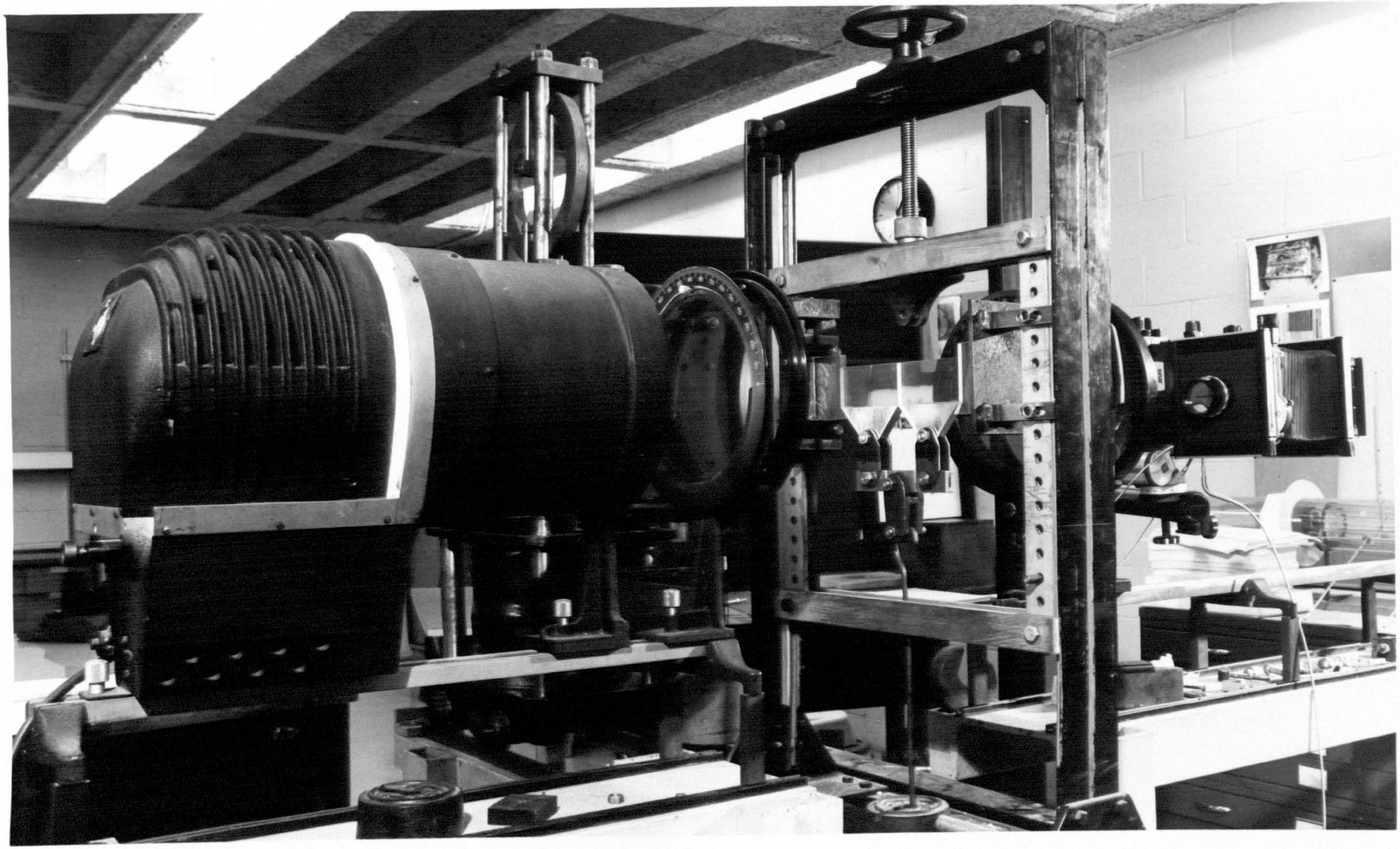

FIG 7.4 Photoelastic set-up

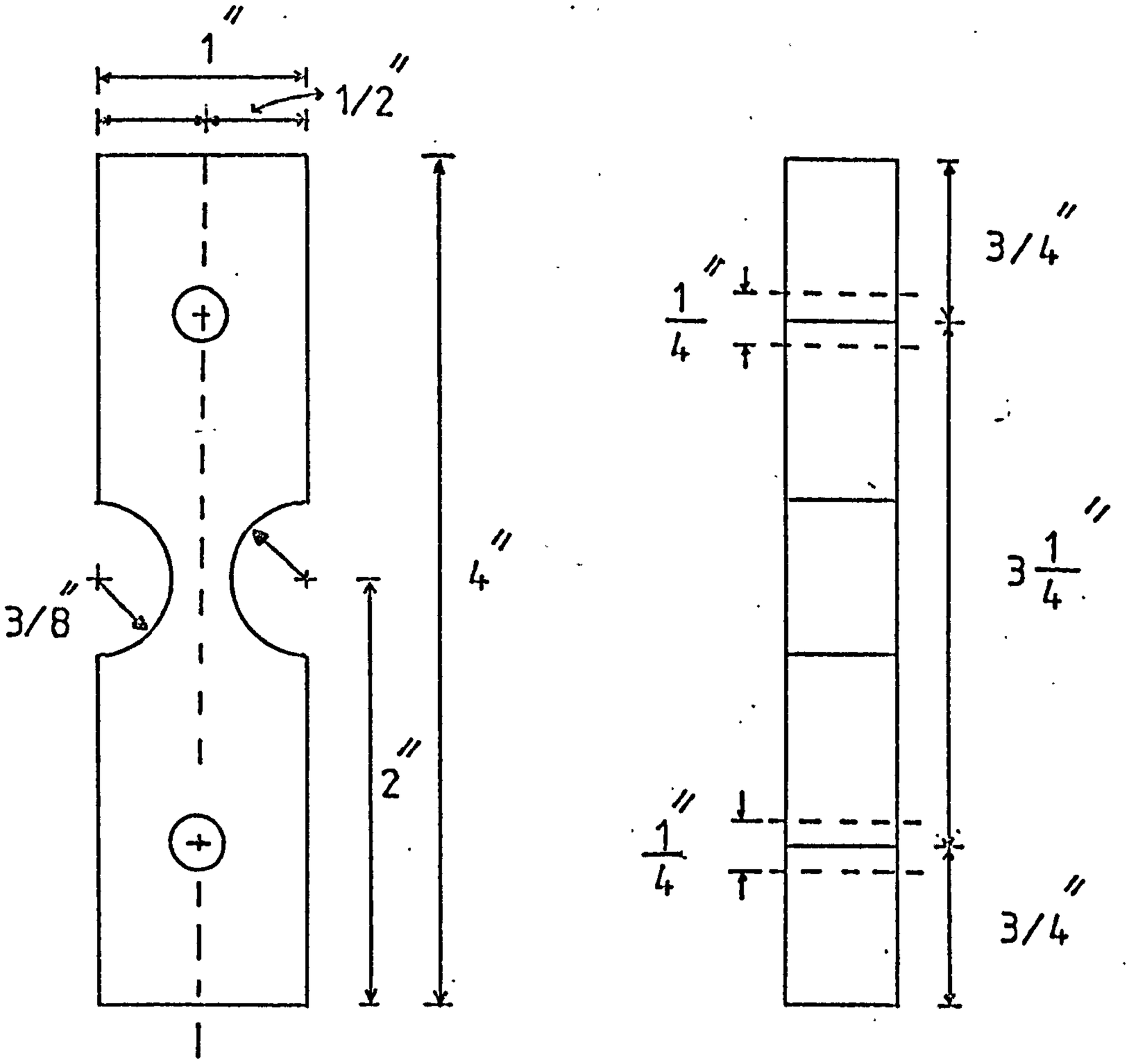

FIG 7.5 Calibration specimen

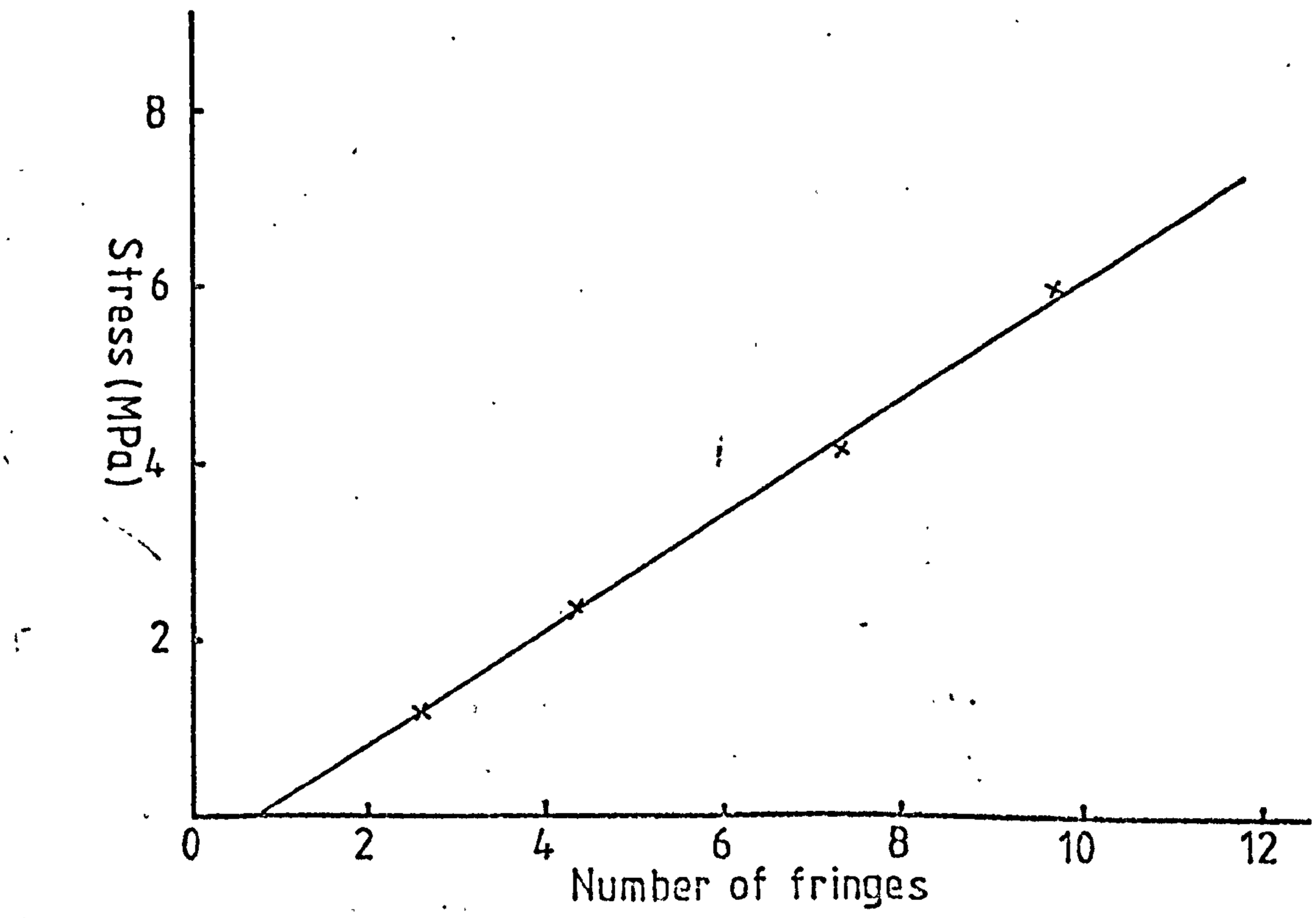

FIG 7.6 Calibration test

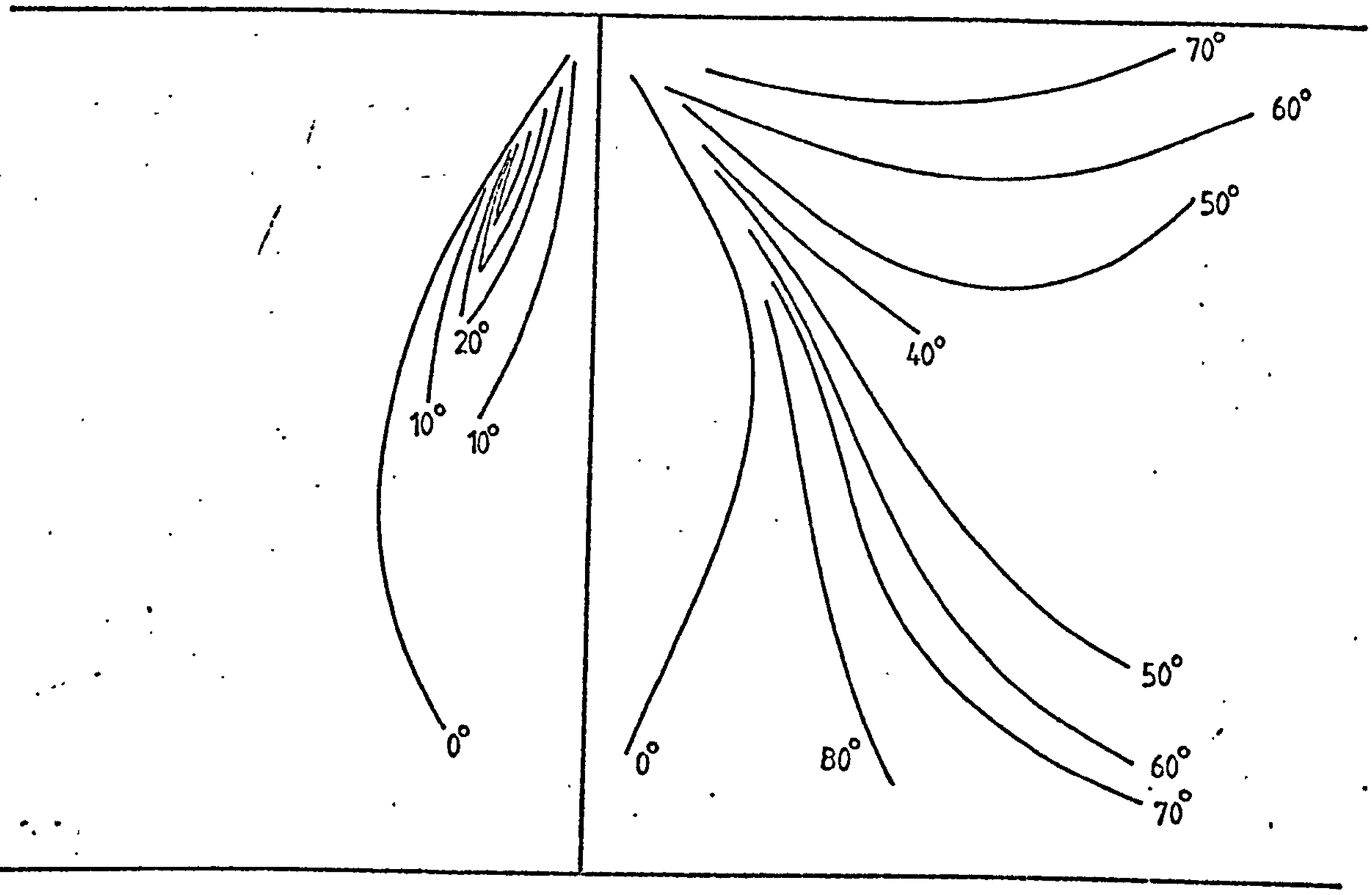

FIG 7.7 ISOCLINICS (S/D = 2.66)

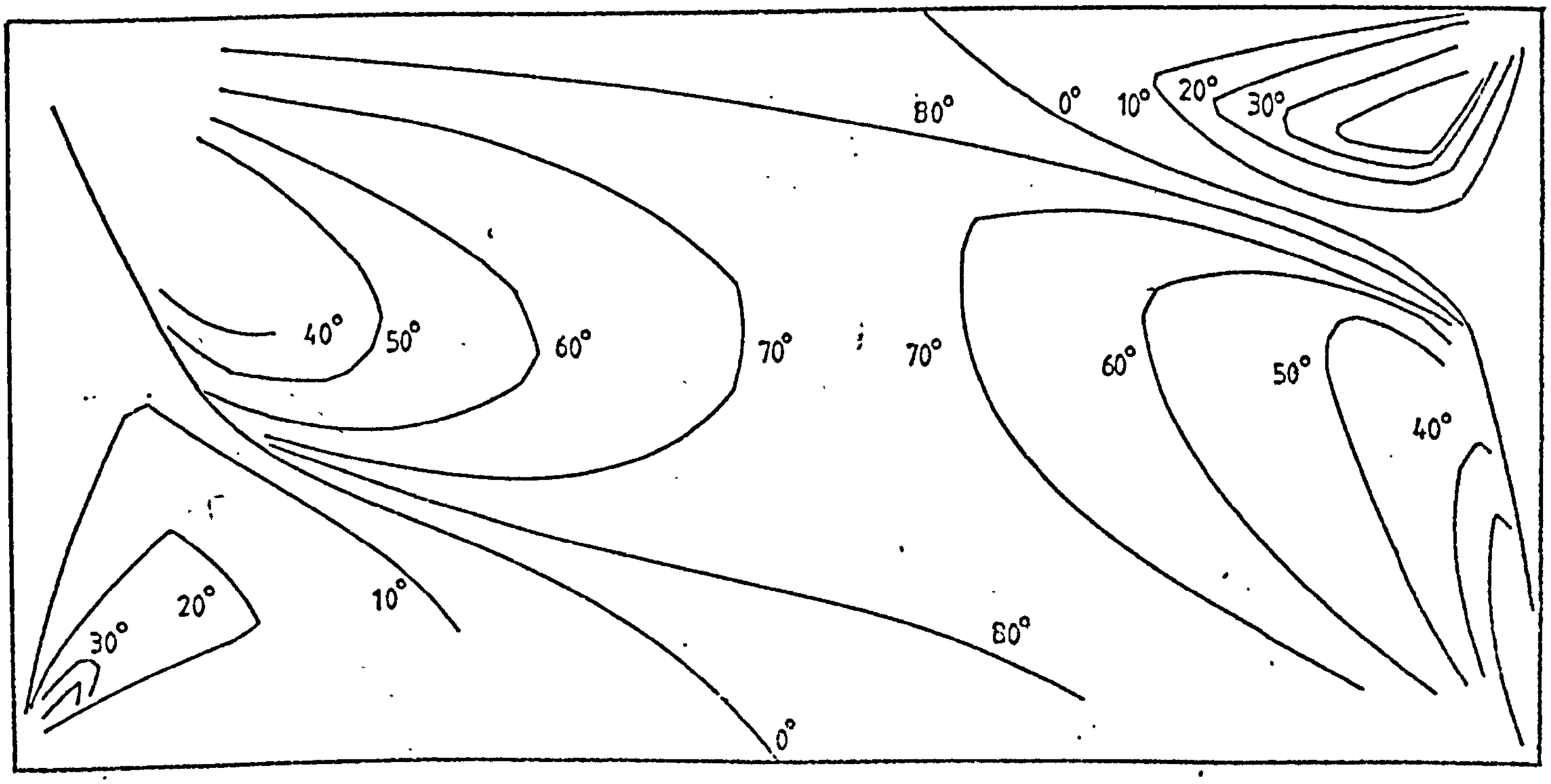

FIG 7.8 ISOCLINICS (S/D = 4)

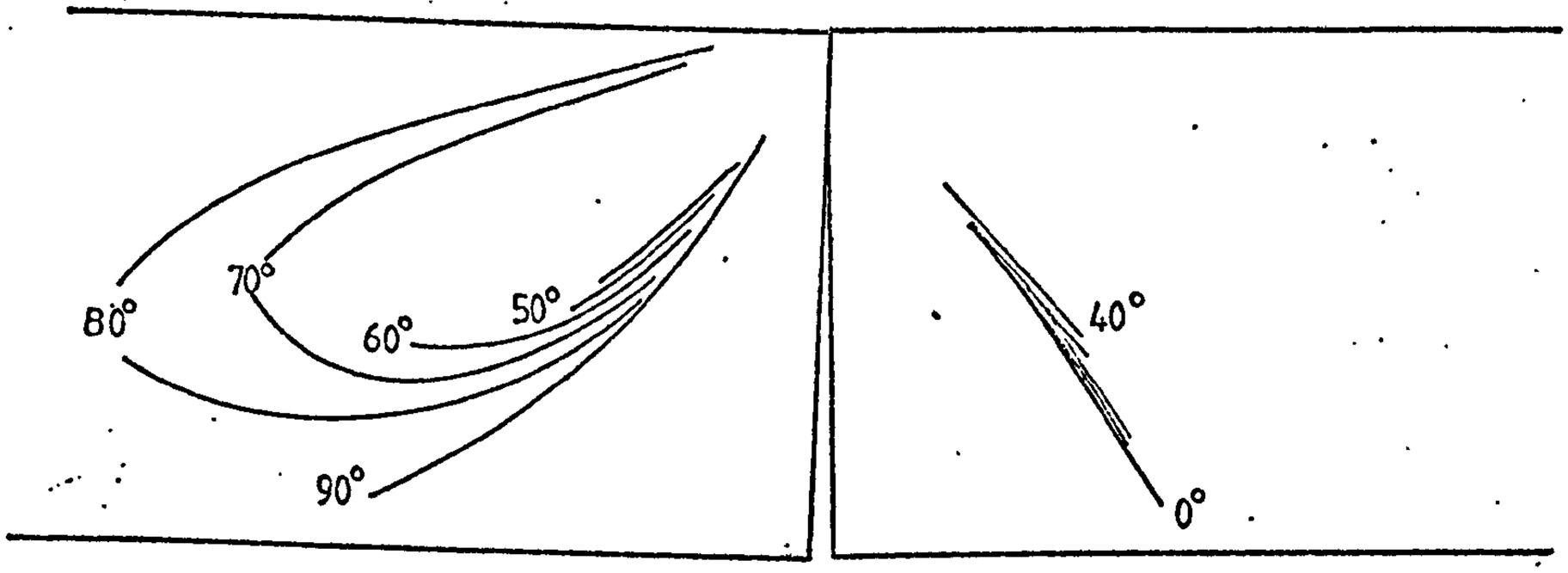

FIG 7.9 ISOCLINICS (S/D = 5.33)

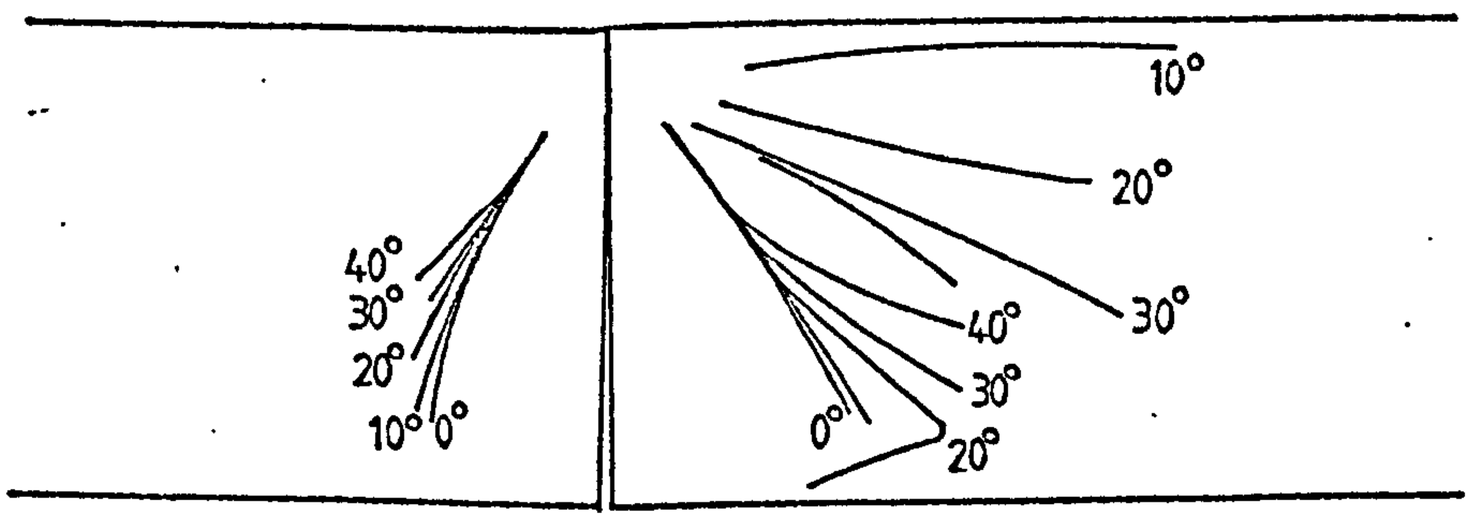

FIG 7.10 ISOCLINICS (S/D = 8)

FIG 7.11 Fringe pattern, S/D = 4

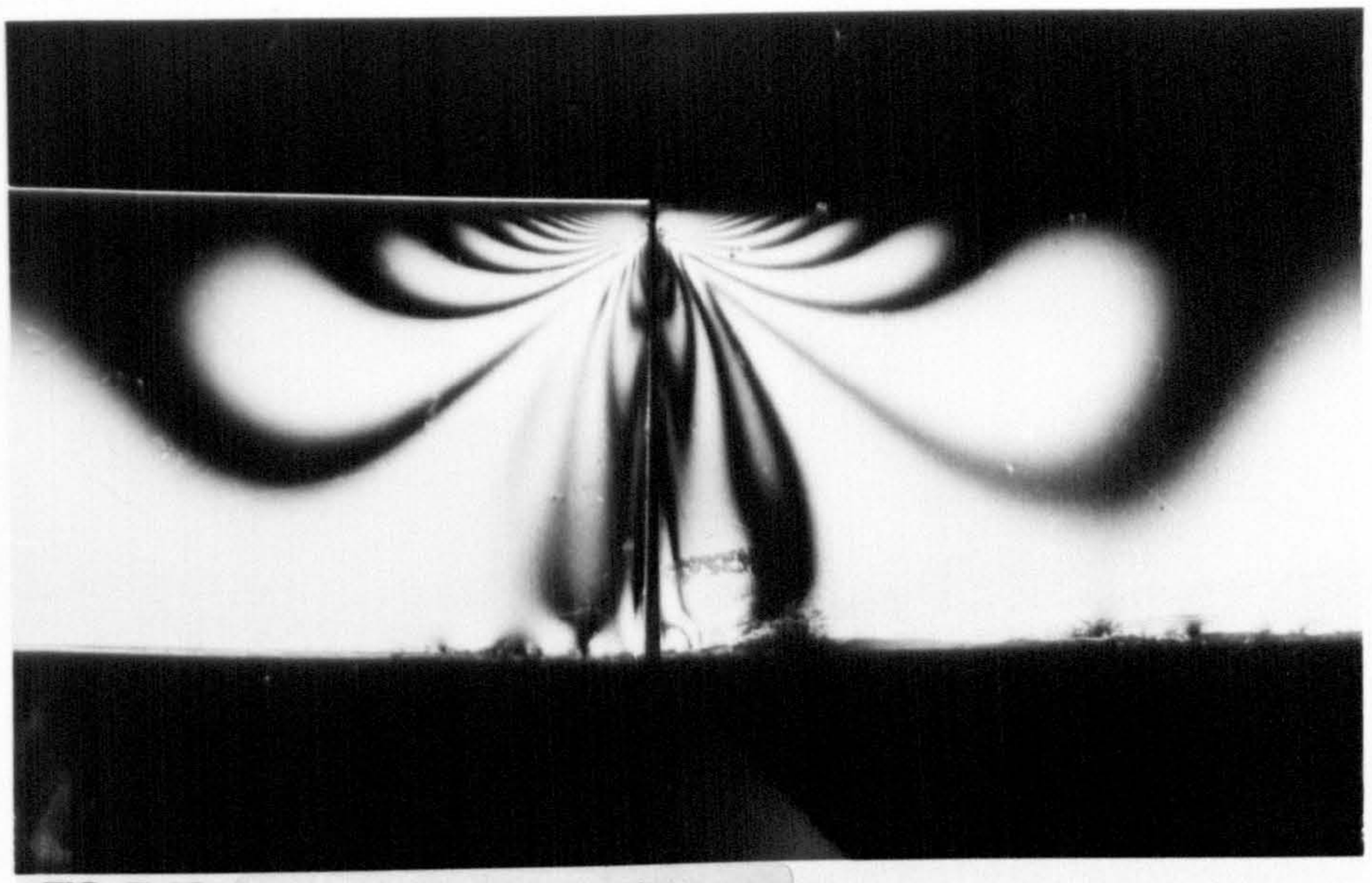

FIG. 7.12 Fringes (S/D=8)

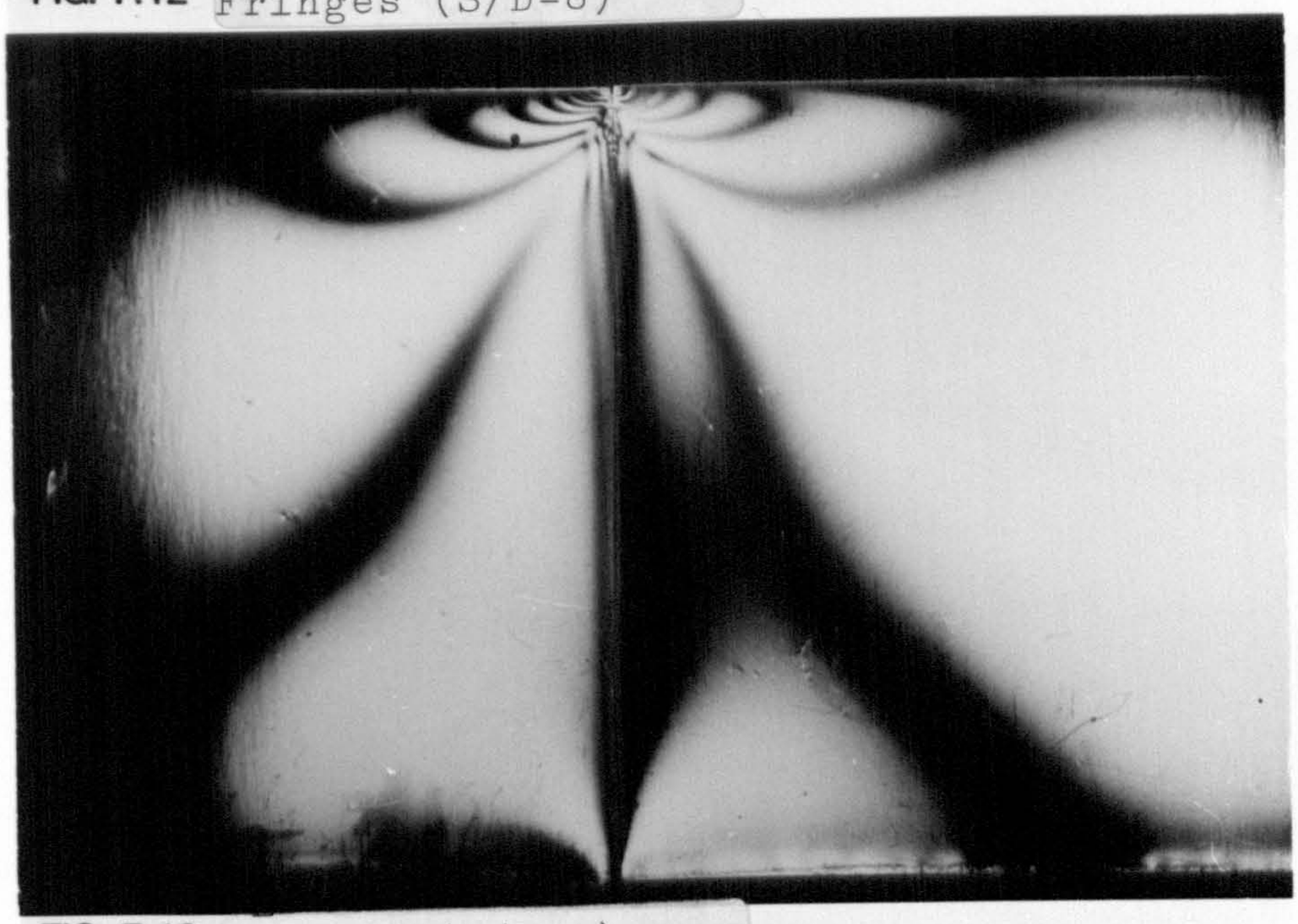

FIG. 7.13 Fringes (S/D=4)

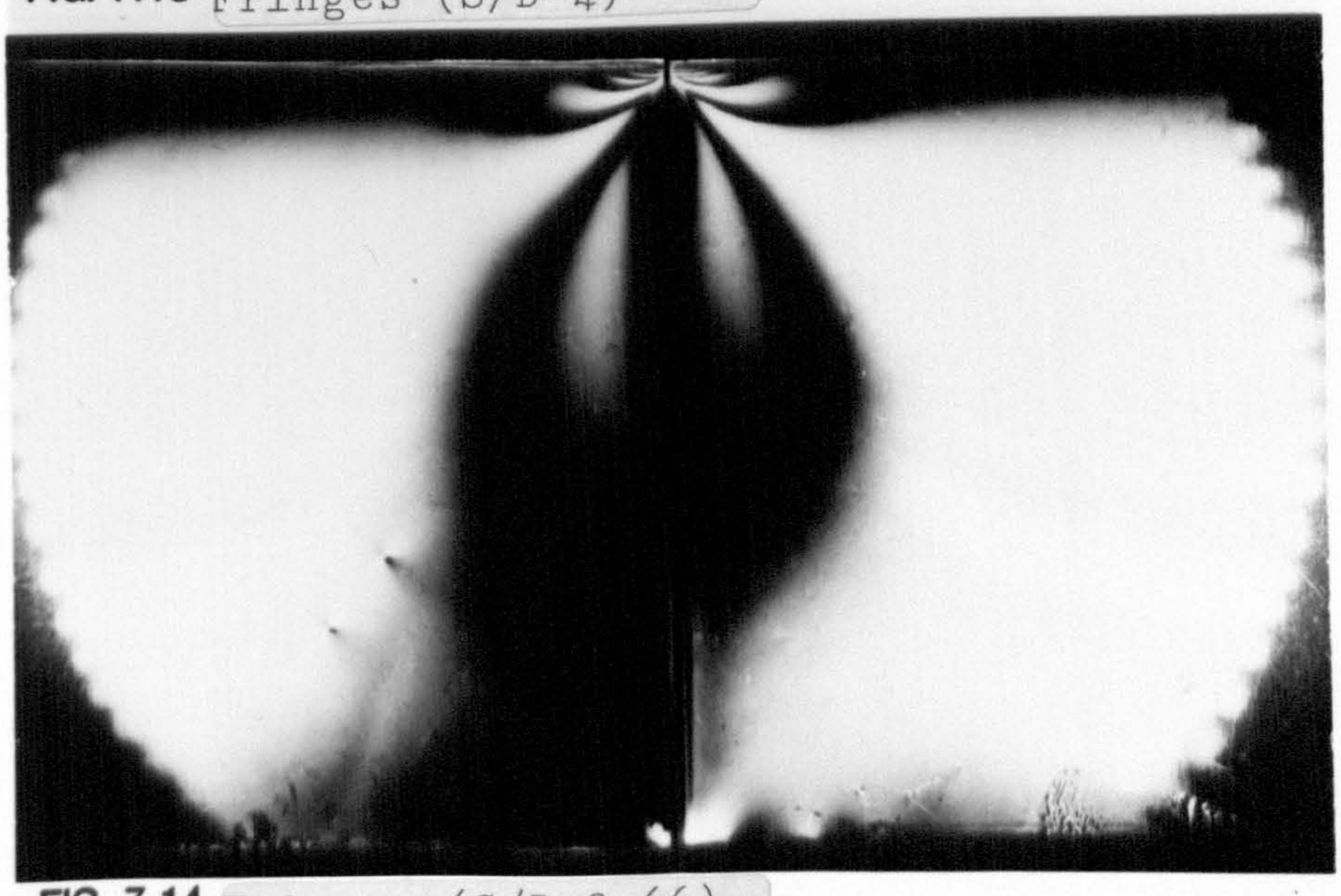

FIG. 7.14 Fringes (S/D=2.66)

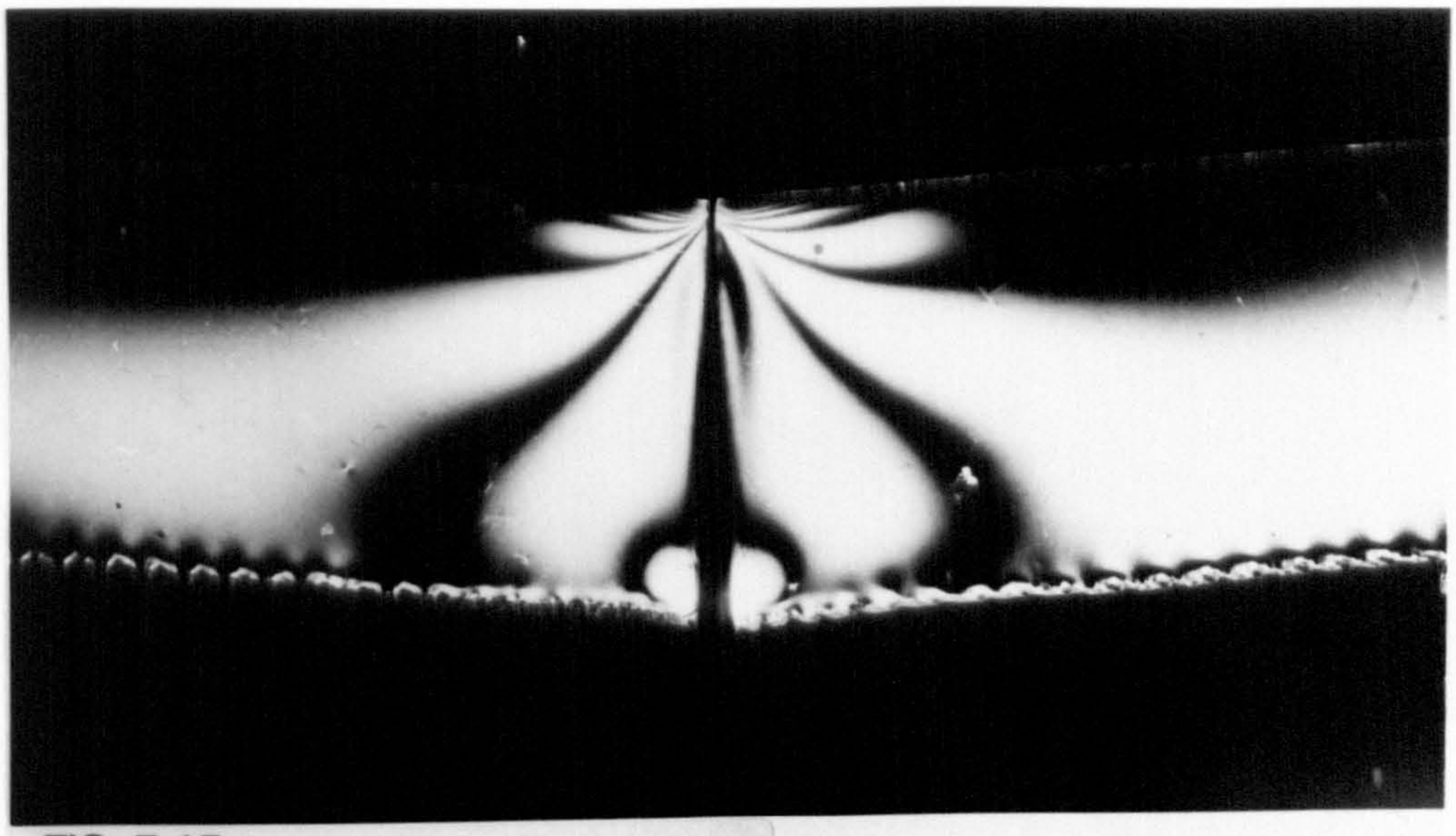

FIG. 7.15 Fringes (S/D=8.63)

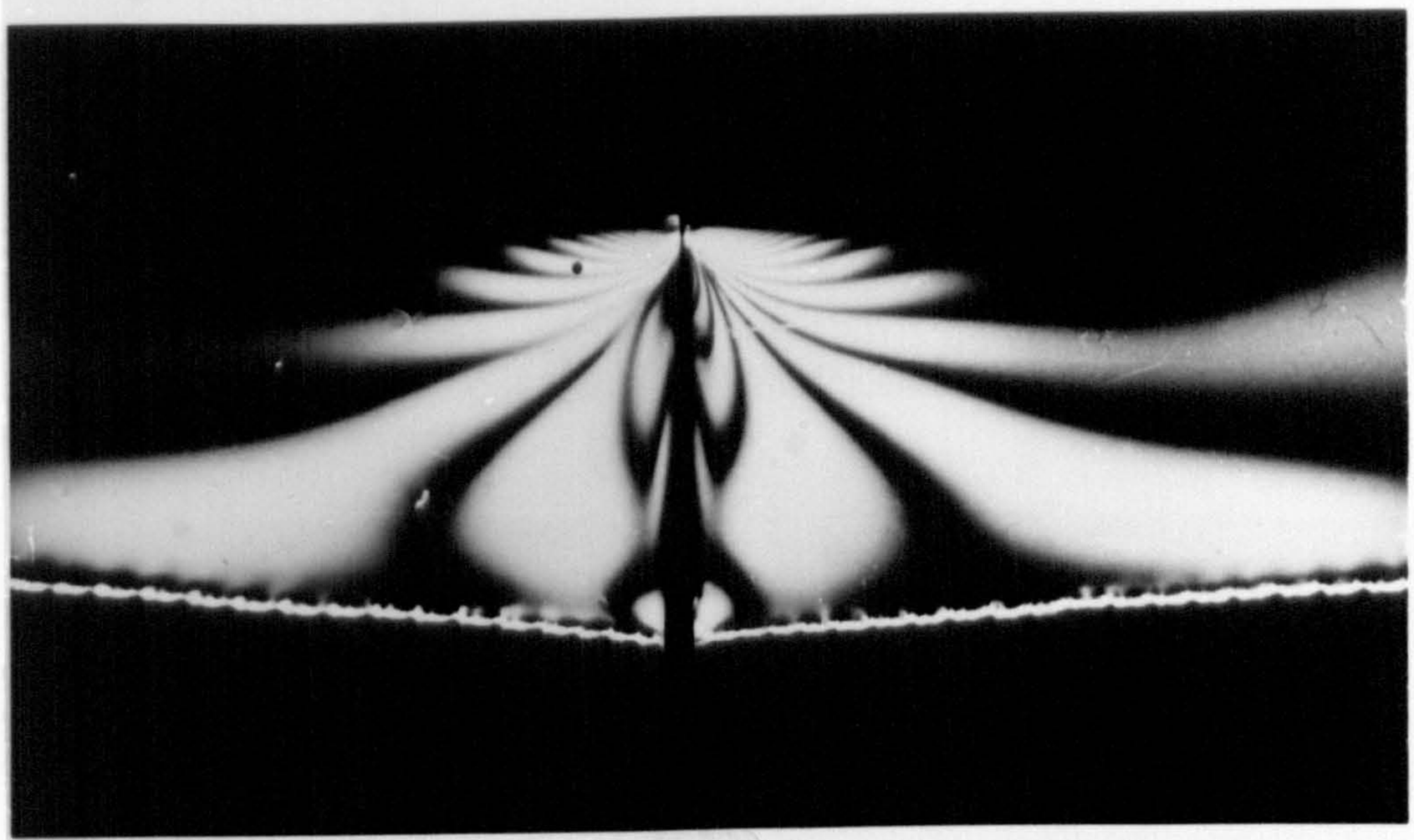

FIG. 7.16 Fringes (S/D=8.63)

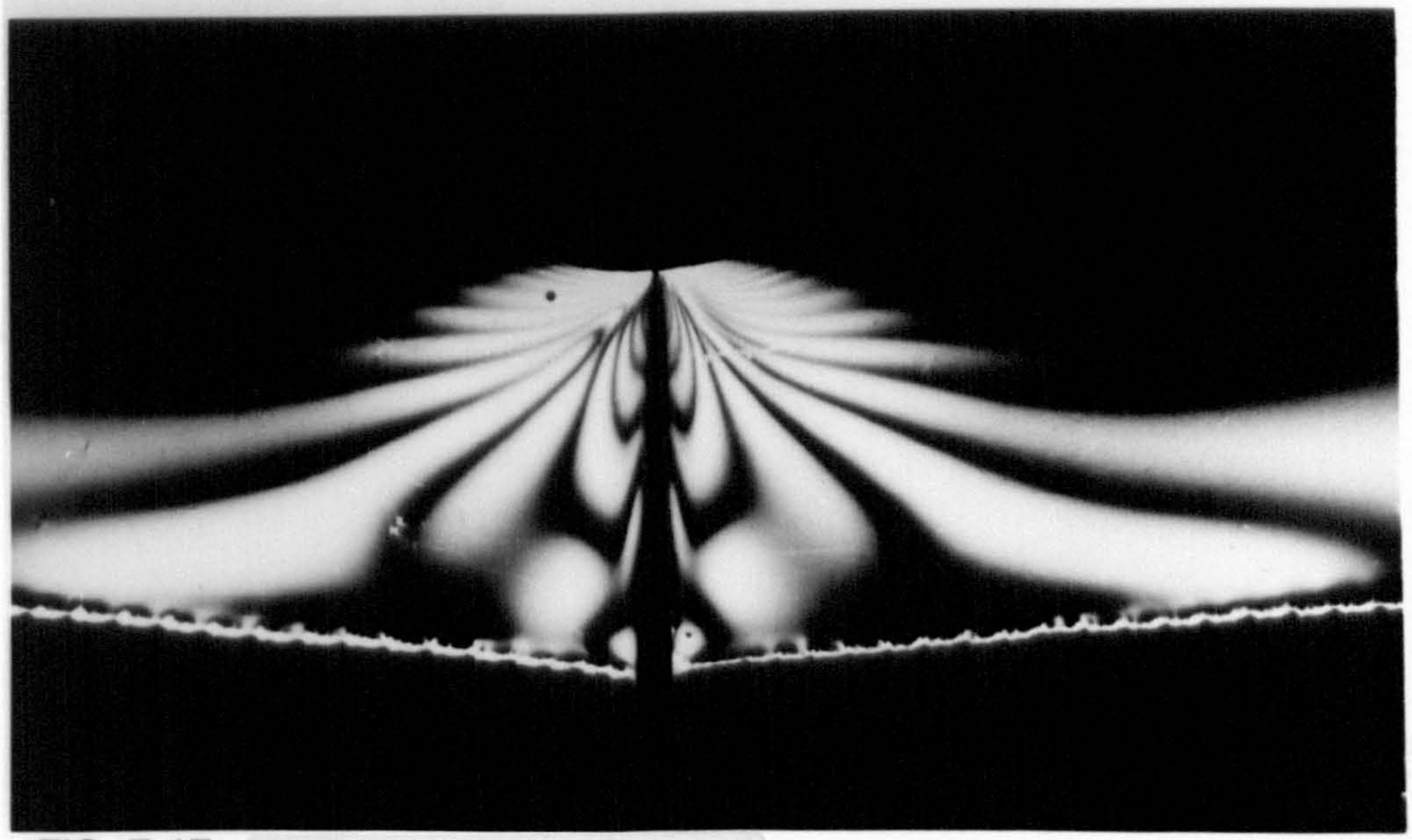

FIG. 7.17 Fringes (S/D=8.63)

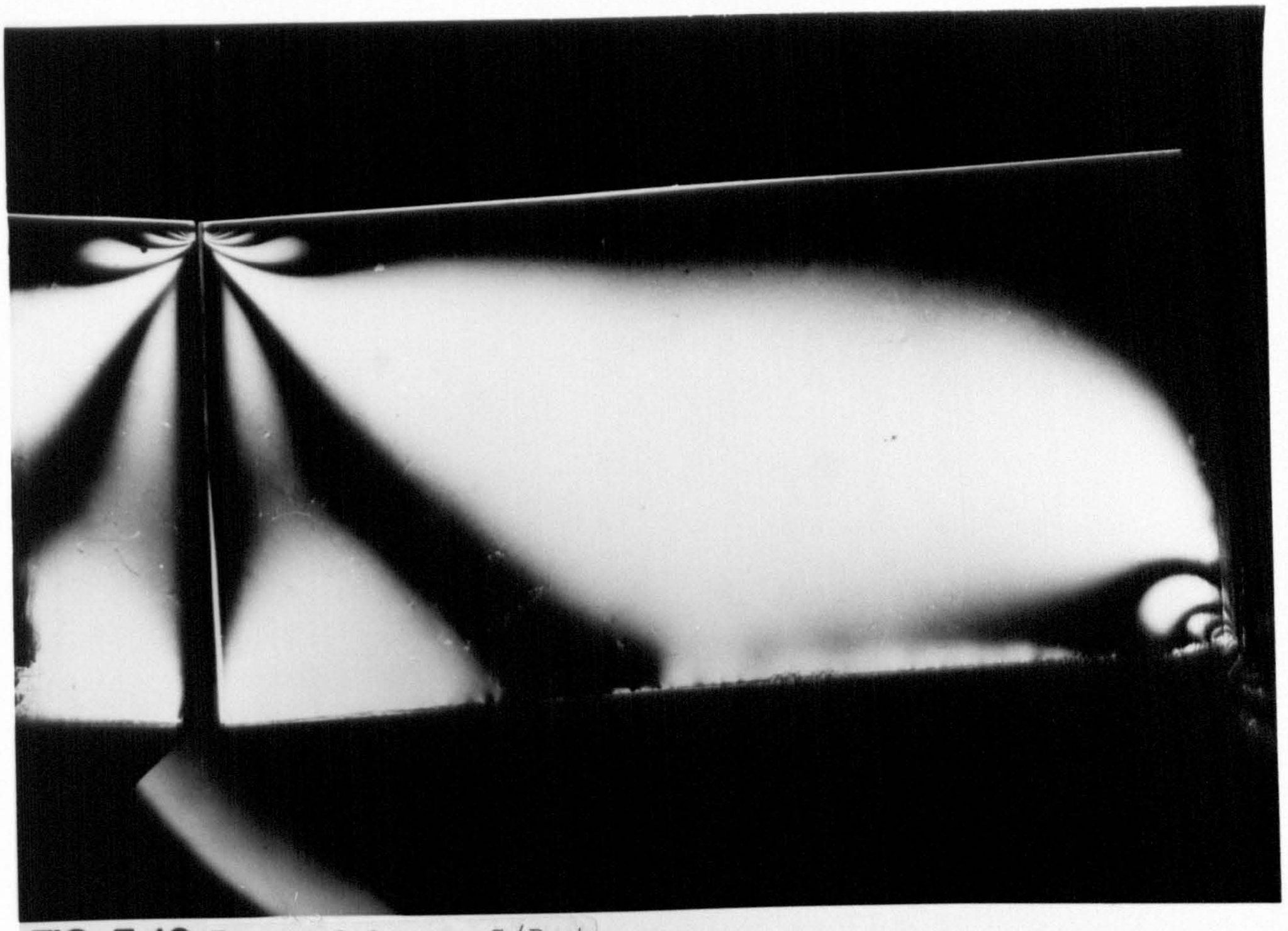

FIG. 7.18 Tapered beams, S/D=4

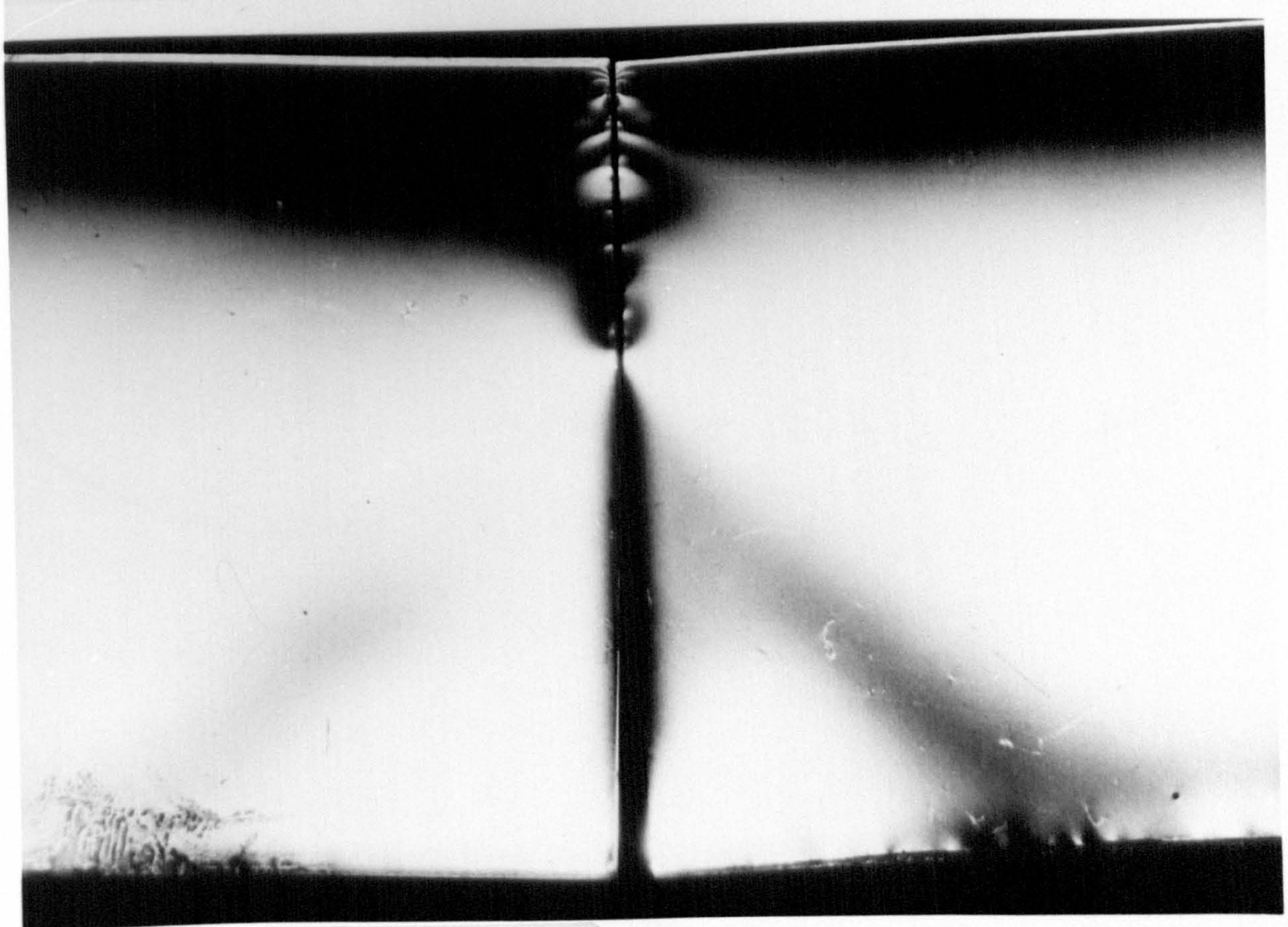

FIG. 7.19 Tapered beams, S/D=4

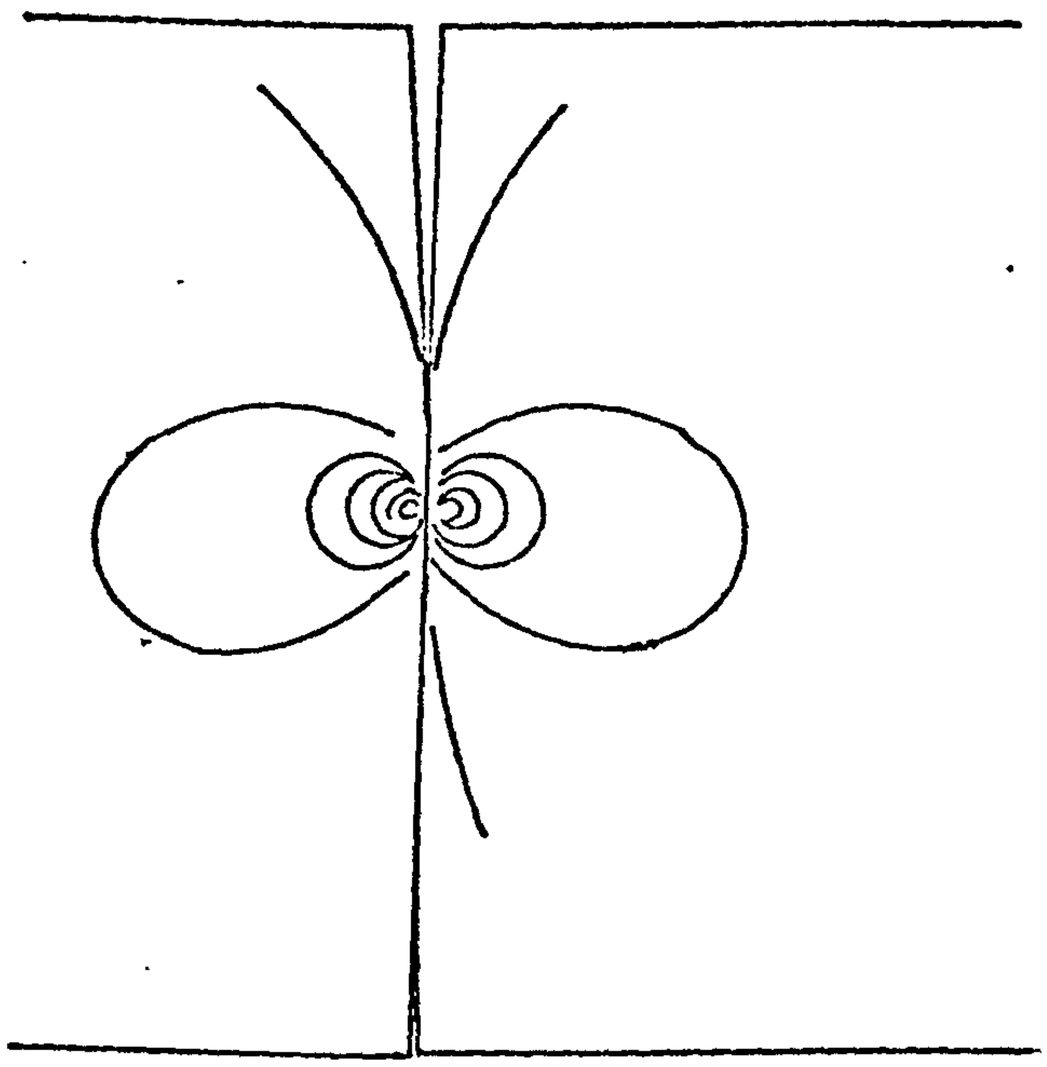

FIG 7.20-A · FRINGE PATTERN OF TAPERED BEAMS

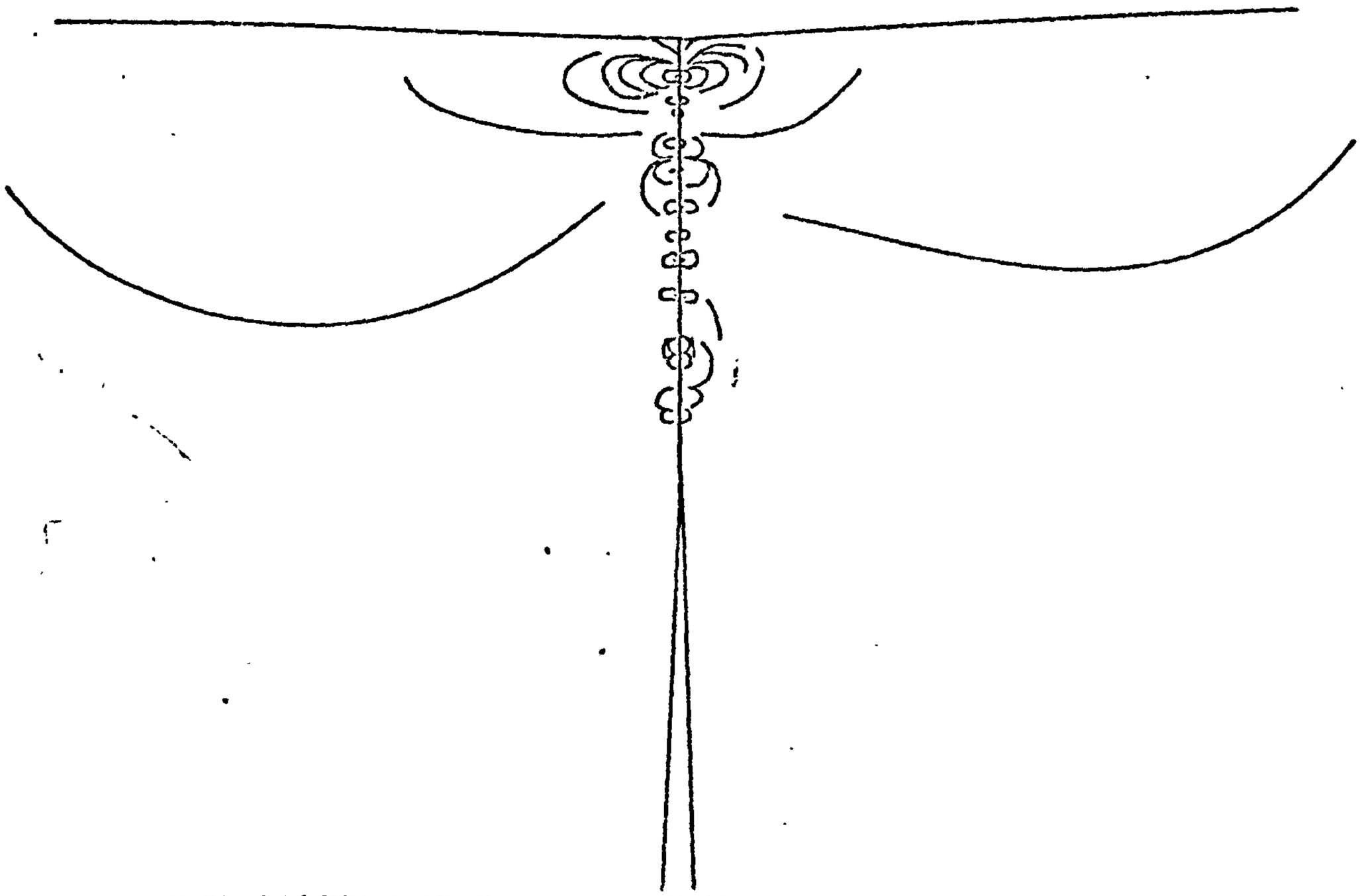

FIG 7.20-B FRINGE PATTERN OF TAPERED BEAMS

FIG 7.21 STRESS TRAJECTORIES (S/D= 4)

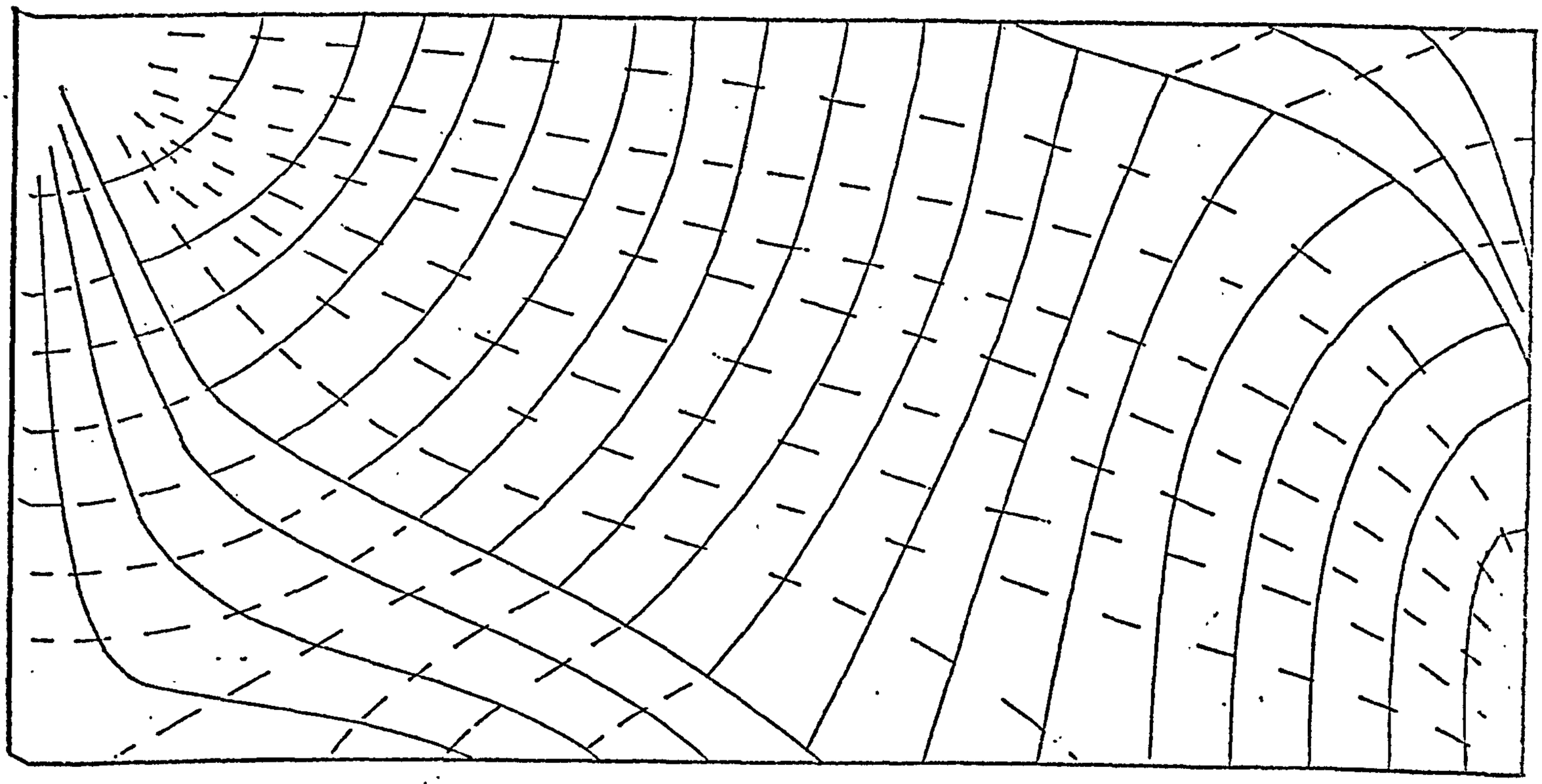

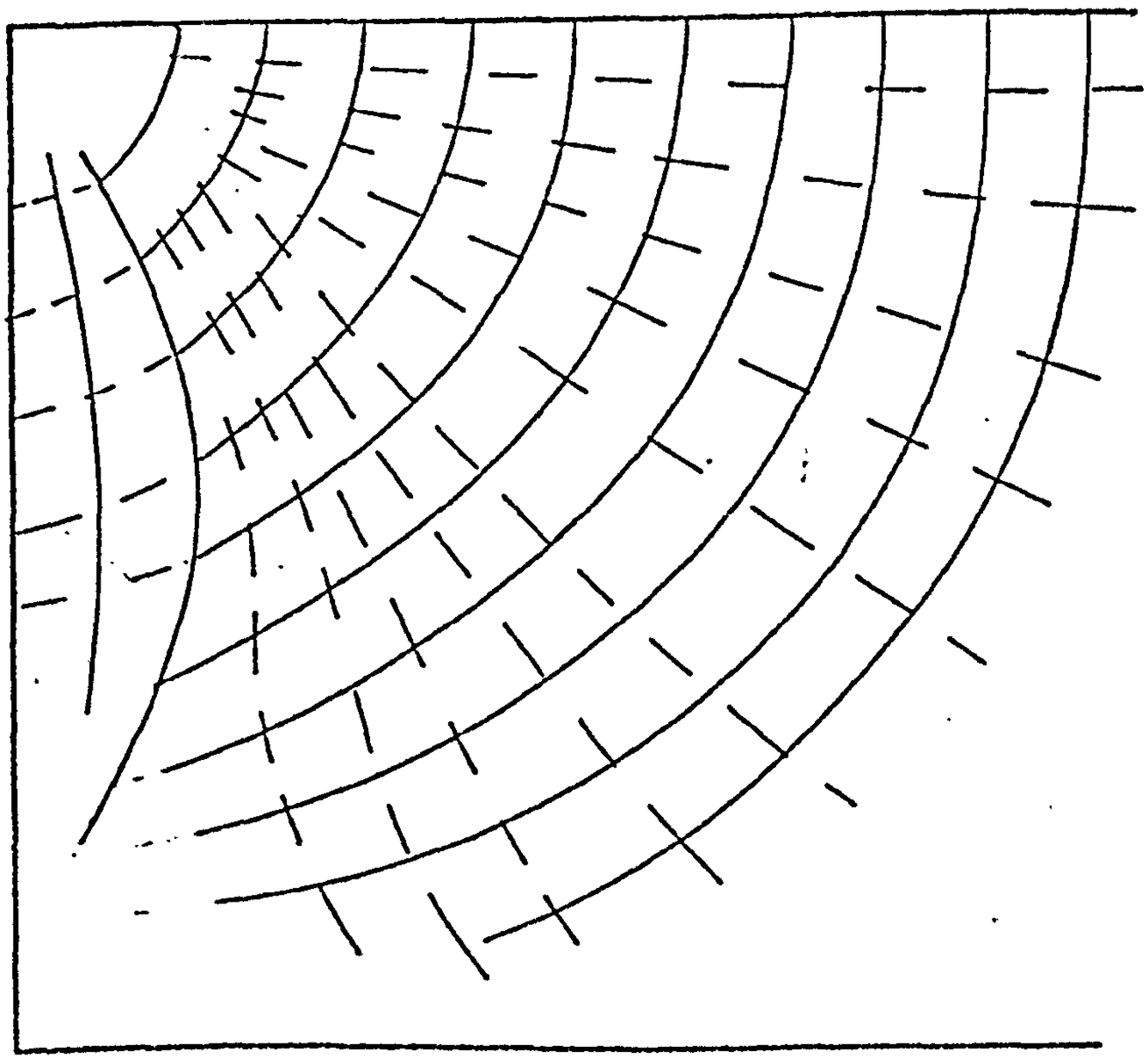

FIG 7.22 STRESS TRAJECTORIES (S/D=2.66)

0	0	0	0	0	0	0
0	0.1	0.15	0.14	0.1	0.1	
-2.5	0.5	0.3	0 2	0.1	0.07	
-1.5		0.3	0.2	008	0 02	
-1	-0.4	0.1	0.1	0 0 5	-0.01	
-0.5	-0.3		-0.02	-0.08	-0.09	
-0.2	-0.1	-0.001	0.0	-0.15	-0.16	
-0.1	-0.12	-0.22	-0.24			

FIG 7.23 MINOR PRINCIPAL STRESSES (S/D = 4)
(applied trasverse stress = 0.195 MPa)

12	7.2	5	3.3	3.1	2.6	2.1	1.5
0	3.4	3.4	2.9	2.5	2.1	1.9	
0	1.4	1.9	2.0	1.9	1.7	1.7	1.2
0		1.2	1.3	1.4	1.3	1.5	
0	-0.1	0.3	0.7	0.9	1.0	1.0	0.9
0	-0.08		0.4	0.6	0.8	0.9	
0	-0.06		0.0	0.4	0.5	0.7	0.6
0		-0.1		0.07		0.2	0.4
0							

FIG 7.24 MAJOR PRINCIPAL STRESSES (S/D = 4)

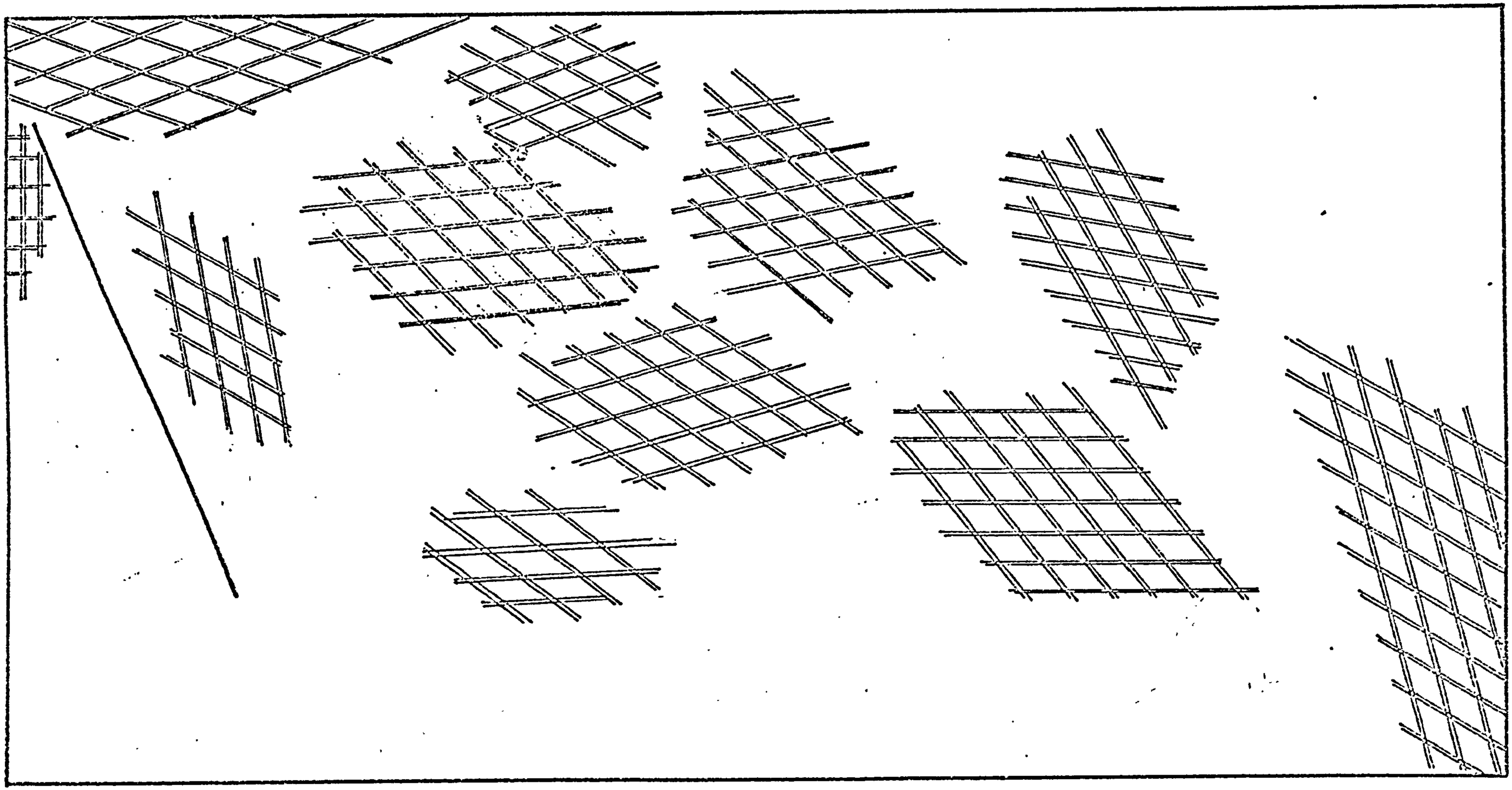

FIG 7.25 EFFECTIVE SHEAR STRESSES ($\emptyset = 50°$) S/D = 4

FAILURE MODES OF MODEL BEAMS

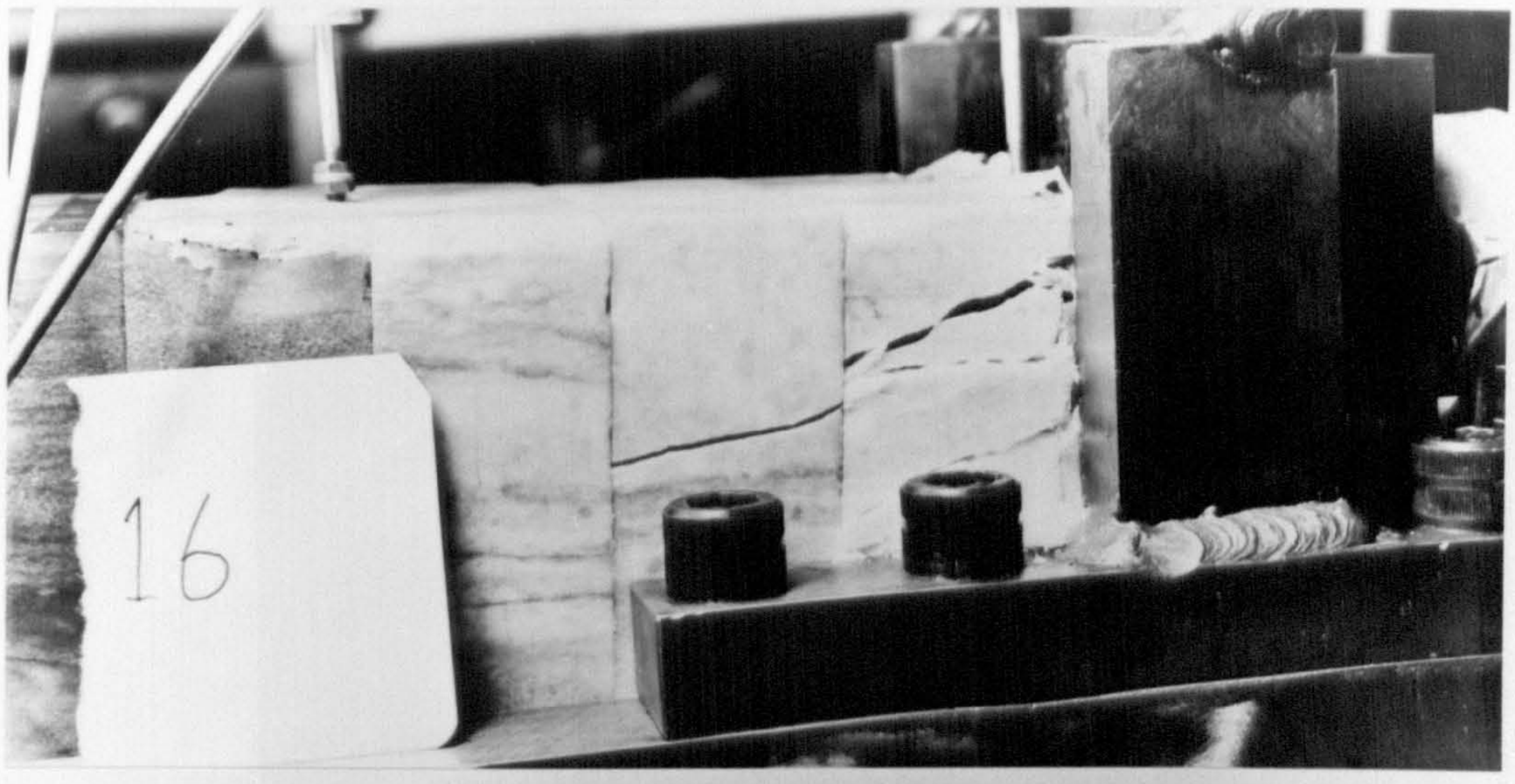

TEST 16

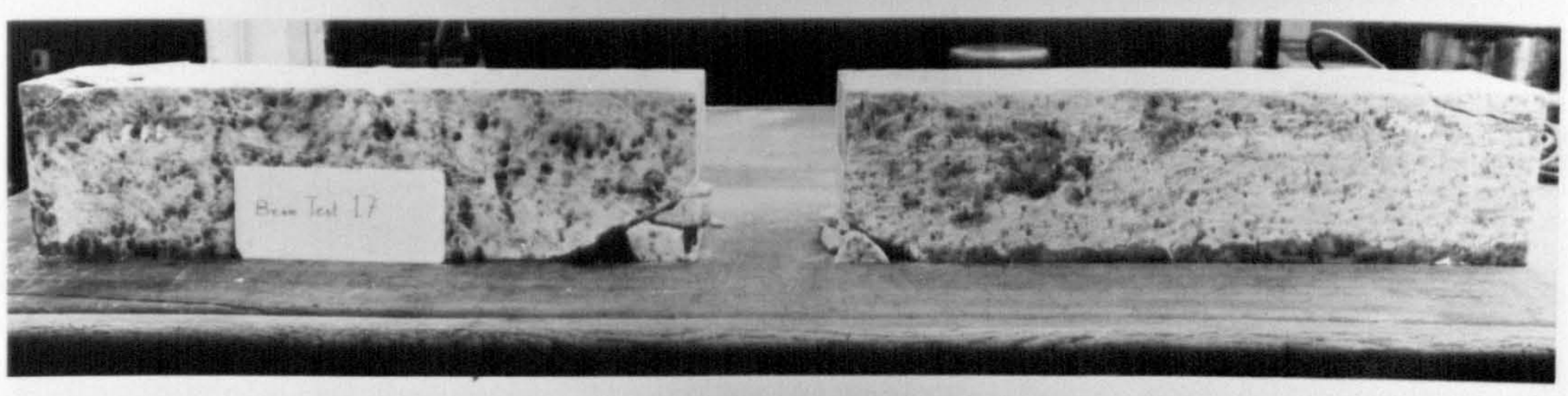

TEST 17

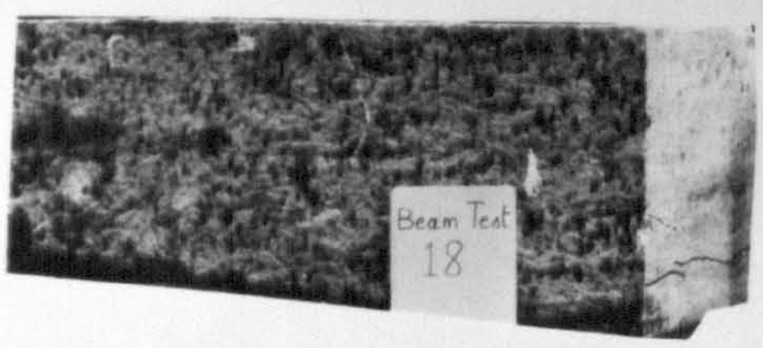

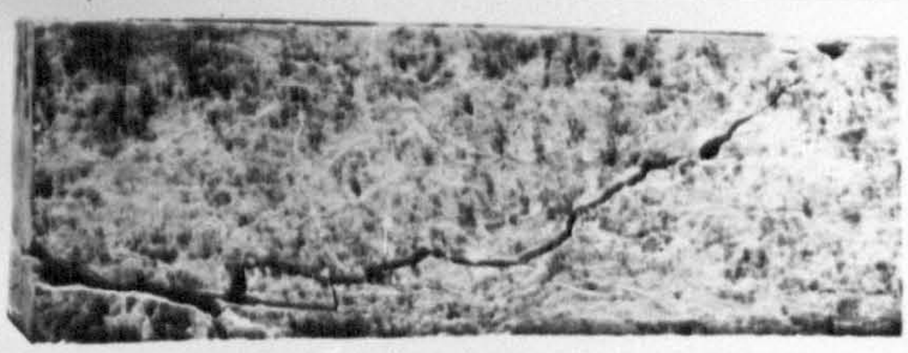

TEST 18

FIG 7.26 (WATSON, 1979)

FAILURE MODES OF MODEL BEAMS

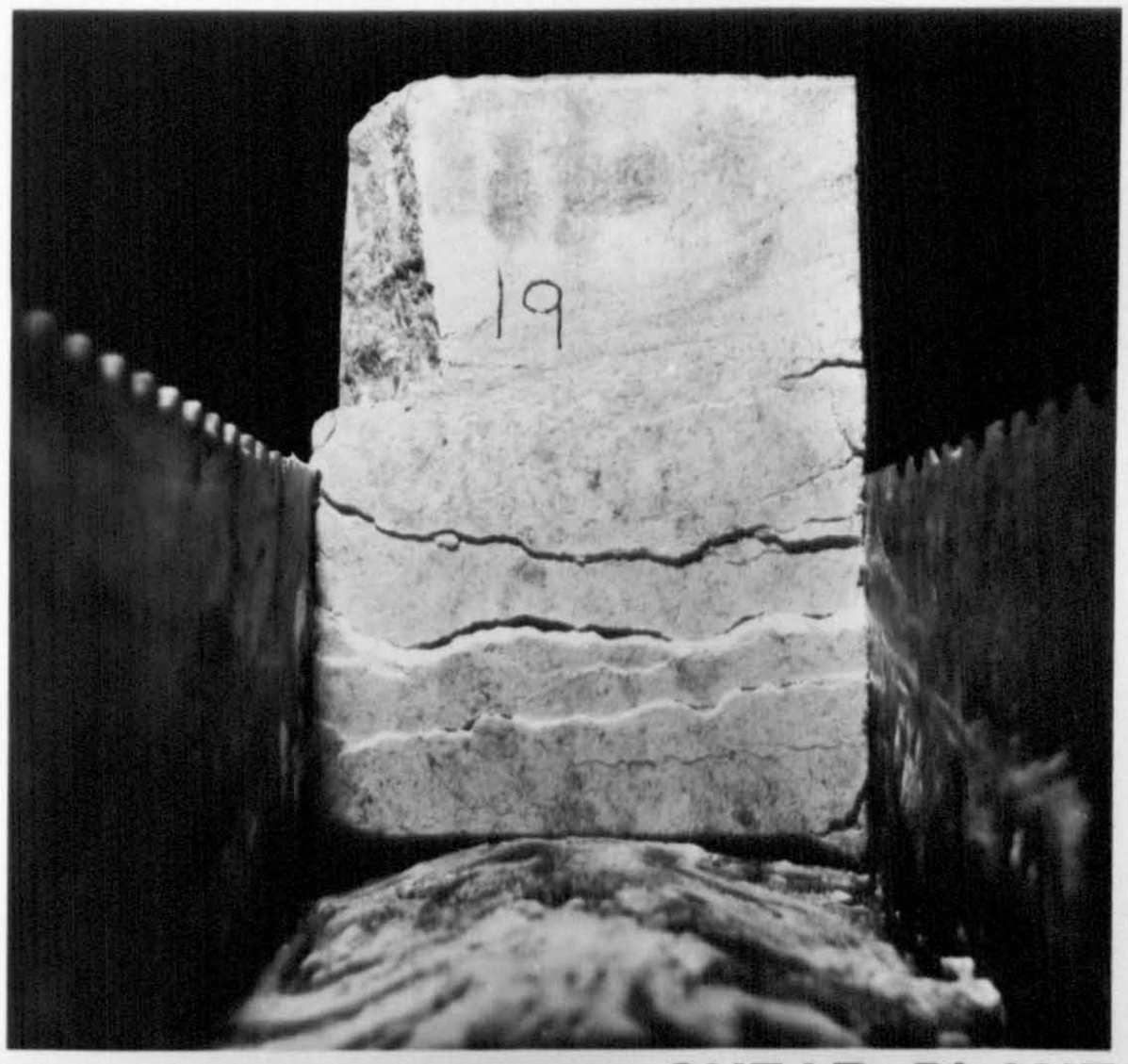

SHEAR PLANES

TEST 19

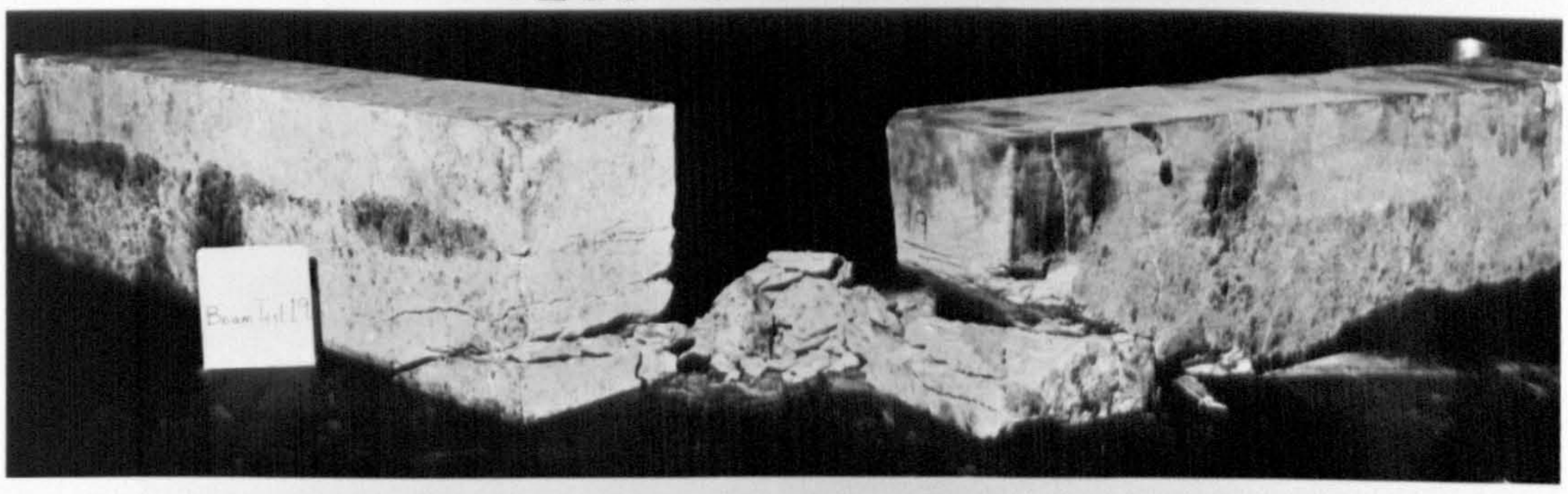

TEST 20

FIG 7.27 (WATSON, 1979)

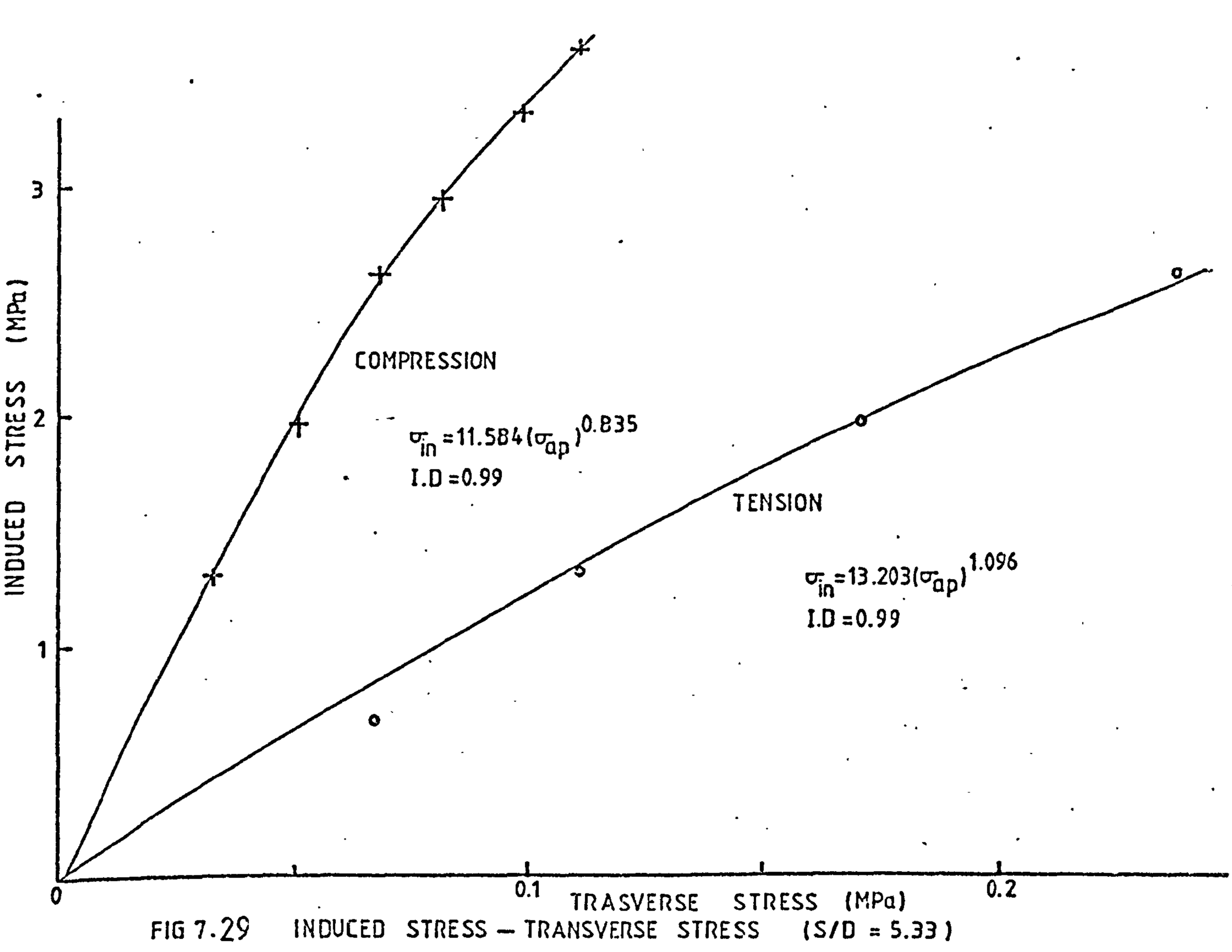

FIG 7.29 INDUCED STRESS — TRANSVERSE STRESS (S/D = 5.33)

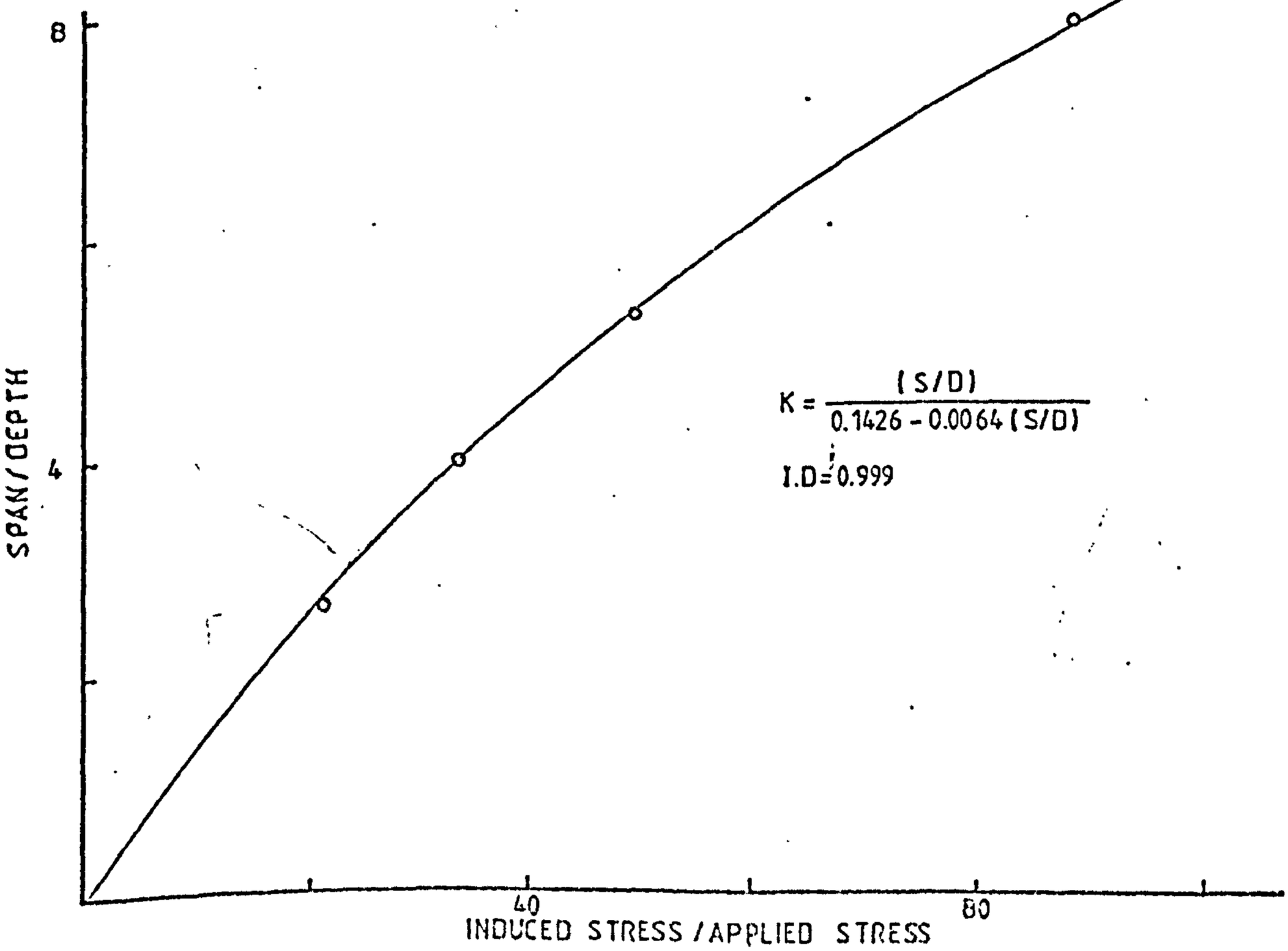

FIG 7.28 EFFECT OF SPAN-DEPTH RATIO

FIG 7.30 DISTRIBUTION OF STRESSES IN BEAM

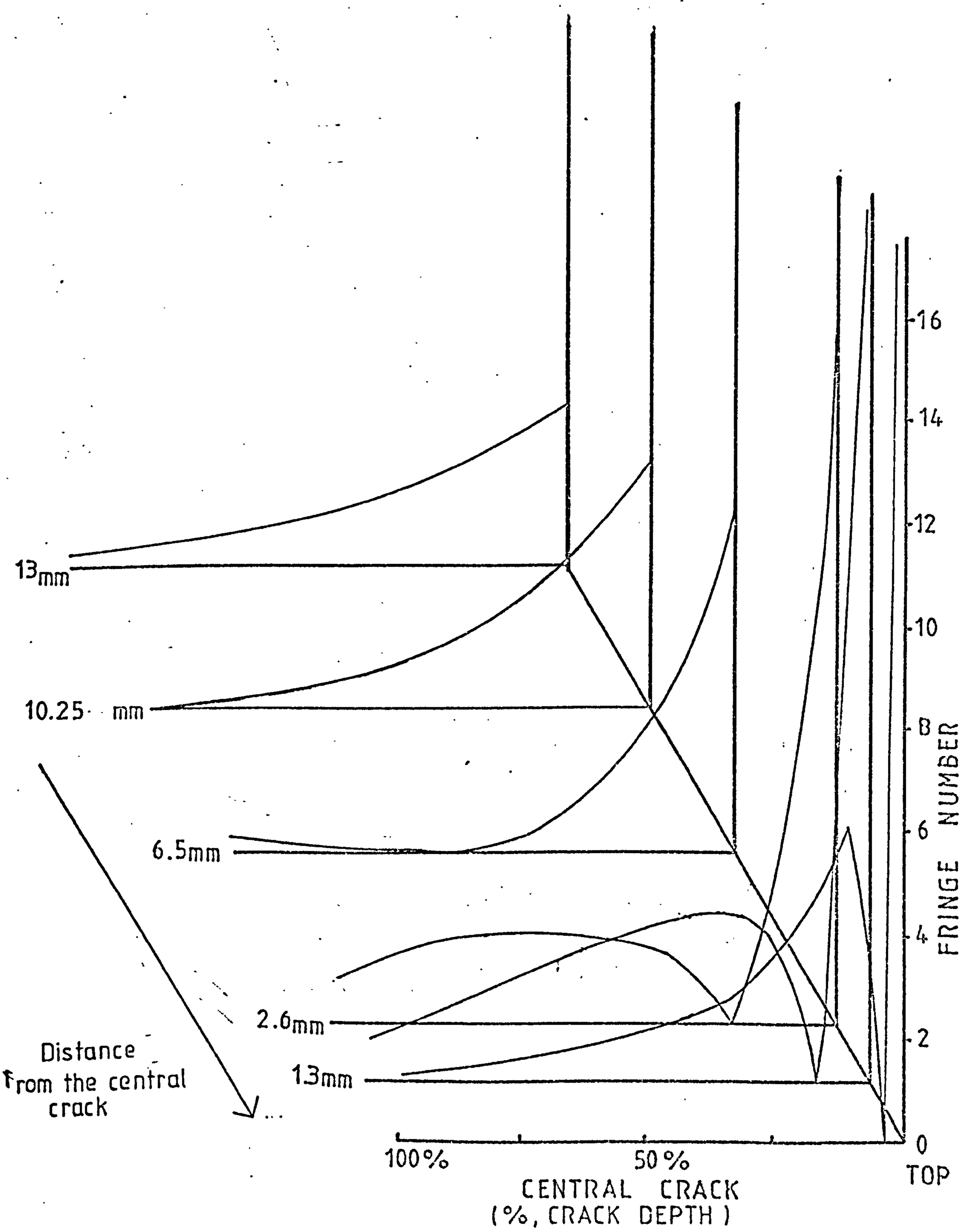

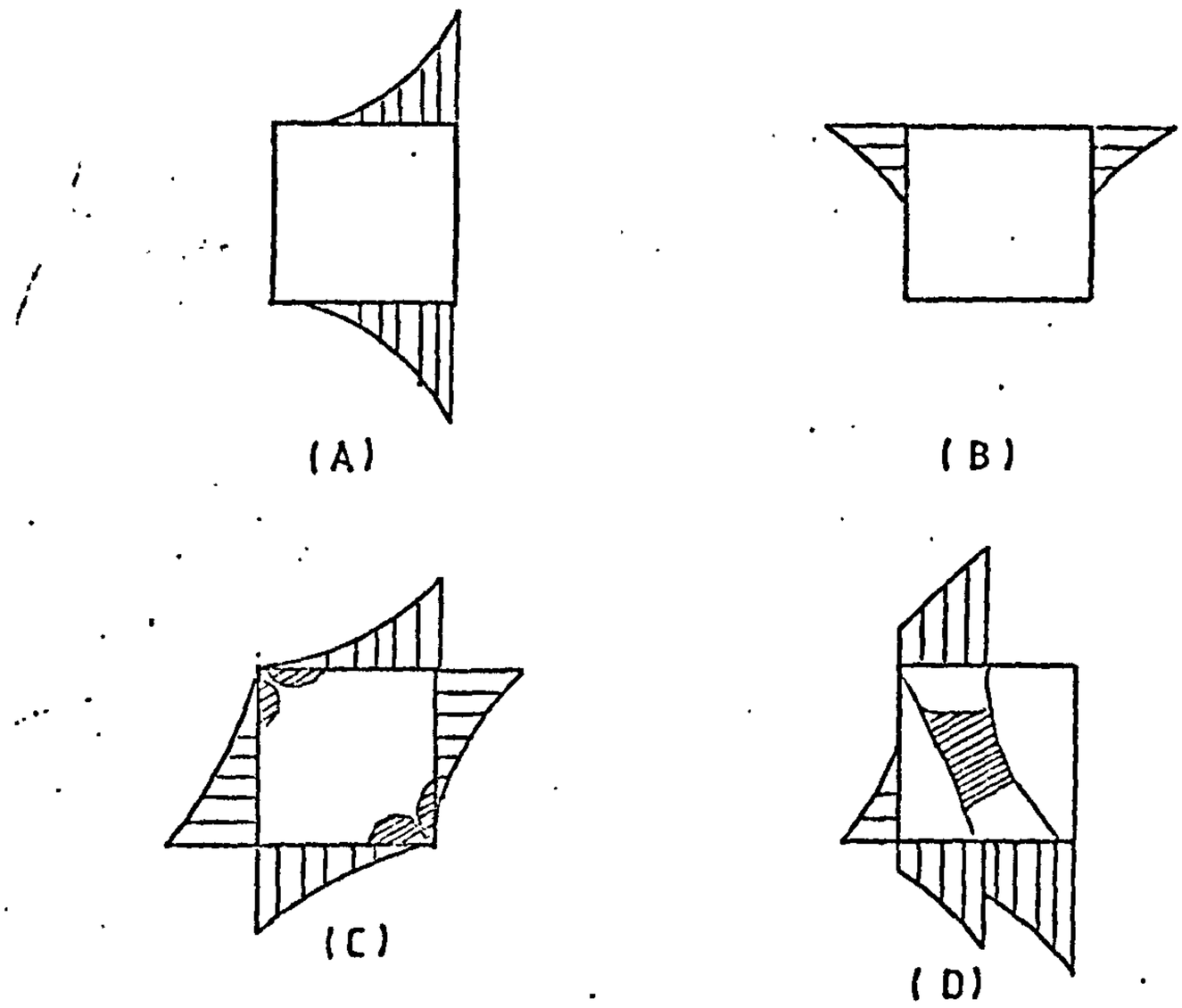

FIG 7.31 Interblock forces (CHAPPELL , 1979)

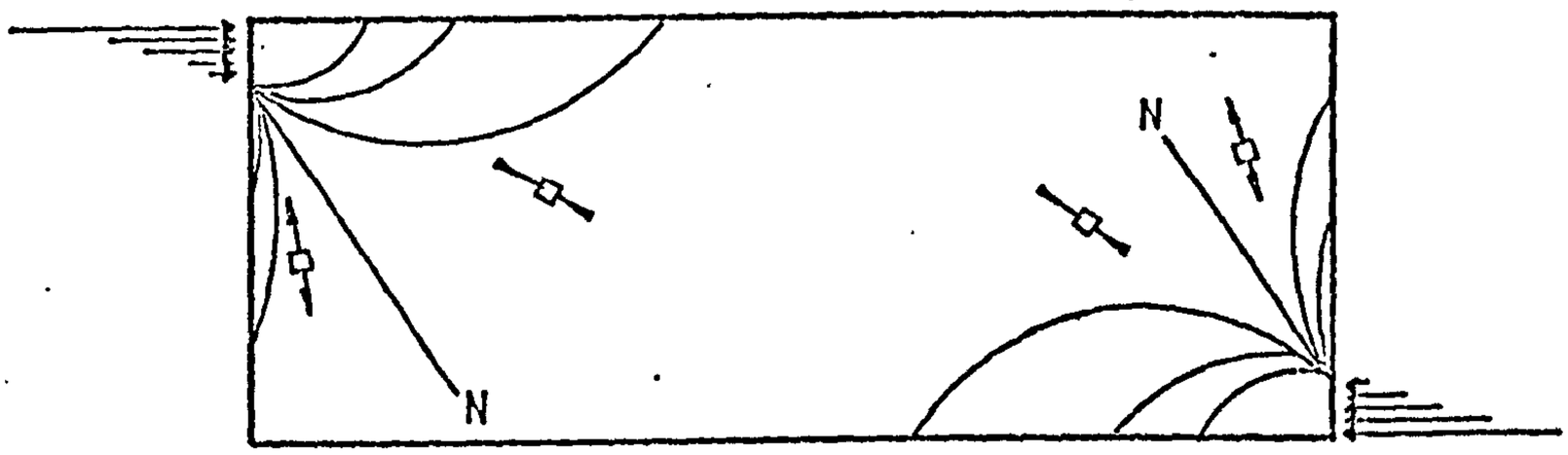

FIG 7.32 DIAGRAMATIC FRINGE PATTERNS

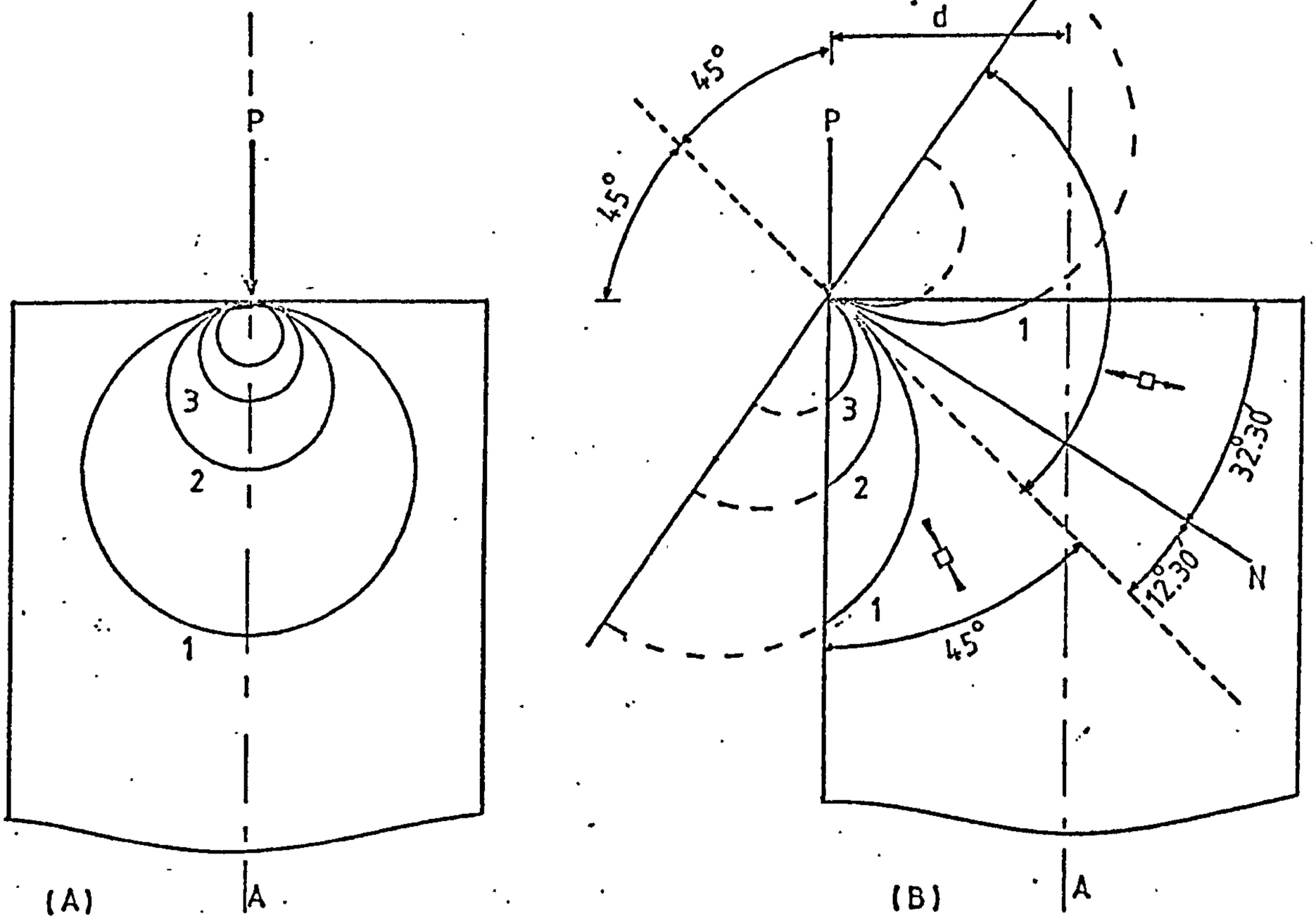

FIG 7.33 CONCENTRATED LOAD THEORETICAL FRINGES (Adapted from the literature)

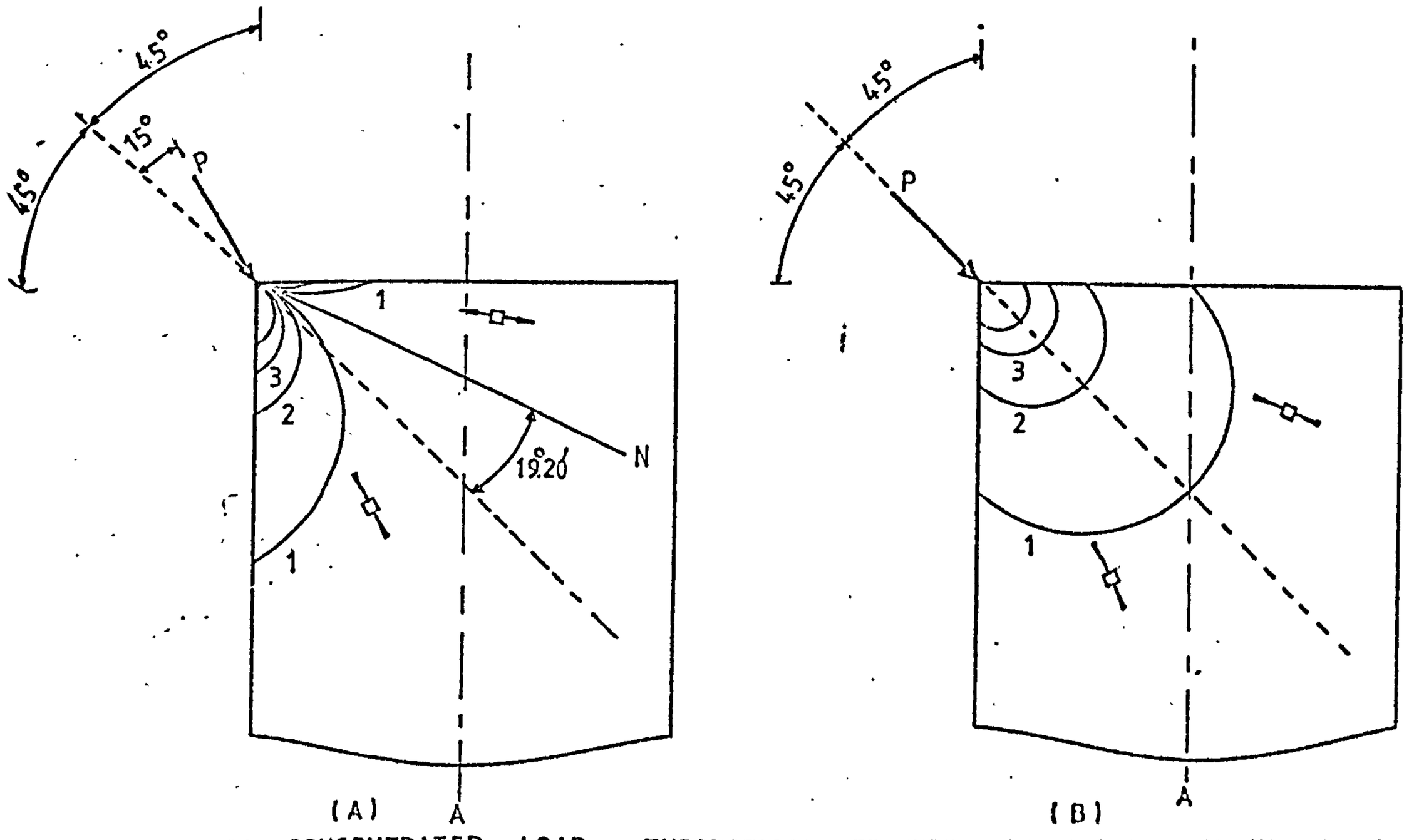

FIG 7.34 CONCENTRATED LOAD THEORETICAL FRINGES (Adapted from the literature)

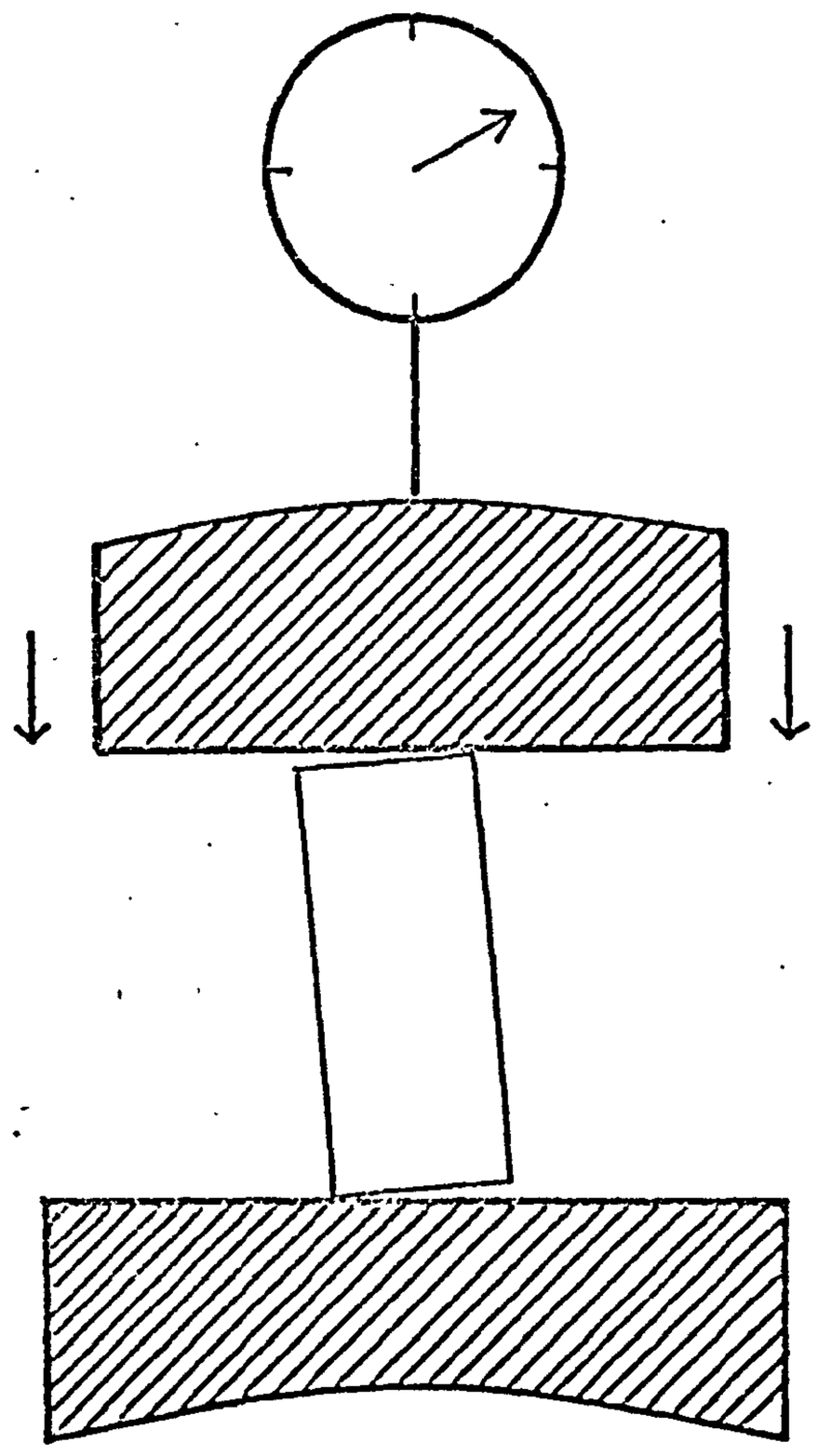

(A)

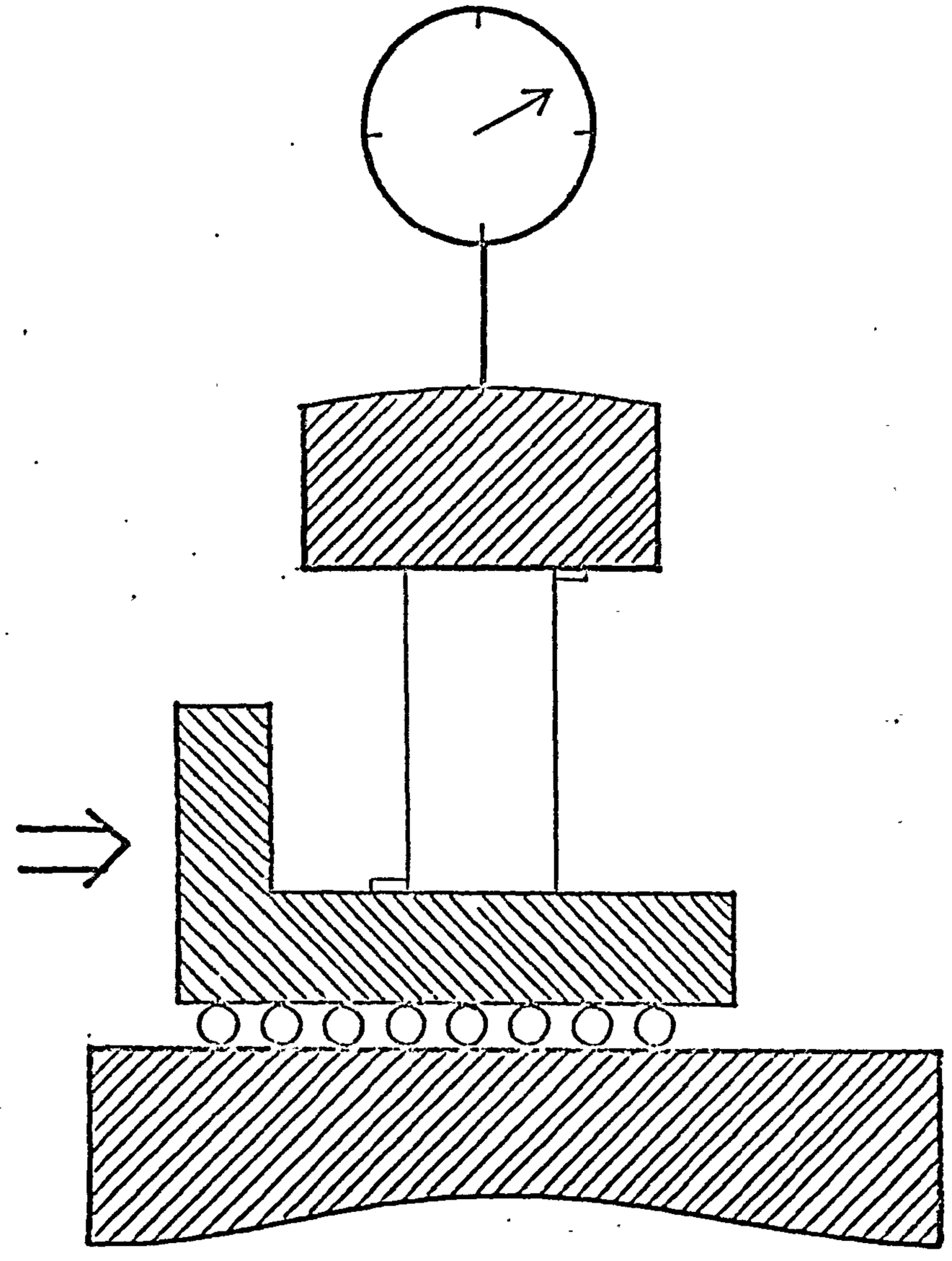

(B)

FIG 7.35 ECCENTRIC LOADING OF GYPSUM SPECIMENS

FIG. 7.36 Eccentrically loaded beams.

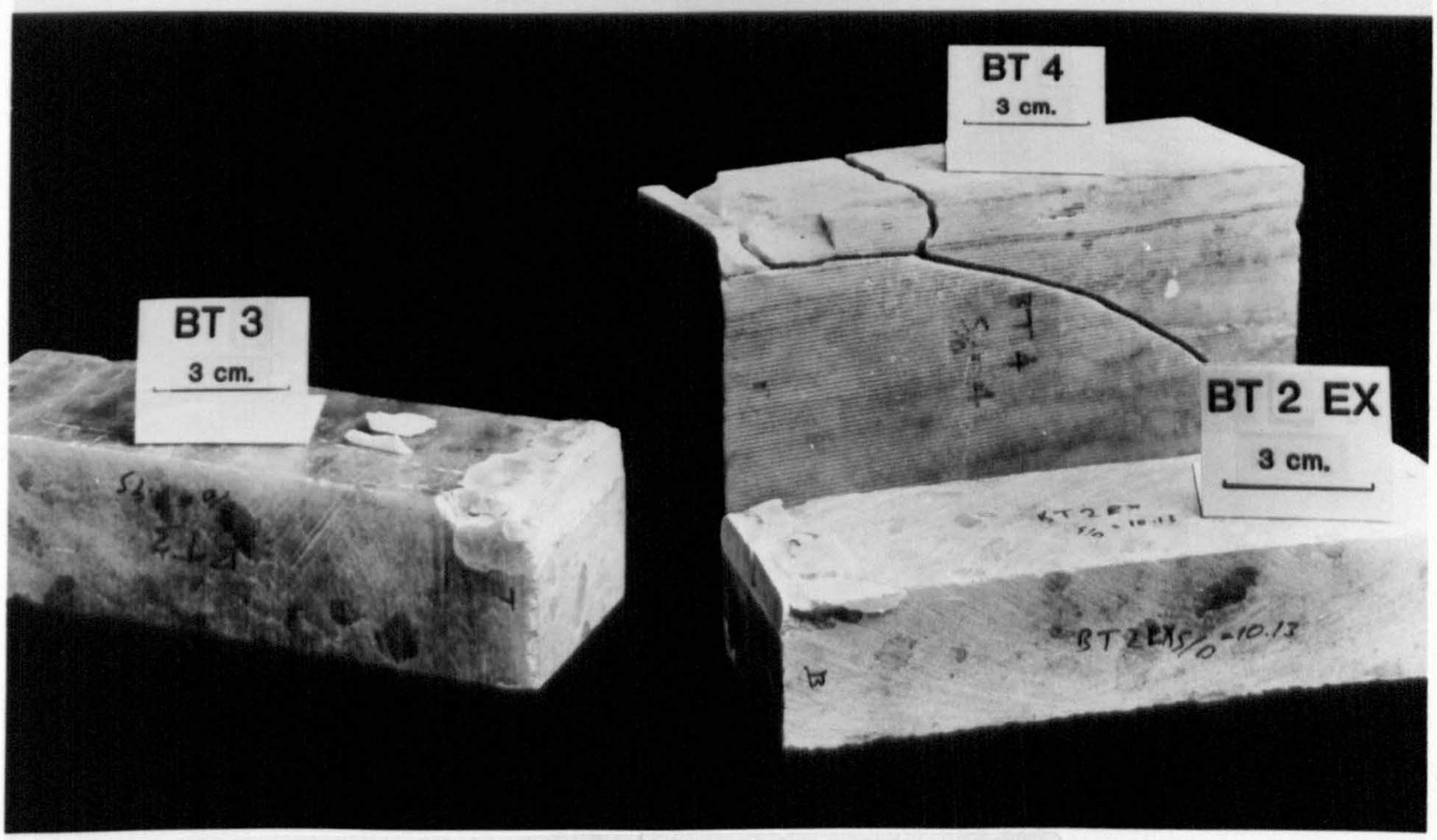

FIG. 7.37 Eccentrically loaded beams

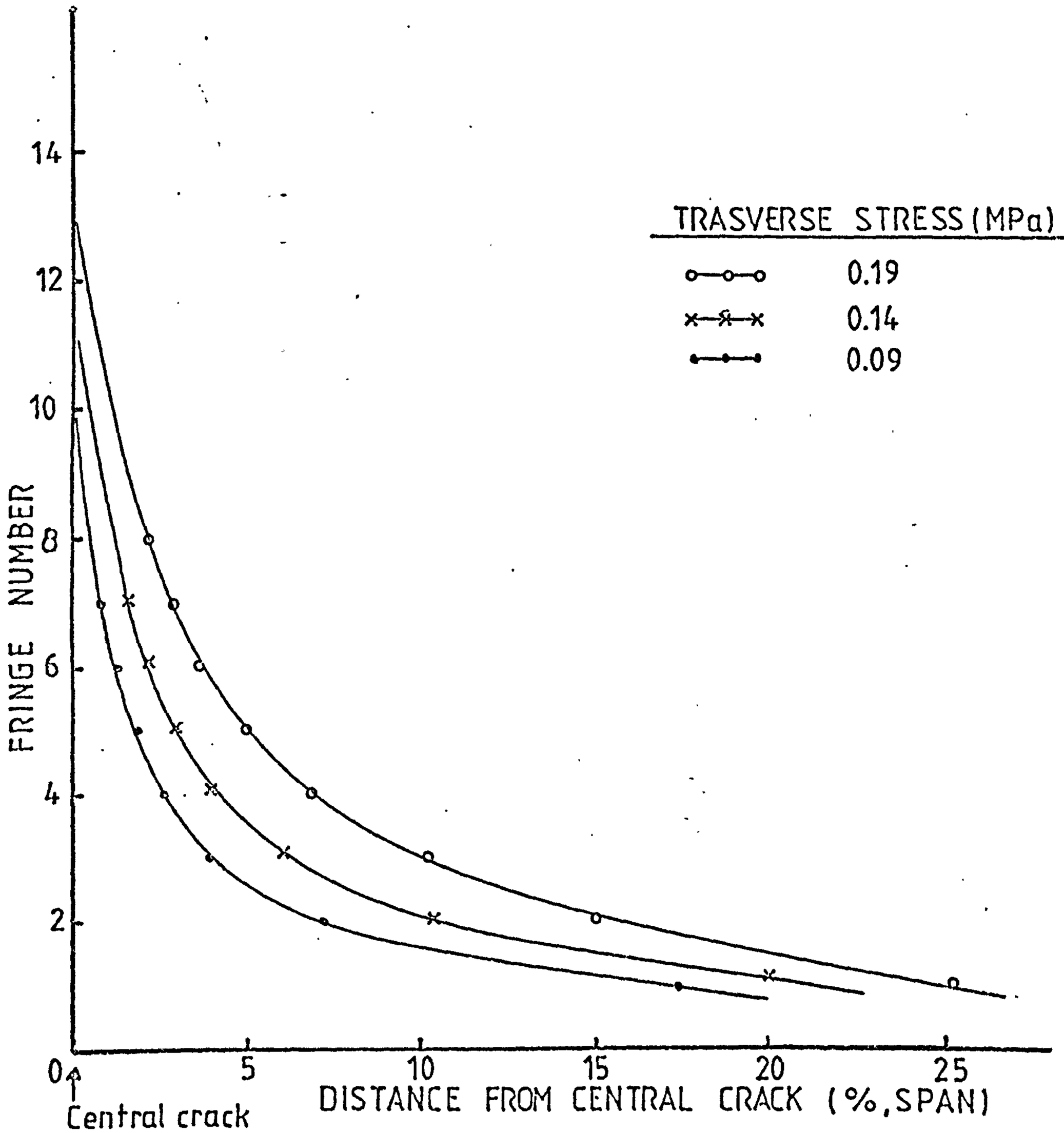

FIG 7.38 EDGE STRESSES (S/D = 4, UPPER EDGE)

TABLE 7.1 PROPERTIES OF PHOTOELESTIC MATERIAL

TYPE OF MATERIAL	EPOXY RESIN
COMMERCIAL NAME	ARALDITE CT-200
TENSILE STRENGTH	72.4 MPa
YOUNG'S MODULUS	2.9 GPa
POISSON'S RATIO	0.35
UNIT FRINGE VALUE	0.6 MPa
FIGURE OF MERIT	4448
UNIT WEIGTH	1.176 TONS/M^3

TABLE 7.2 PHOTOELASTIC MODELS

NO:	SPAN(CM)	DEPTH(CM)	SPAN/DEPTH
1	20.28	7.62	2.66
2	20.28	5.08	4.0
*3	20.28	5.08	4.0
**4	19.16	2.86	6.7
5	20.28	3.81	5.3
6	20.28	2.54	8.0
7	20.28	2.3	8.8

* TAPERED BEAMS
** THREE BEAMS

TABLE 7.3 ECCENTRIC LOADING OF GYPSUM SPECIMENS

NO:	SPAN (Cm)	DEPTH (CM)	SPAN/DEPTH RATIO	ECCENTRICITY (CM)	ULTIMATE AXIAL LOAD (KN)	FAILURE TYPE
1	30.2	5.0	6.04	2.5	23.3	AXIAL
2	30.2	3.8	7.95	1.9	16.6	CORNER
3	30.2	3.0	10.10	1.5	15.5	CORNER
4	30.2	7.5	4.03	3.75	43.1	AXIAL
5	30.2	3.8	7.95	1.9	17.4	CORNER
6	30.2	3.0	10.10	1.5	16.4	CORNER
7	30.2	7.5	4.03	3.75	44.5	AXIAL

8. FINITE ELEMENT STUDIES

8.1 Introduction

The solution of any stress analysis problem requires the formulation of governing differential equations and the establishment of one or more boundary conditions for a special problem. Most of the numerical methods of solving equations are not very suitable for the study of irregular boundaries such as underground excavations, slopes, dam foundations, etc. These considerations led to the development of a new approach in which energy theorems were introduced for the solution of engineering problems and it became known as the finite element method (Jeager and Cook 1979).

Due to the special circumstances of rock engineering, several modifications to the method have been produced, including three-dimensional elasticity, anisotropy, heterogenity, cracks, time-dependent deformation, viscoelasticity, elastoplastic materials, incremental excavations, non-linear elasticity, and jointed rock.

The theoretical basis for the method is fully detailed elsewhere (e.g. Zienkiewicz et al.(1967,1968,1969); Goodman et al.(1968); Smith (1971); PAFEC Manuals 1975); hence no attempt will be made to describe this in the present study.

8.2 The Finite Element Program : PAFEC-75

'PAFEC-75' (Program for Automatic Finite Element Calculations) is a powerful package developed and maintained by PAFEC Ltd. of Nottingham. The program is available in the IBM 370/168 computer of NUMAC (Northumbrian Universities Multi-Access Computer) and is capable of solving two-and three-dimensional problems for either dynamic or static loading conditions using quadrilateral or triangular elements with variable side nodes.

It has manual, automatic or mixed mesh generation facilities and can integrate rectangular, triangular, beam and shell elements for various engineering purposes. The package can handle any linear or non-linear elastic viscoelastic problems for plane strain or plane stress conditions (PAFEC Manuals).

The most importance disadvantage of the program is that it cannot deal with a non-tension analysis or treat discontinuities, weakness planes and fracture planes, which are known to control the deformational characteristics of rock structures to a large extent.

Another Finite Element Program package, 'ANNOLIN' (Program for the Analysis of Non-Linear and Linear Two-Dimensional Continuum), also available at NUMAC system is capable of handling linear elastic, linear viscoelastic, non-tension, limiting tension in two-dimensional continua and has been used by previous investigator, Watson (1979).

In the present study, finite element analysis undertaken is intended, not for design purposes, but for providing supplementary data for the discussions dealt with in the previous sections of this thesis (Sections Two, Three and Six).

8.3 Objectives of Finite Element Analysis

Two separate studies were carried out to examine:

(1) The stress distribution around the excavations under gravity loading to achieve the initial state of stresses and the change in the stress distribution due to failure of simulated gypsum roof beams and part of the overlying marl at various stiffness levels of simulated overlying strata. This study can be considered to be complementary to the physical scale modelling discussed in Sections Two and Three (Figure 8.1).

(2) The distribution of stresses in a mine pillar and in roadway, roof and floor, under uniformly distributed vertical stress and acting along the upper edge of the structure and the change in stress distribution brought about by the presence of soft layers simulating satinspar bands at different horizons along the pillar height, with various thicknesses. This study is complementary to the ideas discussed in Section Six of this thesis (Figure 8.2).

8.4 Finite Element idealisation of room and pillar workings and a roof-beam failure

8.4.1 Mesh Description

The structure considered was a section of strata from the base of a gypsum seam to the surface. Three rooms, each being having a width of 7m, and a height of 3m, and two whole pillars, each having a width

of 5m and two half-pillars along the vertical boundaries of the structure, were modelled. The thicknesses of gypsum roof beam, the Upper Permian Marl, and lacustrian deposits were taken as 1.5m, 13m, and 23m respectively (Figure 8.1).

It was necessary to design a mesh large enough not to permit the boundaries to have an effect on the stress distribution around the opening. In this respect, Kulhawy (1974) recommends a distance of 6 radii beyond the opening centre to the mesh boundary. Due to limitations in the computer resources available, a distance slightly more than 5 radii of the opening was chosen in the study and this was found to be adequate.

The internal meshes were automatically generated using the PAFBLOCK facilities of the package program and the designed model consisted of 156 rectangular elements and 192 main nodes. Too coarse a mesh layout can create inaccurate stress distributions, while indiscriminate use can introduce round-off errors. Therefore, in sections where resolution is required finer mesh layout was used as far as resources available allowed.

The boundary conditions were that the bottom horizontal boundary of the mesh was restrained from vertical movement and the vertical boundaries were restrained from horizontal movement. This appears reasonable when the structure was considered to exist in the centre of the panel and the central room was at a distance from the vertical boundaries.

8.4.2 Analysis

In order to achieve the initial state of stresses around the simulated openings loaded by the self weight of overlying strata, the first set of runs was made without considering a roof beam failure in the central room. Three runs were carried out by altering the rigidity of overlying marl from 4.8 GPa to 0.48 GPa and 0.048 GPa. The lowering of Young's Modulus of marl in steps served to simulate the reduction in the competency of marl due to water and to creep effect.

In the second set of runs the simulated gypsum roof beam was removed from the mesh layout and analyses carried out for varying degrees of competency of marl.

In the third set of runs, a 1.5m thick marl layer was assumed to have dropped out from the crown and the runs were repeated varying the rigidity of the marl. This simulated a possible migration of the void upward in the marl layer.

8.4.3 Results of the Analysis

The deformed shape of the structure, the directions of the principal stresses and principal stress contours for each run were obtained. However, it is not possible to present ample graphical output obtained in this thesis and, therefore, only some of the selected output will be included.

The results of the initial analysis are shown in Figure 8.3. It can be deduced that as the competence of the overlying marl decreases from 4.8 GPa,and 0.48 GPa to 0.048 GPa:

(1) Along the lower section of the simulated gypsum roof beam the maximum principal stresses (tensile) and maximum principal stresses (compressive) increase.

(2) Around the upper section of the simulated gypsum beam the maximum principal stresses (compressive) decrease substantially, while the minimum principal stresses (compressive) increase.

(3) The maximum principal stresses (tensile) and minimum principal stresses (compressive) both increase at abutments for a distance into the rock mass above the pillars.

(4) Both principal stresses and compressive stresses decrease substantially inside the pillar core.

The directions of principal stresses around the workings for two cases (i.e. when Emarl = 4.8 GPa and Emarl = 0.048 GPa) are shown in Figure 8.6a.

It is obvious that, as the competency of the overlying strata decreases, the magnitude of stresses on the pillar also decreases, indicating that the weight of the overlying strata is transferred onto the pillars to a lesser extent and that much of the weight is transferred onto the gypsum roof.

Upon removal of the gypsum roof beam from the central opening magnitudes and directions of stresses change considerably. When the results of the second set of runs (Figure 8.4) are compared to those of the initial study, it can be said that, due to removal of the simulated gypsum roof

from the central opening and at the same time due to lowering the competency of the overlying strata:

(1) Along the lower edge of the unsupported marl roof, the maximum principal stresses (tensile) and the minimum principal stresses (compressive) decrease but they both increase as the competency of the marl layer is reduced.

(2) Around the upper sections of the crown, both principal stresses (compressive) increase but as the Modulus of the marl is reduced,the maximum principal stresses decrease while the others increase.

(3) At the abutment at a distance into the pillar, the maximum principal stresses which were tensile in the initial analysis become compressive and increase with lowering rigidity of the immediate roof. The minimum principal stresses are compressive and increase due to the removal of the gypsum roof beam and due also to the lowering rigidity of the marl layer.

(4) Inside the core of the pillar around the failure zone, the maximum principal stresses (compressive) decrease while the minimum principal stresses (compressive) increase slightly due to the removal of the roof beam and to the lowering of the competency of the marl layer.

The change in direction of the principal stresses due to roof beam failure with decreasing competency of the marl is shown in Figure 8.6b.

The results of the third set of runs which simulated upward migration of the failure zone by removing 1.5 thick marl from the roof of the central opening are shown in Figure 8.1, with various degrees of competency of the overlying strata. Comments on the results obtained during this set of runs will not be made as the graphical outputs are self-explanatory and change in the stress distribution is similar to that obtained in the second set of runs in general (Figure 8.5).

The principal stress directions of the cases models in the third set of runs are shown in Figure 8.6c for the stiff marl (E = 4.8 GPa) and soft marl (E = 0.048 GPa).

8.5 The effect of the presence of satinspar bands in the pillar on stress distribution

The study was carried out to demonstrate the change in the stress distribution due to soft satinspar bands varying in thickness from 0.05m to 0.25m horizontally embedded in different sections of the pillar. This study is supplementary to the experimental programme discussed in Section Six of this thesis.

8.5.1 Mesh Description

The idealised structure is a section of the gypsum seam modelling one-half of a pillar and roadway. The mesh was produced using PAFBLOCKS facility of PAFEC-75. For each run a slightly different mesh had to be prepared in order to simulate varying thickness and location of the satinspar bands. A typical mesh is seen in Figure 8.2. The idealised structure consisted of an average of 343 rectangular elements and 407 nodal points.

The horizontal movements along the vertical boundaries and the vertical movements along the lower horizontal edge of the structure were restrained. Similar mesh designs have been used previously by Crouch (1970); Watson (1979) and by Tincelin et al.(1972) with the absence of a simulated gypsum floor.

8.5.2 Analysis

In all cases modelled, the structure was loaded along the upper edge with a constant stress of 3 MPa and the mechanical properties of satinspar and gypsum were maintained constant and are similar to those given in Section Six.

Initial stress distribution in the pillar cross-section was achieved without simulated satinspar bands.

In the second set of runs, satinspar bands were assumed to be present at the top and at the base of the pillar. The thickness of the bands were varied at each run and were 0.05m, 0.10m, 0.15m, 0.20m and 0.25m.

In the third set of runs, satinspar bands are assumed to be present at an equal distance away (1m) from the pillar base and the top of the pillar. The thicknesses of the satinspar bands were altered for each run as in the previous set of runs.

The fourth, and last, set of runs was carried out assuming that a single satinspar band of varied thicknesses was present at mid-height of the pillar.

8.5.3 Results of Analysis

The results of the analysis have been presented in the form of principal stress contours and stress vectors in Figures 8.7 to 8.12. Although the graphical outputs presented are self-descriptive, the points of some significance will be discussed briefly.

When the results of the second set of runs are compared with those of the initial state of stress (Figures 8.7 and 8.8) it appears that:

(1) the maximum principal stresses (tensile) along the lower edge of the gypsum roof increase as the thickness of the satinspar increases, while minimum prinicipal stresses (compressive) decrease.

(2) The magnitude of the maximum principal stresses (compressive) along the upper edge of the gypsum roof increases with increasing thickness of the satinspar bands, while the minimum principal stresses (compressive) decrease.

(3) the magnitude of the maximum principal stresses (compressive) and minimum principal stresses (compressive) decrease with increasing thickness of the satinspar bands around the pillar skin.

(4) both principal stresses are compressive and decrease with increasing satinspar thickness in the pillar core. This is particularly important for pillar stability.

(5) around the pillar corners, the maximum and minimum principal stresses are compressive, but the latter decrease, while the former increases with increase of satinspar thickness.

As already pointed out in Section Six, the gypsum roof deflected comparatively more than the main body of the pillar and hence effectively prevented excessive expansion of the soft satinspar bands.

When comparing the results of the third set of runs (Figures 8.9 and 8.10) with those of the first set, it emerges that:

(1) At the lower section of the roof beam, the maximum principal stresses (tensile) increase, whereas the minimum principal stresses (compressive) decrease with an increase of satinspar thickness.

(2) At the upper section of the simulated gypsum roof, both stresses are compressive, but the maximum principal stresses increase, while the minimum principal stresses decrease in magnitude as the satinspar thickness increases.

(3) Around the pillar skin, the maximum principal stresses which were compressive in the earlier analysis became tensile in nature and the magnitude increases with increasing thickness of the satinspar band. The minimum principal stresses are compressive but decrease in magnitude with increasing satinspar thickness.

(4) Inside the pillar, both stresses are largely compressive but decrease in magnitude as the thickness of the satinspar increases.

(5) Around the pillar corners, both stresses are compressive and decrease in magnitude with increasing satinspar thickness.

When results of the fourth set of runs (Figures 8.11 and 8.12) are compared to those of the first set of runs, it can be said that:

(1) Around the lower section of the gypsum roof beam and the pillar corners, inside the pillar, the nature and behaviour of stresses are similar to those described in the previous cases, except the change in the magnitude of stresses due to increasing satinspar thickness is less pronounced.

(2) At the upper section of the gypsum beam, both stresses are compressive and decrease with increasing satinspar thickness.

(3) Around the pillar skin, particularly towards the gypsum and satinspar interface, the maximum principal stresses are tensile, and increase considerably with increasing thickness of satinspar, while the minimum principal stresses (compressive) decrease.

In Figure 8.12c, the direction of the principal stresses are shown for the second set of runs and for the fourth set of runs.

The above studies were carried out on a linear elastic idealised structure where satinspar bands were assumed to be perfectly horizontal, uniform in thickness, etc. Furthermore, the studies were made in plane strain conditions which does not make allowance for the effect of the roadway cross-cuts. Therefore, the analysis only provides an estimate of the true in-situ case.

It may be concluded that although failure of the pillar skin is possible due to induced tensile stresses if the thickness and spacing of the satinspar bands are unfavourable the larger section of the pillar, notably the core of the pillar, will be in a confined state.

* * *

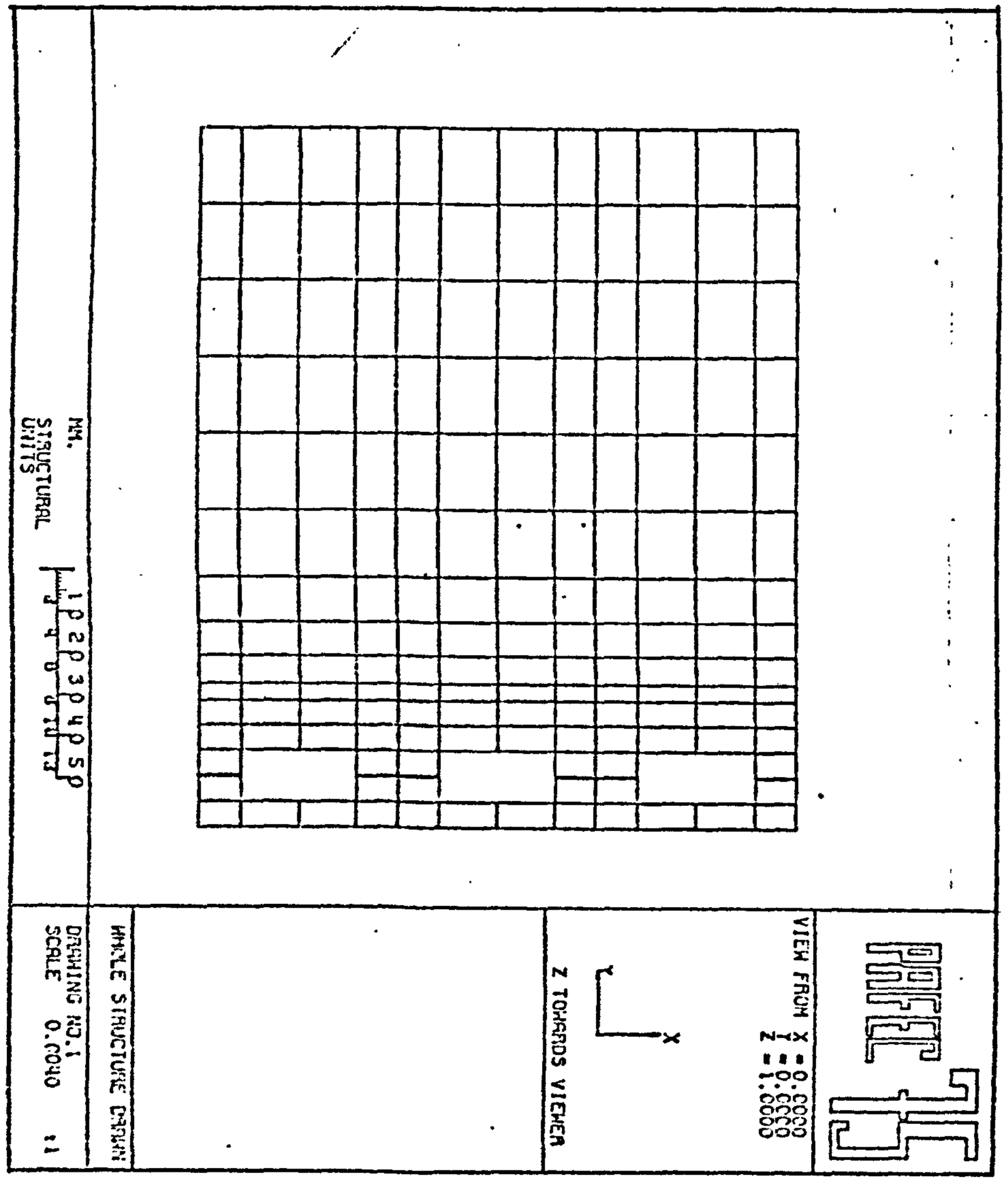
MM.
STRUCTURAL UNITS
0 5 10 20 30 40 50
MULTIPLY BY 10
PAFEC 75
VIEW FROM X = 0.0000
Y = 0.0000
Z = 1.0000
Y
X
Z TOWARDS VIEWER
WHOLE STRUCTURE DRAWN
DRAWING NO.1
SCALE 0.0040 :1

FIG 8.1

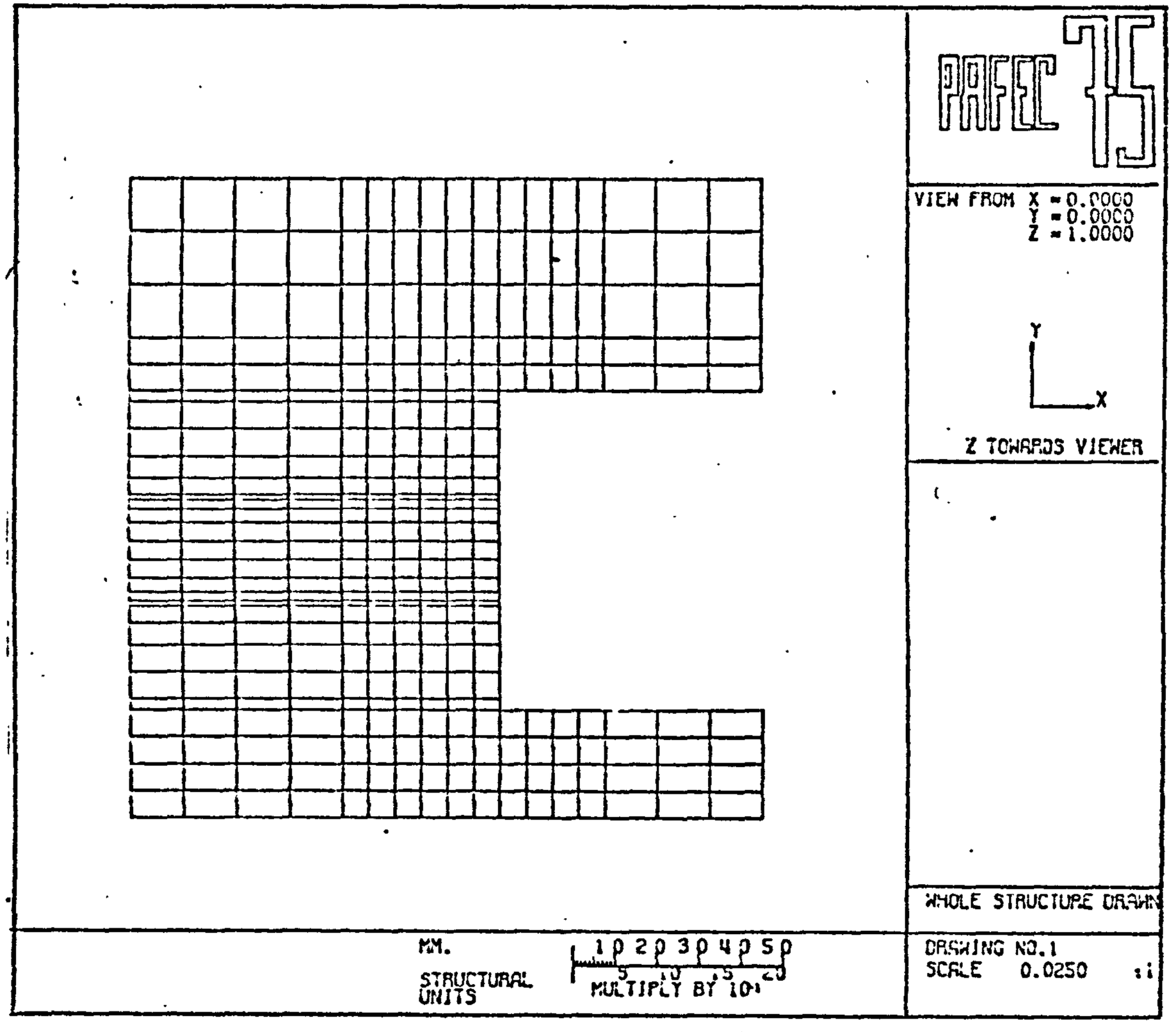
PAFEC 75
VIEW FROM X = 0.0000
Y = 0.0000
Z = 1.0000
Y
X
Z TOWARDS VIEWER
WHOLE STRUCTURE DRAWN
MM.
STRUCTURAL UNITS
0 10 20 30 40 50
MULTIPLY BY 10
DRAWING NO.1
SCALE 0.0250 :1

FIG 8.2

FIG 8.3

TITLE FINITE ELEMENT MODELLING OF MINE WORKINGS E=4.8

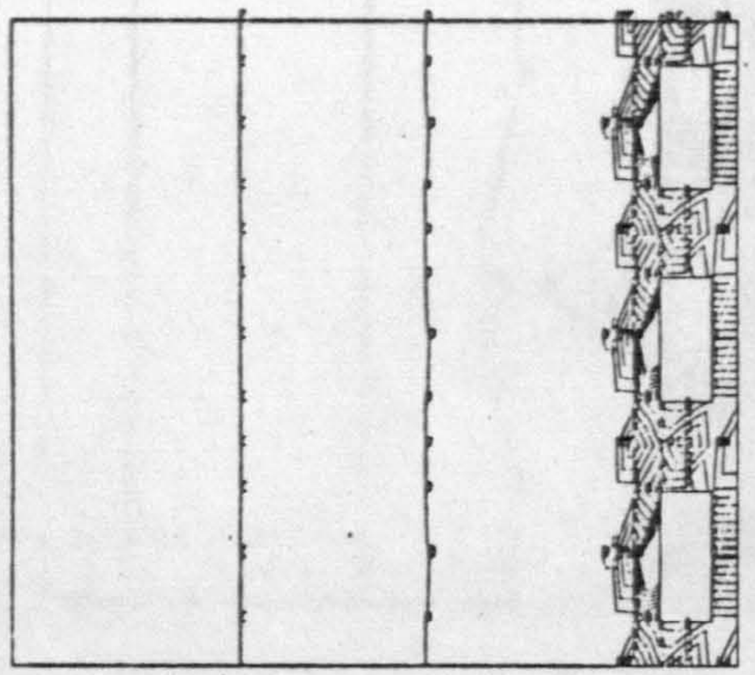

PAFEC 75

VIEW FROM X = 0.0000
Y = 0.0000
Z = 1.0000

Z TOWARDS VIEWER

MAXIMUM PRINCIPAL (MOST POSITIVE) STRESS MULTIPLY BY 10^4

-0.7100
-0.5650
-0.4200
-0.2750
-0.1300
0.0141
0.1590
0.3030
0.4480
0.5930

LOAD CASE =1

WHOLE STRUCTURE DRAWN AS DEFINED IN PARAM.ORDER

MM.
STRUCTURAL UNITS 1 0 2 0 3 0 4 0 5 0
2 4 6 8 10 12

DRAWING NO.4
SCALE 0.0040 :1

TITLE FINITE ELEMENT MODELLING OF MINE WORKINGS (INITIAL, E=0.48)

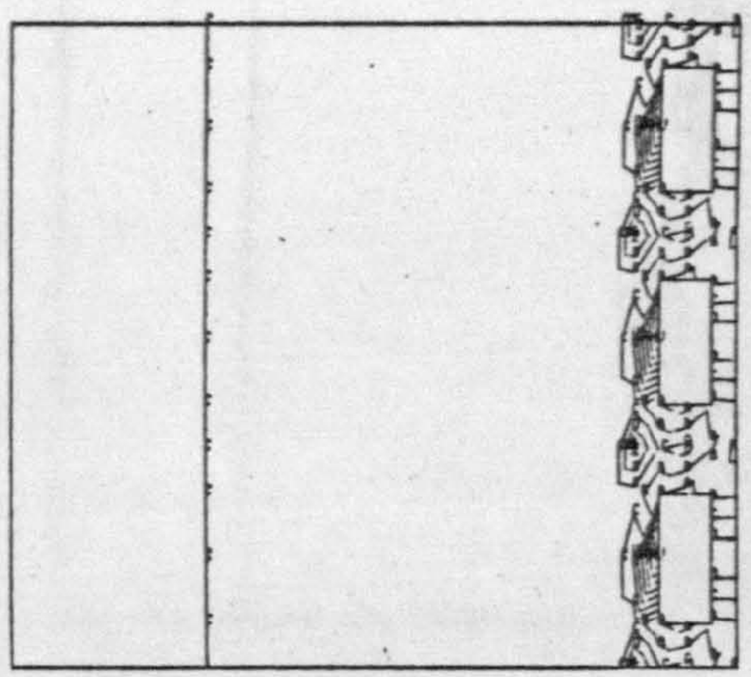

PAFEC 75

VIEW FROM X = 0.0000
Y = 0.0000
Z = 1.0000

Z TOWARDS VIEWER

MAXIMUM PRINCIPAL (MOST POSITIVE) STRESS MULTIPLY BY 10^4

-0.8540
-0.4820
-0.1100
0.2610
0.6330
1.0000
1.3700
1.7400
2.1200
2.4900

LOAD CASE =1

WHOLE STRUCTURE DRAWN AS DEFINED IN PARAM.ORDER

MM.
STRUCTURAL UNITS 1 0 2 0 3 0 4 0 5 0
2 4 6 8 10 12

DRAWING NO.4
SCALE 0.0040 :1

TITLE FINITE ELEMENT MODELLING OF MINE WORKINGS (INITIAL, E=0.048)

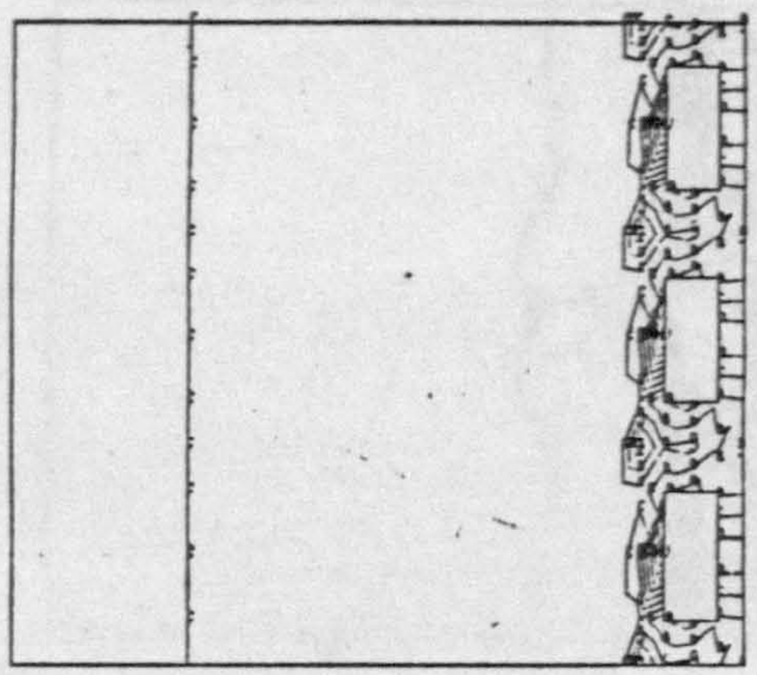

PAFEC 75

VIEW FROM X = 0.0000
Y = 0.0000
Z = 1.0000

Z TOWARDS VIEWER

MAXIMUM PRINCIPAL (MOST POSITIVE) STRESS MULTIPLY BY 10^4

-0.6870
-0.4930
-0.0997
0.2940
0.6880
1.0600
1.4700
1.6700
2.2600
2.6500

LOAD CASE =1

WHOLE STRUCTURE DRAWN AS DEFINED IN PARAM.ORDER

MM.
STRUCTURAL UNITS 1 0 2 0 3 0 4 0 5 0
2 4 6 8 10 12

DRAWING NO.4
SCALE 0.0040 :1

TITLE FINITE ELEMENT MODELLING OF MINE WORKINGS E 4.8

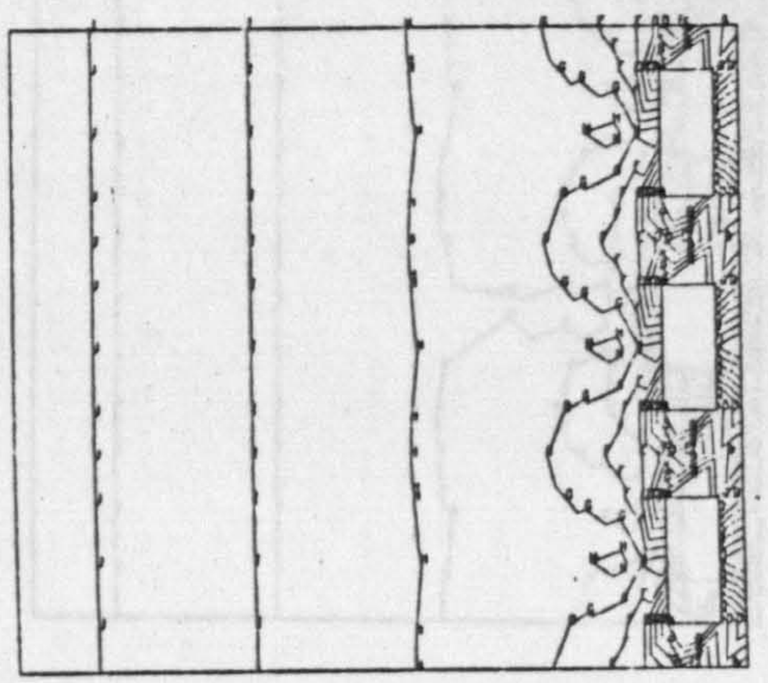

PAFEC 75

VIEW FROM X = 0.0000
Y = 0.0000
Z = 1.0000

Z TOWARDS VIEWER

MINIMUM PRINCIPAL (MOST NEGATIVE) STRESS MULTIPLY BY 10^4

-2.5500
-2.2800
-2.0100
-1.7400
-1.4700
-1.2100
-0.9420
-0.6730
-0.4050
-0.1360

LOAD CASE =1

WHOLE STRUCTURE DRAWN AS DEFINED IN PARAM.ORDER

MM.
STRUCTURAL UNITS 1 0 2 0 3 0 4 0 5 0
2 4 6 8 10 12

DRAWING NO.5
SCALE 0.0040 :1

TITLE FINITE ELEMENT MODELLING OF MINE WORKINGS (INITIAL, E=0.48)

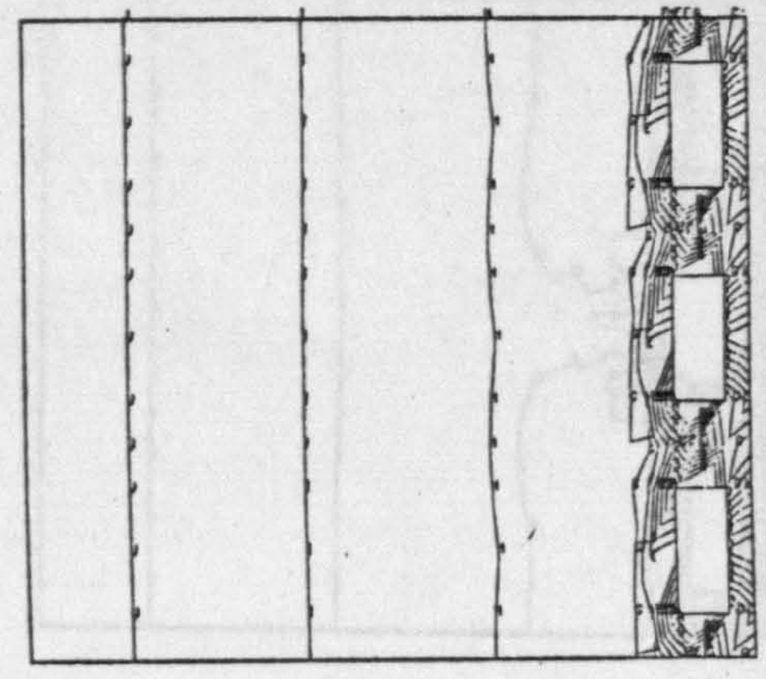

PAFEC 75

VIEW FROM X = 0.0000
Y = 0.0000
Z = 1.0000

Z TOWARDS VIEWER

MINIMUM PRINCIPAL (MOST NEGATIVE) STRESS MULTIPLY BY 10^4

-2.8300
-2.5300
-2.2400
-1.9400
-1.6500
-1.3500
-1.0500
-0.7640
-0.4680
-0.1720

LOAD CASE =1

WHOLE STRUCTURE DRAWN AS DEFINED IN PARAM.ORDER

MM.
STRUCTURAL UNITS 1 0 2 0 3 0 4 0 5 0
2 4 6 8 10 12

DRAWING NO.5
SCALE 0.0040 :1

TITLE FINITE ELEMENT MODELLING OF MINE WORKINGS (INITIAL, E=0.048)

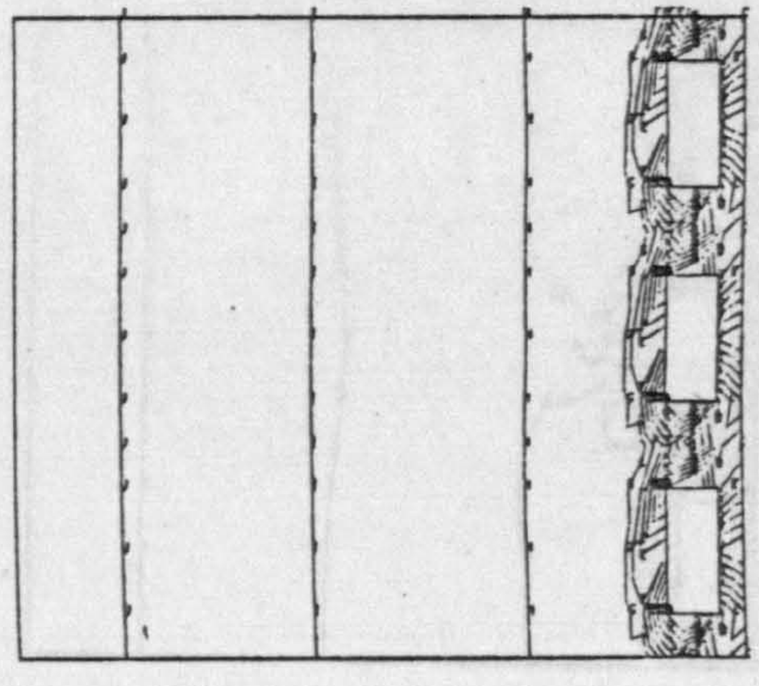

PAFEC 75

VIEW FROM X = 0.0000
Y = 0.0000
Z = 1.0000

Z TOWARDS VIEWER

MINIMUM PRINCIPAL (MOST NEGATIVE) STRESS MULTIPLY BY 10^4

-3.0900
-2.7700
-2.4400
-2.1200
-1.8000
-1.4700
-1.1500
-0.8280
-0.5030
-0.1790

LOAD CASE =1

WHOLE STRUCTURE DRAWN AS DEFINED IN PARAM.ORDER

MM.
STRUCTURAL UNITS 1 0 2 0 3 0 4 0 5 0
2 4 6 8 10 12

DRAWING NO.5
SCALE 0.0040 :1

FIG 8.4

TITLE FINITE ELEMENT MODELLING OF MINE WORKINGS $E_M = 4.8$ GPa

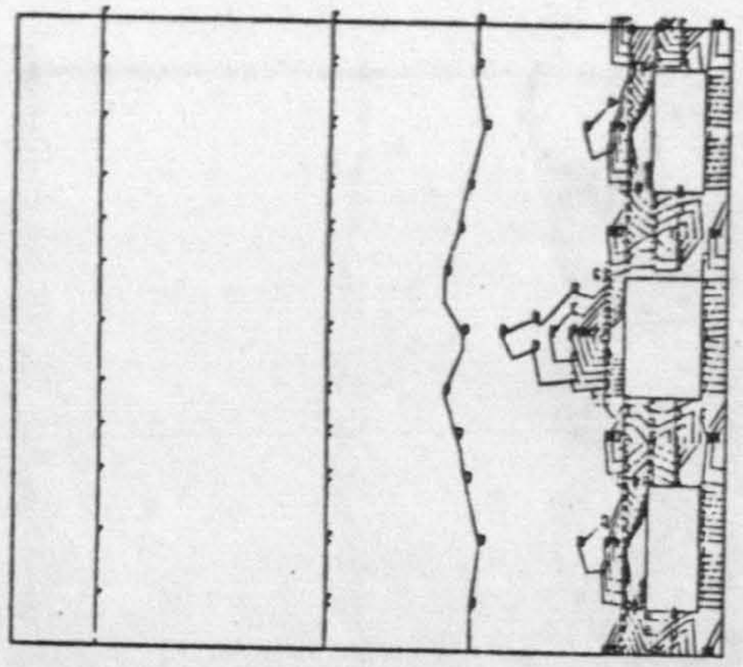

PAFEC 75

VIEW FROM X = 0.0000
Y = 0.0000
Z = 1.0000

Z TOWARDS VIEWER

MAXIMUM PRINCIPAL (MOST POSITIVE) STRESS MULTIPLY BY 10^4

-0.7200
-0.5850
-0.4510
-0.3170
-0.1820
-0.0484
0.0859
0.2200
0.3540
0.4880

LOAD CASE =1

WHOLE STRUCTURE DRAWN
AS DEFINED IN FRONT.GROUP

MM.
STRUCTURAL UNITS 1 0 2 0 3 0 4 0 5 0
2 4 6 8 10 12

DRAWING NO.4
SCALE 0.0040 :1

TITLE FINITE ELEMENT MODELLING OF MINE WORKINGS $E_M = 0.48$ GPa

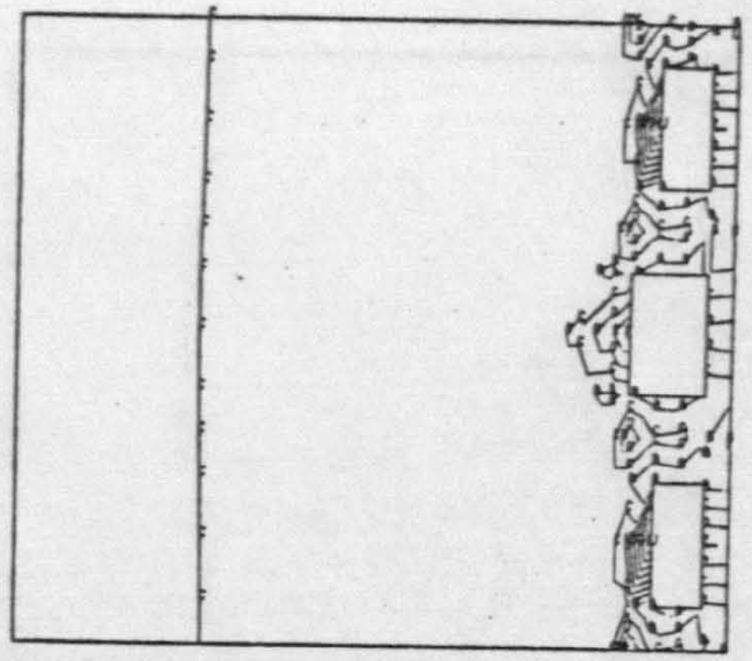

PAFEC 75

VIEW FROM X = 0.0000
Y = 0.0000
Z = 1.0000

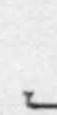

Z TOWARDS VIEWER

MAXIMUM PRINCIPAL (MOST POSITIVE) STRESS MULTIPLY BY 10^4

-0.8800
-0.4930
-0.1060
0.2800
0.6670
1.0500
1.4400
1.8200
2.2100
2.6000

LOAD CASE =1

WHOLE STRUCTURE DRAWN
AS DEFINED IN FRONT.GROUP

MM.
STRUCTURAL UNITS 1 0 2 0 3 0 4 0 5 0
2 4 6 8 10 12

DRAWING NO.4
SCALE 0.0040 :1

TITLE FINITE ELEMENT MODELLING OF MINE WORKINGS $E = 0.047$

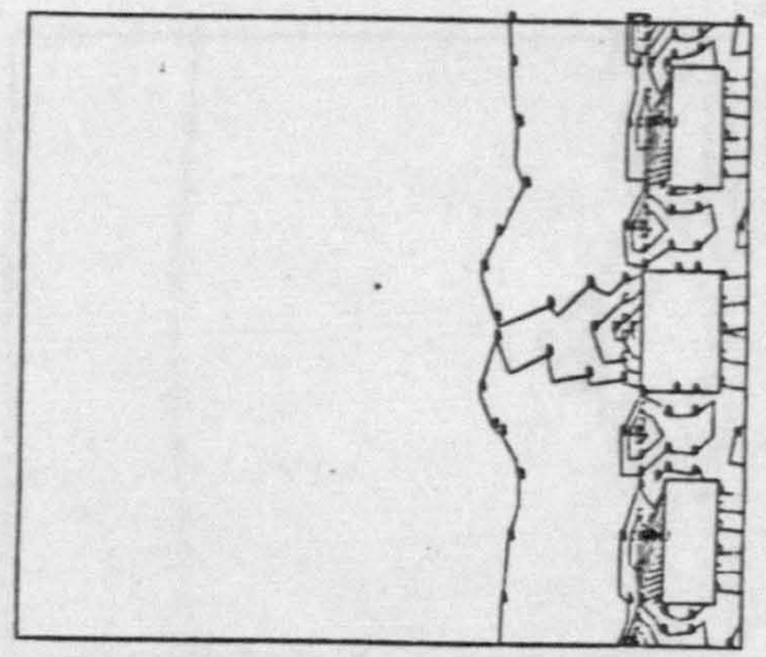

PAFEC 75

VIEW FROM X = 0.0000
Y = 0.0000
Z = 1.0000

Z TOWARDS VIEWER

MAXIMUM PRINCIPAL (MOST POSITIVE) STRESS MULTIPLY BY 10^4

-0.7280
-0.3360
0.0554
0.4470
0.8390
1.2300
1.6200
2.0100
2.4000
2.7900

LOAD CASE =1

WHOLE STRUCTURE DRAWN
AS DEFINED IN FRONT.GROUP

MM.
STRUCTURAL UNITS 1 0 2 0 3 0 4 0 5 0
2 4 6 8 10 12

DRAWING NO.4
SCALE 0.0040 :1

TITLE FINITE ELEMENT MODELLING OF MINE WORKINGS $E_M = 4.8$ GPa

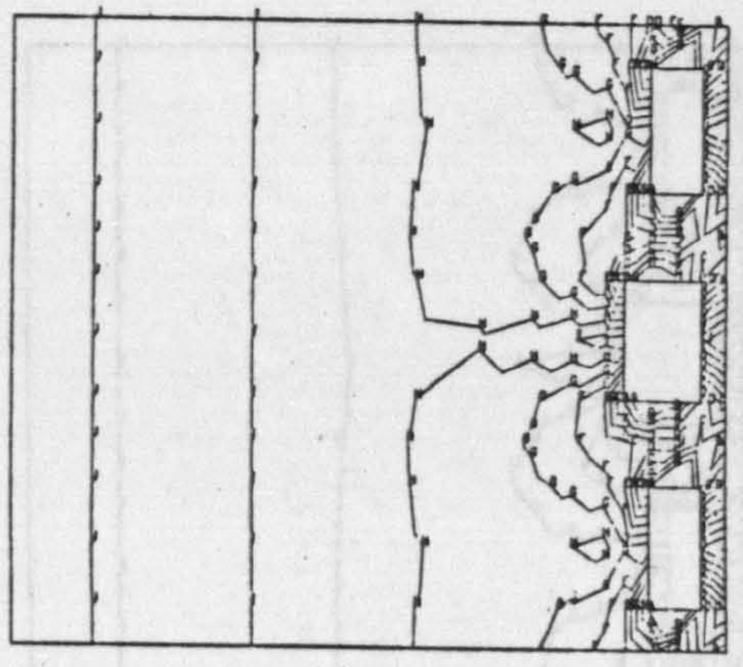

PAFEC 75

VIEW FROM X = 0.0000
Y = 0.0000
Z = 1.0000

Z TOWARDS VIEWER

MINIMUM PRINCIPAL (MOST NEGATIVE) STRESS MULTIPLY BY 10^4

-2.6200
-2.3500
-2.0700
-1.7900
-1.5200
-1.2400
-0.9690
-0.6920
-0.4160
-0.1400

LOAD CASE =1

WHOLE STRUCTURE DRAWN
AS DEFINED IN FRONT.GROUP

MM.
STRUCTURAL UNITS 1 0 2 0 3 0 4 0 5 0
2 4 6 8 10 12

DRAWING NO.5
SCALE 0.0040 :1

TITLE FINITE ELEMENT MODELLING OF MINE WORKINGS $E_M = 0.48$ GPa

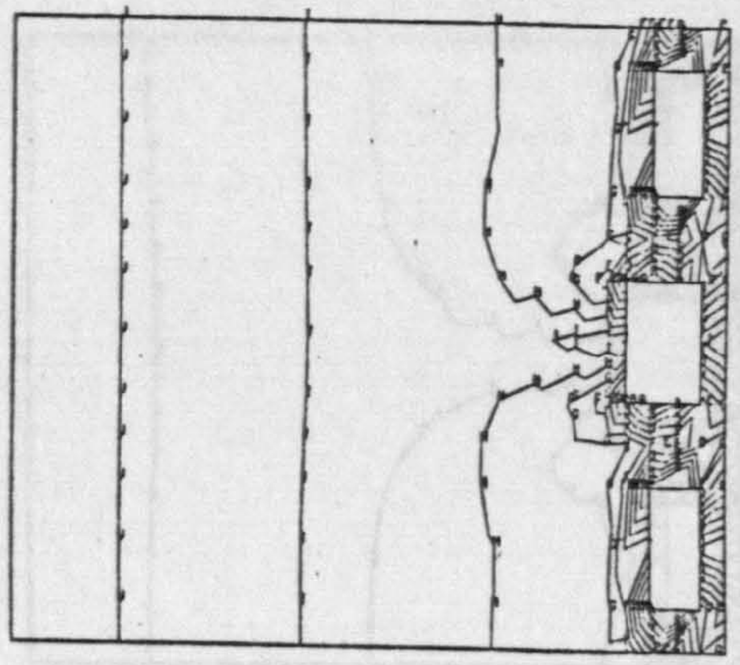

PAFEC 75

VIEW FROM X = 0.0000
Y = 0.0000
Z = 1.0000

Z TOWARDS VIEWER

MINIMUM PRINCIPAL (MOST NEGATIVE) STRESS MULTIPLY BY 10^4

-3.0000
-2.6900
-2.3700
-2.0600
-1.7500
-1.4300
-1.1200
-0.8110
-0.4970
-0.1830

LOAD CASE =1

WHOLE STRUCTURE DRAWN
AS DEFINED IN FRONT.GROUP

MM.
STRUCTURAL UNITS 1 0 2 0 3 0 4 0 5 0
2 4 6 8 10 12

DRAWING NO.5
SCALE 0.0040 :1

TITLE FINITE ELEMENT MODELLING OF MINE WORKINGS $E = 0.048$

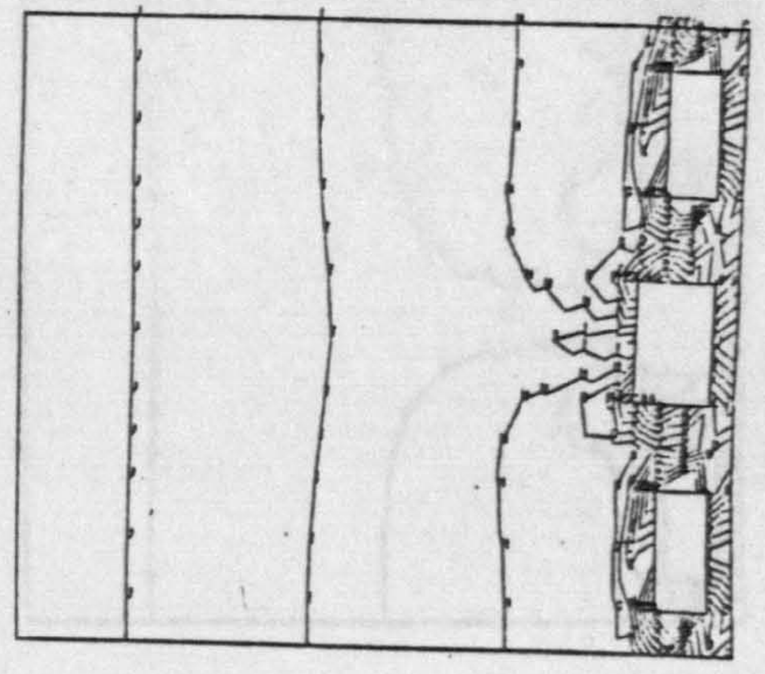

PAFEC 75

VIEW FROM X = 0.0000
Y = 0.0000
Z = 1.0000

Z TOWARDS VIEWER

MINIMUM PRINCIPAL (MOST NEGATIVE) STRESS MULTIPLY BY 10^4

-3.0800
-2.7600
-2.4400
-2.1200
-1.8000
-1.4700
-1.1500
-0.8360
-0.5140
-0.1920

LOAD CASE =1

WHOLE STRUCTURE DRAWN
AS DEFINED IN FRONT.GROUP

MM.
STRUCTURAL UNITS 1 0 2 0 3 0 4 0 5 0
2 4 6 8 10 12

DRAWING NO.5
SCALE 0.0040 :1

FIG 8.5

TITLE FINITE ELEMENT MODELLING OF MINE WORKINGS E = 4.8

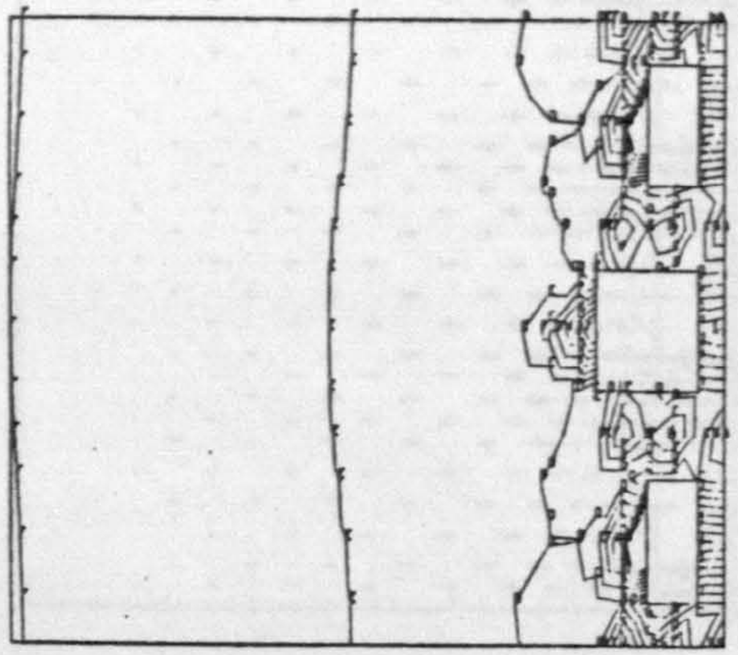

PAFEC 75

VIEW FROM X = 0.0000
Y = 0.0000
Z = 1.0000

Z TOWARDS VIEWER

MAXIMUM PRINCIPAL (MOST POSITIVE) STRESS MULTIPLY BY 10^6

-0.6750
-0.7050
-0.5350
-0.3640
-0.1940
-0.0243
0.1450
0.3160
0.4860
0.6560

LOAD CASE =1

WHOLE STRUCTURE DRAWN AS DEFINED IN FRONT.UNDER

MM. 1 0 2 0 3 0 4 0 5 0
STRUCTURAL UNITS 2 4 6 8 10 12

DRAWING NO.4
SCALE 0.0040 :1

TITLE FINITE ELEMENT MODELLING OF MINE WORKINGS E=0.48

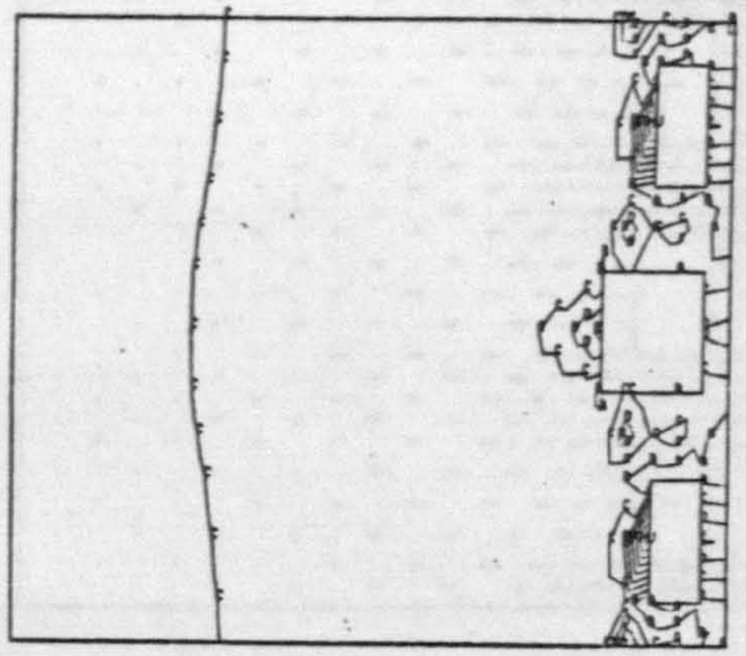

PAFEC 75

VIEW FROM X = 0.0000
Y = 0.0000
Z = 1.0000

Z TOWARDS VIEWER

MAXIMUM PRINCIPAL (MOST POSITIVE) STRESS MULTIPLY BY 10^6

-0.9260
-0.5180
-0.1100
0.2970
0.7060
1.1100
1.5200
1.9300
2.3300
2.7400

LOAD CASE =1

WHOLE STRUCTURE DRAWN AS DEFINED IN FRONT.UNDER

MM. 1 0 2 0 3 0 4 0 5 0
STRUCTURAL UNITS 2 4 6 8 10 12

DRAWING NO.4
SCALE 0.0040 :1

TITLE FINITE ELEMENT MODELLING OF MINE WORKINGS E = 0.048 6P.

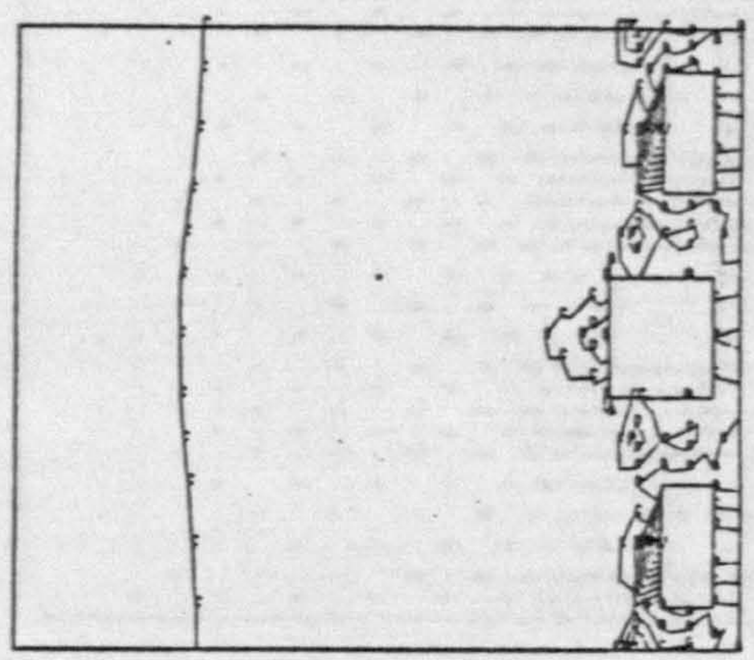

PAFEC 75

VIEW FROM X = 0.0000
Y = 0.0000
Z = 1.0000

Z TOWARDS VIEWER

MAXIMUM PRINCIPAL (MOST POSITIVE) STRESS MULTIPLY BY 10^6

-0.9600
-0.5290
-0.0988
0.3310
0.7620
1.1900
1.6200
2.0500
2.4800
2.9100

LOAD CASE =1

WHOLE STRUCTURE DRAWN AS DEFINED IN FRONT.UNDER

MM. 1 0 2 0 3 0 4 0 5 0
STRUCTURAL UNITS 2 4 6 8 10 12

DRAWING NO.4
SCALE 0.0040 :1

TITLE FINITE ELEMENT MODELLING OF MINE WORKINGS E = 4.8

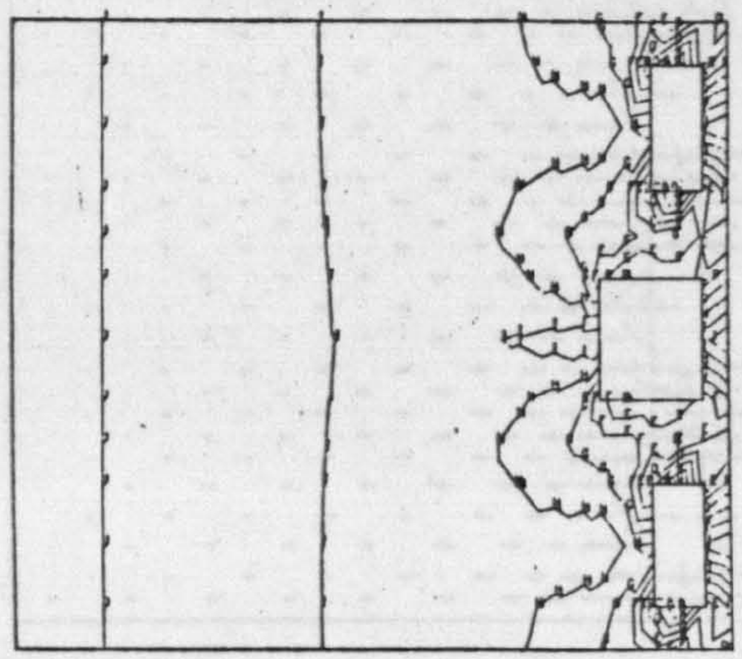

PAFEC 75

VIEW FROM X = 0.0000
Y = 0.0000
Z = 1.0000

Z TOWARDS VIEWER

MINIMUM PRINCIPAL (MOST NEGATIVE) STRESS MULTIPLY BY 10^6

-3.5900
-3.2000
-2.8200
-2.4400
-2.0600
-1.6800
-1.3000
-0.9200
-0.5390
-0.1570

LOAD CASE =1

WHOLE STRUCTURE DRAWN AS DEFINED IN FRONT.UNDER

MM. 1 0 2 0 3 0 4 0 5 0
STRUCTURAL UNITS 2 4 6 8 10 12

DRAWING NO.5
SCALE 0.0040 :1

TITLE FINITE ELEMENT MODELLING OF MINE WORKINGS E=0.48

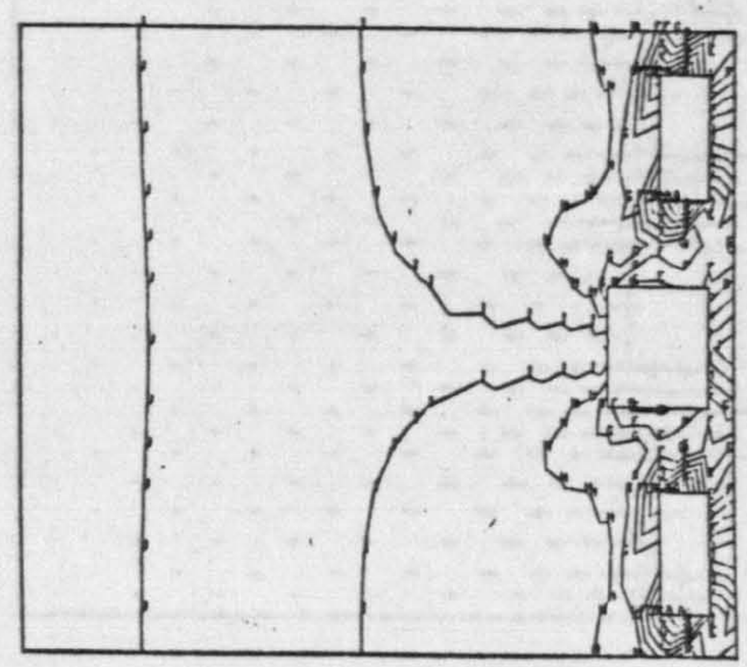

PAFEC 75

VIEW FROM X = 0.0000
Y = 0.0000
Z = 1.0000

Z TOWARDS VIEWER

MINIMUM PRINCIPAL (MOST NEGATIVE) STRESS MULTIPLY BY 10^6

-3.9400
-3.5300
-3.1100
-2.7000
-2.2800
-1.8700
-1.4500
-1.0300
-0.6230
-0.2080

LOAD CASE =1

WHOLE STRUCTURE DRAWN AS DEFINED IN FRONT.UNDER

MM. 1 0 2 0 3 0 4 0 5 0
STRUCTURAL UNITS 2 4 6 8 10 12

DRAWING NO.5
SCALE 0.0040 :1

TITLE FINITE ELEMENT MODELLING OF MINE WORKINGS E= 0.048 6P.

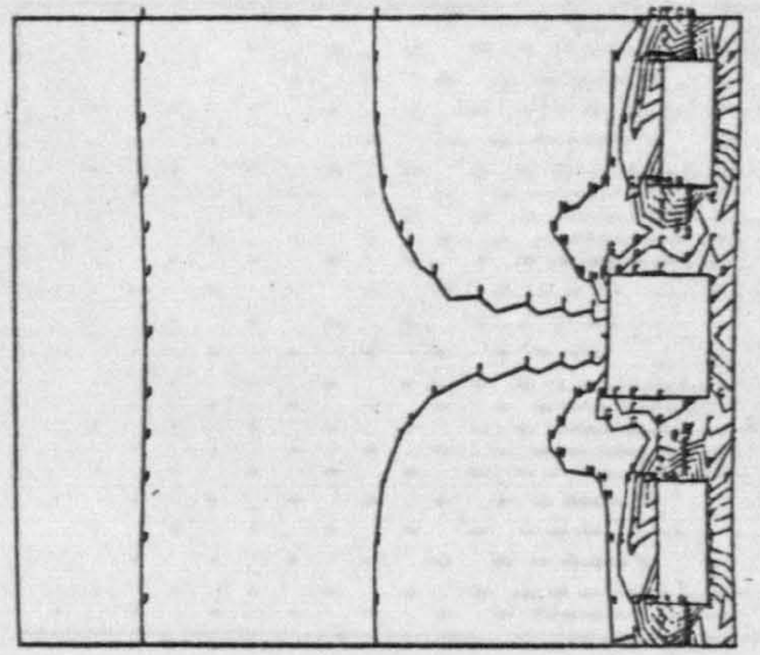

PAFEC 75

VIEW FROM X = 0.0000
Y = 0.0000
Z = 1.0000

Z TOWARDS VIEWER

MINIMUM PRINCIPAL (MOST NEGATIVE) STRESS MULTIPLY BY 10^6

-4.0700
-3.6400
-3.2100
-2.7800
-2.3500
-1.9200
-1.5000
-1.0700
-0.6470
-0.2180

LOAD CASE =1

WHOLE STRUCTURE DRAWN AS DEFINED IN FRONT.UNDER

MM. 1 0 2 0 3 0 4 0 5 0
STRUCTURAL UNITS 2 4 6 8 10 12

DRAWING NO.5
SCALE 0.0040 :1

FIG 8.6

TITLE FINITE ELEMENT MODELLING OF MINE WORKINGS E = 4.8

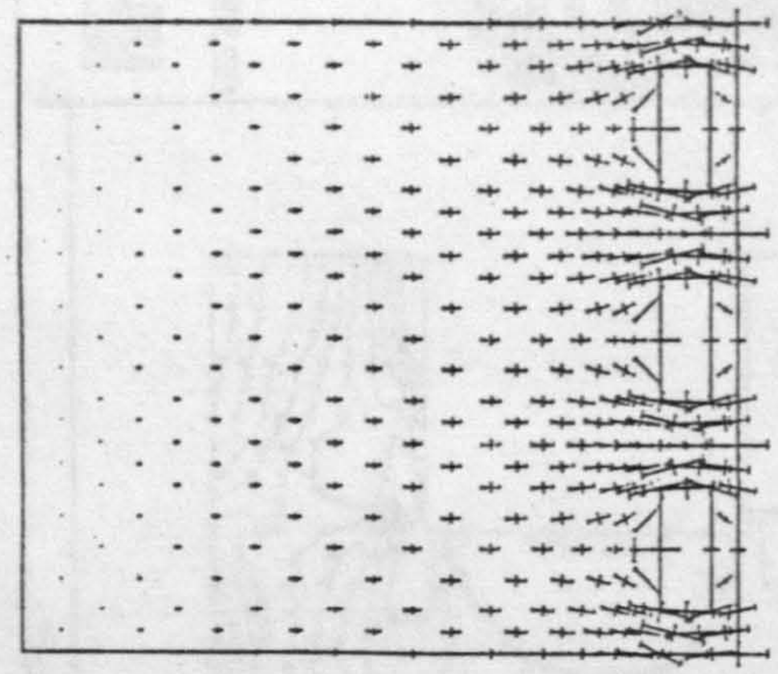

PAFEC 75

VIEW FROM X = 0.0000
Y = 0.0000
Z = 1.0000

Z TOWARDS VIEWER

LOAD CASE =1
SCALE OF VECTORS =
17.4031E+03UNITS/CM.

SHOWN WITH END BARS

WHOLE STRUCTURE DRAWN
AS DEFINED IN FRONT.GROUP

MM.
STRUCTURAL UNITS 1 0 2 0 3 0 4 0 5 0
4 4 6 8 10 12

DRAWING NO.3
SCALE 0.0040 :1

TITLE FINITE ELEMENT MODELLING OF MINE WORKINGS E = 4.8

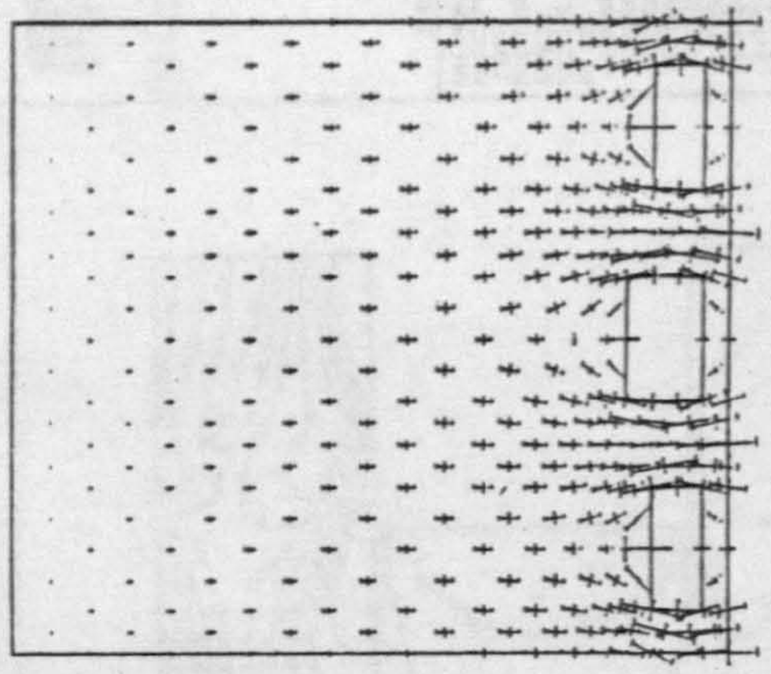

PAFEC 75

VIEW FROM X = 0.0000
Y = 0.0000
Z = 1.0000

Z TOWARDS VIEWER

LOAD CASE =1
SCALE OF VECTORS =
17.9214E+03UNITS/CM.

SHOWN WITH END BARS

WHOLE STRUCTURE DRAWN
AS DEFINED IN FRONT.GROUP

MM.
STRUCTURAL UNITS 1 0 2 0 3 0 4 0 5 0
4 4 6 8 10 12

DRAWING NO.3
SCALE 0.0040 :1

TITLE FINITE ELEMENT MODELLING OF MINE WORKINGS E = 4.8

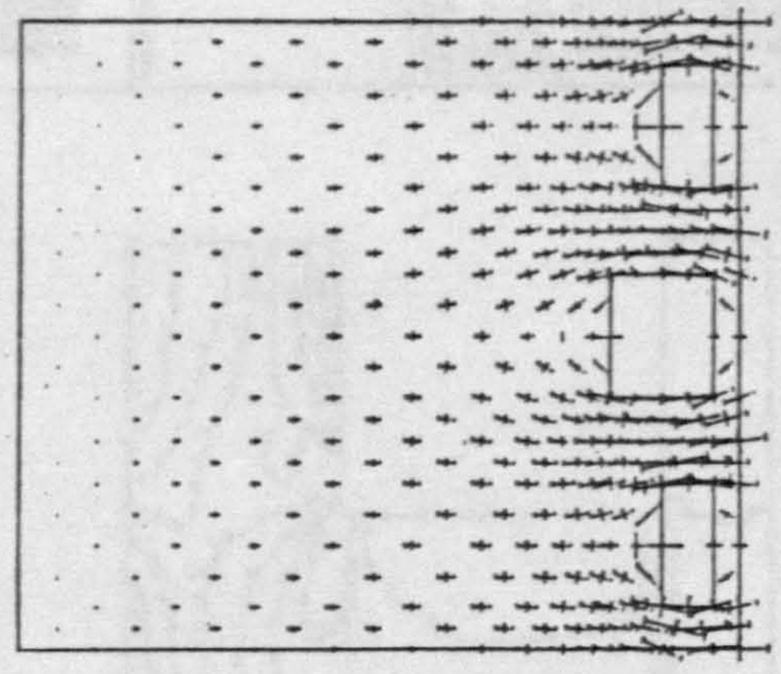

PAFEC 75

VIEW FROM X = 0.0000
Y = 0.0000
Z = 1.0000

Z TOWARDS VIEWER

LOAD CASE =1
SCALE OF VECTORS =
18.9CDEE+03UNITS/CM.

SHOWN WITH END BARS

WHOLE STRUCTURE DRAWN
AS DEFINED IN FRONT.GROUP

MM.
STRUCTURAL UNITS 1 0 2 0 3 0 4 0 5 0
4 4 6 8 10 12

DRAWING NO.3
SCALE 0.0040 :1

TITLE FINITE ELEMENT MODELLING OF MINE WORKINGS (INITIAL, E=0.048)

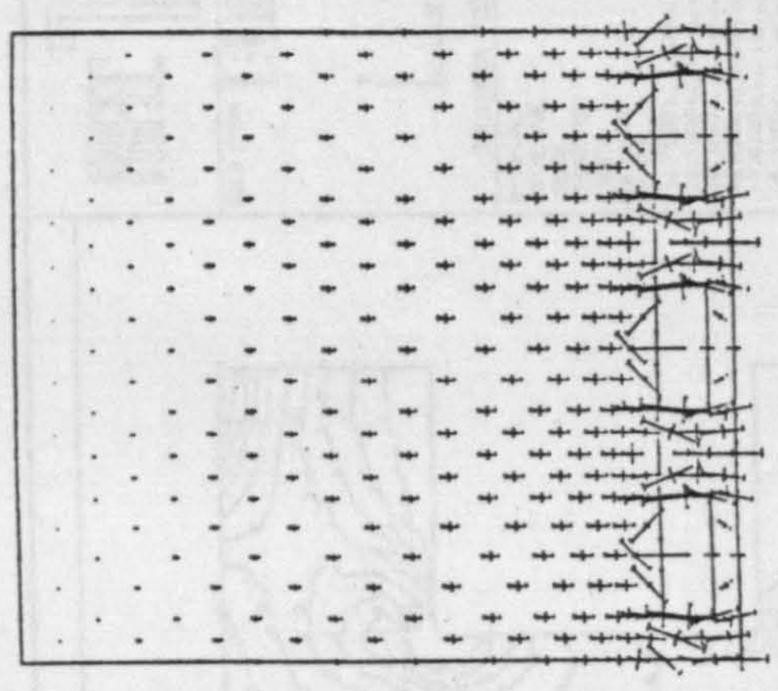

PAFEC 75

VIEW FROM X = 0.0000
Y = 0.0000
Z = 1.0000

Z TOWARDS VIEWER

LOAD CASE =1
SCALE OF VECTORS =
19.6524E+03UNITS/CM.

SHOWN WITH END BARS

WHOLE STRUCTURE DRAWN
AS DEFINED IN FRONT.GROUP

MM.
STRUCTURAL UNITS 1 0 2 0 3 0 4 0 5 0
4 4 6 8 10 12

DRAWING NO.3
SCALE 0.0040 :1

TITLE FINITE ELEMENT MODELLING OF MINE WORKINGS E = 0.0468

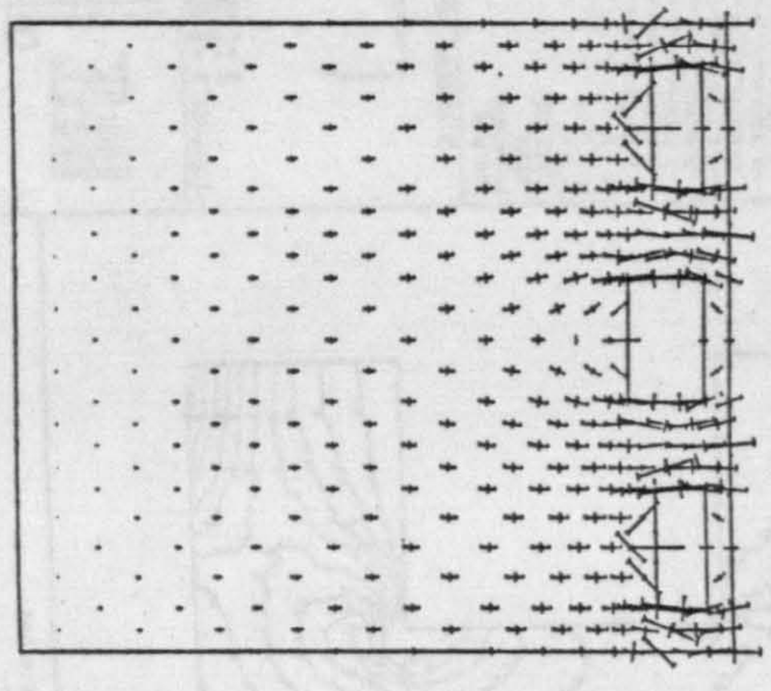

PAFEC 75

VIEW FROM X = 0.0000
Y = 0.0000
Z = 1.0000

Z TOWARDS VIEWER

LOAD CASE =1
SCALE OF VECTORS =
21.0116E+03UNITS/CM.

SHOWN WITH END BARS

WHOLE STRUCTURE DRAWN
AS DEFINED IN FRONT.GROUP

MM.
STRUCTURAL UNITS 1 0 2 0 3 0 4 0 5 0
4 4 6 8 10 12

DRAWING NO.3
SCALE 0.0040 :1

TITLE FINITE ELEMENT MODELLING OF MINE WORKINGS E = 0.048 GPa

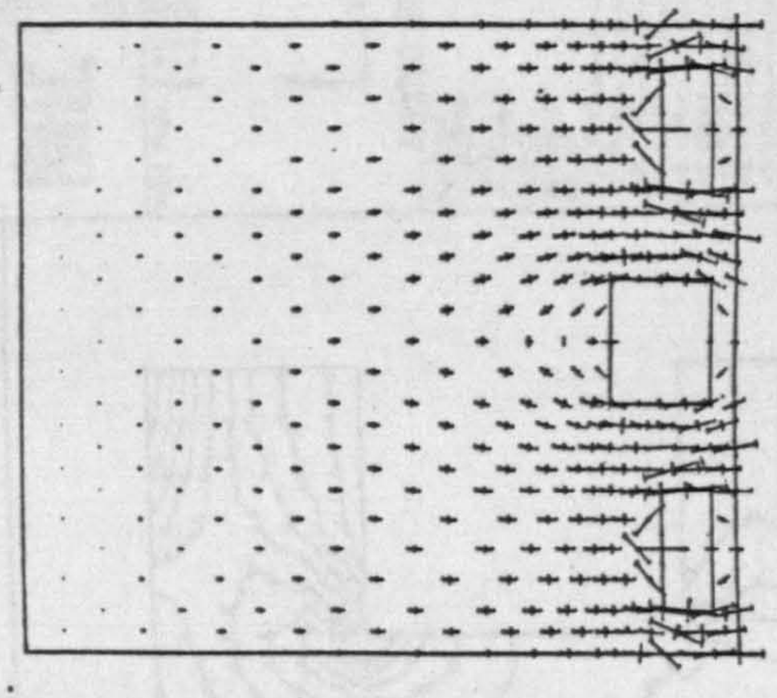

PAFEC 75

VIEW FROM X = 0.0000
Y = 0.0000
Z = 1.0000

Z TOWARDS VIEWER

LOAD CASE =1
SCALE OF VECTORS =
22.7722E+03UNITS/CM.

SHOWN WITH END BARS

WHOLE STRUCTURE DRAWN
AS DEFINED IN FRONT.GROUP

MM.
STRUCTURAL UNITS 1 0 2 0 3 0 4 0 5 0
4 4 6 8 10 12

DRAWING NO.3
SCALE 0.0040 :1

FIG 8.7

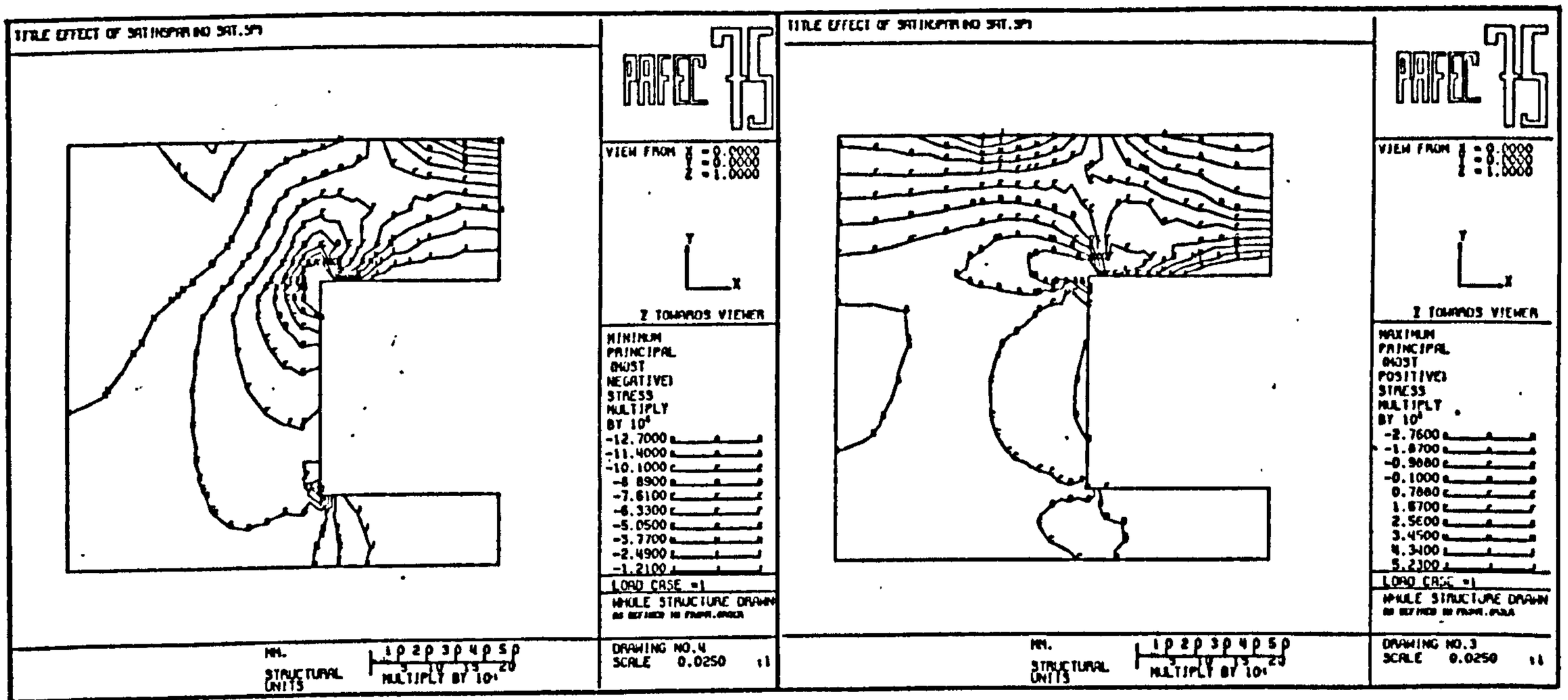
TITLE EFFECT OF SATINSPAR ON SAT.SP
PAFEC 75
VIEW FROM X = 0.0000 Y = 0.0000 Z = 1.0000
Y
X
Z TOWARDS VIEWER
MINIMUM PRINCIPAL (MOST NEGATIVE) STRESS MULTIPLY BY 10^6
-12.7000
-11.4000
-10.1000
-8.8900
-7.6100
-6.3300
-5.0500
-3.7700
-2.4900
-1.2100
LOAD CASE =1
WHOLE STRUCTURE DRAWN
MM.
STRUCTURAL UNITS
1 0 2 0 3 0 4 0 5 0
3 10 13 20
MULTIPLY BY 10^4
DRAWING NO.4
SCALE 0.0250 :1
TITLE EFFECT OF SATINSPAR ON SAT.SP
PAFEC 75
VIEW FROM X = 0.0000 Y = 0.0000 Z = 1.0000
Z TOWARDS VIEWER
MAXIMUM PRINCIPAL (MOST POSITIVE) STRESS MULTIPLY BY 10^6
-2.7600
-1.8700
-0.9680
-0.1000
0.7880
1.6700
2.5600
3.4500
4.3400
5.2300
LOAD CASE =1
WHOLE STRUCTURE DRAWN
MM.
STRUCTURAL UNITS
1 0 2 0 3 0 4 0 5 0
3 10 13 20
MULTIPLY BY 10^4
DRAWING NO.3
SCALE 0.0250 :1

A

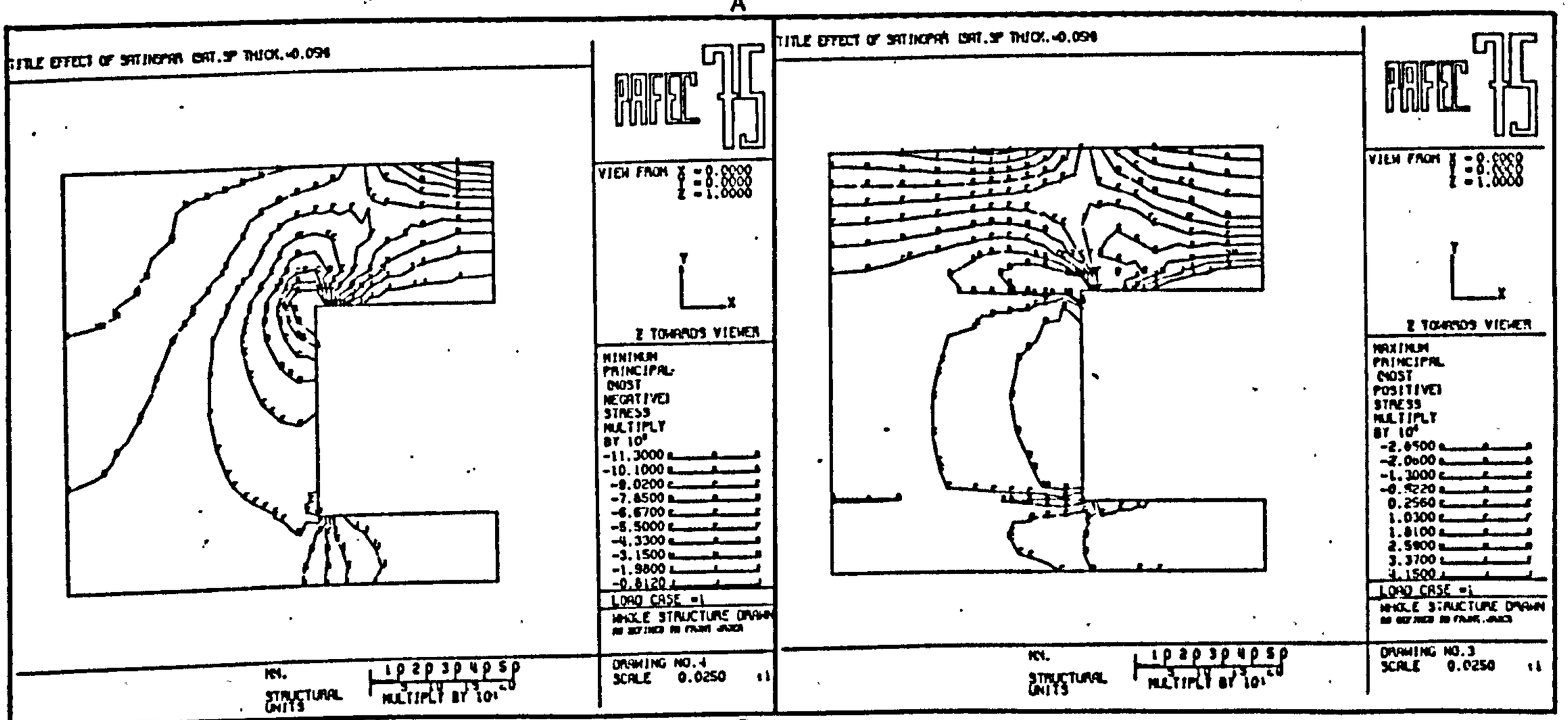
TITLE EFFECT OF SATINSPAR SAT.SP THICK.=0.056
PAFEC 75
VIEW FROM X = 0.0000 Y = 0.0000 Z = 1.0000
Y
X
Z TOWARDS VIEWER
MINIMUM PRINCIPAL (MOST NEGATIVE) STRESS MULTIPLY BY 10^6
-11.3000
-10.1000
-8.9200
-7.8500
-6.6700
-5.5000
-4.3300
-3.1500
-1.9800
-0.8120
LOAD CASE =1
WHOLE STRUCTURE DRAWN
MM.
STRUCTURAL UNITS
1 0 2 0 3 0 4 0 5 0
3 10 13 20
MULTIPLY BY 10^4
DRAWING NO.4
SCALE 0.0250 :1
TITLE EFFECT OF SATINSPAR SAT.SP THICK.=0.056
PAFEC 75
VIEW FROM X = 0.0000 Y = 0.0000 Z = 1.0000
Z TOWARDS VIEWER
MAXIMUM PRINCIPAL (MOST POSITIVE) STRESS MULTIPLY BY 10^6
-2.6500
-2.0600
-1.3000
-0.4220
0.2560
1.0300
1.8100
2.5900
3.3700
4.1500
LOAD CASE =1
WHOLE STRUCTURE DRAWN
MM.
STRUCTURAL UNITS
1 0 2 0 3 0 4 0 5 0
3 10 13 20
MULTIPLY BY 10^4
DRAWING NO.3
SCALE 0.0250 :1

B

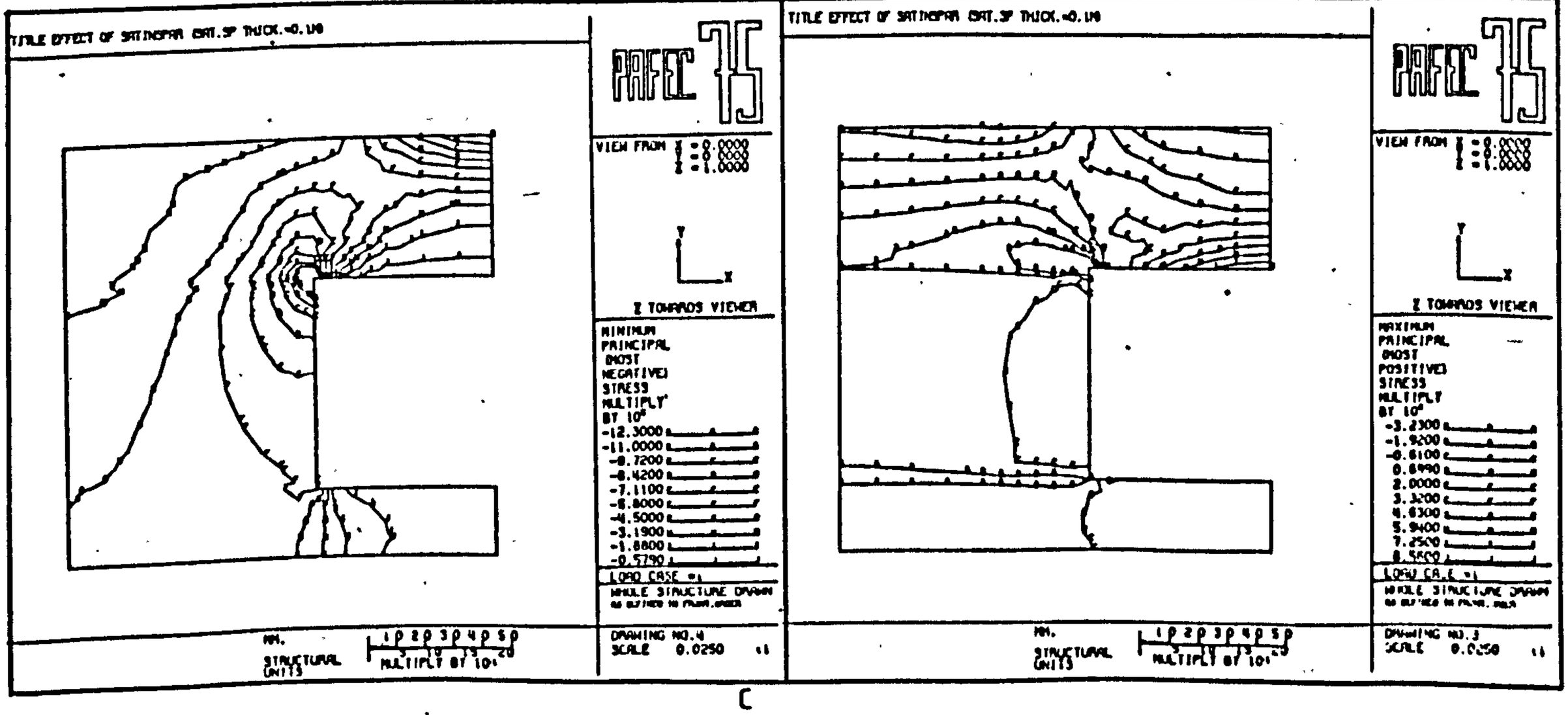
TITLE EFFECT OF SATINSPAR SAT.SP THICK.=0.136
PAFEC 75
VIEW FROM X = 0.0000 Y = 0.0000 Z = 1.0000
Y
X
Z TOWARDS VIEWER
MINIMUM PRINCIPAL (MOST NEGATIVE) STRESS MULTIPLY BY 10^6
-12.3000
-11.0000
-9.7200
-8.4200
-7.1100
-5.8000
-4.5000
-3.1900
-1.8800
-0.5790
LOAD CASE =1
WHOLE STRUCTURE DRAWN
MM.
STRUCTURAL UNITS
1 0 2 0 3 0 4 0 5 0
3 10 13 20
MULTIPLY BY 10^4
DRAWING NO.4
SCALE 0.0250 :1
TITLE EFFECT OF SATINSPAR SAT.SP THICK.=0.136
PAFEC 75
VIEW FROM X = 0.0000 Y = 0.0000 Z = 1.0000
Z TOWARDS VIEWER
MAXIMUM PRINCIPAL (MOST POSITIVE) STRESS MULTIPLY BY 10^6
-3.2300
-1.9200
-0.6100
0.6990
2.0000
3.3200
4.6300
5.9400
7.2500
8.5600
LOAD CASE =1
WHOLE STRUCTURE DRAWN
MM.
STRUCTURAL UNITS
1 0 2 0 3 0 4 0 5 0
3 10 13 20
MULTIPLY BY 10^4
DRAWING NO.3
SCALE 0.0250 :1

C

FIG 8.8

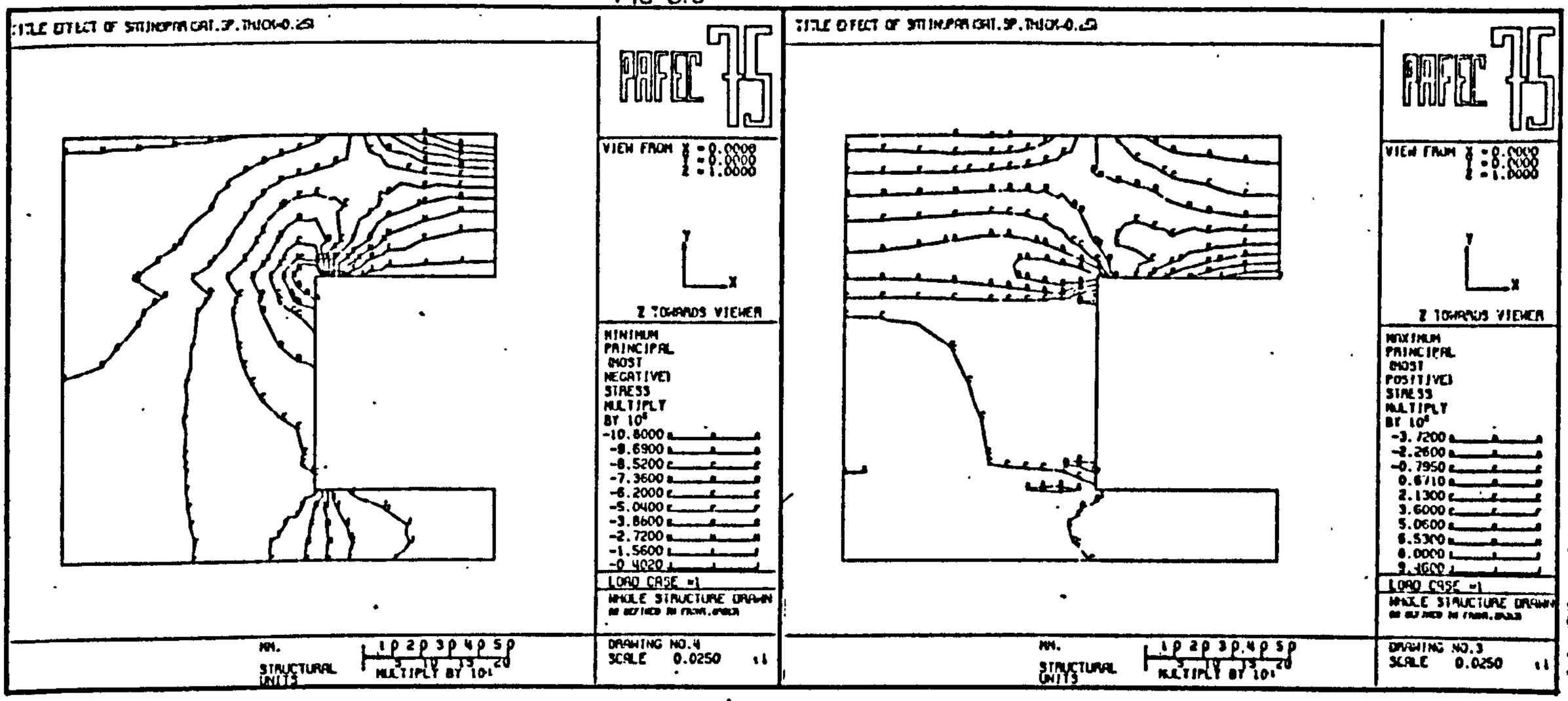
TITLE EFFECT OF SATINSPARSAT.SP.THICK=0.25
PAFEC 75
VIEW FROM X = 0.0000 Y = 0.0000 Z = 1.0000
Y
X
Z TOWARDS VIEWER
MINIMUM PRINCIPAL (MOST NEGATIVE) STRESS MULTIPLY BY 10^6
-10.8000
-8.6900
-8.5200
-7.3600
-6.2000
-5.0400
-3.8600
-2.7200
-1.5600
-0.4020
LOAD CASE =1
WHOLE STRUCTURE DRAWN
MM.
STRUCTURAL UNITS
1 0 2 0 3 0 4 0 5 0
5 10 15 20
MULTIPLY BY 10^1
DRAWING NO.4
SCALE 0.0250 :1
TITLE EFFECT OF SATINSPARSAT.SP.THICK=0.25
PAFEC 75
VIEW FROM X = 0.0000 Y = 0.0000 Z = 1.0000
Z TOWARDS VIEWER
MAXIMUM PRINCIPAL (MOST POSITIVE) STRESS MULTIPLY BY 10^6
-3.7200
-2.2600
-0.7950
0.6710
2.1300
3.6000
5.0600
6.5300
8.0000
9.4600
LOAD CASE =1
WHOLE STRUCTURE DRAWN
MM.
STRUCTURAL UNITS
1 0 2 0 3 0 4 0 5 0
5 10 15 20
MULTIPLY BY 10^1
DRAWING NO.3
SCALE 0.0250 :1

A

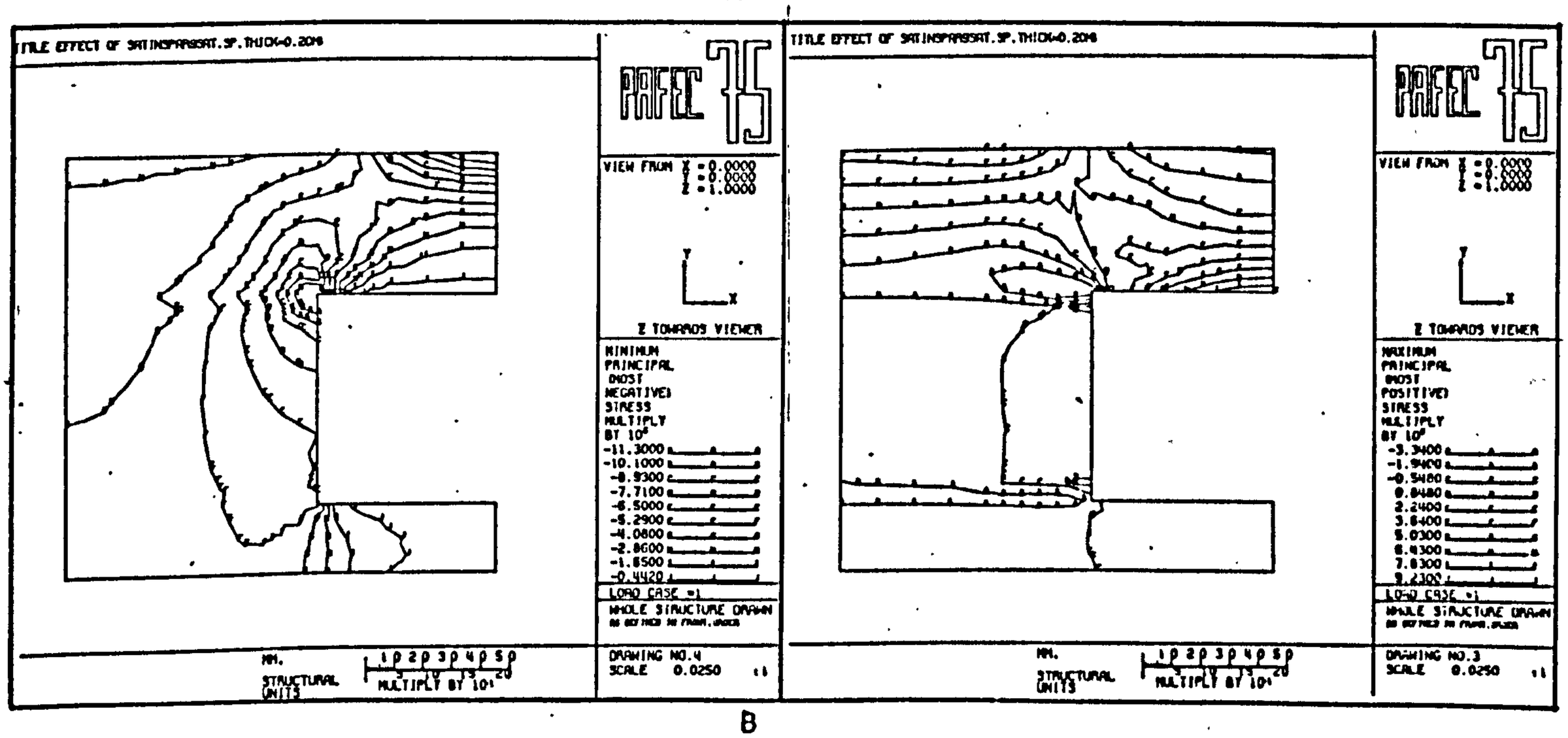
TITLE EFFECT OF SATINSPARSAT.SP.THICK=0.206
PAFEC 75
VIEW FROM X = 0.0000 Y = 0.0000 Z = 1.0000
Y
X
Z TOWARDS VIEWER
MINIMUM PRINCIPAL (MOST NEGATIVE) STRESS MULTIPLY BY 10^6
-11.3000
-10.1000
-8.9300
-7.7100
-6.5000
-5.2900
-4.0800
-2.8600
-1.6500
-0.4420
LOAD CASE =1
WHOLE STRUCTURE DRAWN
MM.
STRUCTURAL UNITS
1 0 2 0 3 0 4 0 5 0
5 10 15 20
MULTIPLY BY 10^1
DRAWING NO.4
SCALE 0.0250 :1
TITLE EFFECT OF SATINSPARSAT.SP.THICK=0.206
PAFEC 75
VIEW FROM X = 0.0000 Y = 0.0000 Z = 1.0000
Z TOWARDS VIEWER
MAXIMUM PRINCIPAL (MOST POSITIVE) STRESS MULTIPLY BY 10^6
-3.3400
-1.9400
-0.5480
0.8480
2.2400
3.6400
5.0300
6.4300
7.8300
9.2300
LOAD CASE =1
WHOLE STRUCTURE DRAWN
MM.
STRUCTURAL UNITS
1 0 2 0 3 0 4 0 5 0
5 10 15 20
MULTIPLY BY 10^1
DRAWING NO.3
SCALE 0.0250 :1

B

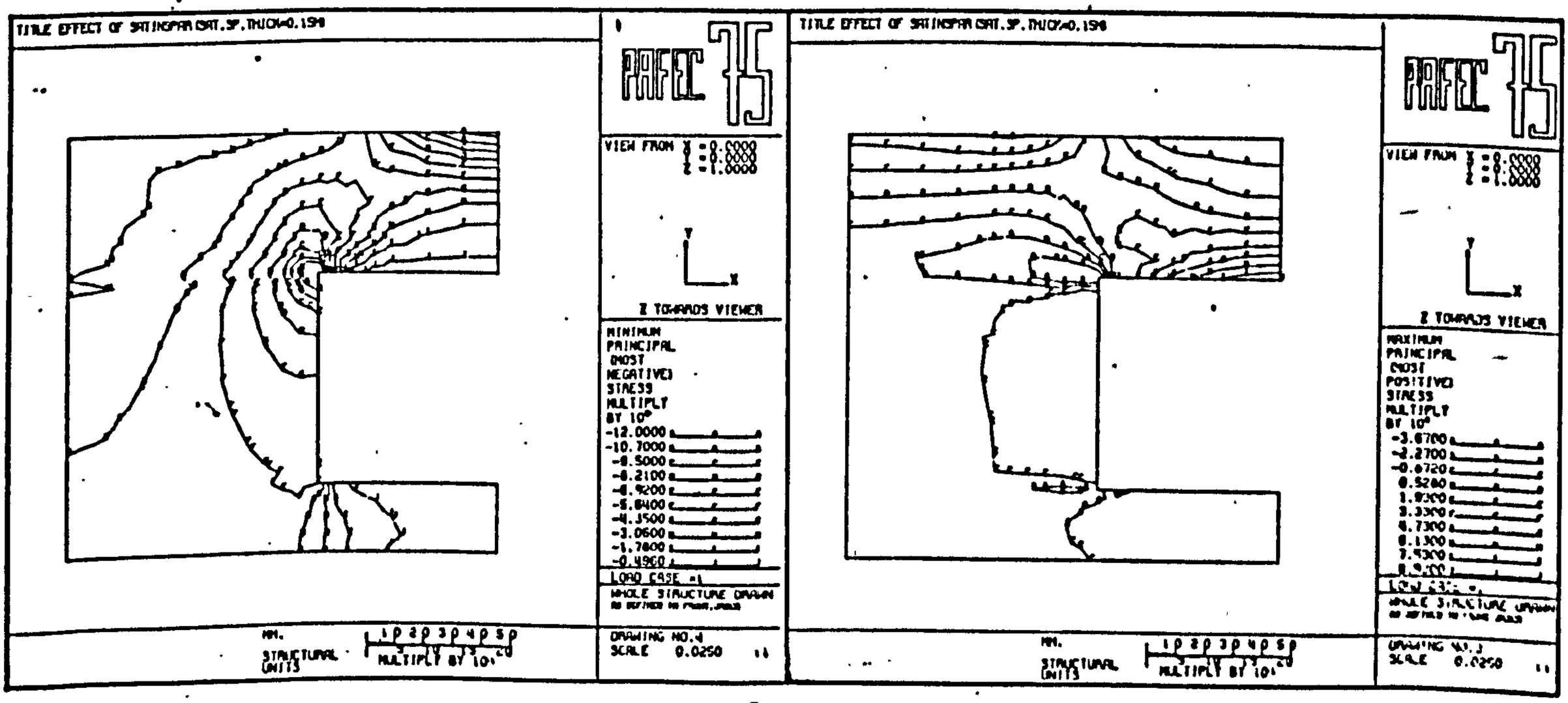
TITLE EFFECT OF SATINSPARSAT.SP.THICK=0.156
PAFEC 75
VIEW FROM X = 0.0000 Y = 0.0000 Z = 1.0000
Y
X
Z TOWARDS VIEWER
MINIMUM PRINCIPAL (MOST NEGATIVE) STRESS MULTIPLY BY 10^6
-12.0000
-10.7000
-9.5000
-8.2100
-6.9200
-5.6400
-4.3500
-3.0600
-1.7800
-0.4900
LOAD CASE =1
WHOLE STRUCTURE DRAWN
MM.
STRUCTURAL UNITS
1 0 2 0 3 0 4 0 5 0
5 10 15 20
MULTIPLY BY 10^1
DRAWING NO.4
SCALE 0.0250 :1
TITLE EFFECT OF SATINSPARSAT.SP.THICK=0.156
PAFEC 75
VIEW FROM X = 0.0000 Y = 0.0000 Z = 1.0000
Z TOWARDS VIEWER
MAXIMUM PRINCIPAL (MOST POSITIVE) STRESS MULTIPLY BY 10^6
-3.6700
-2.2700
-0.8720
0.5280
1.9300
3.3300
4.7300
6.1300
7.5300
8.9300
WHOLE STRUCTURE DRAWN
MM.
STRUCTURAL UNITS
1 0 2 0 3 0 4 0 5 0
5 10 15 20
MULTIPLY BY 10^1
SCALE 0.0250 :1

C

FIG 8.9

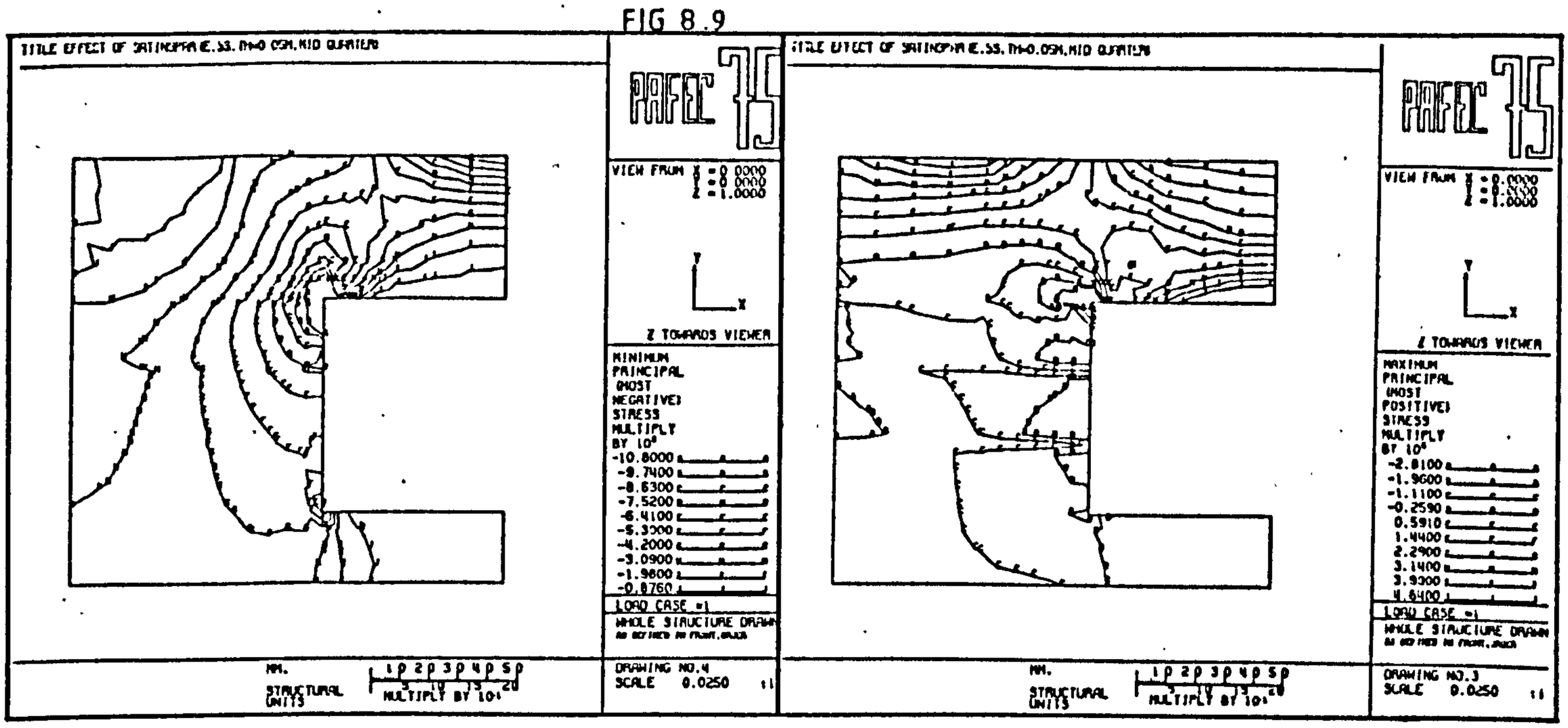
TITLE EFFECT OF SKIINSPAR E.SS. TH=0.05M, MID QUARTER
PAFEC 75
VIEW FROM X = 0.0000 Y = 0.0000 Z = 1.0000
Z TOWARDS VIEWER
MINIMUM PRINCIPAL (MOST NEGATIVE) STRESS MULTIPLY BY 10^8
-10.8000
-9.7400
-8.6300
-7.5200
-6.4100
-5.3000
-4.2000
-3.0900
-1.9800
-0.8760
LOAD CASE =1
WHOLE STRUCTURE DRAWN
MM.
STRUCTURAL UNITS
1 0 2 0 3 0 4 0 5 0
MULTIPLY BY 10^-1
DRAWING NO.4
SCALE 0.0250 :1
TITLE EFFECT OF SKIINSPAR E.SS. TH=0.05M, MID QUARTER
PAFEC 75
VIEW FROM X = 0.0000 Y = 0.0000 Z = 1.0000
Z TOWARDS VIEWER
MAXIMUM PRINCIPAL (MOST POSITIVE) STRESS MULTIPLY BY 10^8
-2.8100
-1.9600
-1.1100
-0.2590
0.5910
1.4400
2.2900
3.1400
3.9900
4.8400
LOAD CASE =1
WHOLE STRUCTURE DRAWN
MM.
STRUCTURAL UNITS
1 0 2 0 3 0 4 0 5 0
MULTIPLY BY 10^-1
DRAWING NO.3
SCALE 0.0250 :1

A

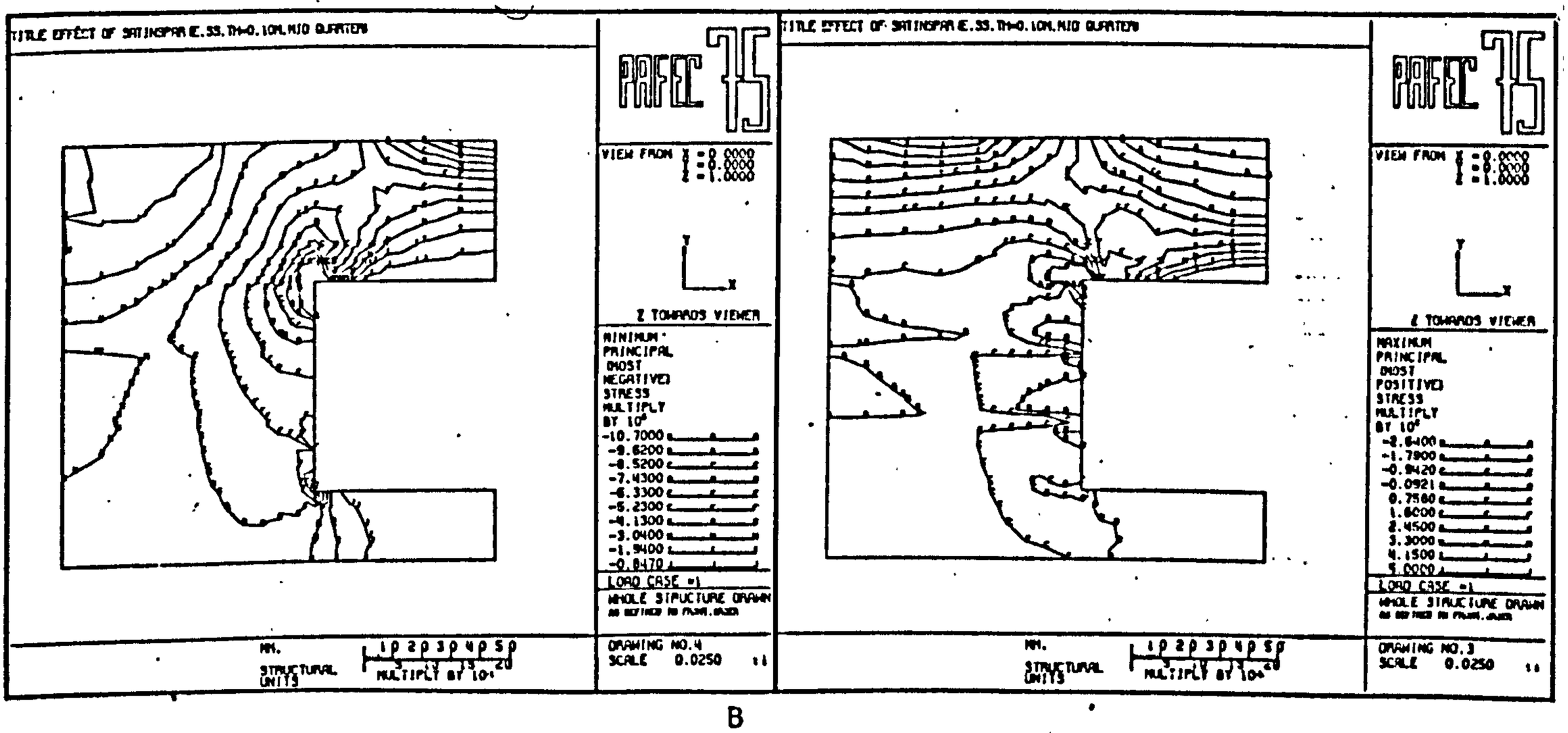
TITLE EFFECT OF SKIINSPAR E.SS. TH=0.10M, MID QUARTER
PAFEC 75
VIEW FROM X = 0.0000 Y = 0.0000 Z = 1.0000
Z TOWARDS VIEWER
MINIMUM PRINCIPAL (MOST NEGATIVE) STRESS MULTIPLY BY 10^8
-10.7000
-9.6200
-8.5200
-7.4300
-6.3300
-5.2300
-4.1300
-3.0400
-1.9400
-0.8470
LOAD CASE =1
WHOLE STRUCTURE DRAWN
MM.
STRUCTURAL UNITS
1 0 2 0 3 0 4 0 5 0
MULTIPLY BY 10^-1
DRAWING NO.4
SCALE 0.0250 :1
TITLE EFFECT OF SKIINSPAR E.SS. TH=0.10M, MID QUARTER
PAFEC 75
VIEW FROM X = 0.0000 Y = 0.0000 Z = 1.0000
Z TOWARDS VIEWER
MAXIMUM PRINCIPAL (MOST POSITIVE) STRESS MULTIPLY BY 10^8
-2.8400
-1.7900
-0.8420
-0.0921
0.7580
1.6000
2.4500
3.3000
4.1500
5.0000
LOAD CASE =1
WHOLE STRUCTURE DRAWN
MM.
STRUCTURAL UNITS
1 0 2 0 3 0 4 0 5 0
MULTIPLY BY 10^-1
DRAWING NO.3
SCALE 0.0250 :1

B

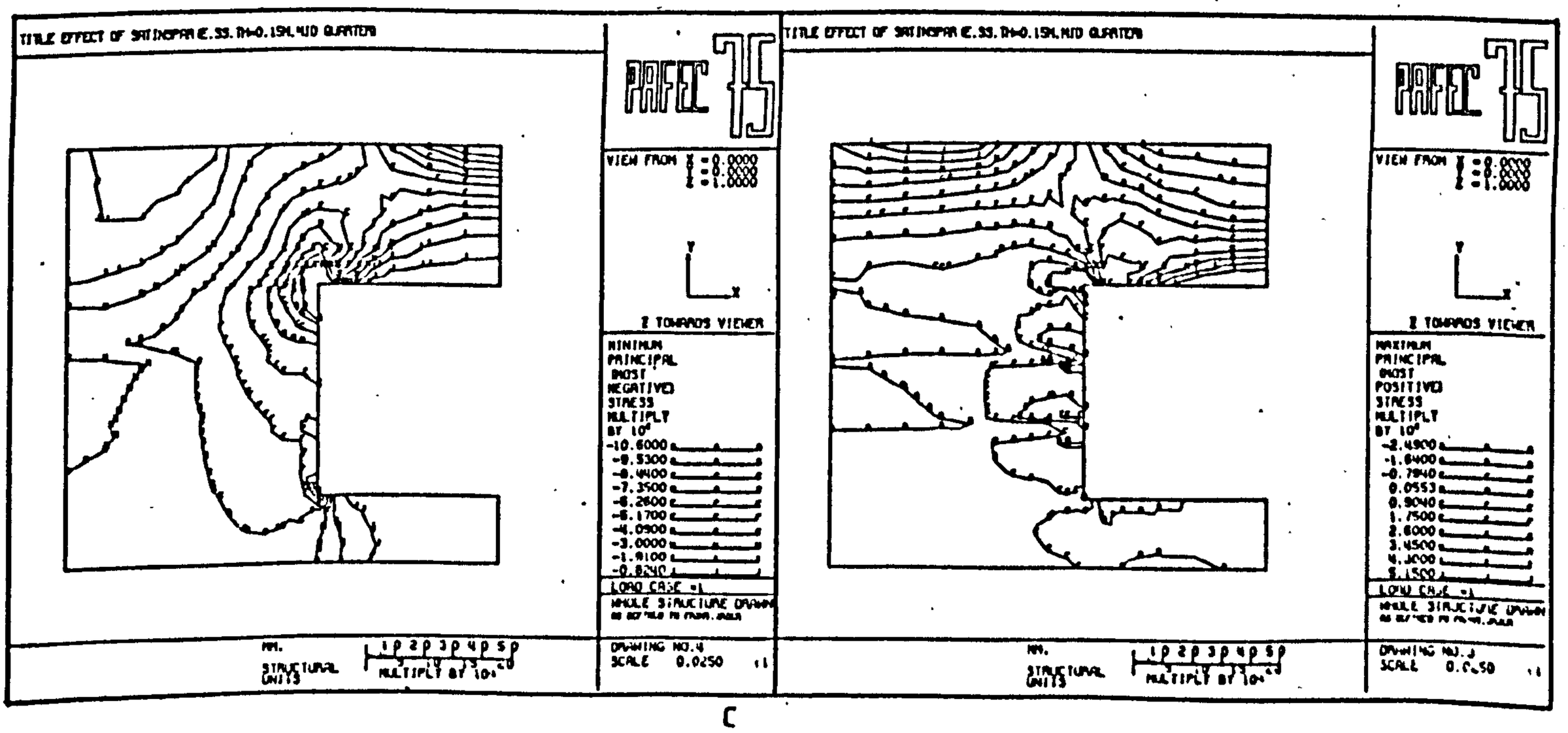
TITLE EFFECT OF SKIINSPAR E.SS. TH=0.15M, MID QUARTER
PAFEC 75
VIEW FROM X = 0.0000 Y = 0.0000 Z = 1.0000
Z TOWARDS VIEWER
MINIMUM PRINCIPAL (MOST NEGATIVE) STRESS MULTIPLY BY 10^8
-10.6000
-9.5300
-8.4400
-7.3500
-6.2600
-5.1700
-4.0900
-3.0000
-1.9100
-0.8240
LOAD CASE =1
WHOLE STRUCTURE DRAWN
MM.
STRUCTURAL UNITS
1 0 2 0 3 0 4 0 5 0
MULTIPLY BY 10^-1
DRAWING NO.4
SCALE 0.0250 :1
TITLE EFFECT OF SKIINSPAR E.SS. TH=0.15M, MID QUARTER
PAFEC 75
VIEW FROM X = 0.0000 Y = 0.0000 Z = 1.0000
Z TOWARDS VIEWER
MAXIMUM PRINCIPAL (MOST POSITIVE) STRESS MULTIPLY BY 10^8
-2.4900
-1.6400
-0.7940
0.0553
0.9040
1.7500
2.6000
3.4500
4.3000
5.1500
LOAD CASE =1
WHOLE STRUCTURE DRAWN
MM.
STRUCTURAL UNITS
1 0 2 0 3 0 4 0 5 0
MULTIPLY BY 10^-1
DRAWING NO.3
SCALE 0.0250 :1

C

FIG 8.10

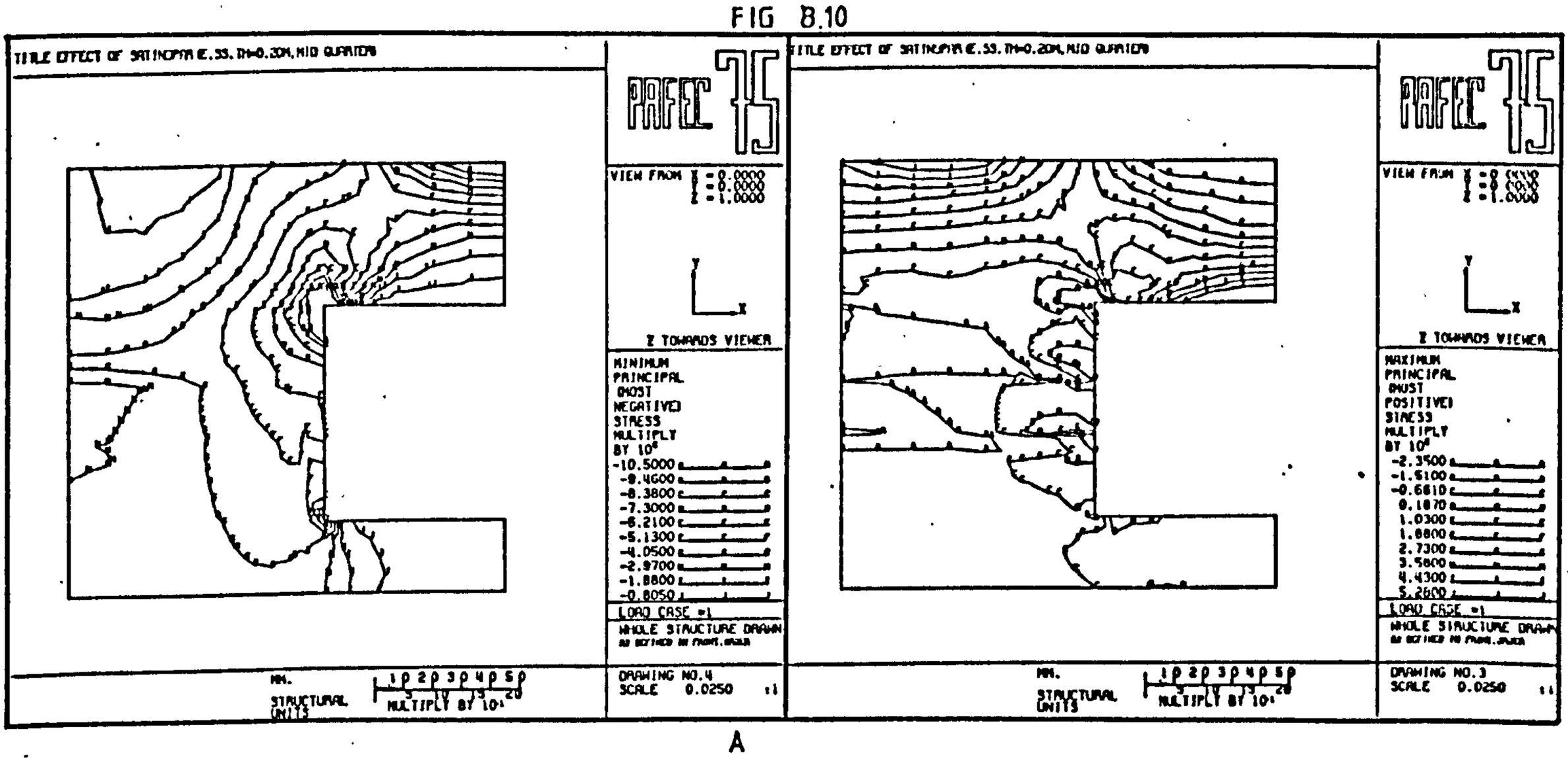
TITLE EFFECT OF SATINSPAR E.SS. TH=0.30M, MID QUARTER
PAFEC 75
VIEW FROM X = 0.0000 Y = 0.0000 Z = 1.0000
Z TOWARDS VIEWER
MINIMUM PRINCIPAL GHOST NEGATIVE) STRESS MULTIPLY BY 10^6
-10.5000
-9.4600
-8.3800
-7.3000
-6.2100
-5.1300
-4.0500
-2.9700
-1.8800
-0.8050
LOAD CASE =1
WHOLE STRUCTURE DRAWN
MM.
STRUCTURAL UNITS
1 0 2 0 3 0 4 0 5 0
MULTIPLY BY 10^-2
DRAWING NO.4
SCALE 0.0250 :1
TITLE EFFECT OF SATINSPAR E.SS. TH=0.30M, MID QUARTER
PAFEC 75
VIEW FROM X = 0.0000 Y = 0.0000 Z = 1.0000
Z TOWARDS VIEWER
MAXIMUM PRINCIPAL GHOST POSITIVE) STRESS MULTIPLY BY 10^6
-2.3500
-1.5100
-0.6810
0.1870
1.0300
1.8800
2.7300
3.5800
4.4300
5.2800
LOAD CASE =1
WHOLE STRUCTURE DRAWN
MM.
STRUCTURAL UNITS
1 0 2 0 3 0 4 0 5 0
MULTIPLY BY 10^-2
DRAWING NO.3
SCALE 0.0250 :1

A

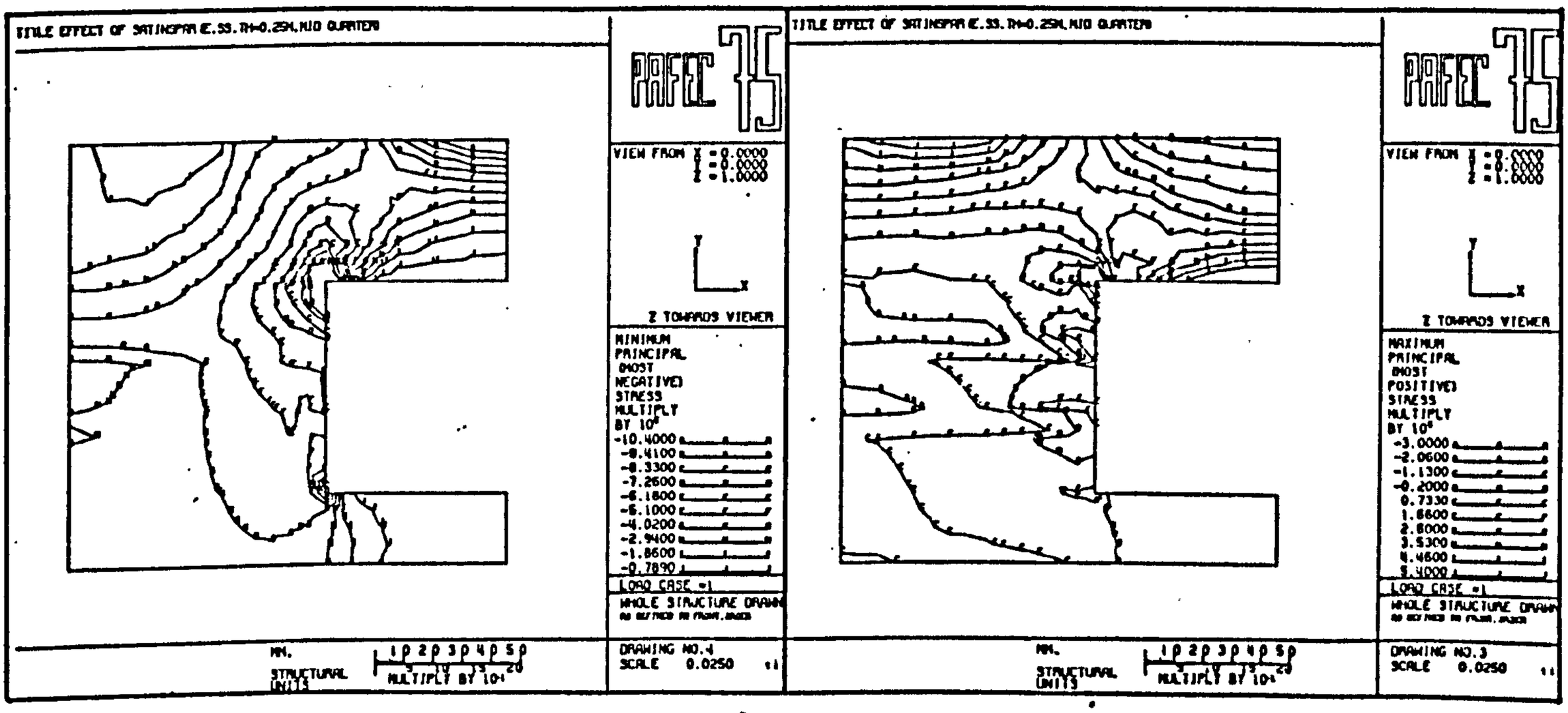
TITLE EFFECT OF SATINSPAR E.SS. TH=0.25M, MID QUARTER
PAFEC 75
VIEW FROM X = 0.0000 Y = 0.0000 Z = 1.0000
Z TOWARDS VIEWER
MINIMUM PRINCIPAL GHOST NEGATIVE) STRESS MULTIPLY BY 10^6
-10.4000
-9.4100
-8.3300
-7.2600
-6.1800
-5.1000
-4.0200
-2.9400
-1.8600
-0.7890
LOAD CASE =1
WHOLE STRUCTURE DRAWN
MM.
STRUCTURAL UNITS
1 0 2 0 3 0 4 0 5 0
MULTIPLY BY 10^-2
DRAWING NO.4
SCALE 0.0250 :1
TITLE EFFECT OF SATINSPAR E.SS. TH=0.25M, MID QUARTER
PAFEC 75
VIEW FROM X = 0.0000 Y = 0.0000 Z = 1.0000
Z TOWARDS VIEWER
MAXIMUM PRINCIPAL GHOST POSITIVE) STRESS MULTIPLY BY 10^6
-3.0000
-2.0600
-1.1300
-0.2000
0.7330
1.6600
2.8000
3.5300
4.4600
5.4000
LOAD CASE =1
WHOLE STRUCTURE DRAWN
MM.
STRUCTURAL UNITS
1 0 2 0 3 0 4 0 5 0
MULTIPLY BY 10^-2
DRAWING NO.3
SCALE 0.0250 :1

B

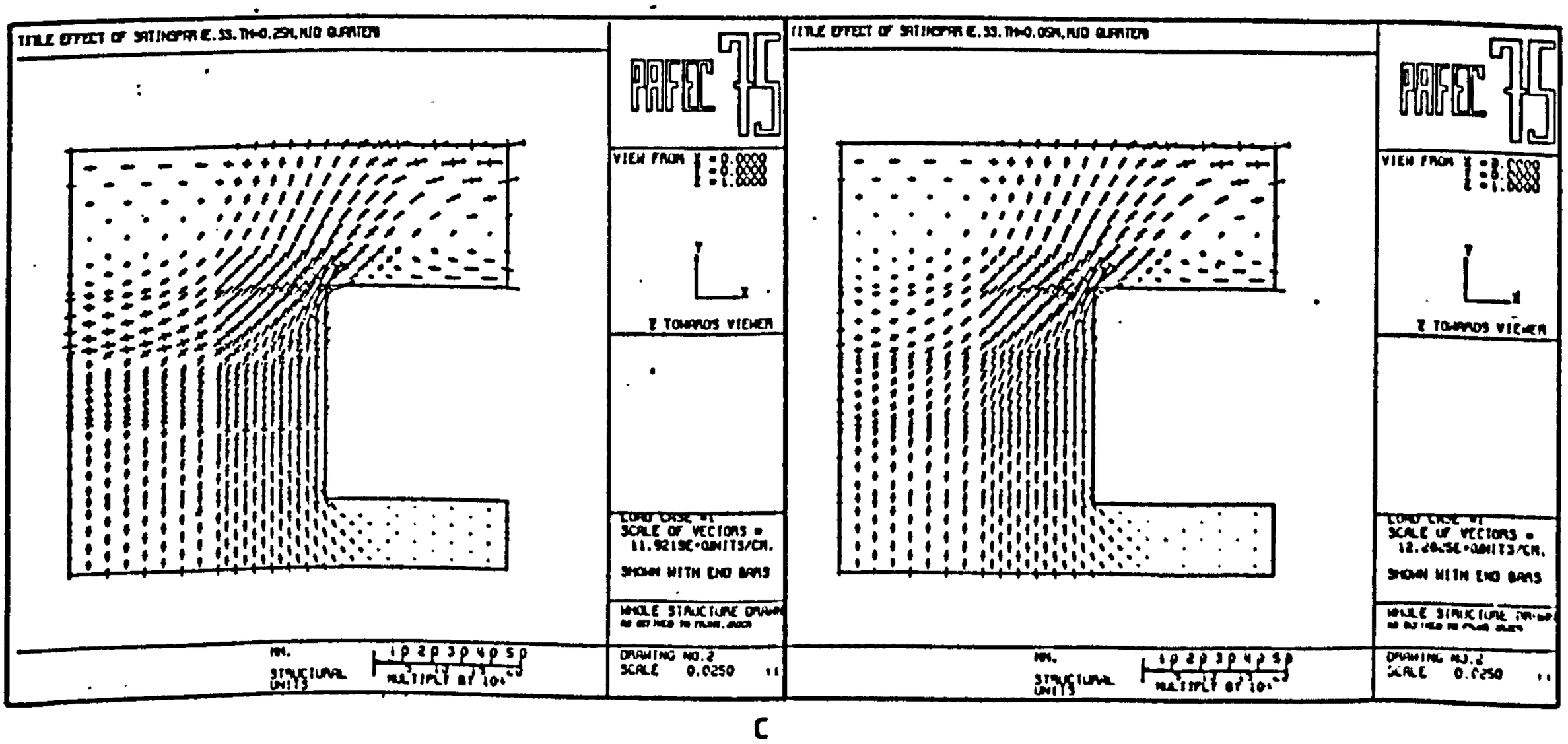
TITLE EFFECT OF SATINSPAR E.SS. TH=0.25M, MID QUARTER
PAFEC 75
VIEW FROM X = 0.0000 Y = 0.0000 Z = 1.0000
Z TOWARDS VIEWER
LOAD CASE #1
SCALE OF VECTORS = 11.9215E-08UNITS/CM.
SHOWN WITH END BARS
WHOLE STRUCTURE DRAWN
MM.
STRUCTURAL UNITS
1 0 2 0 3 0 4 0 5 0
MULTIPLY BY 10^-2
DRAWING NO.2
SCALE 0.0250 :1
TITLE EFFECT OF SATINSPAR E.SS. TH=0.05M, MID QUARTER
PAFEC 75
VIEW FROM X = 0.0000 Y = 0.0000 Z = 1.0000
Z TOWARDS VIEWER
LOAD CASE #1
SCALE OF VECTORS = 12.2035E-08UNITS/CM.
SHOWN WITH END BARS
WHOLE STRUCTURE DRAWN
MM.
STRUCTURAL UNITS
1 0 2 0 3 0 4 0 5 0
MULTIPLY BY 10^-2
DRAWING NO.2
SCALE 0.0250 :1

C

FIG 8.11

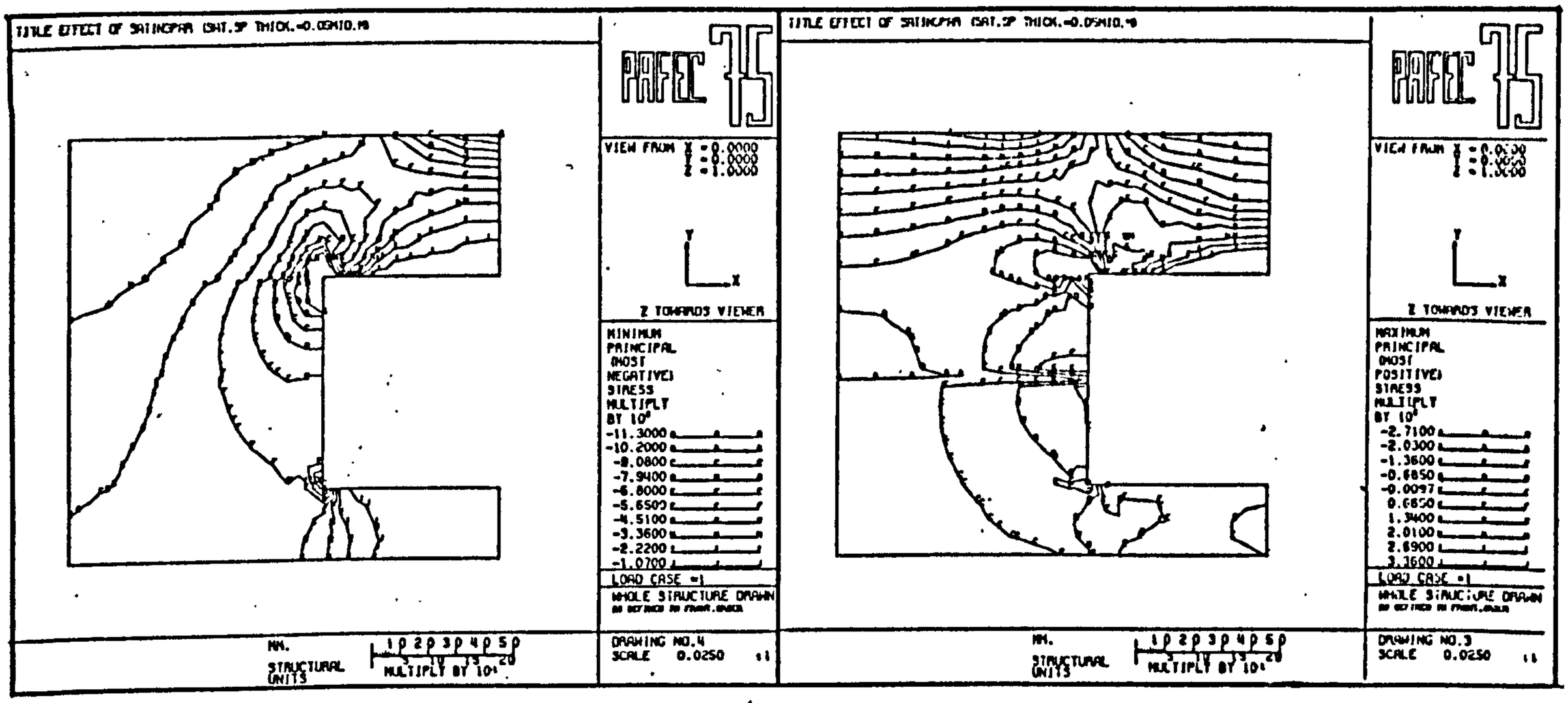
TITLE EFFECT OF SATINSPAR (SAT.SP THICK.=0.05M10.M
PAFEC 75
VIEW FROM X = 0.0000
Y = 0.0000
Z = 1.0000
Z TOWARDS VIEWER
MINIMUM PRINCIPAL (MOST NEGATIVE) STRESS MULTIPLY BY 10⁶
-11.3000
-10.2000
-9.0800
-7.9400
-6.8000
-5.6500
-4.5100
-3.3600
-2.2200
-1.0700
LOAD CASE =1
WHOLE STRUCTURE DRAWN
DRAWING NO.4
SCALE 0.0250
MM.
STRUCTURAL UNITS
MULTIPLY BY 10ⁿ
TITLE EFFECT OF SATINSPAR (SAT.SP THICK.=0.05M10.M
PAFEC 75
VIEW FROM
Z TOWARDS VIEWER
MAXIMUM PRINCIPAL (MOST POSITIVE) STRESS MULTIPLY BY 10⁶
-2.7100
-2.0300
-1.3600
-0.6850
-0.0097
0.6850
1.3400
2.0100
2.6900
3.3600
LOAD CASE =1
WHOLE STRUCTURE DRAWN
DRAWING NO.3
SCALE 0.0250

A

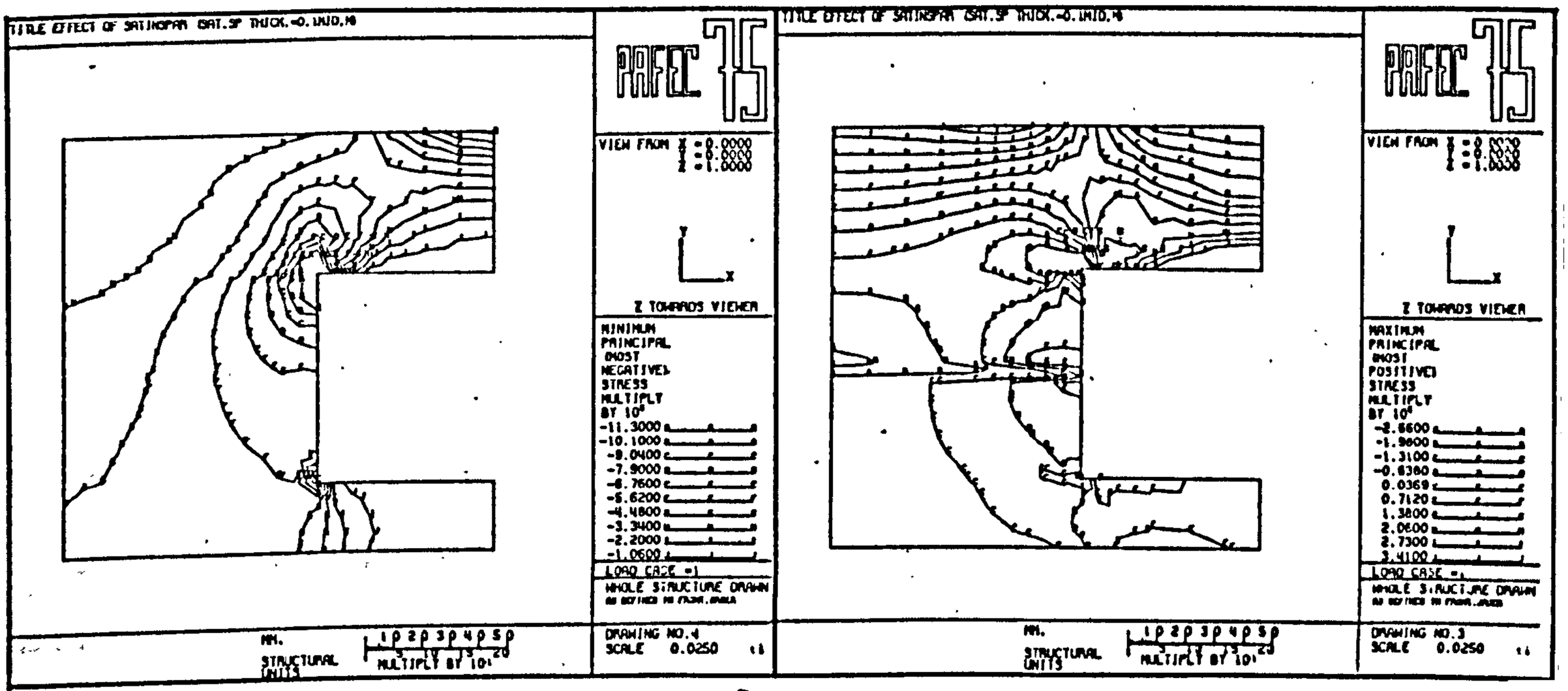
TITLE EFFECT OF SATINSPAR (SAT.SP THICK.=0.1M10.M
PAFEC 75
VIEW FROM X = 0.0000
Y = 0.0000
Z = 1.0000
Z TOWARDS VIEWER
MINIMUM PRINCIPAL (MOST NEGATIVE) STRESS MULTIPLY BY 10⁶
-11.3000
-10.1000
-9.0400
-7.9000
-6.7600
-5.6200
-4.4800
-3.3400
-2.2000
-1.0600
LOAD CASE =1
WHOLE STRUCTURE DRAWN
DRAWING NO.4
SCALE 0.0250
MM.
STRUCTURAL UNITS
MULTIPLY BY 10ⁿ
TITLE EFFECT OF SATINSPAR (SAT.SP THICK.=0.1M10.M
PAFEC 75
VIEW FROM
Z TOWARDS VIEWER
MAXIMUM PRINCIPAL (MOST POSITIVE) STRESS MULTIPLY BY 10⁶
-2.8600
-1.9600
-1.3100
-0.6360
0.0369
0.7120
1.3800
2.0600
2.7300
3.4100
LOAD CASE =1
WHOLE STRUCTURE DRAWN
DRAWING NO.3
SCALE 0.0250

B

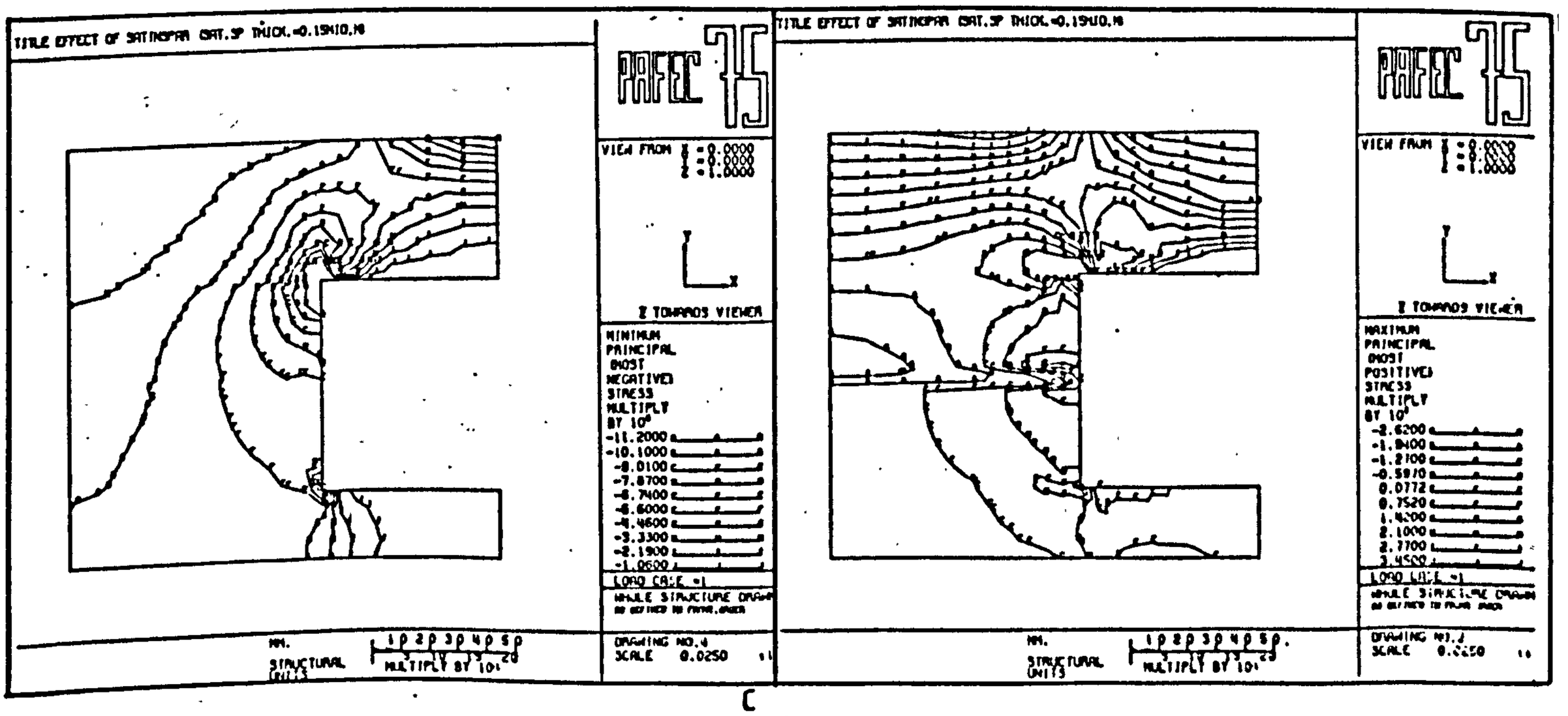
TITLE EFFECT OF SATINSPAR (SAT.SP THICK.=0.15M10.M
PAFEC 75
VIEW FROM X = 0.0000
Y = 0.0000
Z = 1.0000
Z TOWARDS VIEWER
MINIMUM PRINCIPAL (MOST NEGATIVE) STRESS MULTIPLY BY 10⁶
-11.2000
-10.1000
-8.0100
-7.8700
-6.7400
-6.6000
-5.4600
-3.3300
-2.1900
-1.0600
LOAD CASE =1
WHOLE STRUCTURE DRAWN
DRAWING NO.4
SCALE 0.0250
MM.
STRUCTURAL UNITS
MULTIPLY BY 10ⁿ
TITLE EFFECT OF SATINSPAR (SAT.SP THICK.=0.15M10.M
PAFEC 75
VIEW FROM
Z TOWARDS VIEWER
MAXIMUM PRINCIPAL (MOST POSITIVE) STRESS MULTIPLY BY 10⁶
-2.6200
-1.8400
-1.2100
-0.5970
0.0772
0.7520
1.4200
2.1000
2.7700
3.4500
LOAD CASE =1
WHOLE STRUCTURE DRAWN
DRAWING NO.3
SCALE 0.0250

C

FIG 8.12

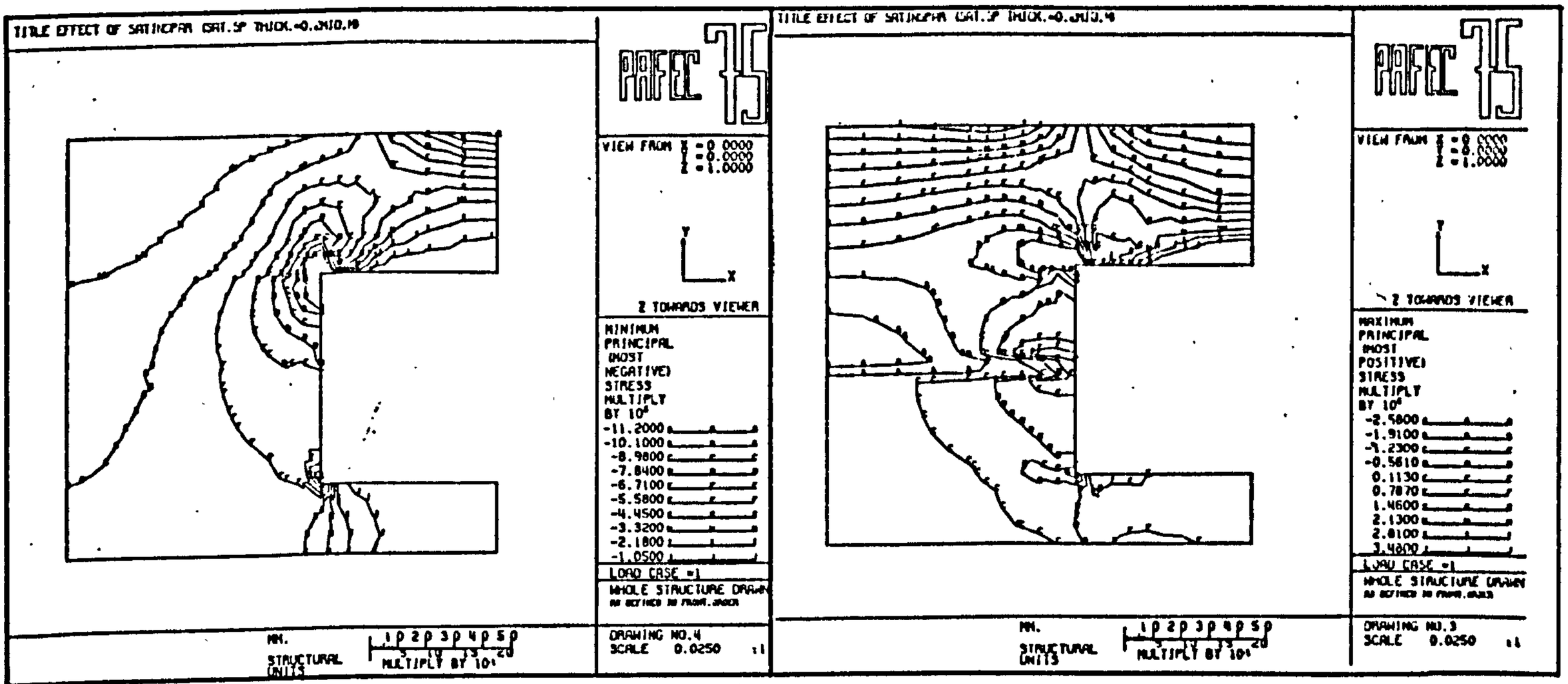
TITLE EFFECT OF SATINSPAR SAT.SP THICK.=0.2510.M
PAFEC 75
VIEW FROM X = 0.0000 Y = 0.0000 Z = 1.0000
Z TOWARDS VIEWER
MINIMUM PRINCIPAL (MOST NEGATIVE) STRESS MULTIPLY BY 10^4
-11.2000
-10.1000
-8.9800
-7.8400
-6.7100
-5.5800
-4.4500
-3.3200
-2.1800
-1.0500
LOAD CASE =1
WHOLE STRUCTURE DRAWN
MM.
STRUCTURAL UNITS
1 0 2 0 3 0 4 0 5 0
MULTIPLY BY 10^1
DRAWING NO.4
SCALE 0.0250 :1
TITLE EFFECT OF SATINSPAR SAT.SP THICK.=0.2510.M
PAFEC 75
VIEW FROM X = 0.0000 Y = 0.0000 Z = 1.0000
Z TOWARDS VIEWER
MAXIMUM PRINCIPAL (MOST POSITIVE) STRESS MULTIPLY BY 10^4
-2.5800
-1.9100
-1.2300
-0.5610
0.1130
0.7870
1.4600
2.1300
2.8100
3.4800
LOAD CASE =1
WHOLE STRUCTURE DRAWN
MM.
STRUCTURAL UNITS
1 0 2 0 3 0 4 0 5 0
MULTIPLY BY 10^1
DRAWING NO.3
SCALE 0.0250 :1

A

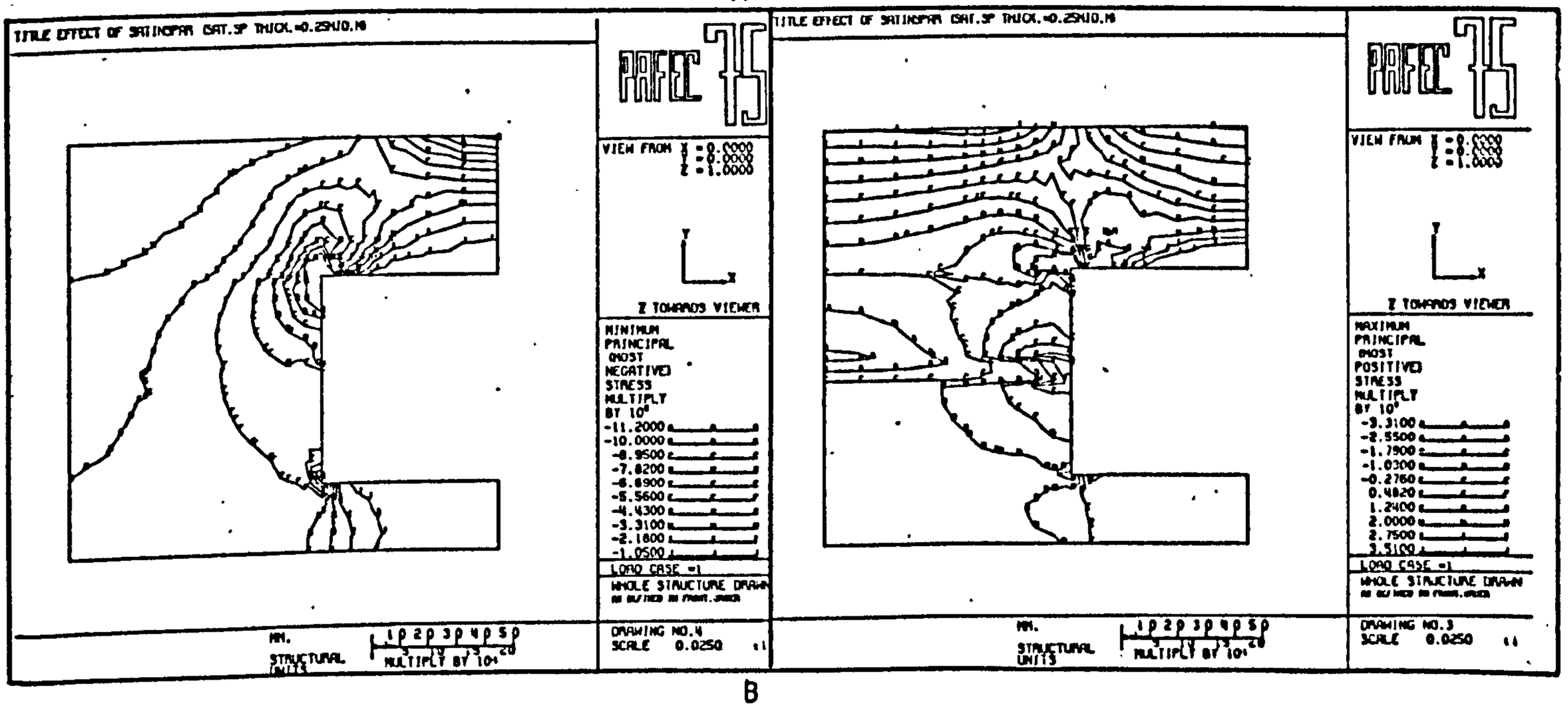
TITLE EFFECT OF SATINSPAR SAT.SP THICK.=0.2510.M
PAFEC 75
VIEW FROM X = 0.0000 Y = 0.0000 Z = 1.0000
Z TOWARDS VIEWER
MINIMUM PRINCIPAL (MOST NEGATIVE) STRESS MULTIPLY BY 10^4
-11.2000
-10.0000
-8.9500
-7.8200
-6.6900
-5.5600
-4.4300
-3.3100
-2.1800
-1.0500
LOAD CASE =1
WHOLE STRUCTURE DRAWN
MM.
STRUCTURAL UNITS
1 0 2 0 3 0 4 0 5 0
MULTIPLY BY 10^1
DRAWING NO.4
SCALE 0.0250 :1
TITLE EFFECT OF SATINSPAR SAT.SP THICK.=0.2510.M
PAFEC 75
VIEW FROM X = 0.0000 Y = 0.0000 Z = 1.0000
Z TOWARDS VIEWER
MAXIMUM PRINCIPAL (MOST POSITIVE) STRESS MULTIPLY BY 10^4
-3.3100
-2.5500
-1.7900
-1.0300
-0.2760
0.4820
1.2400
2.0000
2.7500
3.5100
LOAD CASE =1
WHOLE STRUCTURE DRAWN
MM.
STRUCTURAL UNITS
1 0 2 0 3 0 4 0 5 0
MULTIPLY BY 10^1
DRAWING NO.3
SCALE 0.0250 :1

B

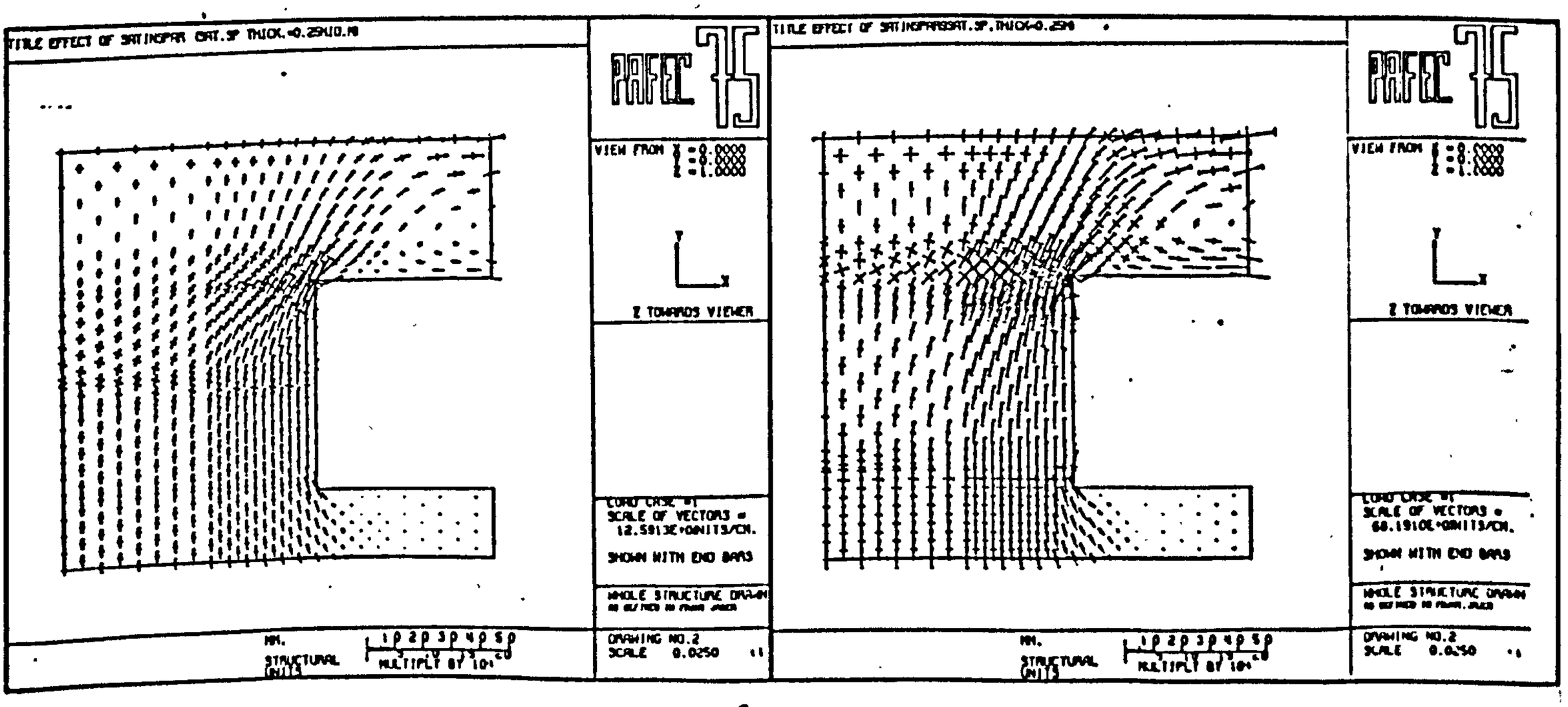
TITLE EFFECT OF SATINSPAR SAT.SP THICK.=0.2510.M
PAFEC 75
VIEW FROM X = 0.0000 Y = 0.0000 Z = 1.0000
Z TOWARDS VIEWER
LOAD CASE =1
SCALE OF VECTORS = 12.5913E+00 UNITS/CM.
SHOWN WITH END BARS
WHOLE STRUCTURE DRAWN
MM.
STRUCTURAL UNITS
1 0 2 0 3 0 4 0 5 0
MULTIPLY BY 10^1
DRAWING NO.2
SCALE 0.0250 :1
TITLE EFFECT OF SATINSPARSAT.SP.THICK=0.2510
PAFEC 75
VIEW FROM X = 0.0000 Y = 0.0000 Z = 1.0000
Z TOWARDS VIEWER
LOAD CASE =1
SCALE OF VECTORS = 68.1910E+00 UNITS/CM.
SHOWN WITH END BARS
WHOLE STRUCTURE DRAWN
MM.
STRUCTURAL UNITS
1 0 2 0 3 0 4 0 5 0
MULTIPLY BY 10^1
DRAWING NO.2
SCALE 0.0250 :1

C

9. SUMMARY, CONCLUSIONS, RECOMMENDATIONS AND FUTURE STUDIES

The work described in this thesis is mainly concerned with the structural behaviour of the overlying strata, pillars and roof structure at Sherburn in the long run, after the abandonment of the mine workings.

Based on previous research and on in-situ observations, some factors which are anticipated to be responsible for a potential instability of the mine workings in the long term have been isolated and each one has been examined in detail, utilising current rock mechanic techniques. A short account of the work carried out is given together with conclusions drawn and recommendations for future studies.

9.1 Physical scale model studies

The possibility of failure of the gypsum roof beam at some districts was considered after completion of mining and physical modelling studies have been undertaken in order to observe the behaviour of simulated overlying strata. The areas of greatest risk in the mine were considered to be those below the aquifer, thus causing the marl to deform and exert extra load on the gypsum roof. In models which simulated a section of the strata from surface to the mining horizon, roof beam failures have been artificially initiated.

A dimensional analysis of the parameters considered important to the model showed that when the mechanical properties of the model material is reduced by the geometrical scale factor selected, linear measurements, such as the height of upbreak, dimensions of disturbed zone on the surface, etc., can be related by the scale factor to the goemetrically similar prototype.

In physical modelling, the applicability of the information obtained from model to the prototype is dependent upon the degree of fulfilment achieved in similitude requirements. Since the Upper Permian Marl, which creeps and swells considerably due to water, is expected to have an appreciable influence upon the state of stability of the roof beam and of the immediate roof after roof beam failure, it is essential to have a model material which exhibits similar behaviour when it comes into contact with water. Therefore, a model material and production procedure were developed. The method is based on statical compaction of ground marl at a predetermined constant moisture content and at a constant compactive effort. The adopted compactive effort was 2.188 MPa. The moisture content was determined from the experimental compaction curve obtained for the ground marl. Some merits of the model material are listed hereunder:

(1) The mechanical properties of the model material can be easily varied by altering some of the components involved in the production process.

(2) Material obtained in this way displays reasonably similar behaviour in water to that of the actual marl.

(3) The material is re-usable and hence is considerably inexpensive.

(4) The material can be moulded or cut into the desired shape easily.

In order to ensure that scaled-down material properties of the Upper Permian Marl were obtained, a number of tests were performed for the determination of uniaxial compressive strength, tensile strength, cohesion, coefficient of friction, Young's modulus, unit weight, slake durability index, swelling strain and pressure index, permeability, liquid and plastic limits. The results indicate some discrepancies, but the material was considered adequate for modelling purposes.

Changes in in-situ conditions depend upon the prevailing circumstances of the water and fracturing level of the Upper Permian Marl. For this reason, models were constructed and tested representing variable crack frequencies:

(a) 1 crack per 5m in one direction and 1 crack per 7.5m in other two directions;

(b) 1 crack per 2.5m in all three directions; and

(c) rather loosely compacted and saturated marl without any fabricated cracks.

The planes of cracks were assumed to be vertical and horizontal in the prototype for simplicity. This allowed circulation of water through the marl blocks, reducing the competency of the mark and hence creating a potentially unstable situation.

Tests were carried out by self-loading in a specially constructed model box with the addition of water. A total of five models were built and tested. The results indicate that:

(1) If the marl in is the dry state it will be competent enough to bridge the unsupported opening and will act as a barrier between the lacustrian deposits and the working horizon even if the crack frequency is one crack per 2.5m in all three directions.

(2) If the water is present, deterioration due to water in the form of swelling and slaking is the controlling mechanism in the failure process and the failure is not a sudden inrush, but a slow degradation of stress relieved zones in the unsupported immediate roof.

(3) In all cases modelled, the failed zone is arch-or dome-shaped but the development of a failure zone is governed largely by the orientation and frequency of simulated weakness planes.

(4) The upward migration of voids can be arrested well below the sand-marl interface provided that orientation and frequency of fracture planes in the marl are favourable such as one crack per 7.5m. The ultimate upbreak of re-stabilised voids will be dependent upon the fracturing level of the marl.

(5) The pose angle of spalled material in a flooded state is approximately 30^{o} from the horizontal.

(6) Even if a void reaches the sand-marl interface the resulting subsidence on the surface is likely to be a flat, well spread depression (Draw Angle = 59^{o}).

(7) It is highly unlikely that the flowing sands can find access to the working horizon because the void is almost filled up by the spalled material.

(8) If three simultaneous roof beam failures happen to occur in the adjacent roadways, the common abutments in the immediate roof above the gypsum pillars will continue to carry the load. Deterioration of common abutments due to water can be expected to be limited.

(9) If a water flooding takes place prior to roof beam failure, the air trapped in the crown of the collapsed roadway effectively reduces the deterioration of marl caused by the water.

In order to assess the risk areas and of the likely behaviour of overlying strata in the event of a gypsum roof failure it is essential to know local conditions such as the presence of water, intensity and orientation of weakness planes in the Upper Permian Marl. This may be achieved by systematically extending the probing boreholes into the Upper Permian Marl and taking cores. The boreholes can be plugged subsequently.

Further modelling studies with various orientations of weakness planes can be carried out and the duration of testing can be prolonged utilising a model box made of a steel frame.

9.2 The effect of water on the pillar stability

In view of water ingress to the workings at different locations it would seem reasonable to predict a partial flooding of some of the sections of the mine after the abandonment of the workings in the distant future. As an aid to the assessment of whether a water flood into the mine workings could develop a potentially unstable situation of the pillars in the long term an experimental programme was initiated. The effect of water on the short term and long term strength characteristics of gypsum specimens from Marbleagis, Fauld, Mountfield and Sherburn mines were investigated. Long term creep tests of gypsum have been carried out in submerged conditions, at a stress level equivalent to 75% of short term wet strength, in an environmentally controlled room. The results of the experiments can be summarised as follows:

(1) The magnitude of percentage reduction in the short term uniaxial strength of the gypsum due to saturation with water was found to be variable with a lowest value of 25% for Sherburn gypsum and with a highest value of 42% for Mountfield gypsum. Brazilian disc tests have indicated a 45% reduction in the dry strength due to saturation.

(2) The factors controlling the deterioration of the gypsum due to water in the long term, are considered to be (a) solubility, (b) solution rate of gypsum,(c) exposed surface area of gypsum, (d) flow velocity of water, (e) ambient temperature, (f) ambient pressure.(g) presence of other dissolved salts, and (h) subsaturation concentration of water. In the case of a mine flooding flow velocity of

of water, ambient temperature, are considered to be of limited importance.

(3) Specimens submerged in mine water and under a constant stress level equal to 75% of short term wet strength have exhibited a decelerating rate of deformation with time with one exception; that of the sample from Mountfield which failed in 699 days. This was attributed to the high porosity of the specimen.

(4) Specimen petrology (porosity, grain size, presence of anhydrite, etc.) played an important role in time-dependent deformation of submerged gypsum. In general, high porosity and the presence of anhydrite caused comparatively larger deformations.

(5) An increase in the stress level from 75% to 81% of short term wet strength caused some specimens to enter the tertiary stage which resulted in rupture.

(6) The duration of the tertiary stage deformation was considerably long giving ample warning of ultimate failure.

(7) Sherburn specimens showed little or no creep when they were dry but started to deform immediately after submersion in water leading to failure within a short period of time under a stress level of 81% of the short term wet strength.

(8) Recrystallisation was a dominant feature of long term submerged creep testing of gypsum.

(9) In the light of the experimental results it may be concluded that the gypsum pillars will be able to carry the overburden load even if the mine workings at Sherburn are flooded.

Interpretation of the long term creep data in mathematical terms required the processing of creep data. A computer package program, PADAS' was utilised for most of the graphs and the regression analysis presented in this thesis.

Initial mathematical analysis of creep data indicated that the equations previously used for the description of creep behaviour were not adequate for the long term creep data of submerged gypsum. Therefore, an empirical, essentially exponential equation was developed for the description of primary stage creep data in the form of:

$$\varepsilon = \varepsilon_o K^{(T^n)} \qquad \ldots\ldots (9.1)$$

An algorithm for the computer fitting of the developed equation by means of the linearisation of the equation for the long term creep data was established. Additional computer programs for processing the raw data were written and utilised during calculations.

A chart, incorporating a power equation, logarithmic equation and the exponential equation (9.1), was constructed for the purpose of demonstrating the fundamental differences between creep behaviours described by these equations. The procedure for extrapolation and rapid determination of constants appearing in the power, logarithmic and proposed equations (9.1) has been explained.

It has been shown that the accelerating and decelerating creep stages can be described mathematically with the above, simple equation (9.1). However, probably because of the stress levels adopted, it was not possible to make use of this property of the equation (9.1) for the creep data at hand.

It is of great importance to be able to predict the exact time of a pending failure of rock structure, particularly when there is a possibility of damage to property, injury to persons and disruption of production. Attempts to predict failure time of creep specimens submerged in water resulted in the development of an equation of the form:

$$\varepsilon = M \, Ln \left(\frac{T_F - T_o}{T_F - T} \right) \qquad \ldots\ldots (9.2)$$

By solving the above equation (9.2) with three data points chosen such that between the strain values of the selected points, the condition $\varepsilon_3 - \varepsilon_2 = \varepsilon_2 - \varepsilon_1$ holds, the failure time can be resolved as:

$$T_F = T_1 - \frac{(T_2 - T_1)^2}{2\,T_2 - T_1 - T_3} \qquad \ldots\ldots (9.3)$$

With the aid of this equation (9.3), it is possible to predict failure time (T_F) using as few as three time values, regardless of the constants appearing in equation (9.2).

The process of failure prediction can be reduced to a much simpler form by resolving the equation (9.3) on the time-strain or time-deformation graph. The method is described fully in Section Five.

The graphical method of determination is extremely easy and offers great flexibility by allowing the use of many sets of three points and the incorporation of the most recent data. The accuracy of prediction is increased by covering longer time spans and by incorporating the most recent readings into the calculations.

The failure of two creep specimens were predicted successfully long before the actual time of failure and any damage to the creep cells were avoided.

A computerised solution has also been presented. Two additional computer programs have been written for the linearisation of the equation (9.3) and for data processing purposes. The constants of equation (9.2) were determined and presented, together with graphical outputs.

It is recommended that further short term and long term creep tests, at various stress levels, should be carried out in order to widen the applicability of the method developed. Application of the prediction process on the full-scale rock structures offers a challenging field of investigation.

9.3 Effect of satinspar bands on the pillar stability

In-situ inspection of pillars at Sherburn has indicated that soft fibrous satinspar bands in the pillar material contributes much to the gradual deterioration of pillar corners. The loosening of corners increases the span of the exposed roof beam which may affect roof stability. On this basis, an experimental program consisting of three main parts, was undertaken to demonstrate the effect of the satinspar present on the

pillar degradation. The first part of the program was aimed at determining the mechanical properties of the satinspar bands of which only short supply was available. In the second part, servo-controlled testing of gypsum specimens was carried out with steel end platens. In the third part, gypsum specimens of mixed shapes were tested on the servo-controlled testing machine with satinspar end pieces of various thicknesses inserted between the specimen ends and the steel platens. The results of the test program can be summarised as follows:

(1) Uniaxial compressive strength, tensile strength, shear strength, Young's modulus, Poisson's ratio, ultrasonic pulse velocity of satinspar specimens were determined and the results indicate that the satinspar bands are possibly the weakest constituents of the pillar forming material.

(2) The complete load deformation curves of gypsum specimens tested with steel end platens indicate a brittle behaviour whereas the load deformation of satinspar specimens was comparatively more ductile.

(3) The peak strength and residual strength of the gypsum specimens increased with decreasing height to width ratio of the specimen. With a sufficiently low height to width ratio (i.e.0.5) the broken material can take considerably high loads provided a certain amount of deformation is permitted to take place.

(4) The failure modes of the gypsum specimens were either single or multiple shear planes or, if present, along visible weakness zones.

(5) When the gypsum specimens were tested with satinspar end pieces, the peak strength was reduced, the magnitude of reduction in the strength with respect to the strength of gypsum tested without satinspar end pieces is dependent upon the height to width ratio of the specimen and the thickness of the satinspar pieces inserted between the specimen ends and the steel platens. An empirical relationship between the peak strength (σ_p) and the ratio of satinspar thickness to gypsum thickness (TS/TG) is established for specimens with a height to width ratio ranging from 0.6 to 1.5.

$$\sigma_p(\text{MPa}) = 22 - 7.49\ (\text{TS/TG}) \qquad \ldots\ldots (9.4)$$

(6) Deformational behaviour of gypsum, loaded with a constant strain rate and tested with satinspar end pieces became semi-ductile and the ductility increased with an increase in the satinspar thickness.

(7) The use of satinspar end pieces altered the failure mode of gypsum from shear along diagonal planes to splitting into long columns with highly compacted inner core. The corners of specimens were particularly liable to fracture.

(8) The specimens tested with satinspar end pieces fractured well below the peak strength value which was revealed along the pre-failure section of the load deformation curve of a number of the intermediate peak points.

(9) Failure modes of the specimens suggested that the tensile stresses were acting horizontally and the satinspar

layers were primarily responsible for the failure of the specimens.

Although test results from small size laboratory specimens cannot be accepted quantitatively in relation to in-situ strength of the pillars, nevertheless, valuable information can be obtained qualitatively.

In the light of the experimental results and conditions prevailing at Sherburn, it may be stated that the corners of pillars containing large amounts of satinspar are liable to loosening and that large blocks may be dislodged. This occurrence does not necessarily mean that the load bearing capacity of the pillar is exceeded. In fact, as long as blocks remain in contact with the surrounding(roof and floor)rock mass the pillar strength is reduced only slightly.

In-situ instrumentation of pillars which contain large amounts of satinspar band and of pillars which contain little or no satinspar bands, if carried out, would provide realistic data on the effect of satinspar bands.

9.4 Linear arch structure and photoelastic modelling

One of the possible structures in the mine at Sherburn is the formation of linear arch structure in the roof. Results from instrumentation of the gypsum roof by previous investigators supported this possibility. In the present study, the linear arch structure was modelled photoelastically in order to obtain an idea of the stress distribution within the elastic range. A number of photoelastic models of linear arch with various span to depth ratios have been tested and analysed on a specially designed loading apparatus. Some points of practical importance are given below:

(1) The highest compressive stress occurs at the top fibres of the beam block around the central crack and the magnitude of maximum compressive stress hyperbolically increases with increase of the span to depth ratio of the beam.

(2) The contact area of the mid-span crack is approximately 15% of the total crack area and increases with an increase in the transverse load.

(3) The distribution of stresses along the contact area may be approximated with a triangular distribution for practical purposes.

(4) As the span to depth ratio of the beam increases, isoclinics and fringe patterns remain essentially the same, although slightly upward shifting is noticable.

(5) The relationship between the stress concentration at the top fibres around the mid-span crack and the applied load is in the form of a power equation which yields slightly better fit than a linear one.

(6) At the lower sections of the beam blocks around the central crack, a pure tension zone is present and the highest vertical tensile stress occurs along the vertical edge of the mid-span crack and may be as much as one-fourth of the maximum compressive stress for the beams with low span to depth ratio.

(7) In each beam block there is a thrust zone acting approximately diagonally, becoming approximately horizontal towards the upper section of the mid-span crack.

(8) Development of tensile stresses is related to the eccentric loading of the beams and to the direction of resultant thrust acting across the contact area.

(9) It is possible that the change in the failure type of the linear arch from axial failure to corner crushing is governed by the magnitude of induced tensile stresses beneath the neutral axis.

For future modelling studies, a centrifugal loading mechanism may be employed by which beams can be loaded to failure, in order to provide further information on the axial failure of the arch.

High stress concentrations along the upper fibres of the beams around the central crack suggest that time-dependent deformation would play an important part in the overall deformational behaviour of the linear arch. Therefore, a long-term creep testing of the linear arch should be initiated.

9.5 Finite Element modelling studies

Two separate finite element studies have been carried out: the first was concerned with the change in the stress distribution around the working zone due to a gypsum roof failure. The second study was intended to illustrate the effect of soft satinspar bands of variable thicknesses and location along the pillar section on the stress distribution of pillars loaded with a constant stress. A recently modified version of PAFEC-75 Finite Element package was utilised for this purpose.

9.5.1 Modelling of a roof beam failure

A section of strata from surface to the base of the gypsum seam including three rooms, two whole and two half pillars, was modelled. The mode of gravity loading was adopted in the studies. In each set of runs the rigidity of the overlying marl was varied in three steps from 4.80 GPa to 0.048 GPa, in order to approximate creep effect of the marl and the effect of water. The results indicate that:

(1) Initial analysis showed that stress distribution is congruous with theoretical prediction around the excavations (i.e. tensional stresses along the lower fibres of the roof beams and at the abutments at a distance into the upper section of the pillars, confined state of the pillar cores). Lowering of marl stiffness caused more load to be thrown onto the roof beams and into the abutments, but less load onto the pillar cores.

(2) When removing the gypsum roof from the F.E. mesh, uniformity of stresses around the excavations is non existent and the stresses around the central opening decrease in magnitude. More load is thrown onto the adjacent pillars due to roof beam failure. As the competency of the marl is reduced, the adjacent roof beams are subjected to an increasing stress. Tensional stresses around the pillar abutments disappear and become compressive after roof beam failure in the central opening. Tensile stresses around the lower section of the roof beam, in the adjacent rooms, however, increases substantially with lowering rigidity of the marl.

(3) Development of a failure zone upward produces similar changes in the stress distribution. More load is thrown onto the roof beams of adjacent rooms and onto the abutments, whereas less load is thrown onto the pillar core. Lowering of marl rigidity substantially increases tensile stresses in the roof beams of adjacent rooms and decreases the level of stresses on the pillars.

9.5.2 Modelling of pillars With and without satinspar bands

Four separate studies were carried out in order to illustrate the effect of soft layers (satinspar) embedded in the pillars on the stress distribution. The idealised structure was one-half of a typical pillar and one-half of a roadway width. The soft layers were assumed to be variable in thickness from 0.05m to 0.25m and in location along the pillar section. The results of the analysis suggest that:

(1) When there is no satinspar band present, the distribution of stresses is in a recognised form (i.e. high stress concentrations around the pillar corners, confined state of pillar core, high tensional stresses along the lower edge of the roof beam and at the abutments towards the upper section of the pillar).

(2) When two satinspar bands, each varying in thickness from 0.05 to 0.25m, are present at the top and base of a pillar, the magnitude and distribution of stresses change. But the change may not be considered critical because the differential deformation of the gypsum roof prevents the expansion of soft

layers and because the two satinspar bands are spaced sufficiently away from each other. Hence, the principal stresses are compressive, inside the pillar core, and around the pillar skin, indicating that the effect of satinspar bands is, in this case, limited.

(3) When the two satinspar bands varying in thickness are present at an equal distance from the roof and floor of the pillar, tensile stresses appear around the pillar skin and the magnitude of these stresses increases with increasing thickness of the satinspar bands. The direction of tensile stresses is in favourable orientation to cause the separation of gypsum blocks from the main body of rock mass. Inside the pillar core both principal stresses are still compressive, but decrease in magnitude with increase in thickness of the satinspar bands.

(4) When there is one single satinspar band present of variable thickness at mid-height of a pillar, tensile stresses occur around the pillar skin at the interface of the gypsum-satinspar band. The magnitude of the tensile stresses increases substantially as the thickness of the satinspar band increases.

Finite element studies were carried out in a plane strain condition assuming perfectly linear elastic deformational behaviour of the materials modelled; therefore they only provide an estimate of the true in-situ condition.

* * *

REFERENCES

AFROUZ A. and HARVEY J.M. (1974): Rheology of rocks within the soft to medium strength range.
Int. Jl. of Rock Mechs. and M. Sci.,Vol.11, pp.281-91.

AHMED S. (1958): Effect of cappi ng on the compressive strength of concrete cubes.
Magazine of Concrete Research. March, pp. 21-4.

AL-CHALABI M. and HUANG C.C. (1974): Stress distribution within circular cylinders in compression.
Int. Jl. of Rock Mechs. and M. Sci., Vol. 11, pp.45-56.

ALDER H.L. and ROESSLER E.B. (1968): Introduction to probability and statistics. 4th Ed.
Freeman Books.

ALI S.A. (1979): Creep properties of evaporite rocks with particular reference to gypsum.
Ph.D. Thesis, Univ. of Sheffield.

ALPAN I. (1957): An apparatus for measuring swelling pressure in expansive soils.
Proc. of 4th Conf. on Soil Mechanics and Foundation Engineering, Vol. 1.

ANDERSON B.G., WHITHEY C.S. and COHEN E. (1955): Design of blast resistant construction for atomic explosion.
Jl. of Amer. Concrete Inst., Vol. 26, pp. 604-83.

ANDRADE E.N. (1910): On the viscous flow in metals and allied phenomena.
Proc. Roy. Soc. A 84, June 9, pp. 1-12.

ATTEWELL P.B. and FARMER I.W. (1976): Principles of Engineering Geology.
Chapman and Hall, London.

AYDAN Ö. (1982): Shaft lining design and its performance.
M.Sc. Thesis, Univ. Newcastle upon Tyne.

BABCOCK C.O.(1969): Effect of end constraint on the compressive strength of model rock pillars.
Trans. Amer. Inst. of Min. & Met., Vol.241,pp.323-28.

BALLA A.(1960):Stress conditions in triaxial compression.
Am. Soc. Civ. Eng.
pp. 57-84.

BENERJI A.K. (1968): Photoelastic investigation of stress distribution in pillars.
M.Sc. Thesis, University of Newcastle upon Tyne.

BARTON N. (1974): Rock slope performance as revealed by a physical joint model.
Proc. of 3rd Congress of the International Society for Rock Mechanics, Advances in Rock Mechanics II-B, pp. 765-73, Denver.

BARTON N. (1976): The shear strength of rock and rock joints.
Int. Jl. of Rock Mechs. and M. Sci.
Vol.13, pp. 253-79.

BARTON N. (1980): The ultimate frictional resistance of rock discontinuities.
Int. Jl. of Rock Mechs. and M. Sci.
Vol. 17, pp. 75-9.

BARTON N. and BANDIS S. (1980): Some effects of scale on the shear strength of joints.
Int. Jl. of Rock Mechs. and M. Sci.
Vol. 17, pp. 69-73.

BAUMGARTNER P. and STIMPSON P. (1979): Development of a tiltable base friction frame for kinematic studies of caving at various depths.
Int. Jl. of Rock Mechs. and M. Sci.
Vol. 16, pp. 265-67.

BELL F.G. (1975): Site investigations in area of mining subsidence.
Newres - Butterworths, London.

BELL F.G. (1979): Foundation engineering in difficult ground.
Newres-Butterworths, London.

BIENIAWSKI Z.T. (1967): Mechanism of brittle fracture of rock.
Parts I, II, III.
Int. Jl. of Rock Mechs. and M.Sci.
Vol. 4, pp. 395-430.

BIENIAWSKI Z.T. (1967): Stability concept of brittle fracture propagation in rock.
Engineering Geology.Vol. 2(3), pp. 149-62.

BIENIAWSKI Z.T. (1968): In-situ strength and deformation characteristics of coal.
Engineering Geology. Vol. 2(5), pp. 325-40.

BIENIAWSKI Z.T. (1970): Time-dependent behaviour of fractured rock.
Rock Mechanics, Rock Mechanics and Engineering Geology.
Vol. 2, pp. 123-37.

BISHOP J.F.W. (1958): On the effect of friction on compression and indentation between flat ends.
Jl. of Mech. & Phys. of Solids, Vol. 6, pp. 132-44.

BLYTH F.G.H. (1960: A geology for engineers.

BONSALL C.J., SMITH S.F. and WHITTAKER B.N. (1982): Model studies of stability of mining tunnels.
Symp. on Strata Mechs. pp. 190-95. Newcastle.

BOWLES J.E. (1979): Physical and geotechnical properties of soils.
McGraw-Hill Book Company.

BRACE W.F. (1972): Laboratory studies of stick-slip and their application to earthquakes.
Tectonophysics. Vol.14, pp. 187-99.

BRADY B.T. (1971a): Effects of inserts on the elastic behaviour of cylindrical materials loaded between rough end plates.
Int. Jl. of Rock Mechs. and M. Sci. Vol.8.pp.357-69.

BRADY B.T. (1971b): Initiation of failure in a radially end-constrained circular cylinder of brittle rock.
Int. Jl. of Rock Mechs. and M. Sci. Vol.8.pp.371-87.

BREKKE T.L. (1965): On the measurement of the relative potential swellability of hydrothermal montmarillorite clay from joints and faults in precambrian and paleozoic rocks in Norway.
Int. Jl. of Rock Mechs. and M.Sci. Vol.2. pp.155-65.

BROCH E. (1974): The influence of water on some rock properties.
Proc. 3rd Cong. of the Int. Society for Rock Mechs., Vol.2A. pp. 33-8, Denver.

BROCH E. (1979): Changes in rock strength caused by water.
Int. Society Rock Mechs. Vol.1.pp.71-6. Montreux.

BROOK N. (1982): Small scale brittle model studies of mine roadway deformation.
Symp. on Strata Mechs. pp.184-89. Newcastle.

BROWN E.T. and TROLLOPE D.H. (1967): The failure of linear brittle materials under tensile stress.
Rock Mechanics. Vol. 5(4). pp. 229-41.

BRYAN A., BRYAN J.C. and FOUCHE (1964): Some problems of strata control in pillar workings.
Mining Engineering. Vol.123. pp. 238-66.

BUCKY P.B. (1934): The effect of approximately vertical cracks on the behaviour of horizontally lying roof strata. Trans. of the Amer. Inst. of Min. & Met. Vol.109. pp. 212-29.

BYERLEE J.D. and BRACE W.F. (1968): Stick-slip stable sliding and earthquakes effect of rock type, pressure, strain rate and stiffness. Jl. Geophys. Res. 73. pp. 6031-037.

CAREY J.R.M. (1965): Photoelastic investigations into the deformation of pillars formed by multiple excavations. M.Sc. Thesis. Univ. of Newcastle upon Tyne.

CHAPPEL A.B. (1974): Load distribution and deformational response in discontinua. Geotechnique. 24. Vol. 4. pp. 641-54.

CHAPPEL A.B. (1975a): Component characteristics of jointed rock masses. Int. Jl. of Rock Mechs. and M.Sci. Vol.2. pp.87-92.

CHAPPEL A.B. (1975b): The effects of constraints on the deformational response of slip along planar joints. Int. Jl. of Rock Mechs. and M.Sci. Vol.12. pp.265-70.

CHAPPEL A.B. (1975c): Numerical evaluation of photoelastic data from discontinuous models. Int. Jl. of Rock Mechs. and M.Sci. Vol.12. pp.353-60.

CHAPPEL A.B. (1979a): Deformational response in discontinuum. Int. Jl. of Rock Mechs. and M.Sci. Vol.16. pp.377-89.

CHAPPEL A.B. (1979b): Load distribution and redistribution in discontinua. Int. Jl. of Rock Mechs. and M.Sci. Vol.16. pp.391-99.

CHUGH A.K. (1977): Stability analysis of a jointed beam. Int. Jl. for Numerical & Analytical Methods in Geomechanics. Vol.1, pp. 323-41.

COATES D.F. (1974): Probability of pillar failure at Elliot Lake. Proc. 3rd Cong. of the Int. Soc. for Rock Mechs. Vol.3. pp. 133-43. Denver.

COKER E.G., FILON L.N.G. and JESSOP W.T. (1957): A treatise on photoelasticity. Cambridge Univ. Press. Sec. Ed.,

CONWAY J.B. (1968): Numerical methods for creep and rupture analysis. Gordon and Breach Science Publishers.

COOK N.G.W. and HOJEM J.P.M. (1966): A rigid 50-ton compression and tension testing machine. S. Afr. Mech. Eng. Vol.16. pp. 89-92.

COOLBACK P.S.B. and WIID B.L. (1965): The influence of moisture content on the compressive strength of rocks.
Proc. Rock Mech. Symp. held at Univ. Toronto. Jan. pp. 65-83.

COTTRELL A.H. (1952): The time laws of creep.
J. Mech. Phys. Solids. Vol.1. pp. 53-63.

COULSON J.H. (1970): The effects of surface roughness on the shear strength of joints in rock.
Univ. Illinois. Tech.Rep. MRD. pp. 2-70.

CRANCK J. (1975): Mathematics of diffusion.
Clarendon Press, Oxford.

CROUCH S.L. (1970): Experimental determinations of volumetric strain in failed rock.
Int. Jl. Rock Mechs. and Min. Sci. Vol.7. pp. 589-604.

CRUDEN D.M. (1971a): Creep law for rock under uniaxial compression.
Int. Jl. Rock Mechs. and Min. Sci. Vol.8. pp. 105-27.

CRUDEN D.M. (1971b): Single increment creep experiments on rock.
Int. Jl. Rock Mechs. and Min. Sci. Vol.8. pp. 127-42.

DEDAME C.D. (1979): Rheologic behaviour of heterogenous salt rocks.
Proc. 4th Int. Conf. on Rock Mechs. Vol. 1. pp. 107-13. Montreux.

DENKHAUS H.G. (1965): Strength of rock material and rock systems.
Int. Jl. Rock Mechs. and Min. Sci. Vol.2. pp. 111-26.

DIDEV I.N. and BERICHUILI N.K. (1974): Study of the effect of stratification cracks filler upon the laminated rock subsidence.
Proc. 3rd Cong. of Int. Soc. for Rock Mechs. Advances in Rock Mechanics. Vol. 2B. pp. 700-04. Denver.

DIXON J.K. (1955): The photoelastic examination of the stress distribution around mine openings.
Ph.D. Thesis. Univ. Durham.

DUNLOP P., DUNCAN J.M. and SEED H.B. (1968): Finite element analysis of slopes in soil. Contract report S-68-3. U.S. Army Engineer Waterways Experiment Station. Vicksburg. M.S.

EINSTEIN H.H., NELSON R.A., BRUHN N.R.W. and HIRSCHFELD R.L. (1969): Model studies of jointed rock behaviour.
Rock Mechanics Theory and Practise.
11th Symp. Part II. pp. 83-105.

EVANS R.H. (1936): The elasticity and plasticity of rocks and artificial stones.
Proc. Leeds Phil. and Lit. Soc. 3. Vol.3. pp.145-58.

EVANS W.H. (1941): The strength of undermined strata.
Time. Vol.50. pp. 475-500.

FARMER I.W. (1980): Face and roadway stability in underground coal mines: Geotechnical criteria.
Report to National Coal Board. Research contract 7220-AC/806.

FLETCHER R. (1971): A modified Marguardt subroutine for non-linear least squares.
AERE Report 6709.

FORREST W. (1978): The Selby Project.
Mining Engineering. Oct. pp. 237-47.

FRANKLIN J.A. and CANDRA R. (1972): The slake durability test.
Int. Jl. Rock Mechs. and Min. Sci. Vol.9. pp. 325-41.

FRIEDEL J. (1964): Dislocations. Inter. series of Monographs on solid state physics. Vol.3.
Pergamon Press.

FUMAGALLI E. (1968): Model simulation of rock mechanics problems.
'Rock Mechanics in Engineering Practice'.
Stagg and Zienkievicz (eds.).
Wiley.

FUMAGALLI E. (1973): Statistical and geomechanical models.
Springer-Verley.

FROCHT M.M. (1948): Photoelasticity I-II.
John Wiley and Sons.

GENEVOIS R. and PRESTININZI A. (1979): Time dependent behaviour of granitic rocks related to their alteration grade.
Proc. 4th Int. Conf. on Rock Mechs. Vol.1.
pp. 107-113. Montreux.

GILBERT M.S. (1981): Shafts in squeezing rock.
Ph.D. Thesis. Univ. Newcastle upon Tyne.

GLANVILLE W.H. (1974): Soil mechanics for road engineers.
Dept. of the Environment. Transport and Road Research Laboratory. 10th Impression.
London.

GLEN J.W. (1958): The mechanical properties of ice.
Advanc. Phys. 7. No. 26. pp. 254-65.

GOODMAN R.E. and BROWN C.B. (1968): Dead load stresses and instability of slopes.
Jl. Soil Mech. & Foundations. Div. ASCE. Vol.89. pp. 103-34.

GOODMAN R.E., TAYLOR R.L. and BREKKE T.L. (1968): A model for the mechanics of jointed rock.
Jl. Soil Mech. & Foundations. Div. ASCE. Vol.98. pp. 637-59.

GOODMAN R.E. (1976): Methods of geological engineering in discontinuous rocks.
West Pub. Co., New York.

GOODMAN R.E. (1977): Finite element analysis for discontinuous rocks.
Numerical methods in geotechnical engineering.
C.S. Desai and J.T. Christian (eds.).

GORDON J.E. (1976): The new science of strong material.
Penguin Books, London. 2nd Ed.

GRIEVES J.R. (1961): The physical properties of coal measures strata with particular reference to strata control and the use of gelatine models for photoelastic analysis of stress around mine roadways.
M.Sc. Thesis. Univ. Durham.

GRIGGS D. (1939): Creep of rocks.
Jl. Geol. Vol. 47. pp. 225-35.

GRIGGS D. (1940): Experimental flow of rocks under conditions favouring recrystallisation.
Bull. Geol. Soc. Am. 51. July. pp. 1001-022.

GROMKO G.J. (1974): Review of expansive soils.
Jl. ASCE. Vol.100. No. GT6. pp. 667-87.

GÜLOGLU R. (1982): Stability of tunnels in hard rock as assessed from field, numerical and physical model studies.
Ph.D. Thesis. Univ. Newcastle upon Tyne.

HANDIN J., HAGER R.V., FRIEDMAN M. and FEATHER N. (1963): Experimental deformation of sedimentary rocks under confining pressure; pore pressure tests.
Am.Ass.Petrol.Geol. Bull. Vol.47. pp. 717-55.

HAQUE M.S. (1974): Investigations of fracture patterns in the gypsum mine at Sherburn-in-Elmet.
Report to British Gypsum. Univ. Newcastle upon Tyne.

HARDY H.R. (1959): Time dependent deformation and failure of geological materials.
Col. Sch. of Mines. Quart. Vol.54. pp. 135-75.

HARDY H.R. (1966): Inelastic behaviour of geologic materials. Part 2. Canada.Dept. Mines and Technology. Survey Report FMP 66/51-P.

HAWKES I. and MELLOR M. (1970): Uniaxial testing in rock mechanics. Engineering Geology. Vol. 4(3). pp. 177-285.

HAYCOCKS C. (1962): Mechanics of the Vaussoir arch as applied to block caving.
Ph.D. Thesis. Missouri School of Mines & Metallurgy.

HEARD H.C. (1960): Transition from brittle to ductile flow in salen hafen limestone as a function of temperature, confining pressure and interstitial fluid pressure in rock deformation.
Geol. Soc. Amer. Mem. Vol.79. pp. 193-226.

HEDLEY D.G.F. (1965): Deformation and failure characteristics of rock salt and potash.
Ph.D. Thesis. Univ. Newcastle upon Tyne.

HENDRY A.W. (1966): Photoelastic analysis.
Pergamon Press, London.

HENDRY A.W. (1977): Elements of experimental stress analysis.
Pergamon Press, SI Ed. Great Britain.

HEYMAN J. (1966): The stone skeleton.
Int. Jl. Solids, Structures. Vol.2. pp. 249-79.

HEYWOOD R.B. (1952): Designing by photoelasticity.
Chapman and Hall Ltd., London.

HIRAMATSU Y. and OKA Y. (1972): A contribution to rational design of rib pillars and openings between them.
5th Int.Strata Contr.Conf.,London. Paper 21.

HOBBS D.W. (1966): Scale model studies of strata movement around mine roadways.
Int. Jl. Rock Mechs. and Min. Sci. Vol.7. pp.163-92.

HOBBS D.W. (1968): Scale model studies of strata movement around mine roadways. I.II.
Int. Jl. Rock Mechs. and Min. Sci. Vol.5. p.219.

HOBBS D.W. (1970): Scale model studies of strata movement around mine roadways. III. Ribside support.
Int. Jl. Rock Mechs. and Min. Sci. Vol.3. pp. 101-27.

HOEK E. and BROWN E.T. (1980): Underground excavations in rock.
Inst. Min. & Metal., London.

HOFFMAN H. (1964): The effect of direction of workings and rate of advance on the scale deformation of a self loaded, stratified model of a large body of ground. Proc. 4th Int. Con. on Strata Contr. & Rock Mechs. held at Columbia Univ., New York. pp. 397-411.

HOLLAND C.T. and OLSEN D.A. (1968): Interfacial friction, moisture and coal pillar strength. Trans. Amer. Inst. Mining & Metal. Vol.241. pp. 323-28.

HÖFER K.H. and KNOLL P. (1971): Investigations into the mechanism of creep deformation in Carnallitite and practical applications. Int. Jl. Rock Mechs. and Min. Sci. Vol.8. pp.61-73.

HUDSON J.A. and BROWN E.T. (1972): Studying time dependent effects in failed rock. New Horizons in Rock Mechans. 14th Symp. on Rock.Mech. Pennsylvania State Univ. pp. 25-34.

HUDSON J.A., CROUCH S.C. and FAIRHURST C. (1972): Soft, stiff and servo-controlled testing machines, a review with reference to rock failure. Engineering Geology. Vol.6. pp. 155-87.

JAEGER J.C. and COOK N.G.W. (1979): Fundamentals of Rock Mechanics. 3rd. Ed. Chapman Hall.

JAMES A.N. and LUPTON A.R.R. (1978): Gypsum and anhydrite in foundations of hydraulic structures. Geotechnique. Vol.28. No.3. pp. 249-72.

JAMES A.N. and KIRKPATRICK I.M. (1980): Design of foundations of dams containing soluble rocks and soils. Jl. Engineering Geology. Vol.13. pp. 189-98.

JOHNSON W. and MELLOR P.B. (1973): Engineering Plasticity.

JONES I.W. (1968): The problems associated with the design and development of workings in stratified deposits with special reference to gypsum. Ph.D. Thesis. Univ. Newcastle upon Tyne.

JONES B. (1970): Laboratory and underground investigations into the stability of mine workings in gypsum. Ph.D. Thesis. Univ. Newcastle upon Tyne.

KENNEDY A.J. (1963): Processes of creep and fatigue in metals. John Wiley and Sons.

KENNEDY B.A. and NIERMEYER K.E. (1970): Slope monitoring systems used in the prediction of a major slope failure at the Chuquicamata Mine, Chile.
Proc. Symp. Planning Open Pit Mines.
Johannesburg. pp. 215-25.

KING M.S. (1973): Creep in model pillars of Saskatchewan Potash.
Int. Jl. Rock Mechs. and Min. Sci. Vol.10. pp.363-71.

KOIDO H., HOSHINO K., ENDO G. and KITAOKA M. (1979): Effect of geological compaction on the deformation of sedimentary rocks.
Proc. 4th Int. Conf. Rock Mechs. Vol.1. pp.211-15.
Montreux.

KRANZ R.L. (1979): Crack growth and development during creep of barre granite.
Int. Jl. Rock Mechs. and Min. Sci. Vol.16. pp. 23-35.

KULHAWY F.H. (1974): Finite element modelling criteria for underground openings in rock.
Int. Jl. Rock Mechs. and Min. Sci. Vol.11. pp. 465-72.

KUSKE A. and ROBERTSON G. (1964): Photoelastic stress analysis.
John Wiley and Sons, England.

LAJTAI E.Z. and LAJTAI V.N. (1975): The collapse of cavities.
Int. Jl. Rock Mechs. and Min. Sci. Vol.12. pp. 81-6.

LAMA R.D. (1970): In-situ and laboratory strength of coal.
12th Symp. on Rock Mech.
Rolla. Missouri. Vol.14. pp. 266-300.

LAMA R.D. (1972): The mechanics of jointed rock.
Proc. Symp. on Rock Mech.
Dhanbad. India. pp. 60-85.

LANCASTER P.R. and MITCHELL D. (1980): Advanced solid mechanics.
The Macmillan Press Ltd.

LANGHAAR H.L. (1951): Dimensional analysis and theory of models.
Wiley, New York.

LAWRENCE D. (1973): Scale model studies of strata movement around mine roadways. III. effects of horizontal and vertical pressure.
Int. Jl. Rock Mechs. and Min. Sci. Vol.10. pp. 173-82.

LECOMTE P. (1965): Creep in rock salt.
Journal of Geology. Vol.73. pp. 469-84.

LEE J.A.N. and COATES R.C. (1957): The use of gypsum plaster as a model material.
Civil Eng. & Public Works Review. Vol.52. November. pp. 1261-263.

LEE J.F. (1969): Thermodynamics. 2nd Ed.

LISK R.D. (1975): The wet and dry strength of 'A' bed gypsum. Kirkby Thore, Cumbria.
M.Sc. Thesis. Univ. Newcastle upon Tyne.

LITTLEJOHN G.S. (1975): Surface stability in areas underlain by old coal workings.
Ground Engineering. March (Reprinted from Ground Eng.)

LITTLEJOHN G.S. (1979): Consolidation of old coal workings.
Ground Engineering May (Reprinted from Ground Eng.)

LIU S.T. and NANCOLLAS G.H. (1971): The kinetics of dissolution of calcium sulphate dihydrate.
J. Inorg.Nuel.Chem. Vol.33. pp. 2311-316.

LOMENICK T.F. and BRADSHAW R.L. (1969): Deformation of rock salt in openings mined for the disposal of radioactive wastes.
Rock Mechanics. Vol.1. pp. 5-30.

LOMNITZ D. (1956): Creep measurements in igneous rocks.
Jl. of Geology. No. 64. pp. 473-79.

LUTTON R.J. (1971): A mechanism for progressive rock mass failure as revealed by loess slumps.
Int. Jl. Rock Mechs. and Min. Sci. Vol.8. pp. 143-51.

McDOWELL E.L., McKEE K.E. and SEVIN E. (1956): Discussion of arching action theory of masonry walls.
Jl. Am. Soc. Civ. Eng. Vol.82. No. ST2.pp.1067-27; 1067-40.

MADSEN F.T. (1979): Determination of the swelling pressures of clay stones and marl stones using mineralogical data.
Proc. 4th Int. Conf. Rock Mechs. pp.237-45. Montreux.

MAIR R.J. (1980): The use of physical models in design.
Design parameters in Geotechnical Engineering.
British Geotechnical Society, London. Vol.4.

MEIKLE P.G. and HOLLAND C.T. (1965): The effects of friction on the strength of model coal pillars.
Trans. Amer. Inst. Min. and Metal. December.

MICHAELS A.S. (1952): Altering soil-water relationship by chemical means.
The role of water in soils.
Proc. Conf. Soil Stab. Massachusetts.

MICHELSON A.A. (1917): The laws of elastica-viscous flow.
Jl. of Geology. Vol.25. No.5. pp. 405-10.

MICHELSON A.A. (1920): The laws of elastica-viscous flow.
Jl. of Geology. Vol.28. No.1. pp.18-20.

MIELENZ and KING (1955): Physical-chemical properties and engineering performance of clays.
Clay. Tech.Bull. Vol.169. pp. 196-254.

MIRZA U.A. (1978): Investigations into the design criteria for underground openings in rock which exhibit rheological behaviour.
Ph.D. Thesis. Univ. Newcastle upon Tyne.

MISRA A.K. and MURELL S.A.F. (1961-1962): Time dependent-strain or creep in rocks and in similar non-metallik materials.
Trans. Amer. Inst. Min. and Metal. Vol.71.pp.355-78.

MOHR F. (1954): Research in rock pressure. A most important function of the mining industry.
Bergbov. Vol.8. pp. 131-35.

MOHR F. (1956): Rock pressure and support. Mine and Quarry Engineering.
June pp. 227-30.

MOSS A.S.E. (1973): Model roadway studies for a deep potash mine.
M.Sc. Thesis. Univ. Newcastle upon Tyne.

MOTT N.F.A. (1953): A theory of work hardening in metals. Part II
Phil. Mag. Vol.44. pp. 742-65.

MOTTAHED P. (1974): The correlation between critical design criteria using data from field and laboratory investigations in gypsum mining.
Ph.D. Thesis. Univ. Newcastle upon Tyne.

MOTTAHED P. and SZEKI A. (1982): The collapse of room and pillar workings in a shaley gypsum mine due to dynamic loading.
Symp. on Strata Mechs. pp. 260-64. Newcastle.

MULLIN J.W. (1982): Crystallisation. 2nd Ed.
Butterworth, London.

MUNDAY J.G.L., MOHAMED A.E. and KHIR R.K. (1977): A criteria for predicting the long term compressive strength of rock.
Conf. on Rock Engg. pp. 127-135.

MURREL S.A.F. (1963): A criterion for brittle fracture of rocks and concrete under triaxial stress and the effect of pore pressure on the criterion.
Proc. 5th Rock Mech.Symp. Univ. of Minnesota. Fairhurst C. (ed.). pp. 563-577.
Pergamon, Oxford.

NADAI A. (1963): Theory of flow and fracture of solids.
McGraw-Hill, I and II. Monographs.

NAIR O.B. and VOD J.E. (1964): Determination of the principal stresses in single pillars using an iterative method.
Proc. 6th Rock Mech. Symp. pp. 391-406.

NELSON R.A. (1968): Modelling of jointed rock mass.
Massachusett Inst. Techn. Dept. Civil Eng. R6870. C8565.

OBERT L. and DUVALL W.I. (1967): Rock mechanics and the design of structures in rocks.
Wiley, New York.

ORCHARD R.J. (1956-57): Surface effects of mining.
The main factors.
TIME. Vol.116. pp. 941-55.

ORCHARD R.J. (1969): The control of ground movements in undersea working.
TIME. Vol.101. pp. 259-72.

PAFEC MANUALS (1978): Pafec Ltd.,
Pafec House, Nottingham.

PANEK L.A. (1952): Centrifugal testing apparatus for mine-structure stress analysis.
Report of Investigation 4883. U.S. Dept. of the Interior.
Bureau of Mines.

PANEK L.A. (1980): Estimating mine pillar strength from compression tests.
Trans. Amer. Inst. Mining, Metal. and Petrol.Eng.
Vol.268. pp. 1749-760.

PAUL B. and GANGAL M. (1967): Initial and subsequent fracture curves for biaxial compression of brittle materials.
Proc. 8th Symp. Rock Mechs. Univ. Minnesota.
Fairhurst (ed.)

PENG S. (1970): Stresses within elastic circular cylinders loaded uniaxially and triaxially.
Int. Jl. Rock Mechs. and Min. Sci. Vol.8. pp.399-432.

PENG S. (1973): Time dependent aspects of rock behaviour as measured by a servo-controlled hydraulic testing machine.
Int. Jl. Rock Mechs. and Min. Sci. Vol.10. pp.235-46.

POMEROY C.D. (1978): Creep of engineering materials. A journal of strain analysis.
Monograph published by Mechanical Eng. Pub. Ltd.

POTTS E.L.J. (1964): The in-situ measurements of stress based on deformation measurements.
Int. Conf. on state of stress in the earth's crust.
Santa Monica.

PRESTON K. (1980): The influence of water on the strength characteristics of gypsiferous rocks.
M.Sc. Thesis. Univ. Newcastle upon Tyne.

PRICE N.J. (1960): The compressive strength of coal measure rocks.
Colliery Engineer. Vol.37. pp. 283-92.

PRICE D.G., WALKIN A.B. and KNILL J.L. (1969): Foundations of multi-story blocks on the coal measures with special reference to old mine workings.
Quarterly Jl. of Engg. Geology. No. 1.pp.271-322.

PRICE A.M. (1979): The effect of confining pressure on the post-yield deformation characteristics of rocks.
Ph.D. Thesis.Univ. Newcastle upon Tyne.

RANKILOR P.R. (1970): An approach to the simulation of mining subsidence phenomena in an elastic layered model.
Quarterly Jl. of Engg. Geology. Vol.3. pp. 55-63.

RANKILOR P.K. (1971): The construction of a photoelastic model simulating mining subsidence phenomena.
Int. Jl. Rock Mechs. and Min. Sci. Vol.8. pp. 433-45.

ROBERTSON E.C. (1960): Creep of Solenhafen limestone under moderate hydrostatic pressure.
Geol.Soc. Am. Mem. No. 79. pp.227-44.

ROBINSON L.H.J.R. (1959): Effect of pore and confining pressure on the failure process in sedimentary rocks.
Col. Sch.Mines Quarter. Vol.54. pp. 177-99.

ROSENBLAD J.L. (1968): Development of a rock like model material.
Proc. 10th Symp. on Rock Mech.
Austin. Texas. Basic and Applied Rock Mechanics.

RUMMEL F. and FAIRHURST C. (1970): Determination of the post-failure behaviour of brittle rock using a servo-controlled testing machine.
Rock Mechanics. Vol.2. pp. 189-204.

RUSSEL G.A. (1935): Crustal growth and solution under local stress.
Am. Mineralogist. Vol.20. pp. 733-37.

RUTTER E.H. (1972a): The influence of interstitial water on the rheological behaviour of calcite rocks.
Tectarophysics. Vol.14. pp. 13-133.

RUTTER E.H. (1972b): On the creep testing of rocks at constant stress and constant force.
Int. Jl. Rock Mechs. and Min. Sci. Vol.9. pp.191-95.

SAITO M. and UGZAWA H. (1965): Failure of soil due to creep.
Proc. 5th Soil.Mech.Found.Eng. Conf. pp. 315-18.

SAITO M. (1965): Forecasting the time of the occurrence of a slope failure.
Proc. 6th Int. Conf. Soil Mech. and Found. Eng.
Vol.2. pp. 537-41.

SAITO M. (1969): Forecasting time of slope failure by tertiary creep.
7th Int. Conf. Soil Mech. Found Eng. Conf. Mexico
pp. 677-83.

SALOMON M.D.G. (1969): Recent developments in the design of board and pillar layouts in South African Coal Mines.
Proc. 9th Commonwealth Mining Metall.Congress.
Vol.1. pp. 13-31.

SALOMON M.D.G. and MUNRO A.H. (1967): A study of the strength of coal pillars.
Jl. South Afr. Inst. Min. & Met. No. 68. pp.55-67.

SANGHA C.M. and DHIR R.K. (1972): The influence of time on the strength, deformation and fracture properties of lower elevation sandstone.
Int. Jl. Rock Mechs. and Min. Sci. Vol.9. pp.343-54.

SAUCIER K. (1967): Development of a material for modelling rock.
U.S. Army Waterways Exprt.Station. Vicksburg. Miss.
Misc. paper. Vol. 6. p.934.

SCHEIDEGGER A.E. (1970): On the rheology of rock creep. Vol.2.
pp. 138-45.

SCHOLZ C.H. (1968a): Mechanism of creep in brittle rock.
J. Geophys. Res. Vol.73. p.10.

SCHOLZ C.H. (1968b): Micrafracturing and the inelastic deformation of rock in compression.
J. Geophys. Res. Vol.73. pp. 1417-432.

SCHOLZ C.H. (1972): Static fatigue of quartz.
J. Geophys. Res. Vol.77. pp. 11.

SERDENGECTI S., BOOZER G. and HILLER K.H. (1962): Effects of pure fluids on the deformation behaviour of rocks subjected to triaxial compression.
Proc. 5th Symp. on Rock Mech. Univ. Minnesota.
pp. 579-625.

SEYMOUR C.A.(1968): An investigation into the properties of linear arches.
B.Sc. (Hons.) Thesis. Univ. Newcastle upon Tyne.

SHOVA E.D. and MASE G.E. (1966): Effect of confining pressure on polycrystalline rock behaviour analysed by rheological theory. Part I.
Proc. 1st Cong. Int. Soc. Rock Mechs. Lisbon,pp.733-41.

SINGH D.P. (1975): A study of creep of rocks.
Int. Jl. Rock Mechs. and Min. Sci. Vol.12. pp.271-76.

SINGH T.N. (1978): Extraction of a thick coal seam in India field and model investigations.
Proc. 11th Commonwealth Mining Metall.Congr. Hong Kong.

SINGH R.D. (1979): Some investigatons into the surface movement due to underground mining by bord and pillar method.
Proc. 4th Int. Conf. Rock Mechs. Montreux.pp.731-37.

SMETHURST B.K. (1975): Laboratory investigations into the criteria of failure of a type of flat arch.
M.Sc. Thesis. Univ. Newcastle upon Tyne.

SMITH J.D. (1963): The condition of stress surrounding a simulated mine opening.
Proc. Rock Mech. Symp. held at Queen's Univ. Canada.
Dec. pp. 27-53.

SMITH G.N. (1971): Introduction to matrix and finite element methods in Civil Engineering.
Applied Science Publishers.

SOWERS G.F. and KENNEDY C.M. (1967): High volume change clays of the south eastern coastal plain.
Proc. 3rd Pan-Am Conf. on Soil Mech. & Found.Eng.
Caracas. Vol.II pp.99-121.

STARFIELD A.M. and McCLAIN N.C. (1973): Project salt vault, a case study in rock mechanics.
Int. Jl. Rock Mechs. and Min. Sci. Vol.10. pp.641-57.

STEPHANSON O. (1971): The stability of single openings in horizontally bedded rock.
Engineering Geology. Vol.5. pp.5-71.

STERLING R.L. and NELSON C.R. (1978): Experimental investigation of the ultimate strength of laterally constrained rock beams.
Experimental Mechanics.
Vol. 18. pp. 261-68.

STEVIC M. and JASAREVIC I. (1977): Analysis of underground room geometry on the basis of secondary stresses for different ratios of horizontal and vertical pressure Tusang Salt Mine.
Rock Mechanics. Vol.9. pp. 145-72.

STIMPSON B. (1970): Modelling materials for engineering rock mechanics.
Int. Jl. Rock Mechs. and Min.Sci. Vol.7. pp.77-121.

SUSHKOV V.V. (1965): Technical Thermodynamics.
Gordan and Breach Science.

SZEKI A. (1978): Report to British Gypsum.

TERZAHGI K.V. (1945): Stress conditions for the failure of saturated concrete and rock.
Proc. Emer.Soc.Test.Mater.Vol.45. pp.777-801.

TINCELIN E., FINE J. and VOILLE G. (1972): A comparison between forecasts calculated by the finite element method and the actual behaviour of mine workings using the small pillar method.
5th Int.Conf. on Strata Control. London. Paper 21.

TINCELIN E. and SINOV P. (1960): Collapse of areas worked by small pillar method practical conclusions and attempt to formulute laws for the phenomenon observed.
Int. Conf. on Strata Control. Paris. Paper G6.

TROLLOPE D.H. (1965-1966): The stability of trapezoidal openings in rock masses.
Rock Mechanics. Vol. 3-4. pp. 232-41.

VARO L. and PASSARIS E.K.S. (1977): The role of water in the creep properties of halite.
Conf. Rock Engg. pp.84-100. Newcastle upon Tyne.

WANG C., BOSHKOV S.H. and WANE M.T. (1967): The application of barodynamic photostress techniques to the study of the behaviour of rock beams loaded by their own weights.
9th Symp. on Rock Mech. Colorado Sch. of Mines. Vol.10. pp. 203-21.

WARDELL K. and EYNON P.A. (1968): Structural concept of strata control and mine design.
Mining Engineering. No. 95. August. pp. 633-56.

WARDELL K. and WOOD J.C. (1966): Ground instability problems arising from the presence of old shallow mine workings.
Proc. Midland. S.M. & Fed.Engg.Soc.Vol.7. pp.5-30.

WATSON S.H. (1979): The characteristics of linear arch structure and its application.
Ph.D. Thesis. Univ. Newcastle upon Tyne.

WAWERSIK W.R. (1972): Time dependent rock behaviour in uniaxial compression.
14th Symp. Rock Mechs. Pensylvania State Univ. New Horizons in Rock Mechanics. pp. 85-105.

WEYL P.K. (1958): Solution kinetics of calcite.
Jl. Geol. Vol.66. pp. 163-76.

WIGLEY T.M.L. (1973): Chemical evolution of the system calcite-gypsum-water
Cong. J.Earth Sci. Vol.10. pp. 306-15.

WIID B.L. (1970): The influence of moisture on the pre-rupture fracturing of two rock types.
Proc. 2nd Int. Symp. Rock Mech. Belgrade. Vol.2. pp. 239-45.

WILLIAMS F.T. and ELIZZI M.A. (1977): Creep properties of Sherburn Gypsum under triaxial loading.
Conf. on Rock Engg. Newcastle. pp. 71-83.

WILSON S.D. (1952): Effect of compaction on soil properties.
Proc. Conf. on Soil Stabilis. Massachusetts.

WILSON J.W. (1965): An investigation into ground movement associated with bord and pillar mining in South Africa.
M.Sc. Thesis. Univ. Newcastle upon Tyne.

WINKLER E.M. and WILHELM E.J. (1970): Salt burst by hydration pressures in architectural stone in urban atmosphere.
Geol. Soc. Amer. Bull. Vol.81. pp. 567-72.

WOODRUFF S.D. (1966): Methods of working coal and metal mines.
Vol.1.
Pergamon Press.

WRIGHT F.D. and AHMED B. (1968): Load-deformation characteristics of model mine pillars before and after crushing.
10th Symp. on Rock Mech. held at Univ. Texas, Austin. Vol.71.

WRIGHT F.D. and MIRZA M.B. (1963): Stress distribution around a vertical crack in a mine roof beam.
Trans. Amer. Inst. Mining & Metall. Vol.226.
pp. 174-79.

WRIGHT F.D. (1972): Arching action in cracked roof beams.
5th Int. Conf. Strata Control. London. Paper 29.

YENGE L. (1981): Analysis of bulk flow of materials under gravity caving process.
Colorado Sch of Mines. July Vol.76. No.3.

ZIENKIEWICZ O.C. and CHENG Y.K. (1967): The finite element method in structural and continuum mechanics.
McGraw-Hill, London.

ZIENKIEWICZ O.C., VALLIADAN S. and KING I.P. (1968): Stress analysis of rock as a non-tension material.
Geotechnique. Vol.18. pp. 55-66.

ZIENKIEWICZ O.C., VALLIADAN S. and KING I.P. (1969): Elasto-plastic solutions of engineering problems; Initial stress/ finite element approach.
Int. Jl. for Num. Methods in Eng. Vol.1. No.1.
pp. 75-100.

* * *

APPENDICES

A RIG B STRAIN-TIME CR. DATA

CURVE TYPE	INDEX OF DETERMINATION	VALUE OF A	VALUE OF B
Y=A+(B*X)	0.8819985	0.3335899	0.0001501
Y=A*EXP(B*X)	0.8722028	0.3336374	0.0004366
Y=A*(X^B)	0.9663770	0.3171776	0.0214196
Y=A+(B/X)	0.4139892	0.3478605	-0.0315934
Y=1/(A+B*X)	0.8619808	2.9968913	-0.0012704
Y=X/(A+B*X)	0.4399256	0.2788522	2.8754964
Y=A+B*LOG(X)	0.9607465	0.3164502	0.0073017

B PROCESSED CR. DATA

CURVE TYPE	INDEX OF DETERMINATION	VALUE OF A	VALUE OF B
Y=A+(B*X)	0.8721936	0.0689759	0.0004366
Y=A*EXP(B*X)	0.7128459	0.0685630	0.0047361
Y=A*(X^B)	0.9981147	0.0352100	0.2612324
Y=A+(B/X)	0.4268426	0.1105866	-0.0938335
Y=1/(A+B*X)	0.4974596	15.0705959	-0.0567544
Y=X/(A+B*X)	0.8319111	22.5503282	9.1159536
Y=A+B*LOG(X)	0.9663833	0.0183824	0.0214197

A RIG A STRAIN-TIME CR. DATA

CURVE TYPE	INDEX OF DETERMINATION	VALUE OF A	VALUE OF B
Y=A+(B*X)	0.9585706	0.3656479	0.0014395
Y=A*EXP(B*X)	0.9135406	0.3710435	0.0030615
Y=A*(X^B)	0.9357094	0.2634522	0.1482545
Y=A+(B/X)	0.2923370	0.5051755	-0.2534009
Y=1/(A+B*X)	0.8509740	2.6746467	-0.0066530
Y=X/(A+B*X)	0.4346779	1.5157283	2.0122355
Y=A+B*LOG(X)	0.8851590	0.2191650	0.0661852

B PROCESSED CR. DATA

CURVE TYPE	INDEX OF DETERMINATION	VALUE OF A	VALUE OF B
Y=A+(B*X)	0.9135426	0.3441649	0.0030615
Y=A*EXP(B*X)	0.7486361	0.3464496	0.0059013
Y=A*(X^B)	0.9994201	0.1515046	0.3262470
Y=A+(B/X)	0.3584797	0.6446054	-0.6113448
Y=1/(A+B*X)	0.5054649	3.0120522	-0.0130918
Y=X/(A+B*X)	0.8087304	5.2787800	1.5917138
Y=A+B*LOG(X)	0.9357085	0.0017178	0.1482546

A RIG 10 STRAIN-TIME CR. DATA

CURVE TYPE	INDEX OF DETERMINATION	VALUE OF A	VALUE OF B
Y=A+(B*X)	0.8846537	0.5873156	0.0003925
Y=A*EXP(B*X)	0.8334612	0.5885543	0.0005570
Y=A*(X^B)	0.9381191	0.3883573	0.1154874
Y=A+(B/X)	0.1679233	0.7440932	-0.3630400
Y=1/(A+B*X)	0.7746657	1.6999061	-0.0008049
Y=X/(A+B*X)	0.2302934	0.9316373	1.3733144
Y=A+B*LOG(X)	0.9070768	0.3143941	0.0776724

B PROCESSED CR. DATA

CURVE TYPE	INDEX OF DETERMINATION	VALUE OF A	VALUE OF B
Y=A+(B*X)	0.8334607	0.2728761	0.0005570
Y=A*EXP(B*X)	0.6439675	0.2567581	0.0014405
Y=A*(X^B)	0.9861063	0.0669801	0.3483567
Y=A+(B/X)	0.1973171	0.4970027	-0.5753642
Y=1/(A+B*X)	0.4098760	4.3560042	-0.0045929
Y=X/(A+B*X)	0.5582127	11.3790223	2.3269467
Y=A+B*LOG(X)	0.9381199	-0.1428680	0.1154876

A RIG 12 STRAIN-TIME CR. DATA

CURVE TYPE	INDEX OF DETERMINATION	VALUE OF A	VALUE OF B
Y=A+(B*X)	0.8380269	0.4552634	0.0002171
Y=A*EXP(B*X)	0.7977362	0.4552532	0.0004251
Y=A*(X^B)	0.9573906	0.3383145	0.0823036
Y=A+(B/X)	0.1995214	0.5305402	-0.1985254
Y=1/(A+B*X)	0.7536993	2.1983216	-0.0008398
Y=X/(A+B*X)	0.2545189	0.9146277	1.9030702
Y=A+B*LOG(X)	0.9387386	0.3111550	0.0406069

B PROCESSED CR. DATA

CURVE TYPE	INDEX OF DETERMINATION	VALUE OF A	VALUE OF B
Y=A+(B*X)	0.7977412	0.2600666	0.0004251
Y=A*EXP(B*X)	0.6383653	0.2507166	0.0012546
Y=A*(X^B)	0.9893609	0.0876736	0.2760348
Y=A+(B/X)	0.2236508	0.4084371	-0.4237279
Y=1/(A+B*X)	0.4412752	4.2458866	-0.0042025
Y=X/(A+B*X)	0.5547219	8.8308955	2.6509165
Y=A+B*LOG(X)	0.9573923	-0.0368115	0.0823037

A

RIG 11 STRAIN-TIME CR. DATA

CURVE TYPE	INDEX OF DETERMINATION	VALUE OF A	VALUE OF B
Y=A+(B*X)	0.8360146	0.2931440	0.0000734
Y=A*EXP(B*X)	0.8230927	0.2931697	0.0002427
Y=A*(X^B)	0.9757652	0.2727000	0.0235548
Y=A+(B/X)	0.3279387	0.3055151	-0.0344917
Y=1/(A+B*X)	0.8096492	3.4107654	-0.0008032
Y=X/(A+B*X)	0.3552517	0.3994549	3.2745567
Y=A+B*LOG(X)	0.9701934	0.2716149	0.0070449

B

PROCESSED CR. DATA

CURVE TYPE	INDEX OF DETERMINATION	VALUE OF A	VALUE OF B
Y=A+(B*X)	0.7727432	0.1005130	0.0001549
Y=A*EXP(B*X)	0.6037329	0.0984724	0.0012741
Y=A*(X^B)	0.9859112	0.0418983	0.2288373
Y=A+(B/X)	0.2944074	0.1404562	-0.1361523
Y=1/(A+B*X)	0.3848603	10.5824572	-0.0115312
Y=X/(A+B*X)	0.7302535	22.6238204	7.2911849
Y=A+B*LOG(X)	0.9821493	0.0131746	0.0245394

A

RIG 6 STRAIN-TIME CR. DATA

CURVE TYPE	INDEX OF DETERMINATION	VALUE OF A	VALUE OF B
Y=A+(B*X)	0.9692676	0.5157006	0.0007930
Y=A*EXP(B*X)	0.9490869	0.5190703	0.0013139
Y=A*(X^B)	0.8840670	0.4119950	0.0883415
Y=A+(B/X)	0.2020816	0.6237451	-0.1963441
Y=1/(A+B*X)	0.9236702	1.9174106	-0.0021923
Y=X/(A+B*X)	0.2546271	0.6241548	1.6157373
Y=A+B*LOG(X)	0.8542491	0.3828215	0.0518635

B

PROCESSED CR. DATA

CURVE TYPE	INDEX OF DETERMINATION	VALUE OF A	VALUE OF B
Y=A+(B*X)	0.9490872	0.1016502	0.0013139
Y=A*EXP(B*X)	0.7134743	0.1053245	0.0064417
Y=A*(X^B)	0.9988191	0.0218329	0.5309576
Y=A+(B/X)	0.2271512	0.2815148	-0.3485489
Y=1/(A+B*X)	0.3135326	11.3357714	-0.0469770
Y=X/(A+B*X)	0.8975480	43.0985060	3.7826333
Y=A+B*LOG(X)	0.8840682	-0.1293778	0.0883414

RIG 12 STRAIN TIME CR. DATA

A

CURVE TYPE	INDEX OF DETERMINATION	VALUE OF A	VALUE OF B
Y=A+(B*X)	0.9626964	0.2888888	0.0007970
Y=A*EXP(B*X)	0.9234100	0.2928097	0.0021803
Y=A*(X^B)	0.9254066	0.2059678	0.1368303
Y=A+(B/X)	0.2464421	0.3881199	-0.1883654
Y=1/(A+B*X)	0.8684960	3.3890602	-0.0060721
Y=X/(A+B*X)	0.3665047	1.8426853	2.6166752
Y=A+B*LOG(X)	0.8768957	0.1705670	0.0476830

B PROCESSED CR.DATA

CURVE TYPE	INDEX OF DETERMINATION	VALUE OF A	VALUE OF B
Y=A+(B*X)	0.9234124	0.2669834	0.0021803
Y=A*EXP(B*X)	0.7202833	0.2685614	0.0051366
Y=A*(X^B)	0.9988909	0.0912737	0.3792179
Y=A+(B/X)	0.3016907	0.5411351	-0.5821716
Y=1/(A+B*X)	0.4033681	4.0315344	-0.0149501
Y=X/(A+B*X)	0.8562003	10.1750355	1.9039395
Y=A+B*LOG(X)	0.9254044	-0.0848187	0.1368302

```
      C  MEHMET  DOKTAN....
      C
      C     THIS PROGRAM HAS BEEN WRITEN FOR THE CALCULATION
      C OF THE INITIAL VALUE OF STRAIN IN THE CREEP FORMULAE
      C 1.FOR EACH SET OF THREE POINTS WHICH SATISFIES THE
      C EQUATION LOG(T1/T2)=LOG(T2/T3) OR T1/T2=T2/T3 ,THE
      C INITIAL VALUE EO IS CALCULATED AND THEN AVERAGED TO
      C OBTAIN A REPRESENTETIVE VALUE.
      C
            INTEGER M,N,G,J,K,P,R,T(100)
            REAL SUM,MEAN,AC,BC,CC,DC,EC,FC,E(100),AE1,AE2,AE3
      C
      C
      C
            AE1=0.0
            AE2=0.0
            AE3=0.0
            SUM=0.0
            MEAN=0.0
            R=35.
            M=0
            WRITE(6,80000)
      80000 FORMAT(//,1H ,'THE RESULTS',//,'RIG NO: A')
      C
            DO 100 N=1,R
            READ(5,10000) T(N),E(N)
      10000 FORMAT(I3,F7.4)
        100 CONTINUE
      C
            DO 200 G=1,R
            DO 200 J=1,R
            DO 200 K=1,R
            IF(T(J).LE.T(G)) GO TO 300
            IF(T(K).LE.T(J)) GO TO 300
            IF(T(J)**2.NE.T(G)*T(K)) GO TO 300
      C
      C
            M=M+1
            WRITE(6,70000)
      70000 FORMAT(//,1H ,'TIME',3X,'STRAIN',3X,'NUMB.',//)
      C
            WRITE(6,20000) T(G),E(G),G
      20000 FORMAT(1H ,I3,3X,F7.4,3X,I3)
      C
            WRITE(6,30000) T(J),E(J),J
      30000 FORMAT(1H ,I3,3X,F7.4,3X,I3)
      C
            WRITE(6,40000) T(K),E(K),K
      40000 FORMAT(1H ,I3,3X,F7.4,3X,I3)
      C
      C
      C
            AE1=E(G)
            AE2=E(J)
            AE3=E(K)
            AC=(ALOG(AE1))*(ALOG(AE3))
            BC=(ALOG(AE2))**2
            CC=(ALOG(AE1))+(ALOG(AE3))
            DC=2.*(ALOG(AE2))
            EC=(AC-BC)/(CC-DC)
            FC=(2.7183)**EC
      C
            WRITE(6,90000) AC,BC,CC,DC,EC
      90000 FORMAT(//,1H ,'AC=',F7.4,X,'BC=',F7.4,X,'CC=',F7.4,X,
           *'DC=',F7.4,X,'EC=',F7.4)
      C
```

```
      WRITE(6,50000) FC,M
50000 FORMAT(//,1H ,'INITIAL VALUE=',F7.4,3X,'NUMB.OF.SET=',I3)
C
      SUM=SUM+FC
  300 P=P+1
  200 CONTINUE
  500 MEAN=SUM/FLOAT(M)
C
      WRITE(6,60000) SUM,M,MEAN
60000 FORMAT(//,1H ,'SUM=',F7.4,2X,'TOT.NUMB.=',I3,2X,'AVERAGE=',F7.4)
C
      STOP
      END
```

d of file

APPENDIX 5.3

Dividing equation (5.9) by (5.10), M is eliminated,

$$\frac{\varepsilon_1}{\varepsilon_2} = \frac{M \, Ln \left(\frac{T_F - T_o}{T_F - T_1}\right)}{M \, Ln \left(\frac{T_F - T_o}{T_F - T_2}\right)}$$ and removing the

logarithm from both sides, one obtains:

$$\frac{T_F - T_o}{T_F - T_2}^{\varepsilon_1} = \frac{T_F - T_o}{T_F - T_1}^{\varepsilon_2}$$ and substituting

$$\frac{(T_F - T_o)^{\varepsilon_1}}{(T_F - T_o)^{\varepsilon_2}} = \frac{(T_F - T_2)^{\varepsilon_1}}{(T_F - T_1)^{\varepsilon_2}}$$ which becomes:

$$(T_F - T_o)^{\varepsilon_1 - \varepsilon_2} = \frac{(T_F - T_2)^{\varepsilon_1}}{(T_F - T_1)^{\varepsilon_2}} \Rightarrow T_F - T_o = \sqrt[\varepsilon_1 - \varepsilon_2]{\frac{(T_F - T_2)^{\varepsilon_1}}{(T_F - T_1)^{\varepsilon_2}}}$$

thus:

$$T_o = T_F - \sqrt[\varepsilon_1 - \varepsilon_2]{\frac{(T_F - T_2)^{\varepsilon_1}}{(T_F - T_1)^{\varepsilon_2}}}$$

Using equation (5.8) and inserting T_o and T_F into this equation we obtain:

$$M = \frac{\varepsilon_1}{Ln(T_F - T_o) - Ln(T_F - T_1)}$$

* * *

APPENDIX 5.4

```
      C MEHMET DOKTAN
      C      THIS PROGRAM HAS BEEN WRITEN FOR THE CALCULATION OF THE
      C FAILURE TIME FROM STRAIN-TIME CREEP DATA ACCORDING TO THE
      C FORMULAE 2 DEVELOPED BY THE AUTHOR.ALL POSSIBLE SETS OF THREE
      C POINTS WHICH SATISFIES,2*E2=E3+E1 ARE FOUND AND TF IS CALCULATED
      C FROM CORRESPONDING T VALUES.
      C
      C
            INTEGER M,N,G,J,K,P,R,T(100)
            REAL SUM,MEAN,AC,BC,CC,DC,E(100),AT1,AT2,AT3
      C
      C
            AT1=0.0
            AT2=0.0
            AT3=0.0
            SUM=0.0
            MEAN=0.0
            R=55
            M=0
      C
            WRITE(6,80000)
      80000 FORMAT(//,1H ,'THE RESULTS',//,'RIG NO: 6')
      C
            DO 100 N=1,R
            READ(5,10000) T(N),E(N)
      10000 FORMAT(I3,F7.4)
        100 CONTINUE
      C
            DO 200 G=1,R
            DO 200 J=1,R
            DO 200 K=1,R
            IF(E(J).LE.E(G)) GO TO 300
            IF(E(K).LE.E(J)) GO TO 300
            IF(2.0*E(J).NE.(E(K)+E(G))) GO TO 300
      C
            M=M+1
            WRITE(6,70000)
      70000 FORMAT(//,1H ,'TIME',3X,'STRAIN',3X,'NUM:',//)
      C
            WRITE(6,20000) T(G),E(G),G
            WRITE(6,20000) T(J),E(J),J
            WRITE(6,20000) T(K),E(K),K
      20000 FORMAT(1H ,I3,3X,F7.4,3X,I3)
      C
      C
            AT1=FLOAT(T(G))
            AT2=FLOAT(T(J))
            AT3=FLOAT(T(K))
            AC=(AT2-AT1)**2
            BC=2.0*AT2-AT1-AT3
            CC=AC/BC
            DC=AT1+CC
      C
      C
            WRITE(6,50000) DC,M
      50000 FORMAT(//,1H ,'FAILURE TIME=',F8.3,3X,'NO:',I3)
      C
            SUM=SUM+DC
        300 P=P+1
        200 CONTINUE
        500 MEAN=SUM/FLOAT(M)
      C
            WRITE(6,60000) SUM,M,MEAN
      60000 FORMAT(//,1H ,'SUM=',F10.3,2X,'TOT.NUMB.=',I3,2X,
           *'AVERAGE=',F8.3)
      C
            STOP
            END
```

APPENDIX 7.1

Radial stresses produced by a concentrated load at the vertex of a wedge is given (Frocth 1944):

$$\sigma_r = -\frac{2p}{r_t}\left(\frac{\text{Cos}\beta \times \text{Cos}\theta}{2\alpha + \text{Sin } 2\alpha} + \frac{\text{Sin}\beta \times \text{Sin}\theta}{2\alpha - \text{Sin } 2\alpha}\right)$$

and $\sigma_\theta = 0$ and $\tau_{r\theta} = 0$ along the neutral axis, where

p = load

r = diameter of fringes

t = thickness of the material

β = angle between the axis of symmetry and direction of load

α = angle between axis of symmetry and the direction of load

σ_r = radial stresses.

The relationship between polar and cartezian coordinates is given by:

$$\sigma_x = \sigma_r \text{Sin}^2$$

$$\sigma_y = \sigma_1 \text{Cos}^2$$

$$\tau_{xy} = \sigma_r \text{Sin}\theta \text{ Cos}\theta \text{ and also}$$

$$\sigma_{1,3} = \frac{\sigma_x + \sigma_y}{2} \mp \sqrt{\left(\frac{\sigma_x - \sigma_y}{2}\right)^2 + \tau_{xy}^2}$$

The line defined by the equation below where σ_r vanishes for the angle θ_o is given

$$\tan \Theta_o = - \frac{1}{\tan\beta} \left(\frac{2\alpha - \mathrm{Sin}2\alpha}{2\alpha + \mathrm{Sin}2\alpha}\right)$$

Also the centres of the circular fringes lie on a line defined by an angle of γ from the axis of symmetry and it is perpendicular to the neutral axis.

By taking $\alpha = 45^o$ and $\beta = 45^o$, i.e. the load is perpendicular to the vertical edge.

$$\tan \Theta_o = - \frac{1}{\tan(-45)} \cdot \frac{\Pi/2 - \mathrm{Sin}\Pi/2}{\Pi/2 + \mathrm{Sin}\Pi/2} \Rightarrow \Theta_o = 12^o.30'$$

is found, i.e. the neutral axis makes an angle of $57^o30'$ with the horizontal edge.

* * *

THESIS COMPOSITE NEGATIVES 90/83

Fig. No.	Neg. No.	Fig.No.	Neg No.
7:11	63/82	3:11	111/81
7:26	83/79	3:12	111/81
7:27	83/79	6:18	9/83
3:1	90/81	6:19	9/83
2:5	101/81	6:20	9/83
4:4	106/81	3:8	106/81
6:2	9/83	3:9	111/81
7:4	63/82	3:2	101/81
4:8	106/81	3:3	90/81
4:9	106/81	3:18	111/81
4:14	62/82	3:19	111/81
7:12	80/82	3:6	101/81
7:13	80/82	3:7	101/81
7:14	80/82	3:20	111/81
7:15	80/82	3:21	1111/81
7:16	80/82		
7:17	80/82		
7:18	72/82		
9:19	72/82		
3:4	101/81		
3:5	101/81		
7:36	117/82		
7:37	130/82		
3:13	111/81		
3:14	111/81		
3:15	111/81		
3:16	111/81		
3:10	111/81		

* * *